UNIVERSIDAD DE CANTABRIA

PROGRAMA DE DOCTORADO
EN INGENIERÍA INDUSTRIAL

Realizada por:
Carmela Oria Alonso
Dirigida por:
Alfredo Ortiz Fernández
Diego Ferreño Blanco

PhD THESIS

An experimental, analytical and numerical study of the mechanical failure of the cellulosic insulation of continuously transposed conductors in power transformers under the influence of short circuits and thermal ageing

TESIS DOCTORAL
Estudio experimental, analítico y numérico del fallo mecánico del aislamiento celulósico de conductores continuamente transpuestos en transformadores de potencia bajo la influencia de cortocircuitos y envejecimiento térmico

Escuela de Doctorado de la Universidad de Cantabria
Santander 2020

UC
UNIVERSIDAD DE CANTABRIA

UNIVERSIDAD DE CANTABRIA

PROGRAMA DE DOCTORADO EN INGENIERÍA INDUSTRIAL:
TECNOLOGÍAS DE DISEÑO Y PRODUCCIÓN INDUSTRIAL

PhD THESIS

An experimental, analytical and numerical study of the mechanical failure of the cellulosic insulation of continuously transposed conductors in power transformers under the influence of short circuits and thermal ageing

TESIS DOCTORAL

Estudio experimental, analítico y numérico del fallo mecánico del aislamiento celulósico de conductores continuamente transpuestos en transformadores de potencia bajo la influencia de cortocircuitos y envejecimiento térmico

Realizada por:
Carmela Oria Alonso
Dirigida por:
Alfredo Ortiz Fernández y Diego Ferreño Blanco

Escuela de Doctorado de la Universidad de Cantabria

Santander 2020

ACKNOWLEDGEMENTS

Mi primer agradecimiento es para los codirectores de esta tesis: Alfredo Ortiz y Diego Ferreño. Alfredo, siempre te agradeceré que me dieses la oportunidad de descubrir mi vocación por la docencia universitaria, que guiases mis primeros pasos cuando todo me resultaba nuevo, y que siempre me hayas tendido una mano en las situaciones complicadas. Diego, gracias por ser un trabajador incansable y un comunicador tan eficaz, por estar siempre pendiente de todos los detalles y por todos tus consejos guiando esta tesis doctoral. Gracias a Inma e Isidro, por aportar toda vuestra experiencia y buen hacer en la parte experimental de esta tesis, por vuestro asesoramiento y todas vuestras horas de trabajo en el laboratorio.

To my colleagues from the Division of Applied Mechanics at Uppsala University. It was an inspiring experience to share those months with you during the summers of 2018 and 2019. I learned a great deal from you, and you always made me feel welcome in the group. Special thanks to Kristofer Gamstedt and Reza Afshar, for your kindness and for all your advice regarding my research.

To David John Cahill, thank you for your great work in the revision of the English language in all the documents that led to this thesis and the related publications.

A mis amigos, por todo el tiempo que no hemos podido compartir durante estos años y por siempre animarme a continuar y darme confianza en que lograría conseguirlo. A mis alumnos, por ayudarme a mejorar cada día y recordarme que el fin al que aspiro es más grande que todos los obstáculos que aparecen por el camino. A mi familia, especialmente, a mis abuelos Antonio y Carmen, por ser un referente de vida, y a mi madre, por estar siempre ahí para todo.

Por último, gracias a Dave, por acompañarme en estos años que ha durado el camino hasta aquí, por haber compartido la felicidad cuando las cosas han salido bien, y por haber sido siempre un apoyo en los malos momentos y ante la incertidumbre.

Santander, julio de 2020

CONTENTS

ACKNOWLEDGEMENTS ..... - 2 -
CONTENTS ..... - 3 -
I. INTRODUCTION ..... - 7 -
II. STATE OF THE ART ..... - 11 -
1. Transformer fundamentals and their importance in the electrical system ..... - 11 -
1.1. Introduction ..... - 11 -
1.1.1. Theoretical fundamentals ..... - 11 -
1.1.2. Transformer electrical characteristics ..... - 14 -
1.1.3. Basic structures and component parts of power transformers ..... - 16 -
1.2. The relevance of power transformers asset management ..... - 20 -
1.2.1. Methods for the estimation of the condition of power transformers ..... - 21 -
1.2.2. Planification of the maintenance of power transformers ..... - 22 -
2. Materials used in power transformers ..... - 23 -
2.1. Introduction ..... - 23 -
2.2. Winding conductors ..... - 24 -
2.2.1. Copper materials ..... - 24 -
2.2.2. Different types of conductors ..... - 26 -
2.3. Insulating materials ..... - 28 -
2.3.1. Relevant electric parameters of dielectric materials ..... - 28 -
2.3.2. Cellulosic insulation: paper and board ..... - 31 -
2.3.3. Insulating liquids ..... - 33 -
3. The ageing of insulating materials and its quantification ..... - 36 -
3.1. Factors producing ageing of dielectric materials ..... - 36 -
3.1.1. Effects of moisture, temperature, oxygen and impurities ..... - 36 -
3.1.2. Effects of voltage and frequency ..... - 40 -
3.2. Parameters used for the assessment of the ageing of oil–paper transformer insulation ..... - 42 -
3.2.1. Degree of polymerisation (DP) ..... - 43 -
3.2.2. Tensile strength and its direct and indirect estimation ..... - 45 -
3.2.3. Furanic compounds ..... - 46 -
3.2.4. Methanol and ethanol ..... - 48 -

3.3. Insulating liquids, their ageing and their interaction with the cellulosic insulation - 49 -

4. Short-circuit currents, electromagnetic forces and mechanical stresses in power transformers - 54 -

4.1. Short-circuit phenomena in transformers - 54 -

4.1.1. Introduction - 54 -

4.1.2. Typical cases of short circuits - 56 -

4.2. Electromagnetic forces in transformers - 57 -

4.2.1. Determination of the electromagnetic forces in power transformers - 57 -

4.2.2. Radial and axial electromagnetic forces in core-type transformers - 59 -

4.2.3. Dynamic behaviour of core-type transformers under short-circuit conditions - 63 -

4.2.4. Mechanical stresses and failure modes caused by short-circuit electromagnetic forces - 64 -

5. Mechanical models applicable to the cellulosic insulation of power transformers - 72 -

5.1. Introduction - 72 -

5.2. Constitutive relations for paper and board - 74 -

5.2.1. Elastic constitutive relations - 74 -

5.2.2. Viscous constitutive relations - 76 -

5.2.3. Plastic constitutive relations and residual stresses - 80 -

5.3. Mechanical models for cellulosic materials - 81 -

5.3.1. Mechanical models for thin paper - 81 -

5.3.2. Influence of the thin paper insulation on the mechanical strength of power transformer windings - 86 -

5.3.3. Mechanical models for board materials - 87 -

5.4. Modes of failure of paper - 103 -

5.4.1. Introduction - 103 -

5.4.2. Analysis of uniaxial tensile fracture of paper - 104 -

5.4.3. Different criteria for the failure of paper materials - 107 -

III. MATERIALS, METHODS AND RESULTS - 111 -

1. Experimental work - 111 -

1.1. Accelerated thermal ageing of the paper insulation - 111 -

1.1.1. Measurement of moisture content of the dielectric paper with the Karl-Fischer titration method - 111 -

1.1.2. Considered ageing states and thermal ageing process - 113 -

1.2. Characterisation of the paper insulation samples - 114 -

1.2.1. Degree of Polymerisation (DP) of the dielectric paper - 116 -

1.2.2. Tensile mechanical properties of the dielectric paper in the MD and in the CD - 119 -

1.2.3. Edgewise mechanical compressive properties of the dielectric paper ..... - 130 -

1.2.4. In-plane shear mechanical properties of the dielectric paper ..... - 142 -

1.3. Three-point bending tests of the insulated CTCs ..... - 147 -

1.3.1. Results of bending tests with a deflection of 20 mm ..... - 149 -

1.3.2. Results of bending tests with a deflection of 10 mm ..... - 153 -

1.3.3. Results of bending tests with a deflection of 5 mm ..... - 156 -

1.3.4. Conclusions after the bending tests ..... - 159 -

1.4. Analysis of the microstructure and fracture patterns in the paper insulation with Scanning Electron Microscope ..... - 162 -

1.4.1. Functioning principle of the Scanning Electron Microscope ..... - 162 -

1.4.2. Results of the analysis of the insulation samples with Scanning Electron Microscope ..... - 164 -

2. Numerical simulation ..... - 174 -

2.1. Description of the model ..... - 174 -

2.1.1. Geometry, material properties and supports ..... - 175 -

2.1.2. Mesh definition and connections ..... - 177 -

2.2. Deformation, stress and strain distributions obtained in the CTC samples through the numerical simulation ..... - 186 -

3. Failure criteria for the paper insulation of the CTC ..... - 206 -

3.1. Introduction ..... - 206 -

3.2. Maximum strain failure criterion ..... - 208 -

3.3. A Modification of the Norris failure criterion ..... - 216 -

IV. CONCLUSIONS ..... - 229 -

1. Problem statement ..... - 229 -

2. Research strategy ..... - 229 -

3. Contributions derived from the experimental research ..... - 230 -

3.1. Thermal ageing of the paper insulation ..... - 230 -

3.2. Tensile, edgewise and in-plane shear mechanical testing of the paper insulation - 230 -

3.3. Three-point bending tests over the insulated CTCs and fracture analysis - 231 -

4. Contributions derived from the FE numerical study ..... - 232 -

5. Contributions derived from the analytical study ..... - 233 -

6. Implications of this work for the estimation of the condition of power transformers in operation ..... - 233 -

BIBLIOGRAPHY ..... - 235 -

APPENDIX: SCIENTIFIC CONTRIBUTIONS ..... - 244 -

1. Publications related to this PhD thesis ..... - 244 -
2. Contributions to international conferences related to this PhD thesis ..... - 244 -
3. Research stays related to this PhD thesis ..... - 244 -
4. Research projects ..... - 244 -

APÉNDICE: RESUMEN, RESULTADOS Y DISCUSIÓN ..... - 245 -

1. Planteamiento del problema ..... - 245 -
2. Estrategia de investigación ..... - 245 -
3. Contribuciones derivadas de la investigación experimental ..... - 246 -
   - 3.1. Envejecimiento térmico del papel dieléctrico ..... - 246 -
   - 3.2. Ensayos mecánicos a tracción, compresión y cortante sobre el aislamiento celulósico ..... - 247 -
   - 3.3. Ensayos de flexión a tres puntos sobre las muestras de conductor continuamente transpuesto con aislamiento de papel y análisis de las fracturas generadas ..... - 248 -
4. Contribuciones derivadas del análisis numérico mediante elementos finitos ..... - 249 -
5. Contribuciones derivadas del estudio analítico ..... - 250 -
6. Contribuciones de este trabajo para el diagnóstico de transformadores de potencia en operación ..... - 251 -

I. INTRODUCTION

Power transformers are electromagnetic conversion devices whose purpose is to transform the alternating voltage and current values in a transmission or distribution line into another voltage and current in a different line, in order to transmit the electrical power minimising the losses, supplying electrical machines at their most suitable voltage level and ensuring the safety of the users in the electrical system. Their correct operation is essential for the reliability and quality of the electrical system.

Insulation is a vital element in any power transformer. It consists of all the materials and components used to insulate parts at different potentials from one another. The most frequently used insulating liquid is still mineral oil, although different types of ester insulating liquids have been increasingly used in recent times. Paper and board are the most common materials used as solid insulation, due to their high dielectric strength, good cooling properties and cost-efficiency. Many factors can affect the correct performance of power transformers reducing their lifespan, the deterioration of the insulation being one of the most significant ones. This is due to the high temperatures and mechanical stresses (produced, for example, by short circuits) to which the transformer is subjected. Besides, chemical reactions take place in the dielectric oil in which the paper is impregnated, producing an irreversible ageing process. As the insulation ages, both its electrical properties (such as resistivity or dielectric breakdown strength) and its mechanical properties (such as tensile strength or elongation to breakage) gradually deteriorate. According to [1], several studies consider that those mechanical and electrical properties are significantly related. For all these reasons, there is an increasing interest among manufacturers to improve the current understanding of the mechanical response and degradation processes of the cellulosic insulation which could lead to the end of life of transformers.

The remainder of this PhD thesis is organised as follows. In part *II.STATE OF THE ART*, the operating principles of a power transformer, its basic components and its relevance in the whole electrical system were reviewed (see section *1.Transformer fundamentals and their importance in the electrical system)*. The main characteristics of the most important materials used in these electrical machines were summarised in section *2.Materials used in power transformers*, with special emphasis on insulating materials (see *2.3.Insulating materials*). All the phenomena and factors which have an impact on the ageing of insulation components, as well as the different measurement methods that can be used for its quantification, were discussed in section *3.The ageing of insulating materials and its quantification*. Section *4.Short-circuit currents, electromagnetic forces and mechanical stresses in power transformers* is devoted to the different kinds of mechanical solicitations that can exist on various types of power transformers, focusing on core-type transformers. Some analytic and also approximate expressions are given for the quantification of forces and stresses, and the main mechanical failure modes observed in real transformers are reported.

There are many available studies focused on the mechanical behaviour of paper materials. Some of them were reviewed and classified in section *5.Mechanical models applicable to the cellulosic insulation of power transformers* and also in [2], but only a few of them are specific for the insulation of power transformers (such as [3]–[7]). The mechanical models for generic paper and board are frequently extremely theoretical and complex, and they rely on many ideal hypotheses, so it is difficult to apply them to the cellulosic insulation of a power transformer. Besides, a mechanical analysis specific for the insulation of transformers should take some particular features into consideration, namely, the influence

of the dielectric oil-impregnation in the mechanical response, the degradation of mechanical material properties due to ageing, an approximate realistic material geometry, and mechanical solicitations similar to those occurring in-service. The failure modes of paper and some criteria for the prediction of mechanical failure are reported in subsection *5.4.Modes of failure of paper*, where the evidence that there is a lack of suitable models specific to the insulation of a power transformer in the literature is specifically highlighted.

The purpose of the experimental part of this PhD thesis is to study the mechanical response of the insulating paper in the winding conductors in a power transformer when they are subjected to deformations (eventually produced by short circuits or other mechanical loads during operation) at different ageing levels during the whole operating life of a power transformer. The main goal is to understand the mechanisms that govern mechanical failure, and to achieve a simple, reliable and conservative criterion, capable of predicting the occurrence of that mechanical failure after different periods of operation of the electrical machine. The mechanical breakage of the cellulosic insulation is relevant by itself, but, besides, it could result in an electric failure of the power transformer. In order to obtain a mechanical failure criterion, first, the mechanical properties of the insulating paper must be determined under different ageing levels; then, the real response of an aged insulated conductor subjected to a particular deformation level should be analysed; finally, a numerical model is needed to quantify the stress or strain field produced in the conductor as a result of the imposed deformation.

Continuously Transposed Conductors (CTC) are often used in power transformers and consist of an assembly of a variable number of enamel-coated rectangular copper strands covered with several layers of insulating paper. In part *III.MATERIALS, METHODS AND RESULTS*, the mechanical response of a CTC of a core-type transformer, with disc-type cylindrical windings arranged concentrically around the core limb (provided by the company Imefy) was analysed, following the sequence represented in Figure 1.

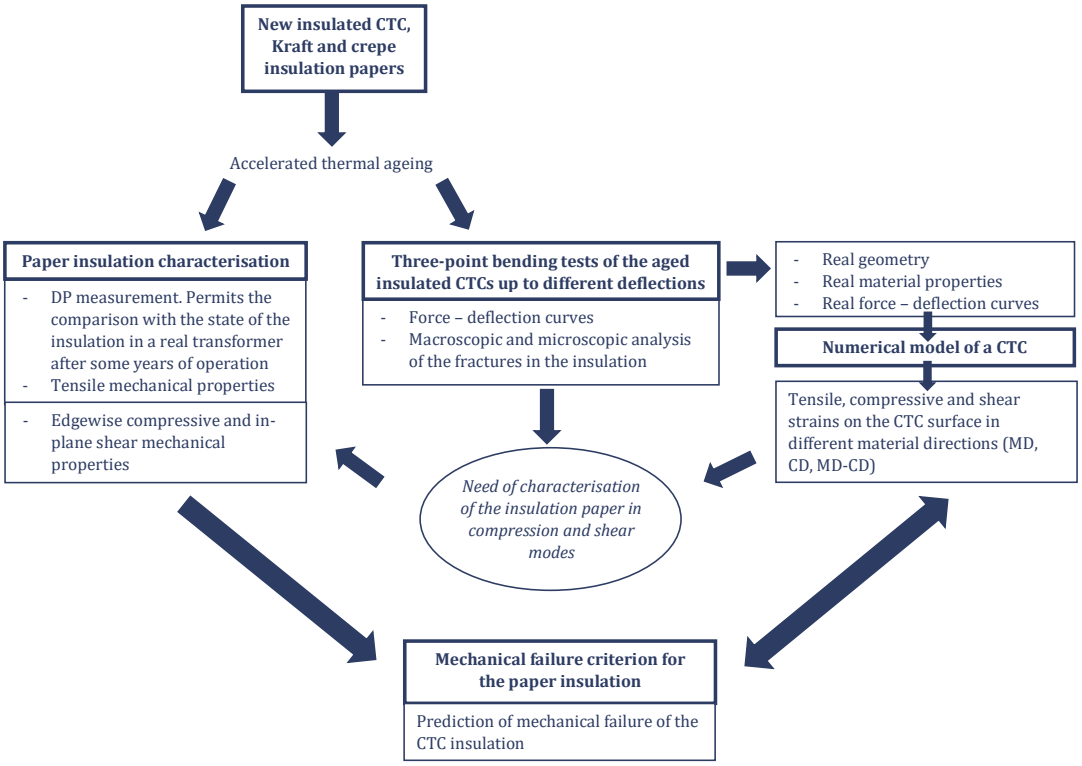

Figure 1. Sequence followed in the experimental process described in III.MATERIALS, METHODS AND RESULTS.

In the first experimental stage of this study, several samples of the analysed CTC were impregnated in naphthenic dielectric oil and subjected to different durations of accelerated thermal ageing, in order to reproduce the process that takes place after several years of operation in a power transformer (see section *1.1.Accelerated thermal ageing of the paper insulation*). The cellulosic insulation was removed from some CTC samples and characterised through the degree of polymerisation (see section *1.2.1.Degree of Polymerisation (DP) of the dielectric paper*) and tensile testing (see section *1.2.2.Tensile mechanical properties of the dielectric paper in the MD and in the CD*). Other insulated CTC samples were subjected to bending tests, in an attempt to reproduce the deformations produced by the short-circuit electromagnetic forces (see *1.3.Three-point bending tests of the insulated CTCs*). After these tests, fracture patterns in the insulation layers were analysed, both macroscopically (see section *1.3.4.Conclusions after the bending tests*) and microscopically by means of a Scanning Electron Microscope (SEM) (see section *1.4.Analysis of the microstructure and fracture patterns in the paper insulation with Scanning Electron Microscope*), and classified according to their size. These results were published in [8].

On the other hand, the mechanical behaviour of the CTC was modelled by means of a Finite Element (FE) model implemented in ANSYS AIM Static Structural, to reproduce the strain field in the copper produced by the bending test carried out in the laboratory (see *2.Numerical simulation* in *III.MATERIALS, METHODS AND RESULTS*). Due to the great intricacy of the phenomenon (complicated geometry of a real CTC, large deformations, plasticity and non-linear analysis, variable friction among components made of different materials, and with different dimensions which require a complex mesh definition, etc.), some simplifications were adopted. This model, whose main characteristics were also described in publication [8], could provide the strain field in the paper for different bending forces and deflections of the CTC, which could be related with the appearance of fractures in the paper insulation observed in the laboratory.

The second experimental stage, also described in part *III.MATERIALS, METHODS AND RESULTS*, was focused on obtaining the strength of the insulation paper under compression and shear stresses. The need for that study arose from the analysis of the fractures in the CTC samples after the bending tests, as the cracks in some areas subjected to compression were more critical than others subjected to tension, especially when the paper insulation was heavily aged. Besides, the results of the numerical simulation (see *2.2.Deformation, stress and strain distributions obtained in the CTC samples through the numerical simulation*) gave compressive and shear stresses in the paper layers which were not negligible in comparison with the tensile ones. Because of this, it was considered that interactions among tension, compression and shear should govern the mechanical failure of the paper insulation in power transformers, and the characterisation of the material was extended in sections *1.2.3.Edgewise mechanical compressive properties of the dielectric paper* and *1.2.4.In-plane shear mechanical properties of the dielectric paper*. For these last experimental analyses, the company Ahlstrom-Munksjö provided samples of insulating paper for power transformers (plain Kraft and crepe papers, very similar to the ones that compose the insulation of the studied CTC). The paper samples were subjected to the same accelerated thermal ageing process prior to their mechanical characterisation.

In the last part of the experimental work in this PhD thesis, a mechanical failure model inspired by a Hill-type failure criterion was developed, see *3.Failure criteria for the paper*

insulation of the CTC in *III.MATERIALS, METHODS AND RESULTS*. This model should consider the interactions among tension, compression and shear strains, and the maximum strains at breakage in the different modes of failure, obtained experimentally for the insulation of the CTC (plain Kraft and crepe papers) in the considered ageing states. This failure criterion made it possible to predict the first areas of the insulation of the CTC in which the cracks appeared, and the correlation between the deformation produced by a bending force acting in the radial direction of the transformer coil and the magnitude of those cracks, for a particular ageing state quantified by the DP of the paper (or by an indirect measurement related to the DP). A critical deformation level for each ageing state could be defined.

A suitable numerical model, together with a failure criterion for the cellulosic insulation, could determine the strain state of the copper CTC that will cause the appearance of cracks and final failure of the paper for each ageing state. That failure model, in combination with engineering measurements, could constitute a useful tool for the estimation of the condition of power transformers and a more accurate prediction of the end-of-life of power transformers. A better understanding of the ageing kinetics and the evolution of the mechanical and electrical properties of the solid insulation of power transformers can contribute to improve the management and planning in electrical systems from a technical and economical point of view, and even to enhance manufacturing techniques, in order to produce more reliable components.

II. STATE OF THE ART

1. Transformer fundamentals and their importance in the electrical system

1.1. Introduction

A power transformer is an electromagnetic conversion device which has two or more windings of wire wrapped around a ferromagnetic core which, through electromagnetic induction, transforms a system of alternating voltage and current into another system of voltage and current usually different, and at the same frequency, with the purpose of transmitting electrical power [9]. The primary and secondary windings are not connected electrically, but coupled magnetically, so the only connection between them is the magnetic flux present within the core. Transformers can be used to either increase or decrease the voltage, depending upon the need and application.

Figure 2. Power transformer in a substation, from https://www.flickr.com/photos/29261037@N02/28923446976/in/photostream/.

This simple and reliable device, which can link circuits with different voltages, has been decisive in enabling universal use of the alternating current system for the transmission and distribution of electrical energy [10], since it has an efficiency ranging from 95% to 99% and it operates more efficiently and with low maintenance costs as compared to rotating electrical machines and most electrical devices [11]. A transformer enables various components of power systems (such as the generators, transmission lines, the distribution networks or the loads) to be operated at their most suited voltage levels. Transformers play a key role in the interconnection of systems at different voltage levels, especially when the voltages are increased up to higher levels in some parts of the power system.

1.1.1. Theoretical fundamentals

The functioning principle of power transformers is based on magnetic circuits. In a transformer, the core is composed of ferromagnetic material with permeability μ (H/m) that is much greater than the permeability of the surrounding air, μ_0 (H/m). The core has a uniform cross-section area, A_c (m^2), and is excited by a winding composed of turns carrying a current, i (A), which produces a magnetic field in the core. The source of this magnetic field is quantified through the magnetomotive force, $\mathcal{F}$ $(A \cdot t)$, and can be obtained as the product of the number of turns of the winding, N (t), by the current flowing through it, i (A):

$$\mathcal{F} = N \cdot i \tag{1}$$

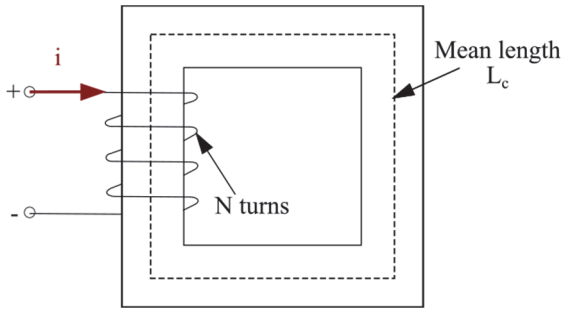

Figure 3. Magnetic circuit, based on [11].

Ampere's law states that the line integral of the magnetic field intensity, H $(A \cdot t/m)$, around a closed path is equal to the net current enclosed by that path, so the magnetomotive force for the magnetic circuit in Figure 3 is given by equation (2):

$$\mathcal{F} = \oint H \, dL \tag{2}$$

Assuming that, for the previous magnetic circuit the magnetic flux density, B (T), is uniform across the core cross-section area, the line integral of H is equal to the scalar product $H_C \cdot L_C$, where H_C is the magnitude of H along the mean flux path, whose length is L_C (m):

$$\mathcal{F} = \oint H \, dL = H_C \cdot L_C \tag{3}$$

From equations (1) and (3):

$$H_C \cdot L_C = N \cdot i = \mathcal{F} \tag{4}$$

For the ferromagnetic material of the core, relationship (5) holds between the magnetic flux density, B, and the magnetic field intensity, H:

$$B = \mu \cdot H \tag{5}$$

Where μ (H/m) is the permeability of the ferromagnetic material of the core, which can be expressed in terms of the relative permeability of the ferromagnetic material, μ_r, and the permeability of free space, $\mu_0 = 4 \cdot \pi \cdot 10^{-7}\ H/m$, as follows: $\mu = \mu_0 \cdot \mu_r$. It should be noted that the relative permeability varies with the magnetic flux density.

The magnetic flux, Φ (Wb), crossing an area is the surface integral of the magnetic flux density, B. According to field theory for the continuity of flux, all the flux that enters the surface enclosing a volume must leave that volume over some other portion of that surface, because magnetic flux lines form closed loops. If the magnetic flux outside the core of Figure 3 is neglected, then the scalar form in equation (6) is obtained:

$$\Phi = \oint B \, ds \rightarrow \Phi_C = B_C \cdot A_C \rightarrow B_C = \frac{\Phi_C}{A_C} \tag{6}$$

Where:

Φ_C (Wb): Magnetic flux in the core.

B_C $\left(\frac{Wb}{m^2} or\ T\right)$: Magnetic flux density in the core.

A_C (m^2): Cross-section area of the core.

Assuming that the permeability, μ, of the ferromagnetic material is constant, and since the magnetic flux density is uniform, equations (7) and (8) can be derived:

$$B_C = \mu \cdot H_C \rightarrow H_C = \frac{B_C}{\mu} \tag{7}$$

$$\mathcal{F} = H_C \cdot L_C \rightarrow \mathcal{F} = \frac{B_C}{\mu} \cdot L_C \rightarrow \mathcal{F} = \frac{\frac{\Phi_C}{A_C}}{\mu} \cdot L_C \rightarrow \mathcal{F} = \Phi_C \cdot \frac{L_C}{\mu \cdot A_C} \tag{8}$$

A transformer works on the principle of electromagnetic induction, according to which a voltage is induced in a coil if it links a changing flux. In a power transformer in no-load condition, that is, when no current flows in the secondary circuit of the transformer, if an alternate sinusoidal voltage, $v_1(t)$ of frequency f (Hz), is applied to the primary winding, N_1, a magnetic flux, $\Phi_m(t)$, will flow through the core of the transformer and will link the primary and secondary windings. In this situation, the current in the primary winding will be the magnetising current $\overline{I_1} = \overline{I_m}$. The generated magnetic flux will pass through the secondary winding, N_2, and will produce, according to Faraday's Law, a voltage $v_2(t)$. Expressions (9)-(13) are obtained if it is assumed that hysteresis is not present in the *B-H* curve of the core material, which is also assumed as linear, and if eddy current losses are neglected.

If the magnetic field in the core varies with time, an induced voltage is produced at the terminals, which is calculated by Faraday's law. The instantaneous value of induced voltage in the winding 1 due to the mutual flux is:

$$e_1 = N_1 \cdot \frac{d\Phi_m}{dt} \tag{9}$$

Since the instantaneous value of the applied voltage, v_1, is sinusoidally varying, the flux, Φ_m, must also be sinusoidal in nature varying with frequency f:

$$\Phi_m = \Phi_{mp} \sin \omega t \tag{10}$$

$$e_1 = N_1 \omega \Phi_{mp} \cos \omega t \tag{11}$$

Where:

Φ_{mp}: Peak value of mutual flux Φ_m

The voltage induced in winding 2 due to the mutual flux, Φ_m, is given by equation (12):

$$e_2 = N_2 \cdot \frac{d\Phi_m}{dt} \tag{12}$$

The ratio of two induced voltages can be derived from equations (11) and (12):

$$\frac{e_1}{e_2} = \frac{N_1}{N_2} = a \tag{13}$$

Where a is known as ratio of transformation.

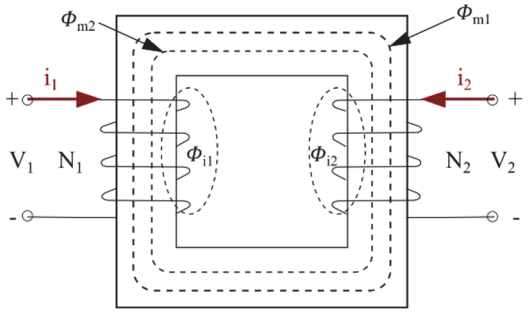

Figure 4. Transformer in which both windings are loaded, from [11].

In the case where the secondary winding is loaded, Figure 4, a secondary current is set up as per Lenz's law such that the secondary magnetomotive force (mmf), i_2N_2, opposes the mutual flux, Φ_m, tending to reduce it. In an ideal transformer, it will be verified that $e_1 = v_1$, because for a constant value of the applied voltage, induced voltage and corresponding mutual flux must remain constant. This can happen only if the primary draws more current ($i_1{}'$) for neutralising the demagnetising effect of secondary ampere-turns. In r.m.s. notations:

$$I_1' \cdot N_1 = I_2 \cdot N_2 \tag{14}$$

Thus, the total primary current is a vector sum of the no-load current (this means magnetising component, $\overline{I_m}$, since core losses are neglected) and the load current, $\overline{I_1'}$:

$$\overline{I_1} = \overline{I_1'} + \overline{I_m} \tag{15}$$

For an infinite permeability magnetic material, magnetising current is zero, so:

$$I_1' \cdot N_1 = I_2 \cdot N_2 \;\; \rightarrow I_1 \cdot N_1 = I_2 \cdot N_2 \tag{16}$$

And this means that, for an ideal transformer (zero winding resistance, no leakage flux, linear $B - H$ curve with an infinite permeability, no core losses), when its no-load current is neglected, primary ampere-turns are equal to secondary ampere-turns.

$$\frac{E_1}{E_2} = \frac{V_1}{V_2} = \frac{N_1}{N_2} = \frac{I_1}{I_2} \;\rightarrow\; V_1 \cdot I_1 = V_2 \cdot I_2 \tag{17}$$

If the secondary winding in Figure 4 is loaded with an impedance Z_2:

$$Z_2 = \frac{V_2}{I_2} \tag{18}$$

Substituting (17) into (18):

$$Z_2 = \frac{(N_2/N_1)V_1}{(N_1/N_2)I_1} \tag{19}$$

Hence, the impedance referred to the primary winding 1 is given by equation (20), and it can be summarised from these equations that, for an ideal transformer, voltages are transformed in ratio of turns, whereas the volt-amperes and power remain unchanged.

$$Z_2' = \frac{V_1}{I_1} = \left(\frac{N_1}{N_2}\right)^2 \cdot Z_2 \qquad Z_2' = a^2 \cdot Z_2 \tag{20}$$

1.1.2. Transformer electrical characteristics

- ***Rated power (kVA):*** The rated power is the output that can be delivered at rated secondary voltage and rated frequency without exceeding the specified temperature rise limitations. The rated power of a three-phase transformer is given by equation (21), and the rated power of the single-phase transformer by equation (22):

$$S_n = \sqrt{3} \cdot U_n \cdot I_n \tag{21}$$

$$S_n = U_n \cdot I_n \tag{22}$$

  Where:
  U_n: Rated voltage.
  I_n: Rated current.

- ***Temperature rise (°C):*** The temperature rise is the difference between the temperature of the part under consideration (usually the average winding temperature rise or the hottest-spot

winding rise) and the ambient temperature. The top-oil temperature rise is the arithmetic difference between the top-oil temperature (the temperature of the top layer of the insulating liquid in a transformer) and the ambient temperature [12]. For oil-immersed transformers, the average temperature rise of the winding is typically 65°C above the ambient temperature and the top-oil temperature rise is 60°C above the ambient temperature [13] .

- ***Impedance voltage (%):*** The impedance voltage or short-circuit impedance is the percentage of the rated primary voltage that has to be applied at the transformer primary winding, when the secondary winding is short-circuited, in order to have the rated current at the primary winding. This parameter is very important because it represents the transformer's impedance, permits the calculation of the voltage regulation due to transformer loading, the distribution of loads in the case of parallel operation of transformers, and the short-circuit current. The higher the short-circuit impedance, the higher the voltage regulation. The lower the short-circuit impedance, the higher the short-circuit current.

- ***No-load losses (W):*** No-load losses include core-loss, dielectric loss, conductor-loss in the winding due to excitation current, and conductor-loss due to circulating current in parallel windings [12]. Core-loss is the power dissipated in the magnetic core subjected to a time-varying magnetising force, and it includes hysteresis and eddy current losses of the core.

- ***Load losses (W):*** Load losses are generated by the carrying of a specified current. They include $I^2 \cdot R$ loss in the current-carrying parts (windings, leads, busbars, bushings), eddy losses in conductors due to eddy currents, and stray loss induced by leakage flux in the tank, core clamps, or other parts [12].

- ***Rated voltages (V):*** The rated primary voltage (input voltage) is the voltage at which the transformer is designed to operate. It determines the basic insulation level (BIL), according to international standards [9], which is a basic transformer characteristic, since it indicates its ability to withstand overvoltages, and the calculation of the winding insulation is based on it. The rated secondary voltage (output voltage) is the voltage at the terminals of the secondary winding at no-load, under rated primary voltage and rated frequency.

- ***No-load current (A):*** The no-load current or excitation current represents the current that the transformer absorbs, when the rated voltage is applied to the primary winding and the secondary winding is open-circuited. The no-load current is expressed as a percentage of the value of the rated primary current.

- ***Overloading:*** The rated overload of a transformer depends on its previous load or the corresponding oil temperature at the beginning of the overloading [11]. The permissible duration and the respective levels of the acceptable overload of commercial oil-immersed distribution transformers are shown in Table 1. The determination of the permissible duration of the overload must be carried out very carefully, since there is a danger that the winding temperature exceeds the critical temperature of 105°C, without this being indicated by the oil temperature, because its time constant is much larger than the time constant for the winding temperature.

- ***Short-circuit current (A):*** The short-circuit current is composed of the asymmetrical and the symmetrical short-circuit current. The first stresses the transformer mechanically, while the second stresses the transformer thermally. In some cases, steady state short-circuit current reaches as high as 10 to 15 times the rated current. Since the mechanical forces are

proportional to the square of the current, they increase to as much as 100 to 225 times the mechanical forces at rated current. Such large mechanical forces can cause appreciable damage to the transformer. Hence, the transformer windings must be designed and constructed to withstand the mechanical forces during short circuits.

Table 1. Permissible duration of overload and level of acceptable overload, from [11].

Previous continuous load (% of rated voltage)	Oil temperature (°C)	Level of overload (% of rated power)				
		10%	20%	30%	40%	50%
		Permissible duration of overload (min)				
50	55	180	90	60	30	15
75	68	120	60	30	15	8
90	78	60	30	15	8	4

1.1.3. Basic structures and component parts of power transformers

The basic structure of a transformer can be either core- or shell-type. In a core-type transformer the windings surround the core, resulting in cylindrically shaped coils, where the low voltage coil is inside the high voltage one. In a shell-type transformer, the core surrounds the windings, so the shape is a flat oval one, called pancakes coils, with the high and low voltage windings assembled on top of each other, generally in more than one layer [14]. Both structures are common, and the use of one or the other sometimes depends on the particular application.

In core-type transformers, Figure 5, the core limb has a circular cross-section, in order to maximise the area carrying the flux, and the coils are also cylindrical and arranged concentrically around their own limb [14]. All these components are generally in vertical position, and each terminal is connected to one coil or several coils in series. The core is made of two or more parallel limbs magnetically coupled to each other in their upper and lower ends by yokes [14].

Figure 5. Core-type transformers, from [14].

In shell-type transformers, Figure 6 and Figure 7, the core structure consists of an assembly of steel laminations laid down horizontally which contour the windings [14]. In three-phase transformers with this structure, there are two configurations which are the most common and depend on the size of the transformer: four-limb or seven-limb configurations.

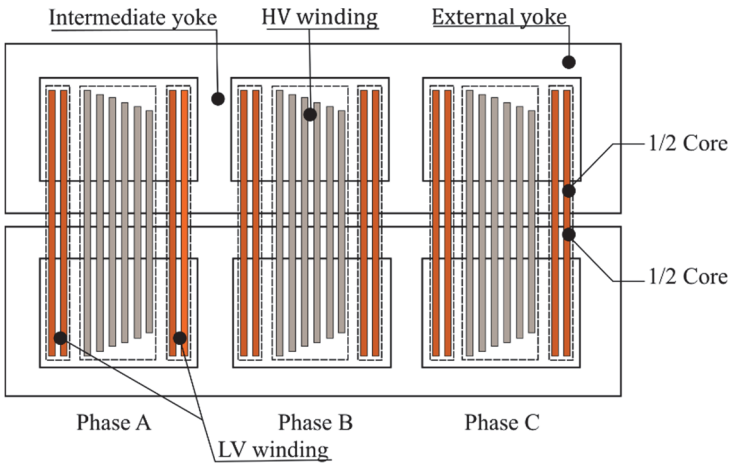

Figure 6. Basic structure of a three-phase shell-type transformer, based on [14].

Figure 7. Images of shell-type transformer windings, from [14].

The main component parts of a power transformer are the following:

- ***Core:*** The laminated iron core is one of the active parts of the transformer, which carries the magnetic flux linked with the transformer windings. It is the size and magnetic stress of this core that determine the capacity and no-load characteristics of the transformer (no-load current, no-load loss, inrush current and magnetic noise of the transformer).

  There are two typical structures for single-phase transformers: one wound limb and two return limbs on each side of the wound, or two wound limbs connected together by an upper and lower yoke, with or without extra return limbs, Figure 8 (a-e). The fluxes in each one of the wound limbs have the same magnitude at any moment [14]. In single-phase transformers with two or more wound limbs, the winding directions alternate to generate flux in opposite directions for adjacent limbs. In three-phase transformers, Figure 8 (f-i), the windings for each of the phases are located on their own limb, so there are three wound limbs magnetically coupled through a upper and lower yoke [14]. Sometimes, there are some particular constructive designs that respond to limits in transportation or manufacturing of very big units.

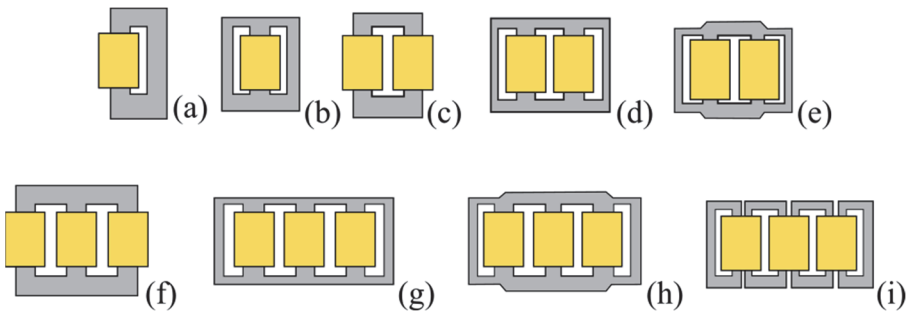

Figure 8. Types of core and coil structures of single-phase (a-e) and three-phase (f-i) transformers, based on [14].

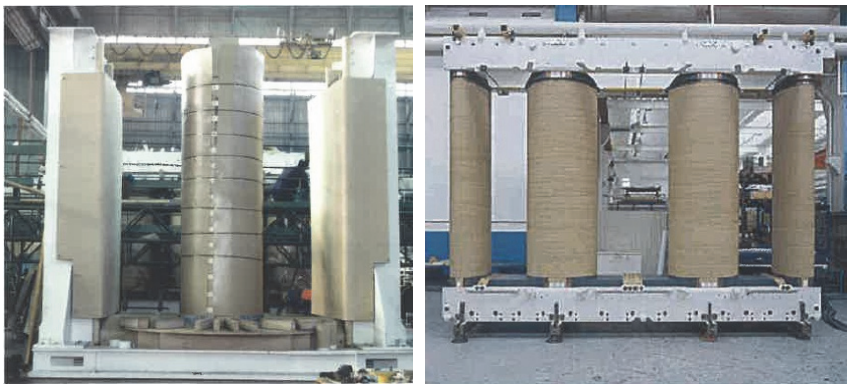

Figure 9. Cores of single-phase transformers, from [14].

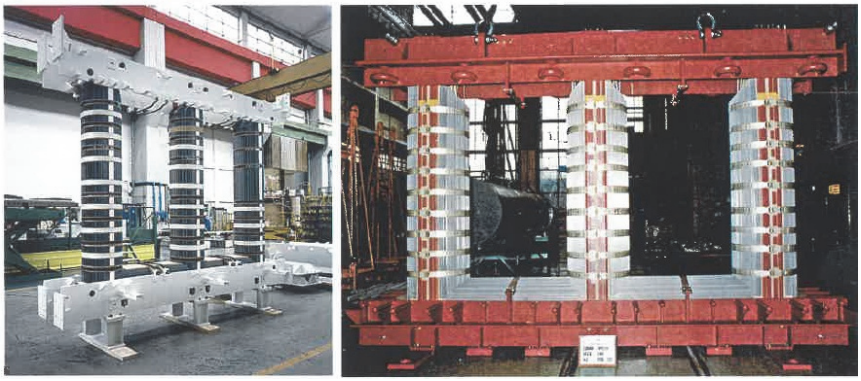

Figure 10. Three-limb magnetic cores of three-phase transformers with different clamping arrangements of the windings, from [14].

- ***Windings:*** The rectangular paper-covered copper conductor is the most commonly used conductor for the windings of medium and large power transformers, although aluminium is increasingly being used in smaller transformers. Despite the fact that copper and aluminium are far from having the best mechanical properties with regard to short-circuit forces, no efforts are made to use wire materials of higher mechanical strength because it would be insufficiently ductile. To enhance the short-circuit withstand capability, the work hardened copper is commonly used instead of soft annealed copper, particularly for higher rating transformers. More information about the employed materials can be found in *2.Materials used in power transformers,* section *2.2.Winding conductors*.

The windings of a transformer are strictly related to its impedance characteristics: the short-circuit impedance, the short-circuit current and the short-circuit forces. The voltage of the transformer is determined by the number of turns of the windings and by the flux, while the cross-sectional area is proportional to the current of the transformer. The winding is expected to meet several requirements in short-circuit strength and withstanding voltage and temperature rises.

In core-type transformers, the windings are arranged concentrically as shells around the core limb [14]. The insulation between two components at different potential (such as two windings or between one winding and the core) is frequently made of paper materials by means of a series of paper sheets placed perpendicularly to the electric field gradient, Figure 11. The windings most typically used in core-type transformers have the following structures: helical-type, disc-type, layer-type, windings for voltage regulation purposes, etc. During the manufacturing of helical and disc-type windings, the alignment of sections and turns respectively at the outside of the insulation is maintained by means of axial sticks and radial spacers attached to them [14].

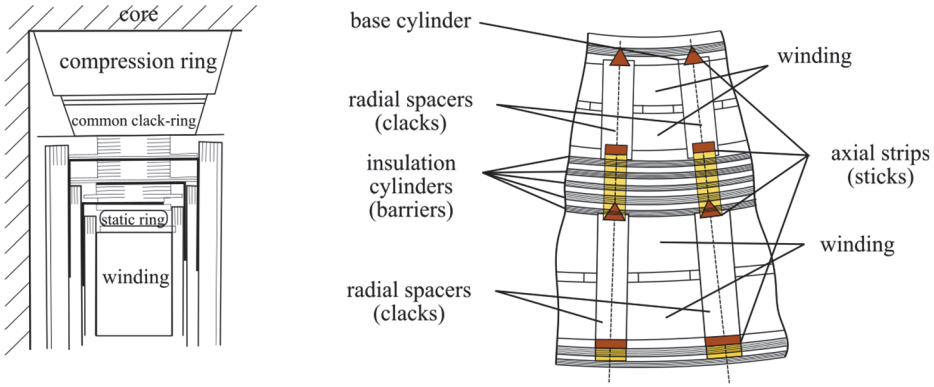

Figure 11. Basic insulation structures of core-type transformers, based on [14].

Helical-type windings, Figure 12 and Figure 13, are mainly used for low-voltage applications, and they are characterised by a relatively low number of electrical turns and many strands (or multiple CTC cables) in parallel. The turns are arranged in a spiral form along the axial extension of the coil, covering its entire radial width, and pressboard spacers are inserted between axial conductors at regular intervals to generate horizontal cooling ducts [14]. In order to equally distribute the current between parallel strands, they all must induce the same voltage, so a transposition of the strands is needed, exchanging their relative position, so that they encircle the same amount of flux. Since transpositions make the manufacturing more complex, the use of a single CTC cable covering the full radial width of the coil is generally preferable, according to [14].

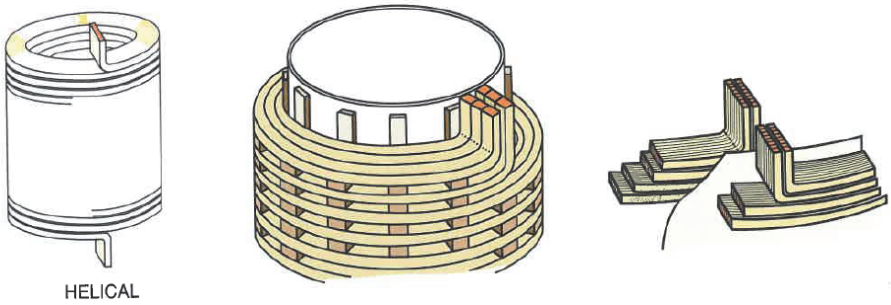

Figure 12. Representation of helical-type windings. Simple helical winding; double helical winding; double-shell configuration, from [14].

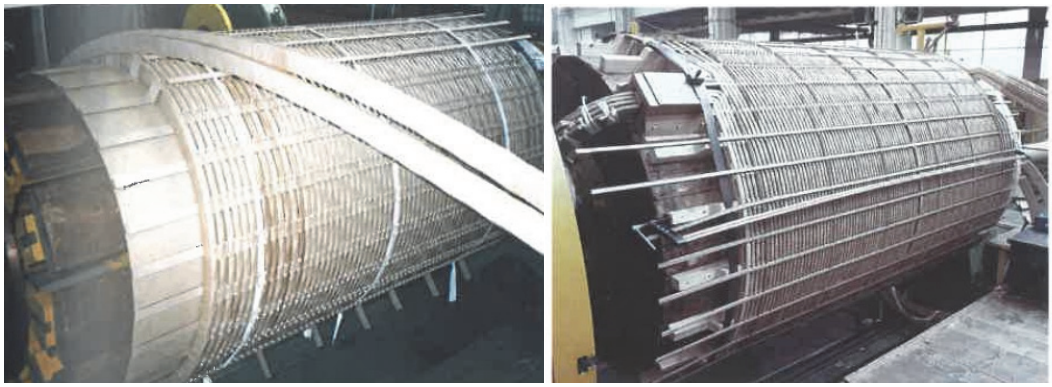

Figure 13. Manufacture of helical-type windings, from [14].

Disc-type windings, Figure 14, are commonly used in windings with a relatively large number of turns and comparatively low current, requiring a low number of strands or CTCs in parallel. This type of winding is built up from an assembly of discs connected in series, and in each of them the turns are wound in radial direction like a spiral and each electrical turn covers just a part of the total radial width of the coil. These windings have radial ducts between turns

or between disc sections for cooling and insulation [14]. Furthermore, there are also *layer-type windings* such as the ones shown in Figure 15.

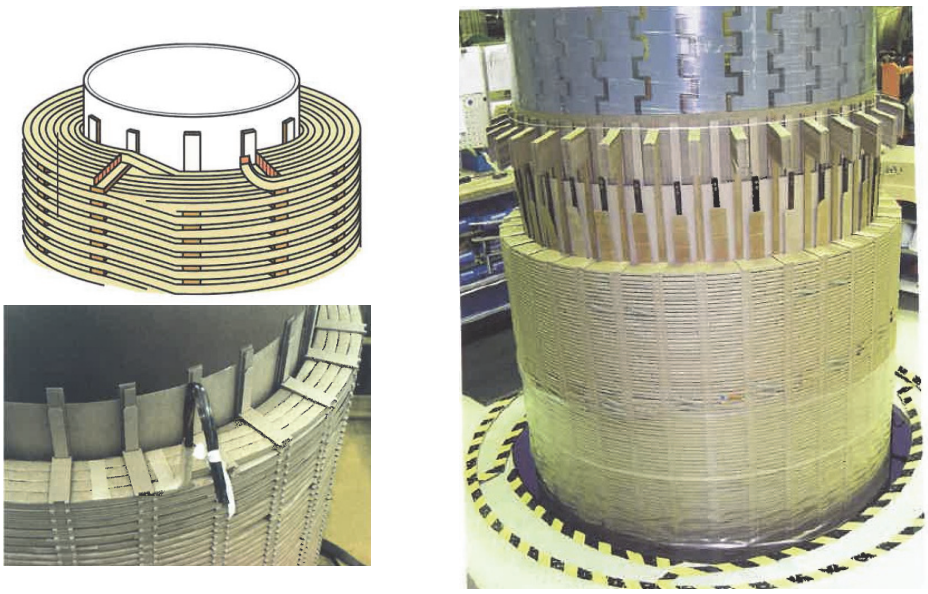

Figure 14. Continuous-disc windings, from [14].

Figure 15. Schematic representation and images of a layer-type coil, from [14].

- ***Insulation and cooling:*** Pre-compressed pressboard is generally used in the windings. The major insulation (between windings, between windings and yoke, etc.) consists of a number of oil ducts formed by suitably spaced insulating cylinders/ barriers. Well profiled angle rings, angle caps and other special insulation components are also used. Mineral oil has traditionally been the most commonly used in electrical insulating medium and coolant in transformers. A high dielectric strength of oil-impregnated paper and pressboard is the main reason for using oil as the most important constituent of the transformer insulation system. Other dielectric liquids have been developed throughout the years, with the purpose to find a non-toxic and environmentally friendly liquid that can be used in transformers. More information about the insulation can be found in *2.Materials used in power transformers* section *2.3.Insulating materials.*

1.2. The relevance of power transformers asset management

The world as we know it today would not be possible without the development of electricity transmission, which is essential for almost every human activity and has been of vital relevance for the progress of industry. Power transformers have played a key role in that development, and they have an essential relevance in our economic environment, where the electric utilities are under constant pressure to reduce operating costs, enhance the reliability of transmission and distribution equipment, and improve the quality of power and services to the customer [15]. Transformers have become a source of concern to utilities in recent years because of the high current values in electrical systems [16], where the consequences of losing

any equipment vital to the transmission and distribution system can be very damaging, and because the time and cost needed for the replacement can be very high. The need for system interconnections has required the installation of large autotransformers, which are more fragile to short circuits due to their considerable low impedance and the reduced capacity of their tertiary windings [14]. In the case of transformers, the purpose is to obtain the longest possible service life, typically assumed to be 25 or 30 years, with minimal lifetime operating costs. If the lifetime is to be maximised, without unwanted interruptions in the system, it is necessary to provide an accurate maintenance schedule for transformer monitoring, repair or replacement.

The focus of operating the power system has changed in recent years, and efforts are being directed to explore new approaches or techniques of monitoring, diagnosis, condition evaluation, maintenance, life assessment, and the possibility of extending the life of existing assets [15]. Transformer management is generally considered to be one of the most significant asset-managements among the power system equipment, mainly because of the substantial investments in these devices and their relevance as one of the major factors affecting the system's reliability [15]. It has been established that the service reliability and life expectancy of power transformers largely depends on the condition of the oil–paper insulation, which is subjected to a complex and irreversible ageing phenomenon [16]. Ageing of the cellulosic insulation results in a reduced ability to withstand the mechanical stresses occurring during inrush currents and short circuits. The problem is accentuated by changes in operational conditions, including increases in acidity and humidity, increased loading, and short-circuit power. The understanding of the ageing mechanisms is essential when optimising asset replacement. To minimise the need for reinvestments and costly maintenance, facilitating long-term planning for replacement of the older unit, and to plan rationally for the future, it is essential to understand and quantify the ageing kinetics and to learn how it may be controlled [16].

1.2.1. Methods for the estimation of the condition of power transformers

Transformer Condition Monitoring (CM) is concerned with the application and development of special-purpose equipment or methods whose purpose is to monitor the condition of a parameter in a power transformer and its data acquisition, focusing mainly on the detection of incipient faults produced by the gradual deterioration of the machine [17]. Online condition monitoring and diagnostics of the insulation over the whole lifetime period of the power transformer allow for the detection of developing faults, thus facilitating economic operation, the determination of the technical end of life of the device, and cost-effective maintenance strategies [18]. Risk management would reduce the overall risk exposure in terms of costs, service reliability and availability.

According to [17], CM has multiple benefits: it reduces the maintenance costs, as it detects faults early; it limits the probability of total failure, allowing the delay of reinvestments for several years and identifying the root causes of the failure. On the other hand, there is an extra added cost due to the monitoring and communication equipment, an increase in the complexity of the control and communication system, the need for new and high-speed systems for data processing and decision making and for suitable memory storage for data base knowledge. For the estimation of the technical condition of a power transformer, the life-cycle characteristics, the overload times and maintenance strategies have to be considered [17]. The basis for a condition evaluation or Condition Assessment (CA) of a power transformer is the

characterisation of its insulation system and how it behaves, for which the development of new analysis techniques is needed, to both predict the trends of the monitored transformer and evaluate its current performance.

- ***Condition assessment by thermal analysis:*** Thermal analysis of the transformers can provide useful information about its condition and be used to detect the inception of any fault, such as overload, as most of the faults produce a change in the measured temperature [15]. A continuous maximum HST (Hottest Spot Temperature) higher than 110°C significantly decreases the expected life of the transformer.

- ***Condition assessment by vibration analysis:*** Generated vibrations (core vibrations, winding vibrations, and on load tap changer vibrations) can be propagated through the transformer oil, until they reach the transformer walls, at which they can be collected via vibration sensors. The health condition of the core and windings can be assessed using the vibration signature of transformer tank [15].

- ***Condition assessment by partial discharge (PD) analysis:*** Partial discharges (PD) occur when the electric field strength exceeds the dielectric breakdown strength of a certain localised area, in which an electrical discharge or discharges partially bridge the insulation between conductors. The dielectric properties of the insulation may be severely affected and even reach complete failure, if subjected to consistent PD activity over long periods. PD measurement is used extensively for the assessment of the insulation and can be detected and measured using piezo-electric sensors, optical fibre sensors, and Ultra High Frequency (UHF) sensors [15].

- ***Condition assessment by dissolved gas analysis (DGA):*** All transformers generate different gases at normal operating temperatures, and the concentration of these gases increases in the presence of a thermal fault, partial discharge or arcing faults. Low temperature decomposition of mineral oil produces relatively large quantities of hydrogen (H_2) and methane (CH_4), and trace quantities of ethylene (C_2H_4) and ethane (C_2H_6). At medium temperatures, the H_2 concentration exceeds that of CH_4, and the amount of C_2H_6 is higher than that of C_2H_4. At the upper end of the thermal fault range, H_2 and C_2H_4 quantities increase and traces of acetylene (C_2H_2) may be produced [15]. The solid insulation begins to degrade at lower temperatures than the oil, therefore, its products are found at normal operating temperatures in the transformer. The thermal decomposition of cellulose produces carbon monoxide (CO), carbon dioxide (CO_2), and water vapour [15]. Analysing the transformer oil for these key gases, by chromatography, helps to know the fault type and its location.

- ***Condition assessment by frequency response analysis:*** When a transformer is subjected to high fault currents, the windings are subjected to severe mechanical stresses causing winding movement, deformations, and in some cases severe damage. Winding damage detection can be accomplished by comparing the fingerprints of a healthy winding (or the calculated response using a transformer equivalent circuit) with the fingerprints of a damaged winding [15].

1.2.2. Planification of the maintenance of power transformers

- **Corrective maintenance:** Corrective maintenance is defined in [15] as the maintenance activity upon occurrence of failure, and was the main maintenance activity in early years. However, it may lead to serious failures and even to losing the asset. Nowadays,

this type of maintenance should be reserved for non-severe defects that have no great consequences, such as failure of some accessories. Its advantages are that it is the least expensive type of maintenance, it saves manpower, it spares the system from unnecessary shutdowns, it performs the maintenance only when it is needed, and it is widely understood by the maintenance personnel [15]. On the other hand, transformer failure becomes costly to repair and may need expensive spare parts, some failures may be irreparable if not detected early and some may cause complete shutdown for a long time [15].

- **Preventive maintenance:** Its objective is to prevent the failure from happening and guarantee long lifetime of the asset.

- ***Time based maintenance (TBM):*** This methodology is based on performing the inspection and the maintenance activities of the transformer at regular time intervals. TBM is the current strategy for many industries and utilities, and although it may prevent many failures, unexpected accidents may still occur in the intervals between maintenance tasks, if the maintenance interval is too large. If the maintenance interval is too small, it may also cause unnecessary outages, wasting manpower, time and money [15].

- ***Condition based maintenance (CBM):*** This technique relys on performing maintenance when the condition monitoring system detects an incipient fault, avoiding the occurrence of a complete failure [15]. The historical data of the transformer's operation parameters, diagnostic tests and the environmental conditions will identify which parameter or component part should be monitored and with which method. Advanced online monitoring and assessment techniques such as dissolved gas analysis, partial discharge, furan analysis (FA), frequency response analysis, and recovery voltage measurement (RVM) play a key role in developing these strategies [15]. When an incipient fault is found, the maintenance activity should take place to avoid the complete failure of the equipment.

- **Reliability centred maintenance (RCM):** This technique can be assumed as the most recent maintenance strategy. RCM combines more than one maintenance strategy in an optimised manner in order to reduce the system's risk and preserve the function or operation with a reasonable cost [15]. For a successful performance, the degree of risk of each fault should be identified to define the optimum maintenance actions.

Its advantages are that the cost of the maintenance operation is optimised based on the risk, it reduces the unnecessary shutdowns for low-risk failures, it reduces the cost of the inspections of a TBM and it guarantees low probability of occurrence of high-risk failures. However, the implementation of the maintenance model is more complex, and the engineers and technicians must be trained. Large amounts of data about failures rates, modes, and consequences are needed [15].

2. Materials used in power transformers

2.1. Introduction

According to [14], the general structure of a power transformer should be as simple and compact as possible to achieve an adequate short-circuit strength, and all the used materials must have good mechanical properties. Each component of the transformer must comply with a particular task that influences the construction characteristics of the component and its constitutive material. Some of the basic materials are magnetic steel for core laminations,

copper for winding conductors, structural steel for the clamping frame and the tank, and cellulosic materials for the insulation.

One of the most important aspects of the design of high-voltage transformers is the definition of all the materials and components used to insulate parts at a different potential from one another, for which the voltage distribution and the voltage stresses arising in the windings of the transformer must be known [1]. The use of appropriate insulating materials, with controlled manufacturing processes, enhances quality and reliability. The insulating materials most commonly used in large high-voltage transformers since their origin are the oil-impregnated cellulose-based products: primarily paper and pressboard, with a typical range of solid to oil ratio of 20–50% [1]. Insulating oil has two important functions: to strengthen the dielectric properties of solid insulation by impregnation, electrically insulating active parts from grounded ones; and to remove heat generated by the windings during service [19]. Among the papers, the most frequently used in oil-filled transformers are Kraft paper and thermally upgraded Insuldur® paper. The main constituents of Kraft paper are about 90% cellulose, 6-7% hemicellulose, 3-4% lignin, and traces of metallic cations [20]. Some chemicals may also be added to the pulp to increase its dielectric constant and oil impregnation [21], [22]. No kind of plastic insulation has so far succeeded in substituting the oil-impregnated paper or pressboard [1], due to their high dielectric strength and excellent cooling properties.

The components of the solid insulation can be categorised into major and minor insulation [10]. The major insulation consists of insulation between windings, between windings and limb/ yoke, and between high voltage leads and ground. The minor insulation consists of internal insulation within the windings (inter-turn and inter-disk insulation). Another purpose of the solid insulation is to provide location of other transformer components, and it must withstand mechanical forces during transportation and service, maintain the shapes and dimensions of the oil ducts when they are electrically stressed and ensure a stable configuration of cooling ducts [14].

2.2. Winding conductors

2.2.1. Copper materials

The copper used in the winding conductors in power transformers should comply with [23], where two types of copper are considered: annealed copper and proof stress copper, the latter having better mechanical properties. The stress-strain curve of copper is non-linear, and it is characterised by a decrease in stiffness as the stress increases. When the material is work-hardened, the elastic regime in the curve is extended. According to [14], when the copper is covered with paper, a certain degree of work hardening is achieved, especially in annealed copper, which increases the yield point stress and its mechanical performance. When determining the strength of a transformer winding, the most relevant parameters are Young's modulus and the yield point, which is generally defined in transformer practice for a deformation of 0.2%.

According to Ramberg-Osgood, equation (23) describes an approximate relationship between stress and strain in copper [14]:

$$\varepsilon = \frac{1}{E_0} \cdot \left(\sigma + \frac{3}{7} \cdot \frac{\sigma^m}{{\sigma_{0.7}}^{m-1}} \right) \tag{23}$$

Where:

E_0 (N/mm^2): Young's modulus in the elastic regime at low stress.

$\sigma_{0.7}$ (N/mm^2): Proof stress of non-proportional elongation 0.7%.

m: Dimensionless exponent which depends on the degree of work hardening.

Young's modulus of copper, [14], can be expressed as:

$$E(\sigma) = \frac{E_0}{1 + \frac{3}{7} \cdot \left(\frac{\sigma}{\sigma_{0.7}}\right)^{m-1}} \tag{24}$$

The tangential modulus of elasticity of copper, [14], can be expressed as:

$$E_t(\sigma) = \frac{d\sigma}{d\varepsilon} = \frac{E_0}{1 + \frac{3}{7} \cdot m \cdot \left(\frac{\sigma}{\sigma_{0.7}}\right)^{m-1}} \tag{25}$$

- **Annealed copper:**

The mechanical characteristics of this material must be guaranteed in the range of working temperatures in the power transformer and up to 120°C [14]. With this material, the stress-strain curve has not a clearly linear region, and there is an uncertainty about the value of the modulus of elasticity. According to [14], annealed copper has the advantages of better workability and faster manufacturing of the windings, but it is very important to require a minimum value of the yield stress of the material. The main properties of this material are listed in Table 2:

Table 2. Physical characteristics of annealed copper (minimum 99.9%), from [14].

PROPERTY	UNITS	VALUE
Density at 20°C	kg/m³	8900
Linear thermal expansion coefficient	1/°C	$1.66 \cdot 10^{-5}$
Average specific heat (between 20 and 100°C)	J/kg·°C	390
Thermal conductivity	W/°C·m	340
Volume resistivity	Ω·mm²/m	0.017241
Modulus of elasticity	N/mm²	$1.1 \cdot 10^5$
Ultimate tensile strength	N/mm²	220-250
Non-proportional elongation 0.2%, $R_{p0.2}$	N/mm²	55-110
Elongation at rupture	%	30-50
Poisson ratio	-	0.35
Specific ohmic loss at 1A/mm² and 75°C	W/kg	2.37
$\sigma_{0.7}$	N/mm²	70
m	-	8

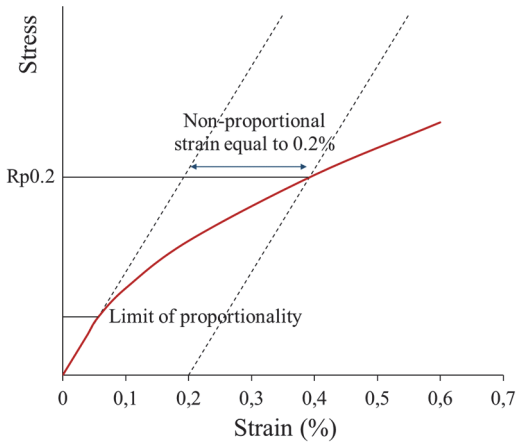

Figure 16. Stress-strain curve of copper and determination of $R_{p0.2}$, based on [14].

- **Work-hardened copper and copper alloys:**

The mechanical properties of copper can be enhanced by cold working process, which consists of rolling, bending, stretching or drawing through a die the material, Figure 17 (a) [14]. The linear portion of the stress-strain curve increases with the amount of cold working, the value of Young's modulus can be defined more precisely, there is a considerable increase in the yield strength and a decrease in the elongation at fracture [14]. The improvement in the properties is maintained in the windings during the life of the transformer. Different types of work-hardened copper have a yield stress between 90 N/mm² and 280 N/mm², Figure 17 (b). There are also some copper alloys, such as those which contain silver or cadmium, with even higher yield stresses. Some properties of this material are listed in Table 3.

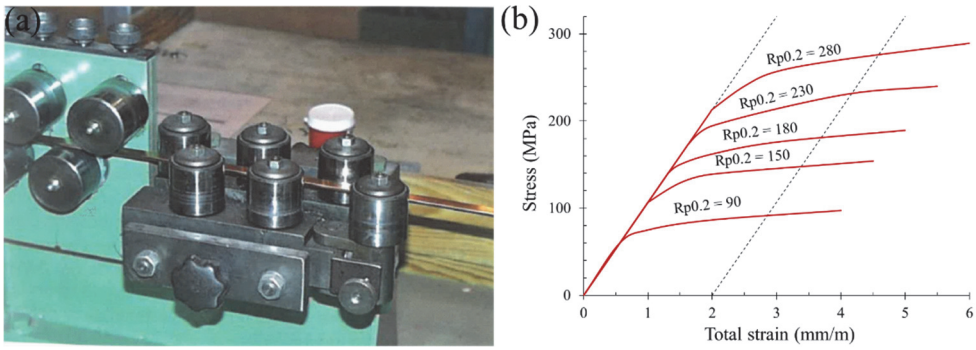

Figure 17. (a) Single copper strand undergoing cold-working process; (b) Stress-strain curves of copper with different degrees of cold working, from [14].

Table 3. Physical characteristics of work-hardened copper, from [14].

PROPERTY	UNITS	VALUE
Modulus of elasticity	N/mm²	$1.1 \cdot 10^5$
Ultimate tensile strength	N/mm²	240-400
Non-proportional elongation 0.2%	N/mm²	110-400
$\sigma_{0.7}$	N/mm²	$R_{p0.2} - 16$
m	-	12

2.2.2. Different types of conductors

There is a wide range of conductors commonly used in the windings of transformers, see Figure 18. The shapes can differ depending on whether the conductor is used in core-type or shell-type transformers. For instance, lower ratios between the width and the thickness of the conductor are used in shell-type transformers, because of the requirements in the leakage flux density [14].

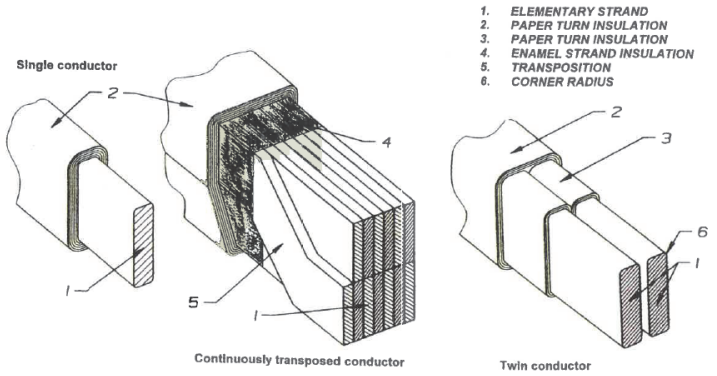

Figure 18. Different copper conductors for core-type transformers, from [14].

- **Rectangular paper-insulated conductors:**

One of the most common types of conductors in medium and large power transformers are the ones with rectangular cross-section formed by copper strips with rounded edges, with common radius between 0.5-0.8 mm. There are also rectangular conductors which consist of twin and triple conductors arranged side by side or quadruple conductors and double twin conductors [14], where several layers of paper insulation, with thicknesses of 0.05-0.13 mm, are arranged in different ways. In core-type transformers, to reduce eddy-current losses, a dimensional range of 1.0-5.6 mm in radial thickness, and of 2.8-16 mm in axial dimension is generally used.

The conductors can be insulated with an individual paper insulation on each strand and an outer overall insulation wrapping the complete conductor, or the individual strands can be insulated with enamel coating on each strand and a common paper insulation [14]. The second option is commonly used in transformers where the voltage between conductors is low and the amount of insulation can be reduced. One common enamel is usually class 120°C polyvinyl acetate (PVA), and the usual thickness of the coating is about 0.1 mm. The enamel should not affect negatively the oil properties at a continuous temperature of 105°C [14].

- **Continuously transposed conductors (CTCs):**

In order to limit eddy-current losses in the windings, especially in large transformers subjected to an alternating magnetic flux, the dimensions of the strands should be reduced (in particular, their width in core-type transformers). However, that reduction in the size generates less robust conductors, with a worse performance in case of a short circuit.

Continuously Transposed Conductors (CTCs) used in core-type transformers consists of a high number of individual strands in parallel (normally an odd number between 5 and 85), whose usual radial thickness is between 1.0-3.0 mm and whose axial height is between 2.8-12.0 mm, insulated individually by means of enamel coating, Figure 19. An automated transposing machine groups the individual strands, transposing them in lengthwise direction at regular intervals of about 12-20 times the strand height, forming a bunch with an approximate rectangular cross-section [14]. The result of the transposition of the strands is a CTC, which can have many possible sizes, which range between 4 and 80 mm in radial direction and between 5 and 25 mm in axial dimension. The standardised insulation is made of paper wrapped around the conductor, with 5-32 paper tapes and an overall insulation thickness between 0.8 and 6 mm [14].

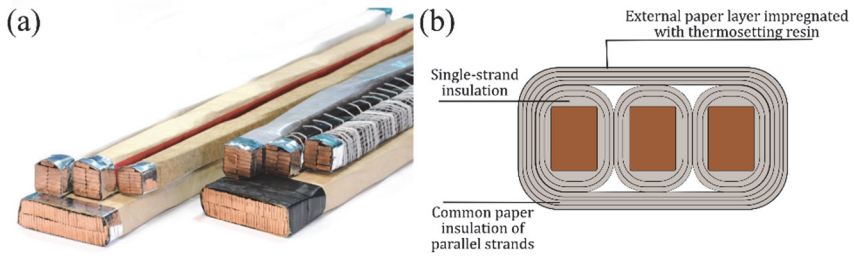

Figure 19. (a) Continuously Transposed Conductors with different number of strands; (b) Multiple strand conductors used with shell-type transformers; from [14].

- **Epoxy-bonded conductors:**

Epoxy-bonded CTCs appeared with the purpose of improving the rigidity of the conductor, in order to avoid buckling under the effect of short-circuit forces. In these conductors, a thin additional layer of a semi-cured epoxy resin is added to each enamel-insulated strand to mutually bond the strands. That additional resin will melt if the conductor is heated at an approximate temperature of 120°C, during the normal drying process, creating a strong permanent bond between adjacent strands [14]. The result is a conductor formed by

a bunch of bonded strands, whose behaviour is comparable to the one of a solid cable with the same external cross-section. The resin must have a long lifetime after the curing process, high stability up to a temperature of at least 120°C and excellent bonding properties. The thermal life of an epoxy-bonded CTC is approximately 80 months at 130°C and approximately 20 months at 140°C [14]. To analyse the response of CTCs of power transformers to forces resulting by short circuits, it is common to subject them to a bending test, Figure 20.

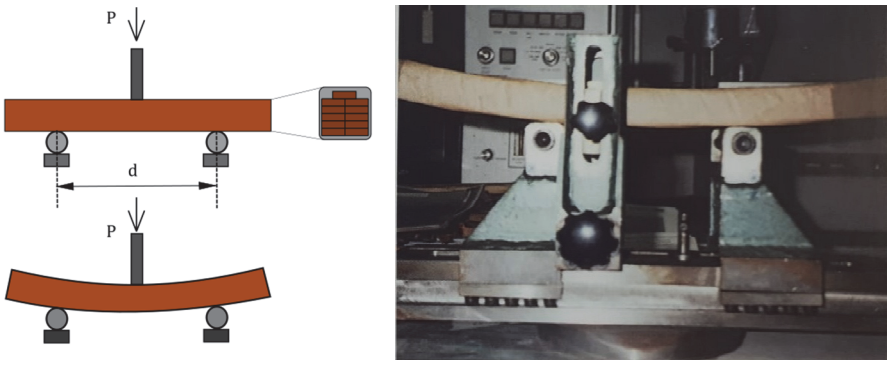

Figure 20. Test set-up to perform the bending test of epoxy-bonded CTC samples, from [14].

2.3. Insulating materials

2.3.1. Relevant electric parameters of dielectric materials

- ***Volume conductivity*** $\boldsymbol{\sigma_v}$, $(\boldsymbol{\Omega \cdot m})^{-1}$: It is the ratio of current density, J, to the applied electric field strength, E: $\bar{J} = \sigma_v \cdot \bar{E}$. Where $\bar{E}(V/m)$ and $\bar{J}\,(A/m^2)$ are vector quantities. In a homogeneous isotropic material, the conductivity is a scalar magnitude. However, machine–made papers are anisotropic in their mechanical properties because of the fibre alignment with the wire during manufacturing. The dielectric properties of paper are a measure of the polarisability of its constituents and depend on the arrangement of the polar groups in the space. As the anisotropy at the fibre level governs the distribution of polar groups in the material, the dielectric properties are anisotropic.

  Paper and board can be considered as three-dimensional orthotropic materials, and their electrical properties have a similar behaviour to their mechanical ones [24]: there are three independent conductivities, one along each of the principal material directions, the machine direction (MD), cross–machine direction (CD), and thickness or direction (ZD), see Figure 21.

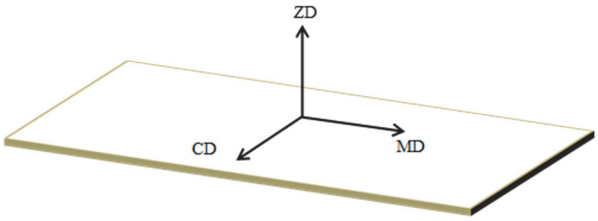

Figure 21. Principal directions of paper material.

- ***Volume resistivity*** $\boldsymbol{\rho_v}$, $(\boldsymbol{\Omega \cdot m})$: This parameter is the reciprocal of the volume conductivity in a given direction of a material. Both ρ_v and σ_v are independent of the specimen and the electrode geometries. It is sometimes useful to consider the ***surface resistivity*** $\boldsymbol{\rho_s}$, **(**$\boldsymbol{\Omega}$**),** which is the resistance measured between the opposite sides of a square on the surface. The standard method for the measurement of volume and surface resistivities is described in Chapter 9 in [24], where some improvements to that method are also detailed.

- ***Permittivity*** $\boldsymbol{\epsilon}$, $(\boldsymbol{F/m})$***:*** It is the proportionality constant between the electric displacement vector, $\bar{D}$ (C/m^2), and the electric field strength, $\bar{E}(V/m)$: $\bar{D} = \epsilon\,\bar{E}$. With homogeneous and

isotropic materials, ϵ is a scalar magnitude, and with anisotropic ones it is a symmetrical second–rank tensor. For paper, assuming orthotropic symmetry, this permittivity tensor has three independent non-zero components, and each of them relates the electrical displacement with field strength in one of the three principal directions [24].

It is usual to define a complex permittivity as: $\epsilon = \epsilon' - i\,\epsilon''$. Both ϵ' and ϵ'' are frequency dependent. In paper, the complex part of permittivity is due to ionic conduction and polarisation losses, which can be attributed to rotation and oscillation of polar groups (dipoles) in the constituents of the fibres.

- ***Dielectric constant k***: It is the ratio of the permittivity of the material and the permittivity of vacuum: $k = \frac{\epsilon}{\epsilon_0}$. This is a dimensionless quantity, always greater than 1 and below 10 for most polymers. The dielectric constant of paper is typically between 2 and 6 depending on the density, moisture content and composition [24]. There is a strong dependence between the concentration of polar groups and the dielectric constant; as the concentration depends on the density of the material, the dielectric constant is expected to vary with density [24]. Any process that increases paper density should also increase the dielectric constant. As the freedom of movement of the polar groups in cellulose is greater in the noncrystalline region than in the crystalline one, the dielectric constant of cellulose decreases with increasing crystalline fraction. The dielectric constant of paper, as for most polymer materials, increases with increasing temperature and decreasing frequency [25]. The simplest way to measure the dielectric constant of paper is described in Chapter 9 of [24].

  It is also usual to define a complex dielectric constant: $k = \frac{\epsilon}{\epsilon_0} = k' - i\,k''$. Paper and board are anisotropic in their dielectric constants, so complex dielectric constants must be defined for each of the three principal directions: MD, CD and ZD [26]. The dielectric constant is a function of the angular displacement between the electric field and the MD of the paper, because of the fibre orientation, and the highest values are obtained when the field is parallel to the MD. If the electric field vector is aligned with each of the three principal directions in the paper, and the values of k' and k'' are analysed as a function of moisture content, Figure 22, the absorbed water apparently reflects the anisotropy of the fibrous structure, although the anisotropy ratio (the ratio of two dielectric constants at a given moisture) increases with increasing moisture [24].

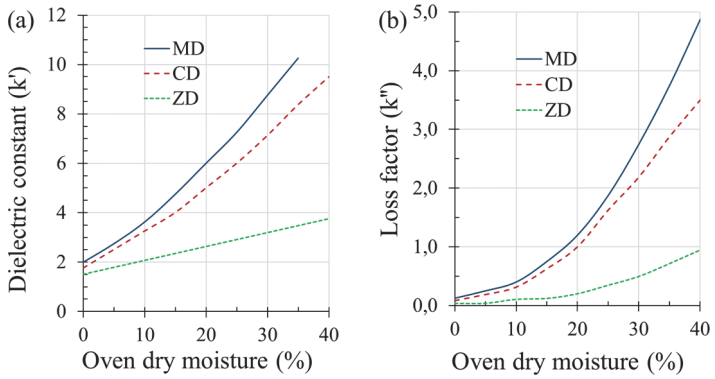

Figure 22. (a) Real part k' and (b) imaginary part k'' of the dielectric constant in the three directions of a board sample as a function of moisture content, based on [24].

- ***Dielectric strength***: It is a measure of the ability of the material to withstand high voltages and maintain its high resistance to current flow, which is usually defined as the maximum electric field strength that can be applied without causing the irreversible failure of the material.

- ***Dielectric breakdown strength*** (kV/mm): It is the value of the breakdown voltage divided by the thickness of the material. If the electric field is uniform throughout the sample, it is also the electric field that causes the breakdown of the dielectric. It is a parameter of great importance in high-voltage or high-power applications. Paper properties with the most significant effect on dielectric breakdown are the air impermeability, the density, the thickness and the uniformity. Paper is a porous material and it should be impregnated with insulating oil or varnished when it is going to be used in high-voltage applications.

  Dielectric breakdown phenomena in polymers can be roughly divided into four categories, according to [27]: *intrinsic breakdown*, which depends on the presence of electrons that can migrate through the material; *thermal breakdown,* which is related to changes in electrical conductivity with temperature; *discharge breakdown* due to the presence of voids in the material; and *electromechanical breakdown* due to mechanical deformation caused by electrical stress.

- ***Dielectric loss:*** It quantifies the dissipation of electromagnetic energy of a dielectric material and depends on the loss angle, δ, or the corresponding loss tangent, $tan\ \delta$. Conduction losses are dominant at high temperatures, whereas polarisation is the reason of dielectric loss at low temperatures. To reduce dielectric loss, it is needed to lower $tan\delta$, which is defined as:

$$tan\delta = \frac{\epsilon''}{\epsilon'} \tag{26}$$

Some factors that affect the dielectric loss tangent are:

- *Lignin content:* It increases dielectric losses, because lignin is essentially polar, Figure 23. However, an excessive removal of lignin (to below 2%) can increase the loss tangent [28].

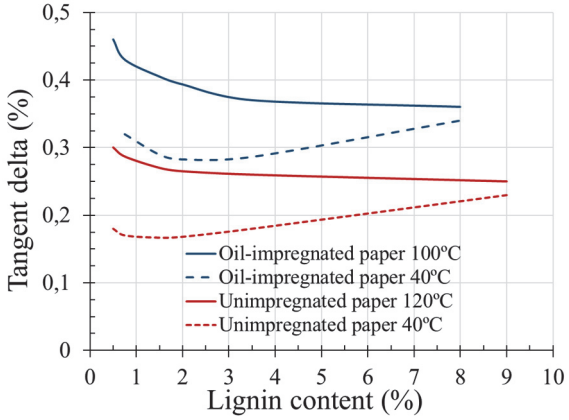

Figure 23. Dielectric loss tangent of paper at different temperatures, as a function of lignin content, based on [24].

- *Hemicellulose content:* According to [29], its effect depends on the temperature. At 80˚C, the loss tangent is independent of hemicellulose content, whereas at higher temperatures an increase in the hemicellulose content will result in a lower loss tangent. Nevertheless, the effect is reversed below 80˚C and the loss tangent will increase slightly with increasing hemicellulose content.

- *Carboxyl groups:* As they are powerful ion-absorption centres, they have a strong negative influence in the loss tangent of paper, which is worse at high temperatures and low frequencies.

- *Crystalline fraction:* The hydroxyl groups of the cellulose chain are believed to have large associated dipole moments when they are no part of a crystalline region. It is impossible to

change the crystalline fraction independently from other properties, for example, the amount of hemicellulose and lignin. Above 100 ˚C, $tan\delta$ increases with the crystalline fraction [30].

- *Ions:* At high temperatures and at commercial frequencies, the dielectric loss tangent is dominated by conduction losses due to metallic ions. Although the number of divalent ions in paper is much greater than the number of univalent ions, the influence of the latter is more remarkable [24]. The most important ions are the cations Na^+, Li^+ and K^+, which are more relevant for electrical conduction than anions. In the absence of an effective cation, the contribution from anions such as Cl^- can become significant. Ionic conduction is increased by the presence of any amount of moisture.

2.3.2. Cellulosic insulation: paper and board

Paper insulation is one of the most critical components of the insulation system, and is required to have high dielectric strength, low dielectric losses and high tensile or breakdown strengths to withstand stresses with both an electrical and a mechanical origin. The steady increase in the voltages of transmission systems has increased the voltage ratings of power transformers, making insulation content a significant portion of transformer cost [31].

The presence of heat, oxygen, water and various chemical and physical processes cause chemical changes in the cellulose molecules and produce insulation ageing, decreasing their electric and mechanical strength against inrush currents or short circuits [32], which is not recoverable once compromised [17]. As the operating temperature is variable throughout the winding [33], the paper insulation can be subjected to non-uniform rates of degradation. The ageing of paper insulation causes a deterioration of mechanical properties first, and a reduction of dielectric strength only afterwards. According to [1], as long as paper retains its mechanical strength and does not break up into pieces, it remains electrically satisfactory.

The electrical, mechanical and chemical degradation of the solid insulation can be considered as the main reason for transformer end of life, causing the failure of the transformer by diverse mechanisms. For instance: the brittle paper can break away from the windings and block ducts; water produced by the degradation reduces the resistivity of paper insulation; in the extreme, local carbonising of the paper increases the conductivity and causes overheating and conductor faults [17]. According to [31], there are two main kinds of failure that usually occur in power transformers. The first involves a complete failure between two electrodes, due to jump/ bulk-oil breakdown, creepage breakdown along oil-solid interface, or a combination of the two. The second one is a local oil failure (partial discharge), which may not immediately lead to failure between two electrodes and can appear both on the surface of the pressboard and inside the insulation. Abnormal operating conditions, such as repetitive overloading for long times and non-sinusoidal loads can also affect the transformer ageing [17].

- **Paper for conductor's insulation:**

In power transformers, paper insulation is a component of the main insulation system between turns and between windings, which should consist of long fibres of pure cellulose with uniform structure [14]. Some physical characteristics of this material are listed in Table 4.

Table 4. Physical properties of paper, from [14].

PROPERTY	UNIT	VALUE	
		Standard type	High-density type
Thickness	mm	0.06-0.09	0.075
Density	g/cm^3	0.75	1.05
Mass per surface unit	g/m^2	40	75
Tensile strength in MD	N/mm^2	> 80	> 110
Tensile strength in CD	N/mm^2	>32	-
Elongation at rupture MD	%	> 2	> 20
Elongation at rupture CD	%	> 4	-
Dielectric strength in air	kV/mm	> 7.5	> 8.0
Dielectric strength in oil	kV/mm	> 35	> 50
Modulus of elasticity	N/mm^2	≃ 1000	-

In papers used for insulation in transformers, it is common practice to specify the mass per square metre (g/m^2), this being the product of thickness and density [1]. The most important electrical properties of paper are its dielectric strength at power frequency (50 to 60 Hz); its dissipation factor, tan δ, which is 10 to $30 \cdot 10^{-4}$; and its resistivity, which is 100-$600 \cdot 10^6$ MΩ [1]. The permittivity of the cellulose is between 5 and 6, and is higher than that of the paper, being this difference due to non-uniform and incomplete filling of the volume of the paper by the cellulose fibres [1]. The same explanation applies to the dielectric strength of the paper, which is inferior to that of the cellulose fibres.

- **Paperboard and high-density pressboard:**

High-density cellulose-based materials are largely used in the major insulation of transformers due to their favourable insulating and mechanical properties, and they have a direct influence on their design and production [7]. The pressboard generally used in large power transformers is a material of high purity without any additives, made of unbleached soft wood sulphate pulp (sulphate cellulose) [14]. The insulation between windings or between windings and yokes consists of oil ducts formed by spaced insulating cylinders and barriers made of pressboard [14], as well as moulded pieces (such as angle rings, insulating discs or stress rings). In fact, part of the mechanical resistance of the complete system relies on those components, which are subjected to both a constant compressive load applied during manufacturing and to a superimposed pulsating compressive force during service [7].

High-density fibre materials are produced in a process that consists of compressing several thin paper layers in a wet condition, under high temperature and pressure, without using any cementing or bonding material. The thinner the individual layers, the better the quality of the board material will be. For instance, in pressboard typically used in transformers there are about 35 layers of 30 μm per mm [1]. In each paper layer, the fibres lay parallel to the surface of board, and they are connected to each other in discrete points by hydrogen bonding created during the drying operation [20], creating a strongly oriented network with open pores of different sizes and shapes. The presence of large pores considerably affects pressboard behaviour, because it allows for oil-impregnability improving dielectric properties, but also causes mechanical weakness, particularly in ZD. According to [7], the oil filling in the pores contributes to the overall stiffness of pressboard when a compressive load is applied in the through-thickness direction. Some of the physical properties of high-density pressboard are listed in Table 5.

Table 5. Physical properties of high-density pressboard, from [14].

PROPERTY	UNIT	VALUE
Tensile strength in MD	N/mm^2	110
Tensile strength in CD	N/mm^2	90
Ultimate compressive strength in ZD	N/mm^2	200
Static modulus of elasticity in ZD	N/mm^2	500-1000
Dynamic modulus of elasticity in ZD	N/mm^2	1000-2000

The density depends on the inter-fibres volume, which is approximately 18% of the apparent volume for high-density pressboard, and can vary from 800 up to 1300 kg/m^3 [14]. The maximum elongation during tensile is 2.3 to 4.6%, depending on the sheet thickness and direction of rolling [1]. However, the behaviour of the pressboard under compression is more relevant in power transformers. Its permanent deformation is small both in the cases of static and dynamic loads, and its elasticity is high. In this respect, there is a considerable difference between calendered and pre-compressed pressboards, the former having a lower modulus of elasticity and a higher permanent deformation than the latter [1].

With respect to electric properties, the dielectric strength of pressboard impregnated with oil under a pressure of $2.7 \cdot 10^{-2}$ mbar lies in the range 200 to 250 kV/cm, and is even higher in thicknesses of 1 to 2 mm. The field strength for inception of a partial discharge is about 70 to 80% of this value [1]. The loss factor, $tan\ \delta$, of pressboard at 20°C is about $40 \cdot 10^{-4}$, and at 130°C about $70 \cdot 10^{-4}$. Its permittivity is 4.4 to 4.5. The surface field strength permissible for pressboard, depending on the creepage distance, falls in the range of 5 - 30 kV/cm, where the higher values apply to shorter distances [1].

2.3.3. Insulating liquids

- **Mineral oil:**

Nowadays, mineral oil is still by far the most common insulating liquid used in power transformers [14]. Historically, mineral oil has shown the best compromise between economical cost and physical properties for most applications, it has a good compatibility with other materials used in power transformers and an adequate stability towards oxidation [14].

Mineral oil is made from crude oil and consists of a variety of hydrocarbon compounds, which are mainly paraffinic, naphthenic or aromatic. Oils containing less than 50% carbons in paraffinic structures are typically defined as *naphthenic oils*; while this value is 56% and above for a *paraffinic oil* [34]. In *isoparaffinic oils*, the molecule is branched, which makes them suitable for use in cold climates. The physical, chemical and electrical properties of insulating oils applicable in transformers are specified by the relevant standards. Three classes of oil are distinguished in [35], see Table 6.

Table 6. Classes of oil, from [1].

	Flash Point (°C)	Pour Point (°C)	Kinematic Viscosity (mm^2/s)
Class I	≧ 140	≦ -30	≦ 16.5 at 40°C
Class II	≧ 130	≦ -45	≦ 11 at 40°C
Class III	≧ 95	≦ -60	≦ 3.5 at 40°C

The density of insulating oil of a satisfactory quality at 20°C should be below 0.895 g/cm^3 [1]. The oil must not contain any inorganic acid or alkali soluble in water, corrosive sulphur or mechanical impurities and should be transparent. These properties depend on the

crude oil used and on the refining process, and most of them do not change either during the treatment following filling of the transformer with oil, or under influences occurring in service. The most important property of the oil with respect to the design of transformer insulation, is its dielectric strength, whose highest value expected in engineering practice is about 330 kV/cm [1]. The breakdown voltage decreases during operation due to the presence of moisture, gases or solid impurities, but it should not be less than 140 kV/cm. If the breakdown voltage drops below this value, the oil should either be regenerated, or changed, according to [1]. Other important properties that oil must have in a transformer are listed in Table 7.

Table 7. Main properties of transformer oil, from [1].

Breakdown voltage at 50 or 60 Hz when the transformer is filled	≥ 200 kV/cm
Interfacial tension at 25°C	$\geq 40 \cdot 10^{-3}$ N/m
Loss factor (tan δ) at 90°C	$\leq 50 \cdot 10^{-4}$
Permittivity (ε)	2.2

Water may be present in the oil in three different ways: in dissolved states, finely distributed (forming an emulsion), and roughly distributed (forming droplets). The higher the temperature and the partial pressure of water vapour present in its environment, more moisture can be kept dissolved by the oil. From 0 to 80°C, oil in contact with atmospheric pressure can retain 30 to 600 ppm dissolved moisture (1 ppm = 1 mg water/1kg oil). Above a moisture content of 40 ppm, the dielectric strength of the oil is considerably deteriorated [1]. The oil becomes unsuitable for further use with moisture present in the finely distributed state, because the turbidity increases, and its dielectric strength decreases considerably. Moisture present in rough distribution tends to accumulate at the deepest point of the tank, because its specific density is higher than that of the oil, causing a drastic drop in local dielectric strength. A high moisture content may be especially hazardous if the oil also contains foreign particles, such as longer fibres, which assume the direction of the field and, in the presence of moisture, constitute a conductive bridge between parts at different potentials causing flashovers [1].

The dielectric strength of the oil may also be reduced by the presence of gases, which may enter the oil either from outside due to its direct contact with the air, or due to the decomposition of the oil itself or of the cellulosic insulation immersed in it [1]. Oil and cellulose are organic substances with little resistance to heat, and their molecular decomposition is detectable at room temperature, and it starts to accelerate considerably at 130°C for the oil and at even lower temperatures for the cellulose. As with moisture, gases can be present in three physical states: dissolved, finely distributed and roughly distributed. At 25°C and at normal atmospheric pressure, the oil can keep the following substances dissolved, expressed as a percentage of the oil volume: 10% air, 8.5% nitrogen, 16% oxygen, 100% carbon dioxide [1]. The percentage of soluble gas increases with rising temperature and pressure.

The dielectric strength of an oil saturated with gas is not much lower than that of an oil free of dissolved gas; but the dielectric strength of the oil can be reduced if a change in its state (decrease of temperature or pressure, or a chemical process) causes a reduction of the quantity of gas the oil can dissolve, and some of the gas is released and appears in the finely distributed state [1]. This state is, however, of a transitory character, because the air bubbles of microscopic size tend to unite to form larger voids of air. Their size keeps growing until the flow resistance is overcome by the lifting force and a bubble starts ascending, tending to approach the surface of the oil. If the bubble reaches the vicinity of parts subject to high electrical stresses, it will cause electrical defects in the transformer.

The presence of gases is also harmful with respect to the useful life of oil. Air or oxygen cause chemical changes that produce permanent deterioration of electrical properties of the oil and the cellulosic insulation. By analysing the composition of the gases dissolved in the oil, conclusions can be drawn about the presence of possible defects in the transformer, such as hot spots or electric discharges. Three main types of defects may be distinguished [1]:

- Discharges release gas bubbles consisting mainly of hydrogen.
- High intensity discharges (sparking and arcing) provoke the development of acetylene.
- Overheated spots within the transformer produce an increase in the quantity of ethylene gas.

Furthermore, the ageing of oil is also indicated by the reduction of interfacial tension. As proven by experiments, at the interface between a new oil of good quality and water, a much higher interfacial tension can be measured than between an aged, highly acidified oil and water. The susceptibility of the oil to degradation caused by oxidation can be reduced by antioxidant additives. The degradation can be decreased or delayed by such inhibitors, and the good insulation properties of the oil can be preserved for a longer time.

- **Ester insulating liquids:**

The variety of insulating liquids for transformers has increased steadily in recent years for several reasons [36]. For instance, natural and synthetic esters have been introduced for transformers located in densely populated areas due to their lower flammability. Moreover, an accidental leakage in a transformer could constitute an environmental hazard because mineral oil is toxic and nonbiodegradable [37]. Synthetic and natural esters used in transformers are reaction products of fatty acids and a polyol. They are abundant, as they are based on renewable resources and do not depend on fossil raw materials; they have a higher biodegradability and can be used in environmentally sensitive places [36]. Glycerol is the naturally occurring polyol in natural esters, while for synthetic esters the polyol is typically pentaerythritol [36]. The composition of fatty acids depends on the nature of the oil seed [38]. To use them as an insulating liquid, the composition can be changed by partial hydrogenation [36], which generates a product thermally more stable and less susceptible to oxidation. Moreover, esters have a higher water solubility, which is claimed to be responsible for a reduced ageing rate of cellulosic insulation compared to mineral oil [36].

According to [37], paper used in power transformers has a relative permittivity higher than that of the insulating mineral oil ($\varepsilon_{mineral\ oil} \simeq 2.2$) and, with that type of oil, the electric stresses under short-circuit conditions will be higher across the oil, resulting in partial discharges. An insulating liquid with a relative permittivity higher than that of mineral oil ($\varepsilon_{natural\ ester} \simeq 3.2$), will increase the oil-impregnated insulation relative permittivity, given by equation (27), and the stress caused by an electric fault will be more equally shared, resulting in an increase in the stress required for the occurrence of a discharge[37].

$$\varepsilon_{oil-impregnated\ paper} = \varepsilon_{paper} \cdot \left[1 - K^2 \left(1 - \frac{1}{1 + K \cdot \left(\frac{\varepsilon_{paper}}{\varepsilon_{oil}} - 1\right)}\right)\right] \quad (27)$$

$$K = \sqrt[3]{\frac{V_{oil}}{V_{paper}}} \quad (28)$$

Where ε_{paper} is the relative permittivity of the paper, ε_{oil} is the relative permittivity of the oil, V_{oil} is the volume of oil and V_{paper} is the volume of paper.

3. The ageing of insulating materials and its quantification

3.1. Factors producing ageing of dielectric materials

The breakdown voltage of a dielectric material is a statistically distributed quantity which is a function of its physical and chemical properties and the impurities present in it, thus failures are not always produced by elevated electrical forces, and sometimes interrelated thermal, chemical and mechanical factors may also have significant influence [31]. The composite oil-solid insulation system exhibits an erratic behaviour, in comparison with other materials, which is increased with the ageing and the deterioration of electrical and mechanical properties.

3.1.1. Effects of moisture, temperature, oxygen and impurities

According to design standards, the temperature rise is the difference between the temperature of a given part of the transformer and that of the cooling medium. The most common types of cooling for oil immersed transformers are *Oil Natural Air Natural (ONAN),* where the heat generated in the core and winding is transferred to the oil due to natural convection and will dissipate in the atmosphere due to the natural air flow around the transformer; *Oil Natural Air Forced (ONAF),* where the heat dissipation is improved by applying forced air on the dissipating surface; *Oil Forced Air Forced (OFAF)*, where the oil is circulated with the help of a pump and forced through the heat exchangers, and then the fans force the compressed air to flow on the heat exchanger; *Oil Forced Water Forced (OFWF),* where forced water flow is used to dissipate heat, and a pump forces the oil to flow through the heat exchanger.

Temperature rises as a result of overloading and of prolonged power-frequency voltage rise may cause defects or permanent deterioration of insulating materials [1]. A sudden increase of load caused, for example, by a short circuit, may lead to a rapid temperature rise of metal parts, which generally does not cause any damage to the transformer because the duration of the short circuit is very short [31]. The transformer is required to withstand the temperature rise, which must not exceed a specified limit such that the properties of the constitutive material are not endangered, during a specified period of time [31]. The permissible temperature limits in the active parts influence the constructional design, size, cost, load carrying capacity and operating conditions of the transformer. The maximum continuous load carrying capacity of the transformer depends on its rating (to which the guaranteed data refer), on the temperature of the cooling medium, and on whether or not the user wants to slow down the ageing of the cellulosic insulation [1].

Due to the short duration of short circuits, practically no heat is transferred to the oil during the flow of a short-circuit current. After the clearing of the fault, the heat transfer begins by convection in the oil and, after a time, the windings return to their normal service temperature [31]. For Class A insulating materials, 115°C is permitted as the highest service temperature. By the temperature of the hottest spot of the winding, the temperature of the hottest inner layer of the disc located at the top of the winding stack is to be understood. For overloads of short duration, 140°C is permitted in [39] as the highest hot spot temperature, whereas in short-circuit conditions, 250°C is the average winding temperature in copper windings, and 200°C in aluminium windings. In practical cases, due to the short fault clearing times and low service current densities, the short-circuit temperature rise limits are not reached.

Several significant experimental studies (such as [17], [18], [20], [32], [40]–[45]) have established that temperature, moisture, and oxygen are major factors influencing gradual

degradation of cellulosic insulation in transformers. The effects of moisture and temperature are generally nonlinear and history-dependent [20], and have been studied over a number of years using, among other parameters, the degree of polymerisation (DP) of the paper [42]. The oil dielectric strength usually increases with temperature in the operating range, but this effect is the opposite for the cellulosic insulation [31]. An electrical overload produces a temperature increase in the power transformer, which reduces both the dielectric strength and the ohmic resistance of paper, resulting in the flow of more current in the insulation [31]. Due to the increase in dielectric loss, insulation temperature goes up higher, and it may finally lead to the current run-away condition and eventual breakdown. Furthermore, as paper is heated, a number of physical and chemical changes affect its properties. In the laboratory, accelerated thermal degradation is used to speed up the natural ageing of paper in order to study its performance.

Until recently, it was thought that the insulation ageing was mainly a function of temperature and stresses arising from short circuits or inrush currents, and the estimation of useful service life was therefore based on an inverse power model, an Arrhenius model (under first order reaction kinetics) or a combination of the two models. The parameters estimated with that life-model were often inaccurate and needed corrections [45]. There is a need for developing models of insulation failure involving moisture [45], as different physical processes cause the absorption of environmental humidity in the transformer and increase the failure probability, accelerating the depolymerisation of paper and reducing the breakdown voltage and dielectric strength of dielectric oil [18], [17], especially when the temperature is high. Moreover, water forms as a reaction product, both during the thermo-kinetic degradation of the cellulose and during the ageing of oil. It has now been realised that moisture in all its forms, in combination with temperature and mechanical stresses, has a tendency to age the insulation and produce failure much more rapidly as compared to dry conditions. Indeed, moisture has been identified by the CIGRE as a major agent of insulation degradation.

In the three-component oil-paper-water system, a definite water content may be present at a given temperature, both in the paper and the oil [1]. The temperature effects are dynamic because a considerable amount of time is required for establishing equilibrium between moisture in the oil and that in the cellulosic solid insulation. The conditions of humidity equilibrium are illustrated by the isothermal curves in Figure 24 (a). For example, at 90°C and with 20 ppm water content in the oil, a state of equilibrium where there is no migration of moisture between oil and paper is that with a moisture content of 0.8%. When there is no humidity equilibrium, there is going to be water migration from oil into the paper and vice versa, and a sudden migration of moisture due to a sudden load increase (and a change in the temperature) can be associated with a further hazardous consequence.

A typical interpretation of moisture content, from [18], is: less than 0.5% when the transformer is produced at the factory; between 0.5-1.5% for dry insulation in a well maintained transformer in-service; between 1.5-2.5% for medium-wet insulation, entering into medium risk; between 2.5-4% for wet insulation, entering into high risk; more than 4% means very wet insulation, imminent failure, bubbling and explosion risk. At 4% moisture content and normal service temperatures, the ageing rate of paper is twenty times higher than at 0.5% moisture content [32]. Moisture content increases with an increase of temperature, and the deterioration will be highly influenced if a threshold value of about 135°C is exceeded [18]. In order to maintain the dielectric strength and to reduce the ageing, the moisture content should be maintained below 0.5% in the paper and below 20 ppm in the oil [1].

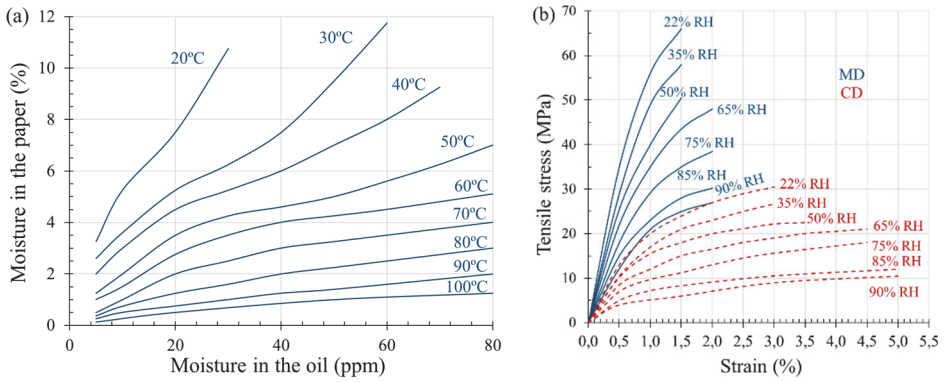

Figure 24. (a) States of equilibrium of moisture contents of oil and paper at different temperatures, based on [1]; (b) Tensile stress-strain curves in MD and in CD for various moisture levels, based on [20].

The dielectric strength of paper insulation is significantly related to its mechanical properties. Ageing of insulation affects its mechanical strength more significantly than the effects of mechanical forces. The Young's modulus (E) of paper decreases with increasing temperature and moisture content [20], see Figure 24 (b). Plastic deformation due to cycling load is larger in moist material tested at high temperature compared to dry material. When there is equilibrium in the moisture content, the Young's modulus and the tensile strength decrease with an increase in temperature, and that decrease is directly coupled to the thermal expansion of the paper and to the loss of strength of the hydrogen bonds [20]. The E_{MD} has been reported to be significantly less affected by temperature and moisture than the E_{CD} and the in-plane shear modulus. The relationship among elastic modulus, temperature and moisture content is generally nonlinear, and temperature and moisture effects may be coupled [40]. When paper is exposed to varying temperature, in nonequilibrium conditions, it frequently displays transient effects, whose precise descriptions are still under active discussion. Tensile strength, breakdown strength, DP, and water content of the paper and pressboard were measured in [42] after an ageing period. The changes were similar for both paper and pressboard. The temperature dependence of acid value, the water content, and the amount of generated gasses were measured for the oils. Above 140°C, insulating papers and pressboards are degraded easily; however, the relation between temperature and the amount of generated gasses has not been investigated at relatively low temperature.

With respect to the electrical properties of the paper, at room temperature and up to 3% moisture content, the breakdown strength is practically constant, and even at 6% water content, it is still around 80% the original value, see Figure 25 (a). At higher temperature, the situation is much worse. The presence of moisture and gases increases the risk of bubble and voids formation under normal allowable hotspot temperature [1], reducing the strength of the cellulosic insulation, and this effect is more significant due to the presence of solid impurities [31]. Since the permittivity of air is lower than that of the paper, a considerably higher electric stress will arise in the voids than in the paper, producing flashovers and partial discharges. That does not cause breakdown of the entire insulation, but the local deterioration may propagate and, after a period of time, lead to the total breakdown of insulation [1]. Figure 25 (b) from [1] shows the breakdown voltage of oil-impregnated paper samples as a function of moisture content at 80°C. When only the mechanism of dielectric breakdown acts (for example, under the effect of a lighting impulse voltage) the breakdown strength drops to about 50% of its original value at 6% moisture content, whereas in the case of combined thermal and

electrical breakdown (power frequency stresses) the breakdown strength is only 15% of the original at the same moisture content.

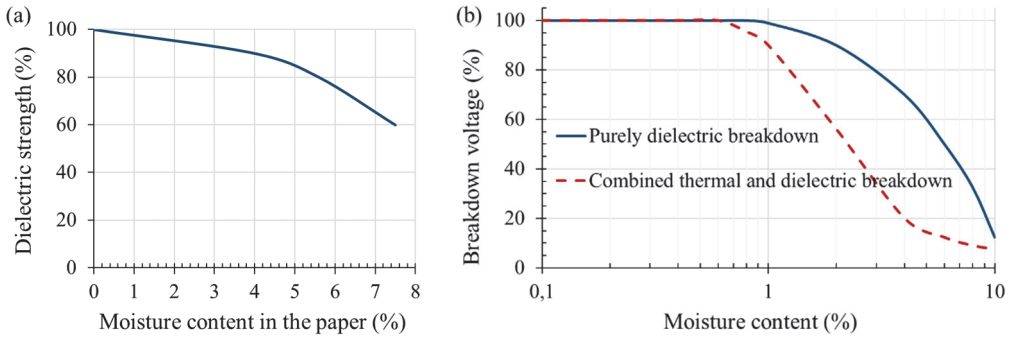

Figure 25. (a) Effect of moisture content on the dielectric strength of oil-impregnated paper at 23°C; (b) Breakdown voltage of oil-impregnated paper samples as a function of moisture content at 80°C, based on [1].

The conductivity of the insulation increases slightly between 0 and 1%, but considerably above 1% moisture content, so the measured resistance indirectly indicates the moisture content [1]. The effect of the accumulation of ageing products on resistivity is less significant. Moisture in the paper also increases its loss factor, $tan\ \delta$, and even thermal instability and subsequent breakdown can be reached. Percentage saturation of moisture content is the decisive factor influencing the dielectric strength of the transformer oil: strength reduces drastically until the saturation point, after which there is no further deterioration [43], [44]. The reduction in dielectric strength of the oil due to presence of cellulose particles is amplified at higher moisture content, due to the higher affinity of paper and moisture [41].

The presence of oxygen is the third factor causing the ageing of paper, although it is less important than water and temperature. According to [1], oxygen at most doubles the ageing rate. Studies of CO production from cellulose aged in a full transformer suggest that the oxygen concentration needs to drop below a threshold of 3000 ppm to reduce oxidative ageing [46]. In [32], the effects of high and low values of relevant parameters (heat, oxygen in the oil and water content in the paper) were analysed through experiments to assess their effectiveness, as well as synergistic and antagonistic interactions between them. Oil-impregnated Kraft and cotton paper samples were aged isothermally in temperature-controlled ovens, with controlled levels of oxygen and water added, as shown in Table 8. The experiments were repeated at temperatures of 120±2°C, 140±2°C and 160±3°C. Samples were removed periodically to measure the DP, Figure 26, and the oil was analysed for furan content. The results in [32] show that heat and moisture are about equally effective individually, with a significant synergistic effect in combination. Oxygen alone and in combination with heat is about one third as effective, but, interestingly, the water-oxygen combination is negative indicating an antagonistic effect at low water levels. This effect might be explained in terms of hydrogen bonding between the oxygen and the free water, causing a "shielding effect", which reduces the reaction between water and cellulose. The implication is that oxygen has a greater affinity to free water than to cellulose below 120°C, so at transformer-operating temperatures, the inhibiting effect of oxygen on the hydrolytic degradation could be stronger.

The effect of oxygen pressure, temperature and copper additives (solid copper in granules and copper naphthenate) on ageing of paper submerged in transformer oil (in terms of DP and the number of chain scissions) was studied in [46]. The DP drops quickly in the early stages of the ageing, whose severity increases with oxygen pressure and temperature. Insignificant differences were observed when the catalyst was changed, and all other

parameters were kept constant. The concentration of water in oil as a function of ageing time seems to increase quickly if the temperature and O_2-pressure is high, but if the temperature is moderate, an initial period with limited H_2O production is observed before a marked increase [46]. Adding copper naphthenate as a catalyst accelerates the production of water in the oil.

Table 8. Ageing experiments, from [32].

Experiment	Water content		Oxygen content in the oil
	Paper (%)	Oil (ppm)	
Low oxygen and low water	<0.1% (low)	8	< 400 ppm (low)
Medium oxygen and low water	<0.1% (low)	10	~ 1% (medium)
High oxygen and low water	<0.1% (low)	20	2.9 – 3.3 % (high)
Low oxygen and high water	5.5-7.5% (high)	8	< 400 ppm (low)
Medium oxygen and high water	5.5-7.5% (high)	10	~ 1% (medium)
High oxygen and high water	5.5-7.5% (high)	20	2.9 – 3.3 % (high)

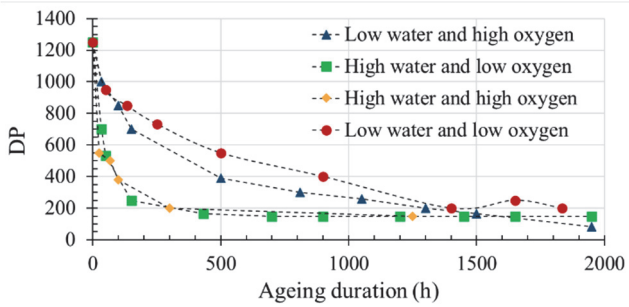

Figure 26. Effects of water and oxygen on DP change during ageing of Kraft paper in oil at 140°C, based on [32].

There are also reactive compounds, such as alkaline and acidic materials, that generate an autocatalytic effect [24]. In [19], oil-impregnated pressboard specimens were aged at 100°C for durations between 300 and 2500 hours, using different metallic catalysts (zinc, copper, aluminium and iron) to study their stability under oxidative conditions. Different oil-to-solid-insulation ratios (20, 10 and 0%, where 0% represents oil without paper) were analysed. The effects of ageing in the content of dissolved decay products, turbidity, oil capacitance, oil dielectric dissipation factor, depolymerisation current, oil conductivity, loss factor of oil, loss factor of pressboard and pressboard tensile strength were also studied in [19]. The thermal stability of paper can be improved both by removing inorganic material and by introducing products such as calcium carbonate that will neutralise the acids in the pulp that otherwise would be very damaging [47].

3.1.2. Effects of voltage and frequency

When an alternating voltage is applied to the cellulosic insulation, initially, the heat on account of dielectric losses is stored inside the insulation and its temperature begins to rise. If the solid insulation temperature continues to rise, its resistance decreases due to the negative temperature coefficient, increasing the current. If the rise in the current continues, losses are further increased, leading to a runaway condition resulting in an eventual breakdown [31]. Thus, with the increase in the time of application of voltage, the dielectric strength at power frequency reduces. Volt-time curves represent the relationship between voltage and time to breakdown: if the voltage is higher, the time to cause breakdown is lower [31]. The dependence of the oil dielectric strength on the duration of voltage application is erratic, as compared to the solid insulation. However, it seems to reduce rapidly after few seconds, and remains more or less constant after a few minutes of application. It requires time for impurities to get lined

up and bridge the gap; hence, the strength is very high when the time of application of the voltage is short [31].

Typical volt-time curves for oil and oil-impregnated pressboard are drastically different from those of the air. Figure 27 (a) from [31] indicates that the oil and solid insulations have flat characteristics after a few microseconds. The breakdown volt-time curve, as expected, is significantly above the partial discharge curve in the microsecond range. However, both curves come very close to each other in the AC long-term region of several minutes, Figure 27 (b). The conclusion is that a partial discharge lasting a very short time is not sufficient to cause the breakdown, but it could cause breakdown if it lasts several minutes.

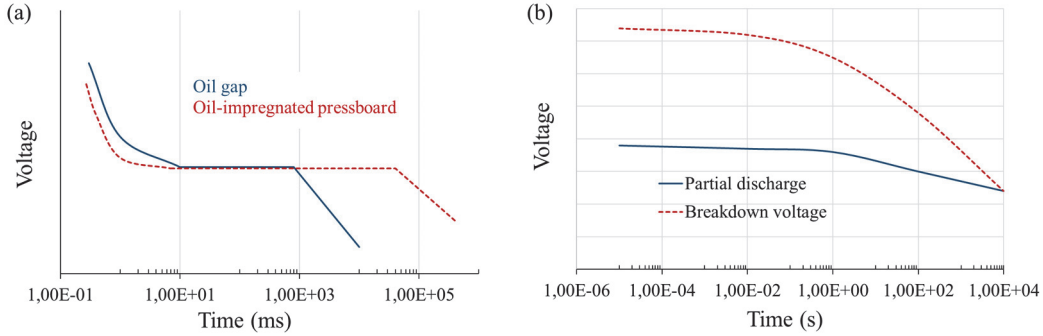

Figure 27. (a) Volt-time curve of oil gap and of oil-impregnated pressboard; (b) Breakdown voltage and partial discharge volt-time curves, based on [31].

In [48] and [49], the breakdown voltage due to a number of voltage impulses (V-N) applied on a deformed CTC conductor wrapped in mineral oil-impregnated Kraft paper was studied. A control system counted the number of applied repetitive voltages, and the voltage waveform was observed with an oscilloscope. The relationship between the amplitude of applied voltage, V, and the number of applied impulses to breakdown, N, was expressed with a simplified Weibull Exponential model: $V = aN^{1/b}$, where a is the breakdown voltage and b the shape parameter. Test samples were firstly subjected to thermal ageing and later to the overvoltage tests: A (equivalent to 0 operating years) and B (equivalent to 80°C for 10 operating years) subjected to lighting impulse, and C (equivalent to 80°C for 20 operating years) subjected to switching impulse. 50% of the breakdown voltage was firstly applied and, then, voltage impulses were applied up to $N = 1000$ times or until breakdown. Breakdown of a transformer winding is not only produced by the electrical accumulative effect of the transient impulse, and mechanical defects, such as axial or radial winding deformation, usually have a great impact on the end of life of transformers, [48], [49]. The paper insulation can be damaged even when the deformed winding appearance is in good condition [49].

Despite the degree of dispersion, the results of [48] indicate that insulation failure cannot happen before applying a certain number of impulses, which have an accumulative effect. It was reported that the insulation layers are damaged from the inside to the outside. More voltage impulse applications (N) are needed if the applied voltage is lower, and N increases fast with the decrease of the applied voltage. According to Figure 28 from [48], 50% breakdown voltage of the transformer equivalent operating 20 years (group C) is 1.2% higher than that of equivalent operating 10 years (group B), which is 13% higher than that of the equivalent operating 0 years (group A). The conclusion is that, with ageing time, both the 50% breakdown voltage and the average breakdown field strength of insulation paper increased, indicating that although thermal ageing weakened the mechanical properties of cellulosic insulation, its ability to withstand impact improved. The reason could be that the damaging of the paper fibre due

to ageing enhances the impregnation of dielectric oil, which has a lower permittivity, into the pores and holes, increasing the breakdown voltage of ageing oil-impregnated paper.

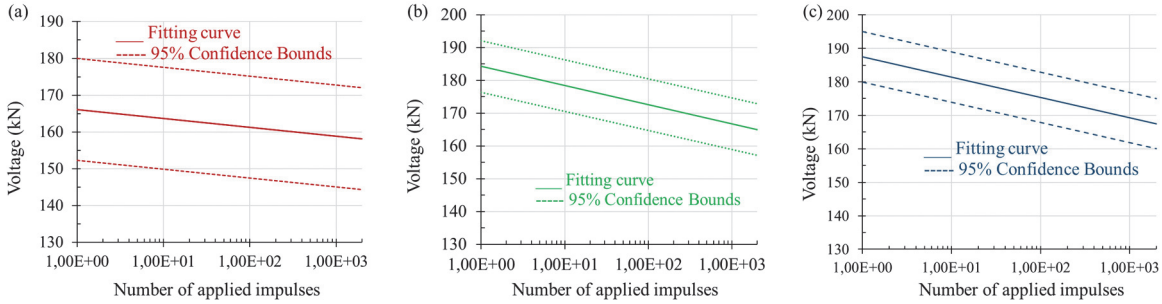

Figure 28. V-N characteristics of equivalent operating (a) group A, (b) group B and (c) group C, based on [48].

Similarly to the duration of voltage application, an increase in frequency increases the dielectric loss and heating, resulting in a reduction of the insulation strength [31]. In dynamic mechanical testing, the properties vary with the oscillating frequency, because at high frequencies there is insufficient time for the polymer chains to change their molecular configuration before the direction of the deformation changes. A more rapid deformation or a high strain frequency results in a more brittle polymer. In a narrow frequency range (0.1–30 Hz), with increasing frequency in the absence of phase transitions, the Young's modulus increases, and the loss factor decreases considerably. The strength does not vary in the linear proportion to the reciprocal of frequency but, approximately, strength $\propto (1/f^{0.137})$, according to [50]. An increase in frequency has a harmful effect on the strength the solid insulation, and a much smaller effect on the oil strength.

It is also important to differentiate between experimental analyses and the real state of an operating transformer. In the laboratory, the transformer is separately and independently subjected to different dielectric tests, such as lighting impulse, switching impulse and short-time/ long-time power-frequency tests. In an actual power system in operation, the transformer may be subjected to superimposed AC and lighting impulse voltages, and the breakdown voltage can be significantly lower [31]. Other factors influencing the oil breakdown strength, are the electrode shape or surface, electrode metal or the gap between electrodes [51], [52].

3.2. Parameters used for the assessment of the ageing of oil–paper transformer insulation

As moisture content is one of the factors with a greater influence on the ageing of the insulation, as discussed in section *3.1.1.Effects of moisture, temperature, oxygen and impurities*, experimental methods for moisture content measurement are needed. The content of water can be measured by the Karl-Fischer titration method. The Polarisation Depolarisation Current method (PDC), where a DC Voltage is applied and the current is measured, can also be used to determine the water content [17]. The Frequency Domain Spectroscopy (FDS), in which an AC voltage with variable frequency is applied and the dissipation factor (tan δ) is measured, also enables the measurement of the water content in the whole insulation system of a transformer. Another method was developed in [17], combining the advantages of FDS and PDC methods, and the duration of the measurement can be significantly shortened.

In addition to electrical and mechanical tests, a number of chemical methods can be used to analyse the state of the oil and paper insulation. According to [19], chemical tests are more sensitive to insulation degradation. Some existing methods for the oil analysis are furfural

concentration in oil using high performance liquid chromatography, gas content of oil using dissolved gas analysis or detection of extracted gases using gas chromatography [17]. The relative content of dissolved decay products can be determined by spectrophotometry, and turbidimetry can be used to analyse solid suspensions.

3.2.1. Degree of polymerisation (DP)

Paper fibres are composed of cellulose that consists of linear, polymeric chains of cyclic, β-D-glucopyranosyl units, which associate in both crystalline and amorphous regions to form microfibrils, which subsequently form fibrils and finally fibres. Most of the mechanical strength of the paper is due to its content of these fibrils and fibres, while the hemicellulose and residual lignin are amorphous, gummy substances which cement them together [16]. The degradation of the solid insulation is directly associated with its mechanical integrity: the shortening of the cellulose chains and their scission are one of the principal causes of the mechanical strength deterioration [19]. In Figure 29, the chemical structure of the cellulose molecule is shown.

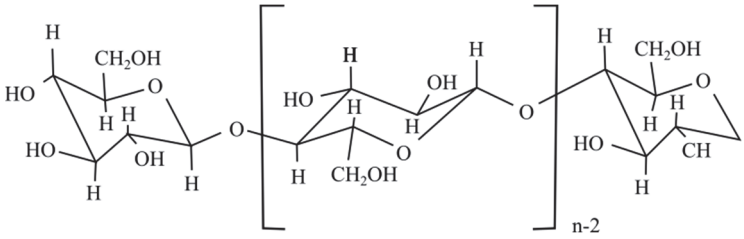

Figure 29. Molecular structure of cellulose.

The average length of the cellulose polymer, measured as the average number of glucose monomer units in the polymer chains, is referred to as degree of polymerisation (DP). The number of anhydroglucose units in the cellulose chain is the direct indication of the decomposition of the cellulose macromolecules and the formation of ageing products, and gives objective information about the paper health and its electrical breakdown strength [18], [17]. In the thermo-kinetic degradation of cellulose macromolecules, cleavage products such as carbon dioxide, carbon monoxide, water, hydrogen, and furans, which are the derivatives of C_6 monomers are produced [18]. In reaction with water, the cellulose molecule is split up and the process of depolymerisation goes on, as the number of glucosic units is reduced. It is quite frequent to describe ageing according to the number of chain scissions, η, given by equation (29), where DP_{new} and DP_{old} are, respectively, the DP-values before and after an ageing period [16]:

$$\eta = \frac{DP_{new}}{DP_{old}} - 1 \tag{29}$$

The DP is frequently used in laboratory tests to determine the overall degradation of the paper insulation of the transformer being sampled, to assess the life expectancy of transformer insulation [53]. There are some standard methods such as [54], [55] or [56], which is specific to transformer paper. In DP measurement, both the sample preparation and the viscosity determination must be carried out very carefully to obtain accurate results [17]. The viscometric method gives very reliable DP results, but it is not usually applied for transformers in operation, because samples of the insulation paper are needed, and that may cause local damage in the winding system or even lead to complete failure [15]. The DP of paper from transformer windings is more variable than that of laboratory aged paper, and the scatter could be due to the non-uniform ageing rates in different positions of the paper in the windings [53].

For instance, the relative standard deviation of the transformer samples described in [53] was approximately between 3-4%, compared to 0.73% for the laboratory-aged samples.

Studies report that new Kraft paper has an average DP of about 1200, and the DP of pre-treated transformer insulation paper gradually decreases from an initial value of about 950 [33]. Below about 500 DP units, the tensile strength starts to decrease in an approximately linear fashion with respect to DP. It is considered that paper under normal operating conditions has a DP higher than 400 [17]. A strong correlation exists between DP and tensile strength of paper materials. Based on the experience of previously retired transformers, it is generally accepted that when the DP is of 200 or less, only about 50% or less of the original tensile strength of the paper remains, meaning the end of life of the solid insulation [33].

In [16], the effect of temperature in ageing rates was analysed for Kraft and Insuldur papers, with a moisture content of 3%, sufficient to promote dissociation of the carboxylic acid groups in the oil and paper. Figure 30 shows that the DP value decreases with ageing duration, and the decrease is more accused at higher temperature. The tensile strength of the paper was analysed through the tensile index (the tensile strength, in N/m, divided by the grammage of the paper). The increase of the tensile index in some points of Figure 31 is a consequence of the highly heterogeneous microstructure of the material, which greatly influences the results of mechanical tests. The deterioration of mechanical properties and the decrease in DP are interrelated, and Kraft was more susceptible than Insuldur paper.

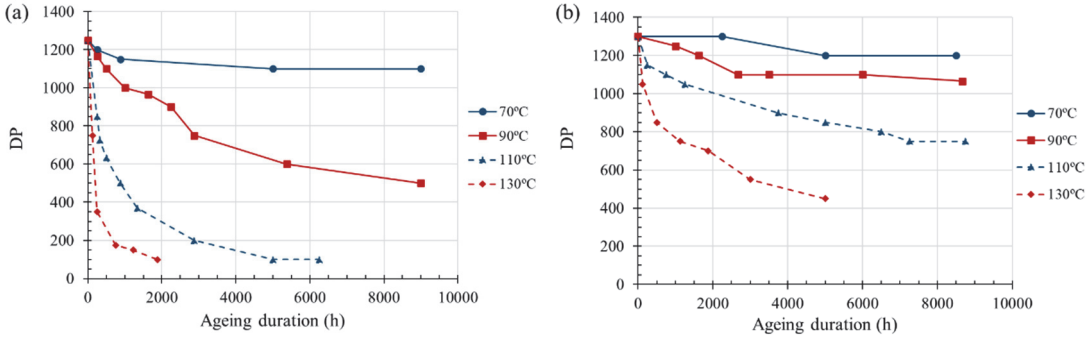

Figure 30. DP value versus time at 3% moisture content (a) for Kraft and (b) for Insuldur papers, based on [16].

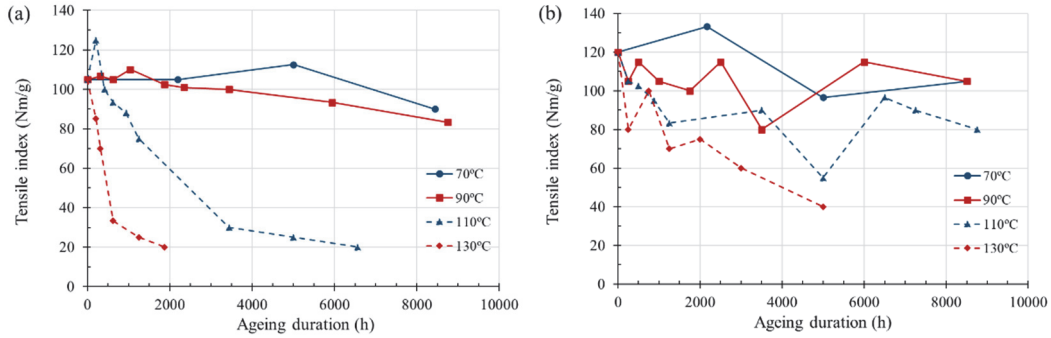

Figure 31. Tensile index versus time at 3% moisture content (a) for Kraft and (b) for Insuldur papers, based on [16].

The rate in the decomposition of cellulose molecules is approximately proportional to the amount of water. Moisture is present at the beginning of the process, but water is also formed by oxidation in the oil and by acid hydrolysis in the paper, increasing the moisture content about 0.5% each time the DP is halved [57]. The variation in the DP of insulation paper samples, with a particular moisture content (1 to 3 %), impregnated with transformer oil, and aged at 90, 110 and 130°C is shown in Figure 32 from [45].

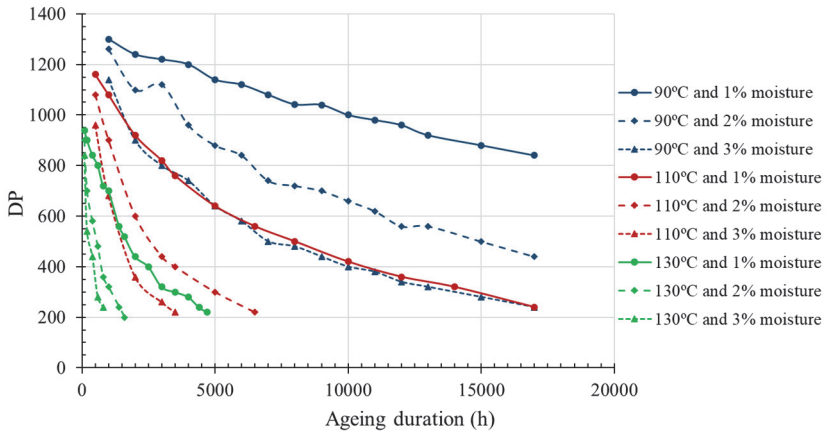

Figure 32. DP as a function of ageing duration at 90°C, 110°C and 130°C, based on [45].

In [33], they developed a non-destructive method capable of local measurement of the DP of aged paper samples taken from a range of transformers and locations on their windings, which combines visible and near infrared diffuse reflectance spectroscopy with multivariate statistical analysis. The DP was predicted with an accuracy of about 30 units in agreement with previous measurements on the same samples using a viscometric method. According to [33], the model can be calibrated to predict the DP of other materials.

Some authors propose an exponential relation for the life-limiting feature of a power transformer depending on the thermal degradation of paper insulation [17], considering temperature, duration of the thermal effect and the extent of ageing. For example, an Arrhenius equation is proposed in [1], which relates the DP with the ageing time, and has been commonly used to model ageing of the paper insulation as a first order process. These equations involve reaction rates or activation energies, which have been analysed in several studies, such as [16], [32], [45], [46], [58].

3.2.2. Tensile strength and its direct and indirect estimation

One of the main mechanical parameters for insulation paper is the tensile strength, which decreases as the paper ages. It is commonly said that the paper insulation reaches its end of life with a 50% retention of tensile strength [42], so the loss of tensile strength provides an end-of-life criterion. The mechanical properties, such as the tensile strength, change more sharply than the electric ones, such as the breakdown voltage. In Figure 33 from [59], the reduction in tensile strength of oil-impregnated cellulosic insulation is shown as a function of ageing time for 140°C, 150°C and 160°C.

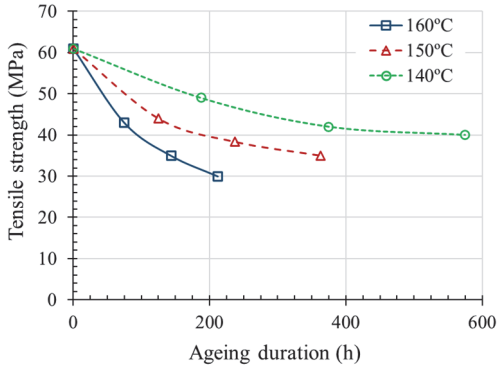

Figure 33. Tensile strength of paper as a function of ageing time and temperatures, based on [59].

As in the measurement of DP, a sample of insulating paper is needed, which makes it unsuitable for operating transformers [15]. To avoid that limitation, some studies try to relate the tensile strength to the production of gases during the ageing of paper materials. There is not a good correlation between CO_2 presence and variation of paper tensile strength [60], because this gas is also produced from oil degradation or even from ingression from the environment. Other researchers consider that the loss of strength can be correlated with level variations in the ratio CO_2/CO. For instance, gas chromatography analysis was used in [59] to measure dissolved gases, as the thermal degradation of cellulose produces CO_2 at low temperature and CO at high temperature. When the ethylene concentration increases, and the CO_2/CO decreases below a ratio of about 6, high rate of paper degradation is expected [15], [43]. At a CO_2/CO ratio less than 2, the probability of failure increases significantly [15]. However, the scatter of measurements performed on service transformers in [43] was so large, see Figure 34, that the transformer service life can only be estimated to within ±10 years based on this phenomenon.

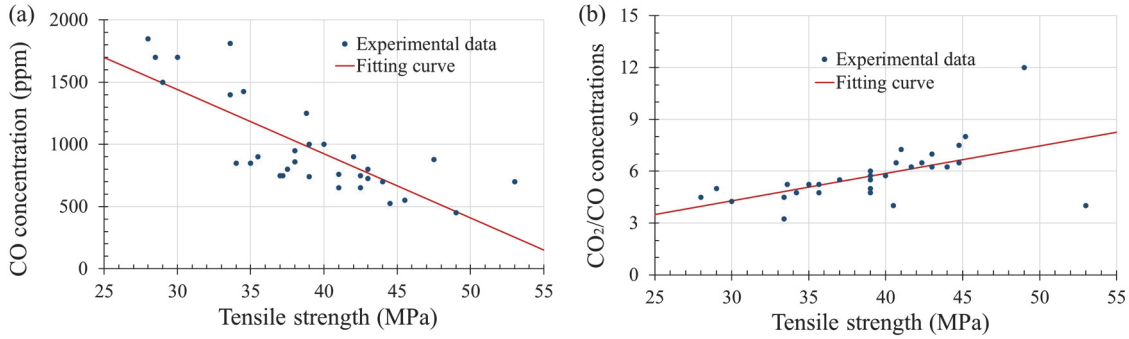

Figure 34. (a) Variation of dissolved CO concentration in oil vs paper tensile strength; (b) Variation of dissolved CO_2 concentration in oil vs paper tensile strength; based on [43].

In [42], the relation between the amount of CO and CO_2 evolving from oil impregnated insulating papers, and the retention of tensile strength, the DP and breakdown voltage strength were studied. Their experimental results were compared with data obtained from insulating papers of transformers with long service life. The content of other gases (such as CH_4, C_2H_2, C_2H_4) in in the insulating oil was also studied, as a function of the duration of the service life (from 0 to 30 years). In [45], CO and CO_2 released due to thermal decomposition of cellulose were monitored throughout the experiment following [61], see Figure 35. When they reached prescribed limiting values, the insulation was considered to have failed.

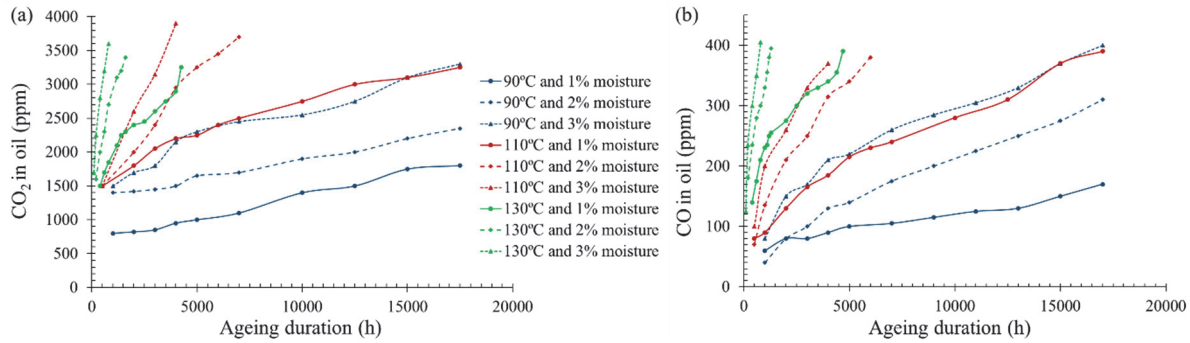

Figure 35. (a) CO_2 (ppm) and (b) CO (ppm) as a function of ageing duration at 90°C, 110°C and 130°C, based on [45].

3.2.3. Furanic compounds

During ageing of the paper insulation, the breaking of the polymer chains generates glucose monomer units that undergo further chemical reactions and become one of a family of derivatives of 2-furaldehyde (2FAL), or what is called furanic compounds, which increase in

the transformer oil with the decrease of the DP of the paper [15]. Furanic compounds are good indicators, especially, of the late stage of paper degradation [62], and are produced from both hydrolysis and pyrolysis, and could also originate from the degradation of pentoses in hemicellulose [63].

Despite both the DP and retained tensile strength tests being reliable methods to assess ageing, the required paper sample limits their practical use in operating transformers. Assessment of the transformer ageing using furanic compounds analysis is growing these days because of its high accuracy without using any paper specimen. Furfuraldehyde has been found to have a strong correlation with the tensile strength and the DP, so empirical relationships have been established to predict them [19]. A linear relationship in logarithmic scale between the total furfural concentration and the DP is commonly accepted [64], see Figure 36. However, the absolute correlation of furanic compounds to DP varies from one transformer to another and depends on humidity, operating temperature, type of oil and paper, and design [9].

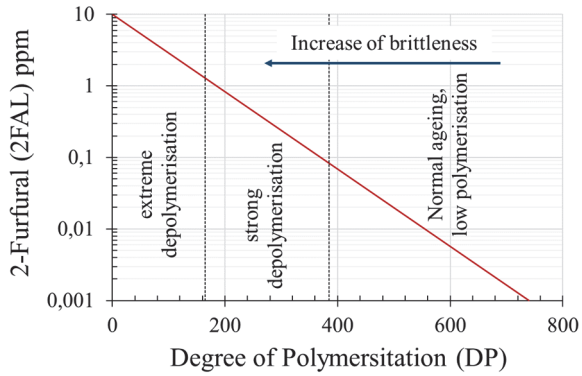

Figure 36. Determination of 2FAL, based on [17].

During the ageing process, when the DP of the paper drops below about 400, the concentration of ageing products in the oil begins to rise exponentially to a maximum value and then decreases, when the paper is fully degraded [32]. The predominant ageing product is always 2-FAL, so the furfural analysis of oil could be particularly useful for the detection of high rates of ageing of paper. For instance, in [45], 2-FAL released due to thermal decomposition of cellulose in Kraft paper insulation was monitored throughout the experiment by high-performance liquid chromatograph, Figure 37.

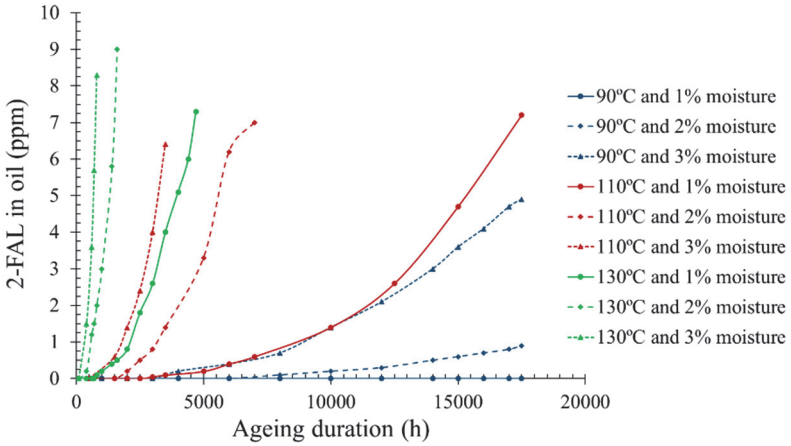

Figure 37. 2-FAL as a function of ageing duration at 90°C, 110°C and 130°C, based on [45].

3.2.4. Methanol and ethanol

Methanol (CH_3OH) and ethanol (C_2H_5OH) in oil were first proposed as indicators for paper ageing in [62], and gas chromatography combined with flame ionisation detection was used to measure them in [65]. Methanol is related to the ageing of cellulose [66], and increases approximately linearly with paper ageing, whereas 2-FAL shows an exponential increase. The production of methanol is higher than the amount of 2-FAL up to a value of the DP of about 400 [67], thus, methanol can be used as an indicator of early ageing state of cellulosic insulation [68]. Furthermore, the measurement of ethanol can be useful as an indicator of abnormal ageing, as it is related with the ageing of levoglucosan, which is a pyrolysis by-product of cellulose ageing [66]. Both methanol and ethanol indicators are stable at transformer working temperatures, but they have some limitations, such as the contributions from components of paper, such as lignin, and from the oil to their generation [60].

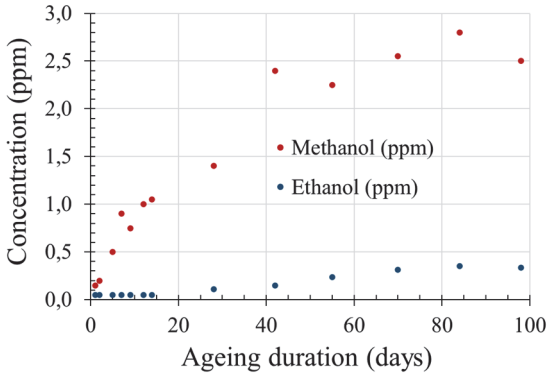

Figure 38. Variation of methanol and ethanol concentration in oil with ageing at 120°C, based on [66].

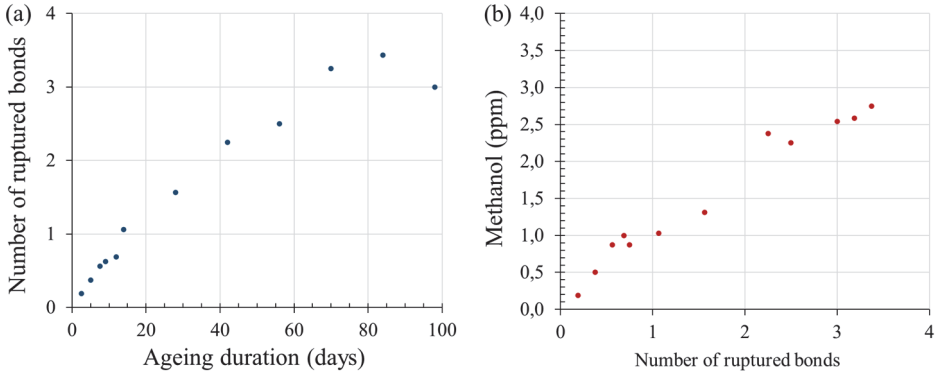

Figure 39. (a) Variation of number of ruptured bonds in paper with ageing at 120°C; (b) Variation of methanol with paper ageing at 120°C; based on [66].

In [66], Kraft paper impregnated in inhibited mineral oil was aged at 120°C inside sealed glass bottles, where CH_3OH and C_2H_5OH in oil were measured through gas chromatography mass spectrometry. Figure 38 shows that methanol rapidly increased during the early stage of ageing, and after that, the increase rate reduced, and the amount of CH_3OH only increased up to approximately 3 ppm at the end of the ageing period. The initial fast increasing rate can be caused by the degradation of weak glycosidic bonds in the amorphous region at the beginning of the ageing process. In the case of C_2H_5OH, the value remains almost constant during the first part of the ageing process, and then increases, but at a substantially lower rate. Figure 39 (a) from [66] shows the variation of the number of ruptured bonds in paper with ageing, which linearly increases during the beginning of the process and reduces to a slower rate at the late ageing stage. Figure 39 (b) shows the linear relationship between CH_3OH in oil and the number of ruptured bonds, indicating that the measurement of CH_3OH could be a useful indicator of paper ageing.

In [60], 2-FAL, methanol and ethanol, moisture content, acidity in oil and tensile strength of the paper were analysed through accelerated ageing tests of Kraft paper with two different types of oil, and the results were compared with the production of those indicators when only oil is aged (without paper). Figure 40 (a) shows methanol and ethanol production, which is similar to the one obtained in [66]. Figure 40 (b) from [60] shows that both CH_3OH and C_2H_5OH increase during the ageing of oil without paper. In the case of CH_3OH, the value at the end of the ageing process is about 10% of the value measured with paper and oil, so it can be considered that the major part of its production was due to the paper. In the case of C_2H_5OH, the value at the end of the ageing process is similar with paper and oil and only with oil, suggesting that the oil ageing produces ethanol, and its production depends on the oil type.

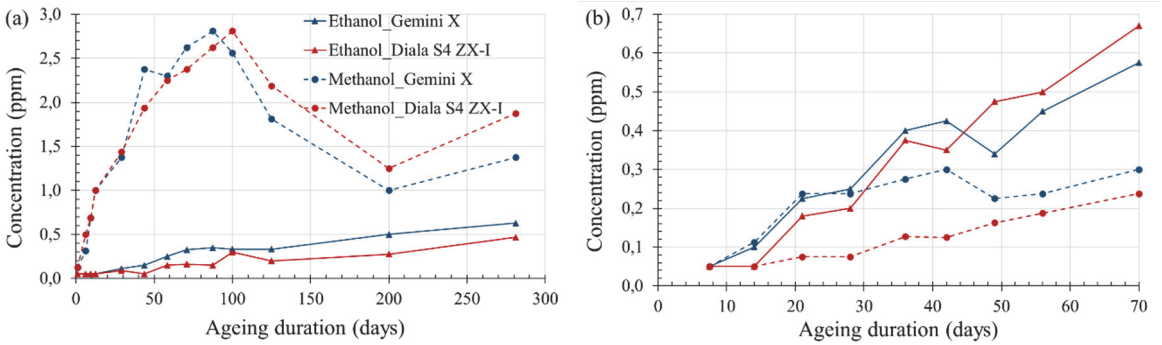

Figure 40. Variation of methanol and ethanol in oil during the ageing at 120°C with (a) oil and paper and (b) oil only samples, based on [60].

3.3. Insulating liquids, their ageing and their interaction with the cellulosic insulation

It is generally considered that the operating life of a transformer is determined by the mechanical strength of the insulating paper wrapped around the windings and it lasts until it can no longer withstand the electromagnetic forces generated by a short circuit. However, transformers used at substations are generally operated under a relatively low load and, therefore, the life of the insulation may be prolonged, making it necessary to consider the influence of degradation of the insulating liquid [69], which typically is mineral oil. Chemical reactions cause the deterioration of several characteristics of that oil, such as its volume resistivity and its dielectric loss tangent [69].

In contrast to water, due to the hygroscopic nature of the cellulose chains, oxygen is predominantly present in the oil and considerably accelerates its ageing, producing oxidation and cleavage of oil molecule bonds [18]. The principal oxidation products are acids, solid constituents (sludge), water, CO_2, CO and scarcely measurable amounts of CH_4. The degradation process of oil is further promoted by dissolved metals with catalytic effects, such as iron and copper. The mechanism of decomposition of oil molecules produces other reactive substances, which make that it continues even when there is a deficiency of oxygen [18].

In [69], the changes in the characteristics of mineral oil samples, as well as the interactions between them, were examined after heat-accelerated degradation tests. Water content, breakdown voltage, volume resistivity, total acid value, and interfacial tension showed a significant deterioration for 10 days of accelerated ageing (equivalent to 10 years of natural ageing) and, except for the total acid value, they also showed a saturation tendency thereafter. Water content appeared to be the major cause for the decrease of the breakdown voltage [69]. After 30 days of heating, the total acid value and the water content showed similar trends. Since the total acid value shows the progress of oxidative deterioration of components in insulating

oil, it was considered to vary depending on the oxygen supply. The volume resistivity was qualitatively dependant on the presence of ionic substances, such as water. However, other results show that, depending on the concentration of ionic substances in the oil, the correlation with the water content may not become obvious, and the volume resistivity also depended on the interfacial tension [69].

In [70], various components detected in transformers subjected to natural ageing, which potentially influence the insulating oil, were added to the base oil to measure some parameters (water content, acidity, interfacial tension, breakdown voltage, dissipation factor, and volume resistivity). Sulfoxides and sulfones produced through the oxidation had an insignificant influence on the degradation of the characteristics of insulating oil. The addition of *organic acids* slightly increased the acidity value. Among organic acids, decanoic acid produced a significant decrease in volume resistivity. Adding *methyl ethyl ketone*, or a kind of ketones, to the oil sample produced a significant decrease in the dissipation factor and volume resistivity. For oil with *aromatic series* added, even though cinnamaldehyde degraded some characteristics, the overall influence on various characteristics was minor. In the case of oil with *phthalate compounds* added, the dissipation factor and volume resistivity degraded when the water content was increased.

Furthermore, it is essential to understand the interaction between the insulating liquid and the cellulosic materials in power transformers. The dielectric strength of paper and board impregnated with oil is considerably above that of either components and greatly depends on the quality of the impregnation. In fact, one of the purposes of the cellulosic material in the combination is to split the oil into minute gaps, or extremely thin oil spaces between fibres and sheets, whose dielectric strength is much higher than that measured between thick-layers of the same oil [1]. As the permittivity of the oil is lower than that of the paper, it takes the greater share of the electric stress. The dielectric strength of oil-impregnated paper insulation of new transformers is 200 to 400 kV/cm, and its permittivity is about 3.5 [1].

There are several studies where the interaction between different insulating liquids, some of them natural esters, and the cellulosic insulation is analysed. For instance, in [36], the ageing of high-density pressboard in nine different insulating liquids was studied: four vegetable oils, one synthetic ester (pentaerythrit ester), one isoparaffinic (isoparaffinic, trace inhibited) and three naphthenic mineral oils (naphthenic, top grade, trace inhibited; naphthenic, standard grade, non-inhibited; naphthenic, medium grade, inhibited). The pressboard samples were aged at 120, 135 and 150°C for up to twelve months and, to simulate the load cycles in a real transformer, the oil was cooled to about 80°C for two hours each day. The water content in the oil was measured weekly during 8 months of ageing at 135°C, Figure 41. With mineral oils, the water content increased steadily throughout the experiment while, with the esters, it started to decrease significantly after four months. The cause is that, at high temperatures and water concentrations, the ester liquids consumed some of the water by hydrolysis. A clear correlation exists between the reduced ageing rate and this reduction in water content.

Figure 42 from [36] shows that the decrease in the DP of pressboard was in the same range when aged in mineral oil as in ester liquids, and only the experiments with long times and/or high temperatures gave a considerably higher degradation in mineral oil. The increase of the conductivity, Figure 43 (a), correlates very well with the increase of the water content in the pressboard. The breakdown voltage of the mineral oils aged for two and four months at

150°C was only about 25% of the initial value, Figure 43 (b), because it was strongly influenced by the amount of free water. Hydrolysis of esters produced longer chain fatty acids, and further investigation is required to determine whether these acids have detrimental effects on other transformer materials at higher concentrations [36]. The different qualities of the mineral oil did not reveal substantial differences of the pressboard ageing rate.

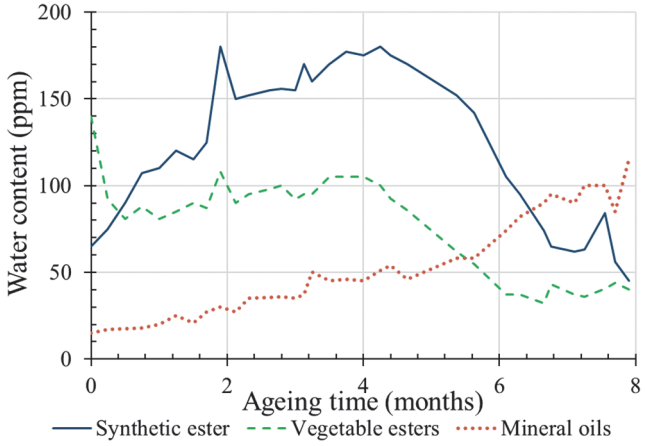

Figure 41. Average water content of insulating liquids, based on [36].

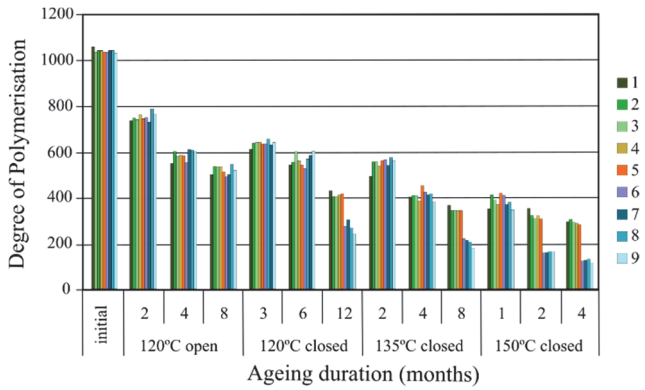

Figure 42. Degree of polymerisation of pressboard, based on [36]. *Liquids 1-4 are vegetable esters, liquid 5 is a synthetic ester, and liquids 6-9 are mineral oils.*

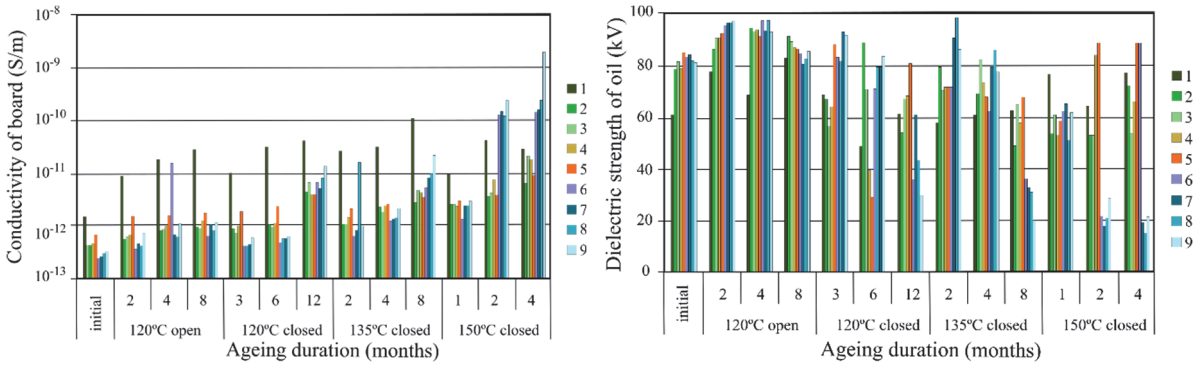

Figure 43. (a) Conductivity of pressboard; (b) Dielectric strength of liquids; based on [36].

An analogous variation in DP and the sudden decrease in water content with the ester were also accounted by [71], where dielectric paper and high-density board were impregnated in mineral oil, natural ester or synthetic ester and aged at 130°C up to 1128 h. Although natural ester produced more soluble acids than the other fluids, they were not damaging for the paper. In [72], paper was impregnated in mineral oil, natural or synthetic ester fluids, and aged at 100°C up to 3100 hours. The increase in dissolved decay products at the end of the ageing process was around 5-7 times higher with mineral oil than with the synthetic ester.

Samples of Kraft paper impregnated in mineral oil and in a newly developed ester fluid, called PKOAE, were aged in [37], and their real and imaginary capacitances and tan δ were measured, at about 60 Hz and 20°C. The variations in tensile strength were also compared, Figure 44 (a), and after 84 days at 150°C, the reduction was 64.6% for mineral oil and only 10.8% for ester-impregnated paper. The degradation rate was slower with the natural ester [37], because it had stronger affinity for water than mineral oil, so the water generated during pyrolysis was absorbed by the ester. The breakdown voltage was analysed using a Weibull distribution function, and it was approximately 42% higher for the ester-impregnated paper and remained almost constant during ageing, Figure 44 (b).

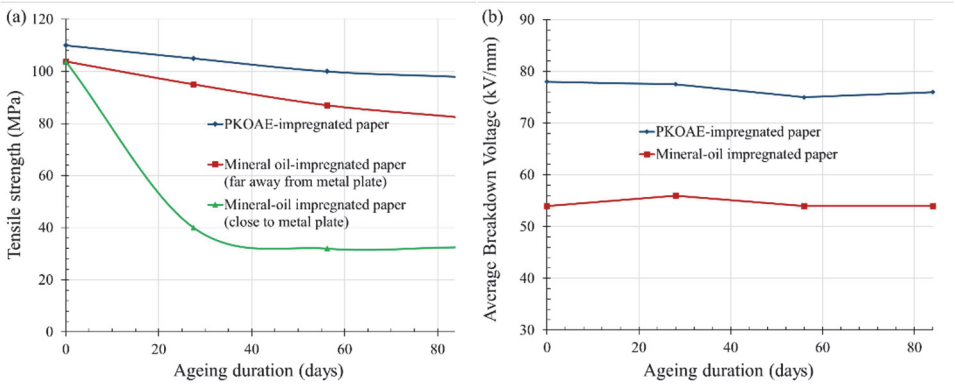

Figure 44. (a)Tensile strength of oil-impregnated paper and (b) average breakdown voltage as a function of ageing duration, based on [37].

Samples of Kraft paper were impregnated in different vegetable oils (palm oil, corn oil, and rice bran oils) and in mineral oil and aged at 90°C in [73]. After the ageing, electrical, mechanical and chemical properties were measured and compared. AC breakdown voltage increased in the first 90 days of ageing duration for all vegetable oils, and did not significantly change for mineral oil, Figure 45 (a). After 180 days of ageing, the samples impregnated in corn oil showed a reduction of AC breakdown voltage. The relative permittivity, Figure 45 (b), was higher with vegetable oils (between 1.8 and 2.0) than for mineral oil (between 1.38 to 1.50) during all the ageing duration. The increase in water content due to cellulose decomposition leaded to the increase in the real part of the relative permittivity of vegetable oil, while there was no significant change in the relative permittivity of mineral oil.

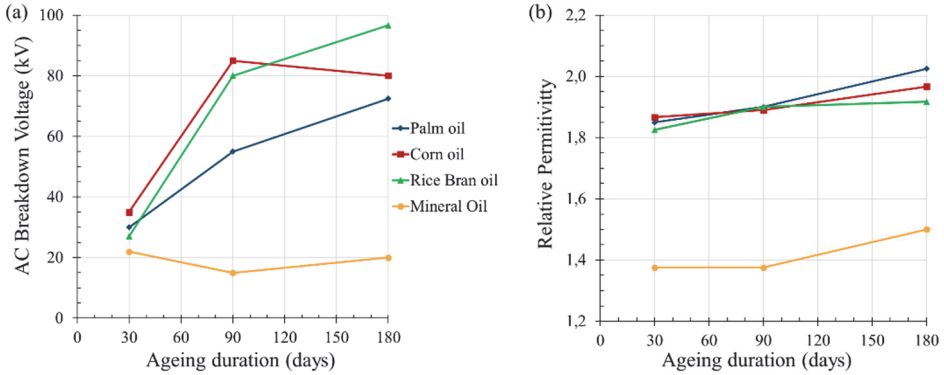

Figure 45. (a) Average AC Breakdown voltage of oil-impregnated paper and (b) relative permitivitty as a function of ageing duration, from [73].

The dielectric losses of all tested oils slightly increased with ageing at 90°C from 30 days to 180 days, and they were higher for vegetable oils than for mineral oil, Figure 46 (a). The resistivity of mineral oil was higher than that of vegetable oil, Figure 46 (b). The variation in the highest reduction of tensile strength of the paper was not significantly different, Figure 47 (a), (about 25.5% in rice bran oil, about 24. 7% in palm oil, 20.7% in mineral oil and 16.2% in corn oil). The moisture content, Figure 47 (b), was between 1200-1500 ppm in vegetable oils

after 30 days and was reduced to 500-600 ppm after 180 days of ageing. The moisture in mineral oil remained very low throughout all the ageing time.

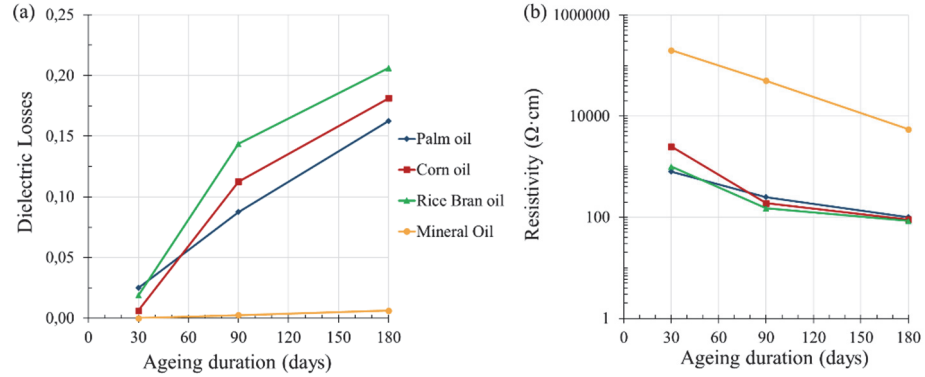

Figure 46. (a) Dielectric losses and (b) resistivity as a function of ageing time, from [73].

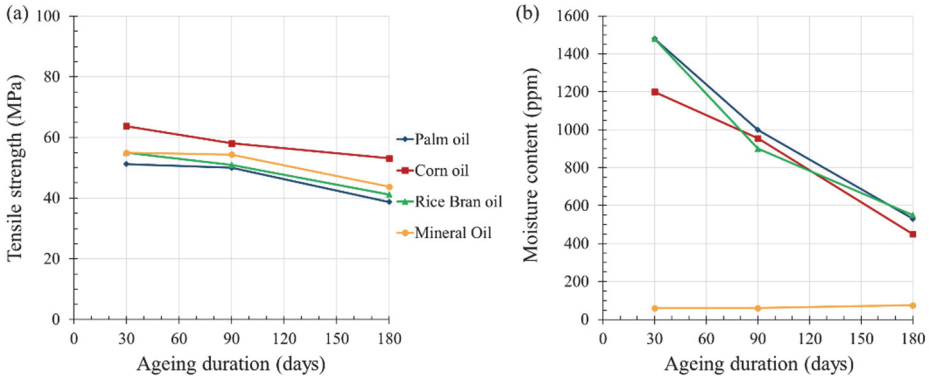

Figure 47. (a) Tensile strength of the paper and (b) moisture in oil as a function of ageing duration, from [73].

In [74], standard and thermally upgraded Kraft paper were impregnated in synthetic dielectric ester or mineral oil and aged at 150°C, and the variation in DP was similar in all cases up to around 1000 hours of ageing. After 2000 hours, the decrease was more severe with the mineral oil, and the thermally upgraded paper degraded more slowly. The paper tensile index (tensile strength divided by the grammage) was around 15% higher when impregnated in synthetic ester. In the last period of ageing, a linear correlation independent of the type of oil, paper and ageing temperature was obtained between the tensile index and the DP. In [75], a vegetable oil derived from karanji was presented as an alternative to mineral oil. The variation on thermal conductivity due to temperature (from 25-70°C) was compared, and it was, respectively, around 22% and 17% higher for new and aged vegetable oil than for new and aged mineral oil. The AC breakdown voltage of the new and aged vegetable oil was, respectively, 129% and 165% higher than that of mineral oil.

Fresh and thermally aged Kraft paper samples, impregnated with mineral oil or with exfoliated hexagonal boron nitride based nanofluid (Eh-BN/MO-NF), were prepared in [76] and the AC breakdown voltage was measured following [77]. The duration of the ageing decreased the dielectric integrity of the material. A Weibull analysis of the instants of breakdown was used for the breakdown probability, and a voltage between 8-15 kV was related with a probability of failure of 5% for the mineral oil-impregnated paper, while values between 9-13 kV were obtained for the nanofluid-impregnated paper. The tensile strength of the nanofluid-impregnated paper suffered less degradation than with the mineral oil, Figure 48, due to a lower moisture absorbance. After 2000 hours of ageing, the mechanical strength was 25% higher with the nanofluid.

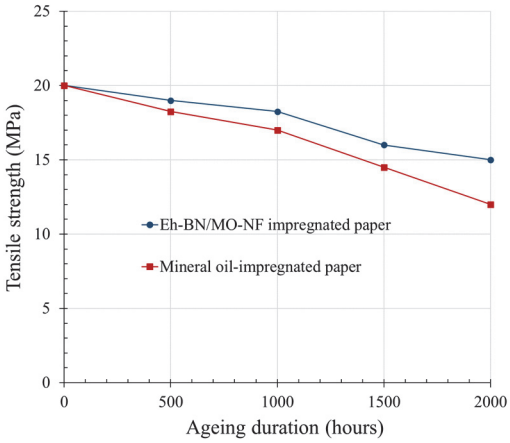

Figure 48. Tensile strength of impregnated paper as a function of ageing duration, based on [76].

4. Short-circuit currents, electromagnetic forces and mechanical stresses in power transformers

4.1. Short-circuit phenomena in transformers

4.1.1. Introduction

The continuous rise in the demand for electrical power by modern societies, has increased the need for generating capacity and interconnections in electrical systems [31]. Because of that, the short-circuit conditions, which are system disturbances that generally produce high-magnitude currents [14], are more severe these days, and the failure of power transformers can have very detrimental consequences for the electrical system. Manufacturers and the electric utility make continuous efforts to improve the performance of power transformers in short-circuit conditions, which must have strength to avoid mechanical collapses in the windings, deformations or damage of clamping structures, or other internal faults [31].

Figure 49. Strokes of lightning on transmission lines is a frequent cause of insulation breakdown, from [14].

There are different types of faults which result in high overcurrents, such as single-phase-to-earth, double-phase with or without a simultaneous earth fault, and three-phase short circuits, with or without a simultaneous earth fault [14]. In high-voltage systems, the most probable type of short circuit is a single-phase-to-earth flashover, generally produced by environmental conditions, equipment failure or failure in the insulation. The relative severity of the different types of faults depends on several factors [14], such as the short-circuit apparent power, ratios between the different internal impedances of the transformer, voltage sources in the terminals, etc. Sometimes, a fault can develop into a more extensive one, and those evolutive short circuits can have higher short-circuit peak currents than the non-evolutive faults [14]. In the majority of cases, the symmetrical three-phase fault, in which the

fault currents are confined to the line conductors only [14], is the most severe one [31]. In a transformer whose input side is supplied at rated voltage and whose output side is short-circuited, the magnitude of currents flowing in its primary and secondary windings depends on its short-circuit impedance, and can be between 8 to 10 times the rated current in larger transformers, and 20 to 25 times in the smaller ones [1].

Assuming a sinusoidal feeding voltage $u\ (t) = \hat{u}\ sin\ (\omega t\ )$ the short-circuit current time history, $i_K(t)$, can be described by equation (30) from [14], with the resistance R, inductance L, and voltage phase angle α. The short-circuit current, $i_K(t)$, has a sinusoidal component and an exponential evanescent component:

$$i_K(t) = \hat{I}_K \left[\sin(\omega t + \alpha - \varphi) - e^{-\frac{t}{\tau}} \sin(\alpha - \varphi)\right] \tag{30}$$

Where:

$$\hat{I}_K = \frac{\hat{u}}{\sqrt{R^2 + (\omega L)^2}}, \tan\varphi = \frac{\omega L}{R}, \tau = \frac{L}{R} \tag{31}$$

For power transformers, the inductance of the coils is usually much higher than the resistance ($L \gg R$), which leads to $\varphi = \pi/2$. To calculate the maximum short-circuit current with this simplification, two special cases shall be distinguished:

- The voltage phase angle, α, equals the angle $\varphi = \pi/2$ of the short-circuit impedance, meaning that the short circuit appears with the maximum voltage. In this situation, the maximum short-circuit current is the steady state short-circuit current, $\hat{I}_K$:

$$i_{K,max} = \hat{I}_K \quad for \quad \alpha = \varphi = \pi/2 \tag{32}$$

- If the short circuit appears during a voltage zero-crossing, $\alpha = 0$, the maximum short-circuit current reaches twice the steady state short-circuit current, $\hat{I}_K$:

$$i_{K,max} = 2 \cdot \hat{I}_K \quad for \quad \alpha = 0, \varphi = \pi/2 \tag{33}$$

As a result of the interaction between the leakage field of the shorted winding system and the current flowing in the turns, short-circuit forces will act on the turns of the windings. These short-circuit forces are proportional to the square of the short-circuit current, so the electrodynamic forces arising during a short circuit may be as high as ten thousand to a million newtons as compared to the few newtons associated with normal operating conditions [1]. The phase position of voltage prevailing at the instant of the short circuit and the time constant of the short-circuit loop determine the maximum short-circuit current and force, and the forces acting on the turns and windings after the first current peak keep the windings and their clamping structures in oscillation at double the network frequency until the short circuit is interrupted [1]. The winding structure should be dimensioned to prevent permanent deformations and movements produced during short circuits.

In the period between the occurrence and clearing of the fault, which usually does not exceed a second, most of the heat developing in the conductor material does not leave the winding but raises its temperature, during a time constant of several minutes [1]. That rise in the winding temperature should not exceed the limit that the insulating materials are capable of withstanding for such periods of time. During short circuits, both mechanical vibration of windings and thermal expansion of the conductors take place simultaneously [1]. The relative

displacements between wire insulation and other components may also injure the insulation, leading to turn faults. These hazards can be avoided by proper dimensioning of windings in accordance with thermal and dynamic criteria, and by pre-compressing the winding system with a force corresponding to the electrodynamic effects of short circuits and firm clamping of current-carrying component parts.

4.1.2. Typical cases of short circuits

According to [14], there are two typical cases of short circuit in power transformers:

- **Two-phase short circuit with two-winding transformers and various winding connections:**

In this type of short circuits, the voltage across each of the two winding phases affected by the fault is $\frac{\sqrt{3}}{2}$ times the rated voltage, and the short-circuit currents will be reduced by the same quantity with respect to the three-phase short-circuit case.

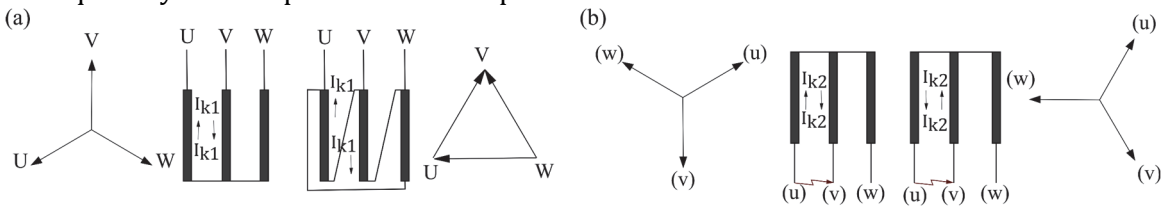

Figure 50.Two-phase short circuit in a three-phase transformer with (a) star/delta winding connection or (b) star/star winding connection, based on [14].

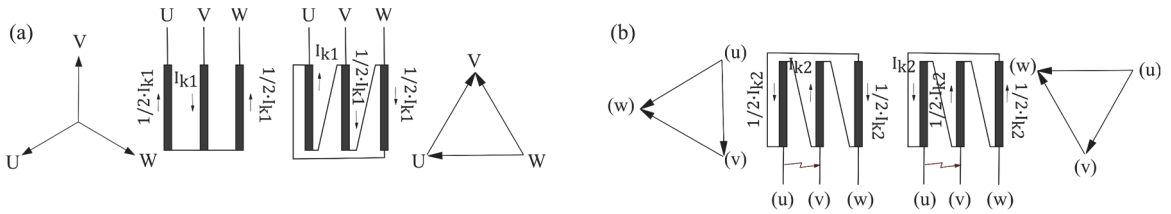

Figure 51. Two-phase short circuit in a three-phase transformer with (a) star-delta winding connection or (a) delta/delta winding connection, based on [14].

- **Single-phase short circuit with three-winding transformers and star/star/delta connection:**

In this case, the magnetomotive force affecting the faulty star-connected phase is balanced by the magnetomotive forces generated by the currents flowing through both primary and delta-connected windings, which are affected by a current that circulates within the delta loop, Figure 52 [14].

The calculation of short-circuit currents is generally based on several simplifications which are valid in most cases. These are that the topological configuration remains constant during a short circuit; only the linear and series branches of the equivalent circuit of the involved component are considered; and the symmetrical short-circuit current can be determined only from the steady-state AC analysis [14]. The method of symmetrical components is used for the study of unbalanced short circuits, and the peak short-circuit current is calculated with the simplification of adding a decaying aperiodic component with a time constant to the steady-state short-circuit current [14]. It is assumed that the magnetomotive forces in the windings are always balanced in the same phase. There are also some special faults in which the topological configuration can change in the interval of time needed to clear the fault, and the peak current can be higher than the one calculated for time-invariant short circuits. It is also possible that a significant unbalance in magnetomotive forces affects the axial electromagnetic forces on the windings of core-type transformers [14].

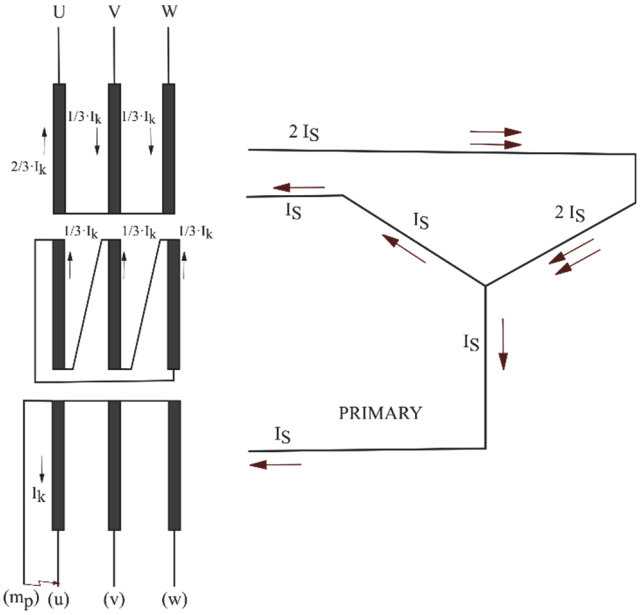

Figure 52. Single-phase short circuit affecting a star-connected winding, based on [14].

4.2. Electromagnetic forces in transformers

4.2.1. Determination of the electromagnetic forces in power transformers

The transient temperature rise in the windings does not represent a serious problem for the power transformer, but the electromagnetic forces that arise, from the linear interaction of winding currents and magnetic leakage flux, are a severe mechanical challenge [14]. These pulsating forces depend on radial and axial magnetomotive force distributions, and asymmetries and displacements of the windings. As the density of the leakage flux is proportional to the currents in the windings, the electromagnetic forces are proportional to the square of the values of the currents, which can be between 10-20 times the rated current in short-circuit conditions. Consequently, electromagnetic forces during short circuits can be multiplied by a factor of 100-400 times the rated forces under normal operating conditions [14]. A mechanical collapse of the winding due to the effect of these forces can produce an electrical fault in the transformer.

A current, I, flowing through a wire and placed in a homogeneous fraction of space would produce a magnetic flux with a determined density around the wire. The differential magnetic flux density at a point, dB_P, produced by a differential length of current, dl, can be obtained according to equation (34), see Figure 53 (a).

$$dB_P = \frac{\mu_0 \cdot \mu_r \cdot I \cdot \cos\alpha \cdot dl}{4\pi^2 \cdot r^2} \tag{34}$$

Where:

dB_P $(T = Wb/m^2)$: Differential flux density at P due to current element $I \cdot dl$.

μ_0 (H/m): Absolute permeability of vacuum, which is $1{,}256 \cdot 10^{-6}$ H/m.

μ_r: Relative permeability of the medium.

I (A): Current.

α: Angle between the distance r and the normal to the element current.

dl: Differential length of the current element.

r (m): Distance from the current element to the point P.

The elementary electrodynamic force acting on an element which is carrying current I (A), with an elementary length $\overline{dl}$, placed in a magnetic field of flux density $\overline{B}$ (T), when α is the

angle between the flux density vector and the current element vector, is given by equation (35). The direction of the electromagnetic force is given by the advance of a right-hand screw if the current is pictured as rotated into the magnetic field, Figure 53 (b).

$$\overline{dF} = I\bar{dl} \; x \; \bar{B} \qquad F = I \cdot l \cdot B \cdot \sin\alpha \tag{35}$$

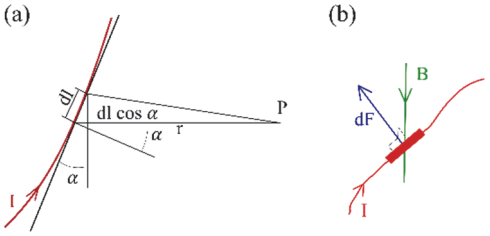

Figure 53. (a) Geometric relationship for the determination of the differential magnetic field intensity at point P produced by a differential element of current dl;(b) Electromagnetic force generated by the interaction between current and magnetic flux, based on [14].

In a power transformer, the windings are surrounded by the leakage or stray flux, and they are the elements carrying current as a result of the electric power which is transferred from the primary source to a secondary load. As a consequence, electromagnetic forces are generated [14]. The distribution of the magnetic leakage flux depends on the geometric characteristics of the core and windings of the transformer, as well as on the relative permeability of the materials. The leakage flux density at various locations in the transformer depends on the reluctance of the air path and is proportional to the magneto-motive force $N \cdot I$ acting in the circuit [14]. The magnetic flux density vector is perpendicular at any point to the current density vector, with the exception of small particular regions of the windings.

The electromagnetic forces depend on the square of the current. If the current is purely sinusoidal, the forces consist of a steady state component with constant amplitude and an alternating component at double frequency. Electromagnetic forces have a repulsive effect between pairs of windings carrying current with opposite directions, and an attractive effect between pairs of windings with equal current direction. According to [14], the force produced by a short circuit follows equation (36), where F^*_{max} is maximum peak force:

$$F^*(t) = F^*_{max} \cdot \left(\frac{1}{2} + e^{\frac{-2 \cdot t}{\tau}} - 2 \cdot e^{\frac{-t}{\tau}} \cdot \cos\omega t + \frac{1}{2} \cdot \cos 2\omega t\right) \tag{36}$$

It can be seen in equation (36) that the electromagnetic force depends on two unidirectional components (one constant and the other decreasing with time), and on two alternating components (one of fundamental frequency decreasing over time, and the other at double frequency with a smaller constant amplitude). Because of the unidirectional component of the current, the value of the force peak is considerably reduced with the number of cycles [14], see Figure 54. Furthermore, it is important to consider that electromagnetic forces are only one of the total forces applied to the conductors during a short circuit, and other forces are due to: gravitation, inertia of conductors, elasticity of insulation materials and winding supports, friction between conductors and insulation, internal solid and viscous damping and hydrodynamic effects of oil motion [14].

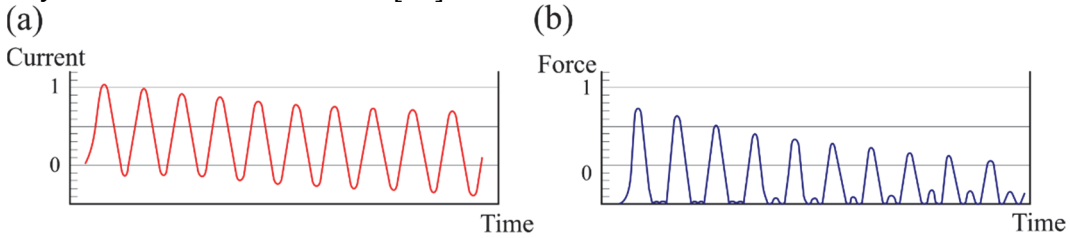

Figure 54. (a) Short-circuit current and (b) electromagnetic force as a function of time, based on [14].

The following electromagnetic forces have to be considered in the different types of power transformers, according to [14]:

- **In core-type power transformers:**

Through the windings, a high current density and a high leakage flux are present, and the force density vector can be expressed according to: $\overline{f(t)} = \overline{J(t)} \times \overline{B(t)}$. If a cylindrical coordinate system is used in core-type power transformers, such as in Figure 55, the current density vector only has a component in winding direction, $\overline{J_\varphi(t)}$, and the windings of the power transformer are only subjected to forces in radial, $\overline{f_r(t)}$, and axial direction, $\overline{f_z(t)}$, [31].

$$\overline{f_r(t)} = \overline{J_\varphi(t)} \times \overline{B_z(t)} \qquad \overline{f_z(t)} = \overline{J_\varphi(t)} \times \overline{B_r(t)} \tag{37}$$

It is usual and appropriate to separate the effect of electromagnetic forces into their radial and axial components [14], since $f_r(t)$ and $f_z(t)$ lead to different kinds of stresses and modes of failure. Radial forces produce circumferential compression on inner windings and tension on outer windings. Axial forces add up from both ends toward the centre [14], so the maximum value appears in layer windings, producing compression on both windings. Any axial imbalance in magnetomotive forces produces thrusts on the windings. In core-type transformers with concentric windings, the predominant force has a radial direction, and the axial component is not significant over approximately 2/3 of the total winding length. However, near the winding ends, the magnetic leakage field lines diverge and the component of the force in axial direction is more important [14].

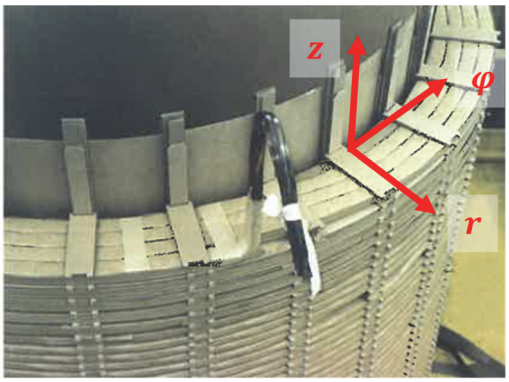

Figure 55. Cylindrical coordinate system of a core-type transformer with disc-type windings.

- **In shell-type power transformers:**
  - Axial forces act perpendicularly to the pancake coil surfaces and tend to increase the gap between windings with opposite magnetomotive forces. In these windings, the compressive forces acting on the spacers are the greatest [14].
  - Radial forces act in the plane of the pancake coils, especially at their contours.

In shell-type transformers, the forces are mainly perpendicular to the pancake coil surfaces and, at the end of the coils, parallel to the pancake coil surfaces. In core-type transformer with concentric windings the radial forces are one order of magnitude larger than axial ones, and the opposite phenomenon can be appreciated in shell-type transformers [14].

4.2.2. Radial and axial electromagnetic forces in core-type transformers

Regarding the disposition of a couple of windings with a uniform axial magnetomotive force in a core-type transformer, three different cases can be distinguished [14], and their axial and radial component of leakage flux density, as well as their integral curve of radial flux density along the HV windings, can be seen in Figure 56:

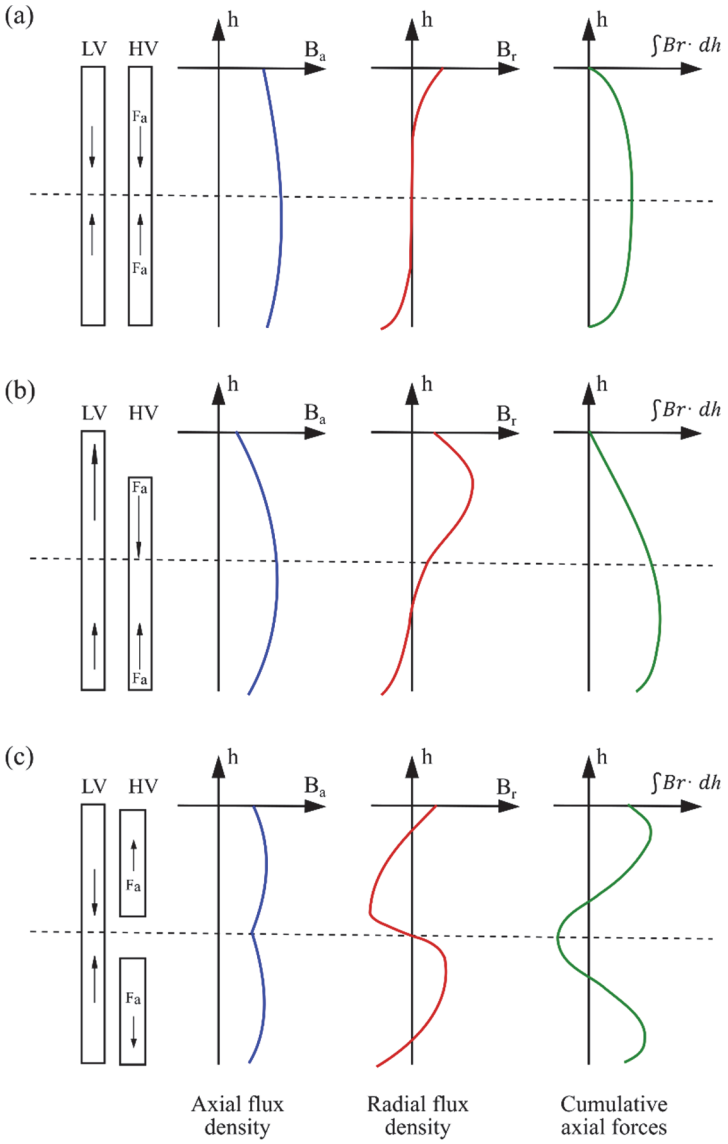

Figure 56. Axial component of leakage flux density, B_a, radial component of leakage flux density, B_r ; and integral curve of radial flux density, based on [14].

- Windings of equal heights aligned at both ends, where the total axial force acting on the conductors is proportional to the area inside the integral curve.
- Windings with lower ends in line and HV winding shorter than LV winding, where the radial component of flux density which affects the outer (HV) winding is larger for the upper part of the winding, and the outer winding is subjected to an axial thrust directed towards the bottom end. By reaction, the inner (LV) winding is subjected to an opposite axial thrust.
- Windings with both ends in line with a gap in the HV winding centre.

- **Radial forces in windings of equal heights aligned at both ends:**

In Figure 57, the conductors close to the main duct between windings are affected by a higher radial force per unit length, and radial forces decrease linearly up to zero in the inside of the inner winding and in the outside of the outer winding [14]. The force pattern causes that a certain amount of force is transferred from the most loaded to the less loaded conductor [14]. The radial forces act outwards on the outer winding, tending to stretch it, producing a tensile stress; whereas the inner winding experiences radial forces acting inwards tending to collapse or crush it, producing a compressive stress [31]. If there are more than two windings, the

direction of the radial force will be the same in the innermost and outermost ones, and will depend on the relative position between the coil and the magnetomotive diagram in the other windings [14].

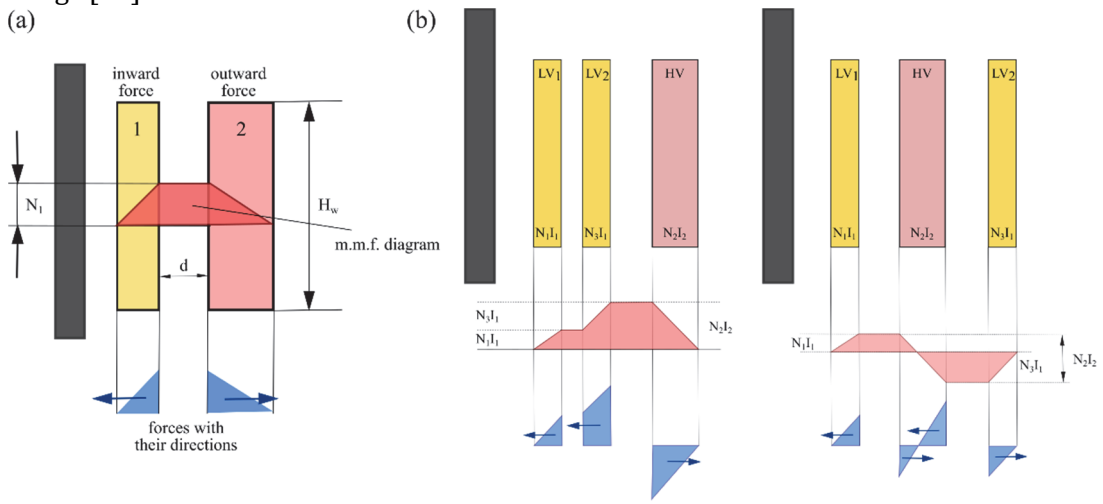

Figure 57. Diagram of magnetomotive force and axial magnetic flux density for (a) a two-winding transformer, (b) in a two-winding core-type transformer with radial-split winding arrangement; based on [14].

In the case where there are two windings, the magnetomotive diagram is trapezoidal and the value of the leakage field increases from zero at the outside diameter to a maximum at the inside diameter. The maximum value of flux density in the gap is approximately given by equation (38):

$$B_{max} = \frac{\sqrt{2}\mu_0 N I_r}{H_w} \tag{38}$$

Where:

μ_0: Permeability of vacuum.

N: Number of winding electrical turns.

I_r: R.m.s. value of the winding rated current.

H_w (m): Winding height.

The average total radial force acting on a winding with a mean diameter of D_m (m) is calculated by equation (39) from [31], which assumes that the winding conductors share the load almost uniformly:

$$F_r = \left[\frac{1}{2}\frac{\sqrt{2}\mu_0 N I_r}{H_w}\right] \cdot \sqrt{2} N I_r \cdot \pi D_m = \frac{\mu_0 (N I_r)^2}{H_w}\, \pi D_m \; (N) \tag{39}$$

Under short-circuit conditions, the first peak amplitude is $k \cdot r$ times higher than the peak value of the rated current, where r is the over-current factor and $k = 1 + e^{-\pi \cdot R/X}$ is the asymmetry factor [14], so the total radial force for the whole winding during a short circuit is:

$$F_r{}^* = \frac{\mu_0 (N I_r)^2}{H_w}\, \pi D_m r^2 k^2 \; (N) \tag{40}$$

- **Axial forces in windings of equal heights aligned at both ends:**

In a core-type power transformer where the windings have equal heights, a uniform magnetomotive distribution, and are radially aligned, the axial forces are mainly directed from the winding ends, where their value is maximum, towards the middle of the coils. However, the total compressive force, which is cumulative, is maximum at the middle of each winding [14]. In a transformer that consists of two windings with the same height, the inner one (usually at

LV) is subjected to a higher axial force because of the leakage flux distribution, Figure 58 (a), (b). In three-phase transformers, there is a mutual influence on the leakage flux between windings of adjacent limbs, and the middle limb is subjected to higher axial forces [14].

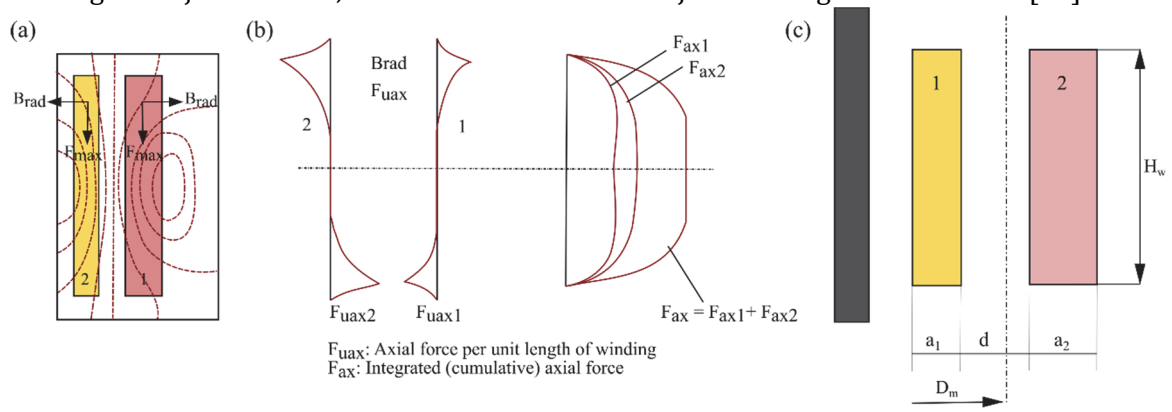

Figure 58. (a) Pattern of leakage flux lines; (b) axial force per axial length of the windings; (c) two-winding core-type transformer arrangement, based on [14].

The approximate formulas giving the total axial force per limb are less rigorous than the ones giving the radial force, according to [14]. This axial component is unequally distributed between the outer and inner windings, due to the presence of the core: the axial force arising in the inner winding is about 65 to 75% of F_a, whereas the force acting on the outer winding is, correspondingly, only 35 to 25% of F_a [31]. This axial resultant force is influenced not only by the vicinity of the core but also by its distance from the tank, the presence of metallic structural parts and the arrangement of adjacent windings. Considering a two-winding core-type transformer, such as the one in Figure 58 (c), the resultant of the axial forces arising in the short-circuit primary and secondary winding is:

$$F_a = F_r \left(\frac{a_1 + a_2}{3} + d\right)\frac{1}{l_s} = \frac{\mu_0 (N I_r)^2}{H_w}\,\pi D_m \left(\frac{a_1 + a_2}{3} + d\right) \tag{41}$$

Under short-circuit conditions, the approximate axial force will be given from equation (42) from [14], where K is the Rogowski factor, given in equation (43):

$$F_a{}^* = F_r{}^* \left(\frac{a_1 + a_2}{3} + d\right)\frac{1}{l_s}\,(2\mathrm{K} - 1) \tag{42}$$

$$\mathrm{K} = 1 - \frac{d + a_1 + a_2}{\pi H_w} \qquad valid\ if\ \frac{d + a_1 + a_2}{\pi H_w} \leq 0{,}25 \tag{43}$$

The sum of axial forces is one order of magnitude lower than the radial force on a single winding. The stresses produced by axial forces under short-circuit conditions depend on the reactive power absorbed in those conditions, whereas the radial stress basically depends on the absorbed active power, according to [14].

- **Radial and axial forces in asymmetrical windings:**

The short-circuit forces arising in windings with unbalanced ampere-turns of transformers tend to increase the existing asymmetry [31]. In ideally symmetrical windings (with fully balanced ampere-turns) the axial forces tend to compress the winding and are in equilibrium with each other, exerting no force on structural parts outside the windings. In cases of asymmetry, the resultant axial force causes a mechanical stress on other structural components as well, such as in the clamping structure [14]. On the other hand, radial forces are not affected by the asymmetry of the windings, so equations (39) and (40) are suitable for determining stresses caused by radial forces both in the case of symmetry and asymmetry [31].

The forces arising in the cases of asymmetry are of considerable magnitude, so in order to avoid them, attempts should be made to eliminate, or at least to reduce the asymmetry whenever it is feasible. However, some asymmetries can be expected to occur, at least to some lesser extentd due to manufacturing inaccuracies or uneven shrinkage of windings in normal service [31]. The supplementary magnetic field developing in an asymmetrical winding system can be explained by the method of superposition, according to [31]. The two windings placed asymmetrically are shown in Figure 59. The field excited by the short winding (2) is the result of the fields excited by windings 2 and 3.

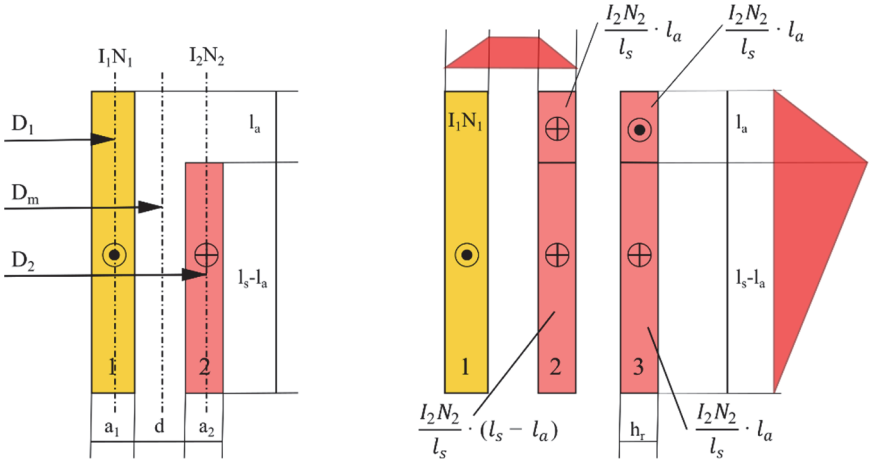

Figure 59. Asymmetry at one winding edge, based on [31].

4.2.3. Dynamic behaviour of core-type transformers under short-circuit conditions

During short circuits, the windings of a power transformer are subjected to different conditions than those arising under static loading. Sometimes, the use of static calculations show inaccuracies when they are compared with experimental results in actual transformers, as the dynamic forces totally differ in magnitude and shape to the static ones [14]. There are many studies of the dynamic behaviour of power transformers during a short circuit, in which the inherent natural vibration frequencies of the windings need to be calculated. According to [14], those calculations are complex and require the assumption of several simplifications, as they depend on many very variable constructional parameters.

The transformer windings along with the supporting clamping structure form a mechanical system with mass and elasticity. The dynamic behaviour is associated with the time-dependence of the instantaneous short-circuit current, which is oscillatory in nature and acts on the elastic system (winding conductors, insulation system and clamping structures), and the corresponding forces and displacements of the windings [31]. The movement of the windings in those situations produce instantaneous modifications in the forces [14], depending upon the relationship between excitation frequencies and natural frequencies of the system, inertia of conductors, frictional forces and reactionary forces of the resilient components [31]. Although the dynamic analysis is quite complex, it improves the understanding of the whole phenomenon and helps designers to enhance the reliability of the transformers under short-circuit conditions [31].

Dynamic mechanical models usually represent the transformer winding, made up of a large number of conductors separated by insulating materials, as an elastic column with distributed masses, which are the conductors, and springs, which are the insulation components. As the winding ends generally are heavily insulated, they can be also represented

by springs. Consequently, the model will be an elastic column restrained between two linear springs, when there is no separation between the conductor and the insulation [14]. The methods for calculating the dynamic response are quite complex. They have to take into account the boundary conditions, such as the degree of axial pre-stress, the stiffness of the clamping structure, the proximity of the tank or other windings, the effects of displacement of conductors and the natural vibration frequency and conditions of resonance [14], [31]. That model permits the calculation of the dynamic load, the displacements and the natural frequencies, but has the limitation of not taking into consideration the non-linearities in the mechanical behaviour of the cellulosic insulation. In fact, the real dynamic response of the cellulosic insulation, especially that of pressboard, is highly non-linear and is affected by the oil impregnation filling its pores. A dynamic compressive force in the transformer causes a flow of oil that will add a viscous component. The dynamic stiffness and damping characteristics can be experimentally determined, as stated by [78] and [79]. Although the dynamic value of Young's modulus can be derived from the static characteristics [80], this approximation may not be valid for oil-impregnated insulation.

In the radial direction, the elasticity of the copper conductors is high and the mass is small, resulting in a natural frequency much higher than the fundamental frequency of the excitation force, 50/60 Hz, and twice the fundamental frequency, 100/120 Hz [31]. Hence, the possibility of an increase in displacements by resonance effects under the action of radial forces is very remote. The energy stored by the displacement of windings subjected to radial forces is almost entirely elastic and the generated stresses approximately correspond with the instantaneous values of the generated forces [31]. On the other hand, the amount of insulation, which is easily compressible, is quite significant along the axial direction. With axial forces acting on the system, the natural frequencies may come quite close to the excitation frequencies of the short-circuit forces, so a resonant condition can be achieved, leading to large displacements and eventual failure of the transformer [31].

Nowadays, there are different software programmes which permit the calculation of short-circuit forces with complex winding arrangements, from a 3D model of the transformer to which the numerical or analytical algorithm for the magnetic field pattern is applied [14]. In most cases, the symmetry of the power transformer (planar or axial symmetry in core-type transformers) permits the simplification of the model to 2D. Once the leakage field distribution in the transformer is obtained, the force pattern is easy to ascertain, as the magnetic induction vector and the resulting force are perpendicular to each other at every point [14].

4.2.4. Mechanical stresses and failure modes caused by short-circuit electromagnetic forces

Although electromagnetic forces acting in power transformers can be approximately calculated with some accuracy, the subsequent mechanical stresses depend on many factors that cannot be easily quantified. According to [14], it is practically impossible to reach a method for the calculation of mechanical stresses on which different manufacturers agree. Moreover, the effect of radial and axial forces on transformer structures is quite different because, although both forces have a pulsating nature, the transformer structure is much more rigid in axial than in radial direction. The conductors of core-type transformers with concentric windings are affected by a magnetic field of mainly axial direction, which generates radial forces. According to [14], these forces induce, among others:

- Tangential tensile stresses on conductors, when the windings are affected by outward electromagnetic forces, and compressive stresses, with inward electromagnetic forces, see Figure 60.
- A radial bending stress between radial supports of inner windings.
- Bending stresses on disc-type windings crossovers and transpositions and on helical-type winding transpositions.

On the other hand, axial electromagnetic forces produce an axial compressive stress on winding conductors and cellulosic insulation, and axial bending stress on the conductors of windings with radial spacers [14]. Apart from the copper conductors and other components of power transformers that can be damaged due to high stress concentrations or high deformations, there are also some allowable compressive, bending and shear stresses for the insulation materials that must be taken into consideration. Some of them are given in Table 9 from [81].

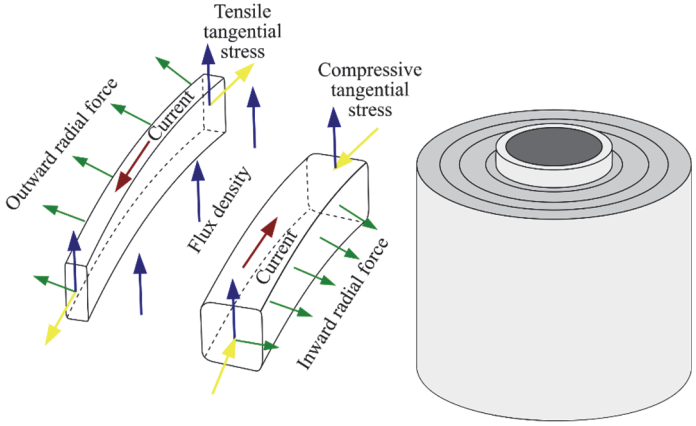

Figure 60. Schematic representation of currents, leakage flux, forces and mechanical stresses in core-type transformers, based on [14].

Table 9. Stress limits for various cellulosic components of a power transformer, from [81].

PROPERTY	VALUE (N/mm²)
Compressive stress on radial spacers (in presence of paper covering the conductors)	≤ 80
Compressive stress on radial spacers (in presence of pure enamel coating of conductors)	≤ 120
Compressive stress on conductor paper insulation with layer-type windings	≤ 35
Compressive stress on pressboard end rings of wound type	≤ 40
Compressive stress on pressboard end rings of stacked type	≤ 80

- **Approximate formulas for the calculation of mechanical stresses on winding conductors of core-type transformers:**

The mean tangential stress in the outer or inner winding of a two-winding core-type transformer, when a short-circuit radial force is applied to the entire winding, can be approximately calculated considering the winding as a pressurised cylindrical vessel subjected to uniform pressure, P^*, applied from the outside to the inside Figure 61 [14]:

$$P^* = \frac{F^*_{rad}}{\pi \cdot D_m \cdot H_w} \quad (N/mm^2) \tag{44}$$

Where:

F^*_{rad} (N): Total radial force.

D_m (mm): Winding average diameter.

H_w (mm): Winding axial length.

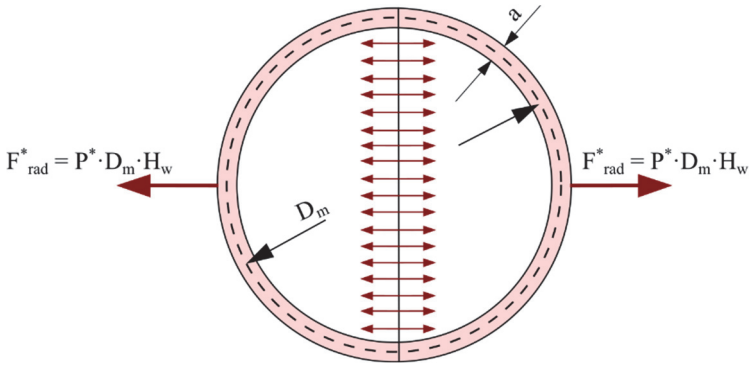

Figure 61. Winding as a cylindrical vessel subjected to uniform pressure, based on [14].

The average tangential stress, which can be of a tensile or compressive nature, will be given by equation (45) from [14]. It is assumed that the steady-state short-circuit current can be expressed as a multiple of the rated current, I_r, which is a valid assumption under a three-phase short circuit:

$$\sigma_t{}^* = \frac{P^* \cdot D_m}{2a} = \frac{F^*{}_{rad} \cdot \cancel{D_m}}{2a \cdot \pi \cdot \cancel{D_m} \cdot H_w} = \frac{\mu_0 (N I_r)^2}{H_w} \cancel{\pi} D_m r^2 k^2 \cdot \frac{1}{2a \cdot \cancel{\pi}} \tag{45}$$

$$\sigma_t{}^* = \frac{\mu_0 (N I_r)^2}{2a\, H_w} D_m r^2 k^2$$

Where a is the equivalent radial thickness of the winding, which depends on the rated current, the number of winding electrical turns, N, the current density value, J_r, and the winding axial length, H_w: $a = \frac{N \cdot I_r}{J_r \cdot H_w}$. When more than two windings are affected by a short circuit in a power transformer, the previous formula shall be modified in order to take into consideration the real magnetomotive force appearing in the windings. The formula in that situation is given in section 9.4.1.1. of [14].

In core-type transformers, the radial forces are predominant, and the conductors tend to equalise their loads and stresses. That is, the most loaded conductors, which are the ones adjacent to the main duct, partially transfer the loads to the less stressed ones, located at the opposite side [14]. In the case of conductors subjected to tensile stress, that tendency to share the load is more accused as the stress in the most loaded conductor approaches the stress at 0.2% non-proportional elongation of the copper material, $R_{p0.2}$ [14]. When $\sigma_t{}^*/R_{p0.2} \simeq 1$, the strain in the inner conductors of the coil starts becoming plastic, the distribution of stresses along the coil width becomes more even and the local compressive stress increases at the points where the spacers are [14]. According to [81], the safety coefficient that shall be considered for the tangential stress is: $\sigma_{t,max}{}^* \leq 0.9 \cdot R_{p0.2}$.

Radial bending of conductors in the windings can happen in the middle of the span between axial sticks and between spacers. If the loads are uniformly shared and the support sticks are assumed to be totally rigid in radial direction, the conductors behave like a series of parallel beams with restrained ends [14]. The maximum stress at radial bending on each conductor will be given by equation (46), and shall comply with $\sigma_{b,max}{}^* \leq 0.9 \cdot R_{p0.2}$ [81].

$$\sigma_b{}^* = \frac{F^*{}_{rad,ul} \cdot l^2}{2 \cdot h \cdot b^2} \ (N/mm^2) \tag{46}$$

Where:

$F^*{}_{rad,ul}$ (N/mm): Average radial force per unit length of conductor.

l (mm): Edge-to-edge distance between consecutive support sticks.

h (mm): Axial height of the strand.

b (mm): Radial thickness of the strand.

Figure 62. Radial bending of strand conductors in a disc-type winding with intermediate cooling ducts, from [14].

According to [14], it is important to consider that the axial sticks at the winding inner side are not substantially rigid supports, and their stiffness depends a lot on the arrangement of the insulation and some manufacturing processes. Other approximate expressions for the bending stress on disc-type winding crossovers and helical-type winding conductor transpositions, as well as bending of conductors between radial spacers of disc and helical-type windings, can be found in sections 9.4.1.3, 9.4.1.4 and 9.4.1.5 of [14]. There are also two complete chapters in [14], 9.5 and 9.6, devoted to mechanical stresses in shell-type transformers.

- **Failure modes of core-type transformers:**

Although there are some failure modes in core-type transformers which depend on the combined effect of radial and axial forces, which can produce distortions at some points of the conductors or instability of the complete windings, in general, the effects of radial and axial forces can be isolated and analysed independently [14]. Here, the analysis is focused on some failure modes for core-type transformers, but chapter 10.4 of [14] also analyses some failure modes for shell-type transformers.

- **Failure modes produced by radial short-circuit forces:**

The windings of core-type transformers will behave considerably differently depending on whether the forces are inward, and they are subjected to compressive stress, or outward, and they are subjected to tensile stress. When the windings are subjected to tensile stresses, the conductors do not have a tendency to change their circular shape, and the design criteria to take into consideration is the yield strength of copper [14]. In this situation, if the yield strength is exceeded, the stretching of the conductor can lead to failure due to a break in the insulation or axial instability of the coil.

However, when the winding conductors are subjected to compressive stresses, they behave like slender bars subjected to an axial load, which may collapse at stresses much lower than the elastic limit of the materials, in both forced-buckling or free-buckling, see Figure 63 [14]. Forced-buckling failure mode happens when the stress exceeds the elastic limit of the copper, and the supporting structure in the inner side is relatively stiff in comparison with the winding conductors. In this mode, the conductors bend inwards in each span or in alternate spans between the axial supporting strips. Free-buckling, which is an unsupported buckling mode, is much more common and occurs when the stiffness of the individual conductor strands is high in comparison to the supporting structure in the inner side. This failure mechanism is based on a complex phenomenon, which depends on the dynamic short-circuit forces, on the composite structure of the winding and on manufacturing processes [14], and produces the inwards and outwards bending of the conductors at one or several points along the circumference of the winding.

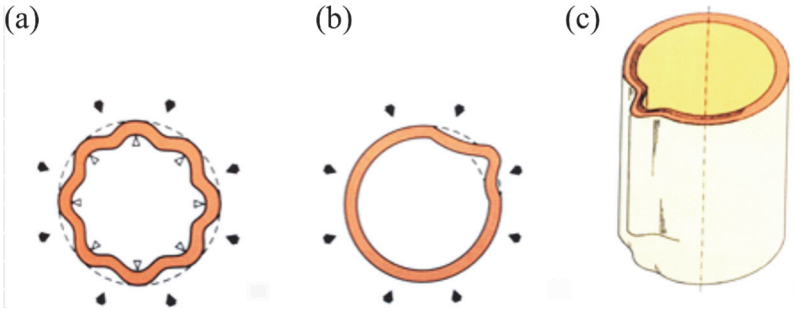

Figure 63. Failure modes of windings under compression; (a) forced-buckling; (b) and (c) free-buckling, from [14].

In theory, buckling occurs at a critical load that depends on the Young's modulus of the material, E, and on geometrical characteristics of the structural element, such as the slenderness ratio, $\frac{b \cdot N}{D_w}$, and is not related to the ultimate strength of the material. The expressions for the calculation of the critical stress for buckling are based on the modification of the Euler's equation, which was only valid for axially compressed slender bars, made by Timoshenko, which is applicable to a uniformly compressed hinged circular arc. A coil between two radial supports can be assimilated to that arc. Equation (47) gives the critical mean tangential compressive stress for buckling is:

$$\sigma_{cr} = \frac{1}{12} \cdot E \cdot \left(\frac{b \cdot N}{D_w}\right)^2 \ (N/mm^2) \tag{47}$$

Where:
N: Number of supports on the circumference.
$E\ (N/mm^2)$: Modulus of elasticity of copper.
$b\ (mm)$: Conductor radial width.
$D_w\ (mm)$: Mean diameter of the winding.

In fact, a winding of a core-type transformer consists of an assembly of non-homogeneous materials, such as copper, paper and pressboard, and according to [14], it is not totally accurate to only base the buckling criterion on equation (47), which states that the critical load essentially depends on the square of the number of supports along the winding inner contour. The reason is that those supports rely on pressboard cylinders and sticks, and paper sheets whose mechanical properties can be highly affected by manufacturing processes (such as drying treatment) and ageing, and that structure cannot guarantee any stiff support to the winding [14]. Moreover, many constructive characteristics, such as conductor transpositions, crossovers, lead exits, etc., make it differ from a perfect cylinder [14]. Due to the complexity of this phenomenon, a complete chapter in [14] is devoted to this topic: *12. Critical compressive stress for free-buckling of core-type transformer windings*.

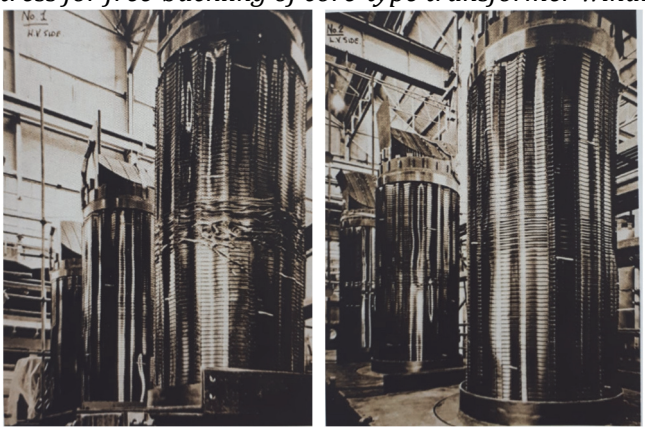

Figure 64. High-voltage and low-voltage windings of a transformer collapsed by forced-buckling produced by a local short circuit in the middle of the LV coil, from [14].

Nowadays, after the experience of short-circuit tests in many different models of power transformers, one of the conclusions is that, no matter how complex the calculation methods are, only a reference to a full-scale short-circuit withstand test will permit validating them completely [14]. The empirical expression (48) given in [14] tries to consider all the parameters which mainly influence the critical stress for free-buckling:

$$\sigma_{cr} = K_1 \cdot K_2 \cdot K_3 \cdot D_w \cdot (1 + K_4 \cdot b \cdot h) \cdot K_5 \cdot K_6 \quad (48)$$

Where:
K_1: Factor depending on the calculated axial pressure on radial spacers.
K_2: Factor depending on the Young's modulus of the conductor material.
K_3: Factor depending on the number of columns of radial supports in a winding.
K_4: Factor depending on centre-to-centre distance of radial supports (spacers). Its value is minimum in case of larger spans and without support.
K_5: Factor depending on the type of wire (standard strand, twin conductor, CTC, epoxy bonding, etc.).
K_6: Factor depending on winding technology and construction.
D_w: Diameter of the winding.
b, h: Radial and axial size of the conductor strand.

It is accepted that the following aspects increase the strength against buckling [14]:

- An increase in the conductor or strand thickness or equivalent thickness (in the case of epoxy-bonded CTC or glued double or triple conductors).
- An increase in the degree of work hardening of the copper material, which increases the value of $R_{p0,2}$.
- Radial compactness of the winding.
- Use of high-density pressboard for radial and axial spacers.
- The designing of self-supporting windings which do not depend on the inside support structure.

On the other hand, the following factors decrease the strength against buckling [14]:

- An increase of the diameter of the winding.
- An increase in the initial eccentricities present in the winding.
- An increase in the conductor's slenderness ratio.
- The presence of axial cooling ducts.
- Large discontinuities in the radial width of the winding and singularities, such as transpositions or crossovers.

According to [14], their experience in ABB has led to some graphs, such as the ones in Figure 65, where the relationship among the critical stress, the value of $R_{p0.2}$ for the copper conductor and the dimensions of the conductors are represented. As these graphs are used by ABB with design purposes, they do not provide the values of the critical stresses for confidentiality. In the graph for resin-bonded CTCs, Figure 65 (b), the radial equivalent thickness is defined by the following equation, where f is the number of strands per CTC cable, b_{sc} is the cable strand width and λ is an empirical factor: $b_{eq} = \frac{1}{2} \cdot f \cdot b_{sc} \cdot \lambda^{1/2}$. Only the cables with a lower value of the equivalent thickness can collapse by buckling [14], so in the part of the graph with high equivalent thickness, the curve represents the stresses for which the conductors collapse due to other phenomena, according to experience.

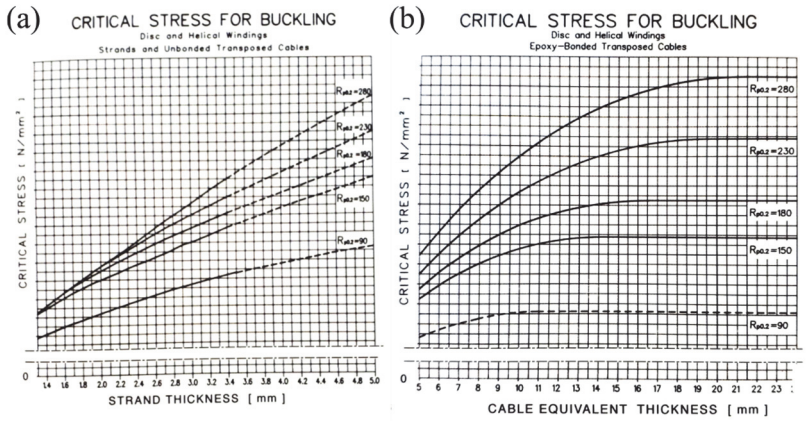

Figure 65. Graphs of critical stress for free-buckling for (a) strand conductors and (b) resin-bonded CTCs, when the winding diameter is 1000 mm, from [14].

Although, in disc-type windings, each coil can be considered as a closed ring with self-supporting resistance against inward radial forces, helical-type windings are characterised by open-turn terminations. When they are subjected to radial compressive forces, as each electrical turn consists of multiple bunches of individual strands or CTCs, the conductors tend to shift circumferentially in another failure mode which is known as *spiralling* [14]. In this failure mode, the windings tend to tighten up on the winding underneath, and an important tangential shift appears especially at the ends of the winding, producing a considerable deviation of the spacers and axial sticks from their original position, as seen in Figure 67 [14]. Moreover, due to the displacements in the conductors and axial supports, spiralling can cause instability of the windings.

Spiralling occurs when the compressive stress originated by radial forces exceeds a critical value. In windings of double-layer helical type, the elements near the main gap are the ones with the highest possibility to suffer spiralling because radial forces are maximum there; while in windings made of resin bonded CTCs the stress limit to prevent spiralling can be more critical than the stress that causes buckling [14]. Some actions that can reduce the probability of spiralling are to wind the conductors as tightly as possible during manufacturing, to minimise radial clearances and radial shrinkage of the inner support or to increase friction forces between conductors and radial spacers as much as possible [14].

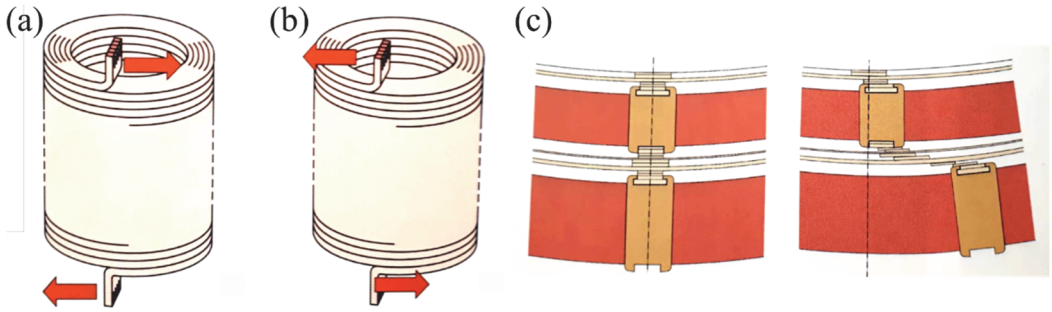

Figure 66. Direction of spiralling forces in helical type windings in (a) radially compressed coils and (b) tensile stressed coils. (c) Original possition of the radial spacers and circunferential shifts caused by spiralling, from [14].

The parameter used for the quantification of the allowable thrust force on exit leads to prevent spiralling, which should be compared with reference experimental values [81], is:

$$T^*_f = \sigma^*_t \cdot A_{wt} \cdot 10^{-3}\ (kN) \tag{49}$$

Where:

$\sigma^*_t\ (N/mm^2)$: Mean tangential compressive stress on the winding.

$A_{wt}\ (mm^2)$: Cross-sectional area of the winding turn.

Figure 67. Spiralling on the outer layer of a double-layer helical-type winding subjected to the short-circuit withstand test, from [14].

- **Failure modes produced by axial short-circuit forces:**

There are different types of failure modes which can be derived from axial forces. One of them is commonly called *tilting* and consists of a loss of winding stability due to a significant turning of the cross-sections of the copper conductors around their axis of symmetry. In this mode, all the adjacent conductors of the winding rotate in the same direction, whereas the next set of conductors turns in the opposite direction, producing a zig-zag pattern in the winding, Figure 68 [14]. The consequences can be the fracture of the insulation, the magnification of the forces due to conductor displacements and internal short circuits [14]. Some theoretical and experimental work has been done with the aim of obtaining a critical axial load or stress that leads to conductor tilting, but it is quite complicated due to the complexity of the phenomenon and the high number of parameters involved [14]. Most of the approaches are static, because they must be based in full-scale experiments, and the performance of dynamic tests is more complex and expensive. In [81], an expression for the critical axial compressive force leading to tilting is given for design purposes.

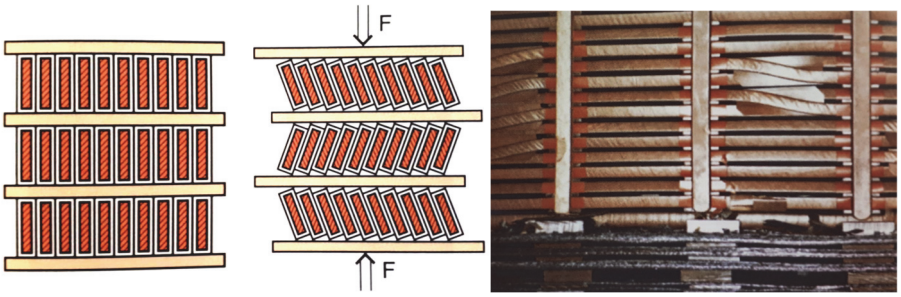

Figure 68. Representation of conductors in normal position and titled conductors, from [14].

Another failure mode is called *telescoping* and is typical of narrow layer-type windings, where axial collapse is derived from the stretching of conductors which make some turns to be driven axially and pass adjacent turns, Figure 69 [14]. An axial inappropriate support of the transformer can also result in telescoping and the consequences can be the damage of the insulation and turn-to-turn faults.

Axial forces can also produce bending of the conductor in axial direction between supporting spacer columns, although this failure mode is less frequent. Other mechanisms could be the collapse of the winding end insulation components and support structures [14].

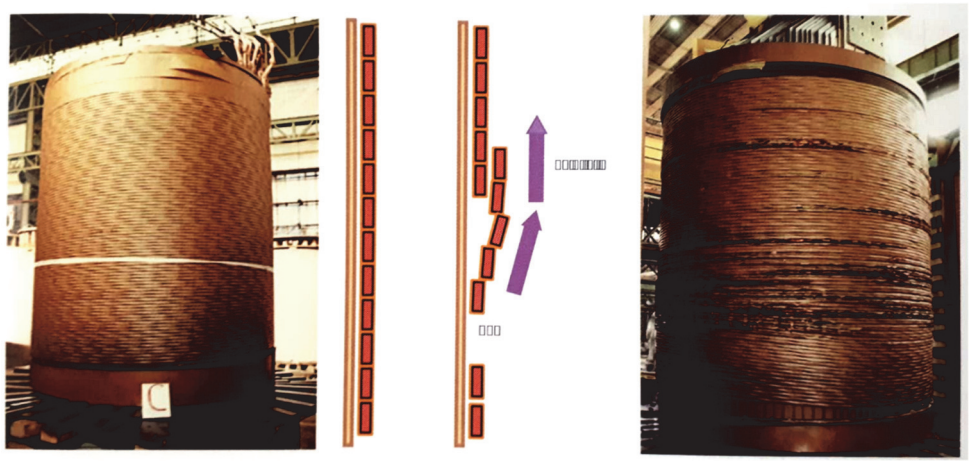

Figure 69. Mechanism of conductor telescoping and axial collapse due to this failure mechanism, from [14].

5. Mechanical models applicable to the cellulosic insulation of power transformers

5.1. Introduction

It is generally accepted that an inadequate response of the cellulosic insulation is one of the basic causes of transformer failure. Although that insulation has, mainly, a dielectric purpose, its mechanical behaviour is also relevant, as it influences the mechanical performance of the transformer itself to some point. That is especially true for the pressboard components of the inner structure of a transformer, such as the winding tables, press rings, and spacers, which can be affected by short circuits, inrush currents, vibrations and constant compressive loads. Thus, a better understanding of its mechanical response and its evolution due to ageing could be very useful to ensure the quality of the cellulosic components during manufacturing, transportation, and life-time services.

The manufacturing processes of paper materials mean that more fibres are aligned parallel with (in MD) than perpendicular (in CD) to the flow of the material through the paper-machine, and there are nearly no fibres aligned with the through-thickness direction (ZD). The macroscopic behaviour can be accurately described by the assumption of orthotropy, and the three main directions of the paper machine can be approximately considered as the principal directions of the material: MD, CD and ZD. The cellulose fibres have a high tensile stiffness and strength along their axis, which are not as high in the direction across the fibre, causing the paper network to be stronger in the in-plane directions (MD and CD) than in the out-of-plane direction (ZD), see Figure 70. The moduli, initial yield strength, and in-plane tensile failure strength in the MD are 2–4 times greater than those of the CD; while the initial yield strength of paperboard in ZD is two orders of magnitude lower than the in-plane initial yield strength values [82], [83]. The mechanical behaviour of different types of paper and board differs in detail, but some characteristics are common, such as: highly anisotropic behaviour, anisotropic hardening, non-linear response, different behaviour in tension and compression, visco-elasticity, strain rate sensitivity, damage evolution, and dependency on the moisture content. Those nonlinear characteristics cannot be considered in any algebraic analysis [84] and make cellulose-based materials very complex to model.

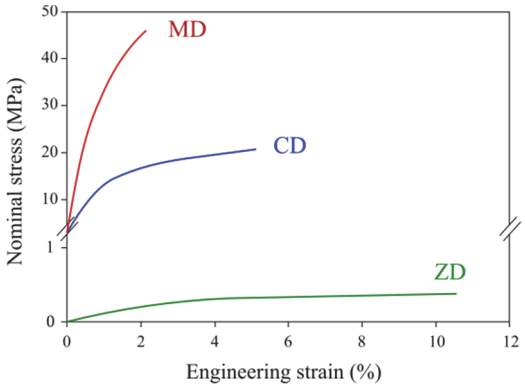

Figure 70. Material behaviour in the principal material directions of a paperboard grade, based on [85].

Microscopically, paper materials have an enormously high degree of heterogeneity, containing millions of pulp fibres, composed mainly of cellulose micro-fibrils made of cellulose chains oriented with respect to the axis of the fibre and embedded in a matrix of hemicellulose and lignin, and with a seemingly infinite number of cracks of different dimensions, which grow with the ageing level [86]. During the drying process in the manufacture of paper, single fibres approach each other closely, and the hydroxyl groups form hydrogen bonds which constitute a rigid and compact structure with high density [38]. The strength of paper (or board) and the processes governing its mechanical behaviour are mainly dependent on the bonding between the individual fibres [39], the geometrical structure of the bonded fibrous network and the existence of damaged zones [12]. One of the principal causes of mechanical strength deterioration is the rupture of those bonds. The bonding mechanisms that are usually considered are hydrogen bonds, mechanical interlocking, electrostatic interactions, interdiffusion of cellulose molecules, and van der Waals forces [40].

Several authors have developed mechanical models for paper and board materials, with various approaches, levels of complexity, and based on different hypothesis and simplifications. Most models are based in macroscopic material properties, but others try to predict the global mechanical response in terms of properties of the cellulose, hemicellulose and lignin, and the presence of fibres, bonds, and the geometrical structure of the network and the existence of damaged zones in the cell wall [20]. Some relevant references have been grouped in Table 10, according to the material directions that they considered. The mechanical behaviour has been considered as elastoplastic in most cases, or as viscoelastic-viscoplastic in others. It is not usual to consider the behaviour as elastic, as that assumption is not realistic in many practical situations. In some studies, the numerical and experimental results have been compared, with a considerably good agreement. Some of the models, such as [87] and [88], do not refer directly to paper material, but cover the theoretical background of viscoelasticity and viscoplasticity in detail, and give many analytical expressions which could be used in polymers. With respect to the remaining analysed models, most of them are focused on the behaviour of board materials (paperboard or pressboard) and there are very few which analyse thin paper ([89]–[92]).

In the case of board materials, the even more evident anisotropy is taken into consideration by all the mechanical models. The coupling between the in-plane and out-of-plane directions was studied in detail by [93] among other authors, and it was found that the in-plane response due to ZD-deformation is negligible in most cases. Thus, the response is commonly separated into in-plane and out-of-plane in many of the studies. Their behaviour in

ZD is relevant, as the insulation in the windings of power transformers is subjected to compressive forces in that direction. The researches which analyse the behaviour in ZD are more frequent in recent literature, and some of them are [4], [5], [99], [6], [79], [93]–[98]. However, there are also some models where the behaviour in MD and CD is studied, such as [84], [85], [100]–[102]. Although some analyses considered the influences of moisture and cyclic stress, these phenomena have not been completely understood yet.

Table 10. Different models proposed in the bibliography. The directions of the material that they consider in the analysis is indicated by X.

	ELASTIC				**ELASTOPLASTIC**				**VISCOELASTIC**				**VISCOPLASTIC**			
		MD	CD	ZD		MD	CD	ZD		MD	CD	ZD		MD	CD	ZD
GENERIC POLYMERIC MATERIALS									[87] [88]	*ISOTROPIC*			[88]	*ISOTROPIC*		
PAPER	[90]	x	x		[89] [92]	*ISOTROPIC*			[91]	x	x		[91]	x	x	
BOARD MATERIALS (PAPERBOARD OR PRESSBOARD)					[85] [100] [101] [102]	x	x	x	[84]	x	x	x	[84]	x	x	x
					[5] [6] [94] [95] [96] [103]			x	[79]			x	[4] [97] [98] [99]			x

5.2. Constitutive relations for paper and board

A constitutive relation is an ideal description of the relationship between loading and deformation for a particular material, which should provide a close approximation to the actual behaviour intended to model [87]. One single constitutive relation cannot accurately describe all the behavioural characteristics of a cellulosic material, because they depend upon several factors, such as the magnitude of stress and strain and its rate of application, temperature or moisture content. It is common to attempt to describe the behaviour according to these categories:

- Constant or time-varying temperature and moisture content.
- Infinitesimal strain or finite strain, depending on whether the deformation is large enough to require the use of finite strain measures or whether the use of infinitesimal strain components would suffice [87].
- Short-time or long-time application of load, which involves creep deformation in the case of paper materials.
- Low or moderate rate of loading or deformation.
- Low, moderate or high stress.

5.2.1. Elastic constitutive relations

Elasticity is defined as the physical property of a material that, when it deforms under external forces, returns to its original shape when the stress is removed. For an elastic material, the stress-strain curve is the same for the loading and unloading process, and the stress only depends on the current strain, not on its history. The initial flexibility matrix in Voigt notation, for a material which exhibits orthotropic symmetry, such as is the case for paper, is:

$$\begin{pmatrix}\varepsilon_{xx}\\ \varepsilon_{yy}\\ \varepsilon_{zz}\\ \gamma_{yz}\\ \gamma_{x}\\ \gamma_{xy}\end{pmatrix}=\begin{pmatrix}\frac{1}{E_x} & -\frac{\nu_{yx}}{E_y} & -\frac{\nu_{zx}}{E_z} & 0 & 0 & 0\\ -\frac{\nu_{xy}}{E_x} & \frac{1}{E_y} & -\frac{\nu_{zy}}{E_z} & 0 & 0 & 0\\ -\frac{\nu_{xz}}{E_x} & -\frac{\nu_{yz}}{E_y} & \frac{1}{E_z} & 0 & 0 & 0\\ 0 & 0 & 0 & \frac{1}{G_{yz}} & 0 & 0\\ 0 & 0 & 0 & 0 & \frac{1}{G_{xz}} & 0\\ 0 & 0 & 0 & 0 & 0 & \frac{1}{G_{xy}}\end{pmatrix}\begin{pmatrix}\sigma_{xx}\\ \sigma_{yy}\\ \sigma_{zz}\\ \tau_{yz}\\ \tau_{xz}\\ \tau_{xy}\end{pmatrix} \quad (50)$$

Where:

E_x, E_y, E_z: Young Moduli in the x, y and z directions.

ν_{ij}: Poisson ratios for strain in the "j" direction when the load is applied in the "i" direction.

G_{yz}, G_{xz}, G_{xy} : Shear Moduli in the yz, xz and xy planes.

For paper materials, it is assumed that the x, y-directions lie in the plane of the sheet (MD and CD) and the z-direction corresponds to the thickness direction of the sheet (ZD). The following must be accomplished when there is orthotropic symmetry: $\frac{\nu_{xy}}{E_x}=\frac{\nu_{yx}}{E_y}$, $\frac{\nu_{xz}}{E_x}=\frac{\nu_{zx}}{E_z}$, $\frac{\nu_{yz}}{E_y}=\frac{\nu_{zy}}{E_z}$. In conclusion, the three-dimensional description of the elastic properties of paper requires the determination of nine independent constants: E_x, E_y, E_z, ν_{xy}, ν_{xz}, ν_{yz}, G_{xy}, G_{xz}, G_{yz}, as seen in equation (51):

$$\begin{pmatrix}\varepsilon_{xx}\\ \varepsilon_{yy}\\ \varepsilon_{zz}\\ \gamma_{yz}\\ \gamma_{x}\\ \gamma_{xy}\end{pmatrix}=\begin{pmatrix}\frac{1}{E_x} & -\frac{\nu_{xy}}{E_x} & -\frac{\nu_{xz}}{E_x} & 0 & 0 & 0\\ -\frac{\nu_{xy}}{E_x} & \frac{1}{E_y} & -\frac{\nu_{yz}}{E_y} & 0 & 0 & 0\\ -\frac{\nu_{xz}}{E_x} & -\frac{\nu_{yz}}{E_y} & \frac{1}{E_z} & 0 & 0 & 0\\ 0 & 0 & 0 & \frac{1}{G_{yz}} & 0 & 0\\ 0 & 0 & 0 & 0 & \frac{1}{G_{xz}} & 0\\ 0 & 0 & 0 & 0 & 0 & \frac{1}{G_{xy}}\end{pmatrix}\begin{pmatrix}\sigma_{xx}\\ \sigma_{yy}\\ \sigma_{zz}\\ \tau_{yz}\\ \tau_{xz}\\ \tau_{xy}\end{pmatrix} \quad (51)$$

In many situations, the stress-strain relations for in-plane loading of thin paper are of main interest, and the assumption of a plane stress state, where the loading is confined in the directions of the plane of the sheet, is a natural simplification. In that situation, $\sigma_{zz}=\tau_{xz}=\tau_{yz}=0$, the relation is given by equations (52) and (53):

$$\begin{pmatrix}\varepsilon_{xx}\\ \varepsilon_{yy}\\ \gamma_{xy}\end{pmatrix}=\begin{pmatrix}\frac{1}{E_x} & -\frac{\nu_{xy}}{E_x} & 0\\ -\frac{\nu_{yx}}{E_y} & \frac{1}{E_y} & 0\\ 0 & 0 & \frac{1}{G_{xy}}\end{pmatrix}\begin{pmatrix}\sigma_{xx}\\ \sigma_{yy}\\ \tau_{xy}\end{pmatrix} \tag{52}$$

$$\begin{pmatrix}\sigma_{xx}\\ \sigma_{yy}\\ \tau_{xy}\end{pmatrix}=\begin{pmatrix}\frac{E_x}{1-\nu_{xy}\nu_{yx}} & \frac{\nu_{xy}E_y}{1-\nu_{xy}\nu_{yx}} & 0\\ \frac{\nu_{yx}E_x}{1-\nu_{xy}\nu_{yx}} & \frac{E_y}{1-\nu_{xy}\nu_{yx}} & 0\\ 0 & 0 & G_{xy}\end{pmatrix}\begin{pmatrix}\varepsilon_{xx}\\ \varepsilon_{yy}\\ \gamma_{xy}\end{pmatrix} \tag{53}$$

Actually, there are limited applications of interest in which paper materials behave purely elastically, and that is why there are not many studies which consider elastic constitutive relations. The assumption of elastic behaviour of paper materials, where the relation between strain and stress is not time-dependent, is only realistic when the strains are small enough that the deformation can be described by the infinitesimal strain components, the duration of loading is relatively short, and the temperature and moisture content are low. The previous conditions are not satisfied by the paper insulation in power transformers, which is subjected to long-time application of loads, dynamic loads of high magnitude and high temperatures.

5.2.2. Viscous constitutive relations

The need of viscous constitutive relations for the modelling of paper materials is due to the viscous properties of their constituents. The fundamental constituent of paper is the pulp fibre, usually produced from wood, which can be modelled as a semi-crystalline viscoelastic composite consisting of highly ordered cellulose chains, with crystallinity in wood fibres of 60-70% [104], embedded in a matrix of amorphous cellulose and lignin, where at least some of the hemicelluloses are arranged parallel to the cellulose fibrils. The microfibrils are load-bearing elements that are aligned at an angle to the axis of the fibre, known as the fibre angle. As cellulose and hemicellulose are polymers, they are very sensitive to moisture and high temperature, which accelerate their ageing and influence their electrical and mechanical performance. In the amorphous phase the molecular chains arrange irregularly, and the density is lower [38]. This amorphous phase is responsible for the association of the fibres with water, viscoelastic behaviour, hygroexpansivity, shrinkage and internal stress state [20]. Paper materials show creep deformations when subjected to long-term loads, caused by the mechanism of internal rearrangement of the polymeric chains.

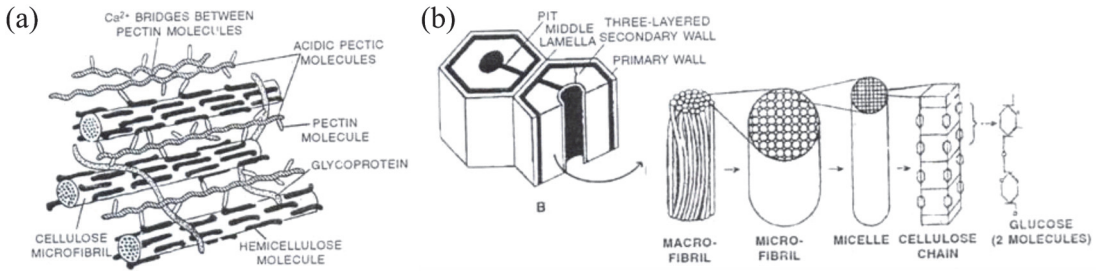

Figure 71. (a) Ultrastructure of primary wall; (b) Detailed structure of the cell wall.

Polymeric materials exhibit rate and time-dependent responses which are usually described by viscoelastic or viscoplastic constitutive models. During a uniaxial load/unload

test, if the stress is below an initial yield stress, σ_y, then their response is rate-independent linear-elastic, and Young's modulus is constant. Beyond σ_y, the stress–strain response at loading is both nonlinear and rate-dependent, but unloading is linear elastic, and therefore rate-independent. However, there are numerous polymer materials whose behaviour is time and rate-dependent at all stages of deformation, and their stress–strain response will depend on the strain rate both below and above the σ_y. For them, the slope during unloading is rate-dependent and may be non-linear, even strongly so. Unloading to zero stress leads to a permanent strain which might diminish with time but does not disappear completely even after a long waiting time. According to [88], all those features can be described by coupled viscoelastic– viscoplastic constitutive models. An extensive description of the mechanical models and testing methods for the viscoelastic behaviour of paper can be found in [24].

Viscoelastic materials are those which exhibit both viscous (dashpot-like) and elastic (spring-like) responses when undergoing deformation. They are characterised by showing creep, stress relaxation, and hysteresis [87]. *Creep loading* is defined as a type of loading where the stresses are constant, but the strains increase with duration of load application. *Stress relaxation* happens when a constant strain is applied to the material, and the stress decreases with the duration of time after the application of the strain. *Hysteresis* appears when the stress-strain curve of the material is different for the loading and unloading process, as in Figure 72.

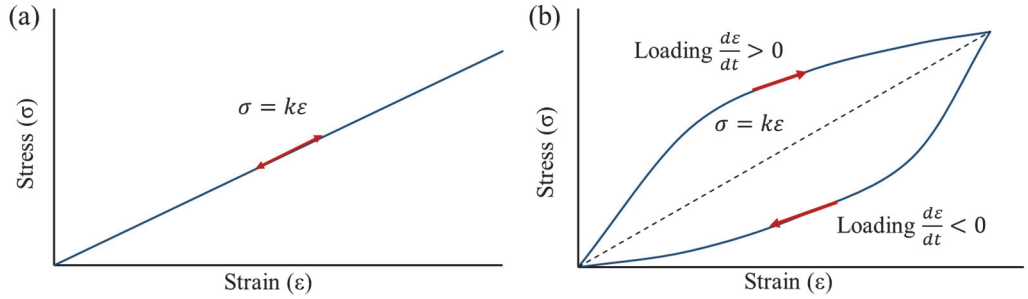

Figure 72. Stress and strain curves during cyclic loading-unloading for (a) a Hookean elastic solid and (b) a Kelvin-Voigt material, based on [87].

The material's behaviour can be described by a *linear viscoelasticity* constitutive law when temperature and moisture content are constant with time and their values are moderate, and if the levels of applied stress or imposed strain are small. However, the linear models are inadequate to describe many materials. *Nonlinear viscoelastic* behaviour is usually exhibited when the deformation is large or if the material changes its properties under deformation. The mechanical response of paper greatly depends on the environment conditions [105]. As paper is highly hygroscopic, moisture content considerably affects its viscous properties: at low moisture, paper is a relatively stiff and brittle material, but it becomes very ductile with moisture uptake. The temperature also affects its degree of viscosity. The nonlinear viscoelastic response of paper may be an effect of the inherent polymeric properties of cellulose in the network structure. Testing of paper regarding its time dependent behaviour under creep, stress relaxation or during cyclical deformation (dynamic behaviour) at specific temperatures and relative humidities could provide a better understanding of its behaviour.

- **Creep and stress relaxation:**

A creep test is accomplished by subjecting the test piece to a constant force or stress, σ_0, and then recording the strain as a function of time, $\varepsilon_c(t)$. The loading may be followed by an unloading at time t_1 at which the recovered strain, $\varepsilon_r(t - t_1)$, is recorded as a function of time, over a period of about 10 times the loading period, see Figure 73 (a). The residual strain,

$\varepsilon_p(t_1)$, is called the permanent set. For a linear viscoelastic material, the permanent set will be small, but for a nonlinear material, there may be a considerable difference between the creep and the recovery. Stress relaxation is defined as the time-dependent dissipation of stress at a constant strain. In a stress relaxation experiment, the test piece is subjected to a strain, ε_0, which is kept constant over time while the reduction of stress is observed, $\sigma(t)$, see Figure 73 (b). If the material is kept under strain for a sufficiently long time (in the case of paper, several days or even weeks) it will attain an equilibrium value.

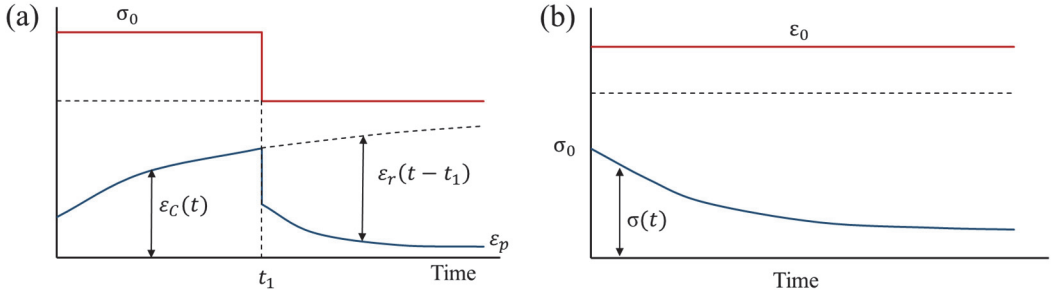

Figure 73. (a) Creep, ε_c, and recovery, ε_r, for a viscoelastic solid subjected to loading and unloading; (b) Stress relaxation of a viscoelastic material, based on [20].

The time dependence of the properties of paper is also emphasised by the straining rate dependence of the stress-strain relationship. The tensile strength of paper increases with increasing strain rate, see Figure 74. The initial slope of the curves, the creep modulus, is higher for the short-time test, where the stress is proportional to the strain and the material exhibits a linear viscoelastic behaviour [106]. For paper materials, there is no agreement in the research community about whether creep and relaxation depend on the bonding between fibres or on structural changes in the fibres themselves [107]. In [108], the mechanical properties of the bonding between fibres, as well as time dependent processes such as creep and relaxation, were studied on the nanometre scale, by static and dynamic loading of individual fibre-fibre bonds up to failure. One of the conclusions is that fibrils, which act as bridging elements, make a very relevant influence in the bonding.

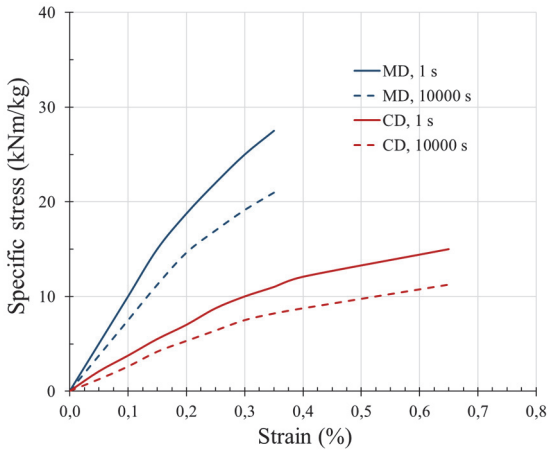

Figure 74. Stress-strain curves for a Kraft liner (185 g/m²) in MD and CD, at short time and at long time, from [20].

- **Cyclical testing:**

Dynamic tests are sometimes used to study the properties of viscoelastic materials. In those tests, the stress (or strain) resulting from an oscillating force or deformation is measured, and the material properties can be characterised as a function of temperature, time, frequency, stress or humidity [87]. The quantities most commonly determined by dynamic mechanical analysis for a linear viscoelastic solid are the storage modulus, *E'*, which quantifies the energy

stored in the material and recovered per cycle and corresponds to the in-phase response; the loss modulus, E'', which characterises the mechanical energy dissipated in the material by converting it to heat by molecular motion, corresponding to the out-of-phase response; and the loss factor, $tan\ \delta$, which is the tangent of the phase angle between the applied stress and strain and also the ratio of the loss modulus to the storage modulus: $\tan\delta = \frac{E''}{E'}$. The storage and loss moduli are related to the complex dynamic modulus, E^*, by equation (54):

$$E^* = \frac{\sigma(t)}{\varepsilon(t)} = \frac{\sigma_0}{\varepsilon_0} cos\delta + i\frac{\sigma_0}{\varepsilon_0} sin\delta = E' + i\,E'' \tag{54}$$

The effect of the strain amplitude must be taken into account when the dynamic mechanical properties of paper are measured, see Figure 75 (a), (b) [109]. Increasing the strain amplitude reduces the absolute value of the complex modulus, $|E^*|$. The loss factor, $\tan\delta$, increases linearly when increasing the applied strain amplitude, Figure 75 (c).

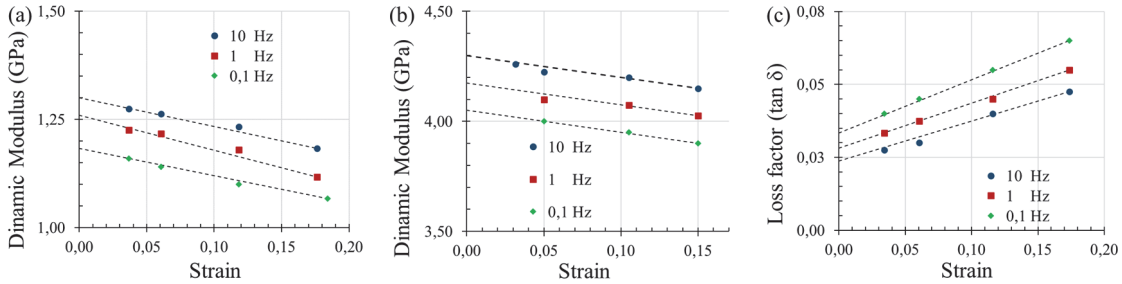

Figure 75. Complex dynamic modulus versus strain amplitude at different frequencies: (a) Freely dried sheet (326 kg/m³) in MD, (b) Restrained dried sheet (799 kg/m³) in the CD; (c) Mechanical loss factor versus strain amplitude at different frequencies, for a freely dried sheet (326 kg/m³) in MD; based on [20].

Oil-impregnation of the pressboard insulation might affect its mechanical behaviour, as the fluid filling the pressboard pores flows in and out during cyclic mechanical load. In [7], compressive tests were performed on both dry and oil-immersed high-density (HD) pressboard in a test set-up designed to reproduce an oil-immersed transformer winding in a small scale. The test pieces were subjected to a creep stress of 5 MPa for 5 minutes; later, a cycling load starting from 5 MPa up to 100 MPa was applied with a frequency of 0.1 Hz. A large non-recoverable deformation was measured in the first load cycle for both dry and oil-immersed pressboard, see Figure 76. The second load cycle showed a much smaller non-recoverable deformation and an increased elastic moduli. The final cycles confirmed that the residual deformation had not significantly increased, and the hysteresis had reduced.

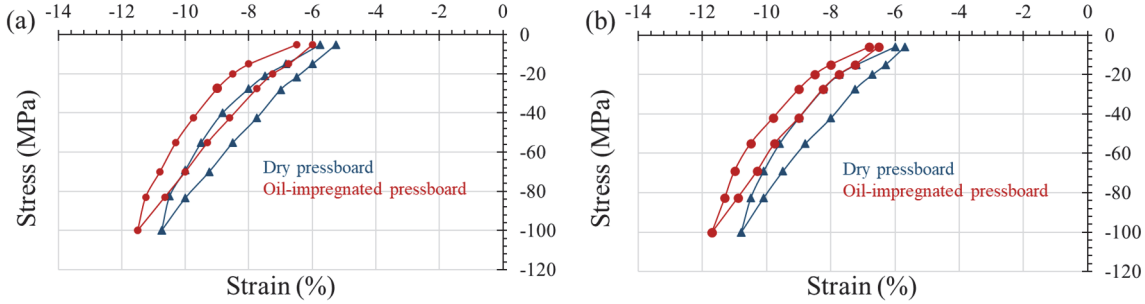

Figure 76. Stress-strain curve representing (a) the first load curve, (b) the second load cycle, based on [7].

The conclusion of [7] was that the influence of oil on the total deformation of pressboard is limited. The largest contribution was measured in the low stress region, whereas no major difference was recorded at higher pressures, where the value of elastic moduli can be considered as almost constant and not-affected by oil-impregnation. Residual deformation at

the low end of the stress-strain curve was not influenced by the oil-impregnation. However, these results were obtained with low range frequency, at higher frequency ranges, such as in-service frequency of 100 Hz or 120 Hz, the oil flow inside the pressboard and at its boundaries might be significantly accelerated and that can considerably change the results.

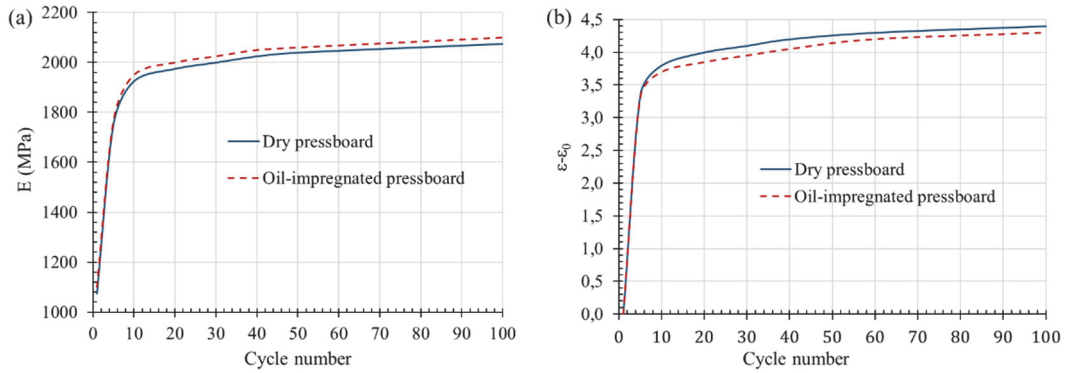

Figure 77. (a) Evolution of the Young's modulus for dry and oil-impregnated materials; (b) Evolution of the residual deformation for dry and oil-impregnated materials, from [7].

5.2.3. Plastic constitutive relations and residual stresses

Plasticity can be defined as the ability of a material to undergo permanent deformation, a non-reversible change of shape in response to the application of external forces. Plastic models are time-independent and are based on the concept of a yield surface for the onset of plastic behaviour, and on the existence of a flow rule for predicting the incremental strains [87]. A yield surface is a multi-dimensional surface in the space of stresses, see Figure 78. If a particular stress state lies inside the yield surface, the material response will be elastic. When the stress state lies in the envelope of the yield surface, the material has reached its yielding. If the deformation continues, the material will behave plastically. The shape and size of the yield surface may change as the plastic deformation evolves. Flow plasticity theories usually assume that the total strain of the material can be decomposed additively (or multiplicatively) into an elastic and a plastic part. The determination of the plastic part of the strain requires a flow rule and a hardening model.

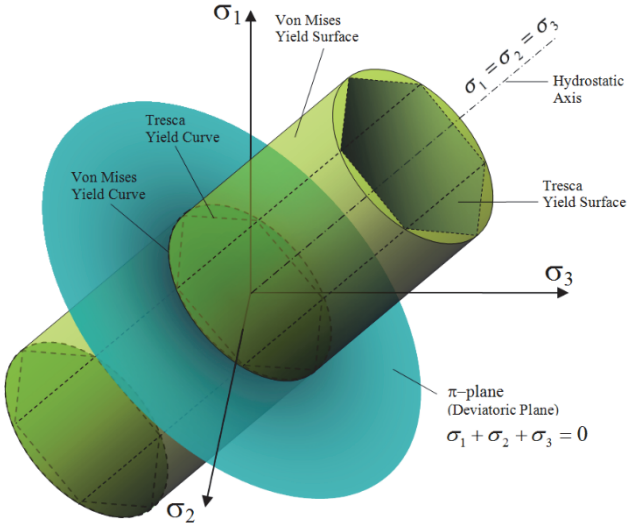

Figure 78. Yield surfaces, from https://es.wikipedia.org/wiki/Archivo:Yield_surfaces.png.

The use of plasticity for paper materials is motivated by their highly non-linear response, even when they are exposed to moderate deformations in comparison to those that cause failure, and because unloading from the non-linear region introduces non-recoverable or

residual strains. The stress-strain response of these materials to uniaxial tensile loading is different from the uniaxial response in compression, and there is plasticity in the three principal directions: MD, CD and ZD. The purpose of plasticity is to predict the nonlinear stress-strain behaviour on loading and unloading cycles. There are several plastic models for these materials in the literature, which will be analysed in section *5.Mechanical models applicable to the cellulosic insulation of power transformers*, which decompose the strain tensor in an elastic and a plastic part, define a yield surface and the hardening of the material. These constitutive models can be implemented into a FE simulation programme, where material parameters can be calibrated with the results of experimental tests.

Furthermore, the mechanical response of paper materials can be influenced by the presence of a residual stress distribution. Paper can be in a state of stress, both at the fibre and network level, even though there are no external forces or constraints acting on their boundary. Many factors during paper manufacturing (such as distribution of the different constituents, fibre orientation, variations in apparent density, consolidation, relative bonded area, differences in shrinkage behaviour between fibres and matrix, drying strategies, calendering or other mechanical treatment) as well as during transformer manufacturing may create or modify the level and distribution of residual stresses [20].

5.3. Mechanical models for cellulosic materials

5.3.1. Mechanical models for thin paper

Some authors consider that the mechanical and electrical properties of the paper insulation used to wrap the conductors in transformer windings are significantly interrelated [1]. Thus, the mechanical response of that thin paper is of relevance, but there are only a few publications in which it is analysed. The main reason could be that the applications in which the mechanical resistance of thin paper is significant are less frequent than those in which paperboard or pressboard are used. Besides, if the analysis is focused to power transformers, its complexity will be considerable: the material geometry, mechanical solicitations, influence of environmental factors and chemical reactions on ageing, etc.

Although there are not many models for thin paper, the main characteristics of some of them are described in section *5.3.1.Mechanical models for thin paper*. In that section, the models are not specific for paper insulation in power transformers, but some of their main characteristics and conclusions could be of use. However, some authors have also studied the influence of the paper insulation on the mechanical response of the components of power transformers, and some of the more relevant publications focused on that are described in section *5.3.2.Influence of the thin paper insulation on the mechanical strength of power transformer windings.*

- **Elastic models for thin paper**

In an assembly of elastic fibres under static compression, each fibre makes contact with a number of other fibres crossing above and below. The distance between fibre contact points is large in a material with low density, while, when density is fairly high, with strong bonds and long fibres, laminate theory can be used to model the in-plane elastic behaviour [90]. For medium-density fibre materials, a model that accounts for differences in stiffness in bonded and unbonded regions would provide a more accurate description. In [90], two alternative methods for the characterisation of elastic properties of fibre materials were compared, which combined macroscopic test methods with a micromechanical model. One was the compression of the material in ZD and the use of a statistical micromechanical model based on first-order

beam theory to describe the deformation. The other was tensile testing of the material and back calculation of the fibre stiffness with a laminate model.

When an external uniaxial pressure is applied in the fibre material, the load is transferred between neighbouring fibres, which act as beams supported at the contact points. The material can then be represented by a finite number of contacts interconnected by segments of the fibres that deflect between two supporting fibres, which can be regarded as a stochastic unit cell. When the network is compressed, more fibre contact points are created, and the beam segments become shorter and stiffer. Using statistical probability methods, model parameters such as the number of fibre contacts and their distribution in the material can be estimated. If the fibre material can be considered as homogeneous orthotropic lamina, whose principal directions are the MD and CD, using invariant properties and lamination parameters, a closed-form formulation for the Young's moduli (E_{MD} and E_{CD}) as a function of the unknown longitudinal and transversal elastic constants of the fibres (E_L, E_T, ν_{LT} and G_{LT}) can be obtained. Several formulas are given in [90] for E_{MD} and E_{CD}, which take into consideration the effect of anisotropy and a non-uniform fibre orientation.

Among the conclusions of [90], one is that first-order beam theory might not be able to describe the deformation mechanism, and other theories that incorporate shear deformation should be considered. It is also probable that local deformation becomes inelastic, which ultimately leads to fibre breakage or crushing. To make the compression method described more useful for a larger variety of wood fibre mats, further model refinements need to be done to describe the deformation mechanisms relevant for these fibre mats.

- **Elastoplastic models for thin paper**

Although the main purpose of [89] was to study the in-plane fracture of paper, a mechanical elastoplastic model was also presented, where the anisotropic elasticity of the paper was modelled by a linear elastic orthotropic in-plane stiffness matrix, D, which connected the rate of the in-plane elastic strain vector, $\dot{\varepsilon}^e$, to the rate of the in-plane stress vector, $\dot{\sigma}$, as: $\dot{\sigma} = D\dot{\varepsilon}^e$, where $\dot{\sigma} = (\dot{\sigma}_1, \dot{\sigma}_2, \dot{\sigma}_3, \dot{\sigma}_6)^T$ and $\dot{\varepsilon}^e = (\dot{\varepsilon}_1, \dot{\varepsilon}_2, \dot{\varepsilon}_3, \dot{\varepsilon}_6)^T$. Sub-indexes 1,2, 3 and 6 denoted the MD, CD, ZD and in-plane shear components, respectively. It was assumed that the out-of-plane stress was zero. The in-plane equations for the orthotropic material, assuming that $E_3/E_1 \simeq 0$ and $E_3/E_2 \simeq 0$, are:

$$\dot{\sigma}_1 = D_{11}\dot{\varepsilon}_1^e + D_{12}\dot{\varepsilon}_2^e + D_{13}\dot{\varepsilon}_3^e \quad (55)$$

$$\dot{\sigma}_2 = D_{12}\dot{\varepsilon}_1^e + D_{22}\dot{\varepsilon}_2^e + D_{23}\dot{\varepsilon}_3^e \quad (56)$$

$$\dot{\sigma}_3 = D_{13}\dot{\varepsilon}_1^e + D_{23}\dot{\varepsilon}_2^e + D_{33}\dot{\varepsilon}_3^e \;;\; \dot{\sigma}_3 = 0 \quad (57)$$

$$\dot{\sigma}_6 = D_{66}\dot{\varepsilon}_6^e \quad (58)$$

$$D_{11} = \frac{E_1}{1-\nu_{12}\nu_{21}}, D_{12} = \frac{E_1\nu_{21}}{1-\nu_{12}\nu_{21}}, D_{13} = \frac{E_3(\nu_{12}\nu_{23}+\nu_{13})}{1-\nu_{12}\nu_{21}} \quad (59)$$

$$D_{22} = \frac{E_2}{1-\nu_{12}\nu_{21}}, \qquad D_{23} = \frac{E_3(\nu_{21}\nu_{13}+\nu_{23})}{1-\nu_{12}\nu_{21}}, D_{33} = \frac{E_3}{1-\nu_{12}\nu_{21}}, D_{66} = G_6$$

To model the anisotropic plasticity in [89], the total strain rate vector, $\dot{\varepsilon}$, was assumed to be the sum of the elastic and the plastic strains as: $\dot{\varepsilon} = \dot{\varepsilon}^e + \dot{\varepsilon}^p$. The used anisotropic yield criterion was based on [110], and captured both the variation in the yield strength and the variation in the plastic straining. The in-plane yield stress rate, $\dot{\sigma}_y$, and the plastic yield strain rate, $\dot{\varepsilon}_y^p$, were assumed to follow the constitutive relation: $\dot{\sigma}_y = H_y\dot{\varepsilon}_y^p$, where $H_y = H_y(\varepsilon_y^p)$ is

the general plastic modulus. An isotropic yield criterion, able to describe all yield surfaces lying between an upper bound (limiting value of the sum of the two greater diameters of Mohr's circle) and a lower bound (the Tresca's yield criterion), expressed as $f = \emptyset - 2\sigma_y^{2k}$, was linearly transformed from the anisotropic stress space to the isotropic one. The evolution laws for the anisotropic plastic strain rate, $\dot{\varepsilon}^p$, follow: $\dot{\varepsilon}^p = \dot{\lambda}_y \frac{\partial f}{\partial \sigma}$, and the analogously for $\dot{E}^p$ and $\dot{\varepsilon}_y^p$.

The experimental mechanical characterisation of newsprint (45 g/m²) and Kraft paper (70 g/m²) was also presented in [89], Table 11, where tensile testing in different in-plane orientations with respect to the MD was performed. The elastic modulus was obtained for low stresses, from the initial linear part of the stress-strain curve. Figure 79 (a) represents the response of Kraft paper, and Figure 79 (b) shows uniaxial tension tests based on [83].

Table 11. Mean values and standard deviations for the results of tensile tests in different orientations, from [89].

	Newsprint paper (45 g/m²)		Kraft paper (70 g/ m²)	
φ (°)	$\sigma_f(MPa)$	$E(GPa)$	$\sigma_f(MPa)$	$E(GPa)$
0	31.9 ± 3.6	4.56 ± 0.78	57.3 ± 3.1	3.47 ± 0.32
22.5	23.6 ± 2.3	2.98 ± 0.18	49.5 ± 1.7	3.58 ± 0.17
45	15.4 ± 0.2	1.48 ± 0.09	41.0 ± 2.3	3.23 ± 0.19
67.5	11.4 ± 1.0	0.93 ± 0.07	37.7 ± 1.6	2.84 ± 0.27
90	10.8 ± 0.4	0.87 ± 0.02	33.1 ± 2.0	2.52 ± 0.10

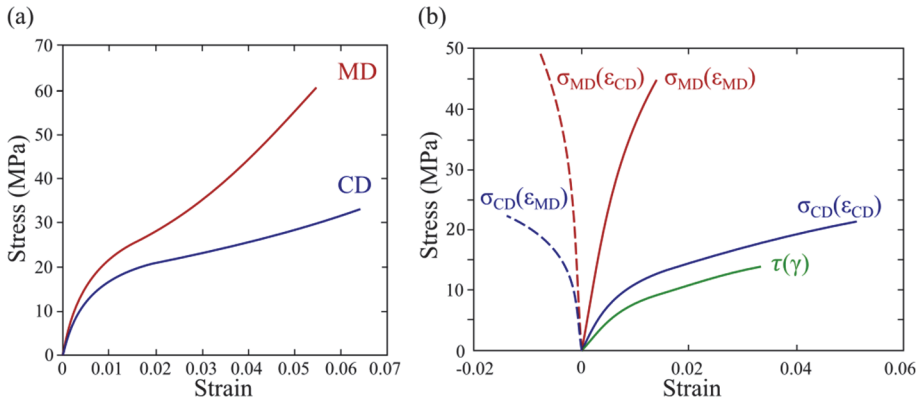

Figure 79. Stress-strain curves (a) for Kraft paper, and (b) due to tension and shear, based on [89].

A mechanical simulation model for a CTC wrapped in dielectric paper was presented in [92], to determine whether critical stress levels are reached in that insulation for reasonable conductor deformations produced by a short circuit, considering different ageing states, number of insulating layers (between 2 and 5) and conductor geometries (CTC types with 4, 12, 22 and 44 strands). The analysis considered the radial short-circuit force component, F_r, acting on one sector of paper-insulated CTC between two supporting sticks. The geometry of the CTC was simplified in [92] neglecting the curvature, homogenising the copper part whose transposition was also neglected, around which the paper is wrapped, and assuming that the copper behaved linear elastically (the stress distribution inside the copper strands was not considered). The insulation in [92] was Kraft paper type 5A2-1M3 with thermal Class 105, thickness of 80 µm and density 800 kg/m², whose anisotropy was neglected, and all properties were measured in MD in three different ageing states, Table 12. In the numerical simulation, the paper was discretised with shell elements with a nonlinear stress-strain characteristic, neglecting the overlap between paper layers and without including the pretension.

Table 12. Ageing dependent Kraft paper material parameters in MD, from [92].

Ageing state	Factory new	102 days at 105°C	134 days at 115°C
Degree of polymerisation, DP	1300	593	179
Young's modulus, E_0 (GPa)	4.7	5.3	3.6
Tensile strength, σ_{max} (MPa)	73.4	55.4	10.7

The contact between the copper core and the first layer was defined as frictionless, while the contact between the paper layers were set to frictional with a coefficient of 1.4. *Augmented Lagrange* method was chosen as contact algorithm, with *Shell Thickness Effects*. The cross-sectional faces of the CTC were set to a fixed support. The electromagnetic force was applied through a nodal force distributed on the mesh nodes. The deformation of the CTC induced shear and normal stresses in the paper layers, and a material damage model for paper was implemented in ANSYS Mechanical based on the assumptions: damage occurred once the stress inside an element reached the tensile strength σ_{max} (deduced from tensile tests); material stiffness for the damaged elements was reduced with a factor of 0.2; while the stiffness for elements under compressive stress remained unchanged. However, the tensile stress inside deteriorated mesh elements was not strictly limited to σ_{max}.

The maximum stress suffered by the paper increased with number of layers of insulation and with the number of strands, as the radial CTC dimension has a direct influence on the maximum stress. The peak stress occurs on the outer layer. The maximum tensile stress over the maximum CTC deflection, for the different geometries and ageing states is shown in Figure 80 from [92]. The curves for DP 593 show an initial increase in tensile stress in comparison to the models with DP 1300, where damage did not start. The CTC with 4 strands and DP 593 did not reach σ_{max} up to a deflection of 1 mm, while the paper with the same ageing and 12, 22 and 44 strands experiences damage at a deflection of around 0.3-0.4 mm.

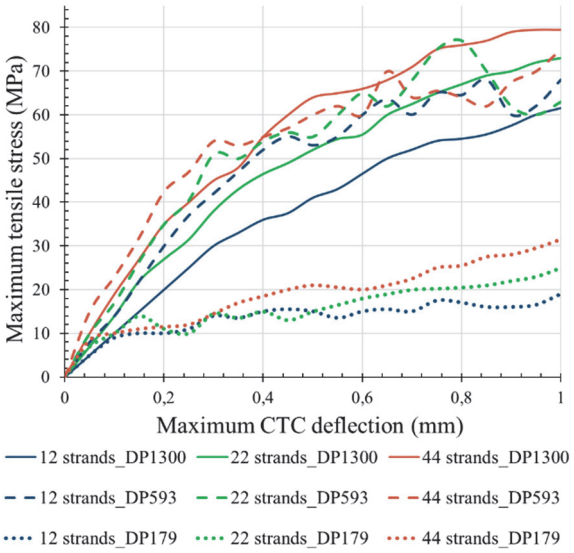

Figure 80. Maximum tensile stress for the models with 5 insulation layers and different ageing states, based on [92].

- **Viscoelastic and viscoplastic models for thin paper**

The non-linear time-dependent mechanical behaviour of three different commercial paper grades was studied in [91] taking into consideration the findings of [111]. The material parameters (elastic modulus *E,* tensile stress at breakage σ_T and strain at breakage ε_T) are given in Table 13. The stress relaxation and creep tests in [91] were performed in a hydraulic

testing machine at 50% RH and 23°C. In stress relaxation tests, the strain was split into a linear and a non-linear part, and a creep compliance was calculated from the stress and the linear part of the strain. Both, the stress relaxation moduli and creep compliances seemed to be independent of the load level and the loading direction (MD/CD) when scaled by the elastic modulus. For creep, the strain can also be split into two parts, but the procedure is more complicated, since the strain depends on time: $\varepsilon(t) = \varepsilon^{linear}(t) + \varepsilon^{nonlinear}(t)$, where $\varepsilon^{linear}(t)$ and $\varepsilon^{nonlinear}(t)$, were identified from the total creep strain, $\varepsilon(t)$, according to Figure 81 from [130]. This procedure was repeated for every time *t*, since the total strain change with time.

Table 13. Structural properties of the studied papers, from [91].

PAPER	Basis weight (g/m^2)	Thickness (μm)	Direction	E (MNm/kg)	σ_T (kNm/kg)	ε_T (%)
Copy paper	80	89	MD	7.84	54.9	1.35
			CD	2.56	20.9	4.96
Fluting, recycled fibres	150	243	MD	8.27	74.0	1.79
			CD	3.41	29.5	2.97
Kraftliner	185	235	MD	10.96	110.8	2.02
			CD	3.99	38.9	3.83

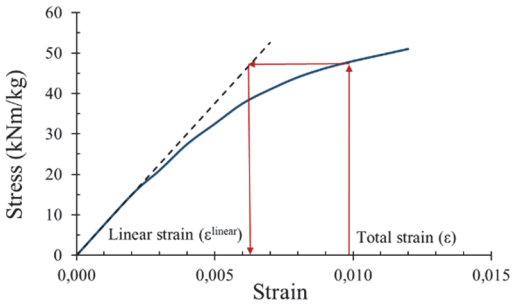

Figure 81. Procedure used for determining the linear part of the strain, based on [91].

The result of a creep test is shown in Figure 82 (a) from [91], where all strains increased with time, but the linear and the nonlinear parts increased at different rates. The nonlinear part increased faster at the end of the test, when the total strain had reached further into the non-linear region. A creep compliance was defined as: $J^{cr}(t) = \frac{\varepsilon^{linear}(t)}{\sigma}$. The stress relaxation modulus was normalised by dividing it by the initial elastic modulus, and the creep compliance by multiplying it by the elastic modulus, to get dimensionless time dependent functions. The stress relaxation modulus was approximately equal to the inverse of the creep compliance, which is a characteristic of linear viscoelastic theory. These values are shown in [91] for all the studied materials. It can be seen in Figure 82 (b), (c), for the Kraftliner in MD and CD, that the time dependent properties scale with the elastic modulus in each direction.

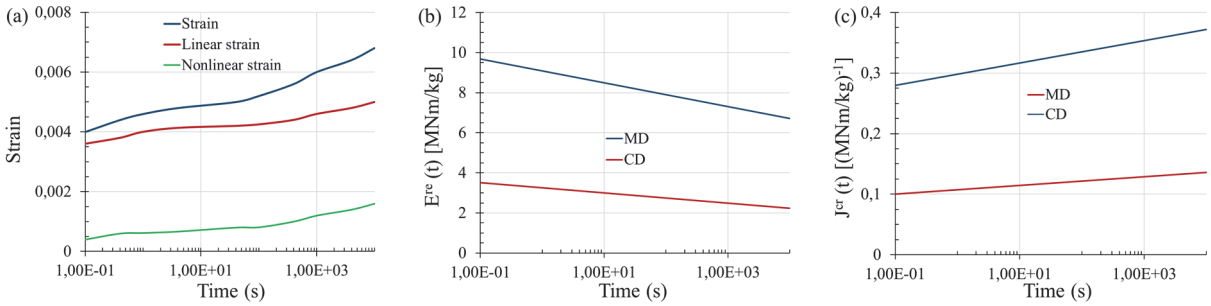

Figure 82. (a) Strain in a creep test for the copy paper, in MD and with a prescribed stress of 25.0 kNm/kg. For the Kraftliner, linear fit of (a) the stress relaxation moduli, (b) and the creep compliances; based on [91].

5.3.2. Influence of the thin paper insulation on the mechanical strength of power transformer windings

To study the influence of the paper insulation wrapping the conductors in the mechanical response of the windings, it is necessary to first characterise the response of the copper conductors alone, without insulation. There are several analytical studies with that purpose. For instance, in [112], large transformer windings were approximated to circular rings to obtain an equation for the radial buckling strength under short-circuit effects. In [113], both the influence of supporting spacers and plasticity of the copper were considered. In [114], a dynamic model for the axial and radial deformation of multilayer disk-type transformer coils was presented, with the simplification of merging the conductors into a homogeneous disk. In [115], the radial buckling strength under the influence of electromagnetic forces of three different CTC types used in power transformer windings was studied, see Table 14. A test stand in which the CTC deformation and the sinusoidal test current could be measured at the same time was used. A FE simulation model, based on a coupled analysis of the magnetostatic force and static structural deformation, was proposed and verified experimentally. The strands of the CTC were modelled independently, but their transpositions were neglected. The nonlinear stress-strain characteristic of the CTC, Figure 83, was introduced in the simulations, and the paper insulation was not included in the simulation nor in the experiments.

Table 14. Characteristics of the modelled CTCs, based on [115].

	N_S	h_S (mm)	t_S (mm)	E_{co} (GPa)	Epoxy coating	Frictional coefficient	Cross-section
CTC-A	19	5.15	1.50	96.0	No	0.08	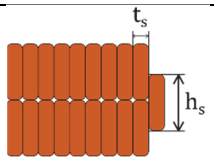
CTC-B	21	8.30	1.40	95.6	No	0.08	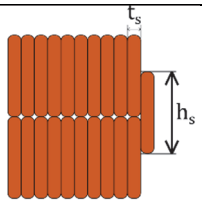
CTC-C	37	5.70	1.13	95.6	Yes	0.30	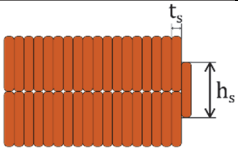

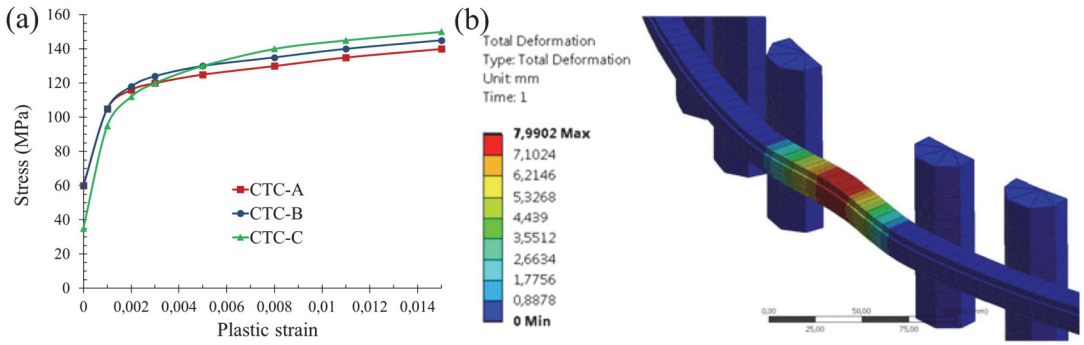

Figure 83. (a) Stress-plastic strain curves for the three types of CTCs; (b) Total deformation in mm after radial buckling for the FE model; from [115].

The current in [115] was applied to the conductor starting with a low value and increasing it in small steps of around 1-2 kA for several hundred milliseconds, Figure 84, until forced buckling in radial direction occurred at the peak current and was recorded with a high-speed camera. The load, $q_r(t)$, was calculated from the current, $i(t)$, using equation (60), where the load factor, k_r, depends on the test strand geometry and the conductor cross-section. The critical buckling load of CTCs, defined by a residual deformation of 0.5 mm, was estimated through tests and simulations with a relatively good agreement. However, the impact of paper wrapping on the buckling strength of CTCs was not taken into consideration in [115].

$$q_r(t) = i^2(t) \cdot k_r \tag{60}$$

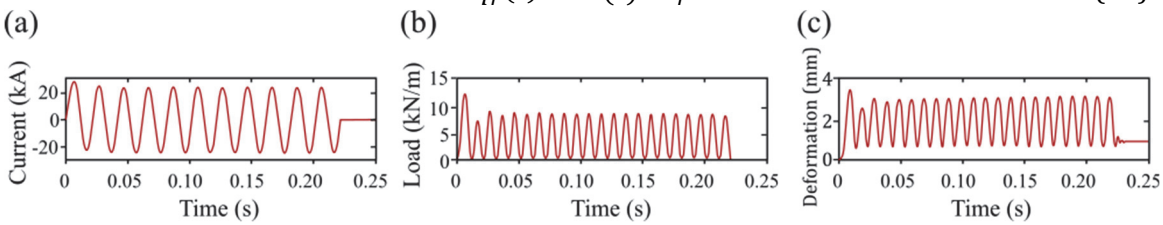

Figure 84. (a) Test current, (b) radial load, (c) radial deflection at the middle turn (inner winding), from [115].

Three CTCs with the same copper cross-sections were tested in [116], to evaluate the influence of different insulation thicknesses (0.45 mm, 0.9 mm and 1.8 mm) on the buckling strength. The short-circuit current was increased in each consecutive test, obtaining a significant total persistent deformation, see Figure 85. There was a visible difference between the thicknesses of 0.45 mm and 0.9 mm. Especially in the range of linear elastic deformation, up to 8 kN/m, the peak deformation when the thickness was 0.45 mm was approximately double than when it was 0.9 mm, and a lower load was needed to generate the same deformation. The beginning of buckling, which was defined by a permanent deformation bigger than 0.5 mm, was 8.5 kN/m for a thickness of 0.45 mm and 11 kN/m for 0.9 mm. However, a further increase in insulation thickness to 1.8 mm showed no significant effects on the mechanical strength, so excessive paper insulation thickness seemed to have no further effect.

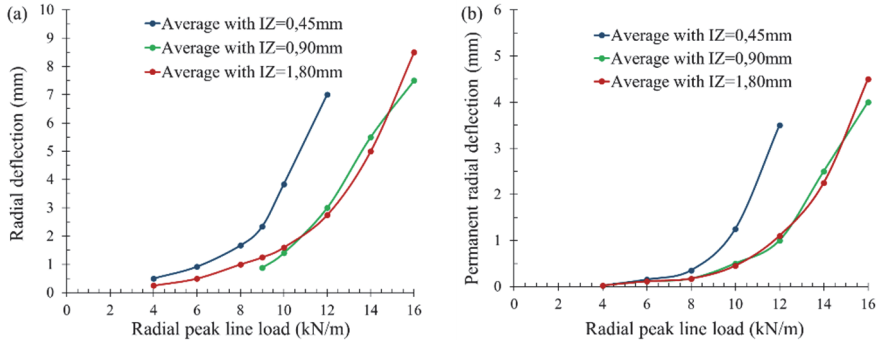

Figure 85. (a) Total peak deformation and (b) total persistent deformation with average curves for the different CTCs, based on [116].

5.3.3. Mechanical models for board materials

Among the literature, the publications studying the mechanical response of paperboard and pressboard are the most common, because there are other applications, such as packaging, in which these materials are used, and their mechanical performance is of relevance. Obviously, those analyses do not consider the environmental conditions that affect solid insulation in power transformers, such as the presence of the dielectric oil, high temperature, chemical reactions or ageing, but some of their main assumptions and conclusions could be useful for improving the understanding of the performance of board materials in power transformers. Most of the publications model the mechanical behaviour as elastoplastic and other consider a viscoelastic or viscoplastic approach.

A mechanical property of board materials which was considered in several of the analyses, was its densification. Pore spaces represent a considerable amount of the volume contained within a piece of paperboard, and can be classified according to their origin [24]. Some of them are originally present in paper fibres, fillers or coating materials. Other are produced by the papermaking or converting process, such as: interfibre gaps, toroidal voids around fibre-fibre bonds or fibre-filler contacts, and in coatings. Most of the pore spaces connect with each other to form an intricate three–dimensional structure which is anisotropic and deformable [103], which can be studied by electron microscopy and other microscopy techniques. That porosity is related to the three distinct responses shown by the compressive curve of board materials: a short linear elastic stage where the fibres deform elastically; a plateau, where the plastic deformation of the network occurs; and a sharp increase in the stiffness caused by densification [117]. In the densification mechanism, inter-fibre pores are squeezed, and new contact surfaces are created [4].

- **Elastoplastic models for board materials**
  - **Mechanical models considering the behaviour in MD, CD and ZD.**

The mechanical properties of a five-layer paperboard (three-layer core constructed from mechanically processed softwood pulp, and two outer stiffer and stronger layers constructed from bleached Kraft pulp) were experimentally obtained in [118]. The material showed an anisotropic elastic–plastic behaviour. The in-plane uniaxial tensile stress–strain curves for the MD, the CD and an orientation 45° from the MD (used to deduce shear properties) are shown in Figure 86 (a). There is a factor of 2–3 difference between MD and CD in the modulus and initial yield strength, and the curves show highly anisotropic strain hardening, which is higher in MD than in CD. The in-plane compression stress–strain curves for the MD and CD, Figure 86 (b), showed anisotropic compressive yield, which were smaller than those in tension by 65% in MD and 25% in CD, respectively. The lateral plastic strain (in CD) versus the axial plastic strain for MD-tension, and also for CD-tension are shown in Figure 86 (c), where the ratio between lateral plastic strain and axial plastic strain was nearly constant until final fracture. Tensile loading/unloading/reloading data showed that, upon unloading, the elastic tensile modulus was nearly unaffected by plastic strain, consistent with traditional models of elastoplasticity. The anisotropic in-plane elastic–plastic properties obtained from the tests are summarised in Table 15.

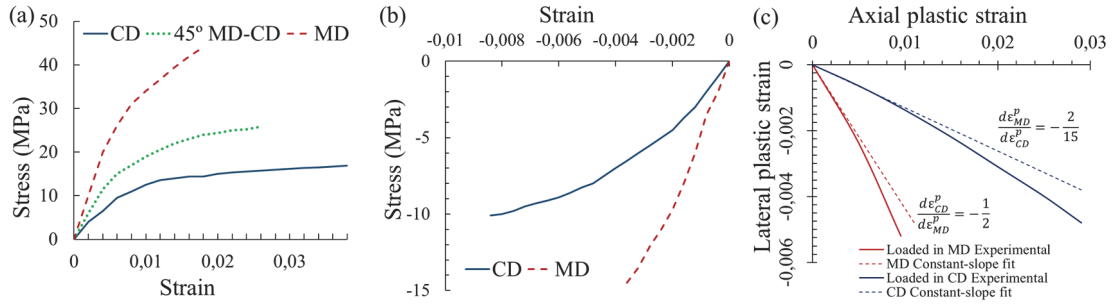

Figure 86. In-plane (a) tensile stress-strain curves; (b) compressive stress-strain curves; (c) Lateral plastic strain vs. axial plastic strain curves for tensile loading in the MD and CD; based on [118].

Table 15. Main mechanical properties of the paperboard, from [118].

	MD	CD	45°
Elastic modulus (GPa)	5.6	2.0	4.1
Tensile yield strength (MPa)	12.0	6.5	8.0
Compressive yield strength (MPa)	7.3	5.0	
Poisson's ratio	0.37	0.12	
Plastic strain ratio ($d\varepsilon^p_{CD}/d\varepsilon^p_{MD}$)	-0.5	-0.133	

The out-of-plane behaviour of the paperboard was also studied in [118] for various loading conditions, Figure 87. In the ZD-tensile curve, the stress increased linearly with strain at the beginning, with $E_{ZD}^{0} = 18.0\ MPa$. The non-linearity was limited before reaching a peak stress of 0.4 MPa and, after the peak, the curve exhibited pronounced softening, which was due to the growth and coalescence of multiple inter-laminar micro-cracks that were observed through a scanning electron microscope near the peak stress. The through-thickness shear curve had similar features, with a transverse shear modulus of $G_{12} = 34$ MPa and a peak shear stress of 1.1 MPa. The amount of lateral (in-plane) strain due to the tensile loading in ZD was negligible, indicating that Poisson's ratios coupling in-plane and out-of-plane responses are close to zero. Compression loading/unloading curves in ZD showed an almost linear relation up to a compressive strain of 3%, and an exponential increase of the stress after that [118]. After unloading from a strain higher than 20%, only a small permanent deformation remained, indicating that the compressive behaviour in ZD was non-linear elastic up to large strains.

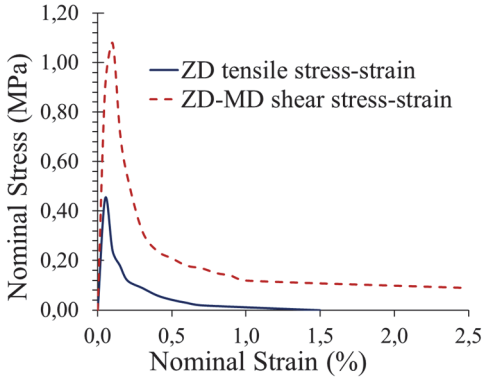

Figure 87. Out-of-plane behaviour of the paperboard, based on [118].

A three-dimensional constitutive model for paperboard was proposed in [100], considering the in-plane behaviour as elastic–plastic and the out-of-plane behaviour as elastic, and whose application was limited to predominant in-plane loading. The through-thickness stresses play a small role in the inelastic deformation and failure of paperboard under in-plane loading, because the strengths (tensile, compressive, shear) in ZD are considerable smaller than in MD-CD. However, the model could be combined with interlaminar decohesion models, to study the behaviour under significant out-of-plane loading. The model can be applied to situations that involve moderately large in-plane strains, as a finite deformation formulation was adopted. Although in the classical metals and polymers plasticity the underlying deformation mechanisms are governed by shear, and yield is driven by the deviatoric stress, there is no such evidence in the case of paper [100], where yielding is micromechanically governed by various forms of inter-fibre interactions. In [100], it was considered that the total stress drives the yield condition.

It is commonly accepted that the yield surface of cellulosic materials is anisotropic, but there are not many studies considering their initial and evolving multi-axial yield surfaces [100]. However, some biaxial failure surfaces of paperboard under combinations of MD and CD normal stress were obtained in [119], see Figure 88 (a) and (b). A similar approach was used in [100], where the initial anisotropic yield behaviour was modelled by a surface constructed from sub-surfaces defined by the experimentally measured initial yield strengths and plastic strain ratios in various loading conditions. A schematic of a four sub-surface system for biaxial loading, with zero in-plane shear stress, is shown in Figure 88 (c), and the model appeared to

be predictive of other in-plane stress–strain behaviour. In cellulose-based materials, strain hardening in a certain loading orientation often leads to softening in other loading directions, due to the reorientation of the polymeric chains into certain preferential directions. The evolution of post-yield plastic behaviour was described in [100] by an isotropic strain hardening model, and the results were compared with experimental results from [118], showing relatively good accuracy for predicting the behaviour under monotonic uniaxial loading, but often led to severe inaccuracy for non-monotonic loading schemes, such as cyclic loading. The authors of [100] claimed that the proposed model can be applied to a wide range of in-plane problems, such as bending or multiaxial in-plane loading.

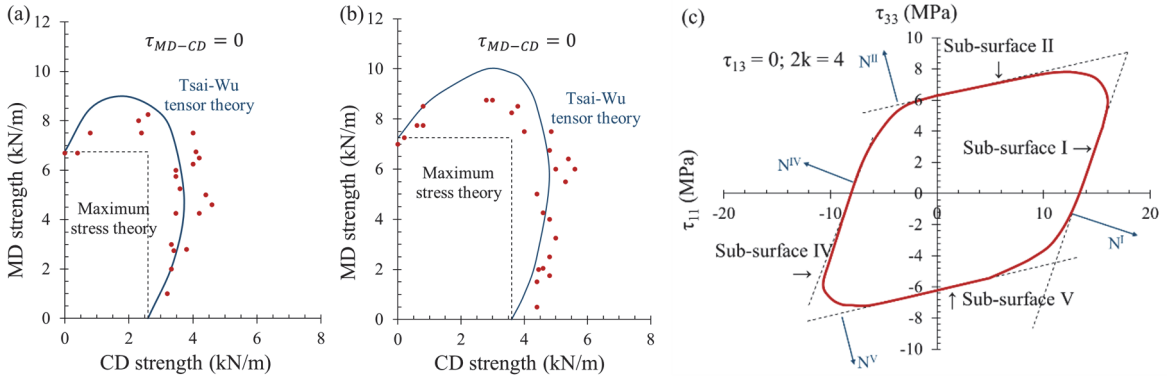

Figure 88. (a), (b) Biaxial failure surfaces, based on [84]*; (c) Initial yield surface for biaxial normal stress loadings where 2k=4, based on* [100].

An elastic–plastic constitutive model was developed in [85], based on small deformation theory, and including anisotropy and parabolic strain hardening, similarly as in [100]. However, in constrast to [100], where the yield condition depended on the total stress, here, the plastic description was based only on the deviatoric stress tensor. As in other models, the total strain tensor, ε, was decomposed into a sum of an elastic and a plastic components: $\varepsilon_{ij} = \varepsilon_{ij}^{e} + \varepsilon_{ij}^{p}$, and it was assumed that the volume is conserved during plastic deformation. The stress tensor, σ, was decomposed into a sum of a hydrostatic and a deviatoric part, and it was assumed that the plastic description can be based only on the deviatoric stress tensor, according to the hypothesis of von Mises. The limit for the initiation of yielding, f, was defined in [85] according to equation (*61*), where σ_e denotes a scalar measure of the effective stress, expressing the severity of the present stress state as a function of the second invariant, J_2, of the deviatoric stress tensor, and H is a scalar hardening function, monitoring the present location of the yield surface. If $f < 0$, the material behaviour is purely elastic; $f = 0$ means that the yield surface is reached, and the condition $f > 0$ is inadmissible and therefore has no physical meaning. Plastic deformation occurs if $f = 0$ and $d\sigma_e > 0$ are satisfied simultaneously.

$$f = \sigma_e(J_2) - H\left(\varepsilon_e^p\right) \tag{61}$$

A more general non-quadratic yield criterion for an isotropic effective stress measure was also considered in [85], based on [110], and expressed according to (62), where k is a factor (between 2/3 and 3/2, to meet the convexity requirement) that determines the influence of the third invariant, J_3, of the deviatoric stress tensor on the effective stress.

$$\sigma_e = \left(k\,(3J_2)^3 + (1-k)\left(\frac{27}{7}J_3\right)^2\right)^{1/6} \tag{62}$$

The results of both, the parabolic and non-quadratic stress–strain relations, were compared in [85] with experimental results, see Figure 89. The experimental and numerical procedures for evaluation of material parameters were described. Three uniaxial tensile tests and three uniaxial shear tests in the principal material directions were required for the calibration of the 17 independent material parameters for the model: nine elastic material parameters (E_1, E_2, E_3, ν_{12}, ν_{13}, ν_{23}, G_{12}, G_{13} and G_{23}) and eight parameters that described the strain hardening and the anisotropy of the material. The model had a good agreement with experimental observations.

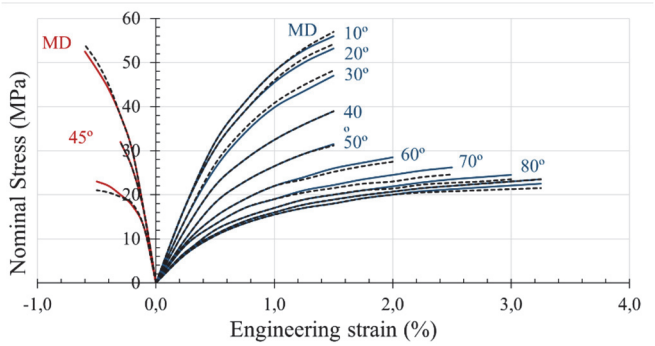

Figure 89. Experimental and numerical results of the non-quadratic formulation, based on [85].

A large-strain anisotropic elastoplastic orthotropic constitutive model for corrugated board (with thickness of 0.32 mm and 150 g/m²) was implemented in ABAQUS in [101]. A yield surface based on the Tsai–Wu failure criterion [120] was adopted, allowing for different yield stresses in the different directions, but also in tension and compression. A non-associated plasticity theory was used to calibrate the model with multi-axial experimental data, which required uniaxial and biaxial loading tests (conducted at 23°C and RH 50%, with a strain rate of 0.8 mm/min). Uniaxial tests in 45° to the MD were used instead of a pure shear test in the MD–CD plane, which was complicated due to the small thickness. In 90 from [101], the results of the experiments and the simulations are shown, and there is a good agreement between both. The uniaxial stress–strain curves up to fracture, 90 (a), showed clear anisotropy and an initial stress–strain linear relation which becomes non-linear after a certain stress value. A compression test in ZD, 90 (b), showed that the out-of-plane deformation was both elastic and plastic. In cyclic loading and unloading, 90 (c), some part of the deformation did not recover, motivating the need of modelling a plastic behaviour. Some material properties obtained from the tests in [101] were: $E_{11} = 3050\ MPa$, $E_{22} = 1172\ MPa$, $E_{33} = 35\ MPa$, $G_{12} = 720\ MPa$, $G_{13} = 10\ MPa$, $G_{23} = 10\ MPa$, $\nu_{12} = 0.3$, $\nu_{13} = 0.01$, $\nu_{13} = 0.01$. An approximate yielding point was considered where the stress–strain curve deviates from the linear-elastic behaviour, and properties related to initial yielding were: $\tau_{MD,\ tension} = \tau_{MD,\ compression} = 7\ MPa$, $\tau_{CD,\ tension} = \tau_{CD,\ compression} = 3\ MPa, \tau_{45º} = 7\ MPa$.

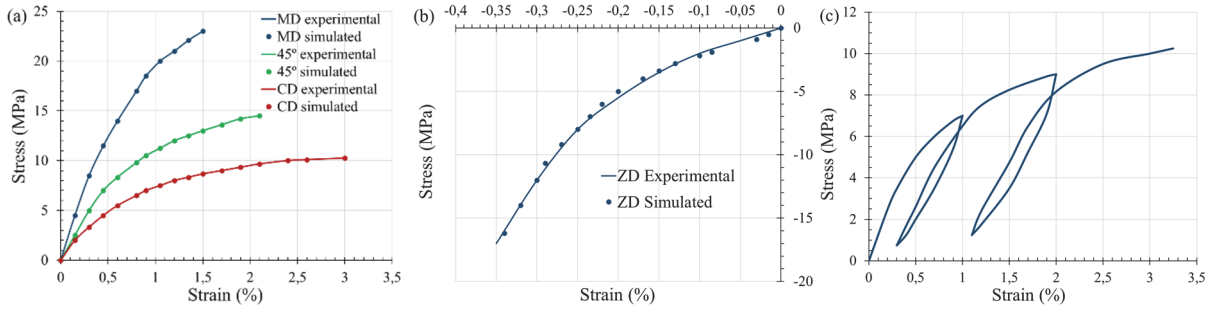

Figure 90. Comparisons of experimental results and simulation. (a) Uniaxial tension test in MD, 45° and CD; (b) Compression test in ZD; (c) Successive loading and unloading in CD; based on [101].

An anisotropic elastoplastic continuum-based model at finite strains for paperboard was presented in [102]. The Tsai–Wu surface, also used in [100] and [101], was introduced as yield criterion to model the softening effects, based on multiple hardening variables and considering that yielding in compression and tension differed. Orthotropy was treated in [102] following the same considerations as in [101]. The out-of-plane response was assumed to be decoupled from the in-plane response. The yield surface in [102] was based on six different sub-yield surfaces, whose hardening in the stress-space was non-isotropic and governed by the effective plastic strain, to consider non-proportional load histories. The yield planes were associated to: MD tension and compression, CD tension and compression, positive and negative oriented shear. An example of yield surface in which the shear stresses are zero can be seen in Figure 91. The required elastic constitutive parameters could be fitted from simple uniaxial tests, while the calibration of the plastic parameters was more complicated. More information about the yield surfaces, the coupling components and the numerical implementation can be found in [102].

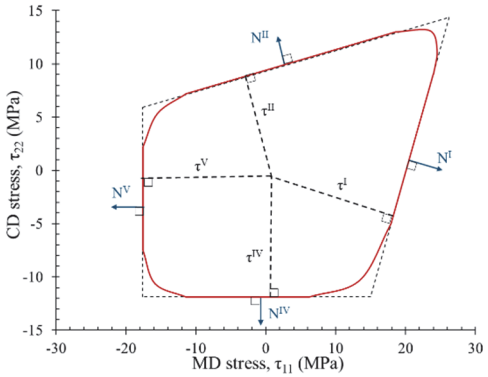

Figure 91. Yield surface for $\tau_{12} = 0$ and k=3, based on [102].

The model proposed in [102] was implemented in a finite element framework to study the response to loading at different angles in the plane and was compared with strain fields obtained from digital image correlation. The testing procedure can be seen in Figure 92 (a) and (b): the large sample was pre-strained until failure (6.5% in CD and 3.1% in MD), and several specimens were then cut out and loaded in the direction perpendicular to the original loading direction. The experimental results for both the situations without and with pre-straining are shown in Figure 92 (c) and (d). For the uniaxial MD and CD tests after pre-straining, a reduction in stiffness (about 25% for the MD direction and 13% in CD) and a reduction in the hardening were observed. The pre-loaded paperboard displayed a softened response which could be modelled by introducing coupling effects (a softening taking place in the direction perpendicular to the loading direction). The model showed a relatively good agreement with experimental results, especially in tension.

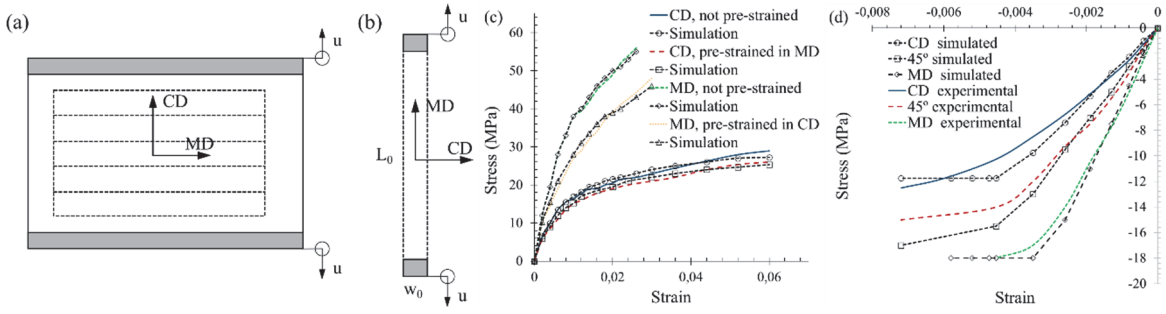

Figure 92. (a) Uniaxial pre-straining of a test-piece in CD; (b) Uniaxial loading of sample in the orthogonal direction to the pre-straining direction in MD; (c) and (d) Uniaxial force vs. displacement curves in CD and MD, based on [102].

The modelling of the behaviour of board materials in ZD is relevant because there are operations during manufacturing and operation in power transformers in which these materials are subjected to a multiaxial stress state, or directly, to loading in ZD. In [94], the elastic-plastic behaviour in ZD was modelled assuming small-strain orthotropic linear elasticity and a quadratic yield function which was assumed to depend on the equivalent plastic strain defined by the rate of plastic work. The yield function for a multiaxial stress state was given by equation (63), where Y is the uniaxial yield stress, A is a symmetric matrix and b is a vector, both containing material constants. The rate of plastic strain was defined with the introduction of a plastic potential.

$$f = \sigma^T A\, \sigma + b^T \sigma\, Y - Y^2 \tag{63}$$

The purpose of the Arcan device is to subject paperboard to testing under simultaneous normal (in ZD) and shear loads [121]. In [94], a modification of the Arcan device for the characterisation of paperboard in ZD was proposed, see Figure 93 (a). The device consisted of two parts: the front, where the test piece was glued with a high viscosity adhesive; and the fixture, with two beams connected to the test piece and to a flexible plate that allowed small movements, designed to suppress deformations of the test piece in all but two directions (ZD and one in-plane direction). With that device, a constant load was firstly applied in ZD, and then a shear test was carried out, with the purpose of defining a biaxial yield surface, Figure 93 (b). The stress-strain curve in ZD initially showed linear elastic behaviour and, above some stress level, a nonlinear elastic-plastic response was initiated. A strain-hardening behaviour was observed between the limit stress and the maximum stress and, after the peak load, paperboard showed strain-softening, mainly due to delaminations. Positive shear in MD had an initial slope between 28.0-37.6 MPa, and a peak stress between 1.02-1.09 MPa. The values for negative shear in MD, were 28.3-31.6 MPa and 1.07-1.17 MPa respectively.

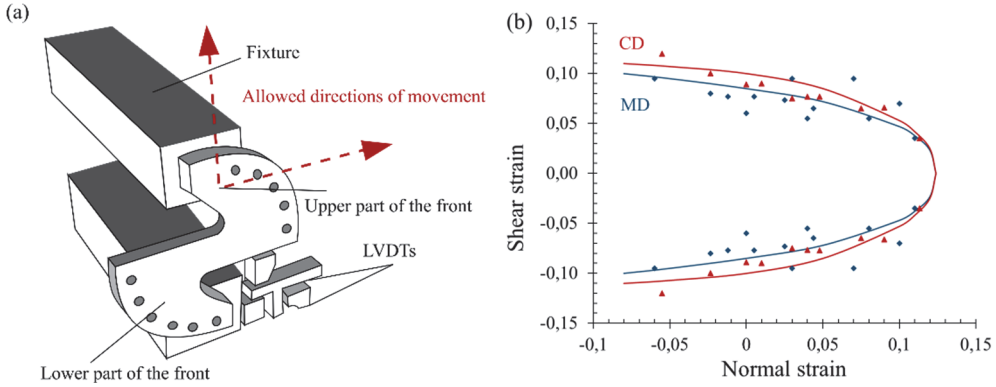

Figure 93. (a) The Arcan device for out-of-plane testing of paperboard; (b) Failure surface in strain-space for tests in MD and CD, and curves fitted using the yield function; based on [94].

The Arcan method was modified in [95], for measuring properties in ZD of five different board materials under ZD tensile, compression and shear loading. The deformation of the test piece was restricted to two directions in the considered plane of deformation, by introducing a fixture that allows only two degrees of freedom and a liquid adhesive with limited penetration into the paperboard. In [95], the paperboard was considered as orthotropic with Poisson's ratios connecting out-of-plane strain with in-plane strains equal to zero: $\nu_{zx} = \nu_{xz} \simeq 0$; $\nu_{zy} = \nu_{yz} \simeq 0$. Due to the uneven surface of paperboard, the small thickness dimension and its porous structure, the moduli in ZD could not be determined with the same precision as the corresponding in-plane properties. Several stress-displacement curves for the different types of board on non-glued and glued test pieces can be found in [95]: normal stress-strain curves

in tension, shear stress-strain curves in xz and yz directions, force-displacement curve, etc. Paperboard showed a strain-hardening behaviour up to peak load, and strain softening after the peak load.

In [103], several tests were performed to characterise the response to compressive, shear and combined loadings of a board material, previously studied in [94],[95]. As no major differences in the ZD behaviour were noticed for shearing in MD and CD, only shearing in MD was considered when illustrating the general behaviour. An elastic–plastic material model for the out-of-plane response of the material subjected to combined shear and high compressive loads in ZD was presented in [103], in which the Poisson effect was omitted, and the only non-zero components of the stress and strain tensors, σ_{ij} and ε_{ij}, were: $\sigma = \begin{pmatrix}\sigma_{zz}\\ \tau_{xz}\end{pmatrix}$, $\varepsilon = \begin{pmatrix}\varepsilon_{zz}\\ 2\varepsilon_{xz}\end{pmatrix} = \begin{pmatrix}\varepsilon_{zz}\\ \gamma_{xz}\end{pmatrix}$. The elastic deformation in ZD was modelled as non-linear, with a stiffer response from a compressed material than from a non-compressed one, because of the porous structure of paperboard; the elastic deformation in ZD shear was modelled as linear. The elastic strain in ZD was split into two parts, deformation of the voids, ε_e^{void}, and deformation of the solid fibre-structure, ε_e^{sol}: $\varepsilon_e = \varepsilon_e^{void} + \varepsilon_e^{sol}$. The voids ratio, r, was used to characterise the porous material: $r = \frac{V_v}{V_s}$, where V_v is the volume of voids, and V_s is the volume of solid fibre-structure.

The in-plane stresses were assumed to have negligible influence on the voids volume, due to their small level compared to the strains in ZD. Only the strain in ZD, ε_{zz}, could change the volume of the voids. Using logarithmic strains, equation (64) was obtained in [103], where σ_{zz} is the stress in ZD, σ_z^t is the tensile strength in ZD and $\varepsilon_{e,zz}^{void}$ is the elastic strain in ZD due to deformation of the voids. The strain related to the voids, $\varepsilon_{e,zz}^{void}$, was determined by the total strain, the plastic strain and the stress in ZD from equation (65). The Young's modulus was a function of the density, whose initial vale was $E_z^{initial}$, and E_z^{end} was the value when the voids had been completely compressed, see equation (66), Where r_p is the voids ratio induced by plastic deformation, which is a function of the plastic volumetric strain $r_p = \left(1 + r_{orig}\right)\left(e^{\varepsilon_{p,vol}^{void}} - 1\right)$.

$$\sigma_{zz} = \sigma_z^t\left(1 - e^{\frac{1+r_0}{\mu}\left(1-e^{\varepsilon_{e,zz}^{void}}\right)}\right) \tag{64}$$

$$\varepsilon_{e,zz}^{void} = \varepsilon_{zz} - \varepsilon_{p,zz} - \frac{\sigma_{zz}}{E_z^{solid}} \tag{65}$$

$$E_z^{solid} = \left(1 + \frac{r_p}{r_{orig}}\right)E_z^{initial} - \frac{r_p}{r_{orig}}E_z^{end} \tag{66}$$

The plastic deformation was modelled in [103] using a parabolic yield surface expanding towards a bounding surface, both with variable size and position according to hardening parameters, and an associative flow rule. Initiation of plastic deformation was governed by that yield function, f, which depended on the out-of-plane stress components, and hardening parameters, K_β $(1, 2, \dots)$, according to: $f = f\left(\sigma_{zz}, \tau_{xz}, K_\beta\right)$. The selection of the hardening parameters and their evolution is explained in [103]. Once the yield surface was reached, plastic deformation was introduced and increased with further loading. The direction of the plastic deformation was determined by a plastic potential. The material parameters were determined experimentally by tensile testing for the failure stress in tension, and several shear tests under different constant compressive loads for the hardening parameters in shear, the

internal coefficient of friction and the initial bounding compressive stress. By combining non-linear elasticity and bounding surface plasticity, the increasing out-of-plane stiffness of the material, both in compression and shear, and increasing shear strength after previous compression were well captured. The model and the shape of the bounding surface can be calibrated for most paper materials, according to [103], through changes of the material and hardening parameters.

A load cycle consisting of consecutive loadings and unloadings at an increasing overall load is shown in Figure 94 (a). The elastic response was nonlinear, as indicated by the unloading curves, and the elastic–plastic behaviour in compression was approximately exponential, with the elastic stiffness increasing with the plastic compression. Some monotonous shear tests were performed in [103], in which different compressive load were first slowly applied, and then followed by shear loading, Figure 94 (b). The material could withstand higher shear loads if it was subjected to compression in ZD and, for high compressive loads, the shear stress approached an asymptote with no clearly visible peak. When the compressive loads were low, there was a distinct peak, which increased if the material was first plastically compressed, followed by subsequent softening, as previously observed by [94], [95] and [100]. In Figure 94 (b), the test pieces were first loaded to a normal stress of -10 or -30 MPa, and then unloaded up to of -3MPa, which was kept constant as the shear load was applied.

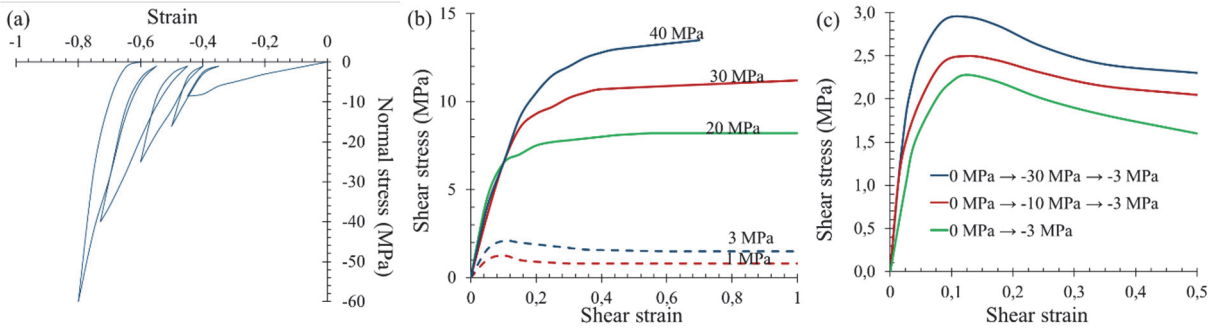

Figure 94. Stress–strain curve (a) under consecutive through-thickness loadings and unloadings; (b) in shear in MD for different compressive loads; (c) in shear in MD at a compressive load of 3 MPa, based on [103].

According to [96], multi-ply paperboard can be represented by a continuum model, in terms of stresses and strains, together with an interface model, in terms of tractions and displacements, as previously introduced by [100]. When paperboard is loaded in ZD tension, the initial response is elastic and almost linear until a peak load is reached, and paperboard deforms in a continuum-like behaviour. After the peak load, local delamination is initiated and the interface cracks. When a compressive load is applied in combination with shear loading, the delamination can be suppressed [96]. In the continuum model in [96], the in-plane and out-of-plane models were uncoupled. The ZD model was elastoplastic in compression, and the plastic behaviour was divided into one yield surface for ZD compression and one for shear. The yield surface in ZD compression was given by equation (*67*), where the hardening is $\sigma_s = B_p\left(C_p\varepsilon_{zz}^p - 1\right)$, where B_p and C_p shall be determined experimentally from the stress-strain curve. The yield surface for shear was given by equation (*68*). The observation that the hardening in shear increased with the compressive stress in ZD, was incorporated into the hardening: $\tau_s = \tau_0 + (A_\tau - \sigma_{zz}B_\tau)\gamma^p$, where τ_0 and A_τ are material constants determined from a shear test, and B_τ is a material constant determined from experiments with combined shear and compressive stresses.

$$f^{comp} = -\sigma_{zz} - \sigma_s \tag{67}$$

$$f^{shear} = \sqrt{\tau_{xz}^2 + \tau_{yz}^2} - \tau_s \tag{68}$$

As in multiply paperboards few fibres cross the interfaces, there are weaker regions in ZD, and delamination between plies is a dominating damage mechanism in which the continuum assumption is no longer valid. Thus, in tension, a cohesive model expressed in terms of tractions and displacements was proposed, sharing some features with the one in [100]. The relative displacement between two opposing surfaces was divided into elastic and plastic parts, referred to the local coordinate system at the interface: $\delta_i = \delta_i^e + \delta_i^p$. Interface damage depended on the interface strength and stiffness, which are functions of the total equivalent plastic displacement. All the material constants have to be determined from experiments. Both the continuum and interface models were implemented into ABAQUS. A cyclic tension ZD test was simulated, Figure 95 (a), and the models together could capture the experimental ZD tension curve well with respect to stress levels. There was one discrepancy in the elastic part, because the elastic stiffness in the interface model was initially set high, in order not to interfere with the continuum model. Simulations were also performed to analyse how the compressive and shear behaviour interact, Figure 95 (b).

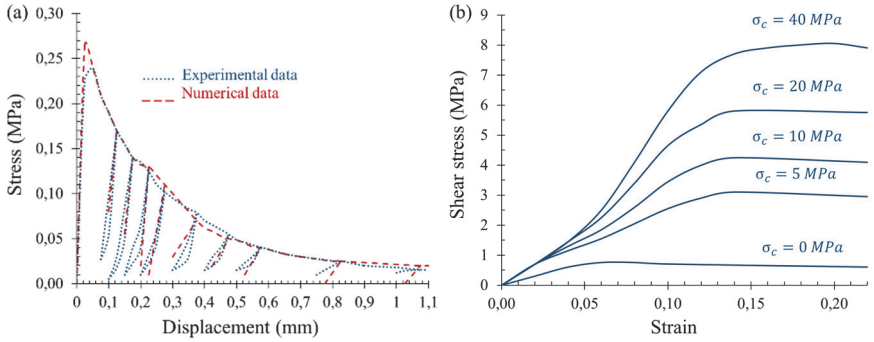

Figure 95. (a) Comparison between experimental and numerical data in a cyclic tensile test; (b) Simulation of a shear test with different compressive stresses, based on [96].

The relation between the microscopic structure of pressboard and the macroscopic response to compression in ZD, and deformation mechanisms occurring in the thickness direction, were studied in [5] and [6]. Pressboard samples were subjected to a compression of 5 MPa in ZD, and subjected to stress relaxation soon afterwards [6]. X-ray micro-computed tomography was used as a non-destructive method to get a picture of the deformation patterns. The Digital Volume Correlation (DVC) method was used for the analysis of the highly heterogeneous microstructure of pressboard and allowed the definition of deformation field and density gradient at different depths from the top surface. The results revealed a strong correlation between the density variation within the sample and the strain calculated from the 3D images. Figure 96 (a) shows the distribution of the relative density on surface parallel to the MD-CD plane sliced at two different depths. At a depth of 160 µm, the density variation caused by the wire marks has almost completely vanished. The relative density within the thickness of the test piece, Figure 96 (b), shows that the compression caused a rather uniform densification, with some increased densification areas nearer to the surfaces and density peaks in the middle section of the sample. The largest deformation occurred when the fibres occupied the free space in the network [6]. On the micrometre-scale, high-density fibre pressboard behaves as a porous material rather than a fibre network.

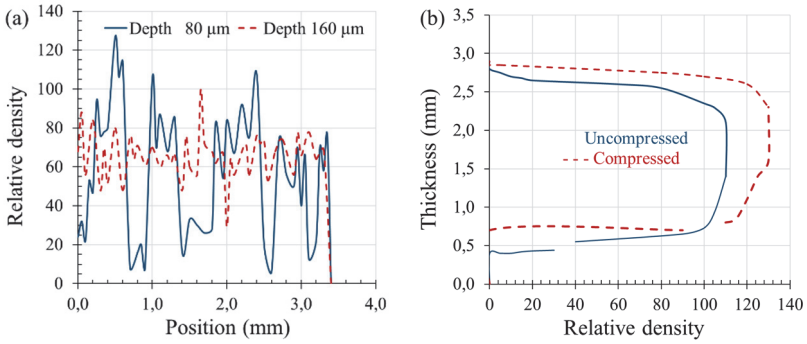

Figure 96. (a) Relative density for unloaded and loaded test piece; (b) Density distribution in the MD-CD plane at different slicing heights from the top surface, based on [5].

- **Viscoelastic and viscoplastic models for board materials**
  - **Mechanical models considering the behaviour in MD, CD and ZD.**

An anisotropic viscoelastic-viscoplastic continuum model for the stationary and transient in-plane and out-of-plane mechanical behaviour of high-density cellulosic materials was presented in [84]. The model was implemented into a finite element programme and required a considerable amount of parameters, whose calibration is described in [84]: 9 orthotropic stationary elastic properties, 10 viscoelastic parameters, 3 parameters defining the anisotropic yield surface, 6 parameters for the densification process, 2 viscoplastic power-law parameters, 10 initial plastic resistances, and 30 strain hardening parameters. In [84], samples of high-density board with thicknesses of 3 and 6 mm were subjected to uniaxial tensile tests in different orientations, see Figure 97 (a), which can be described by a bi-linear stress–strain behaviour: linear elastic in the beginning of the deformation, and a linear hardening during plastic straining. The in-plane anisotropy seemed to be relatively weak (about 20%) in comparison to other materials. There was an asymmetry in tension and compression, Figure 97 (b), which was included in the model. The hardening of the material in MD increased with the applied strain rate, Figure 97 (c), while the initial slope of the stress–strain curve was quite similar for the different strain rates.

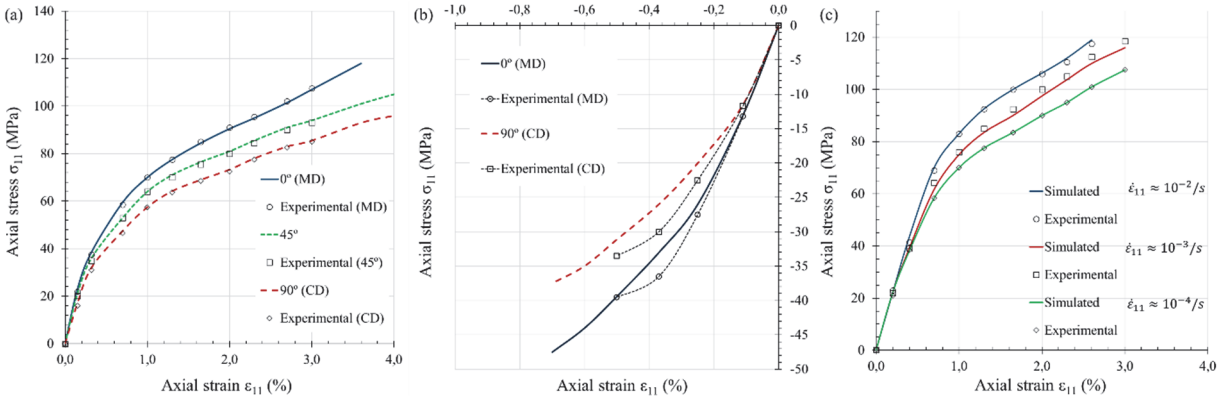

Figure 97. In-plane response of high-density pressboard subjected to uniaxial tension: (a) axial stress, (b) during uniaxial compression, (c) during uniaxial tension with various strain rates, based on [84].

To describe the in-plane time-dependent elastic strain of high-density board, a standard linear viscoelastic constitutive law was applied in [84], such that the overall stress response was related to the magnitude of the elastic strain, as well as the history of the elastic deformation. The anisotropic non-quadratic yield criterion of [100] was modified in [84], particularly in the description of the sub-surfaces associated with in-plane shear components. The positive and negative yield strengths differed, resulting in an asymmetric yield surface.

The post-yield in-plane material behaviour was described by an anisotropic power law viscoplastic model, where the evolution of the accumulated plastic strain during loading was driven by the magnitude and direction of the stress. A power-law equation was used to describe the kinetic relation for the plastic flow-rule incorporating time-dependent plastic behaviour, such as creep and stress relaxation. The continuum elastic–plastic model in ZD initially proposed by [103] was adopted in [84], which accounted for the effects of densification, and the post-yield hardening behaviour was related to the pores-to-fibre ratio via an exponential law previously used in [97]. The initial elastic Young's modulus in ZD and the plastic properties of the material were increased due to densification during compression, through an exponential law. The total plastic resistance or yield strength of the yield sub-surface(s) associated with the out-of-plane normal compressive stress was used to consider the contribution of the densification process.

The stress–strain response during cyclic loading showed hysteresis associated with the viscoelastic effect, but the hysteresis was virtually unaffected by the applied strain rate, Figure 98(a) and (b). The anisotropic–kinematic hardening combined with the lower effective strength under compressive stress state of the model in [84] was able to adequately capture the softening effect, Figure 98 (c) and (d). In some cases, plastic compressive strains developed very early during unloading, even though the material was effectively still under tension. The model predictions and experimental results had a good agreement during in-plane relaxation and creep tests, see Figure 98 (e) and (f).

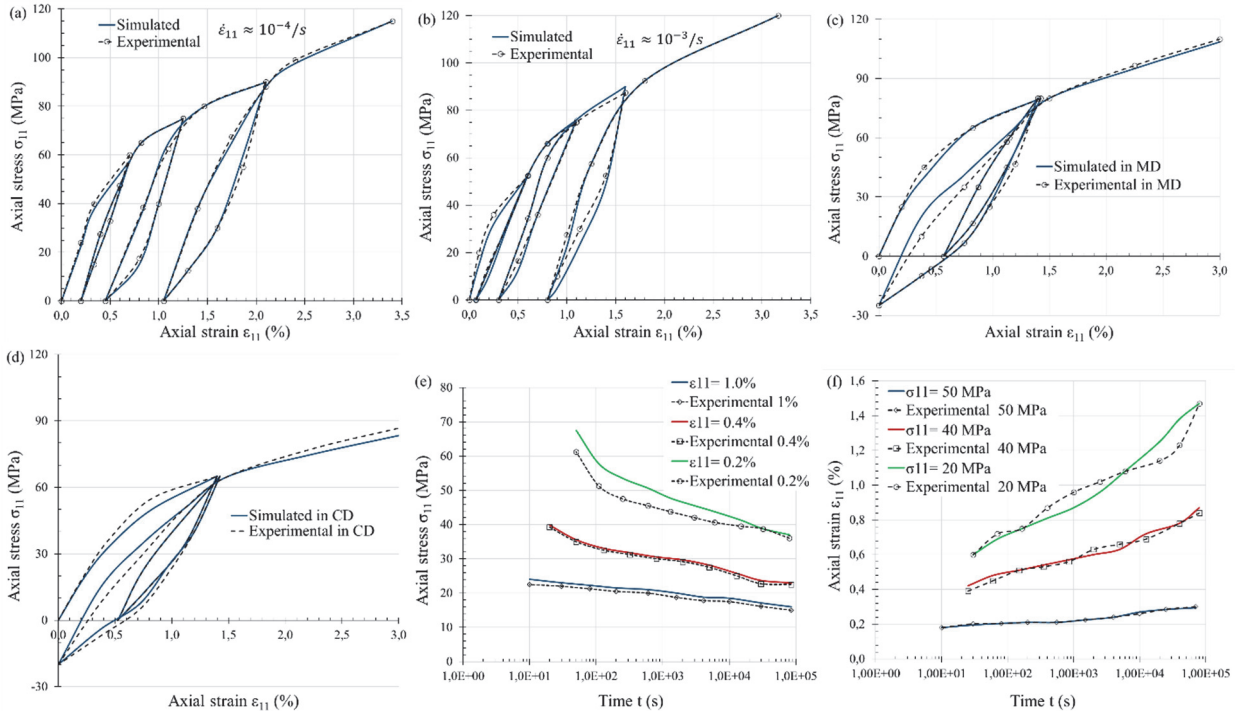

Figure 98. In-plane stress–strain response of high-density pressboard during cyclic tensile loading with strain: (a) with rate 10^{-4} s^{-1}, (b) with rate 10^{-3} s^{-1}; (c) in MD and (d) in CD orientations subjected to extended cyclic loading; (e) In-plane axial stress of high-density pressboard during tensile relaxation test; (f) In-plane axial strain of high-density pressboard during tensile creep test; based on [84].

- **Mechanical models focusing on the behaviour in ZD.**

The dynamic response of pressboard spacers in transformer windings subjected to transient loading similar to the one produced by short circuits was studied in [79]. The transformer coil subjected to axial vibration was considered as a multiple lumped spring-mass

system, Figure 99 (a), where the conductors were the masses and the layers of pressboard and paper insulation between them were the springs. This approach was firstly used in [122], where a three-element model was suggested, which was later extended by [123].The main flexibility of the system was assumed to be in the pressboard, while core and frame were relatively stiff. A simulation of a transformer-coil incorporating the pressboard for the axial dynamic behaviour during short circuits which produce was developed in [79], for predicting the axial vibration response to short-circuit forces which can cause failure of transformer coils.

Many impact tests by means of a mass on a stack of pressboard, impregnated in oil, were performed in [79] to produce large transient forces and displacements, see Figure 99 (b). Stress-strain oscillograms, recording the displacement of the mass and the force on the pressboard immediately after the impact, were used to obtain the dynamic stiffness and damping characteristics at temperatures from 23 to 100°C, preload pressures from 1034 to 5516 kPa, and dynamic stresses over the normal range of operating conditions during a short-circuit. The stress and strain characteristics of pressboard were highly nonlinear, see Figure 100. The stress-strain curves for moderate preload and high preload showed two distinct stiffness regions: one below the preload point with a much lower stiffness, which approximately followed the static stress-strain curve obtained when the pressboard was slowly loaded, and another above it [79]. The initial preload point was on the static curve and, when an impact force was applied suddenly, the oil was subjected to high pressure and started squeezing through the pressboard matrix, which opposed a high flow resistance, and, during this time, an additional stiffness due to the bulk modulus of the oil appeared [79].

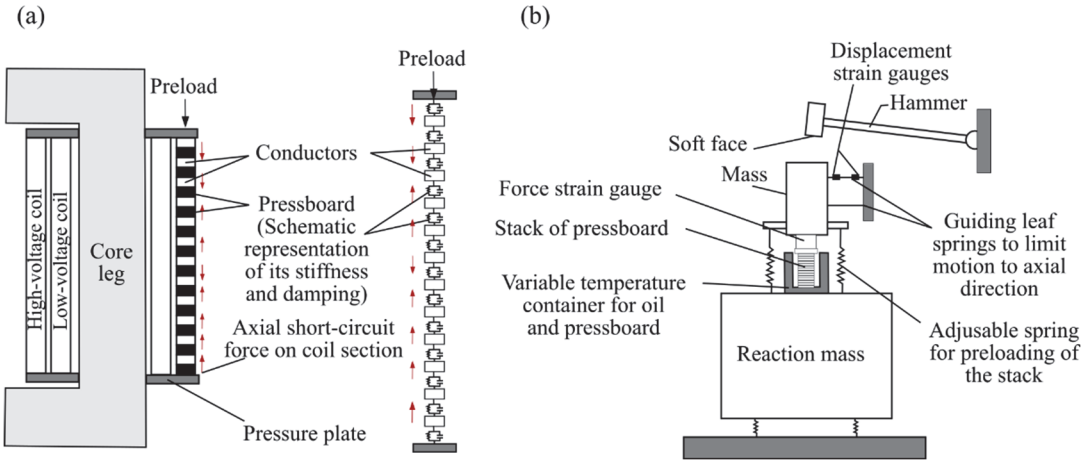

Figure 99. (a) Transformer and dynamic simulation for calculation of short-circuit vibration; (b) Test apparatus for measurement of the dynamic stiffness and damping of transformer coil insulation, from [79].

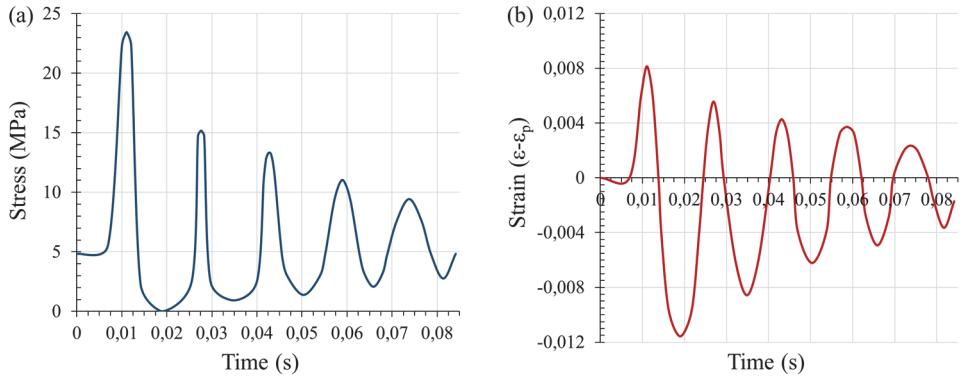

Figure 100. Typical (a) dynamic stress and (b) strain of mass loaded pressboard after impact, at 23°C and 4,83 MPa preload, based on [79].

A closer look at the structure of paper reveals that the density is not constant along its thickness: the regions near the surface have a much lower density and are thus more deformable than the bulk of the material. This is true for paper sheets in which the surface unevenness is the order of few fibre diameters, but will be more marked in pressboard [4]. The response of the material in ZD depends on the compressive stiffness of the fibre network and the size of the contact areas between fibres, which are increased by densification, although that increase is more marked in networks with lower density, where the available space for deformation is larger. This phenomenon accounts for part of the non-linear shape of the stress-strain curve [4]. The relation between density and stiffness in ZD of two pressboards (High Density (HD) 1250 kg/m^3, and on Low Density (LD) 800 kg/m^3) was investigated in [4], through compression tests at different temperatures and moisture contents. A pressboard stack of bits separated by 0.2 mm thin metal plates and inserted between two large steel plates was subjected to compression cycles, see Figure 101 (a), (b). The stress-strain curves for the first and last loading cycles showed that the largest deformation and the lowest elastic modulus were measured during the first cycle. That large permanent deformation was caused by the plastic deformation of cellulose fibres, which adjust and fill in the voids within the material, which had never been subjected to high load before the compression test.

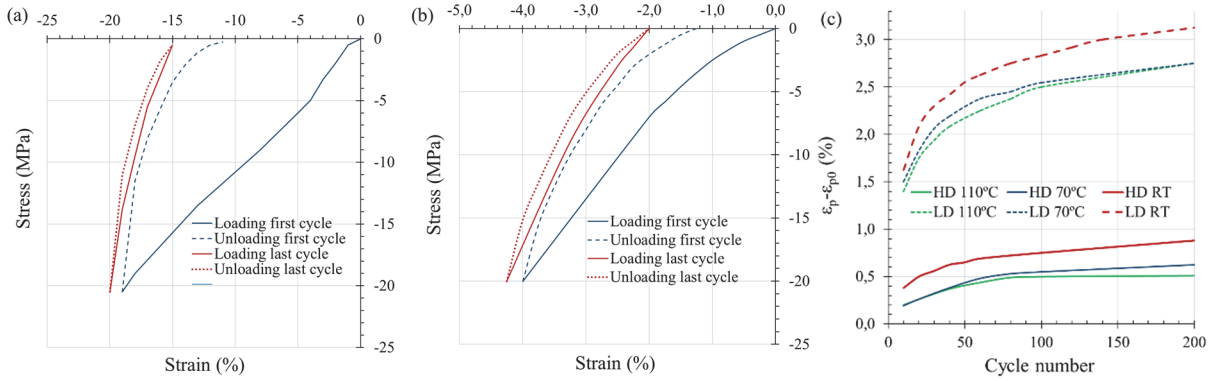

Figure 101. (a) Stress-strain curve for LD moist pressboard at RT; (b) Stress-strain curve for HD moist pressboard at RT, (c) Plastic deformation of LD and HD pressboard at different temperatures during compression cycles; based on [4].

Figure 101 (c) shows the structural changes after the first cycle, by picturing the difference between the total plastic deformation, ε_p, and the plastic deformation of the first cycle, ε_{p0}. After the first few cycles, the slope of plastic displacement was fairly constant with the number of cycles and kept growing until the end of the experiments. A slight difference was noticed in the onset of plastic deformation of RT test pieces compared to high temperature ones. The total deformations after the first cycle and at the end of the load cycles, see Table 16, showed that moisture had a larger effect than high temperature in terms of stiffness reduction and plastic deformation. The compressive stiffness index (CSI) was the elastic modulus, E_z, divided by the initial density, ρ_0, and its value grew with the number of cycles and moist pressboard showed lower stiffness compared to dry and hot material. For LD material, the CSI at 70°C is higher than the one measured at 110°C; while there was almost no difference in the CSI for dry and hot HD.

Table 16. Deformation of the test pieces, from [4].

	HD			LD		
Deformation	RT	70°C	110°C	RT	70°C	110°C
After the first cycle	1.15%	0.75%	0.21%	11.4%	7.5%	2.6%
After 200 cycles	1.95%	1.21%	0.85%	14.5%	10.7%	5.4%

In [97] an orthotropic continuum-based mechanical model for HD pressboard was developed, focusing on the response to ZD stresses which caused both viscous deformation and permanent compaction, and considering the double nature of fibre-network and porous material of the pressboard. Similarly as in [84] or [99], the model in [97] was based on a combined viscoelastic-viscoplastic constitutive law, formulated at infinitesimal strains, where the total strain tensor, ε, was decomposed into: $\varepsilon = \varepsilon_{ve} + \varepsilon_{vp}$. The post-yield behaviour was described, as in [84], using the parameter γ to represent the amount of accumulated plastic strain during loading. The rate of plastic strain was given by: $\dot{\varepsilon}_p = \dot{\gamma}K$, where the tensor K represents the direction of the plastic flow. The mechanical properties of the material were obtained from creep test, monotonic loading and compressibility tests. The constitutive model was implemented into ABAQUS.

The experimental results of compressive loading-unloading sequences with an increasing pressure up to a maximum of 60 MPa were compared with the simulation in [97], and the overall stress-strain behaviour was dominated by the densification mechanism, with a decrease of the pore-to-fibre ratio of up to 50% of the initial value. Thus, the incorporation of densification hardening effects into the model similarly as in [84], through an exponential law in which the out-of-plane elastic moduli depended on a densification factor, was critical to capture deformation in ZD. The slope of the strain in different creep tests was almost identical, Figure 102 (a), suggesting that, within the considered range of creep load, the rate of creep under compression in ZD was not affected by the magnitude of the applied load. These results might differ if the effects of temperature and moisture are included. Both the residual part, C_{res}, and the reversible part, C_{rev}, of the compressibility were evaluated experimentally and with the numerical model, obtaining a compressibility level around 3.8%, Figure 102 (b). The model predicted a slightly lower reversible part (76%) than the experimental one (81%). A qualitatively good agreement between model predictions and experimental observations was obtained in [97], suggesting that all the elements needed to capture creep at RT in moist conditions were included. However, other mechanisms such as material damage development might be considered to improve the overall model predictions.

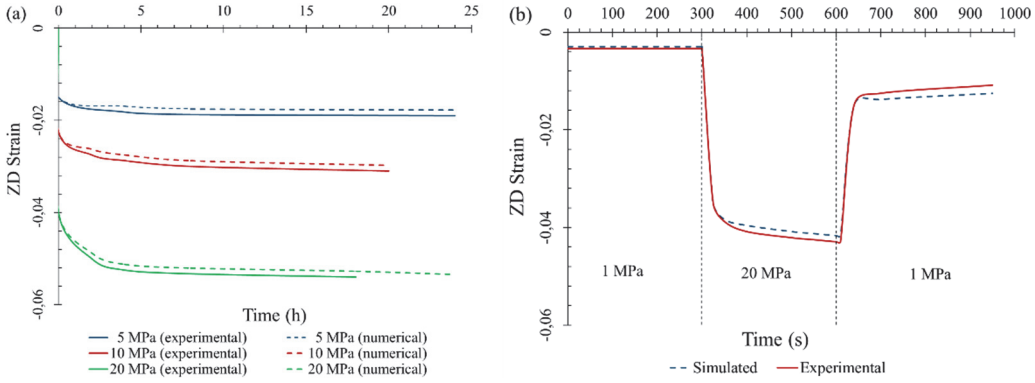

Figure 102. Results of experiments and simulation (a) on the evolution of the compressive strain of HD pressboard during creep, (b) in the compressive strain evolution during standard compressibility test of HD pressboard, based on [97].

The effects of different combinations of temperature, moisture and mechanical load on the deformation in ZD of HD pressboard samples were analysed in [98], and a constitutive model based on a viscoelastic–viscoplastic description was developed. The total strain, ε, was decomposed into the elastic part, ε_e, the plastic part, ε_p, and the thermal/hygro expansion part, ε_v: $\varepsilon = \varepsilon_e + \varepsilon_p + \varepsilon_v$. A standard linear viscoelastic law was applied to describe the time-

dependent behaviour, such that the overall stress response was related to the magnitude of the elastic strain and to the history of the elastic deformation $\sigma = \sigma(\varepsilon_e, \dot{\varepsilon}_e)$. The overall stiffness of the material was considered as non-linear, and depended on temperature (θ) and moisture content (ρ), as given in equation (69), where C_0 was the elastic stiffness at the reference climate condition $C_0 = C_0(\xi, \theta_0, \rho_0)$; ξ was a parameter describing densification in ZD; $\phi^e(\theta)$ was an empirical function representing the effect of temperature; and $\psi^e(\rho)$ was an empirical function representing the effect of moisture.

$$\bar{C} = C_0\, \phi^e(\theta)\, \psi^e(\rho) \tag{69}$$

The post-yield behaviour was described in [98] by an anisotropic viscoplastic model, following a power-law kinetic equation: $\dot{\varepsilon}_p = \dot{\varepsilon}_p(\sigma, S_Y)$, where σ was the stress tensor, and S_Y was the resistance against plastic deformation or yield strength, which was also a function of temperature and moisture: $S_Y = S_0 \phi^p(\theta)\, \psi^p(\rho)$. S_0 was the yield strength at the reference climate condition $S_0 = S_0(\xi, \theta_0, \rho_0)$; $\phi^p(\theta)$ and $\psi^p(\rho)$ were empirical functions characterising the effects of temperature and moisture, respectively, on the overall plastic yield strength. The same hardening model, considered in [97], adopting an exponential law, was also used in [98]. The experimental and simulated temperature and moisture effects on the elastic stiffness and yield strength showed a good agreement, see Figure 103 (a), (b).

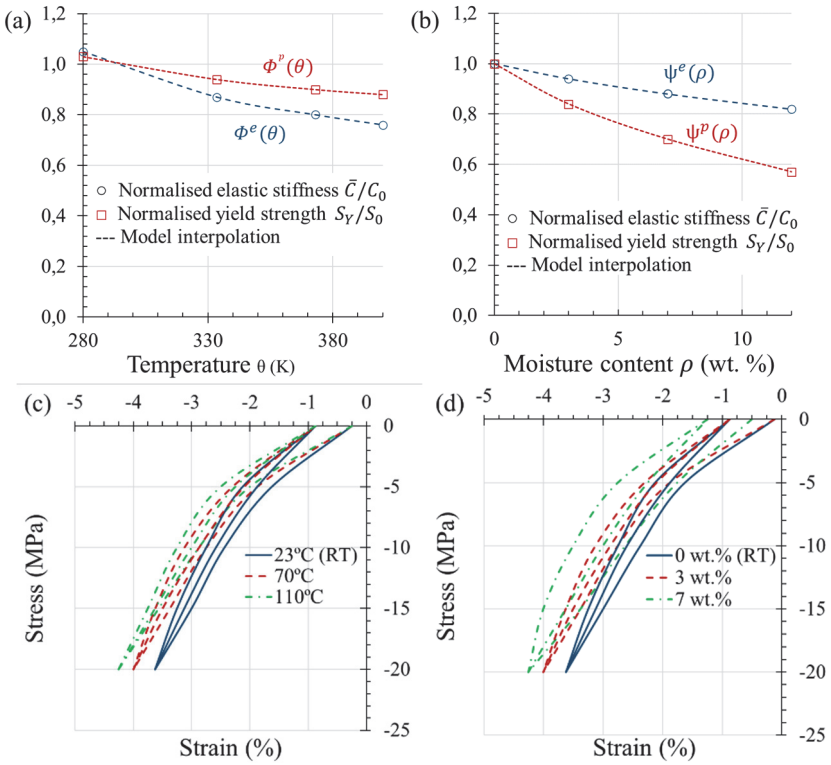

Figure 103. (a) Temperature effects and (b) moisture effects on the overall elastic stiffness and plastic yield strength of pressboard; Stress-strain response (c) of set of experiments I and (d) of set of experiments II from [98].

In [98], consecutive loading-unloading tests were performed on stacks made of HD pressboard bits with a thickness of 3 mm, to analyse the effect of different temperature levels (set I, dry) and the influence of moisture contents (set II, temperature 23°C). The curves represent two cycles, and the first one generated large irreversible deformations. The overall response, particularly the hysteresis, were very similar over the considered range of temperatures, Figure 103 (c), but higher temperature led to a reduction in stiffness, larger compliance, and a lower effective strength. The influence of moisture on pressboard was similar to the one of temperature, Figure 103 (d), but the effects on the stress–strain

hysteresis were more visible: during unloading, a larger amount of permanent plastic strain was observed, indicating that the plastic yield strength was more affected than the elastic stiffness.

In [99], a continuum model was developed for describing the responses of HD board materials subjected to various transient loads in ZD. The standard linear viscoelastic constitutive law applied in [84] was also used in [99]. Both models also adopted the continuum through-thickness elastic–plastic initially proposed by [103], considering the effects densification on the material properties, following the same exponential law for the continuum approximation in porous media from [97]. The constitutive model was simplified into a 1-D formulation, which was implemented into the ABAQUS FE programme. For the validation of the model, pressboard test pieces were subjected to progressive compressive loading–unloading sequences in ZD with an increasing load-peak up to 60 MPa. The slope of the stress–strain curves was relatively high at the beginning of unloading, but decreased quite rapidly as the stress approached zero, mainly due to two mechanisms. The elastic modulus in ZD evolved due to material densification in the first part of the unloading curve. Then, the effects of kinematic hardening (the yield limit in tension affected by the increase in yield stress in compression) started to dominate the overall behaviour. The predictions of the model showed a good agreement with the experiments.

Three different compressive strain levels were applied in the stress relaxation tests in ZD [99]: $\bar{\varepsilon} = -1.2\%, -2.0\%$ and -3.5 %, which corresponded to initial stress levels of σ_0 =-5, -10 and -20 MPa, respectively, Figure 104 (a). The creep behaviour was analysed for various stress levels: $\bar{\sigma} = -5, -10$ and $-20\ MPa$, Figure 104 (b), and the model adequately predicted the experimental response, except for the lowest creep load ($\bar{\sigma} = -5MPa$). The cause could be that, in the low stress regime, the effects of inhomogeneity became more pronounced. During relaxation in ZD, the decay of the material stiffness was dominated by viscoelastic effects, similarly as in the in-plane deformation, and the effect of material densification was not particularly significant, since the level of compressive strain was held constant. In contrast, material densification continuously took place during compressive creep in ZD, with an increasing magnitude of ε, resulting in an increase of the effective material stiffness.

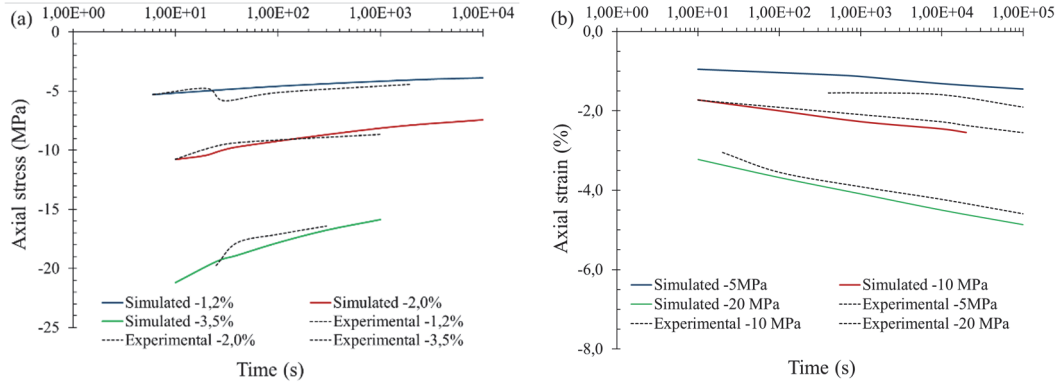

Figure 104. Pressboard responses during (a) relaxation tests; and (b) during creep tests, based on [99].

5.4. Modes of failure of paper

5.4.1. Introduction

Fracture mechanics is the field of applied mechanics that deals with the prediction of crack initiation and propagation in solid materials, and its purpose is to develop a quantitative prediction of fracture loads that make the material to separate into two or more pieces. With

this aim, a failure criterion must be established, which normally takes the form of an equation where an applied quantity, usually a stress or strain or some combination of these, is equated to a material property. Provided the material property is known, a correct failure criterion would allow to predict the stresses or strains that would produce failure in service conditions. Ultimate failure is defined in [20] as the point of loading at which the material can no longer offer significant resistance to further deformation. In paper, ultimate failure is a sequence of failure events beginning at a small size scale which then either escalate in magnitude or coalesce to the largest size scale of the material. Consequently, ultimate failure can be considered as the result of an accumulation of smaller scale events happening during the mechanical deformation of the material.

According to [20], plane stress expressions are generally used for failure analysis of paper materials, in which tensile stress is applied in the plane, and therefore the through-thickness stress is assumed to be zero. The anisotropy of the material must be considered, as failure is highly dependent on the direction of the applied loads relative to the principal material directions (MD, CD and ZD). The microscopic response to tensile forces applied in each of them will be different due to the orientation of the fibre segments and the bonded areas connecting them, which will be subject to different shear stresses [20]. The materials are also heterogeneous, but their heterogeneity depends on the scale of observation. Close observations reveal the heterogeneous nature of the fibre segments and interfibre voids, and examination of the fibres reveals a multilayer cylindrical cellulose micro-fibril composite. When failure analysis is of interest, the non-linear behaviour must be included in the constitutive model [85].

5.4.2. Analysis of uniaxial tensile fracture of paper

Some publications devoted to fracture mechanics of paper materials report that, when subjecting paper strips to uniaxial tensile testing up to fracture, the failure mechanism will depend on the length of the tested paper strips, [89], [124], [125]. If the paper strip is long enough, there will be immediate rupture; if the paper strip is shortened, it will exhibit a non-immediate rupture; and further shortening of the paper strip will result in a stable evolution of the failure zone, as seen in Figure 105 (a).

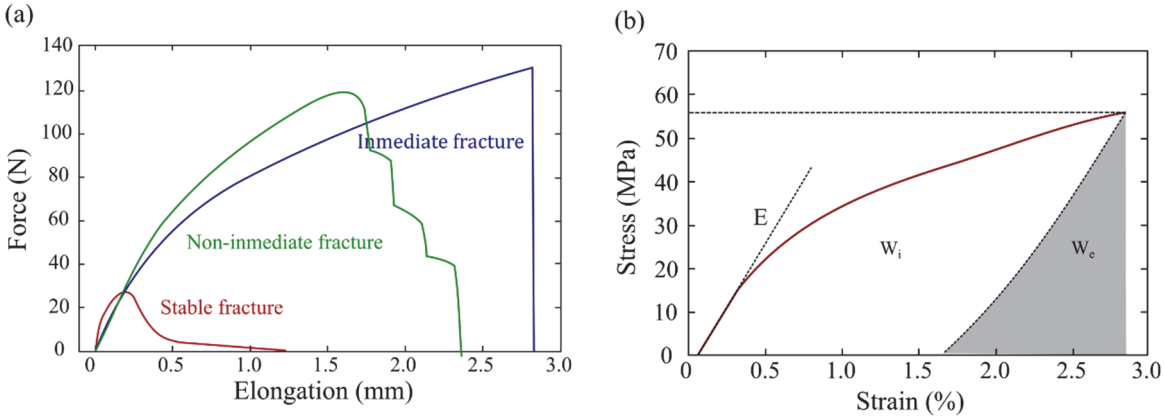

Figure 105. (a) Force- elongation curves for different fracture mechanisms; (b) Loading and unloading stress-strain curve with the elastic and inelastic strain energy; based on [89].

When the length of the paper strip is short enough to show stable fracture, the force-elongation curves are elongated up to the instant when $\varepsilon = \varepsilon_u$ and $\sigma = \sigma_u$, and it can be assumed that further deformation of the paper will be localised in a narrow area [89]. The extension of this damage-process zone along the paper strip can be assumed to be

independent of the length of the paper strip. The localised deformation is assumed to be caused by both plastic and damage softening, until an almost free surface is formed throughout the width of the paper strip, which will be held together only through single fibre bridges. It is known from previous analyses, such as [126]–[128], that the damage evolution in paper is mainly caused by bond failure. When only single fibre bridges hold the paper strip together, a certain amount of work is needed in order to break those fibres and separate the paper strip into two paper strips. The strain energy density, W, at the failure strain, ε_u, is defined as the area under the stress-strain curve, see equation (70). If the paper strip is loaded and unloaded, it behaves as an elastic-plastic material, with plastic deformation at unloading, before reaching the peak stress, σ_u. Thus, the strain energy density, W, consists of an elastic part, W_e, which is recovered during relaxation, and an inelastic part, W_i, which dissipates due to fibre reorientation among other processes: $W = W_e + W_i$, see Figure 105 (b).

$$W = \int_0^{\varepsilon_u} \sigma(\varepsilon) d\varepsilon \tag{70}$$

When stable fracture is achieved in a tensile test, the total elongation measured by the tensile machine, $u\ (mm)$, does not represent a homogenous deformation in the paper strip, but a sum of the local deformation in the fracturing damage band and a uniform strain outside that band, $u_r\ (mm)$, which decreases during the breaking due to the decrease in stress. Consequently, fracture can be assumed to take place in that narrow band while the rest of the paper strip is unloading [89]. It is possible to transform a stable load-elongation curve into a cohesive stress-widening curve that describes the failure properties of the material. The widening of the damage band, $w\ (mm)$ is given by equation (71). The stress-strain relationship for the paper will be determined by unloading tests [89], which indicate that the material properties of paper before the beginning of fracture are elastic-plastic. If the slope of the entire unloading path is assumed to be equal to the Young's modulus, $E\ (MPa)$, the uniform strain during fracture, ε, will be given by equation (72), in which ε_u is the maximum strain at breakage and $\sigma_u\ (MPa)$ is the maximum stress at break. So, the widening damage band, $w\ (mm)$, as a function of the stress, $\sigma(MPa)$, will be expressed as in equation (73).

$$w = u - u_r = u - \varepsilon \cdot L \tag{71}$$

$$\varepsilon = \varepsilon_u - \frac{\sigma_u - \sigma}{E} \tag{72}$$

$$w\ (\sigma) = u - \left(\varepsilon_u - \frac{\sigma_u - \sigma}{E}\right) \cdot L = u - \varepsilon_u \cdot L + \frac{\sigma_u - \sigma}{E} \cdot L \tag{73}$$

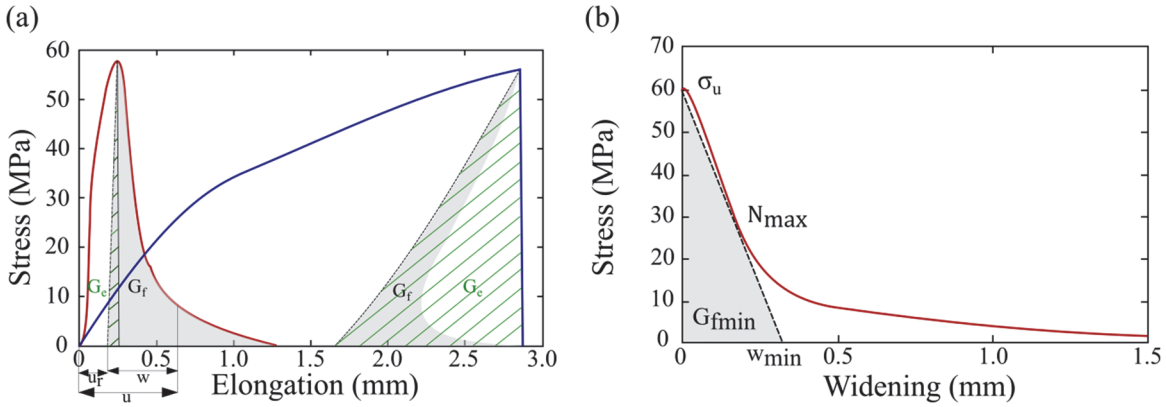

Figure 106. (a) Stress-widening curve; (b) Stress-elongation curves for stable and immediate fracture; based on [89].

The fracture energy, G_f, can be defined as the area under the cohesive stress-widening curve, see equation (74), where w_{max} is the crack widening at a completely separated fracture

surface. The dependence of the descending load-elongation curves on the lengths of the tested paper strips, can be explained through a comparison between the released elastic elongation energy, $G_e = W_e \cdot L$, and the fracture energy, G_f, which are represented in Figure 106. When the length of the paper strip is higher than a determined critical value, the incremental released elastic elongation energy during the entire course of the failure is greater than the incremental fracture energy, $\Delta G_e > \Delta G_f$, so the released elastic elongation energy alone is sufficient to totally separate the material with an immediate brittle fracture (see blue curve in Figure 106 (a)). For intermediate lengths of the tested paper strip, fracture is partly stable and partly unstable, because the incremental released elastic elongation energy, ΔG_e, during the course of failure becomes either higher or lower than the incremental fracture energy, ΔG_f. Finally, strips with a length lower than the stable length will show a stable descending branch with no immediate fall of the stress, because, during the entire failure process $\Delta G_e < \Delta G_f$ (see red curve in Figure 106 (a)) so additional energy must be supplied to completely separate the material [89].

$$G_f = \int_0^{w_{max}} \sigma(w) dw \tag{74}$$

For a particular paper material subjected to tensile testing up to failure, the critical length, $L_{critical}$, is defined as the shortest length of the paper strip for which the load-elongation curve shows an immediate brittle fracture, from a point of instability immediately after the instant of maximum load up to zero load. The length of the longest paper strip which shows a stable descending branch with no immediate fall in the load-elongation curve is the stable length, L_{stable}. Any length of the paper material in between these two values, $L_{critical} > L > L_{stable}$, will show a non-immediate fracture, with a sudden drop of the load from a point of instability to a lower load, not equal to zero [89]. The value of length L_{stable} can be obtained from an analysis the fracture of the paper strip. The total elongation can be expressed as: $u = w + \varepsilon \cdot L$, where w is the widening of the damage band and $\varepsilon \cdot L$ is the uniform elongation of the relaxing undamaged part. That uniform elongation consists of a relaxing elastic part, $\varepsilon^e(\sigma) \cdot L$, and a constant plastic part, $\varepsilon^p \cdot L$, see equation (75).

$$u = (\varepsilon^e(\sigma) + \varepsilon^p) \cdot L + w(\sigma) \tag{75}$$

At the instability point, a virtual change in the elongation is equal to zero $\delta u = 0$, and a virtual change in the load is negative $\delta F < 0$, see equation (76). Equation (77) can be obtained by introducing $\delta F = A \cdot \delta\sigma$, where A is the cross-sectional area and is assumed to be constant. Since $\delta F < 0$ and $A > 0$, it must be that $\delta\sigma < 0$, equation (78) is derived.

$$\delta u = \frac{\partial \varepsilon^e(\sigma) L}{\partial F} \delta F + \frac{\partial w(\sigma)}{\partial F} \delta F = 0 \tag{76}$$

$$\frac{\partial \varepsilon^e(\sigma) L}{\partial \sigma} A \cdot \delta\sigma + \frac{\partial w(\sigma)}{\partial \sigma} A \cdot \delta\sigma = 0 \rightarrow \left(\frac{\partial \varepsilon^e(\sigma)}{\partial \sigma} L + \frac{\partial w(\sigma)}{\partial \sigma} \right) A \cdot \delta\sigma = 0 \tag{77}$$

$$\frac{\partial \varepsilon^e(\sigma)}{\partial \sigma} L + \frac{\partial w(\sigma)}{\partial \sigma} = 0 \tag{78}$$

The stress-strain curve is assumed to be linear during the relaxing of the undamaged part of the strip, $\delta\sigma = E\delta\varepsilon^e$, and the cohesive stress-widening curve, $w(\sigma)$, is a monotonous decreasing function, see Figure 106 (b), for which the slope can be defined as $N(w)$: $\delta\sigma = \frac{\partial \sigma}{\partial w} \delta w = -N(w)\delta w$. The combination of the previous equations gives equation (79). As the stable length will be determined by the steepest part of the stress-widening curve, $w(\sigma)$, that

is, when $N(w) = N_{max}$, the value of the stable length can be obtained from equation (79). If that slope is considered in the stress-widening curve of Figure 106 (b), the corresponding fracture energy is given by the area of the grey triangle, see equation (80). So, another expression for the stable length from [89] will be given by equation (81).

$$\frac{\delta\sigma}{E}L - \frac{\delta\sigma}{N(w)} = 0 \rightarrow \left(\frac{L}{E} - \frac{1}{N(w)}\right)\delta\sigma = 0 \rightarrow L = \frac{E}{N(w)} \rightarrow L_{stable} = \frac{E}{N_{max}} \quad (79)$$

$$G_{fmin} = \frac{1}{2}\sigma_u w_{min} = \frac{1}{2}{\sigma_u}^2 \frac{1}{N_{max}} \rightarrow N_{max} = \frac{{\sigma_u}^2}{2G_{fmin}} \quad (80)$$

$$L_{stable} = \frac{2EG_{fmin}}{{\sigma_u}^2} \quad (81)$$

5.4.3. Different criteria for the failure of paper materials

- **Introduction to lamina failure analysis**

The purpose of a failure criterion for a lamina is to determine its strength and mode of failure in a state of combined stress. Paper and board are frequently considered as orthotropic materials, and most of the criteria consider two-dimensional stress states and are basically phenomenological, so detailed microscopic failure processes are not described [129]. In orthotropic materials, the strengths and elastic constants depend on the direction, and an infinite number of strength values can be obtained through uniaxial tests, depending on the direction of load application. For prediction purposes, the number of relevant strengths can be limited to five strengths in the principal material directions: longitudinal tensile and compressive strengths, transverse tensile and compressive strengths, and shear strength. It is important to consider that, although these criteria take into consideration one of the main features of paper material, which is its lack of isotropy in terms of macromechanical variables (strengths in different directions of the material), they do not account for another fundamental characteristic, which is its lack of homogeneity. That lack of homogeneity is sometimes one of the causes that govern lamina failure.

The following modes of failure are considered in [129]:

- *Fibre Breakage*: The longitudinal stress, σ_{MD}, or the longitudinal strain, ε_{MD}, dominates lamina failure.
- *Transverse Matrix Cracking:* The transverse stress, σ_{CD}, or transverse strain, ε_{CD}, dominates lamina failure.
- *Shear Matrix Cracking:* The shear stress, τ_{MD-CD}, or shear strain, γ_{MD-CD}, dominates lamina failure.

According to [129], the failure criteria can be classified into:

- *Limit Criteria:* These criteria predict failure load and mode by comparing lamina stresses σ_{MD}, σ_{CD}, and τ_{MD-CD} (or strains ε_{MD}, ε_{CD}, and γ_{MD-CD}) with the corresponding strengths separately. Interaction among the stresses (or strains) is not considered in these criteria.

- *Interactive Criteria:* These criteria predict the failure load by using a single quadratic or higher order polynomial equation involving all stress (or strain) components. Failure is assumed when the equation is satisfied. The mode of failure can be determined indirectly by comparing the stress/strength ratios.

The strengths of a material can be experimentally obtained by subjecting prepared samples of the material to loads that produce simple stress fields in the test specimen and by determining the load at which the failure happens. The accuracy of the failure criteria depends

on the availability of reliable material strength data ($\sigma_{MD,t}^{max}, \sigma_{MD,c}^{max}, \sigma_{CD,t}^{max}, \sigma_{CD,c}^{max}, \tau_{MD-CD}^{max}$) or the corresponding ultimate strains ($\varepsilon_{MD,t}^{max}, \varepsilon_{MD,c}^{max}, \varepsilon_{CD,t}^{max}, \varepsilon_{CD,c}^{max}, \gamma_{MD-CD}^{max}$). Except for longitudinal and transverse tensile strengths $\sigma_{MD,t}^{max}$ and $\sigma_{CD,t}^{max}$, good measurements of the compressive and shear strengths are not easy to obtain [129], which makes the use of the lamina failure criteria more complicated. If reliable uniaxial strength properties are available, failure loads of a lamina must be determined for a combined state of stress; that is, at least two of the three stress components, σ_{MD}, σ_{CD} and τ_{MD-CD}, must be present.

- **Limit criteria**

The following criteria are generalised for either tensile or compressive stresses (or strains). The corresponding tensile or compressive strength value must be chosen based on the sign of the applied stress [129].

- **Maximum stress:** According to this criterion, failure will occur if any of the stresses in the principal material axes exceeds the corresponding allowable stress. If any of the following inequalities is accomplished, the material will fail in a failure mode associated with the allowable stress.

  - Fibre failure:

$$\sigma_{MD} \geq \sigma_{MD}^{max} \tag{82}$$

  - Transverse matrix cracking:

$$\sigma_{CD} \geq \sigma_{CD}^{max} \tag{83}$$

  - Shear matrix cracking:

$$\tau_{MD-CD} \geq \tau_{MD-CD}^{max} \tag{84}$$

- **Maximum strain:** This criterion states that failure of the material will occur if any of the strains in the principal material axes exceeds the corresponding allowable strain.
  - Fibre failure:

$$\varepsilon_{MD} \geq \varepsilon_{MD}^{max} \tag{85}$$

  - Transverse matrix cracking:

$$\varepsilon_{CD} \geq \varepsilon_{CD}^{max} \tag{86}$$

  - Shear matrix cracking:

$$\gamma_{MD-CD} \geq \gamma_{MD-CD}^{max} \tag{87}$$

When the actual stress field (or strain field) is simple, a direct comparison can be made between the values of the field and the strengths of the material. However, a direct comparison may not be valid if the material is subjected to a biaxial stress state. According to [129], the Maximum Stress (or Strain) criterion is not adequate for predicting the transverse matrix cracking failure mode where σ_{MD} is present.

- **Interactive criteria**

An interactive failure criterion aims at predicting strengths of materials under biaxial stress states using strength data obtained from uniaxial tests. The interactive criteria predict failure of the material for lower stresses (or strains) compared to those predicted by the maximum stress (or strain) criterion. The largest differences between the predictions of the

limit and interactive criteria occur at the points where the maximum stress criterion predicts a change in the failure mode, for instance, from the shear mode to the longitudinal or transverse tensile failure modes. The interactive criteria predict a smoother variation of the strength of the material than the limit criteria.

- **Hill-type criteria:** Several failure criteria for orthotropic materials subjected to combined stresses have been proposed by different authors following the Hill-type condition. Among those criteria, maybe the one commonly known as Tsai-Hill failure criterion [130] is the most frequently used:

$$\left(\frac{\sigma_{MD}}{\sigma_{MD}^{max}}\right)^2 + \left(\frac{\sigma_{CD}}{\sigma_{CD}^{max}}\right)^2 - \frac{\sigma_{MD}\cdot\sigma_{CD}}{(\sigma_{MD}^{max})^2} + \left(\frac{\tau_{MD-CD}}{\tau_{MD-CD}^{max}}\right)^2 \geq 1 \tag{88}$$

The Tsai-Hill criterion in (88) considers a transversely isotropic material [131] and defines an envelope in the stress space, and if the stress state (plane stress) lies outside this envelope, that is if the sum of the terms which include the failure strengths of the material is equal to or greater than unity, then failure is predicted [132]. This criterion takes into account the interaction between different failure modes, such as axial, transverse tensile and shear failure. However, it does not intrinsically consider the differences between the values of the tension and compression strengths [131], so it would be necessary to introduce the values of the strengths in tension or compression ($\sigma_{MD,t}^{max}$, $\sigma_{MD,c}^{max}$, $\sigma_{CD,t}^{max}$, $\sigma_{CD,c}^{max}$), according to stresses σ_{MD} and σ_{CD}, which is a time-consuming procedure as it leads to four different criteria in the four quadrants. Besides, the failure mechanism is not specifically identified, such as for maximum stress and maximum strain criteria.

The Norris criterion [133] does not differ between tension and compression either, and follows equation (89):

$$\left(\frac{\sigma_{MD}}{\sigma_{MD}^{max}}\right)^2 + \left(\frac{\sigma_{CD}}{\sigma_{CD}^{max}}\right)^2 - \frac{\sigma_{MD}\cdot\sigma_{CD}}{\sigma_{MD}^{max}\cdot\sigma_{CD}^{max}} + \left(\frac{\tau_{MD-CD}}{\tau_{MD-CD}^{max}}\right)^2 \geq 1 \tag{89}$$

The Hoffman criterion [134] includes linear terms of the differences between tensile and compressive strengths, see equation (90), where both the tensile and compressive strengths must be introduced with a positive sign (in absolute value).

$$\frac{{\sigma_{MD}}^2}{\sigma_{MD,t}^{max}\cdot\sigma_{MD,c}^{max}} + \frac{{\sigma_{CD}}^2}{\sigma_{CD,t}^{max}\cdot\sigma_{CD,c}^{max}} - \frac{\sigma_{MD}\cdot\sigma_{CD}}{\sigma_{MD,t}^{max}\cdot\sigma_{MD,c}^{max}} + \left(\frac{\tau_{MD-CD}}{\tau_{MD-CD}^{max}}\right)^2 + \frac{\sigma_{MD,c}^{max}-\sigma_{MD,t}^{max}}{\sigma_{MD,c}^{max}\cdot\sigma_{MD,t}^{max}}\sigma_{MD} + \frac{\sigma_{CD,c}^{max}-\sigma_{CD,t}^{max}}{\sigma_{CD,c}^{max}\cdot\sigma_{CD,t}^{max}}\sigma_{CD} \geq 1 \tag{90}$$

- **Tsai-Wu:** This criterion is designed for use in all quadrants of the stress plane [120].

$$F_1\cdot\sigma_{MD} + F_2\cdot\sigma_{CD} + F_{11}\cdot{\sigma_{MD}}^2 + F_{22}\cdot{\sigma_{CD}}^2 + 2F_{12}\cdot\sigma_{MD}\cdot\sigma_{CD} + F_{66}\cdot(\tau_{MD-CD})^2 \geq 1 \tag{91}$$

Where:

$$F_1 = \frac{1}{\sigma_{MD,t}^{max}} - \frac{1}{\sigma_{MD,c}^{max}} \tag{92}$$

$$F_2 = \frac{1}{\sigma_{CD,t}^{max}} - \frac{1}{\sigma_{CD,c}^{max}} \tag{93}$$

$$F_{11} = \frac{1}{\sigma_{MD,t}^{max}\cdot\sigma_{MD,c}^{max}} \tag{94}$$

$$F_{22} = \frac{1}{\sigma_{CD,t}^{max} \cdot \sigma_{CD,c}^{max}} \quad (95)$$

$$F_{66} = \frac{1}{(\tau_{MD-CD}^{max})^2} \quad (96)$$

In equations (91)-(96), both the tensile and compressive strengths must be introduced with a positive sign (in absolute value). In equation (91), the interaction term, F_{12}, needs to be experimentally determined through a biaxial test. The criterion in [120] considers stability conditions in relation to strength tensors and magnitudes of the interaction term, and establishes: $-\sqrt{F_{11} \cdot F_{22}} < F_{12} < \sqrt{F_{11} \cdot F_{22}}$. Some authors propose to use $F_{12} = -\frac{1}{2\sigma_{MD,t}^{max} \cdot \sigma_{MD,c}^{max}}$, and several studies found that $F_{12} = 0$ gave adequate accuracy for engineering purposes, as that term is insignificant for many practical cases [129].

In 2-D plane stress, Tsai-Wu is essentially Hill-Tsai with additional linear terms in σ_{MD} and σ_{CD}, which allow Tsai-Wu to account for compressive and tensile stresses. According to [135], the Tsai-Wu failure criterion overestimates the strength of paper in some parts of the biaxial tension region, and that could be corrected by adding two cubic terms to the criterion. Such a polynomial cannot be related to the concept of deformation energy [129]. Due to the different tensile and compressive failure mechanisms, there is no reason for the lamina failure envelope to be described by a single equation as suggested by Tsai-Wu. It is not acceptable from a physical point of view, for instance, that failure of a composite under biaxial tension should depend on its compressive strength properties and vice versa. Although the Tsai-Wu criterion could be mathematically more convenient, it may cause unreasonable failure predictions.

III. MATERIALS, METHODS AND RESULTS

1. Experimental work

1.1. Accelerated thermal ageing of the paper insulation

In the first stage of this study, twenty CTC samples with a length of 120 mm, Figure 107 (a), were obtained from the copper coil and vacuum-dried in an oven at 100°C for 3 hours, Figure 107 (b), in order to reduce their moisture content. These CTC samples were impregnated in mineral dielectric oil, whose properties are listed in Table 17, and subjected to thermal ageing for different periods and, after that, some of them were used for obtaining the paper samples for characterisation in tension (see *1.2.2.Tensile mechanical properties of the dielectric paper in the MD and in the CD*), and other insulated CTC samples were subjected to three-point bending tests (see *1.3.Three-point bending tests of the insulated CTCs*).

In a second experimental stage, some paper samples were prepared for the characterisation of the mechanical response of the material in compression and shear modes. The insulation samples were also vacuum-dried in an oven at 100°C for 3 hours, Figure 107 (c), and, afterwards, they were impregnated in naphthenic oil and introduced into three sealed vessels. Some pieces of the copper conductor were introduced into the vessel, with approximately the same mass ratio of copper and paper that exists in the CTC conductor, to include any possible catalytic effect of this material in the ageing of the paper insulation.

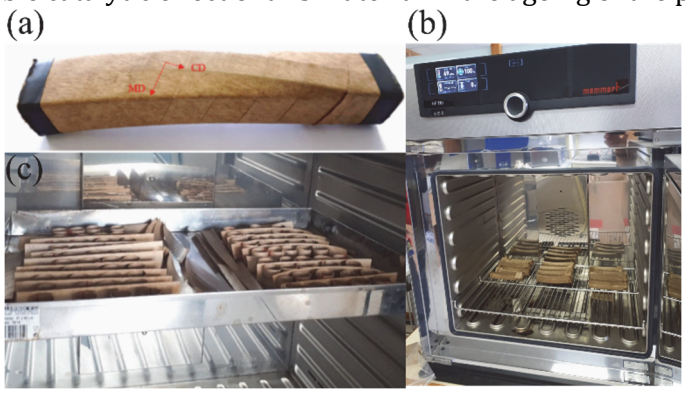

Figure 107. (a) CTC sample with the main directions of the paper material; (b) Samples for tensile testing before the preconditioning process; (c) Samples for compressive and shear testing before the preconditioning process.

After this preconditioning process, a final average moisture content of 1.99% for the paper of the CTC samples, and an average final moisture content of 1.50% for the paper samples prepared for compressive and shear tests, were measured using the Karl-Fischer titration method (KF) [136], and a Sartorius Moisture Analyser (Electronic moisture analyser model MA45).

1.1.1. Measurement of moisture content of the dielectric paper with the Karl-Fischer titration method

Coulometric KF determination of water content is based on the standard reaction equation for the Karl-Fischer reaction:

$$ROH + SO_2 + 3RN + I_2 + H_2O \rightarrow (RNH) \cdot SO_4R + 2(RNH)I \quad (97)$$

In coulometry, however, the iodine is generated electrochemically by anodic oxidation at a generator electrode, also called generator cell, which is incorporated into the glass titration cell, in accordance with the following half-reaction: $2\,I^- \rightarrow I_2 + 2e^-$. The generator

cell is close to the measuring electrode, a double pin platinum electrode, which is monitoring the potential of the sample solution by voltametric technique during coulometric titration. The classical coulometric cell consists of two parts: the anode compartment and the cathode compartment, separated by a diaphragm. The anode compartment contains the anolyte, which consists of sulfur dioxide, imidazole and iodide salts, as well as methanol or ethanol used as solvent. The anolyte is the KF electrolyte required for the oxidation in order to generate iodine by applying a current at the generating electrode. The negative iodide ions release electrons and form iodine, which subsequently reacts with water. The coulometer used in the laboratory is shown in Figure 108.

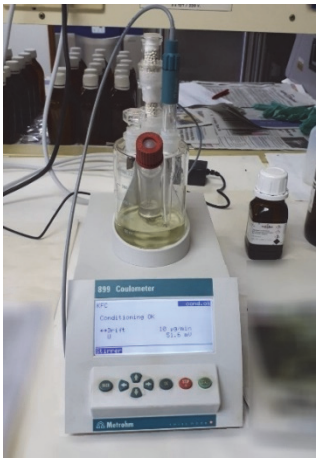

Figure 108. Coulometer used in the laboratory for the measurement of the initial moisture in the paper material.

The oxidation reaction in the anolyte compartment is completed by a reduction reaction in the catholyte compartment, which contains either a manufacturer special reagent or the same reagent as used in the anode compartment. At the cathode, the positive hydrogen ions are reduced to hydrogen, which is the main product formed and this production is promoted by the addition of ammonium salt to the catholyte: $2\,[RN]H^+ + 2e^- \rightarrow\ H_2 + 2RN$.

The amount of water titrated by the coulometric technique is determined by the amount of electrical current given in Coulomb, C, used to generate iodine. To produce one mole of a chemical substance, one electron and 96485 C of current are required, and the value 96845 C/mol is known as the Faraday's constant. In Karl-Fischer reaction, two iodide ions, I^-, are oxidised to one molecule of iodine, I_2, releasing two electrons at the anode, and subsequently, iodine reacts with water: $2I^- \rightarrow I_2 \rightarrow H_2O$.

Therefore, 2 x 96485 C/mol is required for 1 mole of water. Since the molar mass of water is 18.015 g/mol, 1 mg of water corresponds to a consumption of 10.712 C electrical current. For an electrochemically optimised Karl Fischer's cell, the current conversion efficiency for iodine production is assumed to be 100%, and since current and time can be accurately measured, no standardisation of the coulometric KF reagents is necessary. For this reason, coulometry is designated as an absolute method and it is used as a reference method for the determination of water content.

The rate of iodine generation is adjusted by varying the current pulse duration and frequency and the pulse height (of 400, 300, 200 and 100 mA). The maximum pulse height depends on the conductivity of the anolyte, which is influenced by the samples and additional solvents; and on voltage and surface of the generator electrode, which depend on the type of coulometer. In addition, the conductivity of the anolyte is influenced by the samples and

additional solvents. With standard conductivity values, the coulometer operates with current pulses of 400 mA, having an iodine generation rate which corresponds to a maximum of 2240 µg water/min. At very low conductivities (i.e. less than 3–4 µS/cm), the maximum possible current applied by the instrument is 100 mA.

1.1.2. Considered ageing states and thermal ageing process

A very long time would be needed to study the effects of ageing if the temperature is maintained within realistic values in operating transformers. Shorter experiments at elevated temperature are widely used but it will be noticed that, due to the more extreme conditions, the degradation might not be totally representative of the system aged under service conditions [46]. After the preconditioning process, the test pieces were aged isothermally in temperature-controlled ovens. As there are many references in the literature that relate the Degree of Polymerisation (DP) of the paper insulation with the number of years for which the power transformer has been operating under usual conditions, the measurement of the DP detailed in section *1.2.1* could be used to correlate the mechanical response of the material in the following ageing states with the expected response of the paper insulation in a realistic situation. The considered ageing states were:

- *AGEING STATE 0:* Four test pieces were not aged.

The remaining CTC samples were impregnated in dielectric naphthenic oil and subjected to four different ageing durations.

- *AGEING STATE I:* Four test pieces were aged for a week at 150°C.
- *AGEING STATE II:* Four test pieces were aged for four weeks at 150°C.
- *AGEING STATE III:* Four test pieces were aged for nine weeks at 150°C.
- *AGEING STATE IV:* Four test pieces were aged for twenty-eight weeks at 150°C.

Table 17. Main properties of the mineral dielectric oil used in the experiments.

PROPERTIES	Method	Value
Density at 20°C (g/cm^3)	ISO 12185	0.84
Viscosity at 40°C (mm^2/s)	ASTM D445	10.3
Viscosity at 100°C (mm^2/s)	ASTM D445	2.7
Viscosity at -30°C (mm^2/s)	ASTM D445	807
Freezing point (°C)	ASTM D97	-48
Interfacial tension (dynes/cm)	ASTM D971	42
Acidity (mg KOH/g)	ASTM D974	<0.01
Water content (mg/kg)	IEC 60814	15
Furfural content (mg/kg)	IEC 61198	<0.05

Consequently, in the first stage of the experiments, there was a total of sixteen insulated CTC test pieces which were impregnated in naphthenic oil (properties summarised in Table 17). Two sealed vessels filled with that dielectric mineral oil were used, and four samples were introduced in each of the vessels, Figure 109, with a ratio of 10 g paper/400 g oil. After that, the vessels were vacuum-sealed, Figure 110, and subjected to the mentioned ageing durations. In the second experimental stage, the paper samples needed for obtaining the edgewise compressive properties and the in-plane shear properties of the material were introduced into the vessels with some pieces of the copper conductor, with the same ratio paper/copper that the insulated CTC samples have. The vessels were filled with the same naphthenic oil, introduced into convective ovens, and aged for the different time periods. In

this second stage, only Ageing States 0-III were considered, because these are the states that better represent the potential performance of the paper insulation in an operating transformer.

Figure 109. Test pieces in the vessel filled with dielectric oil.

Figure 110. Vessels containing the oil-impregnated samples being vacuum-sealed.

An inert atmosphere was created by introducing nitrogen into the free space created in the vessel after the removal of air, as seen in Figure 111 (a), before introducing the vessels into the oven in order to start the ageing process, Figure 111 (b).

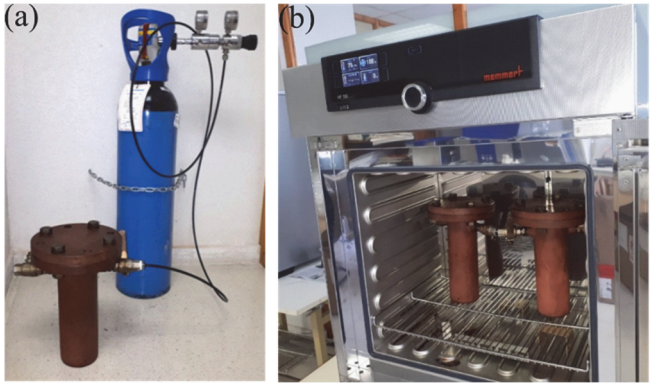

Figure 111. (a) Introduction of nitrogen into the vessels; (b) Vessels containing the oil-impregnated samples being introduced in the convective oven to start the ageing process.

1.2. Characterisation of the paper insulation samples

Once the ageing process had finished, both the copper CTC samples wrapped in insulating paper (for tensile characterisation and bending tests) and the paper samples (for compression and shear characterisation) were washed five times, using hexane, to remove the remaining dielectric oil. Hexane is one of the de-oiling solvents suggested by standards, but benzene or chloroform can also be used [53]. The degreased material was then allowed to dry by exposition to open air until it reached equilibrium with atmospheric humidity, to be

later subjected to mechanical tests and DP measurement. The removal of the residual naphthenic oil in which the insulation is impregnated is an essential factor in the preparation of the samples, as well as the measurement of the moisture content of the paper, to obtain an accurate measurement of the dry weight [53].

It is a well-known fact that paper is an anisotropic material, and the differences in the mechanical response in the different material directions, the MD and the CD (or other directions of interest), should be considered in any mechanical analysis or mechanical failure model. Besides, the response to different mechanical solicitations (tension, compression or shear) are also distinct. The various kind of loads which affect the windings of power transformers and, subsequently, the conductors and their cellulosic insulation, produce complex strain-stress states which, in general, will not be aligned with any of the main directions of the paper material. As the strength is variable in the different directions of paper, there will be a tendency for the cracks to spread in the weaker direction.

In the first stage of the characterisation, tensile tests were performed, see section *1.2.2.Tensile mechanical properties of the dielectric paper in the MD and in the CD*. The insulating paper was extracted from one test piece of each of the ageing states (five CTC samples). Two samples from each of the four layers were extracted, to measure material properties in MD and CD, and several samples of each layer were used to measure the DP. Although there were only two different materials in the insulation of the CTC, plain Kraft paper in the internal layers (named as layers 1 and 2) and crepe paper in the external ones (named as layers 3 and 4), whose manufacturing properties are summarised in Table 18, the four layers were characterised, because, in that stage of the experimental work, it was of interest to determine if thermal ageing had a different impact on the layers depending on their position. For instance, layer 1 was in direct contact with the copper CTC and layer 4 was in direct contact with the dielectric oil, while layers 2 and 3 were between two layers of paper insulation. The conclusions after tensile testing, were that the position of the insulation layer was not relevant, except in the case of layer 1, in direct contact with the copper CTC, which was the most deteriorated. That extreme deterioration of layer 1 was artificially increased due to the high temperature selected for the ageing process.

Table 18. Properties of the paper insulation materials used in the CTC.

PROPERTY	UNIT	TEST METHOD	Plain Kraft paper	Crepe paper
Nominal Grammage	g/m^2	ISO 536	62.0	80.0
Nominal Thickness	µm	ISO 543	82	80
Nominal Density	kg/m^3	ISO 543	760	1000
Minimum Tensile Strength in MD	MPa	ISO 1924	93.5	87.5
Minimum Tensile Strength in CD	MPa	ISO 1924	33.9	25
Minimum Elongation at break in MD	%	ISO 1924	2	15
Minimum Elongation at break in CD	%	ISO 1924	4	5

In a second stage of the experimental work, some samples of plain Kraft and crepe insulations were prepared for the experimental characterisation of the edgewise compressive properties and the in-plane shear properties, as described in sections *1.2.3.Edgewise mechanical compressive properties of the dielectric paper* and *1.2.4.In-plane shear mechanical properties of the dielectric paper*. In this case, the paper samples were not obtained from the aged CTC samples, and the analysis does not distinguish between the different layers of the insulation. Here, insulation paper sheets provided by the company

Ahlstrom-Munksjö were used for obtaining the paper samples. The reason was that it was not possible to get paper samples with the needed dimensions from the CTC insulation. Besides, all the relevant conclusions about the differences in the ageing of the four layers of the insulation were derived from the tensile tests (*1.2.2.Tensile mechanical properties of the dielectric paper in the MD and in the CD*).

1.2.1. Degree of Polymerisation (DP) of the dielectric paper

- **Method for the determination of the DP of paper**

The purpose of [55] is to describe a standardised method for determining the average viscometric degree of polymerisation, $\overline{DPv}$, of any kind of new and aged cellulosic insulating materials for electrical use. In this study, the DP of the paper samples was measured after the ageing process, for each paper layer and each ageing state. Sufficient quantity of aged paper which was going to be subjected to evaluation was cleaned of grease, in order to have a mass of degreased paper of approximately 3 g. The degreased material was allowed to dry, exposing it to the open air until it reached equilibrium with atmospheric humidity. The paper under evaluation had to be handled only with gloves or with tweezers. Samples had to be cut into pieces small enough to facilitate further operations. For very thin papers, as was the case, the materials can be cut into small pieces, Figure 112, with the help of scissors. The cellulose fibres must be separated to facilitate dissolution in the Cuen solution, and the samples under evaluation must be weighed before the dissolution. The concentration of the solution to be used depends on the expected $\overline{DPv}$ value, as indicated in Table 19, based on [55].

Figure 112. Paper sample being prepared to perform the DPv measurement

Table 19. DPv values of the samples, based on [55].

Condition of the sample	Expected value of $\overline{DPv}$	Approximate concentration (g/ dl)
Factory - new	1000 – 2000	0.05 – 0.15
Good	650 – 1000	0.08 – 0.25
Intermediate	350 – 650	0.15 – 0.45
Aged	< 350	0.25 – 0.80

In this study, the small pieces of paper subjected to evaluation were immersed in a solution composed of 22.5 ml of deionised water and 22.5 ml of copper (II) ethylenediamine. According to [55], for most papers (with a $\overline{DPv}$ > 350), a stirring time of 16 hours generally guarantees total dissolution. In this case, the solution was stirred for 48 hours, Figure 113.

Figure 113. Devices used in the laboratory for weighing and stirring the solution.

The viscometer tube used in the laboratory was selected and kept in a constant temperature bath at 20°C ± 0.1 K, Figure 114. It must be ensured that the viscometer tube is dry, dust-free and carefully filled with nitrogen. It was necessary to wait from 5 min to 10 min before the first measurement of the viscosity, to ensure the solution had reached its equilibrium temperature.

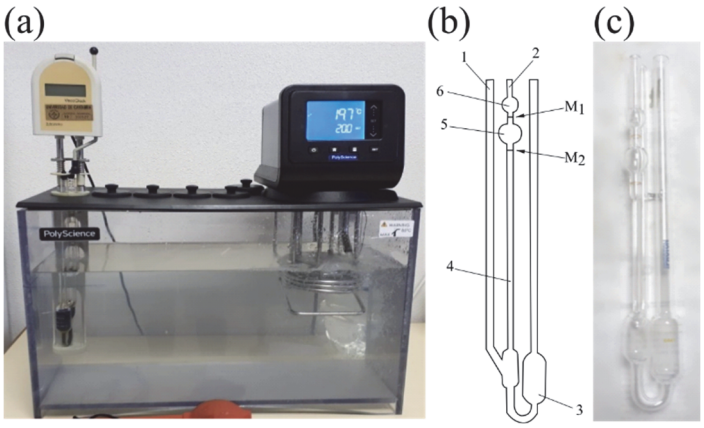

Figure 114. (a) Bath controlled by a thermostat adapted for immersion of viscometer tubes; (b) Parts of a viscosimeter; (c) Viscosimeter used in the laboratory.

In the viscometer shown in Figure 114, the ventilation tube (1) must be covered with the finger, a stopper or a plastic film, and vacuum must be applied to the capillary tube (2) until filling the lower reservoir (3), the active capillary (4), the timing bulb (5), and the upper tank (6). The vacuum is then removed, and the viscometer is sealed. It must be ensured that the liquid separates in the lower part of the capillary. The time interval (t_{1A}, efflux duration) in which the liquid moves between the two timing-marks M_1 and M_2 in the timing bulb (5) must be measured and recorded with an accuracy of ± 0.5 s. The measurement must be repeated in the same sample, in order to get the value of t_{1B}. The difference in percentage between the two results is then noted. It must be verified that the efflux duration is within the allowed range and that the two results differ by less than 1%. The information, concerning the tube constant used and the efflux times (C_1, t_{1A} and t_{1B}), must be recorded. After that, the procedure is repeated using a second sample. If the two results obtained from the second test differ by more than 1%, the viscometer must be cleaned, and the measurement repeated with a new sample of the same solution. In the case that no pair of results differ by less than 2%, the pair of results that are closest must be accepted and recorded with the corresponding information of the tube constant used, such as C_2, t_{2A} and t_{2B}. The test report should indicate the lack of consistency between the results.

The concentration of the solution is calculated according to equation (98), where m_D is the dry paper mass, v_{H_2O} is the volume of water added to the solution and v_{Cu} is the volume of Cuen added to the solution.

$$c = \frac{m_D}{v_{H_2O} + v_{Cu}} \ (g/dl) \tag{98}$$

The average time, *t*, of efflux for the sample of paper solution is calculated from t_{1A} and t_{1B}. The average time, t_0, of efflux for the diluted solvent is calculated from t_{0A} and t_{0B}. The cinematic viscosity of the solution, ν, and that of the solvent, ν_0, is then calculated in accordance with equation (99), where t and t_0 are the average efflux times, and C_1 and C_0 are the calibration constants of the tube.

$$\begin{aligned} \nu &= C_1 \cdot t \ (mm^2/s) \\ \nu_0 &= C_0 \cdot t_0 \ (mm^2/s) \end{aligned} \tag{99}$$

The specific viscosity, ν_S, is obtained from equation (100), and the intrinsic viscosity is calculated using Martin's empirical formula, see equation (102), where $[\nu] \cdot c$ is given in annex D of standard [55] as a function of ν_S, and k = 0.14 for Kraft paper.

$$\nu_S = \frac{\nu - \nu_0}{\nu_0} \tag{100}$$

$$\nu_S = [\nu] \cdot c \cdot 10^{k \cdot [\nu] \cdot c} \tag{101}$$

The average viscometric degree of polymerisation, $\overline{DP\nu}$, and the intrinsic viscosity, $[\nu]$, are correlated by equation (102), where K and α are the constants of Mark Howink: $K = 0.0075$ and $\alpha = 1$.

$$[\nu] = K \cdot \overline{DP_\nu}^{\alpha} \tag{102}$$

- **Results of the DP measurement of the plain Kraft and crepe insulation paper after the accelerated thermal ageing**

The results of the DP measurement are summarised in Table 20. It can be seen that the non-aged insulation has a DP comprised between 650 – 1000, which is catalogued as "good" in Table 19 of [55]. The crepe paper used in the external layers has a higher initial DP than the plain Kraft paper used in the internal layers, which can be related with its better mechanical properties. The average reduction in DP after one week of thermal ageing, in Ageing State I, with respect to Ageing State 0, is very similar for both materials: the DP of plain Kraft paper reduced in 15.4%, while the DP of the crepe paper reduced 15.9%, approximately. This initial reduction in DP has the most accused slope, see Figure 115, and after the first week of ageing, the reduction in DP seems to be approximately linear until the end of Ageing State III (1562 hours), for the two different types of paper. After that, the DP reduction is slowed down up to the end of the ageing process (State IV).

Table 20. Results of average viscometric Degree of Polymerisation measurements.

	Plain Kraft paper		**Crepe paper**	
AGEING STATE	**Layer 1**	**Layer 2**	**Layer 3**	**Layer 4**
0	745.10		870.39	
I	600.85	660.07	713.87	750.00
II	467.87	542.67	627.20	652.20
III	252.87	320.20	482.80	525.03
IV	111.38	207.50	342.79	397.10

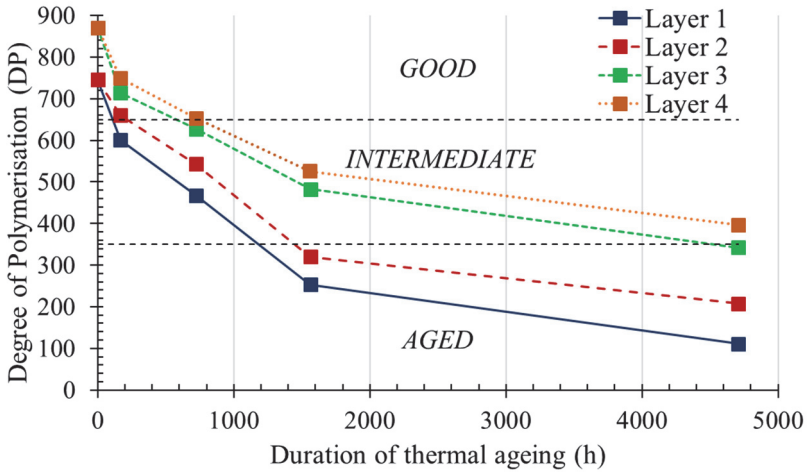

Figure 115. Reduction of the DP in the different layers of the insulation as a function of the duration of thermal ageing.

After four weeks at 150°C, in Ageing State II, all the layers were in a state of intermediate ageing (between 350 and 650). The DP decreased approximately the same in layers 2 and 3 (27.2% and 27.9%), slightly less in layer 4 (25.1%), and considerably more in the most inner layer (37.2%). The differences in the decrease of DP in layers 2, 3 and 4 at that ageing level are not relevant, but it becomes clear that layer 1, in direct contact with the copper CTC, is the most deteriorated. The reason was that layer 1 was considerably damaged in the extraction after the ageing process at 150°C and before the DP measurement, as it was glued to the copper due to the melting of the enamel surrounding the strands of the CTC which were in contact with layer 1, and it suffered breaking of the cellulose fibres that could result in a lower value of the DP.

After four weeks of thermal ageing, in State III, the internal layers were in an aged condition (DP lower than 350) while the external ones remained in an intermediate condition (between 350 and 650). The DP decreased 66.1% in layer 1, 57% in layer 2, 44.5% in layer 3 and 39.7% in layer 4 (with respect to State 0). At the end of the ageing process, in State IV, the DP had decreased 85% in layer 1, 72.2% in layer 2, 60.6% in layer 3 and 54.4% in layer 4. Consequently, it can be concluded that thermal ageing affected plain Kraft paper used in the inner layers in a deeper way than crepe paper. To be in contact with the CTC negatively affected ageing at very high temperatures, as can be seen in the results for layer 1, while no harming effect is reported about being in direct contact with the naphthenic oil, as it was the case for layer 4. These results also justify the temperature chosen for analysis: a lower ageing temperature would have required ageing periods of more than seven months in order that the crepe paper insulation (layers 3, 4) reaches a DP ≃ 350 (aged conditions). The purpose of the first stage of this investigation is to analyse the mechanical response of the insulation of power transformers under different ageing levels, even when the transformer is close to the end of its useful life.

1.2.2. Tensile mechanical properties of the dielectric paper in the MD and in the CD

The standard [137], applicable to all types of paper and paperboard, specifies a method for the measurement of tensile strength, elongation to break, energy absorbed by paper and paperboard and tensile stiffness. According to [137], a paper sample of given dimensions must be subjected to tensile up to fracture, with a constant rate of elongation of 20 mm/min, using a testing machine that automatically records both the tensile force and the elongation. The tensile testing machine must have two jaws, to fix the paper sample with a width of 15 ±

0.1 mm. Each jaw must be designed to secure the specimen firmly along a straight line across its entire width, but preventing damage of the sample or sliding, and must have a means of adjusting the clamping force. The surfaces of the jaws must be in the same plane and aligned in such a way that they hold the specimen in that same plane during the whole test. According to [137], the jaws must be placed so that the average distance between the fixing lines is (180 ± 1) mm. Consequently, the strain rate proposed by the standard is given by (103):

$$\dot{\varepsilon} = \frac{\varepsilon}{t} = \frac{\frac{20\ mm}{180\ mm}}{1\ min} = \frac{0.11}{60\ s} \simeq 0.00185\ s^{-1} \tag{103}$$

The testing machine records the load (N) by means of the load cell, and the elongation of the paper sample (mm) by the moving crosshead. The uniaxial load-elongation curves are recorded by a PC. To transform the measured data to stress-strain curves, relationships (104) and (105) have to be considered:

$$\varepsilon\ (\%) = \frac{L_f - L_0}{L_0} \cdot 100 \tag{104}$$

$$\sigma\ (MPa) = \frac{F}{A} = \frac{F}{w \cdot t} \tag{105}$$

Where:

$L_f\ (mm)$: Elongation recorded by the tensile machine.

$L_0\ (mm)$: Initial distance between jawns in the tensile test.

$F\ (N)$: Force recorded by the tensile machine.

$A\ (mm^2)$: Cross-sectional area of the paper strip, which is the product of the width by the thickness, $A = w \cdot t$.

According to [89], the ascending part of the stress-strain curves finishes when the tensile strength is reached, and then, a localised failure zone is developed. The failure mechanism in paper subjected to uniaxial tension is related to the length of the tested paper strip: paper strips whose length is higher than a particular critical length, $L_{critical}$, will show sudden fracture; if the length is lower than a particular value, L_{stable}, there will be a stable evolution of the failure zone; intermediate lengths of the paper strip between those two values will show a non-immediate rupture.

- **Characterisation of the tensile properties of the CTC insulation in MD**

In some circumstances, for example, when the product has a limited size, a smaller test length can be used, but specimens must have a width of (15 ± 0.1) mm and must be long enough to be fixed between the jaws, according to [137]. In the present study, the purpose was to reproduce an ageing process as realistic as possible, so the paper samples were extracted from the aged CTC samples. That imposed a limitation in the number of available paper samples and in their size. Indeed, in the tensile test for the characterisation of the material in MD, the paper samples were 15 mm wide with parallel sides, and with a length of 140 mm, because it was the only way in which two paper samples could be extracted from each insulation layer in the CTC samples. Some of the paper samples can be seen in Figure 116 (a), (b). The insulation strip samples were held by pneumatic vice-action grips between two parallel textured jaw faces, Figure 116 (c), and the initial distance between jaws was $L_0 =$ 100 mm, so the rate of elongation must be changed to maintain the proposed strain rate calculated in equation (103): $0.00185\ s^{-1} \cdot 100\ mm \cdot \frac{60\ s}{1\ min} = 11.11\ \frac{mm}{min}$. A speed of elongation of 11.11 mm/min was used in the tensile tests for the characterisation of the insulation in MD.

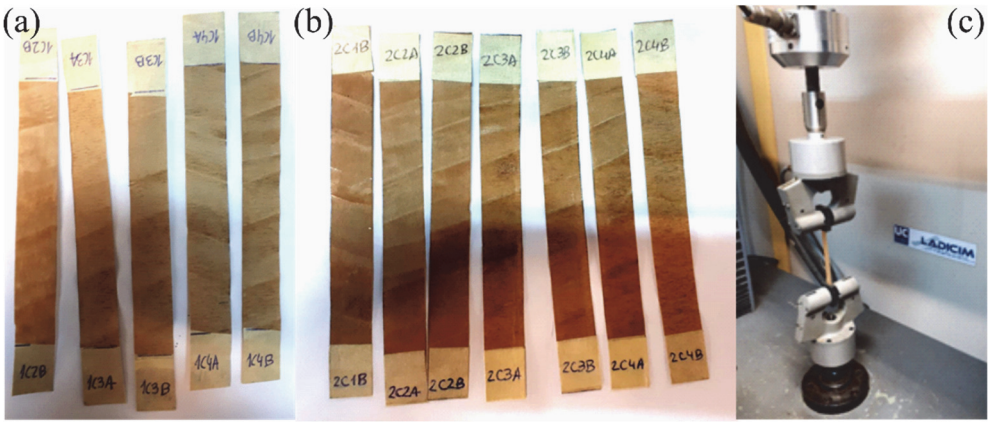

Figure 116. Some paper samples for tensile testing in MD of (a) Ageing State I and (b) Ageing State II; (c) Tensile test for the characterisation of the paper samples in MD.

The analysis in MD initially considered 5 ageing states x 4 paper layers in each copper conductor piece x 2 paper strips for each layer = 40 paper strips. In the cases where notable differences were noticed between the results of two tests for the same layer and ageing state (such as a variation of more than 50%), a third or fourth paper strips were tested. All the paper strips were characterised, obtaining their stress-strain curves up to fracture, from which the maximum tensile stress, $\sigma_{MD,t}^{max}$, and their strain at breakage, $\varepsilon_{MD,t}^{max}$, can be obtained. It became clear that the stress-strain curves did not show a descending part, but they exhibited immediate fracture, so $L_{critical} < 100\,mm$ both for the plain Kraft and crepe papers.

Table 21 summarises the results of tensile tests in MD for all the layers and ageing states (0-IV). Those results show that the mechanical properties of the plain Kraft paper (layers 1, 2) radically differ from the ones of the crepe paper (layers 3, 4). The first paper behaves as a purely plastic material, while the second behaves as a hyperelastic one. The tensile strength of the crepe paper is, in most tests, slightly higher than in the plain paper, but especially the strain at breakage is much greater in the crepe paper, because of its hyperelastic behaviour. The tests also showed that the response of both materials to ageing differs, especially when the ageing is very extreme.

In Figure 117, representative tensile stress-strain curves in MD are shown for the same layer and different ageing states. As mentioned in section *1.2.1*, it must be noted that layer 1 was considerably deteriorated in the extraction after the ageing process at 150°C and before the tensile tests, as it was glued to the copper due to the melting of the enamel surrounding the strands of the CTC which were in contact with that layer, and it suffered local delaminations. In fact, it was not possible to extract layer 1 for its characterisation in Ageing State IV, because it was totally glued to the CTC. Because of that reason, the fragility of layer 1 in ageing states I, II and III was not totally representative of the response of the material to ageing at normal conditions. The thermal class of the enamel was not high enough to withstand 150°C, so these results can be regarded as a representation of what would happen if a power transformer is accidentally subjected to more extreme conditions than its rated ones. However, as stated in section *1.2.1.Degree of Polymerisation (DP) of the dielectric paper*, that elevated temperature was selected in order to mechanically characterise the dielectric paper in an aged condition (DP < 350), as is the case at the end of the ageing duration.

Table 21. Results of the tensile tests for the different layers in MD and for the different ageing states.

Ageing state	State 0 (Not aged)			
	Plain Kraft paper		Crepe paper	
	Layer 1	Layer 2	Layer 3	Layer 4
Tensile strength, $\sigma_{MD,t}^{max}$ (MPa)	80.7 ± 2.8	77.4 ± 9.7	92.0 ± 5.5	96.6 ± 8.8
Strain at breakage, $\varepsilon_{MD,t}^{max}$ (%)	3.42 ± 0.25	3.12 ± 0.28	23.85 ± 1.08	22.33 ± 1.84
Ageing state	State I (Aged for a week at 150°C)			
	Plain Kraft paper		Crepe paper	
	Layer 1	Layer 2	Layer 3	Layer 4
Tensile strength, $\sigma_{MD,t}^{max}$ (MPa)	58.7 ± 7.1	80.3 ± 7.0	96.6 ± 17.2	111.8 ± 17.3
Strain at breakage, $\varepsilon_{MD,t}^{max}$ (%)	2.07 ± 0.18	2.54 ± 0.22	20.74 ± 0.73	23.47 ± 1.30
Ageing state	State II (Aged for four weeks at 150°C)			
	Plain Kraft paper		Crepe paper	
	Layer 1	Layer 2	Layer 3	Layer 4
Tensile strength, $\sigma_{MD,t}^{max}$ (MPa)	42.1 ± 5.0	63.0 ± 2.2	81.9 ± 2.3	80.8 ± 6.7
Strain at breakage, $\varepsilon_{MD,t}^{max}$ (%)	0.99 ± 0.05	2.03 ± 0.16	19.96 ± 0.87	20.91 ± 0.57
Ageing state	State III (Aged for nine weeks at 150°C)			
	Plain Kraft paper		Crepe paper	
	Layer 1	Layer 2	Layer 3	Layer 4
Tensile strength, $\sigma_{MD,t}^{max}$ (MPa)	38.3 ± 2.0	63.4 ± 7.2	59.1 ± 10.4	68.3 ± 6.2
Strain at breakage, $\varepsilon_{MD,t}^{max}$ (%)	0.82 ± 0.03	1.19 ± 0.05	17.50 ± 2.28	17.85 ± 0.30
Ageing state	State IV (Aged for twenty-eight weeks at 150°C)			
	Plain Kraft paper		Crepe paper	
Tensile strength, $\sigma_{MD,t}^{max}$ (MPa)	-	39.4 ± 0.4	26.7 ± 0.7	24.0 ± 0.9
Strain at breakage, $\varepsilon_{MD,t}^{max}$ (%)	-	0.68 ± 0.01	2.31 ± 0.24	1.51 ± 0.07

In layers 2, 3 and 4, an unexpected result was obtained: the strength seemed to be higher in Ageing State I than when the paper sample was not aged (see Figure 117 (b), (c) and (d)). The reason could be that the initial impregnation in dielectric oil, filling the voids of the paper material improved its mechanical resistance in comparison with the paper alone. However, for layers 2 and 3, the strain at breakage was lower in Ageing State I than when the paper was not aged. In the case of layer 4 (Figure 117 (d)), both the tensile strength and the strain at breakage were higher in Ageing State I than in State 0, and that could be caused by specific defects in the non-aged samples, producing a lower resistance in them.

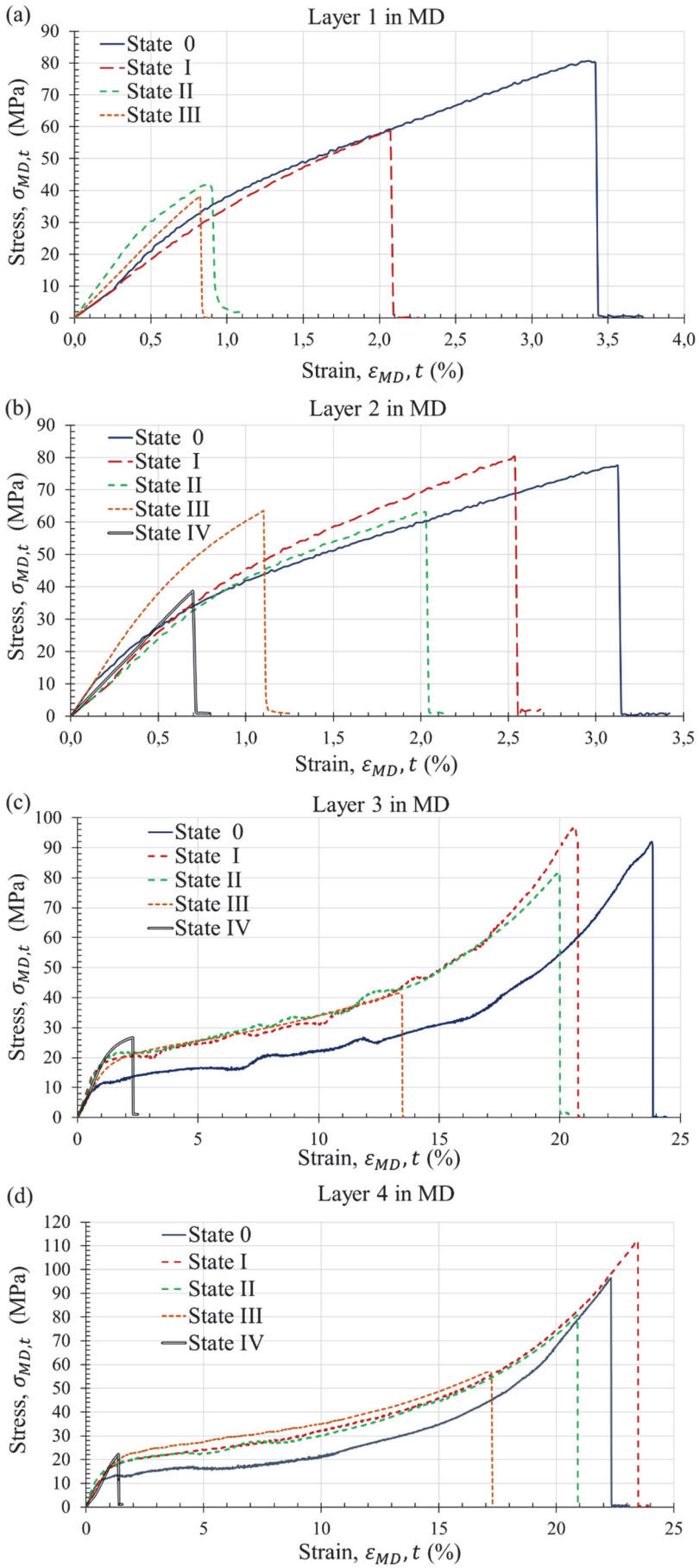

Figure 117. Tensile test in MD for layer (a) 1, (b) 2, (c) 3 and (d) 4, in the different ageing states.

The results in MD for the samples obtained from the same layer and ageing state, see Table 21, highlight the high degree of heterogeneity of the insulation material, which is one of its main features and is primarily due to its microstructure and local defects such as micro cracks or small delaminations, sometimes produced during manufacture and magnified by the ageing process. The average values of tensile strength and strain at breakage, and the variability obtained in the tensile tests in MD, are shown in Figure 118. The coefficient of variation of the results reduced as the ageing level increased, so it can be inferred that the accused reductions in tensile strength or strain at breakage in some of the tested paper samples was due to a particular local defect in those samples. On the other hand, when the material is aged, its response is more homogeneous.

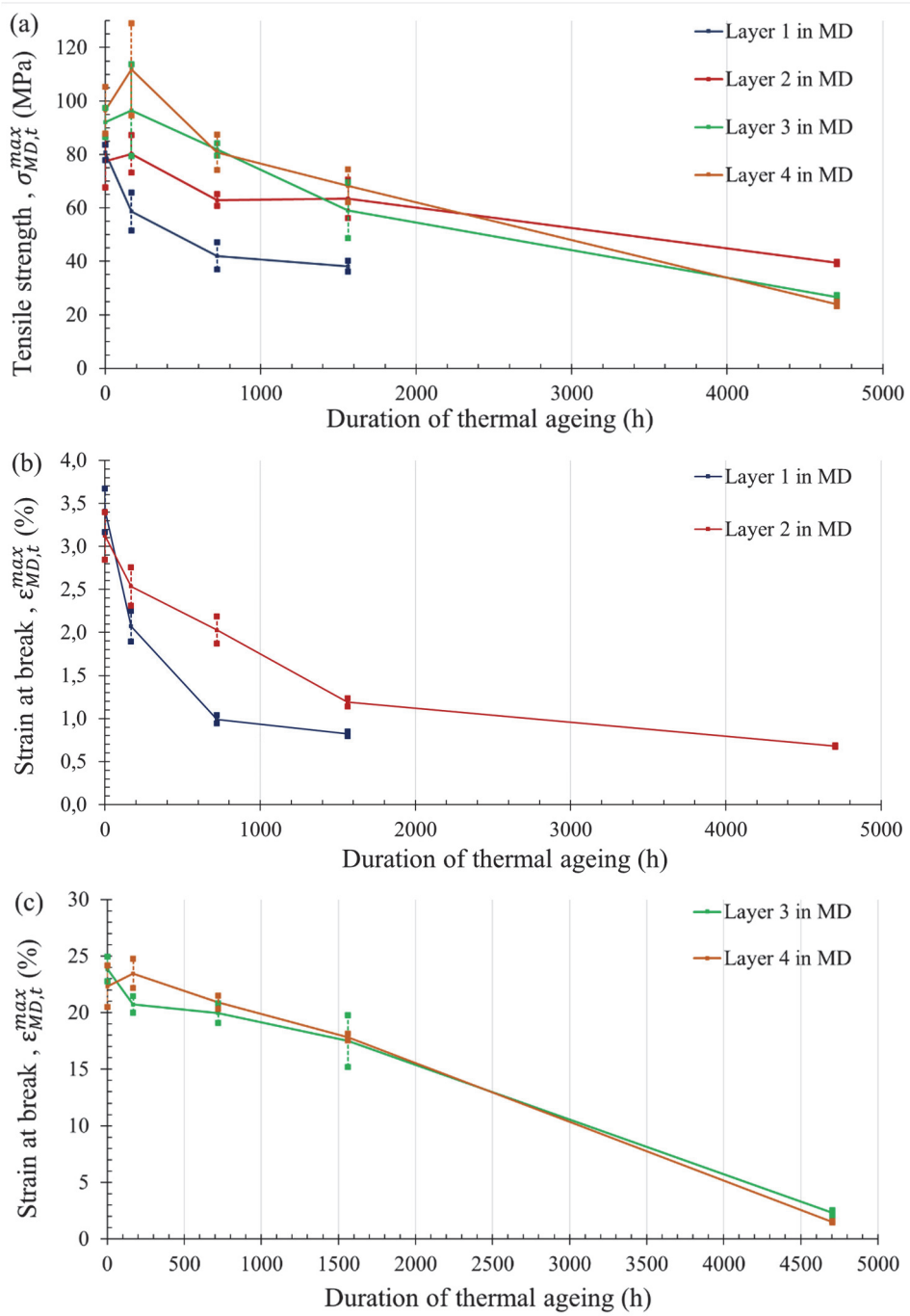

Figure 118. Average values ± standard deviations of the (a) tensile strength, σ_{MD}^{max}, and (b), (c) strain at breakage, ε_{MD}^{max}, as a function of ageing duration.

The variation in the tensile strength in MD due to thermal ageing can be seen in Figure 118 (a). At the beginning of the ageing process, the reduction of strength was maximum in layer 1, because it became glued to the CTC due to the enamel melting. The increase in the strength due to oil-impregnation after one week of ageing can be seen for layers 2, 3 and 4, but the strength started decreasing later, up to the end of the ageing process. Although the initial strength of the plain Kraft was lower than the one of the crepe paper, the strength of layers 3 and 4 suffered a higher descent after Ageing State I and up to the end of the ageing process. Regarding the variation in strain in MD, Figure 118 (b) and (c), there was a great difference in the maximum strain at breakage between the plain and crepe papers. For layers 1 and 2, the decrease in strain was maximum in the first hours of ageing, and at the end of the process, the maximum strain at breakage was less than one third of the initial one. For the crepe paper (layers 3 and 4), there was also a decrease in the strain at breakage, which was not very accused between the first two ageing states. However, after Ageing State II, the strain at breakage decreased radically up to a final value of around 1-2%. At the end of the ageing duration, both materials were very fragile and had similar values of the strain at breakage.

- **Characterisation of the tensile properties of the CTC insulation in CD**

The characterisation of the material in CD was a technical challenge, because of the narrowness of the insulation strips in the CTC. The tested paper samples, Figure 119 (a), had average length of 17 mm and width of 15 mm and, as the sample length was remarkably different to those recommended in [137], the elongation rate was reduced proportionally up to 1.7 mm/min. That short length of the paper strips in CD affected the obtained stress-strain curves and, in this case, the observed failure mechanism was different than in MD. Instead of the immediate fracture, a non-immediate rupture was exhibited in CD, so it can be inferred that $L_{stable} < 17\ mm < L_{critical}$, at least when the paper was not heavily aged. Most of the tensile tests in CD showed consecutive bond-ruptures in the paper, which caused a decrease in the stress that the paper held. That was especially evident when the paper was not aged (State 0); on the other hand, some tests in CD with the heavily aged paper (State IV) showed a sudden rupture.

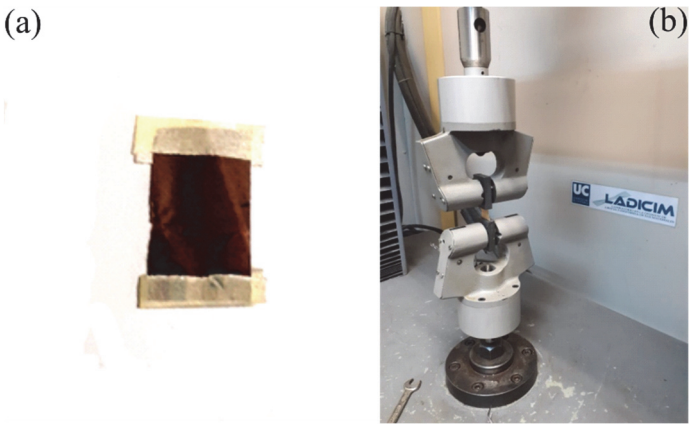

Figure 119. (a) Paper sample for the characterisation in CD; (b) Tensile test for the characterisation in CD.

With that type of non-immediate fracture mechanism, the elongation measured by the tensile machine in CD does not correspond to a homogenous deformation in the tested paper strip, but is the sum of the local deformation in the fracturing damage band and a uniform strain outside that damage band, which decreases during the fracture process due to the decrease in stress, according to [89]. However, it must be taken into consideration that the real length in CD of the strips which serve as insulation of the studied CTC is about 25 mm, and that length will also be between L_{stable} and $L_{critical}$, so the failure mechanism of the paper in CD in a real situation in that particular CTC will be similar to the one shown by the

performed tensile tests. It must be noted that the interest of this experimental work is to characterise the mechanical response of the insulation paper in a power transformer in operation, with the particular features that the material has in that situation, such as its geometry. The tensile testing of samples in CD with the dimensions proposed in [137] would not be representative for studying failure of the insulation of the analysed CTC in that material direction.

Table 22 summarises the results of the tensile tests in CD for all the insulation layers in the different ageing states, which are also shown in Figure 120.

Table 22. Results of tensile tests in CD for the different layers in the different Ageing States.

Ageing state	State 0 (Not aged)			
	Plain Kraft paper		Crepe paper	
	Layer 1	Layer 2	Layer 3	Layer 4
Tensile strength, $\sigma_{CD,t}^{max}$ (MPa)	45.6 ± 3.2	40.2 ± 2.9	12.1 ± 1.0	15.5 ± 1.3
Strain at breakage, $\varepsilon_{CD,t}^{max}$ (%)	8.78 ± 0.83	7.65 ± 0.79	12.20 ± 0.83	11.43 ± 0.81
Ageing state	State I (Aged for a week at 150°C)			
	Plain Kraft paper		Crepe paper	
	Layer 1	Layer 2	Layer 3	Layer 4
Tensile strength, $\sigma_{CD,t}^{max}$ (MPa)	25.6 ± 1.6	35.9 ± 2.7	19.6 ± 0.5	18.6 ±0.4
Strain at breakage, $\varepsilon_{CD,t}^{max}$ (%)	7.39 ± 0.54	7.38 ± 0.80	9.06 ± 0.28	11.68 ± 0.43
Ageing state	State II (Aged for four weeks at 150°C)			
	Plain Kraft paper		Crepe paper	
	Layer 1	Layer 2	Layer 3	Layer 4
Tensile strength, $\sigma_{CD,t}^{max}$ (MPa)	22.7 ± 1.1	36.1 ± 2.0	18.3 ± 1.4	20.1 ± 1.6
Strain at breakage, $\varepsilon_{CD,t}^{max}$ (%)	5.00 ± 0.62	6.09 ± 1.09	8.01 ± 0.29	7.57 ± 0.19
Ageing state	State III (Aged for nine weeks at 150°C)			
	Plain Kraft paper		Crepe paper	
	Layer 1	Layer 2	Layer 3	Layer 4
Tensile strength, $\sigma_{CD,t}^{max}$ (MPa)	22.5 ± 3.5	33.3 ± 5.8	16.7 ± 0.9	17.8 ± 0.9
Strain at breakage, $\varepsilon_{CD,t}^{max}$ (%)	4.08 ± 0.47	5.50 ± 0.88	3.48 ± 0.35	3.44 ± 0.33
Ageing state	State IV (Aged for twenty-eight weeks at 150°C)			
	Plain Kraft paper		Crepe paper	
Tensile strength, $\sigma_{CD,t}^{max}$ (MPa)	-	13.6 ± 0.3	13.6 ± 0.4	10.9 ± 0.3
Strain at breakage, $\varepsilon_{CD,t}^{max}$ (%)	-	1.45 ± 0.03	1.45 ± 0.09	1.75 ± 0.09

Representative strain-stress curves of the tensile tests for the strips of insulation in CD can be seen in Figure 120, where it can be noticed that some curves show a really irregular pattern, especially the ones for the aged crepe paper. In those curves, the maximum stress was considered to be the tensile strength of the material in CD, $\sigma_{CD,t}^{max}$, and the strain for that stress was considered to be $\varepsilon_{CD,t}^{max}$.

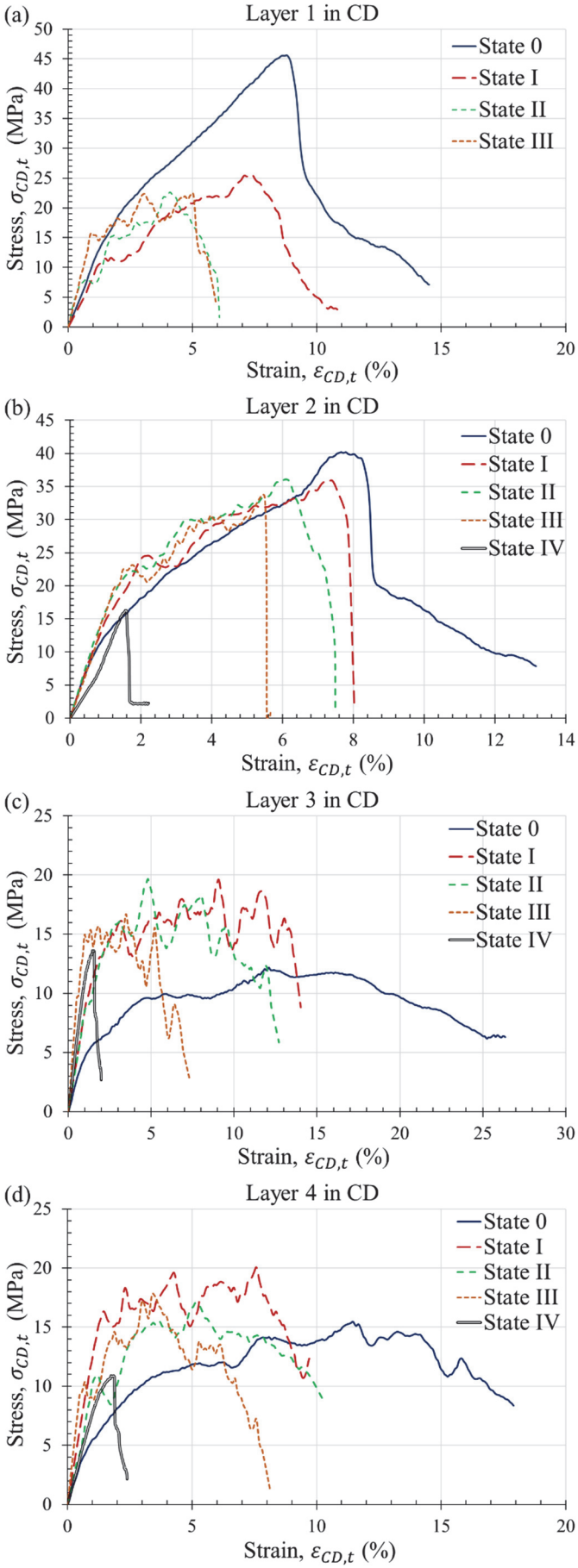

Figure 120. Tensile test in CD for layer (a) 1, (b) 2, (c) 3 and (d) 4, in the different ageing states.

The results of the tensile tests in CD showed that, for the plain Kraft paper, Figure 120 (a) and (b), the strain at breakage was between 2 and 6 times higher in CD than in MD. Besides, the effect of the ageing duration in the strain at breakage of the plain Kraft was similar in MD, with a reduction of around 75% between Ageing States 0 and IV, and in CD, where the reduction was around 80%. Regarding the tensile strength, the values in MD are between 1.5 and 2 times higher than the ones in CD, and the effects of thermal ageing in the strength are similar in both directions of the paper material. Only at the end of the ageing process, in Ageing State IV, had the strength in CD reduced more than the one in MD.

For the crepe paper, the tests in Figure 120 (c) and (d) showed that, in the first stages of ageing, States 0 and I, the strain at breakage is between 1.5 and 2 times higher in MD than in CD. In States II and III, the $\varepsilon_{MD,t}^{max}$ was between 2.5 and 3 times higher than the $\varepsilon_{CD,t}^{max}$, so that means that the decrease of strength was more accused in CD. At the end of the ageing process, State IV, the strain at breakage in MD and CD were of the same order of magnitude. Regarding the tensile strength, its value is higher in MD than in CD for all the ageing states, but the ratio between them, $\sigma_{MD,t}^{max}/\sigma_{CD,t}^{max}$, decreases from a value around a 6-7 when the paper is not aged, up to a value of about 2 in Ageing State IV, indicating that the reduction of strength in MD due to ageing is higher than in CD.

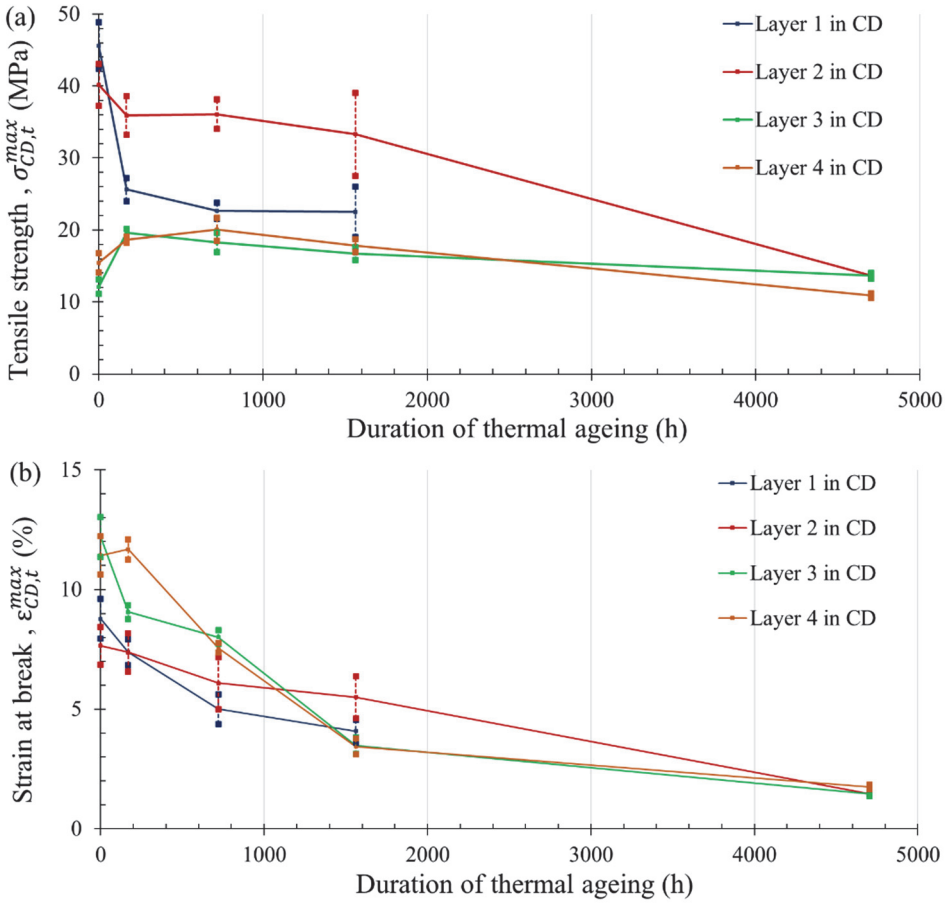

Figure 121. Average values ± standard deviations of the (a) tensile strength, σ_{CD}^{max}, and (b) strain at breakage, ε_{CD}^{max}, as a function of ageing duration.

In conclusion, the tensile properties of two different dielectric papers (plain Kraft and crepe paper) were analysed in the laboratory under different ageing states, and the accused differences in their mechanical behaviour were noticed. In view of the experimental results, it seemed that there were no significant differences in the impact of ageing between layers 3

and 4. For each ageing state, both the tensile strength, σ_t^{max}, and strain at breakage, ε_t^{max}, remained similar for both layers, considering the heterogeneity of the material, so the impact that being in direct contact with the naphthenic oil (as in the case of layer 4) has on the ageing was not relevant.

- **Conclusions**

In conclusion, the tensile properties of two different dielectric papers (plain Kraft and crepe paper) were analysed in the laboratory under different ageing states, and the accused differences in their mechanical behaviour were noticed. In view of the experimental results, it seemed that there were no significant differences in the impact of ageing between layers 3 and 4. For each ageing state, both the tensile strength, σ_t^{max}, and strain at breakage, ε_t^{max}, remained similar for both layers, considering the heterogeneity of the material, so the impact that being in direct contact with the naphthenic oil (as in the case of layer 4) has on the ageing was not relevant.

- In tension in MD, the differences in the mechanical behaviour of the crepe and plain Kraft papers are evident. The first has a plastic response, while the second shows marked hyperelasticity.

- In tension in MD, $\sigma_{MD,t}^{max}$ was higher for the crepe paper during the beginning of the ageing duration. For Ageing States III and IV, the values were similar for both materials.

- In tension in MD, $\varepsilon_{MD,t}^{max}$ was considerably higher for the crepe paper, except at the end of the ageing process, in Ageing State IV, when both materials have similar values. When the material was not aged, the value of the strain at breakage was approximately 7.5 times higher in the crepe paper than in the plain paper.

- In tension in CD, the mechanical response was not markedly different between the plain and crepe papers, and the stress-strain curves had similar aspects.

- In tension in CD, $\sigma_{CD,t}^{max}$ was higher in the plain Kraft paper at the beginning of the ageing duration. Only at the end, in Ageing State IV, were the values similar for both materials.

- In tension in CD, $\varepsilon_{CD,t}^{max}$ was higher in the crepe paper from the beginning of the ageing duration and up to Ageing State III. In this case, for the non-aged material, the strain was less than 2 times higher in the crepe paper than in the plain Kraft paper.

- For both types of insulation, $\sigma_{max,t}^{MD} > \sigma_{max,t}^{CD}$, as is expected for paper materials.

- For the crepe paper $\varepsilon_{max,t}^{MD} > \varepsilon_{max,t}^{CD}$, except in Ageing State IV, were the maximum strain at breakage was similar for both directions. On the contrary, for the plain Kraft paper $\varepsilon_{max,t}^{MD} < \varepsilon_{max,t}^{CD}$ for all the ageing states.

- It could be concluded that, in the crepe paper, the CD will be the preferential one for crack propagation, as both the strain at breakage and the tensile strength are lower in CD.

1.2.3. Edgewise mechanical compressive properties of the dielectric paper

In a multiaxial stress state, such as the one that the windings of a power transformer and their conductors suffer under the influence of a short circuit, the mechanical failure of the paper insulation depends on the interaction among the stresses and strains in the different directions of the material. Because of that, the compressive properties are also of relevance, especially when the insulation paper is aged and more fragile. Actually, the results of the bending tests performed in the CTC samples and described in *1.3.Three-point bending tests of the insulated CTCs*, showed that big cracks appeared in areas of the sample subjected to compression when the insulation was deeply aged, see Figure 122.

Figure 122. CTC sample of Ageing State IV after the bending test with final deflection of 20 mm.

Although there are applicable standardised methods for obtaining the tensile properties of thin paper, such as [137], those kind of accepted standards do not exist for its characterisation in compression. There are several methods proposed in the bibliography to determine the compressive properties of pressboard and paperboard, but, according to [20], they give results which can differ in 30% or more, as the obtained compressive strength depends on the way in which it is measured. The main sources of variation among test methods are the sample size, the strain rate, the structural contribution to failure, and the sample preparation and its shape, which could be cylindrical or planar [20]. The basic challenge of compression tests for paper materials is to introduce a pure compressive force into the plane of the sheet that causes pure in-plane deformation and failure, although the failure itself will involve out-of-plane deformations, such as bending or buckling [20]. The difficulties are mainly related to the small thickness of the material, so it is even more complicated to obtain the properties of thin paper than the ones of paperboard or pressboard. Indeed, there are no published works that report in-plane compressive properties of thin paper.

In order to measure compressive properties reliably, the experimental process should avoid the strength degradation due to damaged edges or stress concentrations close to clamps, and the structural response and structural instability of the material should be eliminated as far as possible. Besides, instabilities of fibres within the sheet influence the real behaviour under compression of the material, so they must not be inhibited to avoid an artificial increase in the compressive strength of the material [20]. With thin materials, such as the paper insulation studied here, the most easily applicable methods need to use cylindrical specimens. A method for the determination of the edgewise compressive strength of paper and paperboard using cylindrical samples is specified in [138], which is applicable to all paper and paperboard with a thickness between 100 µm and 580 µm. For samples with a thickness below 280 µm, test values can result from a combination of both buckling failure and pure compression, according to [138]. The normalised method is thought for board used

in the manufacture of fibreboard shipping containers. However, the dielectric insulation studied here has a thickness of 80-82 µm, so it is essential to adapt the proposed experimental method in order to study the insulation response to edgewise compression.

First, it must be considered that if the sheet of paper is formed into a cylinder, its structural stability is increased, and that the mechanical response of the cylinder when it is subjected to compression depends on its particular geometry. The classification of the mechanical behaviour of cylinders under compression shown in Figure 123 and Table 23 is reported in [20]. To obtain the maximum edgewise compressive strength and reduce the influence of structural buckling, the tested cylinder should be in the short range. That introduces a problem when analysing dielectric papers (plain Kraft and crepe), because with a thickness of 80 µm, the expression from Table 23 would be:

$$\frac{H^2}{Rt} = \frac{H^2}{R \cdot 80 \cdot 10^{-3}} < 1 \tag{106}$$

And, considering that the minimum height of the cylinder which is feasible to test in the laboratory is about H = 5 mm, a radius larger than 312.5 mm would be needed, which means a rectangular paper sample with an approximate length of 2 m. The conclusion is that it is impracticable to make a cylindrical paper sample in the short range.

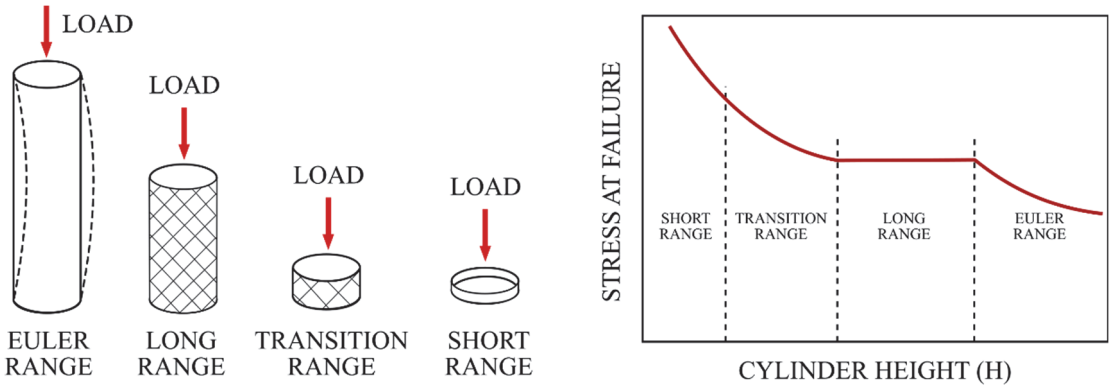

Figure 123. Different mechanical responses of a thin cylinder under compression, based on [20].

Table 23. Intervals for the different mechanical responses of a thin cylinder to compression, where H is the free height, R is the radius and t is the thickness, from [20].

Euler column	$\frac{H^2}{Rt} \gg 100$
Long range	$\frac{H^2}{Rt} > 100$
Transition range	$1 < \frac{H^2}{Rt} < 100$
Short range	$\frac{H^2}{Rt} < 1$

However, the purpose of the present work is to estimate the edgewise compression strength of the insulation material of a CTC in a power transformer, and there, the geometry clearly affects the mechanical response. The ideal maximum edgewise compressive strength of the material is not of interest here, but the edgewise compressive strength of the paper insulation with a particular geometry and in a particular ageing state. The insulation of the CTC consists of two inner layers of plain Kraft paper, and two outer layers of crepe paper. The paper is wrapped around the copper conductor, the layers have a width of approximately 25

mm and they are overlapped, see Figure 124. Thus, the chosen cylindrical sample for compressive testing should have a similar response to the real CTC insulation.

Figure 124. General view of an insulated CTC sample.

In the same way as there are modifications to the Ring Crush Test proposed in the literature, such as the one in [139], where the edges of the cylinder were reinforced with wax and a glueline was used, see Figure 125 (a), a modification is proposed here to measure the edgewise compressive properties of the insulation with the equipment available in the laboratory. As the paper insulation of the CTC consists of two layers of plain Kraft and two layers of crepe paper, a paper sample consisting of two concentric cylinders was used here for the tests. To obtain a trade-off among the avoidance of an accused structural buckling for low loads, dimensions manageable in the laboratory, and a response similar to the real one, the cylinders were made of two concentric layers of paper with H = 20 mm and R = 10 mm. Instead of using the glueline proposed in [139], a sewing thread was used, with the intention of constraining the cylinder to open circumferentially, but trying to avoid an artificial rigidisation as far as possible, see Figure 125 (b). With the strain rate proposed in [137], of 0.00185 s^{-1}, which is equivalent to 0.25 mm/min, and transmitting the loading force through a plastic plane surface, to reduce damage of edges or stress concentrations, see Figure 126, it was observed that the response of the cylinder in compression was quite stable and could be considered as representative.

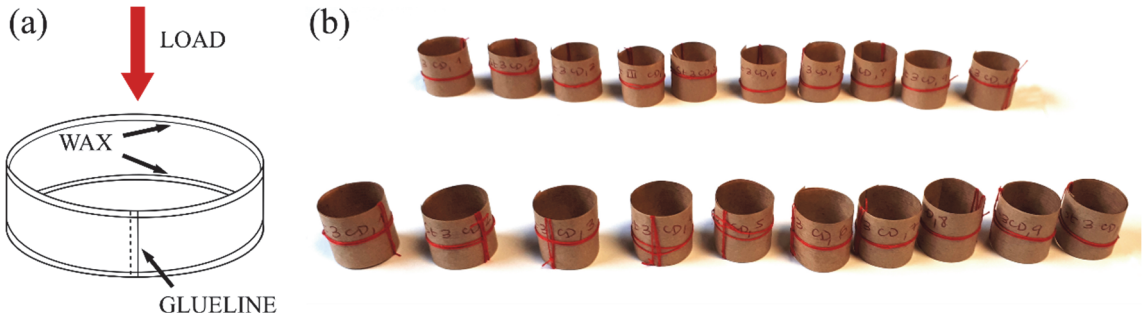

Figure 125. (a) Sample for the Modified Ring Crush Test, based on [139]; (b) Paper cylinders for compressive testing before the ageing process.

As the edgewise compressive properties of the plain Kraft and the crepe papers could differ in the MD and CD, ten cylindrical samples were prepared in each of the directions for the two materials and four ageing states were considered (Ageing States 0-III). That means 2 materials x 2 directions x 4 ageing states x 10 samples = 160 cylindrical samples for the characterisation of the edgewise compressive properties. The testing machine records the compressive load (N) by means of the load cell, and the elongation of the paper sample (mm) by the moving crosshead. The uniaxial load-elongation curves are recorded by a PC. To transform the measured data to stress-strain curves, relationships (107) and (108) have to be considered:

$$\varepsilon\ (\%) = \frac{H_0 - H_f}{H_0} \cdot 100 \quad (107)$$

$$\sigma\ (MPa) = \frac{F}{A} = \frac{F}{4\pi \cdot 10 \cdot t} \quad (108)$$

Where:

$H_f\ (mm)$: Elongation recorded by the tensile machine.

$H_0\ (mm)$: Initial height of the cylindrical sample.

$F\ (N)$: Force recorded by the tensile machine.

$A\ (mm^2)$: Cross-sectional area of the cylinder that is in contact with the plastic loading surface, $A = 2\ (2\pi R \cdot t) = 4\pi R \cdot t = 4\pi \cdot 10 \cdot t\ mm^2$

$t\ (mm)$: Thickness of the material.

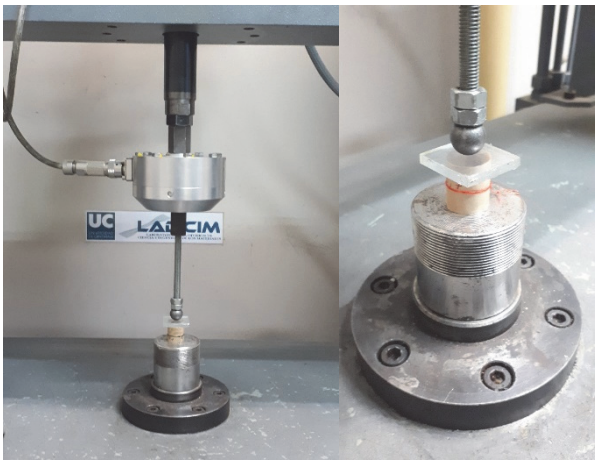

Figure 126. Cylindrical paper sample being subjected to a compressive test.

- **Characterisation of the edgewise compressive properties of the plain Kraft paper**

Figure 127 shows the results of the compressive tests over the cylindrical samples made of plain Kraft paper and whose edges are oriented in the MD of the material, for the different ageing states (0-III). Note that the strains are compressive, although they have been represented in absolute value in the horizontal axis. Figure 128 shows the stress-strain curves for the compressive tests over cylindrical samples made of plain Kraft paper and whose edges are oriented in the CD of the material, for the different ageing states (0-III). Figure 129 shows two cylindrical paper samples made of plain Kraft paper after the compressive tests. The cylinders have undergone local buckling and wrinkle formation which was the cause for the reduction in the mechanical resistance that can be seen in the stress-strain compressive curves.

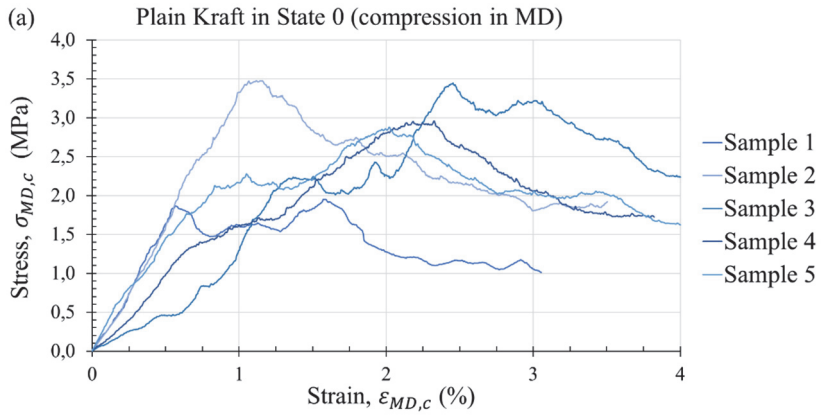

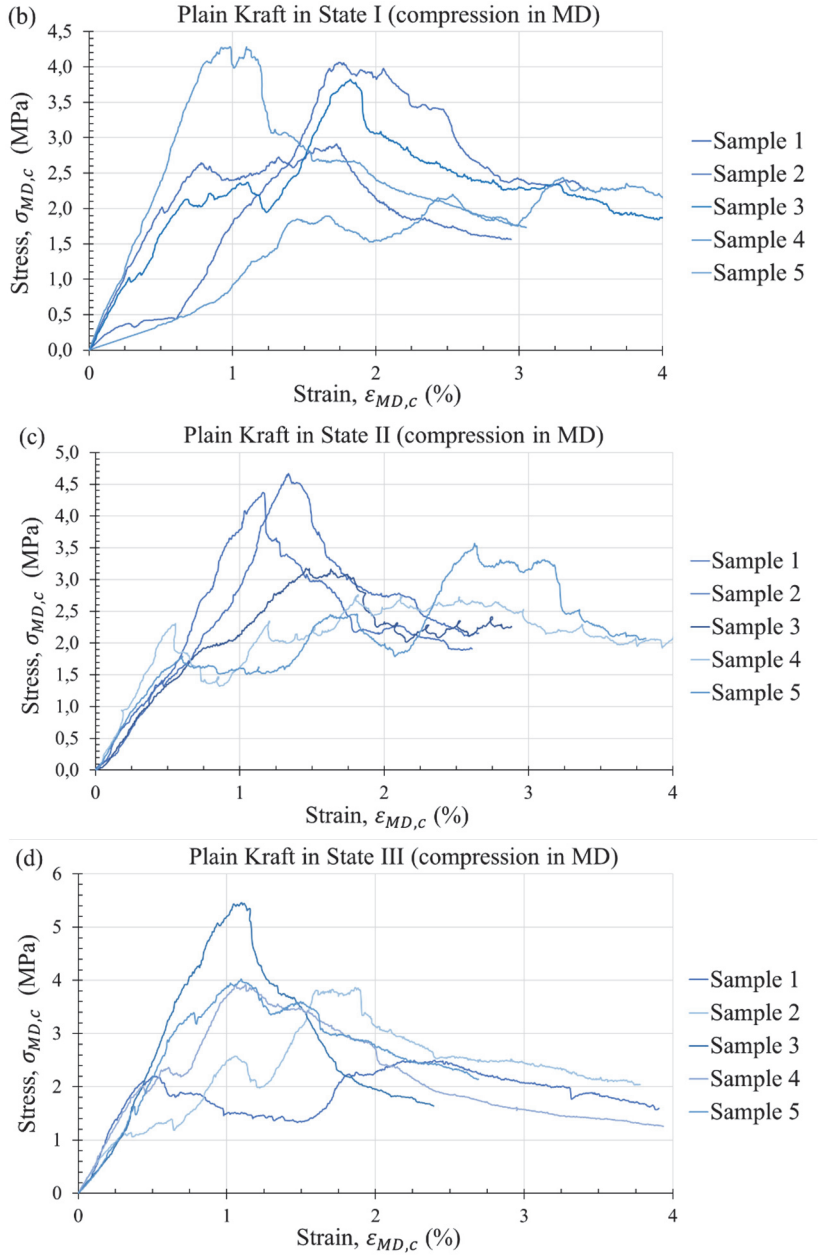

Figure 127. Edgewise compression in MD for the plain Kraft paper in ageing states (a) 0, (b) I, (c) II and (d) III.

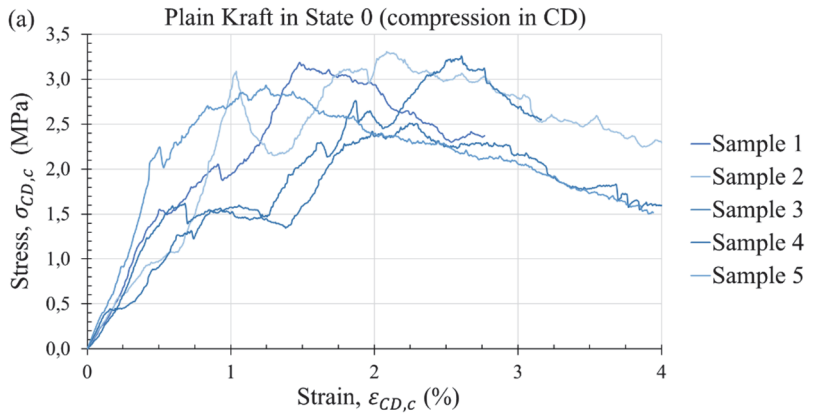

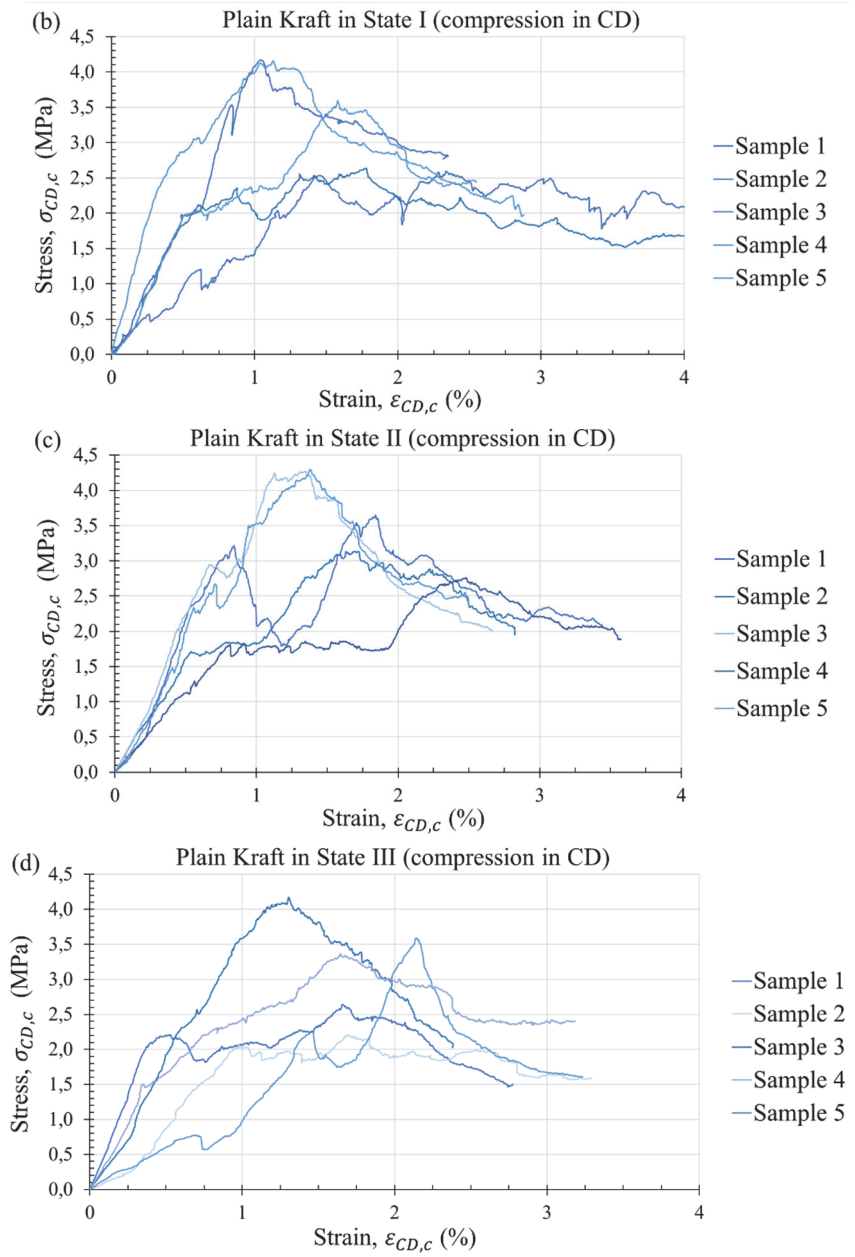

Figure 128. Edgewise compression in CD for the plain Kraft paper in ageing states (a) 0, (b) I, (c) II and (d) III.

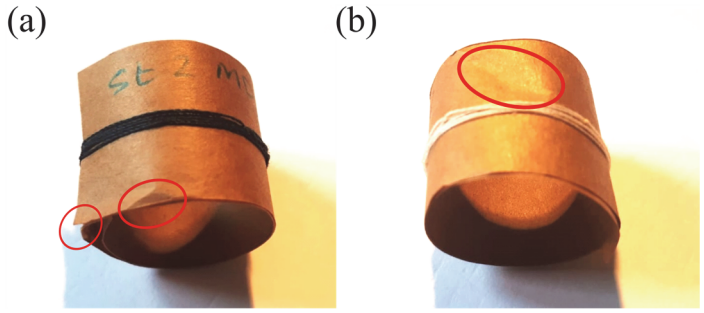

Figure 129. Defects in the cylindrical samples made of plain Kraft paper after being subjected to compressive tests.

- **Characterisation of the edgewise compressive properties of the crepe paper**

Figure 130 shows the results of the compressive tests over the cylindrical samples made of crepe paper and whose edges are oriented in the MD of the material, for the different ageing states (0-III). Here the strains are also compressive strains and have been represented in absolute value. Figure 131 shows the stress-strain curves for the compressive tests over cylindrical samples made of crepe paper and whose edges are oriented in the CD of the material, for the different ageing states (0-III). Figure 132 shows the most common mechanical failure observed in two cylindrical paper samples made of crepe paper after the tests: local buckling and wrinkle formation.

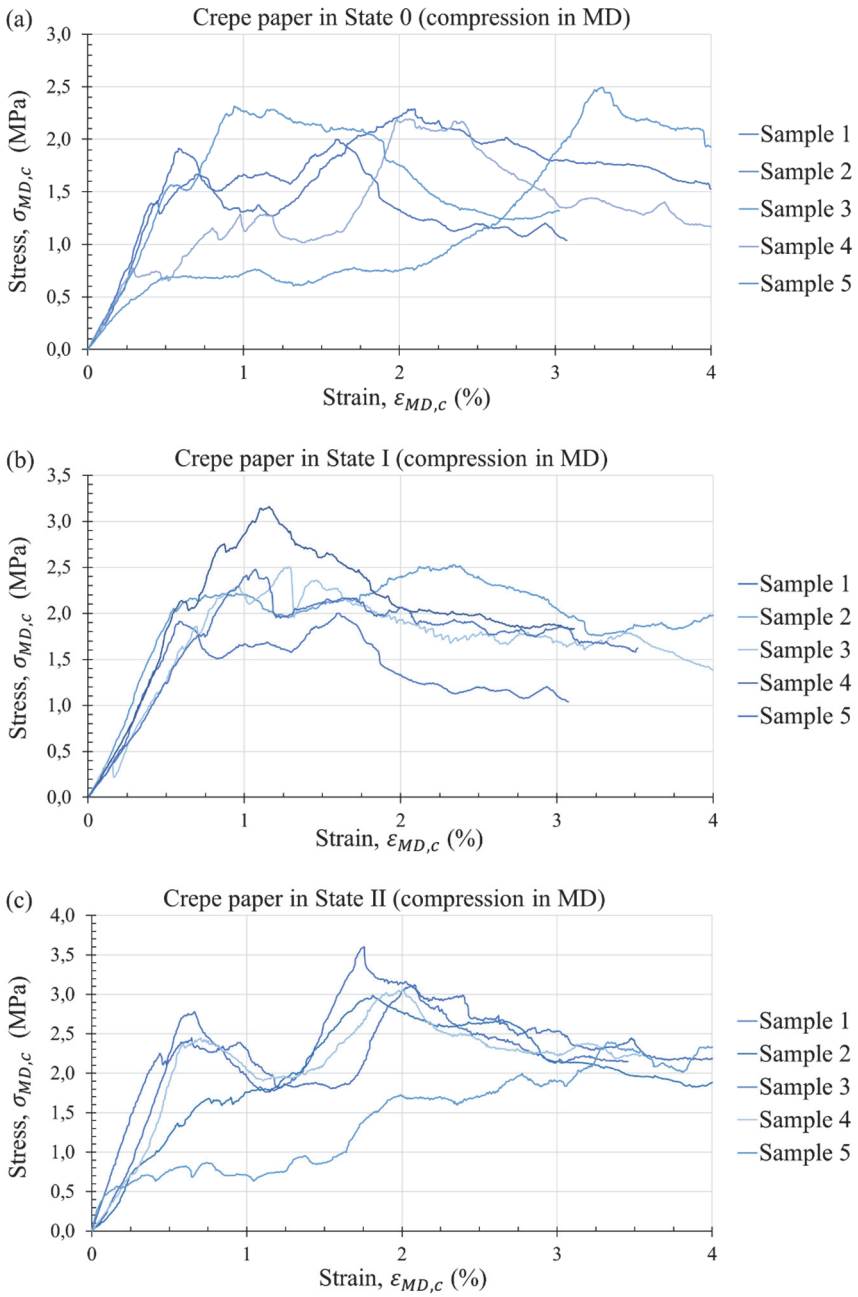

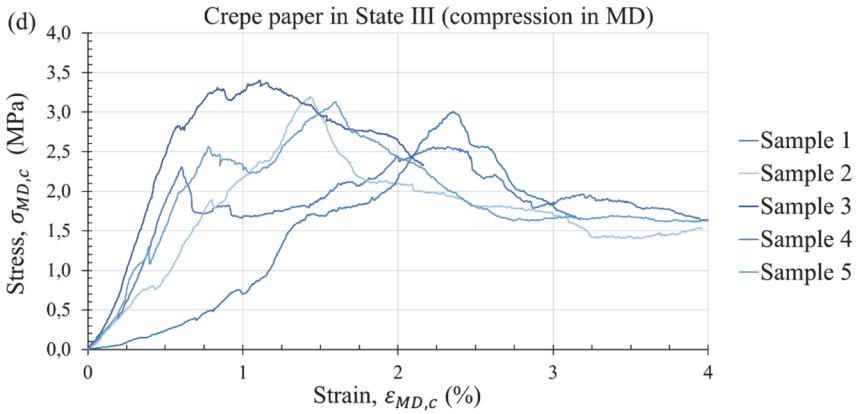

Figure 130. Edgewise compression in MD for the crepe paper in ageing states (a) 0, (b) I, (c) II and (d) III.

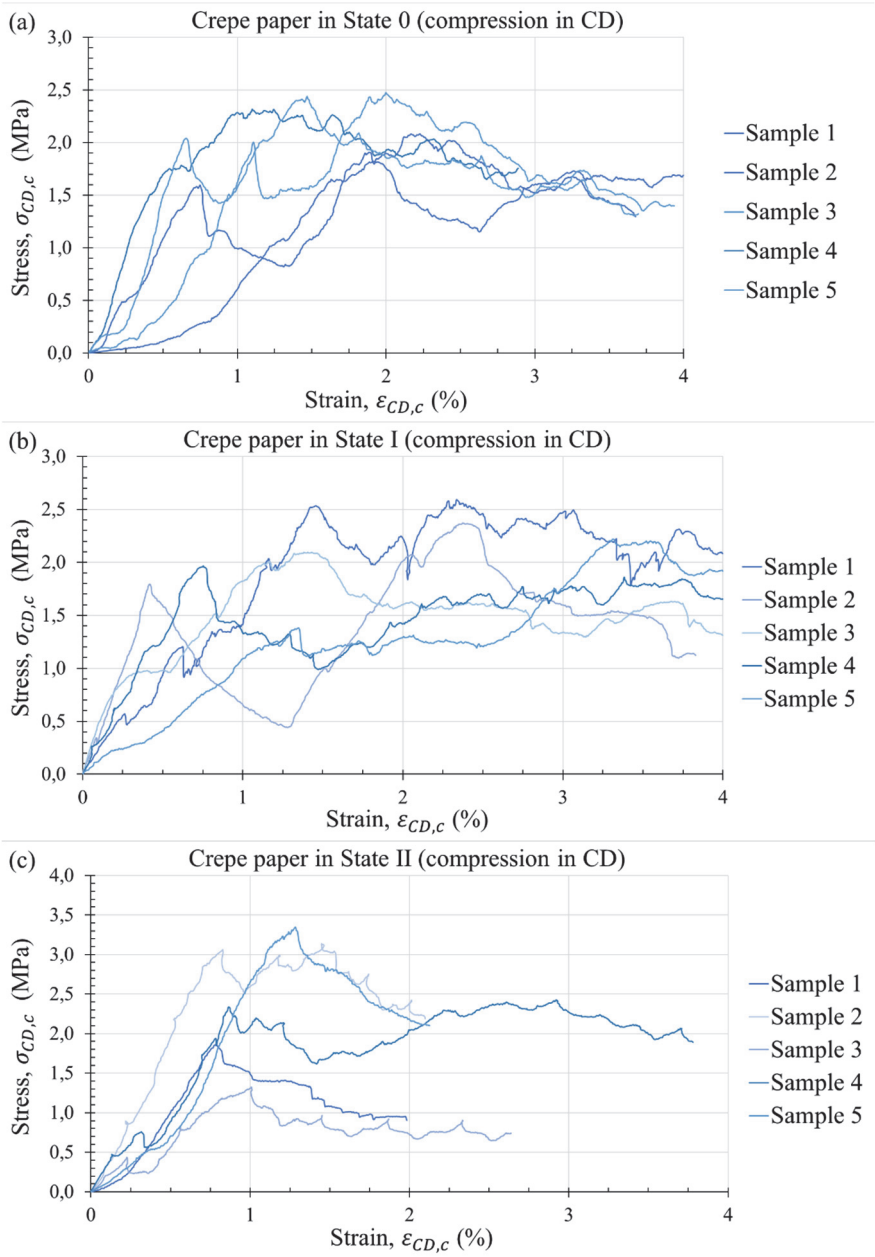

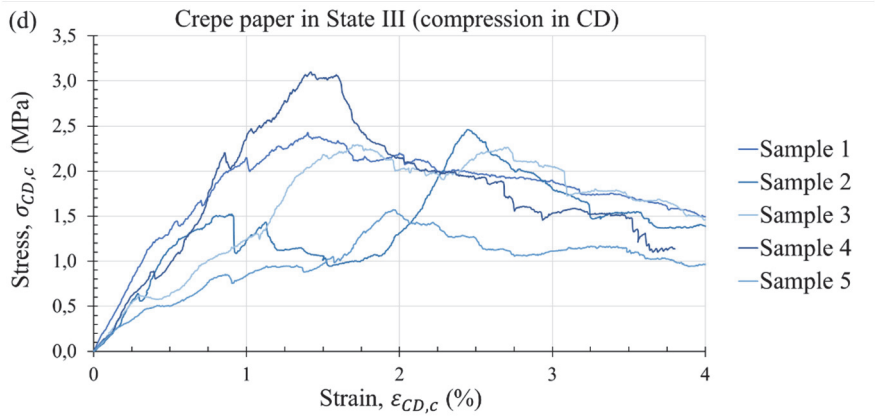

Figure 131. Edgewise compression in CD for the crepe paper in ageing states (a) 0, (b) I, (c) II and (d) III.

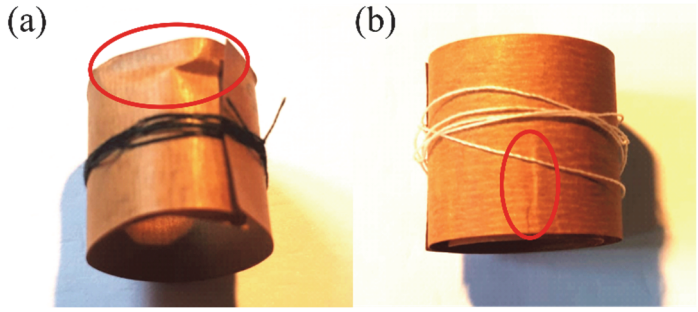

Figure 132. Defects in the cylindrical samples made of crepe paper after being subjected to compressive tests.

- **Conclusions**

The compressive stress-strain curves over a considerable number of cylindrical samples showed an initial peak stress, a subsequent reduction in the stress, and a second peak stress afterwards (see Figure 127, Figure 128, Figure 130 and Figure 131). That may be explained based on the configuration of the cylindrical samples, which consist of two concentric cylinders made of paper insulation. As these two layers are not glued to each other, any superficial unevenness in the contact area between the sample and the loading plastic plane surface could result in initial buckling of one of the concentric layers. After the first concentric layer buckles, it leans on the adjacent insulation layer, and they are loaded together, so the stress increases again. Due to the construction of a real insulated CTC, in which there are several individual layers of paper wrapped around the conductor, it is expected that the previous behaviour is also present there.

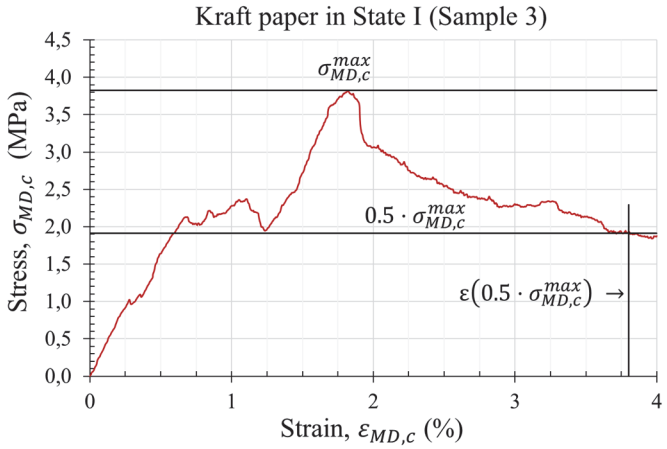

Figure 133. Geometrical construction for obtaining the strain which corresponds to the 50% of the peak compressive stress.

It is not straightforward to translate the information provided by the stress-strain compression curves into an actual in-service deformation of a CTC. Although almost all the compressive curves display a characteristic peak compressive stress, σ_c^{max}, these curves show that the deformation ability of the paper remains beyond that value and that the material retains a relevant compressive strength after reaching that peak stress. In view of the experimental difficulties to determine the "ultimate strain" of the material in compression mode, a conservative value was selected here, which is defined as the strain corresponding to 50% of the peak compressive stress, $0.5 \cdot \sigma_c^{max}$, after reaching that peak stress. The geometrical construction for obtaining $\varepsilon\left(0.5 \cdot \sigma_{MD,c}^{max}\right)$ can be seen in Figure 133.

Table 24 summarises the results of the compressive tests over the cylindrical samples made of both insulation materials, in the different orientations and ageing states (0-III). The average maximum compressive stress, σ_c^{max}, ± the standard deviation was calculated for the different paper samples made of each type of paper (plain Kraft or crepe) and orientation (MD or CD) and for the different ageing levels. The same process shown in Figure 133 was carried out for all the cylindrical samples and average values of $\varepsilon(0.5 \cdot \sigma_c^{max})$ ± the standard deviation were obtained for each material, orientation and ageing state.

Table 24. Results of the compressive tests for the plain Kraft and the crepe papers in the different ageing states.

Ageing state	State 0 (Not aged)			
	$\sigma_{MD,c}^{max}$ (MPa)	$\varepsilon\left(0.5 \cdot \sigma_{MD,c}^{max}\right)$ (%)	$\sigma_{CD,c}^{max}$ (MPa)	$\varepsilon\left(0.5 \cdot \sigma_{CD,c}^{max}\right)$ (%)
Plain Kraft paper	2.9 ± 0.6	4.01 ± 0.57	3.0 ± 0.3	4.38 ± 0.85
Crepe paper	2.3 ± 0.1	5.03 ± 1.13	2.2 ± 0.3	5.54 ± 1.80
Ageing state	State I (Aged for a week at 150°C)			
	$\sigma_{MD,c}^{max}$ (MPa)	$\varepsilon\left(0.5 \cdot \sigma_{MD,c}^{max}\right)$ (%)	$\sigma_{CD,c}^{max}$ (MPa)	$\varepsilon\left(0.5 \cdot \sigma_{CD,c}^{max}\right)$ (%)
Plain Kraft paper	3.5 ± 0.8	4.07 ± 1.99	3.4 ± 0.8	3.94 ± 1.37
Crepe paper	2.5 ± 0.4	5.00 ± 1.22	2.2 ± 0.2	5.53 ± 1.65
Ageing state	State II (Aged for four weeks at 150°C)			
	$\sigma_{MD,c}^{max}$ (MPa)	$\varepsilon\left(0.5 \cdot \sigma_{MD,c}^{max}\right)$ (%)	$\sigma_{CD,c}^{max}$ (MPa)	$\varepsilon\left(0.5 \cdot \sigma_{CD,c}^{max}\right)$ (%)
Plain Kraft paper	3.7 ± 0.8	3.27 ± 1.17	3.6 ± 0.7	3.20 ± 0.68
Crepe paper	3.2 ± 0.3	5.00 ± 0.82	2.4 ± 0.8	3.13 ± 1.18
Ageing state	State III (Aged for nine weeks at 150°C)			
	$\sigma_{MD,c}^{max}$ (MPa)	$\varepsilon\left(0.5 \cdot \sigma_{MD,c}^{max}\right)$ (%)	$\sigma_{CD,c}^{max}$ (MPa)	$\varepsilon\left(0.5 \cdot \sigma_{CD,c}^{max}\right)$ (%)
Plain Kraft paper	4.0 ± 1.0	2.96 ± 1.06	3.2 ± 0.8	3.15 ± 0.82
Crepe paper	3.1 ± 0.3	3.61 ± 0.91	2.3 ± 0.8	4.46 ± 0.91

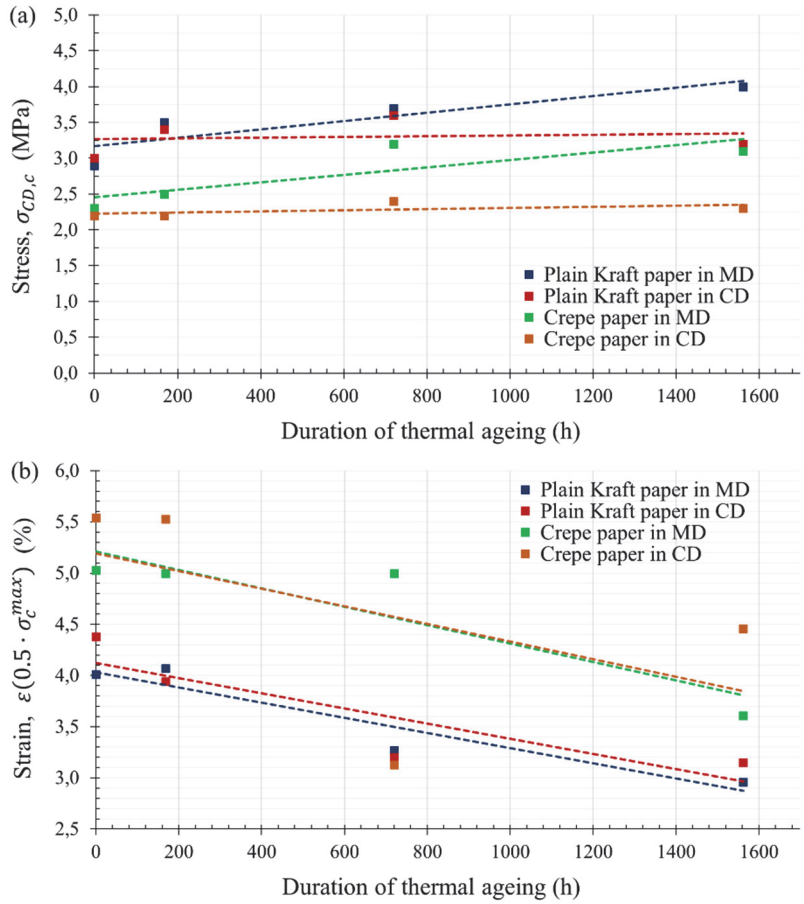

Figure 134. (a)Peak stress and (b) average compressive strain for the peak stress with their trendlines for each material and orientation, as a function of ageing duration.

Figure 134 (a) shows the evolution of the average peak stress, σ_c^{max}, for the plain Kraft and crepe paper in MD and CD. The peak compressive stress in MD is higher than the one in CD for both materials from Ageing State I and up to the end of the ageing process. It can be seen that the ageing has a different impact depending on the material direction: $\sigma_{CD,c}^{max}$ remains almost constant during the ageing duration, while $\sigma_{MD,c}^{max}$ seems to increase. It is not uncommon that a material subjected to ageing increases its strength while reducing its ductility. That behaviour supports the hypothesis that the mechanical failure process is controlled by the deformation level instead of by the stress level, so it would be more convenient that a failure model for paper materials is expressed in terms of strains.

The variations in the average $\varepsilon\left(0.5 \cdot \sigma_{MD,c}^{max}\right)$ and $\varepsilon\left(0.5 \cdot \sigma_{CD,c}^{max}\right)$ for the plain Kraft and crepe papers suggests a downward sloping relationship with the ageing condition of the material, see Figure 134 (b). Nevertheless, it is important to bear in mind the large uncertainties of the experimental results, which are not surprising in such heterogeneous materials. If the trend lines are considered as representative of the variation of the $\varepsilon(0.5 \cdot \sigma_c^{max})$, the differences between the behaviour in compression in MD and CD for both types of paper are almost negligible, especially for the crepe paper. Therefore, for the sake of simplicity, no differences will be considered between the maximum compressive strain at failure in MD and CD for the plain Kraft and crepe papers. An average value of $\varepsilon(0.5 \cdot \sigma_c^{max})$ for each ageing state, in which all the cylindrical samples made of each insulation material for one state were considered, was calculated and represented in Figure 135, indicating that the mean value of the deformation which corresponds to 50% the maximum compressive stress, $\varepsilon(0.5 \cdot \sigma_c^{max})$, is higher for the crepe paper than for the plain Kraft and reduces with the

ageing duration for both materials. The estimated values for the maximum compressive strain at different ageing levels were obtained from that linear fit and are summarised in Table 25.

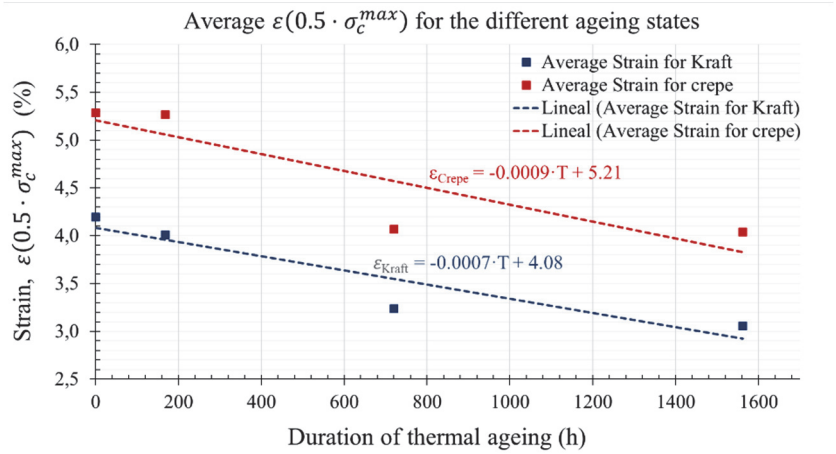

Figure 135. Average strain, $\varepsilon(0.5 \cdot \sigma_c^{max})$, with their trendlines for each material as a function of ageing duration.

Table 25. Equations of the trendlines $\varepsilon_c^{max}(T)$, depending on the ageing duration (T), and estimated values for the compressive strain at failure at the different ageing states.

Trendline	State 0	State I	State II	State III
$\varepsilon_{c,Kraft}^{max} = -7 \cdot 10^{-4}T + 4.08$	4.08 ± 0.71	3.96 ± 1.68	3.58 ± 0.92	2.99 ± 0.95
$\varepsilon_{c,Crepe}^{max} = -9 \cdot 10^{-4}T + 5.21$	5.21 ± 1.45	5.06 ± 1.43	4.56 ± 1.10	3.80 ± 0.92

Besides, the analysis of the results obtained from the compressive tests leads to the following conclusions:

- There is a great variability among the curves obtained for the same material in one particular orientation and ageing state; indeed, the average coefficient of variation for $\varepsilon(0.5 \cdot \sigma_c^{max})$ is around 27.8%. That variability is even higher than the one shown by the insulation materials in their characterisation in tension, see section *3.2.2.Tensile strength and its direct and indirect estimation*.

- Although there are some differences in the maximum compressive stress that a cylinder withstands, σ_c^{max}, see Figure 134 (a), the obtained values remain very similar for both insulation papers, in the different material orientations and ageing states, and is $\sigma_c^{max} \simeq 3\ MPa$.

- The average coefficient of variation of the maximum compressive stress, σ_c^{max}, is around 20 %, which is lower than the variation in the strain $\varepsilon(0.5 \cdot \sigma_c^{max})$.

- There is a moderate influence of the ageing level in the difference between $\sigma_{MD,c}^{max}$ and $\sigma_{CD,c}^{max}$ for one insulation material. The plain Kraft shows an average $\sigma_{MD,c}^{max} > \sigma_{CD,c}^{max}$ in Ageing State III and the same happens for the crepe paper in states II and III.

- The kind of mechanical failure observed in many of the cylindrical samples made of paper insulation after the compressive tests performed in the laboratory is buckling of one paper layer and a subsequent formation of wrinkles in the cylinder (see Figure 129 and Figure 132). That phenomenon was also observed after the bending tests over the insulated CTC samples described in section 1.3. However, the cylindrical samples did not show formation of cracks, something that was frequent in the insulated CTCs, especially when the insulation was heavily aged (see Figure 122). This can be explained

because the insulation of a real CTC is much more constrained due to the pretension imposed during manufacture, and that inhibits the free formation of wrinkles, and it can even be considered as a source for crack initiation. However, buckling and formation of wrinkles require less energy than crack-formation, so the results presented here for the maximum compressive stress withstood by the cylindrical samples and the corresponding strain are conservative ones.

1.2.4. In-plane shear mechanical properties of the dielectric paper

It is commonly accepted that mechanical failure of sheet materials is considerably affected by their shear properties. In fact, shear matrix cracking of a lamina is reported in [129] as a mode of failure itself, in which the shear stress, τ_{MD-CD}, or shear strain, γ_{MD-CD}, are critical for the breakdown of the material. The most popular interactive failure criteria for orthotropic materials subjected to the combined stresses are based on the Hill-type condition [140], and they include in-plane shear stress and strength.

However, the determination of the shear strength in paper materials is an open issue, as it is very difficult to generate a pure shear stress condition while testing thin structures, which involve stability problems, such as buckling. One possible method implies the torsion of a hollow cylinder, as described in [141], but it requires special equipment for applying a torsional moment that is not frequently available. Due to that difficulty in experimental measurement, the majority of studies propose to obtain the shear stress-strain curve from several approximations. For instance, [142] gives an expression for the shear strength of an anisotropic sheet based on a tensile test performed at any angle, ϕ, measured from the longitudinal direction of the material (MD). Other authors, such as [83], [85], [89], [101], [118], propose to infer the shear properties of paper from in-plane uniaxial tests at 45º to the MD, as that off-axis tensile test generates a biaxial stress state that is equivalent to a state of pure shear. However, in those tests, in-plane tensile and compressive stresses appear, and their contributions are difficult to separate from those produced by the shear stresses. Because of the lack of suitable standards for shear-testing and the variability in the mechanical properties of different paper materials, it is difficult to validate the published results.

In [140], an equation is proposed for obtaining the in-plane shear strength of paper, based on experimental results of tensile tests in different orientations from the MD (represented by a variable angle θ) for three types of paper. When a tensile stress, F_θ, is applied to a paper sample whose longitudinal direction is oriented at an angle θ to the MD, the stress components in the principal in-plane axes are:

$$\sigma_{MD} = F_\theta cos^2\theta \quad (109)$$

$$\sigma_{CD} = F_\theta sin^2\theta \quad (110)$$

$$\tau_{MD-CD} = F_\theta \sin\theta \cos\theta \quad (111)$$

The values of the strengths $\sigma_{MD}^{max}, \sigma_{CD}^{max}$ and τ_{MD-CD}^{max} were estimated in [140] by introducing the values of F_θ at failure into equations (109), (110) and (111), and they were plotted with respect to the angle θ for different types of paper. The result was that the estimated τ_{MD-CD}^{max} was maximum when θ was approximately equal to 35º to MD. Another analysis based on data from [143] showed that the dependence on the angle θ for the strain at breakage components $\varepsilon_{MD}^{max}, \varepsilon_{CD}^{max}$ and γ_{MD-CD}^{max}, also gave a maximum value of γ_{MD-CD}^{max} when $\theta \simeq 35º$. Therefore, the authors considered that this angle pronounced the shear stress component while reducing the effect of normal stress components.

In a subsequent paper of the same authors, [144], they designed an asymmetric four-point bending test for the estimation of the in-plane shear strength of the same three types of paper and compared the results with the ones estimated in [143]. It was impossible to avoid buckling of the thinner paper samples, so the strength obtained using that method was not considered as representative, but, with the thicker paper that did not buckle during the tests, the results were consistent with the ones based on tensile tests performed at 35º to MD. In [145], the same authors performed tensile tests with paper samples with two circular holes on their axial centreline and two slits cut asymmetrically to each other, which induced shear stresses in the region between the hole edges. The results of [145] showed a good correlation with the ones estimated in [143] for two of the tested materials (the sack paper and the copy paper). Consequently, it is considered here that tensile testing at 35º could give a first estimation of the shear strength of paper, as the use of other experimental methods for its measurement is not feasible.

Ten paper samples, with the same geometry used in [140], Figure 136 (a), were prepared for each insulation material (plain Kraft and crepe papers) and ageing state (States 0, I, II and III). The purpose of this geometry is to limit the major part of the deformation to the central area of the sample, whose length is 30 mm and whose width is 10 mm. Paper tape was used to avoid the indentation of the machine grips in the paper samples, Figure 136 (b), and then the samples were subjected to tensile forces up to fracture, Figure 136 (c), with a constant rate of elongation of 3.33 mm/min, to comply with the strain rate proposed in [137].

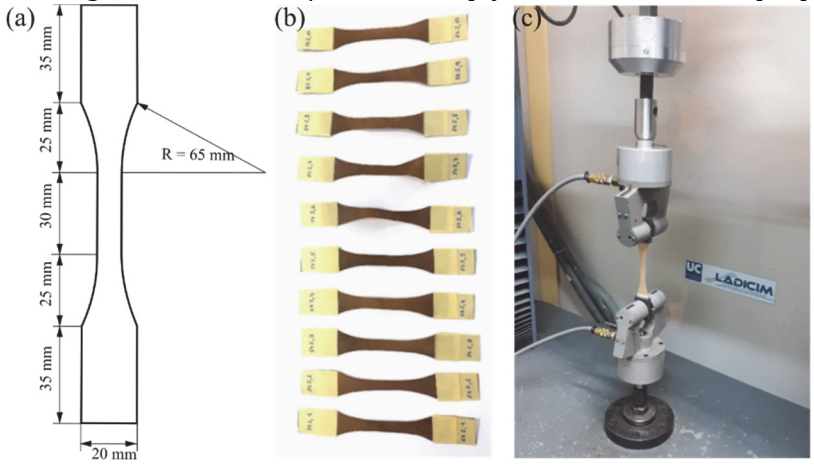

Figure 136. (a) Geometry of the paper samples; (b) Ten plain Kraft paper samples of Ageing State I; (c) Paper sample being subjected to a tensile test.

Figure 137 shows the results of the tensile tests at 35º from the MD over the plain Kraft insulation, as well as an average stress-strain curve ± the standard deviations. The shear strength of the material was estimated from the average tensile strain, $\sigma_{35^\circ}^{max}$, for the insulation material in a particular ageing state, and it was considered that $\varepsilon_{35^\circ}^{max} \simeq \varepsilon_{MD-CD}^{max}$. The same process was carried out in Figure 138 for the tensile tests at 35º from the MD over the crepe insulation. In this case, the shape of the stress-strain curves for both types of paper was not so distinct as in the tensile tests in MD, and both of them showed a sudden failure mechanism, but there are also differences in the tensile strength, $\sigma_{35^\circ}^{max}$, and the strain at breakage, $\varepsilon_{35^\circ}^{max}$. The tensile strength of the plain Kraft paper remained between 31-33% higher than the one of the crepe paper, up to Ageing State III, where the crepe paper was considerably more deteriorated and its $\sigma_{35^\circ}^{max}$ was 2.3 times lower. On the contrary, the strain at breakage, $\varepsilon_{35^\circ}^{max}$, was more than 5 times higher for the crepe insulation when the material was not aged, but the ratio between them reduced to around 1.4 times in Ageing State III. That means that, when the crepe insulation is deeply aged its mechanical performance is not much better than the one of the plain Kraft.

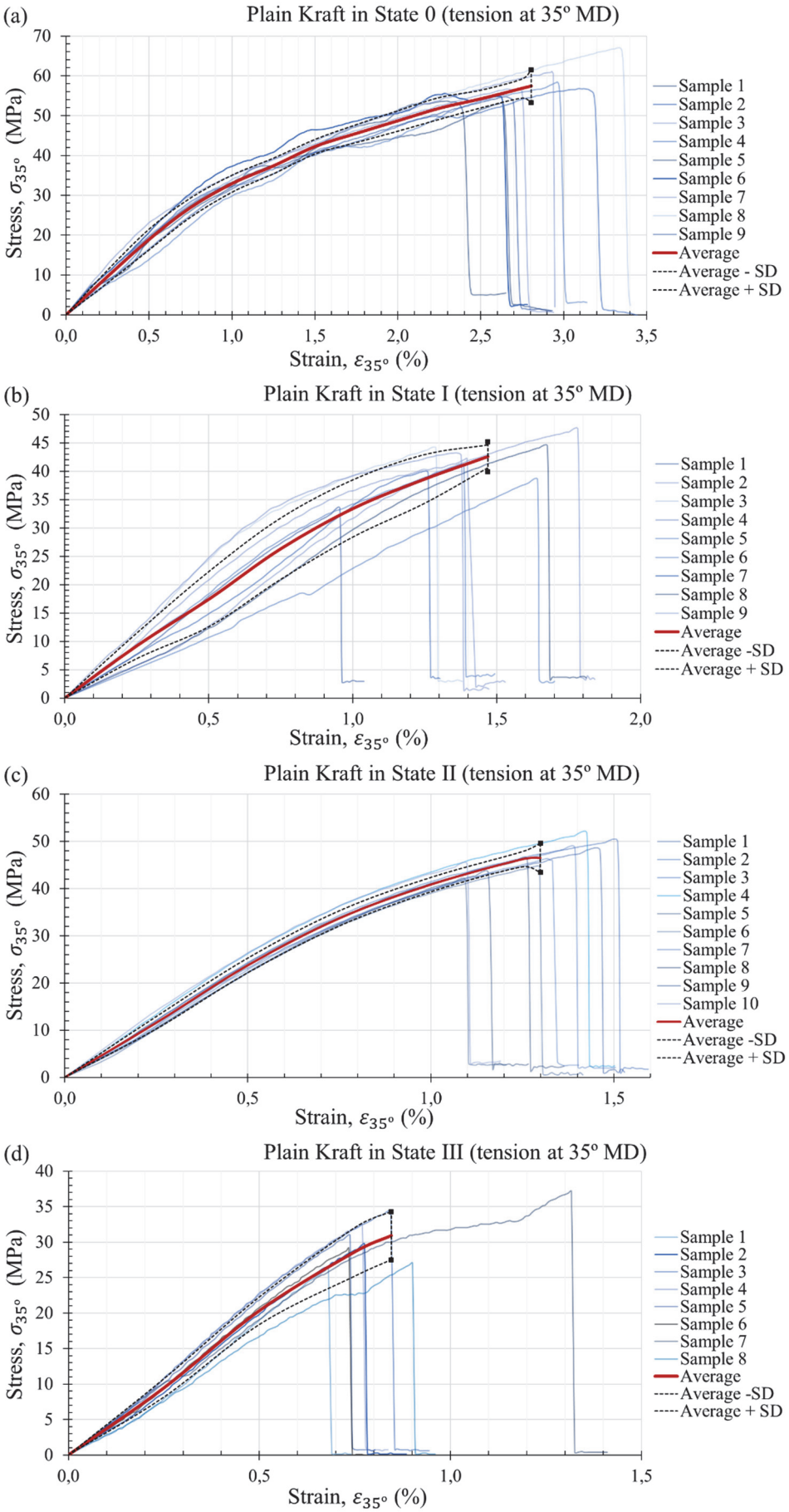

Figure 137. Tensile test at 35° MD for the plain Kraft paper in ageing states (a) 0, (b) I, (c) II and (d) III.

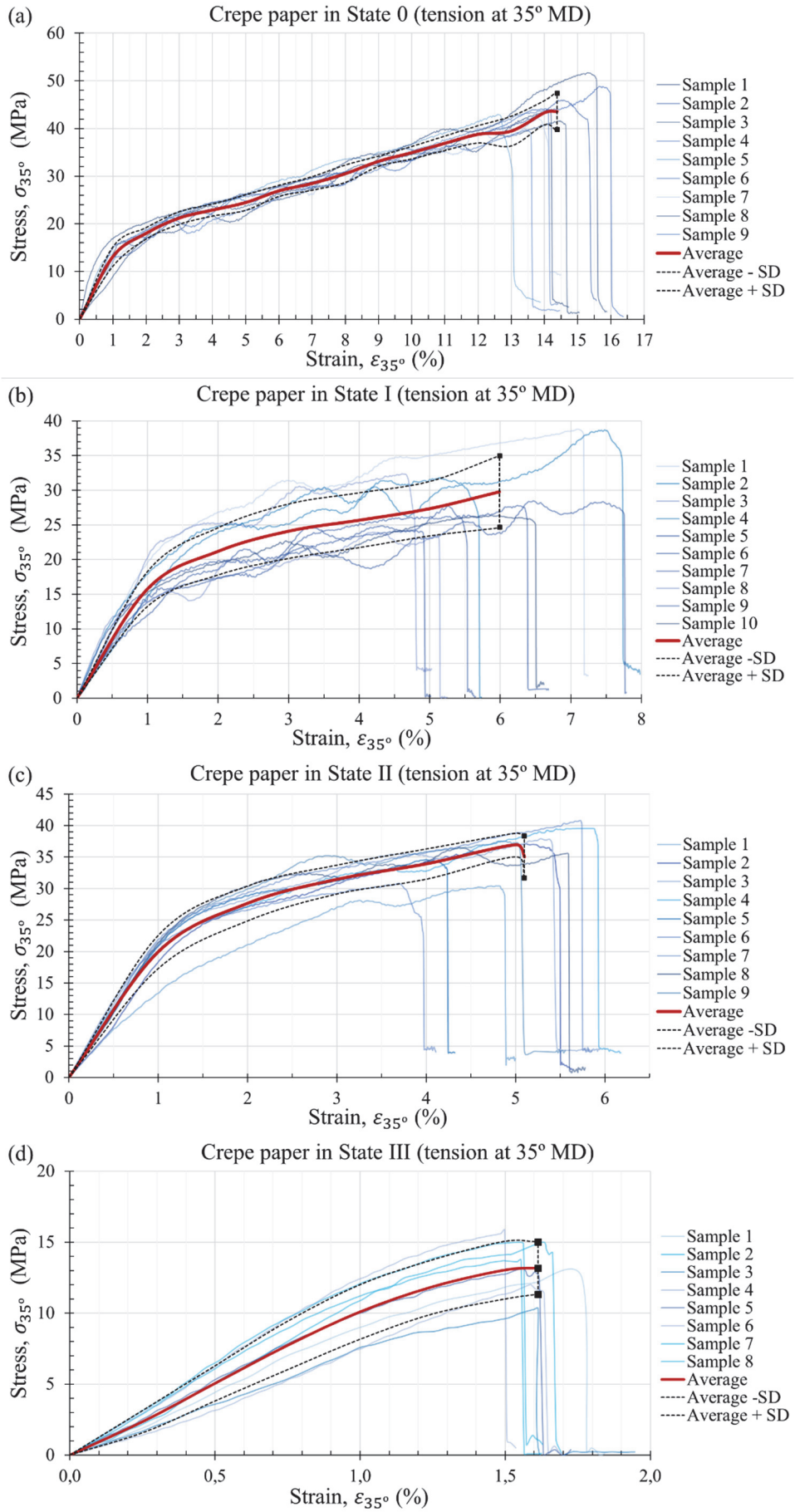

Figure 138. Tensile test at 35° MD for the crepe paper in ageing states (a) 0, (b) I, (c) II and (d) III.

- **Conclusions**

Table 26 summarises the results of tensile tests at 35º of MD for both insulation materials and ageing states (0-III). The variation in the estimated shear strain at breakage, $\varepsilon_{MD-CD}^{max}$, is shown in Figure 139.

Table 26. Results of the tensile tests at 35º of MD for the plain Kraft and the crepe papers in different ageing states.

Ageing state	State 0 (Not aged)	
	Plain Kraft paper	Crepe paper
Tensile strength, $\sigma_{35^o}^{max}$ (MPa)	57.4 ± 4.2	43.6 ± 4.2
$\varepsilon_{35^o}^{max} \simeq \varepsilon_{MD-CD}^{max}$ (%)	2.80 ± 0.29	14.38 ± 0.96
Ageing state	State I (Aged for a week at 150°C)	
	Plain Kraft paper	Crepe paper
Tensile strength, $\sigma_{35^o}^{max}$ (MPa)	42.6 ± 2.0	29.8 ± 5.2
$\varepsilon_{35^o}^{max} \simeq \varepsilon_{MD-CD}^{max}$ (%)	1.47 ± 0.26	5.99 ± 1.09
Ageing state	State II (Aged for four weeks at 150°C)	
	Plain Kraft paper	Crepe paper
Tensile strength, $\sigma_{35^o}^{max}$ (MPa)	46.5 ± 3.1	35.0 ± 3.3
$\varepsilon_{35^o}^{max} \simeq \varepsilon_{MD-CD}^{max}$ (%)	1.30 ± 0.15	5.10 ± 0.73
Ageing state	State III (Aged for nine weeks at 150°C)	
	Plain Kraft paper	Crepe paper
Tensile strength, $\sigma_{35^o}^{max}$ (MPa)	30.9 ± 3.4	13.18 ± 1.85
$\varepsilon_{35^o}^{max} \simeq \varepsilon_{MD-CD}^{max}$ (%)	0.84 ± 0.20	1.61 ± 0.08

In conclusion, the shear strain at breakage was indirectly estimated following [140] for two different dielectric papers (plain Kraft and crepe paper) under different ageing states and the results showed that:

- The estimated shear strain at breakage, $\varepsilon_{MD-CD}^{max}$, of the non-aged paper insulation (in State 0) is more than 5 times higher for the crepe paper than for the plain Kraft paper.

- The reduction of the estimated shear strain at breakage, $\varepsilon_{MD-CD}^{max}$, after one week of ageing was the most accused of the whole ageing duration. That decrease was more accused for the crepe paper (58.3% between State 0 and State I) than for the plain Kraft paper (47.5%).

- Between Ageing State I and Ageing State III, the reduction of the estimated shear strain at breakage, $\varepsilon_{MD-CD}^{max}$, was almost linear. After nine weeks of ageing, the estimated $\varepsilon_{MD-CD}^{max}$ for the crepe paper had reduced approximately 88.8% with respect to the initial value and the decrease was around 70% for the plain Kraft.

- As happened with the tensile properties (see section *1.2.2.Tensile mechanical properties of the dielectric paper in the MD and in the CD*), although the initial mechanical performance of the crepe insulation was superior, that material was also

more affected by the ageing process. At the end of Ageing State III, the mechanical response of both materials was similar.

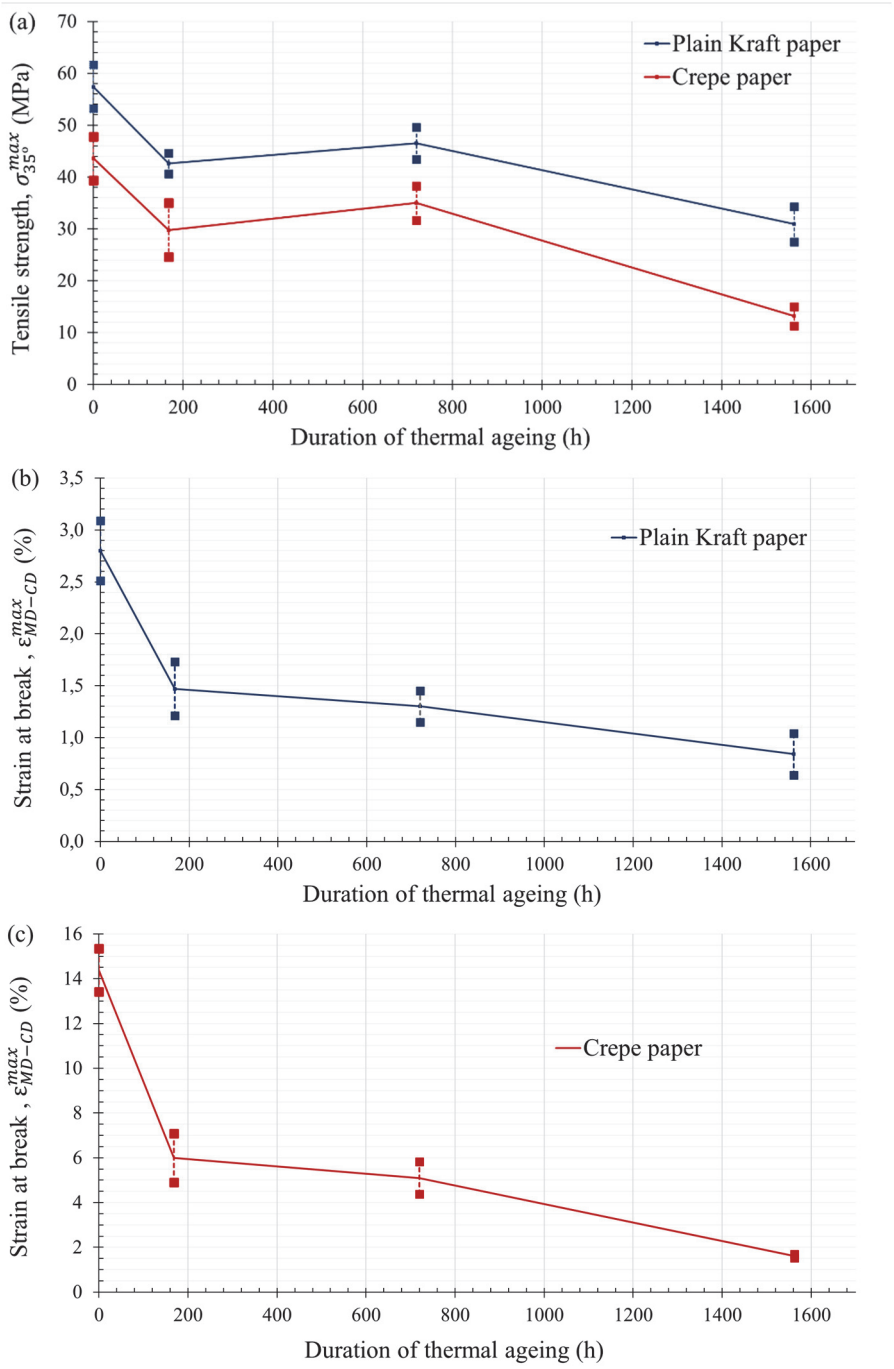

Figure 139. (a) Tensile strength $\sigma_{35°}^{max}$ for both materials and estimated shear strain at breakage, $\varepsilon_{MD-CD}^{max}$, (b) for the plain Kraft and (c) for the crepe paper as a function of ageing duration.

1.3. Three-point bending tests of the insulated CTCs

The studied CTC was made of enamelled annealed copper and covered in four layers of dielectric paper, as seen in Figure 140, where the cylindrical coordinate system of a coil, (r, φ, z), is also represented.

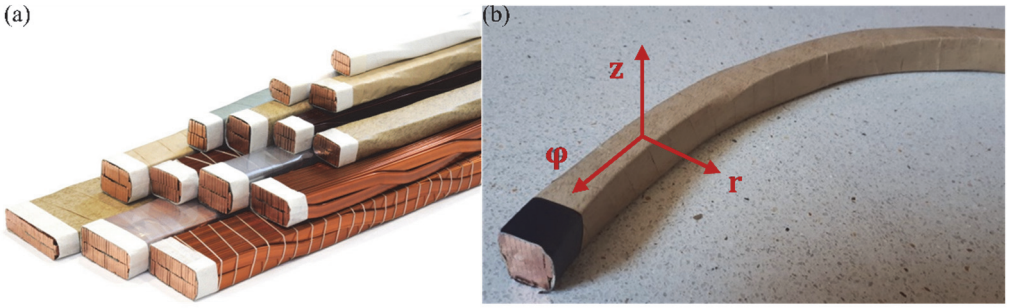

Figure 140. (a) Continuously Transposed Conductors (CTC); (b) Cylindrical coordinate system and main directions of the CTC.

One of the most extreme mechanical solicitations that can affect a power transformer during operation and even result in its end-of-life is a short circuit, see section *4.Short-circuit currents, electromagnetic forces and mechanical stresses in power transformers* in *II.*STATE OF THE ART. Short circuits produce a transient temperature rise in the windings that does not usually represent a serious problem, but the generated electromagnetic forces can be about 100-400 times the forces under normal operating conditions [14]. The force density vector is the product of the current density vector and the magnetic flux density, see equation (112), where $\overline{I(t)}$ is the current vector, $\overline{B(t)}$ is the leakage flux vector and L is the winding length.

$$\overline{f(t)} = \overline{J(t)} \times \overline{B(t)} = L \cdot \overline{I(t)} \times \overline{B(t)} = L \cdot \begin{pmatrix} I_\varphi(t) \cdot B_z(t) \\ 0 \\ -I_\varphi(t) \cdot B_z(t) \end{pmatrix} = \begin{pmatrix} f_r(t) \\ f_\varphi(t) \\ f_z(t) \end{pmatrix} \quad (112)$$

That force has only two components in the cylindrical coordinate system of a core-type transformer with disc-type windings: the radial, $f_r(t)$, and the axial one, $f_z(t)$. The most critical component of that force vector is $f_r(t)$, because the bending stiffness of a CTC is much lower in radial than in axial direction. Because of that, and also for the sake of simplicity, the electromagnetic short-circuit force acting on the windings of the transformer considered in this work was purely radial. It is also known that real short-circuit forces are dynamic, with a sudden initial peak of short duration, which is considerably reduced with the number of cycles. Although we are aware that the mechanical response to dynamic forces differs from the response to static ones, both the experimental tests in the laboratory and the simulation were carried out considering a static force, for the purpose of simplicity. It could be interesting to perform a dynamic analysis in the future.

Figure 141. Three-point bending test of copper samples.

Several insulated CTC samples of each of the ageing states (fifteen test conductor-pieces in total) were subjected to three-point bending tests under displacement control in the laboratory, measuring the force-displacement curve up to a certain deflection, Figure 141. After the bending with different final deflections (d), which could be reasonably produced by severe short-circuit forces, according to experimental results reported in [14], the wrapped paper was visually analysed in order to determine in which layers fracture occurred or not, as well as to characterise the magnitude of those fractures, which were classified in section *1.3.4.Conclusions after the bending tests* into: no cracks, small cracks (< 5 mm), medium cracks (5-10 mm), big cracks (> 10 mm), and total fracture (paper so deteriorated that it does not accomplish any insulating purpose).

1.3.1. Results of bending tests with a deflection of 20 mm

The external aspect of a CTC sample after being subjected to a bending test with deflection d = 20 mm is shown in Figure 142, in this case for Ageing State 0. The cylindrical coordinate system of a coil is also shown, (r, φ, z), as well as the main directions in the paper material, (MD, CD).

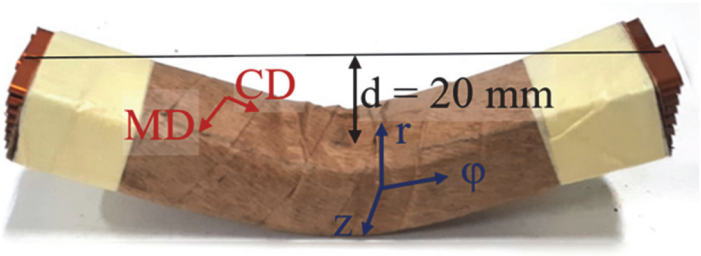

Figure 142. CTC sample after a bending test with d = 20 mm.

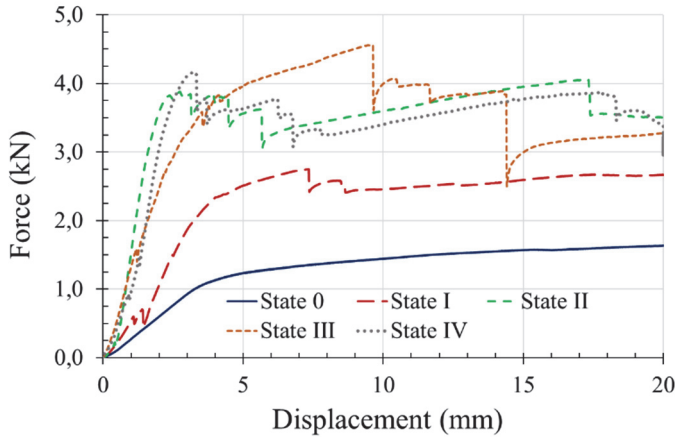

Figure 143. Force - displacement curves for d = 20 mm and different ageing states.

The real geometry of the copper CTC, which consisted of enamelled copper strands made into an assembly with a transposed strand, was the cause of the considerable differences among the force–displacement curves for the different CTC samples, such as the ones shown in Figure 143. Firstly, the response of the non-aged CTC samples considerably differed from the one of the aged samples, in which the melted enamel initially bonded adjacent strands and made the assembly more rigid, but that bonding between some strands broke after a certain deformation, and they started to slide. On the contrary, in the non-aged samples, the sliding was possible since the beginning of the test. Secondly, as the position of the transposed strand was not exactly the same in all the CTC samples, their response to the bending test was different, and the way in which the strands slid on each other also differed.

The consequence was that the vertical force needed to produce a deflection of 20 mm in the conductor was highly variable. For instance, in these tests, the force was between 1.6 kN (in State 0) and 4.6 kN. These results confirmed that the behaviour of a real CTC cannot be accurately described by the simplification of a rectangular cross-section with the same outer dimensions, as it had been previously suggested by [115], and the consideration of the individual copper strands in the mechanical model is essential.

In the bending test for Ageing State 0 and d = 20 mm, no major irregularities in the force-displacement curve were noticed, Figure 143, because the copper strands were not glued by the enamel melting. The bending test of that insulated CTC sample did not produce facture of the insulation in any of the paper layers, where only some wrinkles appeared, as seen in Figure 144 (a). In the bending test for Ageing State I and d = 20 mm, the mentioned breaking of the enamel bonding happened at the beginning of the test, with a displacement of only 1-2 mm, and more markedly with a displacement of 7-8 mm, see Figure 143. In this case, fracture did not happen in the crepe paper (layers 3 and 4), Figure 144 (b). However, after only one week of ageing at 150°C, some medium sized cracks appeared in layer 2, while the cracks in layer 1 were considerably larger, see Figure 144 (c). This marked deterioration of layer 1 was caused by the already mentioned melting of the enamel, which glued the insulation to the adjacent copper strands. It can be then inferred that the cracks are always going to appear first in layer 1 when this type of commercial CTC is subjected to extreme ageing.

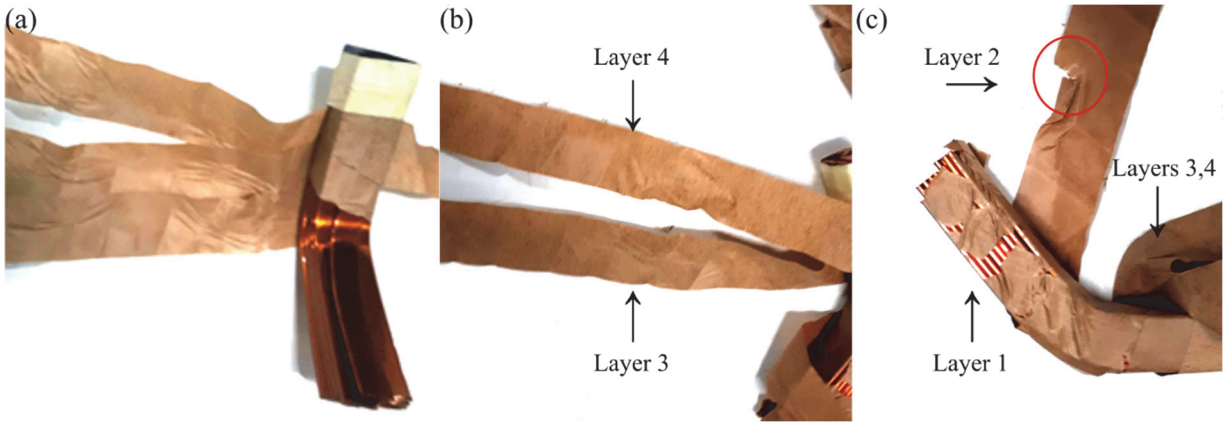

Figure 144. (a) Insulation layers of the sample in Ageing State 0 and d = 20 mm; (b) Insulation layers 3 and 4, and (c) layers 1 and 2 of the sample in Ageing State I and d = 20 mm.

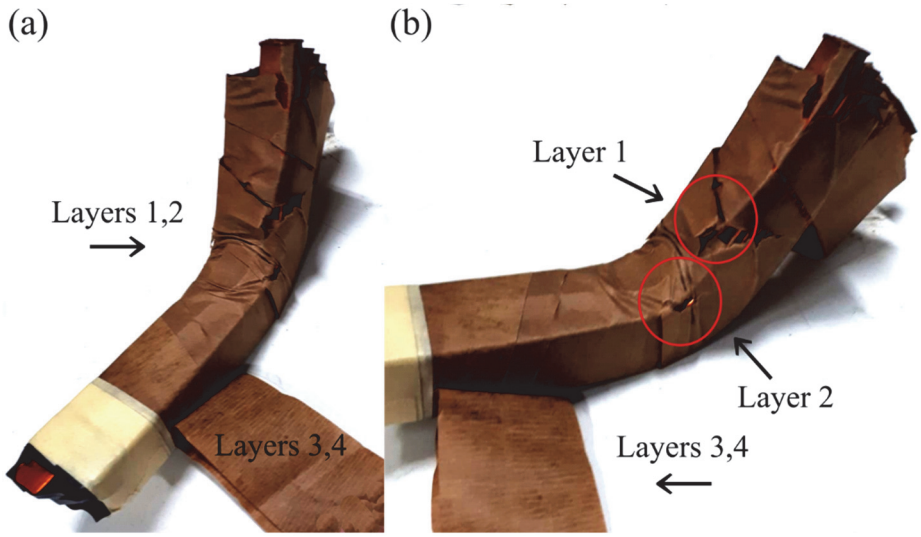

Figure 145. Insulation layers of the sample in Ageing State II and d = 20 mm.

In the bending test for Ageing State II and d = 20 mm, the breaking of the bonding among copper strands happened repeatedly at different deformation levels, see Figure 143. In Ageing State II, cracks did not appear in layers 3 and 4, but the fracture of layer 2 was more evident than in State I and the cracks can be classified as big (larger than 10 mm), Figure 145. That shows that the resistance of layer 2 considerably diminished between states I and II, after four weeks at 150°C. In this case, the cracks in layer 1 were of the same order of magnitude than in the previous ageing state.

In the bending test for Ageing State III and d = 20 mm the characteristic breaking of the bonding among copper strands can also be appreciated, see Figure 143. In this case, the first small cracks (of about 2-3 mm) appeared in layers 3 and 4, see Figure 146, indicating that the fracture had just started in these external layers for this ageing state and deformation. Furthermore, Figure 147 shows that the cracks were very large in layers 2 and 1, which can be considered as almost completely broken.

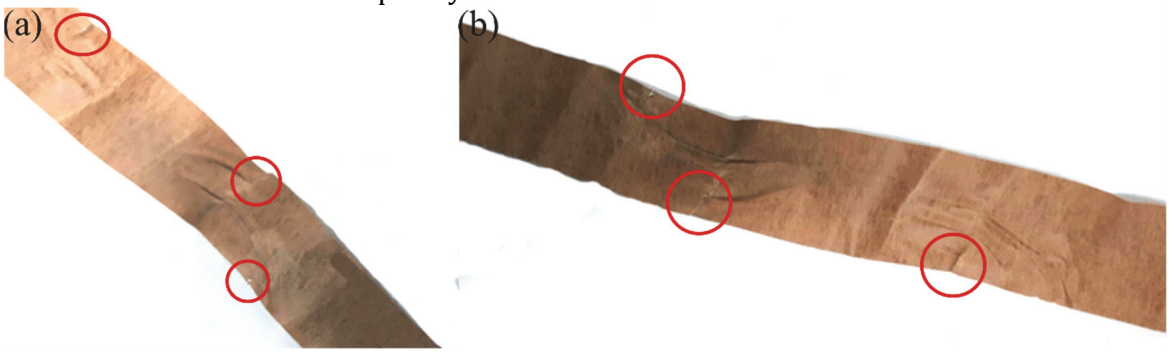

Figure 146. (a) Insulation layer 4 and (b) insulation layer 3 of the sample in Ageing State III and d = 20 mm.

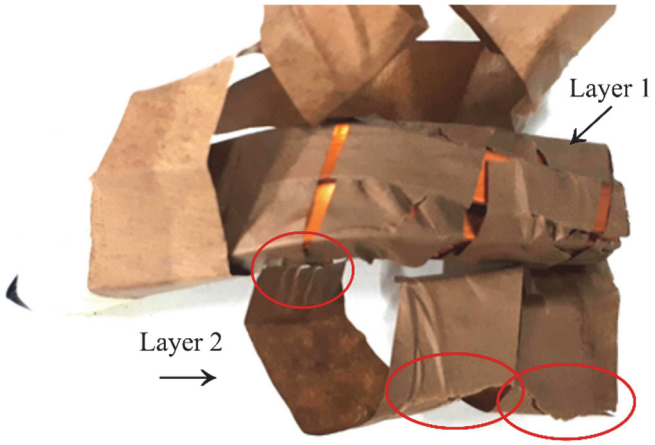

Figure 147. Insulation layers 1 and 2 of the sample in Ageing State III and d = 20 mm.

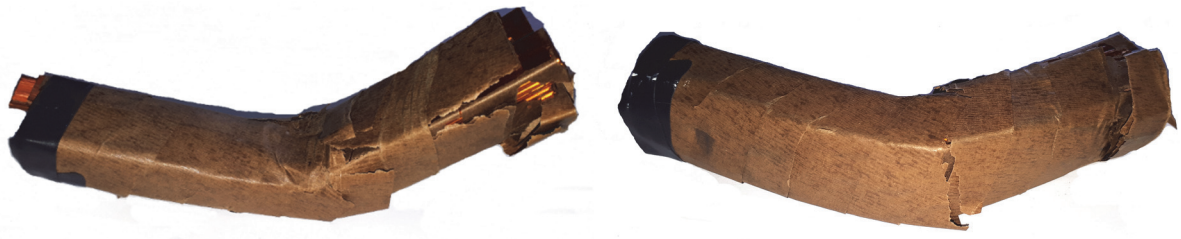

Figure 148. CTC sample after a bending test with d = 20 mm in Ageing State IV.

The external aspect of the CTC samples for Ageing State IV and d = 20 mm can be seen in Figure 148. In this situation, the cracks in the two external layers (3 and 4) were big (> 10 mm), as seen in Figure 149 and Figure 150. Moreover, the plain Kraft was totally broken into pieces, see Figure 151 and Figure 152, specially in layer 1. It is worth noting that the material

in the inner layers was more damaged in the areas of the CTC sample subjected to compression, where the embrittled paper could not resist the wrinkling. Moreover, the higher deformations suffered near the transposed strand were another cause for the fracture growth in the plain Kraft paper.

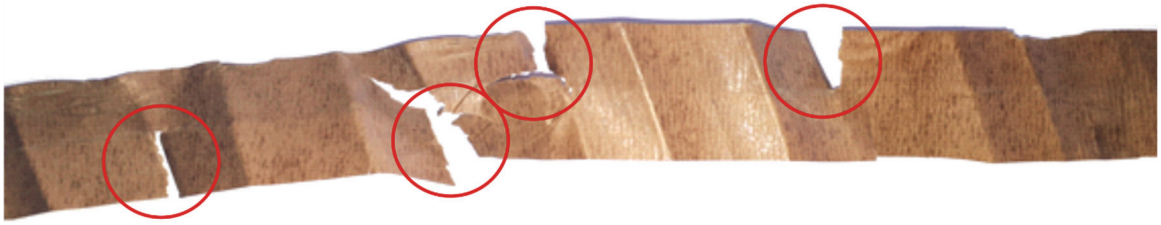

Figure 149. Insulation layer 4 of the sample in Ageing State IV and d = 20 mm.

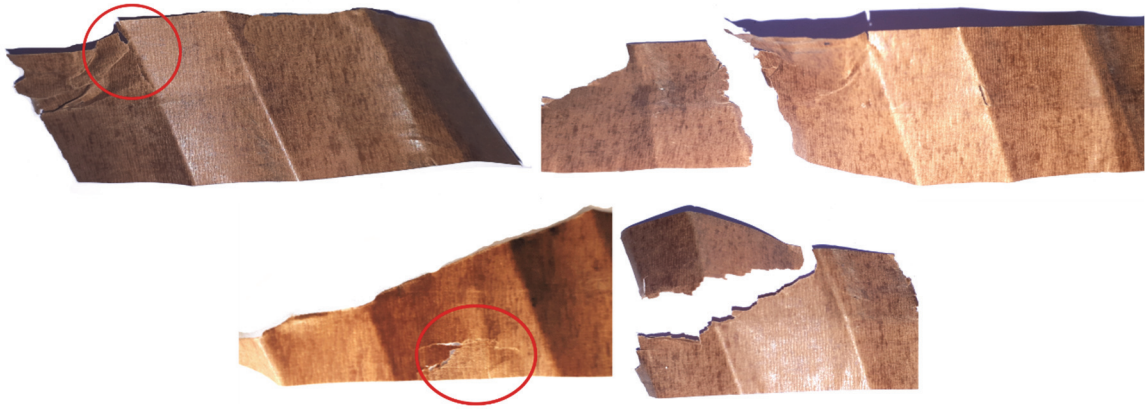

Figure 150. Insulation layer 3 of the sample in Ageing State IV and d = 20 mm.

Figure 151. Insulation layer 2 of the sample in Ageing State IV and d = 20 mm.

Figure 152. Insulation layer 1 of the sample in Ageing State IV and d = 20 mm.

1.3.2. Results of bending tests with a deflection of 10 mm

As Ageing State III and d = 20 mm seemed to be the limit at which fracture of layers 3 and 4 started, it was of interest to determine the lower limit for the initiation of fracture in layers 1 and 2. Because of that, after the performance of the previous bending tests, some tests were performed with a final deflection of 10 mm. The peak forces withstood by the CTC samples were between 3.3 kN and 4.2 kN, and the mentioned sliding among copper strands also happened repeatedly, as seen in Figure 153.

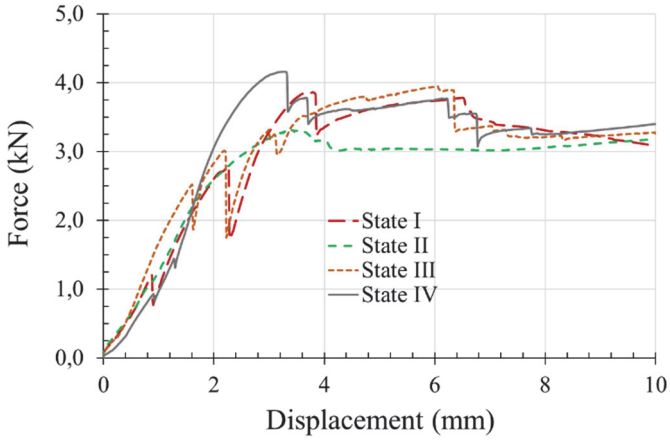

Figure 153. Force - displacement curves for d = 10 mm and different ageing states.

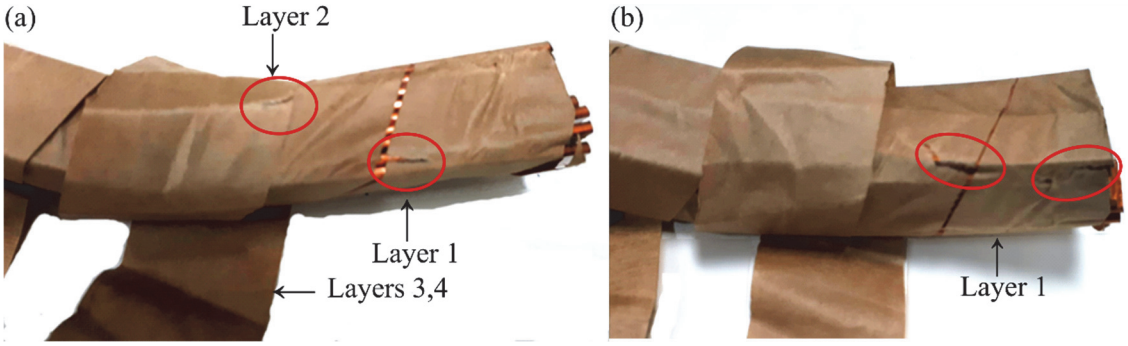

Figure 154. (a) Insulation layers 1 and 2, and (b) Insulation layer 1 of the sample in Ageing State I and d = 10 mm.

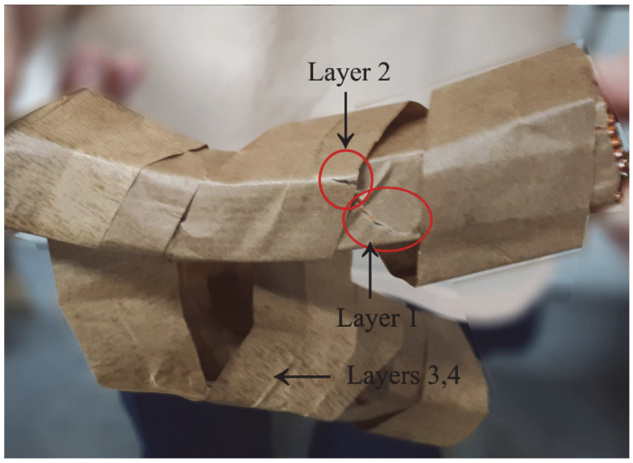

Figure 155. Insulation layers 1 and 2 of the sample in Ageing State II and d = 10 mm.

In Ageing State I, the bending tests with d = 10 mm did not produce fractures in layers 3 and 4, as expected. A few small cracks appeared in layer 2, of about 5 mm, such as the one shown in Figure 154 (a). The visible fractures in layer 1 were big, some of them larger than 10 mm, Figure 154 (b). Although both the cracks in layers 1 and 2 and State I were smaller

with this deflection than when d = 20 mm, a deflection of 10 mm was enough to initiate fracture in the plain Kraft paper in this ageing state. In Ageing State II and with d = 10 mm, the crepe paper was not damaged, as expected. The cracks which appeared in layers 2 and 1 were of similar sizes that in the test for Ageing State I and the same deflection, Figure 155 and Figure 156.

Figure 156. Insulation layer 1 of the sample in Ageing State II and d = 10 mm.

A deflection of 10 mm was not enough to initiate fracture of the crepe paper in Ageing State III, after 9 weeks at 150°C. It can be inferred then that a deflection in the CTC higher than 10, and probably closer to 20 mm, is necessary to start fracture in the crepe paper. The cracks in layer 2 were larger in this case, in comparison with Ageing State II, and can be classified as big (larger than 10 mm) as seen in Figure 157. Layer 1 was totally fractured, see Figure 158. However, the size of the cracks in this case was slightly lower than in the test with the same ageing state and d = 20 mm.

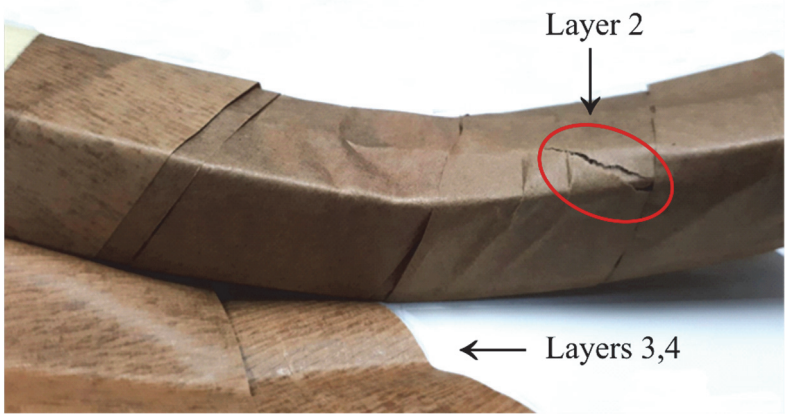

Figure 157. Insulation layers of the sample in Ageing State III and d = 10 mm.

Figure 158. Insulation layer 1 of the sample with Ageing State III and d = 10 mm.

The external appearance of the CTC sample in Ageing State IV and after the bending tests with d = 10 mm can be seen in Figure 159. After these tests, the fractures in the crepe paper were of medium size (between 5-10 mm), see Figure 160 and Figure 161, and mainly localised in the edges of the CTC sample, perpendicular to the wrapping direction of the paper around the copper conductor. Some big cracks appeared in layer 2, Figure 162, and layer 1 suffered total fracture, Figure 163, although in this case the cracks were smaller than in the tests with d = 20 mm.

Figure 159. CTC sample after a bending test with d = 10 mm in Ageing State IV.

Figure 160. Insulation layer 4 of the sample in Ageing State IV and d = 10 mm.

Figure 161. Insulation layer 3 of the sample in Ageing State IV and d = 10 mm.

Figure 162. Insulation layer 2 of the sample in Ageing State IV and d = 10 mm.

Figure 163. Insulation layer 1 of the sample in Ageing State IV and d = 10 mm.

1.3.3. Results of bending tests with a deflection of 5 mm

Some bending tests were performed with d = 5 mm, in order to determine the deflection level at which the first cracks appear in the inner layers of plain Kraft paper. In these bending tests, the sliding among copper strands was less relevant than in the previous cases, but also appeared in ageing state II and IV, as seen in Figure 164. The maximum forces that the CTC samples withstood to get that final deflection were between 2.9 kN and 3.8 kN.

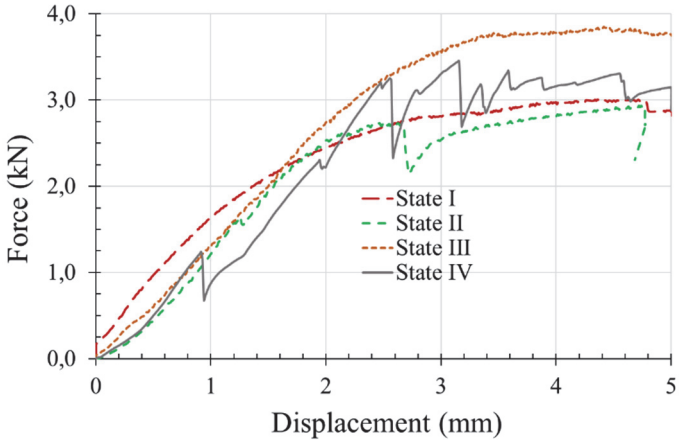

Figure 164. Force - displacement curves for a deflection of 5 mm and different ageing states.

In Ageing State I and with d = 5 mm, factures did not appear in layers 2, 3 and 4, see Figure 165 (a). However, a deflection of 5 mm was enough to initiate fracture in the plain Kraft paper in layer 1. There were only a few small cracks (smaller than 5 mm) in the innermost layer, which can be seen in Figure 165 (b). Analogously, fractures did not appear in layers 2, 3 and 4 in Ageing State II with d = 5 mm, see Figure 166 (a). As expected, a few cracks appeared in layer 1, but their size was not significantly larger than in Ageing State I, see Figure 166 (b).

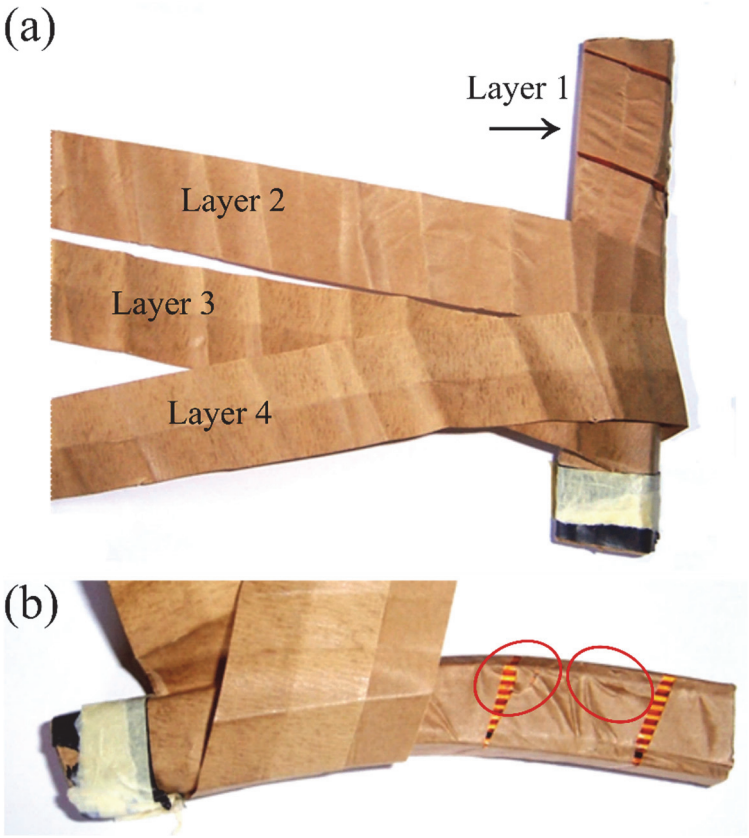

Figure 165. (a) Insulation layers and (b) insulation layer 1 of the sample in Ageing State I and d = 5 mm.

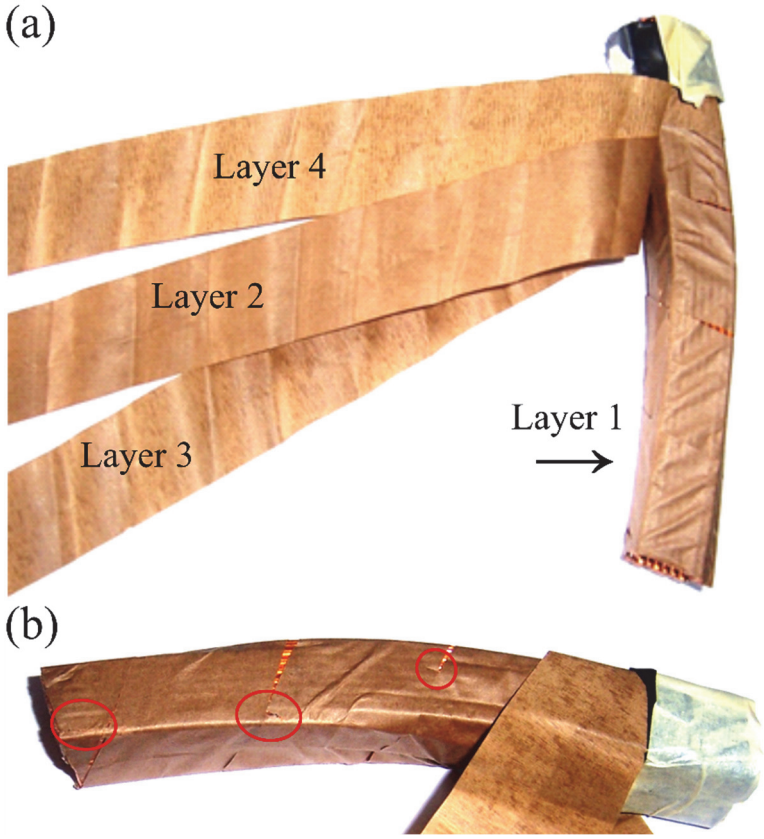

Figure 166. (a) Insulation layers and (b) insulation layer 1 of the sample in Ageing State II and d = 5 mm.

In Ageing State III with d = 5 mm, cracks did not appear in layer 2, 3 and 4, see Figure 167. The cracks in layer 1 were slightly larger than in the previous ageing states, see Figure 168, and can be classified as medium size (between 5 and 10 mm).

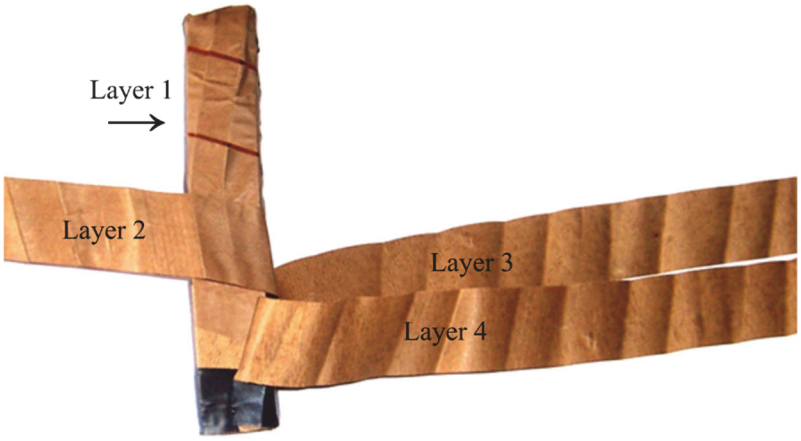

Figure 167. Insulation layers of the sample in Ageing State III and d = 5 mm.

Figure 168. Insulation layer 1 of the sample in Ageing State III and d = 5 mm.

Figure 169. CTC sample after a bending test with final d = 5 mm in Ageing State IV.

Finally, the aspect of the CTC samples after the bending tests with d = 5 mm in Ageing State IV can be seen in Figure 169. The external layer, made of crepe paper, was not damaged

in the areas of the sample subjected to tension, but the wrinkle formation in the compressed areas produced very small cracks, of around 2-3 mm in layer 4, Figure 170. Some small cracks also appeared in layer 3, Figure 171. However, after 28 weeks of ageing at 150°C, a deflection of 5 mm was enough to produce big fractures in the inner layers (1 and 2), Figure 172 and Figure 173. In this case, most of the cracks in layer 1 also appeared near the transposed strand.

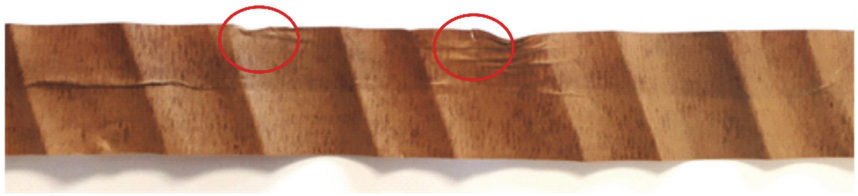

Figure 170. Insulation layer 4 of the sample in Ageing State IV and d = 5 mm.

Figure 171. Insulation layer 3 of the sample in Ageing State IV and d = 5 mm.

Figure 172. Insulation layer 2 of the sample in Ageing State IV and d = 5 mm.

Figure 173. Insulation layer 1 of the sample in Ageing State IV and d = 5 mm.

1.3.4. Conclusions after the bending tests

The results of all the three-point bending tests carried out with the aged insulated CTC samples (Ageing States I, II, III and IV) are summarised in Figure 174, where an average force – displacement curve, together with the standard deviation (SD) of the results, are also pictured. The response to these bending tests showed that both the cellulosic materials, the plain Kraft and crepe papers, are very resistant and can withstand substantially high deformations of the copper CTC without breaking when they are not aged. The effect of the thermal ageing in the mechanical response of the oil-impregnated paper was of radical

relevance. After only a week of ageing (Ageing State I), layer 1 was fractured for every deflection of the CTC sample higher than 5 mm, and cracks appeared in layer 2 for any deflection higher than 10 mm.

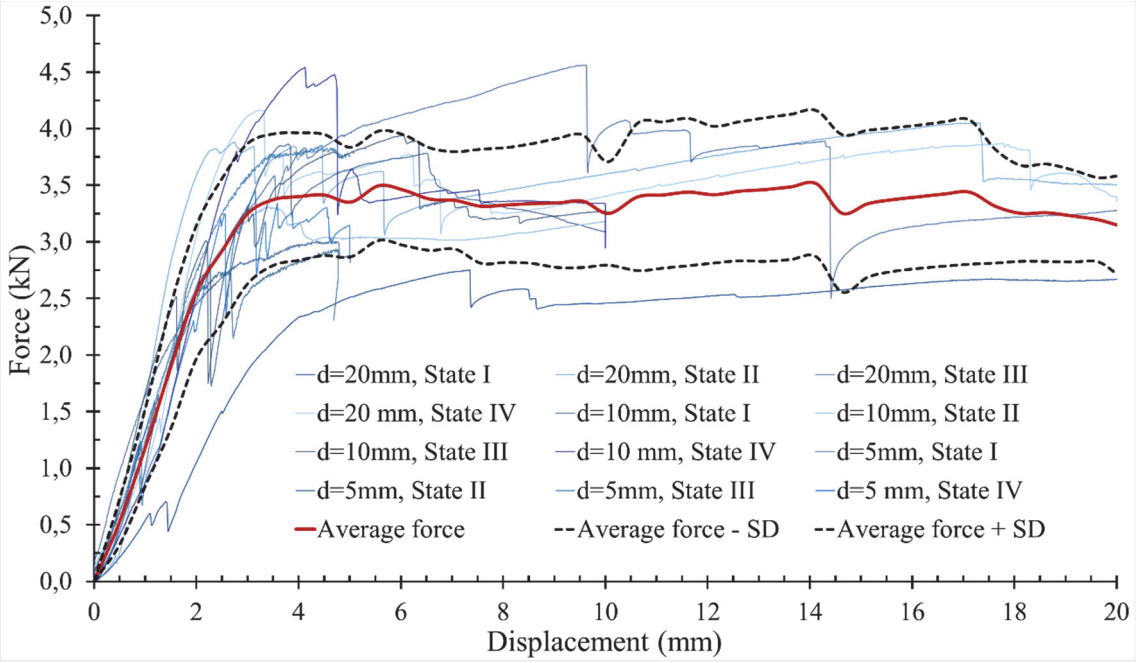

Figure 174. Force-displacement curves for different deflections and different ageing states.

The difference between two and four weeks of ageing (Ageing States I and II) was not very marked, except in the bending test with d = 20 mm, where the fracture of the plain Kraft paper was more accused. However, the effects of thermal ageing markedly augmented with an increase in ageing duration, and after nine weeks of ageing at 150°C (Ageing State III), d = 5 mm was enough to produce relevant cracks in the most inner layer, d = 10 mm produced big cracks in the two inner layers, and d = 20 mm started the fracture in the two external layers, made of crepe paper. After maintaining a temperature of 150°C for 28 weeks, in Ageing State IV, both materials were in a very bad condition. Any deflection of the CTC higher than 5 mm produced big fractures in the plain Kraft paper and small cracks in the crepe paper, which grew with the increase in the deflection. The results of all the tests are summarised in Table 27.

Some conclusions can be drawn after the analysis of the results of the bending tests over the insulated CTC samples:

- Failure in the paper insulation of this commercial CTC is always going to start in the innermost layer, which is in contact with the copper strands. If the enamel melts, the insulation becomes glued to the copper core and breaks due to big deformations of the strands or due to the slidings between them.

- In the innermost layer, a common source for crack initiation is the presence of the transposed conductor, which suffers higher deformations than other parts of the CTC.

- In layers 2, 3 and 4, some cracks appeared due to stress concentrations in local defects. Another source of stress concentrations was the wrapping of the paper around the copper CTC. Many cracks were initiated in that direction, which coincides with an angle of 70º clockwise from the MD, because the pretension imposed on the paper material during manufacturing impedes the free deformation of the insulation. The kind of

failure in areas of the CTC samples subjected to tension is the sudden onset of cracks, such as the ones shown by the paper samples tested in section *1.2.2.Tensile mechanical properties of the dielectric paper in the MD and in the CD.*

- When the paper is heavily aged, areas subjected to compression are more critical for crack initiation and growth than areas subjected to tension. When the deformation of the conductor is not very high, the first defects that appear in areas subjected to compression are wrinkles and local buckling, very similar to the ones observed in the characterisation described in section *1.2.3.Edgewise mechanical compressive properties of the dielectric paper*, see Figure 144 and Figure 169. However, when the CTC deformation increases, the paper insulation cannot continue buckling as happened in the cylindrical samples tested in *1.3.Three-point bending tests of the insulated CTCs*, because it is constrained due to its wrapping around the copper conductor, and that produces a change in the failure mode, being the source of cracks in areas subjected to compression in the fragile aged paper. That can be clearly seen in Figure 145.

- A very high temperature and duration of the ageing is needed for the cracks to grow, in order to consider that the insulation reaches its end of life.

- Crepe paper has a much better response to ageing and big deformations of the CTCs than the plain Kraft paper. However, if the thermal ageing is very extreme, the final condition of the crepe paper is similar to the one of the plain Kraft.

Table 27. Summary of the results of bending tests and fracture sizes in the paper insulation.

		Layer	DP	Deflection 20 mm	Deflection 10 mm	Deflection 5 mm
AGEING STATE 0	Plain Kraft	1	745.1	*No cracks*	*No cracks*	*No cracks*
		2				
	Crepe	3	870.4			
		4				
AGEING STATE I	Plain Kraft	1	600.9	*Big cracks (> 10 mm)*	*Big cracks (> 10 mm)*	*Small cracks (< 5mm)*
		2	660.1	*Medium cracks (5-10mm)*	*Small cracks (< 5mm)*	*No cracks*
	Crepe	3	713.9	*No cracks*	*No cracks*	*No cracks*
		4	750.0	*No cracks*	*No cracks*	*No cracks*
AGEING STATE II	Plain Kraft	1	467.9	*Big cracks (> 10 mm)*	*Big cracks (> 10 mm)*	*Small cracks (< 5mm)*
		2	542.7	*Big cracks (> 10 mm)*	*Small cracks (< 5mm)*	*No cracks*
	Crepe	3	627.2	*No cracks*	*No cracks*	*No cracks*
		4	652.2	*No cracks*	*No cracks*	*No cracks*
AGEING STATE III	Plain Kraft	1	252.9	*Total fracture*	*Total fracture*	*Medium cracks (5-10mm)*
		2	320.2	*Total fracture*	*Big cracks (> 10 mm)*	*No cracks*
	Crepe	3	482.8	*Small cracks (< 5mm)*	*No cracks*	*No cracks*
		4	525.0	*Small cracks (< 5mm)*	*No cracks*	*No cracks*
AGEING STATE IV	Plain Kraft	1	111.4	*Total fracture*	*Total fracture*	*Big cracks (> 10 mm)*
		2	207.5	*Total fracture*	*Big cracks (> 10 mm)*	*Big cracks (> 10 mm)*
	Crepe	3	342.8	*Big cracks (> 10 mm)*	*Medium cracks (5-10mm)*	*Small cracks (< 5mm)*
		4	397.1	*Big cracks (> 10 mm)*	*Medium cracks (5-10mm)*	*Small cracks (< 5mm)*

1.4. Analysis of the microstructure and fracture patterns in the paper insulation with Scanning Electron Microscope

1.4.1. Functioning principle of the Scanning Electron Microscope

The Scanning Electron Microscope (SEM) is commonly used for the observation of specimen surfaces. Its basic functioning principle is that, when the sample is irradiated with a fine electron beam, the specimen surface emits secondary electrons, making it possible to observe the topography of the surface by the two-dimensional scanning of the electron probe over the surface, and to acquire images from the detected secondary electrons. The main components of the SEM, Figure 175 (a), are an electron optical system which produces an electron probe, a specimen stage where the sample is placed, a secondary-electron detector to collect secondary electrons, an image display unit, and an operation system to perform various operations. Subsequently, the electron optical system consists of an electron gun, a condenser lens and an objective lens, a scanning coil to scan the electron probe, and other components. The inside of the electron optical system and the specimen chamber (a space surrounding the specimen) are generally evacuated by a diffusion pump, as they must be kept at a high vacuum of 10^{-3} to 10^{-4} Pa.

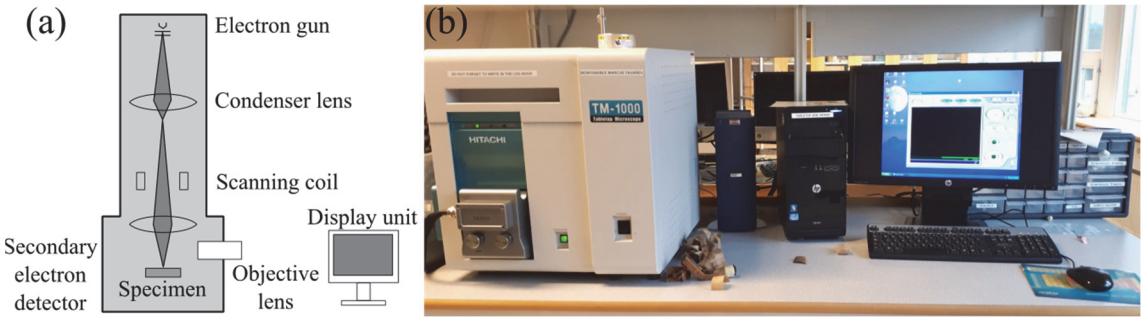

Figure 175. (a) Main components of a Scanning Electron Microscope; (b) SEM used in the tests.

In the electron gun, thermoelectrons are emitted from the cathode, a filament made of a thin tungsten wire, by heating the filament at a very high temperature of about 2800 K. By applying a positive voltage (1 to 30 kV) to the anode, which is a metal plate with a hole at its centre, the thermoelectrons are gathered as an electron beam, flowing through the hole of the anode. The current of that electron beam can be adjusted by placing an electrode between the cathode and anode and applying a negative voltage. Two-stage lenses, the condenser and objective lenses, are located below the electron gun and enable the adjustment of the diameter of the electron beam, Figure 176 (a).

The secondary electrons emitted from the specimen are detected by the secondary electron detector, Figure 176 (b). A scintillator (fluorescent substance) is coated on the tip of the detector and a high voltage of about 10 kV is applied to it, and attracts the secondary electrons from the specimen, which generate light when they hit the scintillator. This light is directed to a photo-multiplier tube (PMT) through a light guide, converted to electrons, and these electrons are amplified as an electric signal. A supplementary electrode, the collector, is placed before the scintillator and a voltage of a few hundred volts is applied to it in order to help the scintillator to collect a controlled number of secondary electrons. The output signals from the secondary electron detector are amplified and then transferred to the display unit. Since the scanning on the display unit is synchronised with the electron-probe scan, brightness variation, which depends on the number of the secondary electrons, appears on the monitor screen on the display unit, thus forming a SEM image. In general, the scan speed of the electron probe can be changed. An extremely fast scan speed is used for observation and a slow scan speed is used for acquiring or saving images.

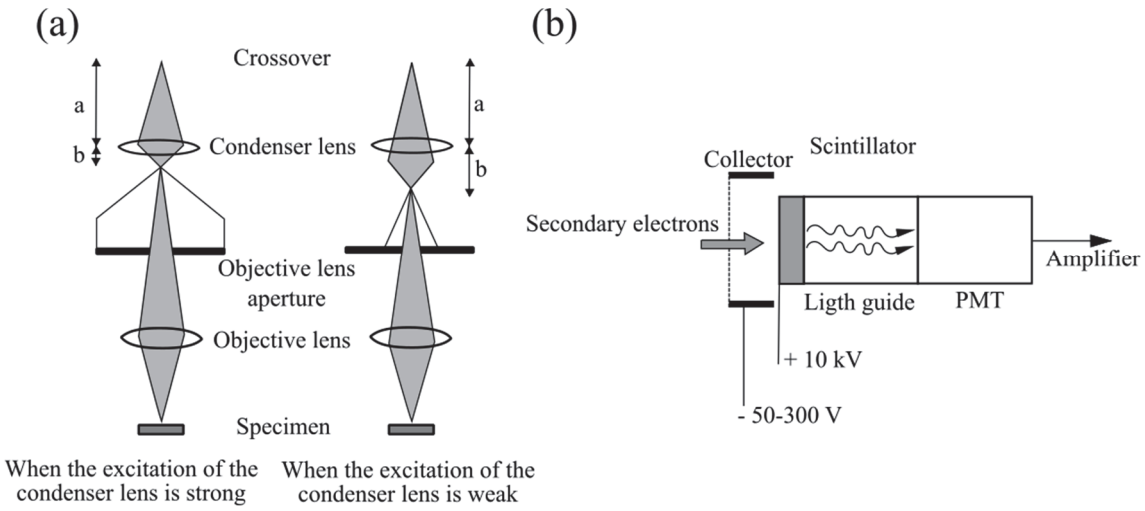

Figure 176. (a) Formation of the electron probe by the lenses; (b) Functioning of the secondary electron detector.

When using SEM, the specimen can be observed at a high magnification, and it is stably supported by a specimen stage, Figure 177, which is required to smoothly perform horizontal movement (X, Y), vertical movement (Z), specimen tilting (T), and rotation (R). The X and Y movements are used for the selection of a field of view, while the Z movement provides the change of image resolution and the depth of focus.

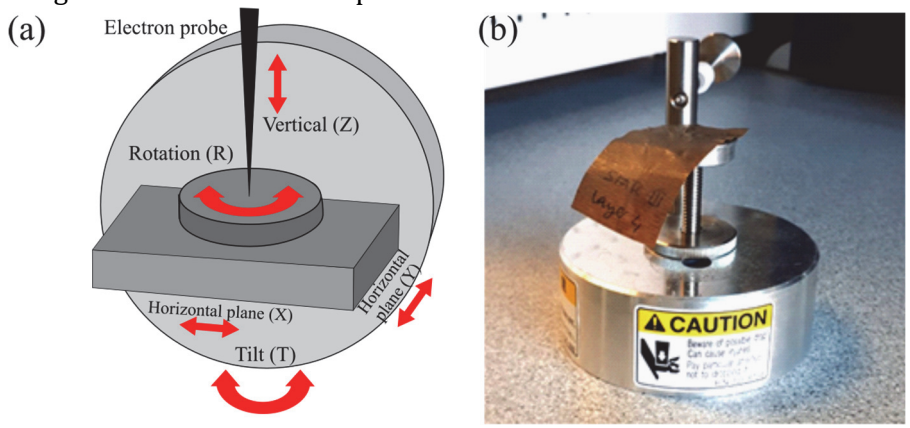

Figure 177. (a) Degrees of freedom of the specimen stage; (b) Specimen stage used in the laboratory with one paper sample.

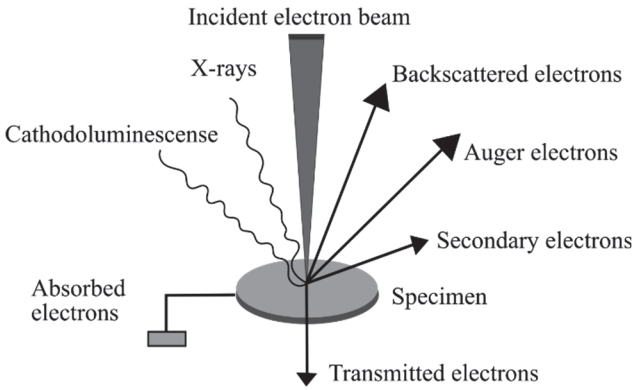

Figure 178. Emission of various electrons and electromagnetic waves from the specimen.

When electrons enter the specimen, they are scattered within it and gradually lose their energy and are absorbed by the specimen. The scattering range of the electrons inside the specimen is different depending on the electron energy, the atomic number of the elements which constitute the specimen and the density of the atoms. If the energy is higher, the scattering range is larger; while if the atomic number and density are large, the scattering

range is smaller. Figure 178 illustrates various signals emitted from the specimen when the incident electron beam enters it, which are used by the SEM to observe and analyse the specimen surface. As the accelerating voltage is higher, the penetration depth of the incident electrons is larger, and information from the inside of the specimen can be obtained.

If a specimen is conductive, the electrons flow through the specimen stage; however, if it is nonconductive, the electrons stop in the specimen, which becomes charged, and the number of the electrons flowing to the specimen is not equal to that those which exit from it. If the charging occurs, the electron probe that scans over the specimen is deflected by the repulsive force from a charged potential, resulting in a positional shift of the electron probe and producing distortion of the image. On the other hand, if the charging is very small and the electron-probe scan is not affected, secondary electrons with a small energy are influenced by a local charging, giving rise to a difference in the detection efficiency of secondary electrons or disturbance of the secondary electron trajectory. As a result, part of the image appears bright or dark.

The most typical method to prevent the charging is conductive coating, which consists of ion sputtering of a highly-conductive thin metal film, with a thickness ranging from a few to 10 nm of a noble metal (such as Au, Pt, Au-Pd, Pt-Pd), and vacuum evaporation to coat a nonconductive specimen. The reason for using a noble metal is that it is highly stable, and its secondary-electron yield is high. In order to reproduce the true surface of the specimen, it is necessary to prepare a thin film. Figure 179 shows the schematic diagram of the ion-sputter coater, whose inside is kept at a low vacuum, and the particles of the sputtered target metal collide with many residual gas molecules. Therefore, the metal particles are strongly scattered and attached to the specimen surface from every direction, forming a uniform film on the surface.

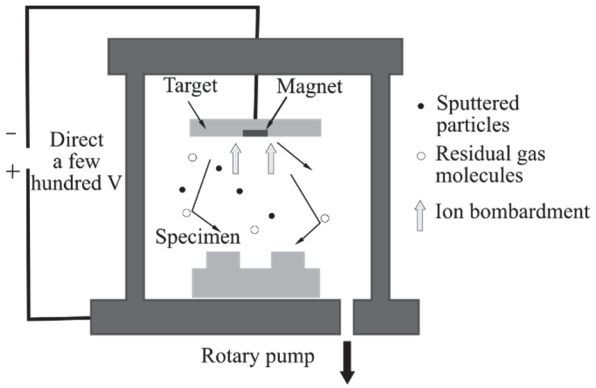

Figure 179. Functioning of the ion-sputter coater

1.4.2. Results of the analysis of the insulation samples with Scanning Electron Microscope

Before the ageing process, the different microstructure of non-damaged plain Kraft and crepe papers could be clearly appreciated through the SEM. The plain Kraft used in layers 1 and 2 can be seen in Figure 180 (a), where the matrix in which the cellulose fibres are embedded is less dense and the voids among fibres are more visible. On the other hand, the crepe paper used in layers 3 and 4 can be seen in Figure 180 (b). The visible wrinkles of the crepe paper, see Figure 181, are a manufacturing characteristic of this material and their extension is the cause of the hyperelasticity seen in the tensile tests. The preferent orientation of the fibres in MD is more evident in the crepe paper. Those microscopic structures are maintained in non-damaged areas of the paper materials during the ageing process, indicating that crack initiation and growth is mostly a local phenomenon.

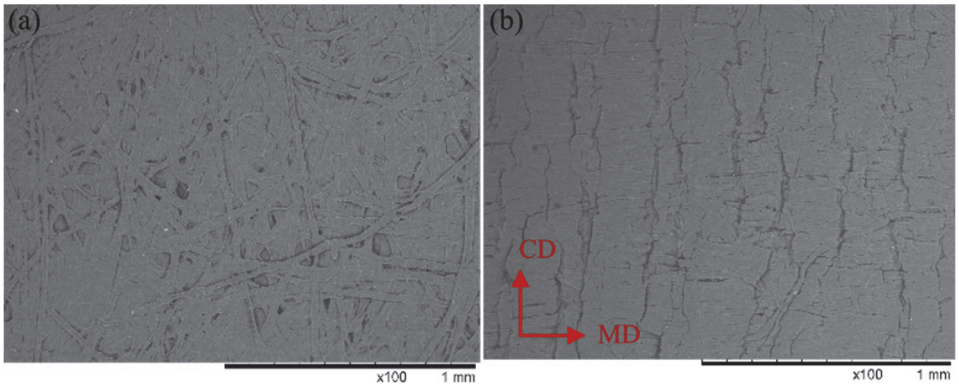

Figure 180. (a) Plain Kraft paper used in layer 2 and (b) crepe paper used in layer 3.

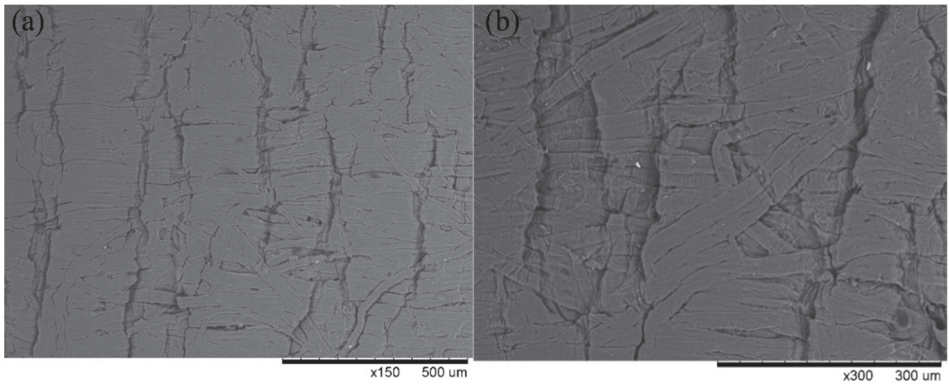

Figure 181. Closer view of the crepe paper in (a) layer 3 and (b) layer 4, where the wrinkles in the non-damaged material can be appreciated.

Table 28. Characteristics of SEM image Figure 180 and Figure 181.

Characteristics of SEM image Figure 180 (a)		*Characteristics of SEM image Figure 180 (b)*	
Accelerating Voltage	15000 Volt	Accelerating Voltage	15000 Volt
Working Distance	7.40 mm	Working Distance	7.01 mm
Emission Current	44700 nA	Emission Current	44700 nA
Micron Marker	1000000	Micron Marker	1000000
Characteristics of SEM image Figure 181 (a)		*Characteristics of SEM image Figure 181 (b)*	
Accelerating Voltage	15000 Volt	Accelerating Voltage	15000 Volt
Working Distance	7.01 mm	Working Distance	6.69 mm
Emission Current	44700 nA	Emission Current	44400 nA
Micron Marker	500000	Micron Marker	300000

The purpose of using SEM here was to locate the areas where fracture initiation took place, and to improve the understanding of the fracture growth process that leads to big cracks or total failure of the insulation. Two frequent causes for crack initiation were noticed in this analysis. On the one hand, local defects in the material, such as the ones shown in Figure 182, were affected by stress concentrations in areas of the CTC subjected to tension during the bending test, due to the big deformations suffered by the copper conductor, and grew as a result. These local defects, were magnified during the ageing process that, particularly in the plain Kraft, reduced the bonding among fibres, see Figure 183. The wrapping of the paper around the copper CTC during the manufacturing process contributed to generating stress concentrations coinciding with the edges of the CTC.

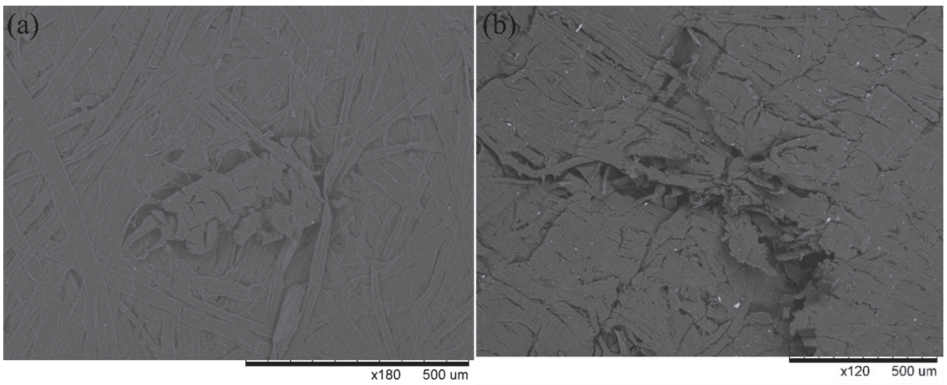

Figure 182. Local defect in (a) layer 2 and (b) layer 3 Ageing State II.

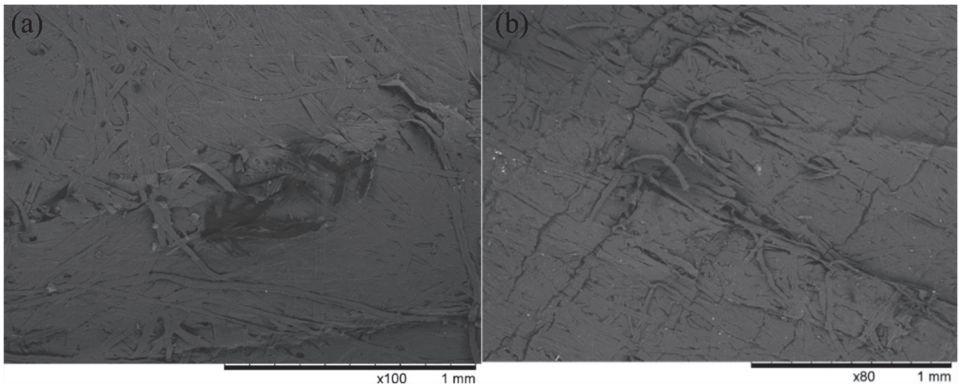

Figure 183. Local defects in (a) layer 2 and (b) layer 3, both in Ageing State III.

Table 29. Characteristics of SEM image Figure 182 and Figure 183.

Characteristics of SEM image Figure 182 (a)		*Characteristics of SEM image Figure 182 (b)*	
Accelerating Voltage	15000 Volt	Accelerating Voltage	15000 Volt
Working Distance	6.85 mm	Working Distance	6.46 mm
Emission Current	42700 nA	Emission Current	43700 nA
Micron Marker	500000	Micron Marker	500000
Characteristics of SEM image Figure 183 (a)		*Characteristics of SEM image Figure 183 (b)*	
Accelerating Voltage	15000 Volt	Accelerating Voltage	15000 Volt
Working Distance	7.62 mm	Working Distance	6.46 mm
Emission Current	42700 nA	Emission Current	43700 nA
Micron Marker	1000000	Micron Marker	1000000

On the other hand, in areas of the windings of a power transformer in which the CTCs are subjected to compression due to electromagnetic forces, wrinkle formation can also result in cracks, especially if the paper is heavily aged. In the tests, some wrinkles appeared in both insulation papers after the bending, Figure 184 and Figure 185. In the plain Kraft, the cellulose fibres were initially embedded in a matrix of hemicellulose and lignin, which formed a whitish cement that can be appreciated in Figure 186. The bonding among fibres was also visible in the microstructure of the crepe paper, Figure 187. Near local defects, such as wrinkles, the increased deformation of the insulated CTC samples produced delamination of the paper, and some cellulose fibres got out of the matrix that bonded them together, producing defects as the ones in Figure 188 and Figure 189. A closer view, see Figure 190, shows the points in which the fibres had broken and that the bonding did not cement them any longer.

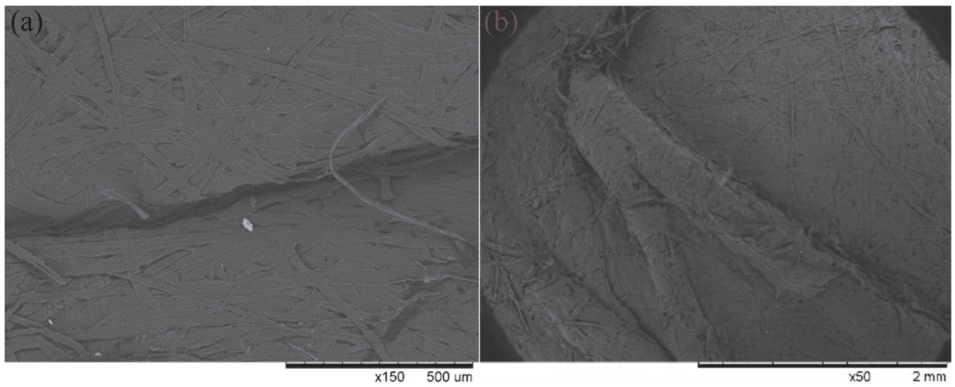

Figure 184. (a) Small and (b) bigger wrinkle produced in areas subjected to compression by the bending test, both in layer 2 and Ageing State II.

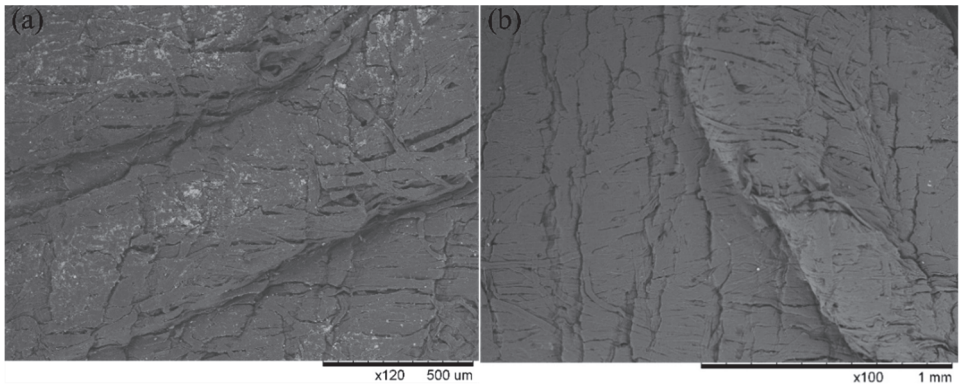

Figure 185. Wrinkles produced in areas subjected to compression by the bending test, (a) in layer 3 and (b) in layer 4 and Ageing State III.

Table 30. Characteristics of SEM image Figure 184 and Figure 185.

Characteristics of SEM image Figure 184 (a)		*Characteristics of SEM image Figure 184 (b)*	
Accelerating Voltage	15000 Volt	Accelerating Voltage	15000 Volt
Working Distance	6.57 mm	Working Distance	6.30 mm
Emission Current	43200 nA	Emission Current	43400 nA
Micron Marker	500000	Micron Marker	2000000
Characteristics of SEM image Figure 185 (a)		*Characteristics of SEM image Figure 185 (b)*	
Accelerating Voltage	15000 Volt	Accelerating Voltage	15000 Volt
Working Distance	6.69 mm	Working Distance	6.69 mm
Emission Current	44700 nA	Emission Current	44700 nA
Micron Marker	500000	Micron Marker	1000000

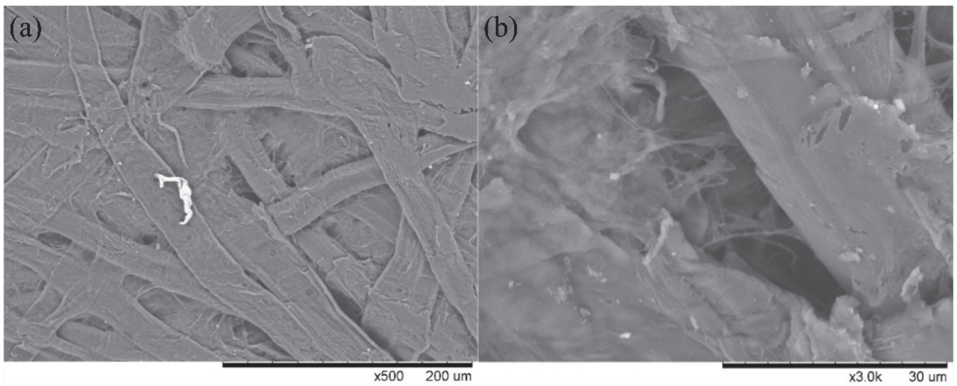

Figure 186. Close view of the microstructure of the plain Kraft paper used in layers 1 and 2, where the cellulose fibres and their bonding can be appreciated.

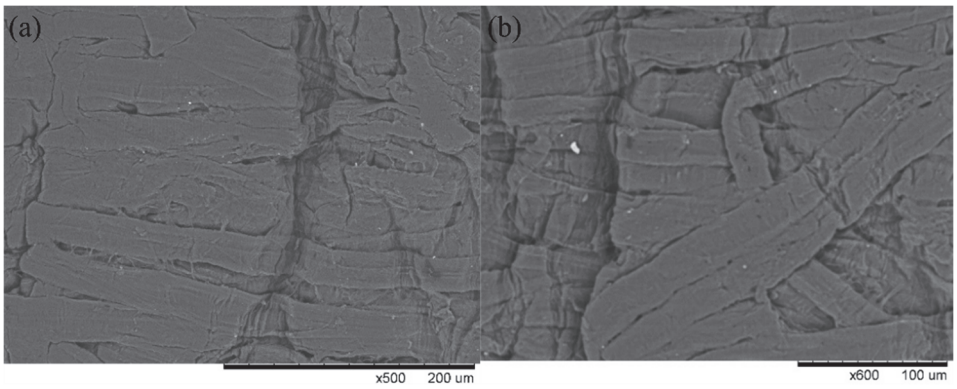

Figure 187. Close view of the microstructure of the crepe paper used in layers 3 and 4, where the cellulose fibres and their bonding can be appreciated.

Table 31. Characteristics of SEM image Figure 186 and Figure 187.

Characteristics of SEM image Figure 186 (a)		*Characteristics of SEM image Figure 186 (b)*	
Accelerating Voltage	15000 Volt	Accelerating Voltage	15000 Volt
Working Distance	6.67 mm	Working Distance	6.67 mm
Emission Current	43700 nA	Emission Current	43700 nA
Micron Marker	200000	Micron Marker	30000
Characteristics of SEM image Figure 187 (a)		*Characteristics of SEM image Figure 187 (b)*	
Accelerating Voltage	15000 Volt	Accelerating Voltage	15000 Volt
Working Distance	7.01 mm	Working Distance	6.69 mm
Emission Current	44900 nA	Emission Current	44400 nA
Micron Marker	200000	Micron Marker	100000

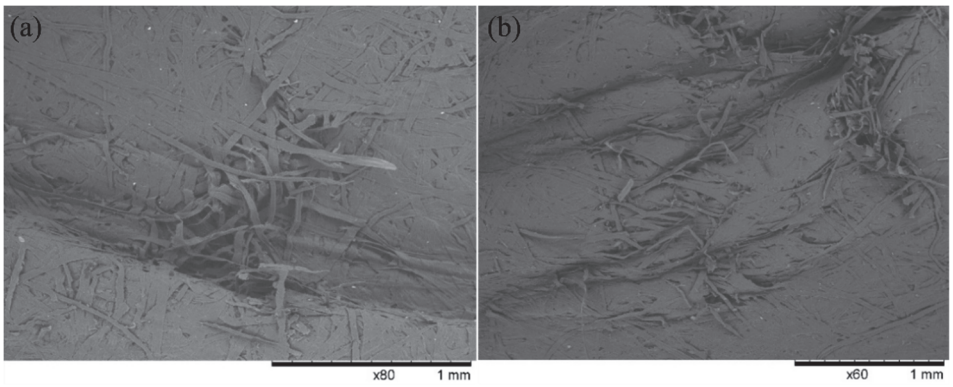

Figure 188. (a) Small and (b) bigger local defects produced in a wrinkle in layer 2 and Ageing State II.

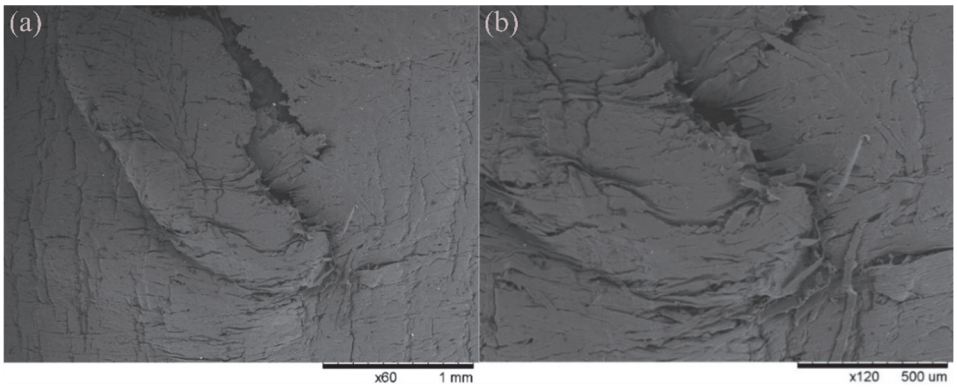

Figure 189. Local defects and cracks produced near a wrinkle in layer 4 and Ageing State III.

Table 32. Characteristics of SEM image Figure 188 and Figure 189.

Characteristics of SEM image Figure 188 (a)		*Characteristics of SEM image Figure 188 (b)*	
Accelerating Voltage	15000 Volt	Accelerating Voltage	15000 Volt
Working Distance	6.91 mm	Working Distance	6.57 mm
Emission Current	43700 nA	Emission Current	43900 nA
Micron Marker	1000000	Micron Marker	1000000
Characteristics of SEM image Figure 189 (a)		*Characteristics of SEM image Figure 189 (b)*	
Accelerating Voltage	15000 Volt	Accelerating Voltage	15000 Volt
Working Distance	6.69 mm	Working Distance	6.69 mm
Emission Current	44400 nA	Emission Current	44700 nA
Micron Marker	1000000	Micron Marker	500000

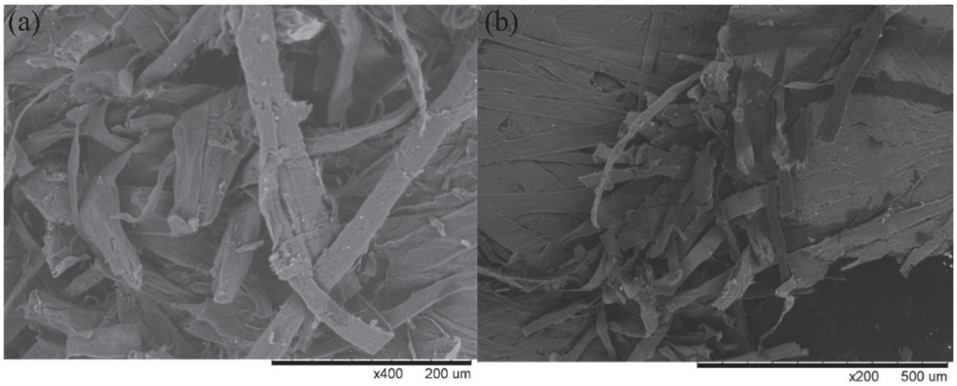

Figure 190. Close view of the microstructure of the plain Kraft paper used in layer 2 and (a) Ageing State II and (b) Ageing State III, where the broken cellulose fibres can be appreciated.

Table 33. Characteristics of SEM image Figure 190.

Characteristics of SEM image Figure 190 (a)		*Characteristics of SEM image Figure 190 (b)*	
Accelerating Voltage	15000 Volt	Accelerating Voltage	15000 Volt
Working Distance	6.91 mm	Working Distance	7.62 mm
Emission Current	43900 nA	Emission Current	43900 nA
Micron Marker	200000	Micron Marker	500000

In Figure 191, the aspect of small and medium-size cracks in the plain Kraft paper after a week at 150°C, in Ageing State I, can be seen. The big deflections of the insulated CTC samples after the bending tests, of 10 mm or 20 mm, made the defects grow in areas of stress concentrations. A closer view, Figure 192, shows the points at which the cellulose fibres broke. After four weeks at 150°C, in Ageing State II, the cracks in layer 2 were small in the bending test with d = 10 mm, Figure 193, but large when d = 20 mm, Figure 194.

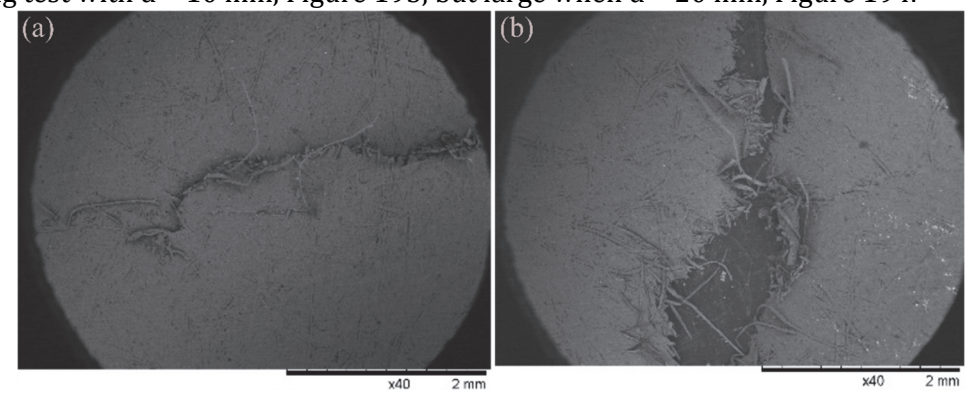

Figure 191. (a) Small crack and (b) part of a medium-size crack in layer 2 and Ageing State I.

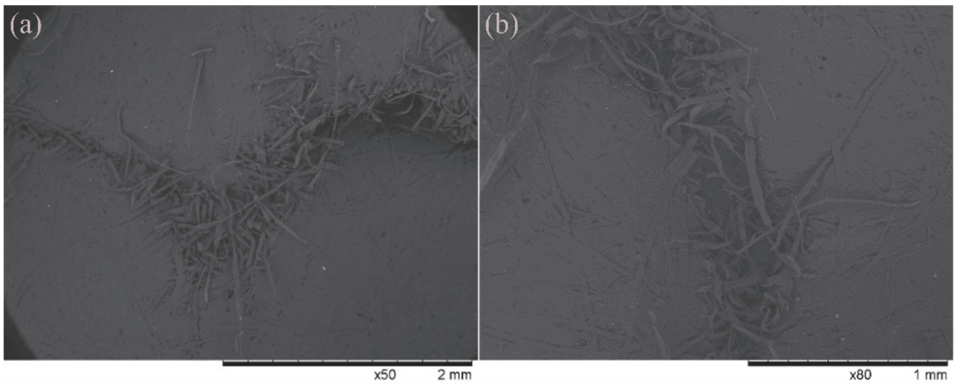

Figure 192. Closer view of the cracks in layer 2 and Ageing State I.

Table 34. Characteristics of SEM image Figure 192.

Characteristics of SEM image Figure 192 (a)		*Characteristics of SEM image Figure 192 (b)*	
Accelerating Voltage	15000 Volt	Accelerating Voltage	15000 Volt
Working Distance	6.97 mm	Working Distance	6.41 mm
Emission Current	44200 nA	Emission Current	42700 nA
Micron Marker	2000000	Micron Marker	1000000

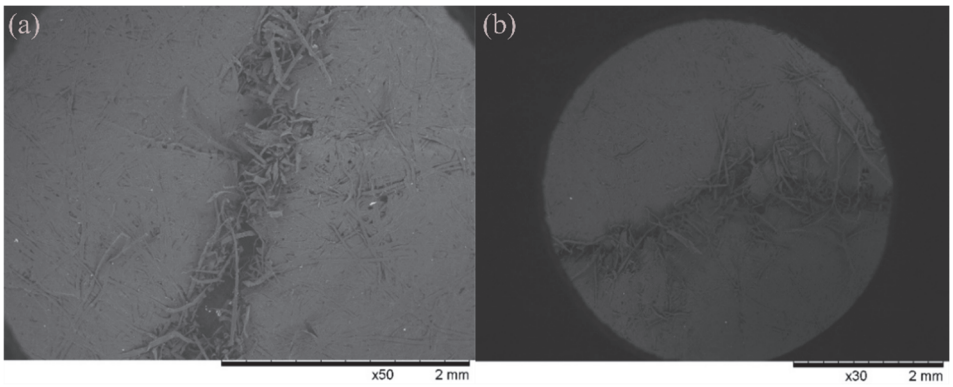

Figure 193. Small cracks in layer 2 and Ageing State II, after the bending test with d = 10mm.

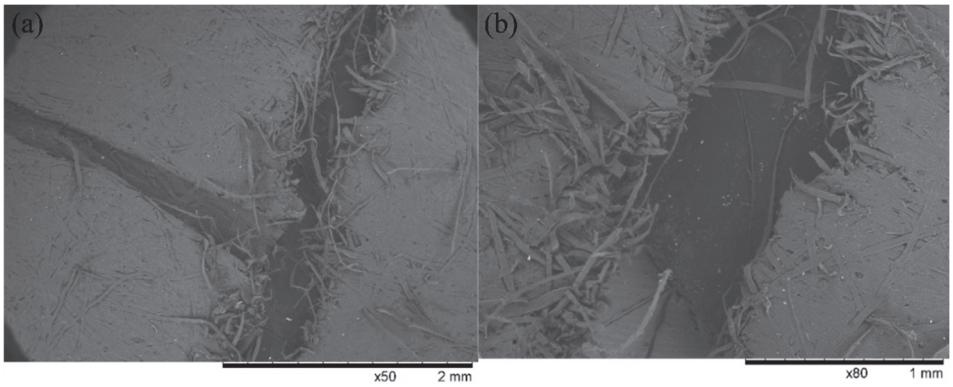

Figure 194. Big cracks in layer 2 and Ageing State II, after the bending test with d = 20mm.

Table 35. Characteristics of SEM image Figure 193 and Figure 194.

Characteristics of SEM image Figure 193 (a)		*Characteristics of SEM image Figure 193 (b)*	
Accelerating Voltage	15000 Volt	Accelerating Voltage	15000 Volt
Working Distance	6.91 mm	Working Distance	7.39 mm
Emission Current	43700 nA	Emission Current	42200 nA
Micron Marker	2000000	Micron Marker	2000000
Characteristics of SEM image Figure 194 (a)		*Characteristics of SEM image Figure 194 (b)*	
Accelerating Voltage	15000 Volt	Accelerating Voltage	15000 Volt
Working Distance	6.91 mm	Working Distance	6.91 mm

Emission Current	44200 nA	Emission Current	43700 nA
Micron Marker	2000000	Micron Marker	1000000

After three weeks of ageing at 150°C, in Ageing State III, there were some areas of layer 2, made of plain Kraft paper, where the cracks still had small or medium sizes, such as the ones seen in Figure 195. However, in the bending tests with deflections of 10 or 20 mm, the cracks grew up to large size or even total fracture of the material, as seen in Figure 196 and Figure 197.

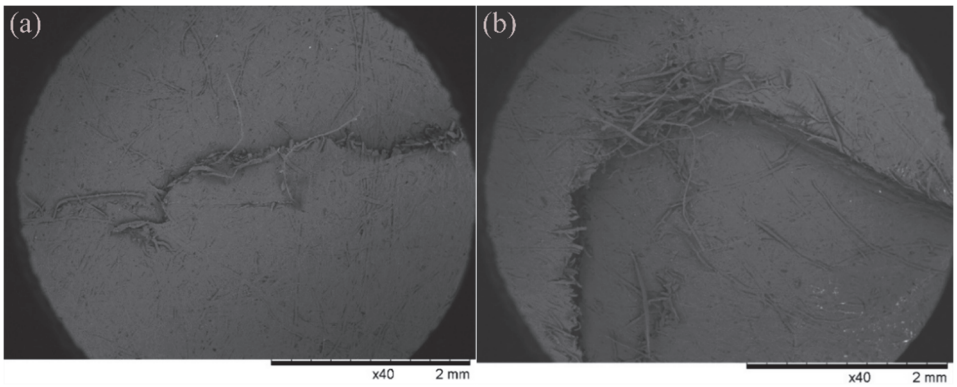

Figure 195. Some small and medium-size cracks in layer 2 and Ageing State III.

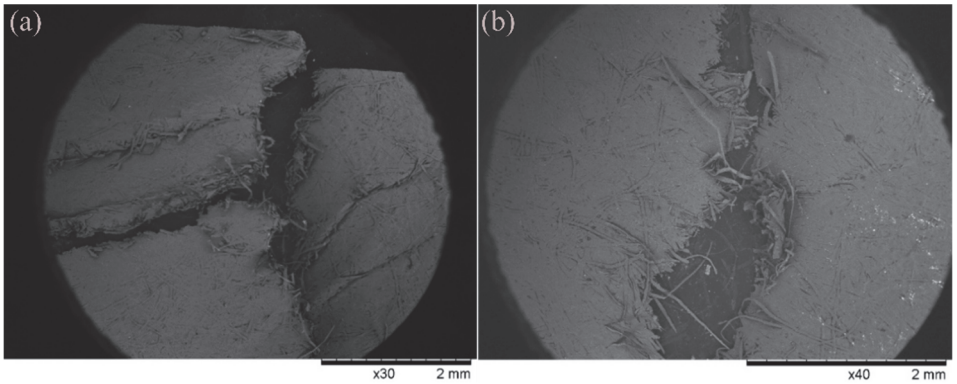

Figure 196. Parts of big cracks in layer 2 and Ageing State III.

Table 36. Characteristics of SEM image Figure 195 and Figure 196.

Characteristics of SEM image Figure 195 (a)		*Characteristics of SEM image Figure 195 (b)*	
Accelerating Voltage	15000 Volt	Accelerating Voltage	15000 Volt
Working Distance	7.26 mm	Working Distance	7.57 mm
Emission Current	42700 nA	Emission Current	43000 nA
Micron Marker	2000000	Micron Marker	2000000
Characteristics of SEM image Figure 196 (a)		*Characteristics of SEM image Figure 196 (b)*	
Accelerating Voltage	15000 Volt	Accelerating Voltage	15000 Volt
Working Distance	9.35 mm	Working Distance	7.57 mm
Emission Current	43400 nA	Emission Current	44200 nA
Micron Marker	2000000	Micron Marker	2000000

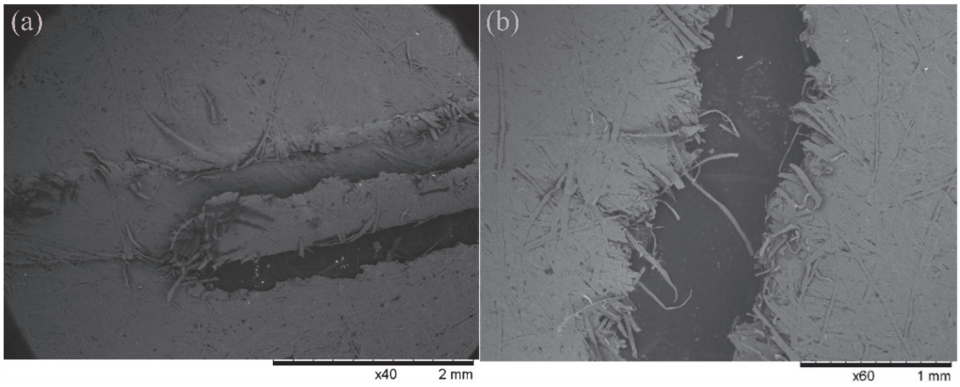

Figure 197. Parts of big cracks in layer 2 and Ageing State III.

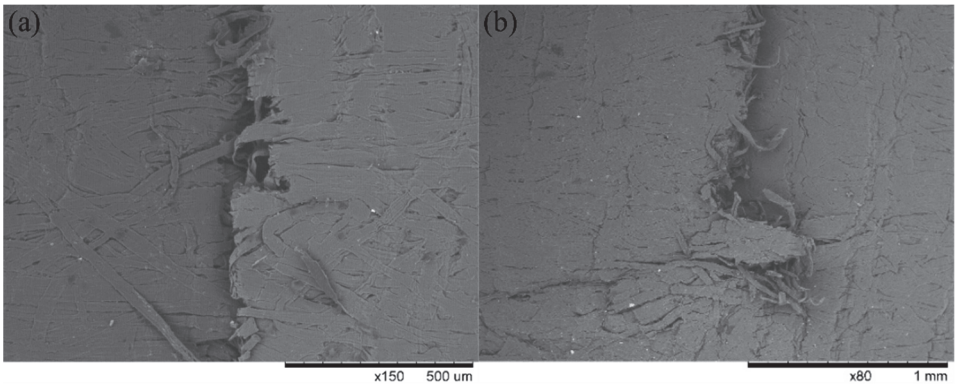

Figure 198. Cracks oriented in CD in layer 3 and Ageing State III.

Table 37. Characteristics of SEM image Figure 197 and Figure 198.

Characteristics of SEM image Figure 197 (a)		*Characteristics of SEM image Figure 197 (b)*	
Accelerating Voltage	15000 Volt	Accelerating Voltage	15000 Volt
Working Distance	9.35 mm	Working Distance	7.57 mm
Emission Current	43900 nA	Emission Current	43900 nA
Micron Marker	2000000	Micron Marker	1000000
Characteristics of SEM image Figure 198 (a)		*Characteristics of SEM image Figure 198 (b)*	
Accelerating Voltage	15000 Volt	Accelerating Voltage	15000 Volt
Working Distance	7.01 mm	Working Distance	7.01 mm
Emission Current	44700 nA	Emission Current	44700 nA
Micron Marker	500000	Micron Marker	1000000

In Ageing State III, after the tests with d = 20 mm, the first cracks of small size appeared in layers 3 and 4 of the insulation, made of crepe paper. Some of them were originated in small defects initially present in the material which grew due to ageing and can be seen in Figure 198 - Figure 203. In the crepe paper, the preferential orientation of the cellulose fibres was more evident, and some longitudinal cracks were produced in CD, which is the less resistant direction of the material both in terms of maximum stress and maximum strain at breakage, see Figure 198. In areas of stress concentrations in the insulation of the CTC samples, the cracks grew to produce small holes such as the ones seen in Figure 200. Where the degradation of the material was more accused, the cracks were slightly larger, Figure 201, but their maximum dimension remained smaller than 5 mm in this Ageing State.

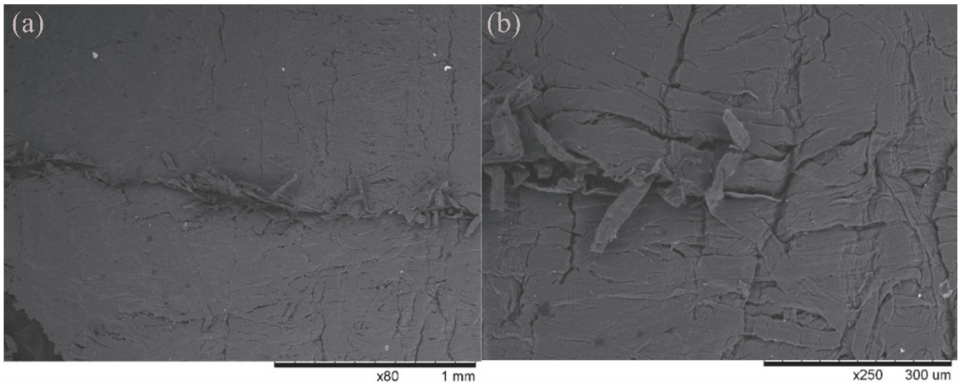

Figure 199. Small crack in layer 4 and Ageing State III.

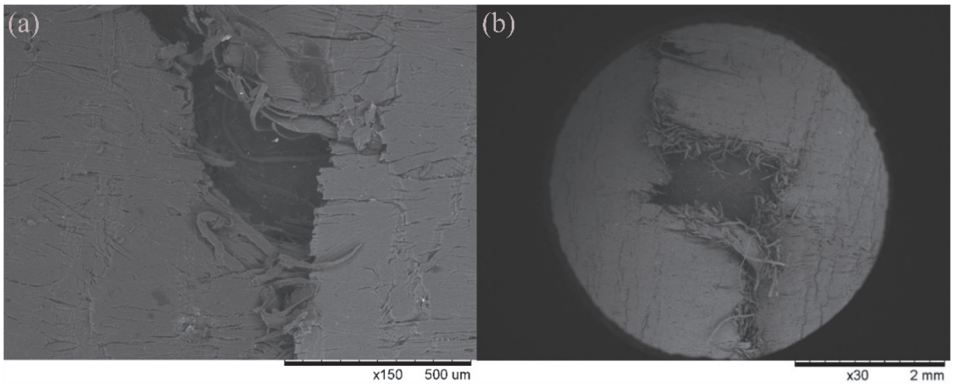

Figure 200. Small cracks in layer 3 and Ageing State III.

Table 38. Characteristics of SEM image Figure 199 and Figure 200.

Characteristics of SEM image Figure 199 (a)		*Characteristics of SEM image Figure 199 (b)*	
Accelerating Voltage	15000 Volt	Accelerating Voltage	15000 Volt
Working Distance	6.69 mm	Working Distance	6.69 mm
Emission Current	44400 nA	Emission Current	44400 nA
Micron Marker	1000000	Micron Marker	300000
Characteristics of SEM image Figure 200 (a)		*Characteristics of SEM image Figure 200 (b)*	
Accelerating Voltage	15000 Volt	Accelerating Voltage	15000 Volt
Working Distance	7.01 mm	Working Distance	7.01 mm
Emission Current	44700 nA	Emission Current	44700 nA
Micron Marker	500000	Micron Marker	2000000

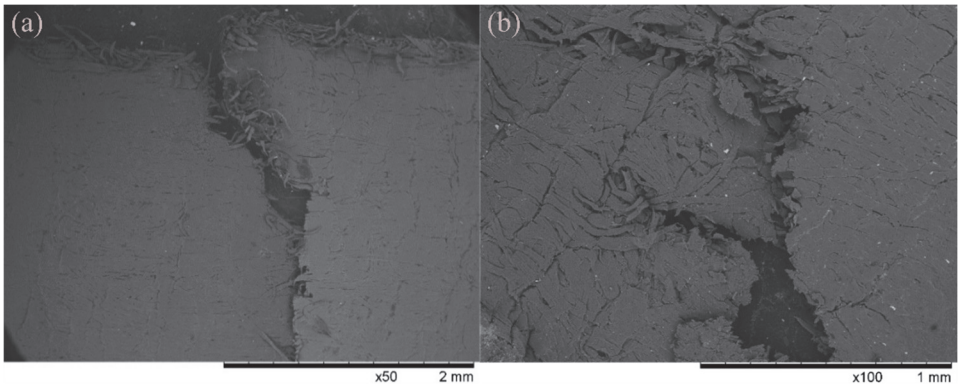

Figure 201. Small cracks in layer 3 and Ageing State III, after the bending test with d = 20 mm.

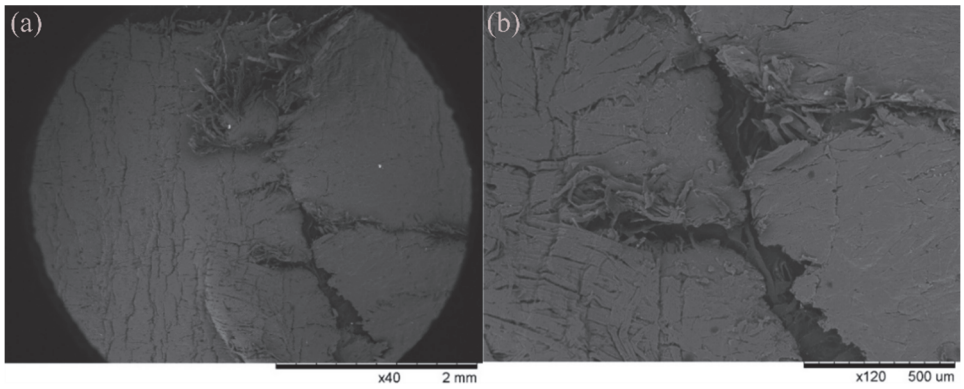

Figure 202. Small cracks in layer 4 and Ageing State III, after the bending test with d = 20 mm.

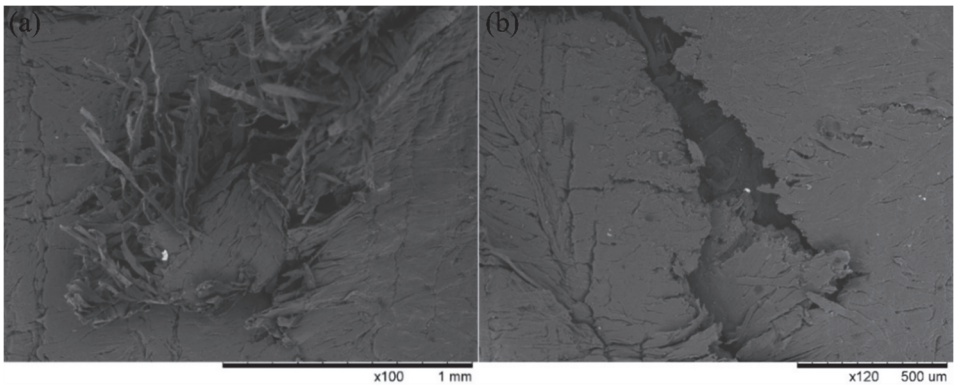

Figure 203. Closer view of the cracks in layer 4 and Ageing State III, after the bending test with d = 20 mm.

Table 39. Characteristics of SEM image Figure 201, Figure 202 and Figure 203.

Characteristics of SEM image Figure 201 (a)		*Characteristics of SEM image Figure 201 (b)*	
Accelerating Voltage	15000 Volt	Accelerating Voltage	15000 Volt
Working Distance	7.10 mm	Working Distance	6.46 mm
Emission Current	44700 nA	Emission Current	43700 nA
Micron Marker	2000000	Micron Marker	1000000
Characteristics of SEM image Figure 202 (a)		*Characteristics of SEM image Figure 202 (b)*	
Accelerating Voltage	15000 Volt	Accelerating Voltage	15000 Volt
Working Distance	6.69 mm	Working Distance	6.69 mm
Emission Current	43900 nA	Emission Current	44400 nA
Micron Marker	2000000	Micron Marker	500000
Characteristics of SEM image Figure 203 (a)		*Characteristics of SEM image Figure 203 (b)*	
Accelerating Voltage	15000 Volt	Accelerating Voltage	15000 Volt
Working Distance	6.69 mm	Working Distance	6.69 mm
Emission Current	44400 nA	Emission Current	44700 nA
Micron Marker	1000000	Micron Marker	500000

2. Numerical simulation

2.1. Description of the model

The mechanical response of the analysed copper CTC was modelled using ANSYS AIM Static Structural. The Finite Element (FE) simulation model described here attempts to reproduce the mechanical effects of the bending test over the CTC samples, and to obtain the deformations produced in the copper conductor that will subsequently affect the paper insulation. As the bending tests in the laboratory were carried out under displacement control, a displacement was applied in the different steps of the mechanical model to reproduce the bending test, using *Direct Solver* type and large deflections. The strain field

obtained in the external faces of the CTC can be correlated afterwards with the appearance of fractures in the insulation, their location and magnitude, which were analysed experimentally.

2.1.1. Geometry, material properties and supports

Although the real CTC samples have curvature, it was neglected in the FE model for simplicity, analogously to in [92], where the authors considered that the big winding diameters of large power transformers and the high number of supporting sticks result in a negligible curvature. The transposition of the copper strands in the CTC was also neglected, to avoid the complexity of the geometry and because its relevance in the general mechanical response of the CTC was considered to be limited. The results of the simulation model and their correlation with experimental observations, described in *1.3.Three-point bending tests of the insulated CTCs* and *Deformation, stress and strain distributions obtained in the CTC samples through the numerical simulation*, were satisfactory enough so these initial hypotheses did not need to be reconsidered.

The CTC sample consists of two independent stacks, named in the model as A and B, each of them formed by eight copper strands, plus the transposed one, Figure 204 (a). That real geometry was approximated in the model by a cross-section modelled in SpaceClaim, composed of 18 rectangular strands (nine strands in each stack), Figure 204 (b), with a width of 11 mm and a thickness of 1.9 mm, rounded corners similar to the ones of the real cross-section and a symmetrical disposition. It is noticed that, in a previous analysis [146], a solid rectangular cross-section with the same outer dimensions was considered for simplicity and the results of the numerical simulation were radically different to the ones obtained in the laboratory: that approximation gave a deflection 25 times smaller than the one measured experimentally. Because of that, it can be concluded that the sliding between copper strands is an essential characteristic of the mechanical response of CTCs, and the strands need to be modelled independently to obtain reliable results.

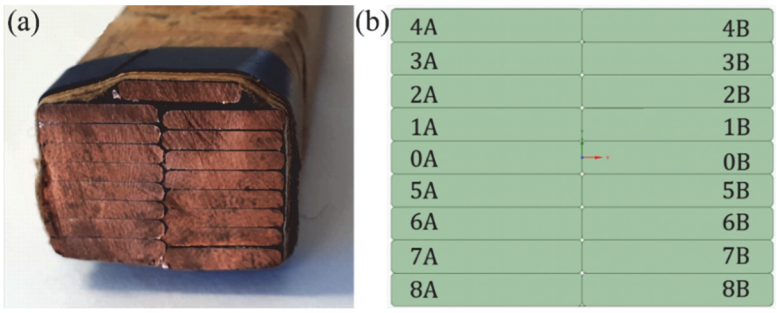

Figure 204. Cross-sectional view of the (a) real and (b) modelled CTC.

The modelled CTC sample had a length of 120 mm, the same as the samples tested in the laboratory, and the loading and supporting cylinders required for the three-point bending test were also modelled with their real diameters of 20 mm and 25 mm, respectively, Figure 205 (a). The copper strands were modelled as flexible solids with nonlinear effects and made of Copper Alloy, and some the properties of this material set by defect in the ANSYS library "Engineering Data Sources → General materials" were modified to meet the properties of the annealed copper used in the conductors of the windings of power transformers, which were measured in the laboratory, Figure 205 (b).

(a)

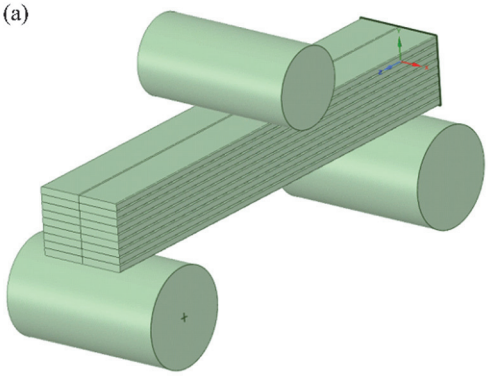

(b)

Properties of Outline Row 3: Copper Alloy

	A	B	C
1	Property	Value	Unit
2	Material Field Variables	Table	
3	Density	8300	kg m^-3
4	Isotropic Secant Coefficient of Thermal Expansion		
6	Isotropic Elasticity		
7	Derive from	Young's Modulus and P...	
8	Young's Modulus	1,1E+11	Pa
9	Poisson's Ratio	0,34	
10	Bulk Modulus	1,1458E+11	Pa
11	Shear Modulus	4,1045E+10	Pa
12	Bilinear Isotropic Hardening		
13	Yield Strength	2,2E+08	Pa
14	Tangent Modulus	8E+08	Pa
15	Tensile Yield Strength	2,2E+08	Pa
16	Compressive Yield Strength	2,2E+08	Pa
17	Tensile Ultimate Strength	4,3E+08	Pa
18	Compressive Ultimate Strength	0	Pa

Figure 205. (a) 3-D view of the CTC sample with the loading cylinder and the two supporting cylinders for the three-point bending tests; (b) Properties of copper material introduced in the numerical simulation.

The three cylinders were defined as rigid elements, as they are considerably more rigid than the copper CTC and their flexible behaviour was not of interest in this analysis. The modelled CTC sample was supported on the two rigid supporting cylinders, to the bases of which two remote displacements (Remote Displacements 2 and 3, Figure 206 (a)) were applied and all degrees of freedom were impeded: X, Y, Z, Rotation X, Rotation Y and Rotation Z were set to 0, as seen in Figure 206 (b). The other rigid loading cylinder was used to apply the bending load in direction *"-Y"* on the modelled CTC sample. A remote displacement was applied on the base of this third cylinder, impeding all the degrees of freedom except the *Y*-component which was set as "*Free*", Figure 207. As the bending test in the laboratory was carried out under displacement control, its reproduction in the numerical model consisted of several steps in which the magnitude of the displacement of the load cylinder in *Y*-direction was varied, and the force reaction in the contact between that cylinder and the CTC was measured in the different steps. Besides, according to [147], applying the loads through imposed displacements is more stable than doing it through imposed forces or pressures.

(a)

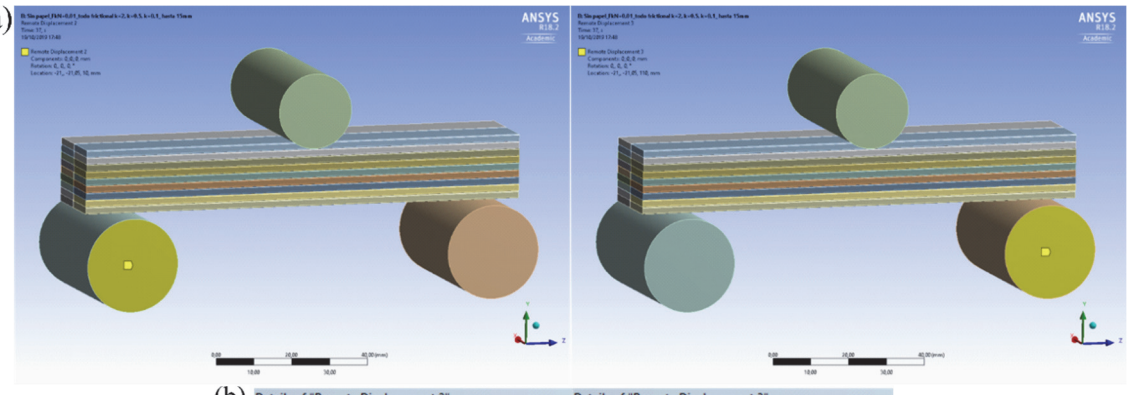

(b)

Details of "Remote Displacement 2"		Details of "Remote Displacement 3"	
Scope		**Scope**	
Scoping Method	Geometry Selection	Scoping Method	Geometry Selection
Geometry	1 Face	Geometry	1 Face
Coordinate System	Global Coordinate System	Coordinate System	Global Coordinate System
X Coordinate	-21, mm	X Coordinate	-21, mm
Y Coordinate	-21,05 mm	Y Coordinate	-21,05 mm
Z Coordinate	10, mm	Z Coordinate	110, mm
Location	Click to Change	Location	Click to Change
Definition		**Definition**	
Type	Remote Displacement	Type	Remote Displacement
X Component	0, mm (ramped)	X Component	0, mm (ramped)
Y Component	0, mm (ramped)	Y Component	0, mm (ramped)
Z Component	0, mm (ramped)	Z Component	0, mm (ramped)
Rotation X	0, ° (ramped)	Rotation X	0, ° (ramped)
Rotation Y	0, ° (ramped)	Rotation Y	0, ° (ramped)
Rotation Z	0, ° (ramped)	Rotation Z	0, ° (ramped)
Suppressed	No	Suppressed	No
Behavior	Deformable	Behavior	Deformable
Advanced		**Advanced**	

Figure 206. (a) General view of the model, where Remote Displacements 2 and 3 can be seen; (b) Details of Remote Displacements 2 and 3, respectively in support cylinders 1 and 2.

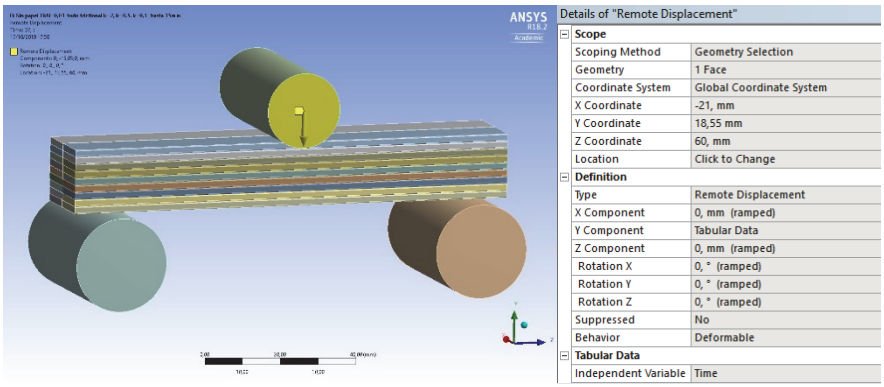

Figure 207. General view and details of the Remote Displacement 1 in the load cylinder.

2.1.2. Mesh definition and connections

Initially, we tried to include the four layers of dielectric paper in the numerical model as flexible solid elements with thickness of 80-82 μm and with the mechanical properties obtained in the laboratory (see *1.2.Characterisation of the paper insulation samples), wrapped around the copper CTC sample*). However, defining the contact conditions among the four layers of paper insulation and their contact with the copper core was a numerical challenge because of the small thickness of the paper. Since one copper strand is almost 24 times thicker than one layer of paper insulation, the compatibility between adjacent meshes implied that the mesh size must have been significantly smaller than the paper thickness; and this entailed an unmanageable number of elements for the whole model. Since the contribution of the paper insulation to the mechanical response of the whole CTC is negligible, the FE model did not include the insulation, but only the copper core. Due to the adherence between the first layer of dielectric paper and the core, the strain field in that layer can be assimilated with the strain field at the surface of the CTC. The other layers of the insulation will be subjected to a lower strain level, because their sliding is not impeded, so the assumption that they are affected by the same strains that as the copper CTC will be conservative in any case.

- **Mesh definition**

The general preferences in the mesh definition can be seen in Figure 208 (a). The *Physics Preference* option must be in accordance with the physics of the analysis, which in this study is *mechanical*. The *Relevance* predetermines the fineness of the mesh for the whole geometry, which is going to influence the accuracy of the result. Here, the relevance was set at its maximum value, that is 100, because the results are considered to strongly depend on the mesh quality.

The *Size Function* option enables the user to have a greater control over some refinement mechanisms of the mesh [148], such as:

- Angles between normals for adjacent mesh elements, through the *curvature* option.

- Number of mesh elements employed in the gaps between two geometric entities, through the *proximity* option.

- Gradation between minimum and maximum sizes of the mesh, based on a specified growth rate, through all *size functions*.

Here, the *curvature size function* was used, which focuses on the curvature on edges and faces and computes element sizes on these entities such that the size will not violate the maximum size or the curvature normal angle, which are either automatically computed by the mesher or defined by the user. The purpose of using the curvature function here was to have more mesh elements in the rounded corners of the strands, in order to avoid sharp

edges that could lead to stress concentrations, Figure 208 (b). The curvature size function is defined by the following properties [148]:

- *Relevance centre*, which establishes the gauge of the relevance slider control in the default group. The available options are coarse, medium and fine. A *fine relevance centre* was selected here.

- *Maximum Face Size*, which is the largest size that the mesher uses in face elements, except on hard edge sizes or floating-point arithmetic, where face element may be larger. The default value was used here.

- *Defeature Size*, which establishes the global tolerance for defeaturing. The default value was used here.

- *Transition,* which conditions the rate at which adjacent elements will grow. The transitions will be smooth if *Slow* is selected, and more abrupt if *Fast* is selected. Here, slow was selected.

- *Growth Rate*, which represents the increase in element edge length with each succeeding layer of elements. The default value was used here, which was calculated by the mesher based on the values of the *Relevance* and *Transition* options.

- *Span Angle Centre*, which subdivides the mesh along a region with curvature until the individual elements span this angle. There are three options: *coarse* (from 91 to 60°), *medium* (from 75 to 24°) and *fine* (from 36 to 12°). Here, fine was selected.

- *Minimum Size*, which is the smallest size that the mesher uses, except in local feature sizes or other geometric anomalies, where some element sizes may be smaller. The default value was used here.

- *Max Tet Size*, which is the largest size that the mesher uses in solid elements. The default value was used here.

- *Curvature Normal Angle*, which is the maximum allowable angle that one element edge is allowed to span given a certain geometry curvature. The default value was used here.

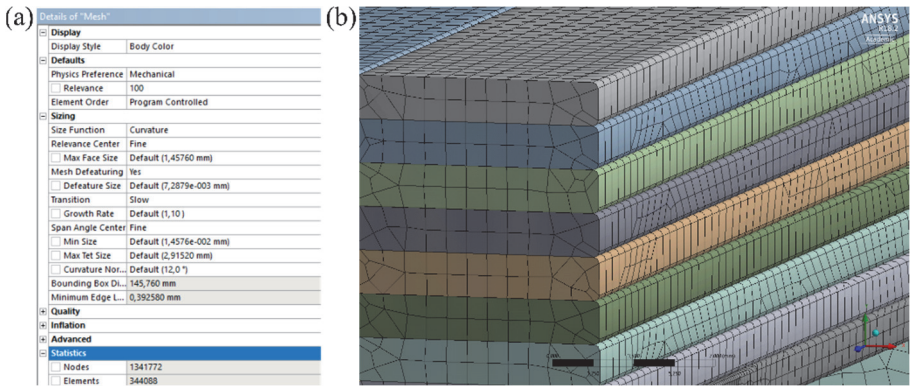

Figure 208. (a) Preferences in the mesh definition; (b)Detail of the mesh in the rounded corners of the copper strands.

According to [148], a *sizing control* permits to set:

- The element size for a selected body, face, or edge.

- The number of divisions along an edge.

- The element size within a user-defined *sphere of influence* that can include a selected body, face, edge, or vertex. This control, which must be attached to a coordinate system except when its centre is a vertex of the geometry, is recommended for local mesh sizing.

- The element size within a user-defined body of influence, which will influence the mesh of the body to which it is scoped, but the body of influence itself will not be meshed.

- The minimum mesh sizing used for a selected body, face or edge. This setting revokes the default global sizing.

Here, a *body sizing* with a minimum element size of 1 mm was applied to the 18 copper strands which form the CTC sample, to obtain a sufficiently small general meshing. As major problems with convergence will appear where the load and support cylinders are in contact with the CTC, some *Element Size on Contacts* were introduced between the load cylinder and strands 4A and 4B, Figure 209, and between the support cylinders and strands 8A and 8B, Figure 210, with an element size of 0.25 mm, to improve contact convergence in the most problematic areas.

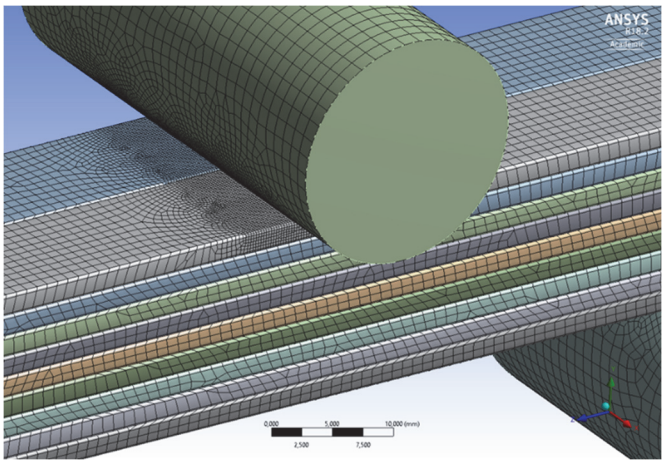

Figure 209. Close view of the mesh sizing of 0.25 mm in the contact between the load cylinder and copper strands 4A and 4B.

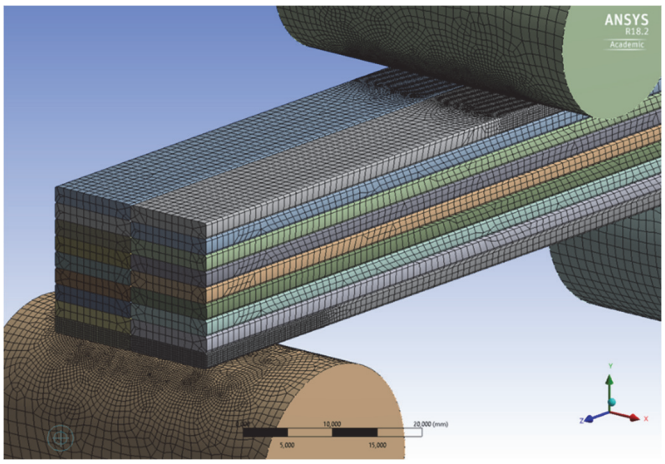

Figure 210. Close view of the mesh sizing of 0.25 mm in the contact between the support cylinders and copper strands 8A and 8B.

- **Contact definition**

For nonlinear solid body contact of faces, two penalty-based contact formulations, the *Pure Penalty* or *Augmented Lagrange* formulations can be used. In both methods, expression (113) is accomplished, see Figure 211, and the penetration will be lower if the normal stiffness is higher:

$$F_{Normal} = k_{Normal} \cdot x_{penetration} \tag{113}$$

Where:

F_{Normal} (N): Finite contact force.

k_{Normal} (N/mm): Contact stiffness.

$x_{penetration}$ (mm): Penetration.

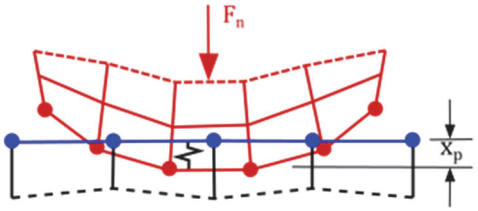

Figure 211. Criterion for the Augmented Lagrange contact formulation.

However, when the *Augmented Lagrange Contact Formulation* is used, equation (113) is transformed into equation (114), in which the contact force is increased:

$$F_{Normal} = k_{Normal} \cdot x_{penetration} + \lambda \tag{114}$$

Compared to the *Pure Penalty Contact Formulation*, the *Augmented Lagrange Contact Formulation* usually leads to better conditioning and is less sensitive to the magnitude of the contact stiffness coefficient [147], because of the extra term λ. However, in some analyses, the *Augmented Lagrange* method may require additional iterations, especially if the deformed mesh becomes too distorted. Besides, this method augments the stiffness matrix by adding extra DOF terms, by means of contact pressure, to reconcile the contact. That produces a larger stiffness matrix but makes ill-conditioning less probable. The *Augmented Lagrange Contact Formulation* can be used with any type of contact behaviour, with both the iterative or direct solvers, and symmetric or asymmetric contact behaviours are available.

According to [147], the amount of penetration between the contact and target surfaces in ANSYS relies on the values of FKN, the *Normal Stiffness* of the contact, and FTOLN, the *Penetration Tolerance Factor*, which is a factor based on the thickness of the element which is used to calculate the allowable penetration. If the value of FKN is high, the amount of penetration will be smaller, but that can lead to ill-conditioning of the global stiffness matrix and to convergence difficulties. On the other hand, if the value of FKN is small, there will be a certain amount of penetration or slip that could result in an inaccurate solution. The ideal goal will be to use a value of the normal stiffness of the contacts which is high enough to produce an acceptable penetration or slip, but small enough to make the convergence easy [149]. For surface-to-surface contact elements, the normal stiffness is usually between 0.001-100, with a default value of 1.0, which is appropriate for bulk deformation. In mechanical problems where bending deformation dominates, as it is the case we are studying here, smaller values of FKN, from 0.01-0.1, usually result in a better performance [147]. Many convergence failures in contact analyses are produced by a too large value of FKN [149].

When solving a numerical simulation with complicated contacts, it is recommended in [147] to start with a low value of FKN, because that requires shorter solution times, despite the excessive penetration. During the solution process, the penetration and the number of

equilibrium iterations used in each substep must be controlled: if the global convergence difficulty is caused by too much penetration, rather than by residual forces and displacement increments, FKN may be underestimated or FTOLN may be too small [149]. When the solution process finishes, it is necessary to check the penetration values and, if these values are too high, the solution process must be then restarted with higher values of FKN [147].

It is stated in [150] that the value of FKN is the most important parameter affecting both accuracy and the convergence behaviour. They changed that parameter and analysed how much that affected the results of the simulations, and it was observed that decreasing the normal stiffness by 100 times increases the penetration values by 100 times, but the pressures and stresses in the contacts only changed about 1%. Although a zero penetration in contacts will be, theoretically, the ideal value, small or negligible penetrations could be accepted numerically, because zero penetration is not possible with penalty-based methods. In [150], a decrease in FKN was translated into a better agreement between numerical and experimental results, and the subsequent raise in the allowed penetration could be interpreted as more flexibility in the contact.

In the initial stages of this analysis, after introducing the individual copper strands, the contacts between them were modelled as bonded, and the normal stiffness was varied in order to diminish the rigidity of those contacts and to obtain numerical results more similar to the experimental ones. As the force-deflection diagrams had been previously obtained experimentally from the three-point bending tests (see *1.3.4.Conclusions after the bending tests*), a remote force was applied in consecutive steps into the base of the load cylinder, starting from $F = 0\ kN$ and up to $F = 3.5\ kN$. The numerically obtained deformations, in mm, were then compared to the experimental ones. With $FKN = 0.1$, the maximum deflection obtained with the numerical FE model was 17-18 times smaller than the experimentally measured one. With all the contacts set to bonded and $FKN = 0.01$, the maximum deflection was around 7 times smaller than the experimentally measured one, Figure 212. The cause was that those models were not able to represent the behaviour of the CTC samples under bending, because they did not involve any relevant sliding between adjacent copper strands, in contrast with the results of the laboratory experiments, in which that phenomenon was really evident.

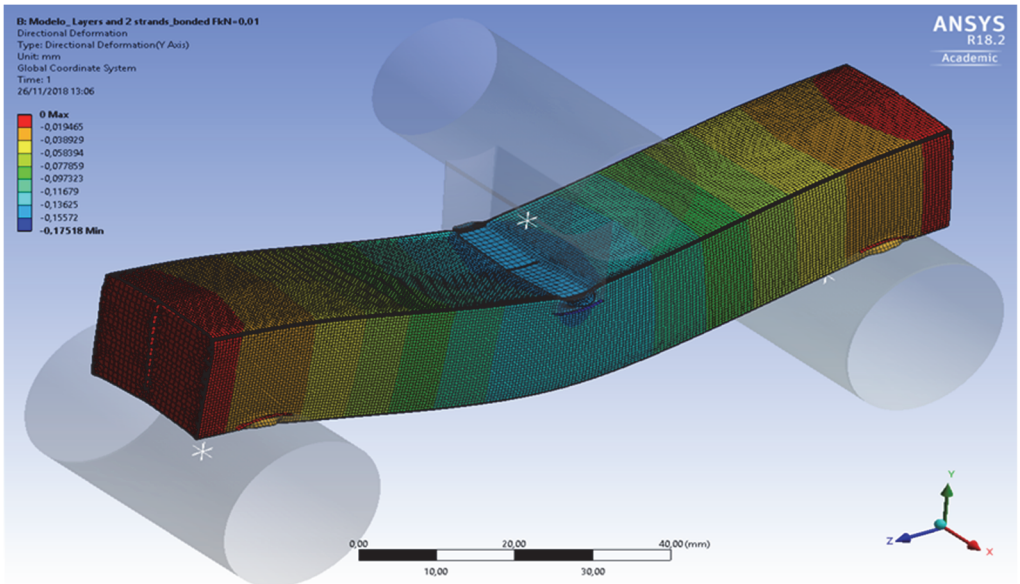

Figure 212. Directional deformation (Y Axis) in the model with all the contacts set as bonded and normal stiffness 0.01.

After those initial analyses, it became clear that some degree of sliding between strands must be introduced into the numerical model to represent the response observed in the laboratory. A *frictional contact* is one in which the interface between the two contacting geometries can withstand shear stresses up to a certain magnitude, before the relative sliding between them starts. That is also known as a "sticking" between two surfaces in contact, which is precisely the behaviour that was observed after the bending tests of the CTC samples in the laboratory. With frictional contact, there is a shear stress at which sliding begins, and that stress is defined by the solver as a fraction of the contact pressure. That type of contact is characterised by a *coefficient of friction*, which can have any non-negative value.

Some different analyses with variable frictional coefficient, k, were carried out in order to capture, firstly, the elastic part of the force-deflection curve. The result was that a frictional coefficient of k = 2.0 was the one that better captured the elastic behaviour of the CTC sample under bending, see Figure 213. Consequently, the contacts between copper strands in the CTC sample were defined as frictional, with *Augmented Lagrange* formulation, a normal stiffness factor $FKN = 0.01$ which was updated in *Each Iteration*, and setting *Add Offset, No Ramping* as interface treatment, Figure 214 (a). In the contacts between the rigid cylinders and the strands, the normal stiffness was updated in *Each Iteration, Aggressive,* Figure 214 (b). The contacts between two adjacent strands were defied as symmetric, while the contact between the rigid cylinders and the strands were defined as asymmetric. When selecting to update the normal contact stiffness with the augmented Lagrange method, the value of the normal stiffness will be changed at each iteration, depending on the mean stress of the underlying elements and the allowable penetration tolerance [149]. For other characteristics of the contact, such as the *detection method*, *penetration tolerance*, *elastic trip tolerance* or the *pinball region*, the *Program Controlled* option was used.

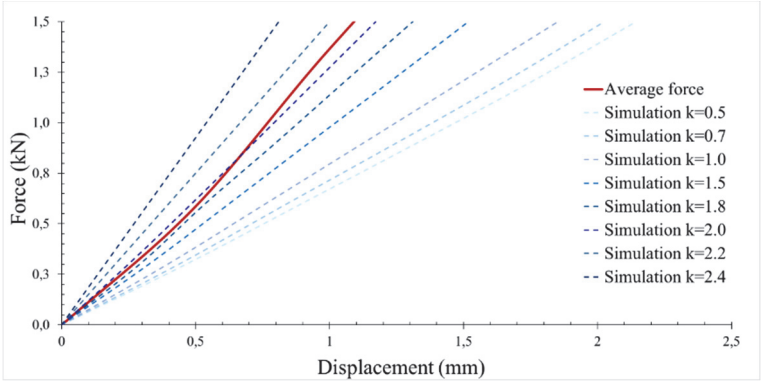

Figure 213. Elastic part of the Force-Displacement curve with different frictional coefficients.

(a)

Details of "Frictional - Cop Lay 4B To Cop Lay 3B"	
Scope	
Scoping Method	Geometry Selection
Contact	3 Faces
Target	3 Faces
Contact Bodies	Cop Lay 4B
Target Bodies	Cop Lay 3B
Definition	
Type	Frictional
Friction Coefficient	2,
Scope Mode	Automatic
Behavior	Symmetric
Trim Contact	Program Controlled
Trim Tolerance	0,3644 mm
Suppressed	No
Advanced	
Formulation	Augmented Lagrange
Small Sliding	Program Controlled
Detection Method	Program Controlled
Penetration Tolerance	Program Controlled
Elastic Slip Tolerance	Program Controlled
Normal Stiffness	Manual
Normal Stiffness Factor	1,e-002
Update Stiffness	Each Iteration
Stabilization Damping Factor	0,
Pinball Region	Program Controlled
Time Step Controls	None
Geometric Modification	
Interface Treatment	Add Offset, No Ramping
Offset	0, mm
Contact Geometry Correction	None
Target Geometry Correction	None

(b)

Details of "Frictional - Cop Lay 8A To Support cylinder 1"	
Scope	
Scoping Method	Geometry Selection
Contact	3 Faces
Target	1 Face
Contact Bodies	Cop Lay 8A
Target Bodies	Support cylinder 1
Definition	
Type	Frictional
Friction Coefficient	2,
Scope Mode	Automatic
Behavior	Asymmetric
Trim Contact	Program Controlled
Trim Tolerance	0,3644 mm
Suppressed	No
Advanced	
Formulation	Augmented Lagrange
Small Sliding	Program Controlled
Detection Method	Program Controlled
Penetration Tolerance	Program Controlled
Elastic Slip Tolerance	Program Controlled
Normal Stiffness	Manual
Normal Stiffness Factor	1,e-002
Update Stiffness	Each Iteration, Aggressive
Stabilization Damping Factor	0,
Pinball Region	Program Controlled
Time Step Controls	None
Geometric Modification	
Interface Treatment	Add Offset, No Ramping
Offset	0, mm
Contact Geometry Correction	None
Target Geometry Correction	None

Figure 214. Characteristics of the frictional contact (a) between two adjacent copper strands, and (b) between a copper strand and a rigid cylinder.

Commands

```
!   Commands inserted into this file will be executed just after the contact region definition.
!   The type number for the contact type is equal to the parameter "cid".
!   The type number for the target type is equal to the parameter "tid".
!   The real and mat number for the asymmetric contact pair is equal to the parameter "cid".
!   The real and mat number for the symmetric contact pair(if it exists) is equal to the parameter "tid".

!   Active UNIT system in Workbench when this object was created:  Metric (mm, kg, N, s, mV, mA)
!   NOTE:  Any data that requires units (such as mass) is assumed to be in the consistent solver unit system.
!               See Solving Units in the help system for more information.

MPDE,MU,cid
TB,FRIC,cid,,,ISO    ! Activate isotropic friction model
TBFIELD,TIME,0.0
TBDATA,1,2.0
TBFIELD,TIME,1.0
TBDATA,1,2.0
TBFIELD,TIME,2.0
TBDATA,1,2.0
TBFIELD,TIME,3.0
TBDATA,1,2.0
TBFIELD,TIME,4.0
TBDATA,1,2.0
TBFIELD,TIME,5.0
TBDATA,1,0.5
TBFIELD,TIME,6.0
TBDATA,1,0.5
TBFIELD,TIME,7.0
TBDATA,1,0.5
TBFIELD,TIME,8.0
TBDATA,1,0.5
TBFIELD,TIME,9.0
TBDATA,1,0.5
TBFIELD,TIME,10.0
TBDATA,1,0.5
TBFIELD,TIME,11.0
TBDATA,1,0.5
TBFIELD,TIME,12.0
TBDATA,1,0.5
TBFIELD,TIME,13.0
TBDATA,1,0.5
TBFIELD,TIME,14.0
TBDATA,1,0.5
TBFIELD,TIME,15.0
TBDATA,1,0.5
TBFIELD,TIME,16.0
TBDATA,1,0.5
TBFIELD,TIME,17.0
TBDATA,1,0.5
TBFIELD,TIME,18.0
TBDATA,1,0.5
TBFIELD,TIME,19.0
TBDATA,1,0.5
TBFIELD,TIME,20.0
TBDATA,1,0.5
TBFIELD,TIME,21.0
TBDATA,1,0.5
TBFIELD,TIME,22.0
TBDATA,1,0.5
TBFIELD,TIME,23.0
TBDATA,1,0.5
TBFIELD,TIME,24.0
TBDATA,1,0.5
TBFIELD,TIME,25.0
TBDATA,1,0.5
TBFIELD,TIME,26.0
TBDATA,1,0.5
TBFIELD,TIME,27.0
TBDATA,1,0.5
TBFIELD,TIME,28.0
```

Graphics Commands

Figure 215. Command for the definition of a variable frictional coefficient. At time step t = 5.0 the frictional coefficient was reduced from 2.0 up to 0.5.

After achieving a relatively good agreement between the experiments and the results of the numerical simulation in the elastic part of the force-displacement curve, the next goal was to model the plastic part of that curve. After some attempts at calibrating the parameters influencing the plastic response in the *Engineering Data* menu of ANSYS AIM, first through the simplification of *Bilinear Isotropic Hardening*, and later through *Multilinear Isotropic Hardening*, it could then be concluded that the behaviour observed in the laboratory tests was heavily conditioned by the rupture of the bonding between some strands, previously created by the melted enamel, more than by the plastification of the copper material. In fact, that rupture was appreciated during the tests, as it produced abrupt decreases in the force at some points in the force-deflection curves (see Figure 174 in *1.3.4.Conclusions after the bending tests*). That behaviour could be modelled by means of a variable frictional coefficient in the different steps of the analysis, which was included by inserting some Commands (APDL) into the contacts, see Figure 215.

Initially, the previous command was inserted into all the contacts between strands, resulting in a very marked decrease in the force at the step in which the frictional coefficient was reduced. For instance, Figure 216 shows the force-displacement diagram for a simulation where the frictional coefficient was k = 2.0 from the beginning of the loading process, up to a deflection of 3 mm and, after that, the frictional coefficient changed to k = 0.5 up to a deflection of 5 mm. The cause of that marked difference between the experimental results and the numerical simulation was that, in the real three-point bending tests over the CTC samples, the sliding did not occur between all the strands at the same time, but there were several consecutive slidings at different deformation levels.

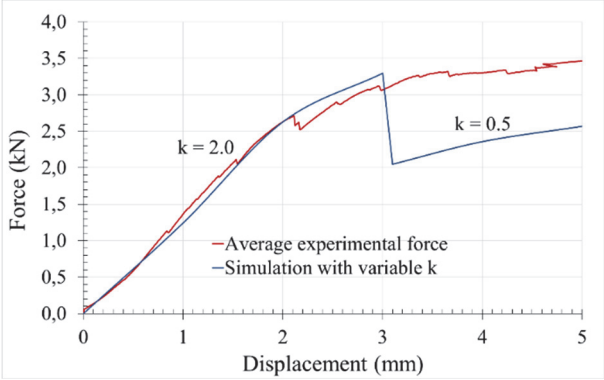

Figure 216. Force-Displacement diagram for the simulation with an initial frictional coefficient of k=2.0, which was reduced to k=0.5 after a deflection of 3 mm for all the contacts between strands.

To reproduce the bending test over the CTC samples up to a final deflection of 20 mm, the vertical displacement was applied in consecutive steps, and the sliding between copper strands was introduced at different levels of deformation, trying to approximately reproduce the average force-deflection curve obtained from the laboratory experiments, see Figure 174, and to remain between the standard deviations. It had been noticed in the laboratory experiments that the initial planes of sliding in the CTC samples appeared between pairs of strands, as seen in Figure 217, and if the deformation continued, the bonding between individual strands also broke afterwards, so that pattern was introduced in the simulation. The ruptures of the bonding at different levels of deformation was represented, firstly, with a reduction of the frictional coefficient from k = 2.0 to k = 0.5, secondly, with a reduction of the coefficient from k = 0.5 to k = 0.1 and, finally, from k = 0.1 to k = 0.01. These values were selected after a long trial and error process, in which some frictional coefficients were introduced into the contact for the plastic part of the force-deflection curve, the curve obtained with the simulation was compared to the experimental one, and the required changes were introduced afterwards. Finally, the variable frictional coefficient used in the different steps, which gave a considerably good agreement between numerical and experimental results, are shown in Table 40.

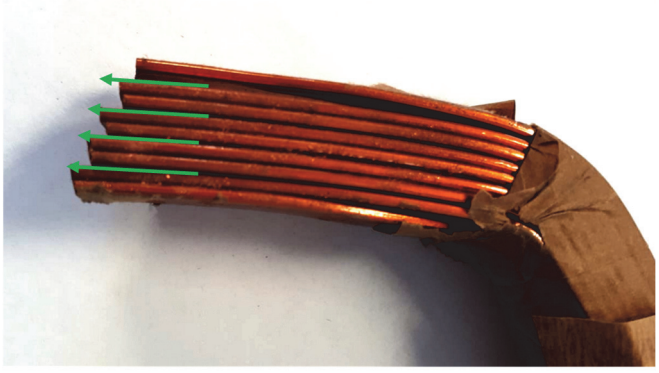

Figure 217. Sliding planes in the CTC sample after the bending test with deflection of 20 mm.

Table 40. Vertical displacement and frictional coefficients between strands in the different steps of the analysis.

Steps	Displacement in Y-direction	Frictional coefficient between adjacent strands			
		k = 2.0	k = 0.5	k= 0.1	k= 0.05
0	0.00	All the contacts	-		
1	-1.00	All the contacts	-		
2	-2.00	All the contacts	-		
3	-3.00	All the contacts	-		
4	-3.50	All the contacts	-		
5	-3.55	0-1, 1-2, 3-4, 0-5, 5-6, 6-7, 7-8	Sliding between 2-3. 2-3	-	
6	-4.50	0-1, 1-2, 3-4, 0-5, 5-6, 6-7, 7-8	2-3	-	
7	-4.55	1-2, 3-4, 0-5, 5-6, 6-7, 7-8	Sliding between 0-1. 0-1, 2-3	-	
8	-5.00	1-2, 3-4, 0-5, 5-6, 6-7, 7-8	0-1, 2-3	-	
9	-5.50	1-2, 3-4, 0-5, 5-6, 7-8	0-1, 2-3	-	
10	-5.55	1-2, 3-4, 0-5, 5-6, 7-8	Sliding between 6-7. 0-1, 2-3, 6-7	-	
11	-6.00	1-2, 3-4, 0-5, 5-6, 7-8	0-1, 2-3, 6-7	-	
12	-6.50	1-2, 3-4, 0-5, 7-8	0-1, 2-3, 6-7	-	
13	-6.55	1-2, 3-4, 0-5, 7-8	Sliding between 5-6. 0-1, 2-3, 5-6, 6-7	-	
14	-7.00	1-2, 3-4, 0-5, 7-8	0-1, 2-3, 5-6, 6-7	-	
15	-7.50	1-2, 3-4, 0-5	0-1, 2-3, 5-6, 6-7	-	
16	-7.55	1-2, 3-4, 0-5	Sliding between 7-8. 0-1, 2-3, 5-6, 6-7, 7-8	-	
17	-8.00	1-2, 3-4, 0-5	0-1, 2-3, 5-6, 6-7, 7-8	-	
18	-8.50	1-2, 3-4, 0-5	0-1, 2-3, 5-6, 6-7, 7-8	-	
19	-9.00	3-4, 0-5	0-1, 2-3, 5-6, 6-7, 7-8	-	
20	-9.05	3-4, 0-5	Sliding between 1-2. 0-1, 1-2, 2-3, 5-6, 6-7, 7-8	-	
21	-9.50	3-4, 0-5	0-1, 1-2, 2-3, 5-6, 6-7, 7-8	-	
22	-10.00	3-4, 0-5	0-1, 1-2, 2-3, 5-6, 6-7, 7-8	-	
23	-10.50	3-4, 0-5	0-1, 1-2, 2-3, 5-6, 6-7, 7-8	-	
24	-10.55	0-5	Sliding between 3-4. 0-1, 1-2, 2-3, 3-4, 5-6, 6-7, 7-8	-	
25	-11.00	0-5	0-1, 1-2, 2-3, 3-4, 5-6, 6-7, 7-8	-	
26	-11.50	0-5	0-1, 1-2, 2-3, 3-4, 5-6, 6-7, 7-8	-	
27	-12.00	0-5	0-1, 1-2, 2-3, 3-4, 5-6, 6-7, 7-8	-	
28	-12.05	-	Sliding between 0-5. 0-1, 1-2, 2-3, 3-4, 0-5, 5-6, 6-7, 7-8	-	
29	-12.50	-	0-1, 1-2, 2-3, 3-4, 0-5, 5-6, 6-7, 7-8	-	
30	-13.00	-	0-1, 1-2, 2-3, 3-4, 0-5, 5-6, 6-7, 7-8	-	

Steps	Displacement in Y-direction	Frictional coefficient between adjacent strands			
		k = 2.0	k = 0.5	k= 0.1	k= 0.05
31	-13.05	-	1-2, 3-4, 0-5, 5-6, 6-7, 7-8	Sliding between 2-3 and 0-1. 0-1, 2-3	-
32	-13.50	-	1-2, 3-4, 0-5, 5-6, 6-7, 7-8	0-1, 2-3	-
33	-14.00	-	1-2, 3-4, 0-5, 5-6, 6-7, 7-8	0-1, 2-3	-
34	-14.05	-	1-2, 3-4, 0-5, 6-7, 7-8	Sliding between 5-6. 0-1, 2-3, 5-6	-
35	-14.50	-	1-2, 3-4, 0-5, 6-7, 7-8	0-1, 2-3, 5-6	-
36	-15.00	-	1-2, 3-4, 0-5, 6-7, 7-8	0-1, 2-3, 5-6	-
37	-15.05	-	1-2, 3-4, 0-5, 6-7	Sliding between 7-8. 0-1, 2-3, 5-6, 7-8	-
38	-15.50	-	1-2, 3-4, 0-5, 6-7	0-1, 2-3, 5-6, 7-8	-
39	-15.55	-	1-2, 3-4, 6-7	Sliding between 0-5. 0-1, 2-3, 0-5, 5-6, 7-8	-
40	-16.00	-	1-2, 3-4, 6-7	0-1, 2-3, 0-5, 5-6, 7-8	-
41	-16.05	-	1-2, 6-7	Sliding between 3-4. 0-1, 2-3, 3-4, 0-5, 5-6, 7-8	-
42	-16.50	-	1-2, 6-7	0-1, 2-3, 3-4, 0-5, 5-6, 7-8	-
43	-16.55	-	1-2	Sliding between 6-7. 0-1, 2-3, 3-4, 0-5, 5-6, 6-7, 7-8	-
44	-17.00	-	1-2	0-1, 2-3, 3-4, 0-5, 5-6, 6-7, 7-8	-
45	-17.05	-		Sliding between 1-2. 0-1, 1-2, 2-3, 3-4, 0-5, 5-6, 6-7, 7-8	-
46	-17.50	-		0-1, 1-2, 2-3, 3-4, 0-5, 5-6, 6-7, 7-8	-
47	-17.55	-		0-1, 1-2, 3-4, 0-5, 5-6, 6-7, 7-8	Sliding between 2-3. 2-3
48	-18.00	-		0-1, 1-2, 3-4, 0-5, 5-6, 6-7, 7-8	2-3
49	-18.05	-		1-2, 3-4, 0-5, 5-6, 6-7, 7-8	Sliding between 0-1. 0-1, 2-3
50	-18.50	-		1-2, 3-4, 0-5, 5-6, 6-7, 7-8	0-1, 2-3
51	-18.55	-		1-2, 3-4, 0-5, 5-6, 7-8	Sliding between 6-7. 0-1, 2-3, 6-7
52	-19.00	-		1-2, 3-4, 0-5, 5-6, 7-8	0-1, 2-3, 6-7
53	-19.05	-		1-2, 3-4, 0-5, 7-8	Sliding between 5-6. 0-1, 2-3, 5-6, 6-7
54	-19.50	-		1-2, 3-4, 0-5, 7-8	0-1, 2-3, 5-6, 6-7
55	-19.55	-		1-2, 3-4, 0-5	Sliding between 7-8. 0-1, 2-3, 5-6, 6-7,7-8
56	-20.00	-		1-2, 3-4, 0-5	0-1, 2-3, 5-6, 6-7,7-8

2.2. Deformation, stress and strain distributions obtained in the CTC samples through the numerical simulation

The force-displacement curves obtained experimentally and from the numerical simulation are shown in Figure 218, where it can be seen that the agreement between them is rather good up to a deformation of about 17 mm. The abrupt decreases in the force at some

levels of deformation are caused by the initiation of the sliding between two adjacent copper strands, modelled through a variable frictional coefficient, something that was also observed in the laboratory tests (see Figure 174 from *1.3.4.Conclusions after the bending tests*). For deformations larger than 19 mm, the force obtained with the numerical simulation exceeds the *Average Force + Standard Deviation* calculated from the experimental results. However, the average peak force in the three-point bending tests with final deflection d = 20 mm, is around 3.89 kN, which is very similar to the maximum reaction force obtained with the simulation, F ≃ 3.8 kN when d = 20 mm. Consequently, it is considered that the strain states obtained from this simulation when d = 20 mm could be feasible in a realistic situation. The directional deformation in the different areas of the CTC sample was obtained with the numerical simulation, for maximum deflections of 5 mm, 10 mm and 20 mm, respectively, in Figure 219-Figure 221.

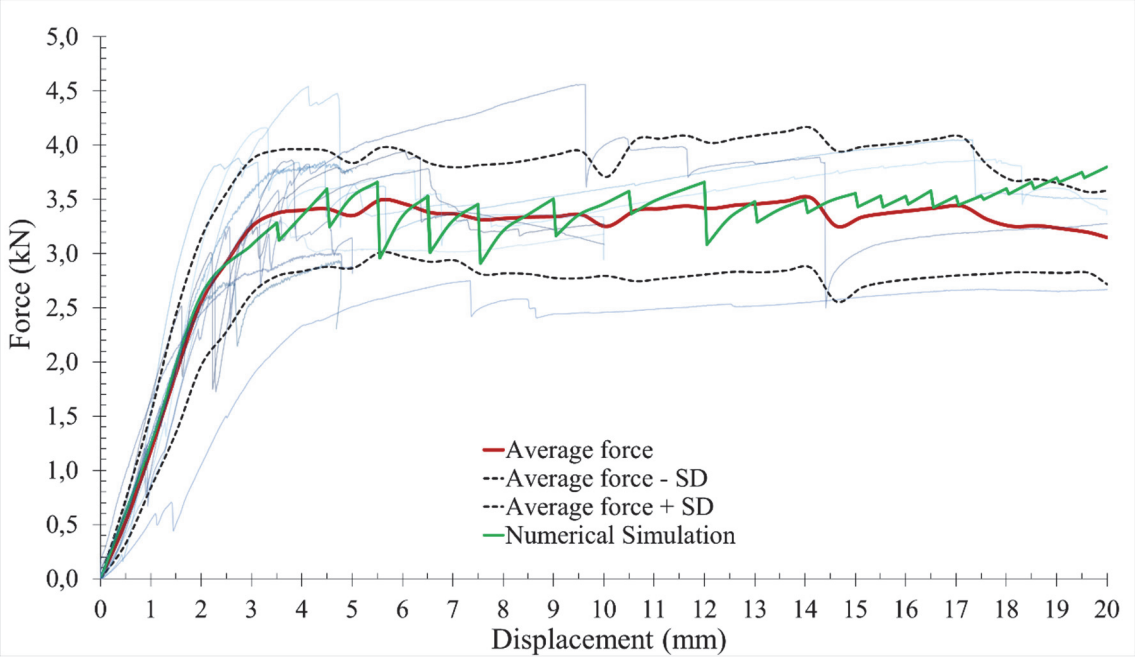

Figure 218. Comparison of the experimental and simulated force-displacement curves.

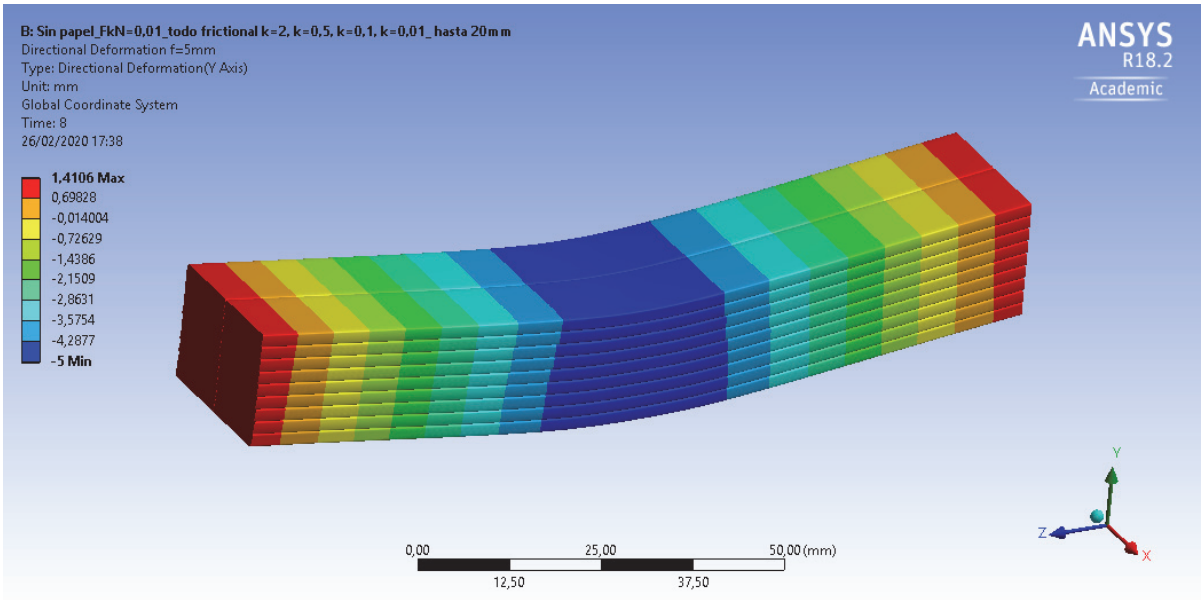

Figure 219. Directional deformation (in -Y direction) for the simulated bending test with final deflection of 5 mm.

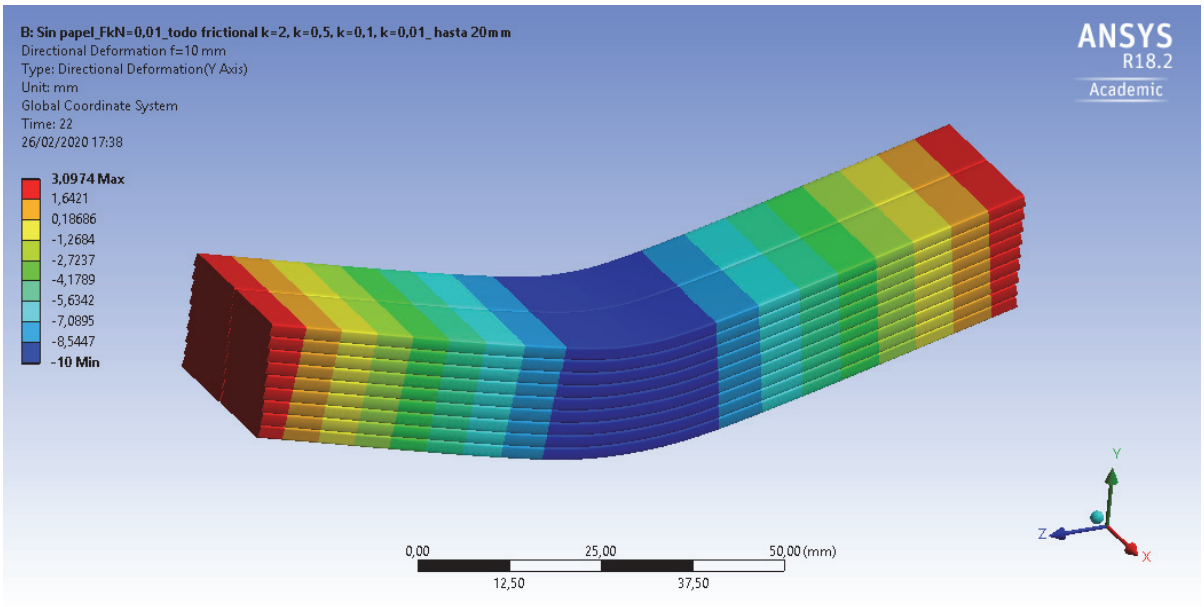

Figure 220. Directional deformation (in -Y direction) for the simulated bending test with final deflection of 10 mm.

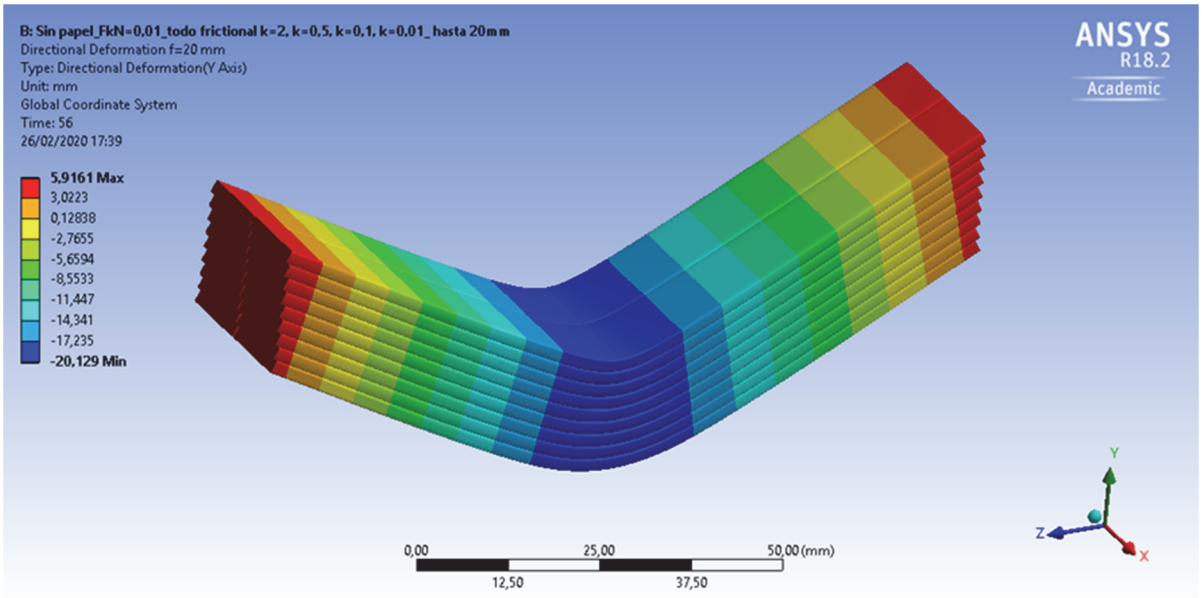

Figure 221. Directional deformation (in -Y direction) for the simulated bending test with final deflection of 20 mm.

The equivalent stress suffered by the copper CTC sample is relevant because the stress level determines the areas of the conductor which will plastify. In those areas, the strain is non-reversible and larger than in the non-plastified areas, and that will cause the strains in the paper to be higher also. The central area, where the load cylinder contacts the CTC sample, is the most stressed, reaching stresses higher than 200 MPa when the deflection is $d = 5\ mm$, and that area will be the first to get irreversible deformations. It can be seen in Figure 222-Figure 224, how the stress level increases when the final deflection rises from 5 mm up to 20 mm. The relevant growth in the extension of plastified areas in the copper CTC sample due to that increment in the final deflection can be seen in Figure 225-Figure 227.

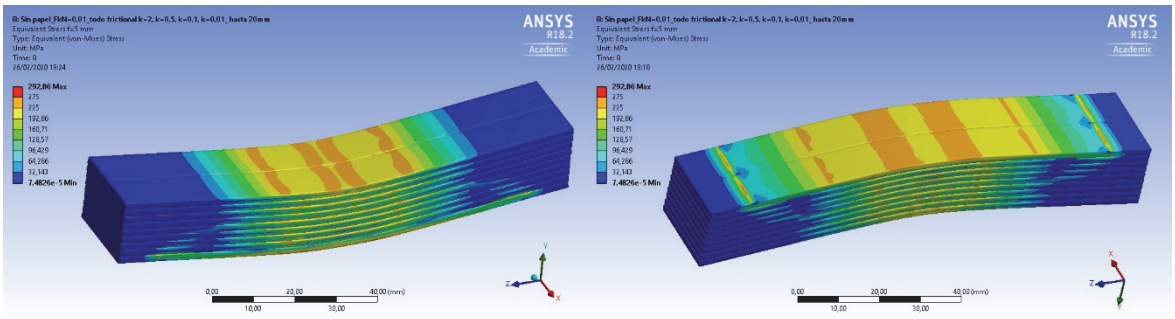

Figure 222. Equivalent (von-Mises) stress for the simulated bending test with final deflection of 5 mm.

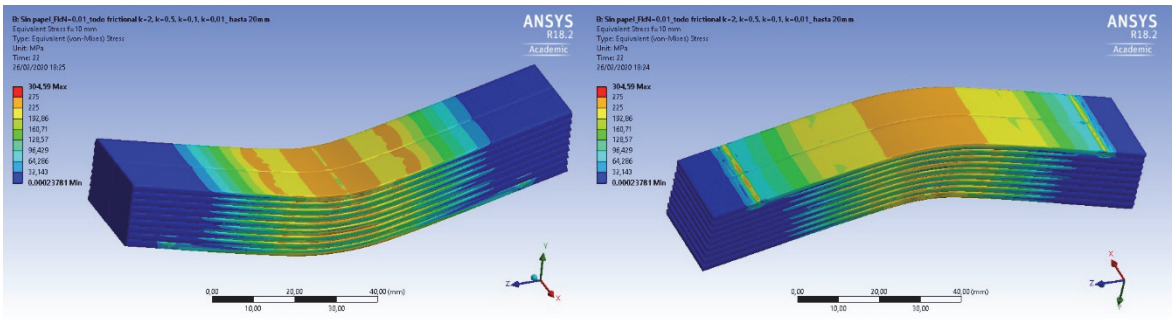

Figure 223. Equivalent (von-Mises) stress for the simulated bending test with final deflection of 10 mm.

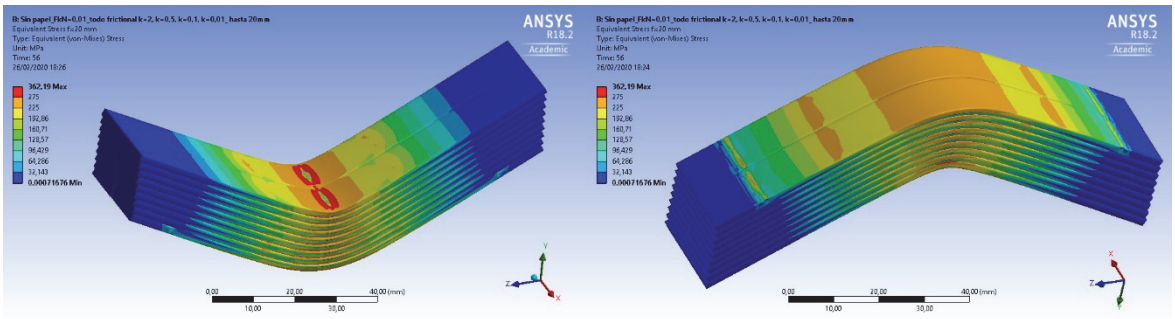

Figure 224. Equivalent (von-Mises) stress for the simulated bending test with final deflection of 20 mm.

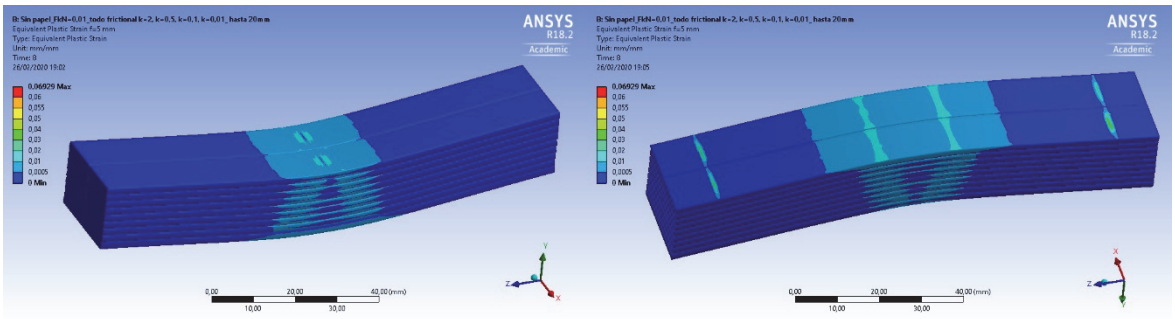

Figure 225. Equivalent plastic strain in principal axes for the simulated bending test with final deflection of 5 mm.

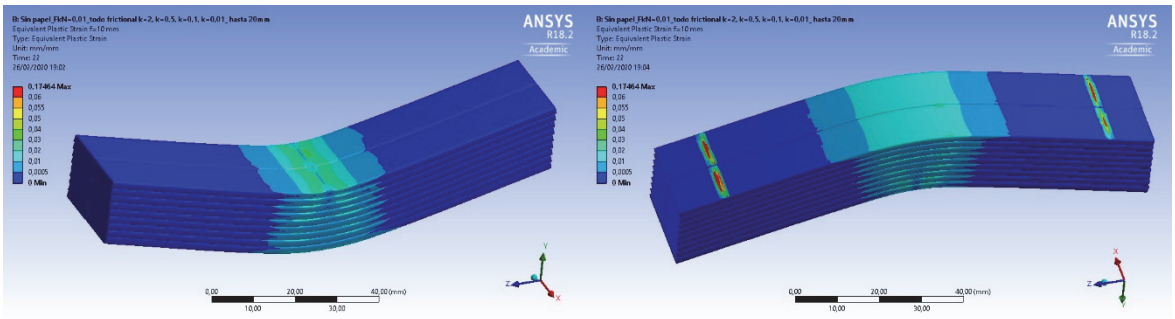

Figure 226. Equivalent plastic strain in principal axes for the simulated bending test with final deflection of 10 mm.

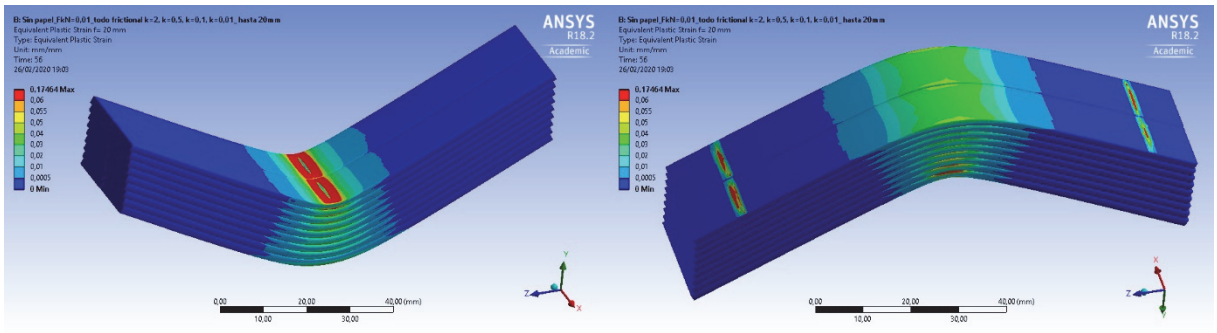

Figure 227. Equivalent plastic strain in principal axes for the simulated bending test with final deflection of 20 mm.

However, as the paper material was not included in the numerical model, only the strain field in it can be estimated, by assuming that it is similar to the one on the external surfaces of the copper conductor. As mentioned before, this is a conservative assumption, as the strain values will always be lower than those predicted in the copper surface, as the insulation layers are able to slide (except in the case of layer 1, which is glued to the CTC sample as a result of the ageing process, and will be subjected to the same strains as the CTC surface). Because of that, the construction of a failure model for the paper insulation described in *3.Failure criteria for the paper insulation of the CTC* has to be based on strains. As the maximum-strain-at-break values of paper insulation subjected to different mechanical solicitations are known only along the principal material axes (MD, CD, ZD), see *1.2.Characterisation of the paper insulation samples*, before comparing the results of the simulation with those values, a transformation of axes is needed, from the calculated strain field in (X, Y, Z) to those material axes. A uniaxial stress (or strain) applied in any direction other than the principal material axes generates multiaxial stresses (or strains) along the principal material axes. Besides, the orientation of the main material directions in the paper insulation changes in the different sides of the CTC sample, according to the wrapping direction. On the upper and the lower faces of the CTC, Figure 228 and Figure 229, Y-direction of the CTC coordinate system coincides with ZD of the paper coordinate system, and directions (MD, CD) can be obtained after performing a clockwise rotation of 20º in axes (X, Z). On the other hand, in the lateral sides of the CTC, Figure 230, X-direction of the CTC coordinate system coincides with ZD of the paper coordinate system, and directions (MD, CD) can be obtained after performing a clockwise rotation of 30º in axes (Y, Z).

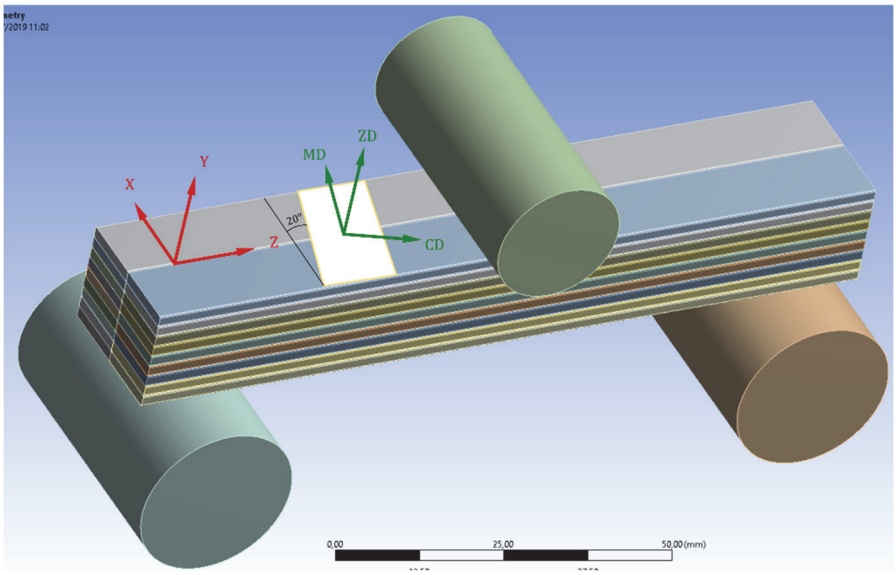

Figure 228. Coordinate systems of the model (X, Y, Z) and of the paper material (MD, CD, ZD) in the upper faces.

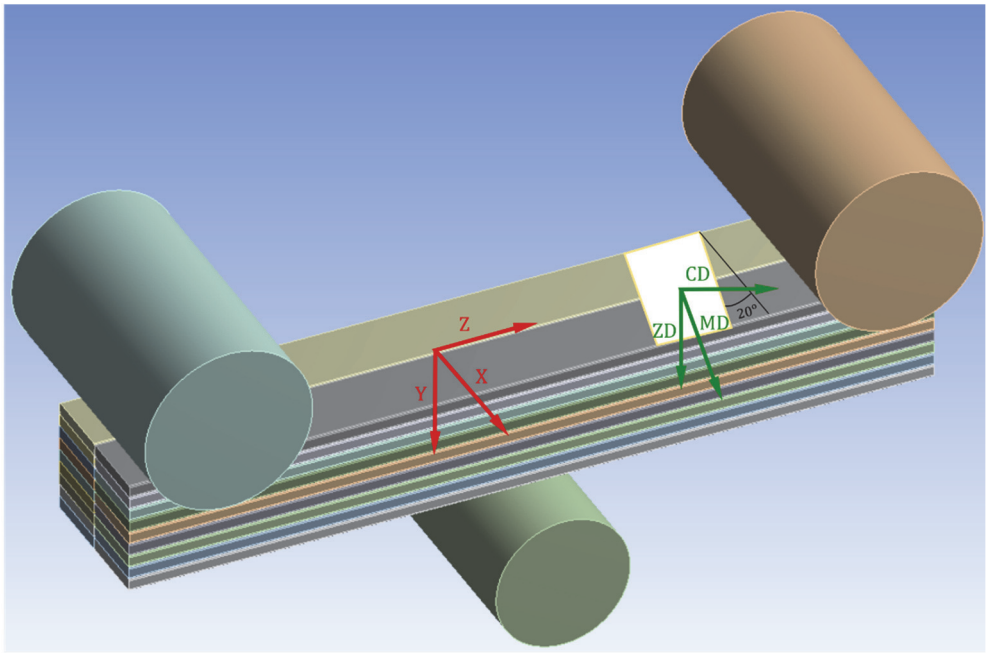

Figure 229. Coordinate systems of the model (X, Y, Z) and of the paper material (MD, CD, ZD) in the lower faces.

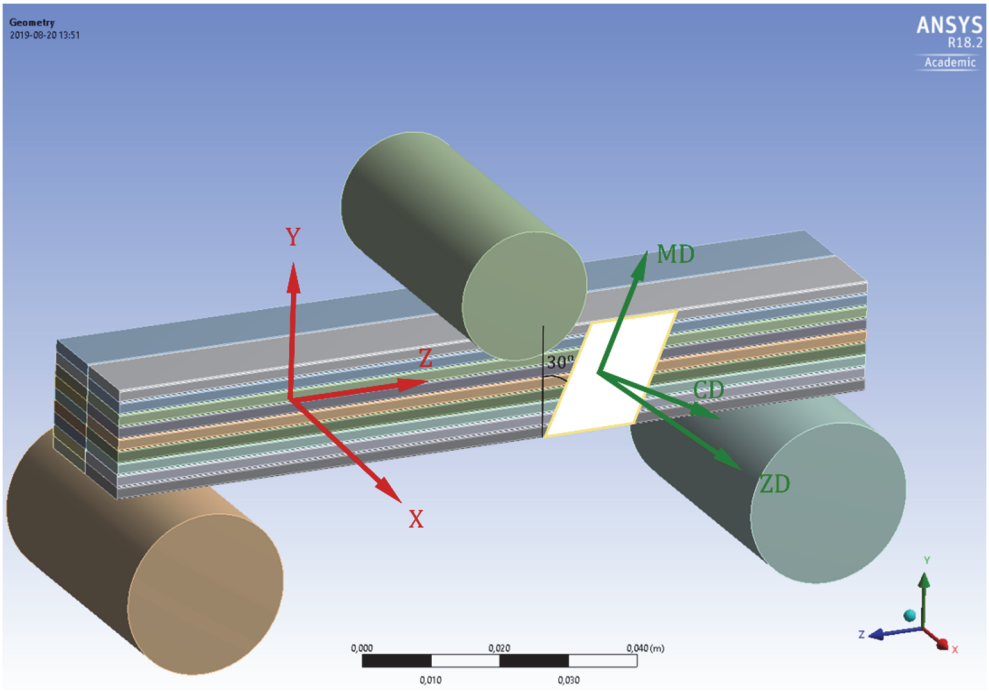

Figure 230. Coordinate systems of the model (X, Y, Z) and of the paper material (MD, CD, ZD) in one lateral face.

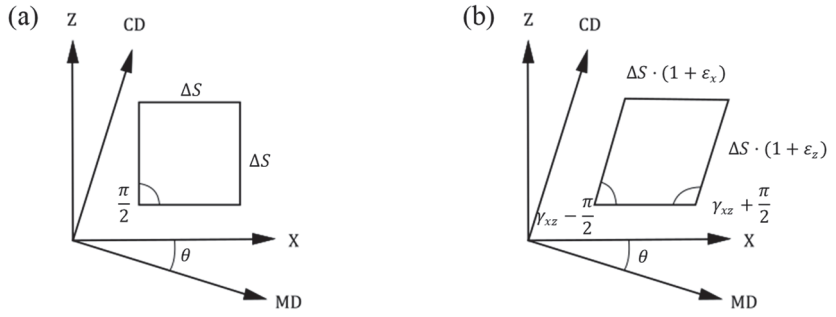

Figure 231. (a) Non-deformed and (b) deformed surface element, with the coordinate systems of the CTC (X, Z) and of the paper material (MD, CD)

In Figure 231, a surface element contained in the XZ plane is represented before and after being deformed, and both the coordinate systems can be seen. If the strains $(\varepsilon_X, \varepsilon_Z, \gamma_{XZ})$ in the original coordinate system (X, Z) are known, the strains in the coordinate system of the paper material (MD, CD) can be obtained from equations (115), (116) and (117), according to [151]:

$$\varepsilon_{MD} = \varepsilon_X cos^2\theta + \varepsilon_Z sin^2\theta + \gamma_{XZ} \sin\theta \cos\theta = \left(\frac{\varepsilon_X + \varepsilon_Z}{2}\right) + \left(\frac{\varepsilon_X - \varepsilon_Z}{2}\right) \cos 2\theta + \frac{\gamma_{XZ}}{2} \sin 2\theta \quad (115)$$

$$\varepsilon_{CD} = \varepsilon_X sin^2\theta + \varepsilon_Z cos^2\theta - \gamma_{XZ} \sin\theta \cos\theta = \left(\frac{\varepsilon_X + \varepsilon_Z}{2}\right) - \left(\frac{\varepsilon_X - \varepsilon_Z}{2}\right) \cos 2\theta - \frac{\gamma_{XZ}}{2} \sin 2\theta \quad (116)$$

$$\gamma_{MD-CD} = 2(\varepsilon_Z - \varepsilon_X) \sin\theta \cos\theta + \gamma_{XZ}(cos^2\theta - sin^2\theta) = (\varepsilon_Z - \varepsilon_X) \sin 2\theta + \gamma_{XZ} \cos 2\theta \quad (117)$$

It should be noted that there are two usual notations to working with strains, the scientific and the engineering ones, which are indicated in equation (118). The engineering shear strains $(\gamma_{xy},\ \gamma_{xz}, \gamma_{yz})$ are twice the tensor shear strains $(\varepsilon_{xy}, \varepsilon_{xz}, \varepsilon_{yz})$ in scientific notation:

$$\{\varepsilon\} \equiv \begin{pmatrix} \varepsilon_x & \varepsilon_{xy} & \varepsilon_{xz} \\ \varepsilon_{xy} & \varepsilon_y & \varepsilon_{yz} \\ \varepsilon_{xz} & \varepsilon_{yz} & \varepsilon_z \end{pmatrix} \equiv \begin{pmatrix} \varepsilon_x & \frac{1}{2}\gamma_{xy} & \frac{1}{2}\gamma_{xz} \\ \frac{1}{2}\gamma_{xy} & \varepsilon_y & \frac{1}{2}\gamma_{yz} \\ \frac{1}{2}\gamma_{xz} & \frac{1}{2}\gamma_{yz} & \varepsilon_z \end{pmatrix} \quad (118)$$

To obtain the strains ε_{MD}, ε_{CD} and γ_{MD-CD} with ANSYS AIM, four named selections were defined in the external faces of the modelled CTC sample: one on the upper faces, another on the lower faces, and two more in both lateral sides, Figure 232. Some *User Defined Results* were defined with *Scoping Method = Named Selection*, using expressions (115), (116) and (117) for obtaining the strains in MD and CD from the total strains (elastic, $EPEL$, and plastic, $EPPL$, strains) in the principal directions. In ANSYS, $EPELXZ$ and $EPPLXZ$ represent the elastic and plastic engineering strains, $\gamma_{xz\ elastic}$ and $\gamma_{xz\ plastic}$.

On the upper and lower faces of the CTC sample, equations (119), (120) and (121) were introduced as *User Defined Results*:

$$\varepsilon_{MD} = \big((EPELX + EPPLX) * cos^2 20 + (EPELZ + EPPLZ) * sin^2 20 + (EPELXZ + EPPLXZ) * \sin 20 * \cos 20\big) * 100 \quad (119)$$

$$\varepsilon_{CD} = \big((EPELX + EPPLX) * sin^2 20 + (EPELZ + EPPLZ) * cos^2 20 - (EPELXZ + EPPLXZ) * \sin 20 * \cos 20\big) * 100 \quad (120)$$

$$\gamma_{MD-CD} = ((-(EPELX + EPPLX) + (EPELZ + EPPLZ)) * \sin(2 * 20) + (EPELXZ + EPPLXZ) * \cos(2 * 20)) * 100 \quad (121)$$

Analogously, on the lateral sides of the CTC sample, equations (122), (123) and (124) were introduced as *User Defined Results*:

$$\varepsilon_{MD} = \big((EPELY + EPPLY) * cos^2 30 + (EPELZ + EPPLZ) * sin^2 30 + (EPELYZ + EPPLYZ) * \sin 30 * \cos 30\big) * 100 \quad (122)$$

$$\varepsilon_{CD} = \big((EPELY + EPPLY) * sin^2 30 + (EPELZ + EPPLZ) * cos^2 30 - (EPELYZ + EPPLYZ) * \sin 30 * \cos 30\big) * 100 \quad (123)$$

$$\gamma_{MD-CD} = ((-(EPELY + EPPLY) + (EPELZ + EPPLZ)) * \sin(2 * 30) + (EPELYZ + EPPLYZ) * \cos(2 * 30)) * 100 \quad (124)$$

Where:

$EPELX, EPELZ, EPELXZ$: Elastic strains in directions X, Z and XZ, respectively.

$EPPLX, EPPLZ, EPPLXZ$: Plastic strains in directions X, Z and XZ, respectively.

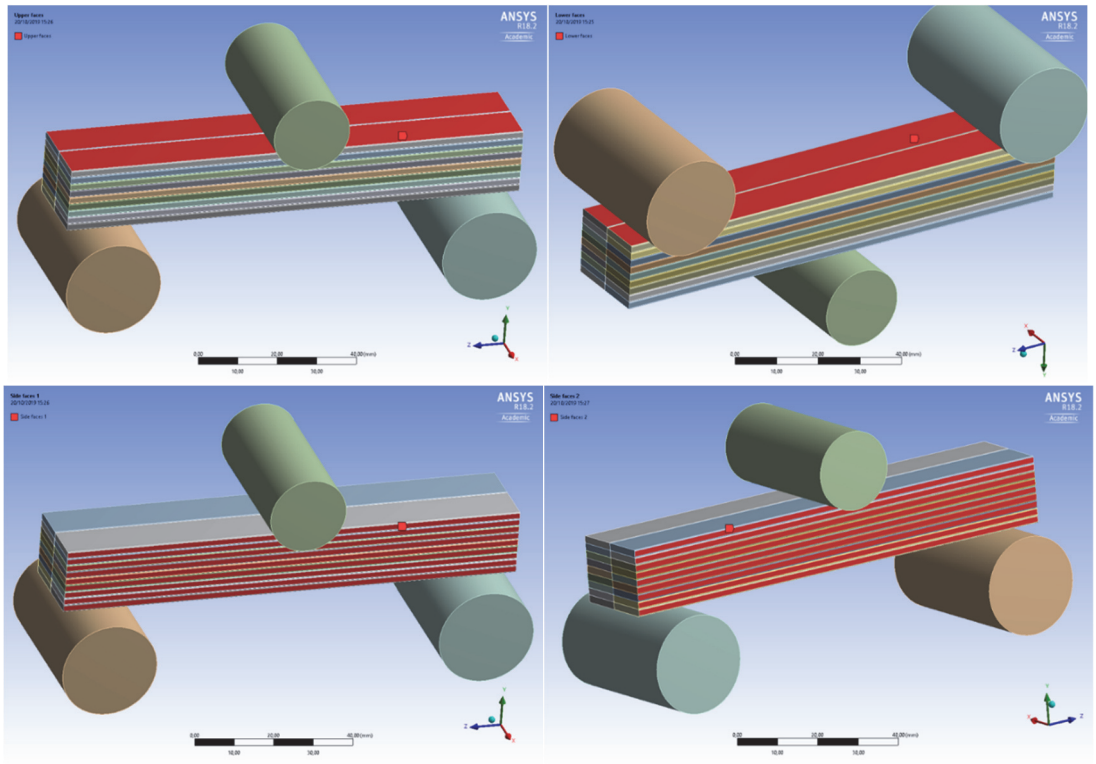

Figure 232. Named selections on the upper, lower and lateral faces of the CTC sample.

The total strains in the main directions of the paper material, on the upper faces of the CTC sample, can be seen in Figure 233-Figure 241. For all the numerical simulations with final deflections between 5 and 20 mm, the strain values in CD and shear in MD-CD were considerably higher than the strains in MD. Regarding the strains in MD, almost the whole surface of the upper faces is subjected to tension, but some small areas are subjected to compression. The maximum tensile strains in MD increased from around 0.4% up to around 1% between d = 5 mm and d = 10 mm, and up to 2.5% when d = 20 mm. The highest compressive strains in MD were around -0.14% when d = 5 mm, and around -0.5% when d = 20 mm.

Regarding the strains in CD on the upper faces of the CTC sample, almost the whole surface is subjected to compression and the strain values in the central part are between -1 and -1.2% when d = 5 mm, between -1.5 and -2.861% when d = 10 mm, and between -3 and -10.434% when d = 20 mm. Consequently, there was a considerable increase in the value of ε_{CD} between those deflections, which will contribute to the appearance of fractures in the paper. With respect to the shear strains, $\gamma_{\mathrm{MD}-CD}$, they were of a very similar order of magnitude than the strains in CD. The maximum values are between -1 and -1.2% when d = 5 mm, between -1.5 and -3.464% when d = 10 mm, and between -3 and -9.998% when d = 20 mm.

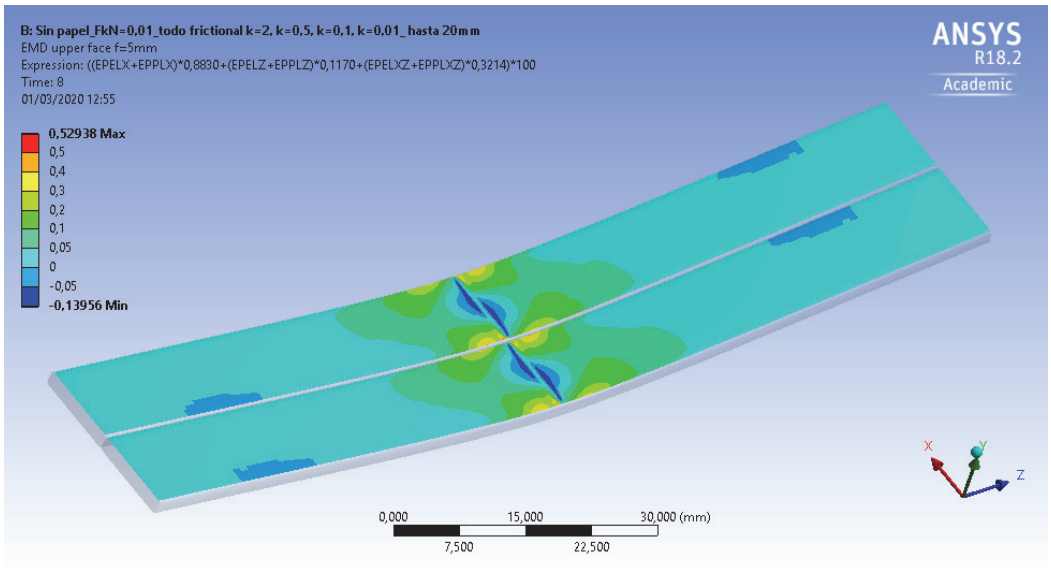

Figure 233. Strain ε_{MD} (%) on the upper face, for a final deflection of 5 mm.

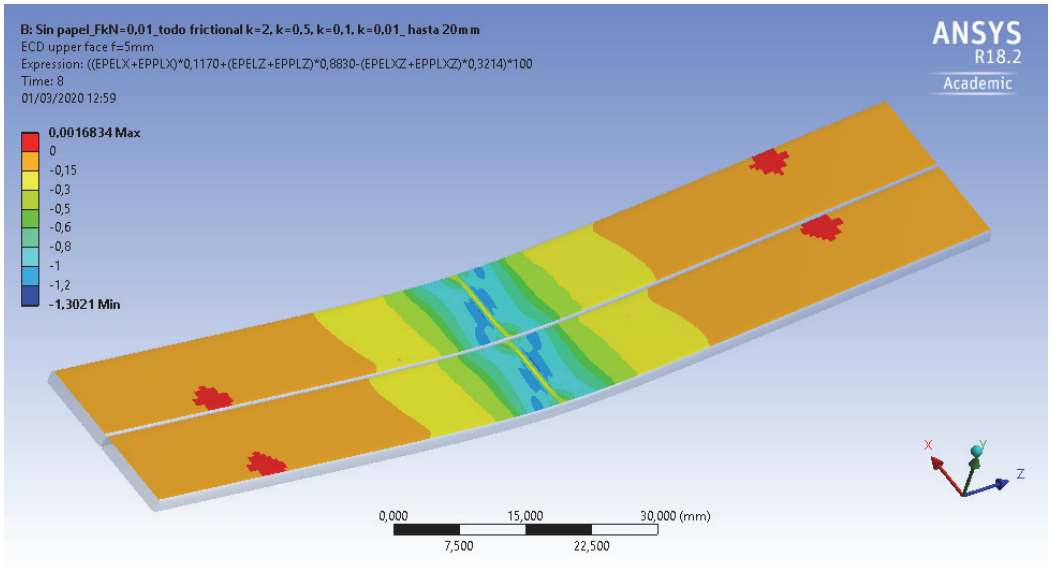

Figure 234. Strain ε_{CD} (%) on the upper face, for a final deflection of 5 mm.

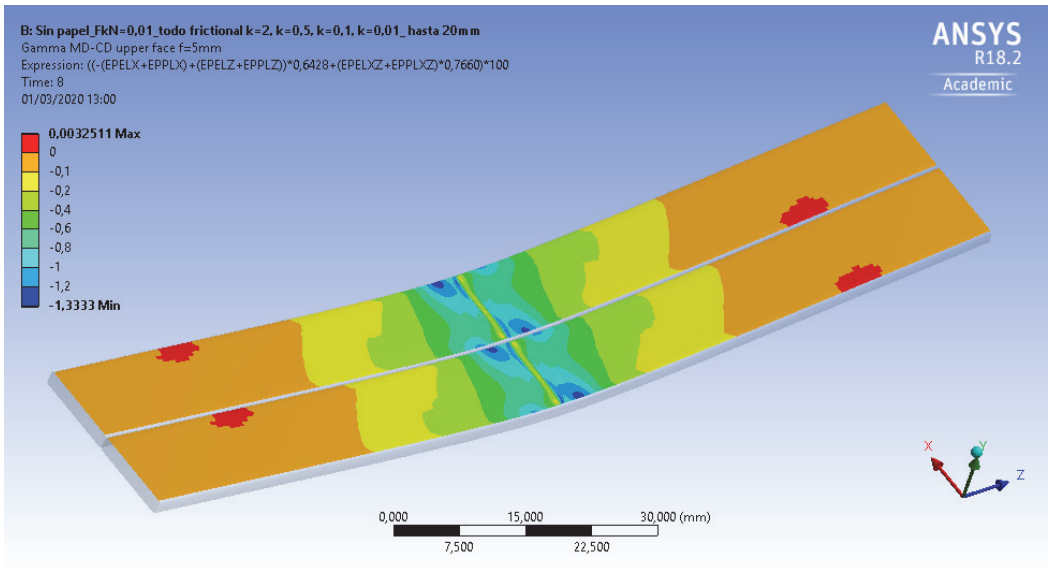

Figure 235. Shear strain γ_{MD-CD} (%) on the upper face, for a final deflection of 5 mm.

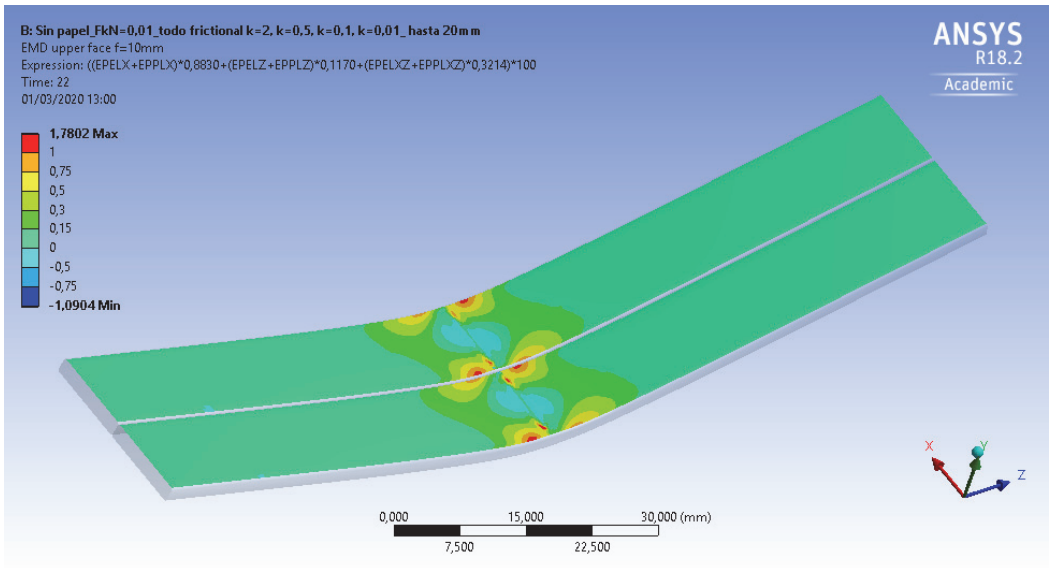

Figure 236. Strain ε_{MD} (%) on the upper face, for a final deflection of 10 mm.

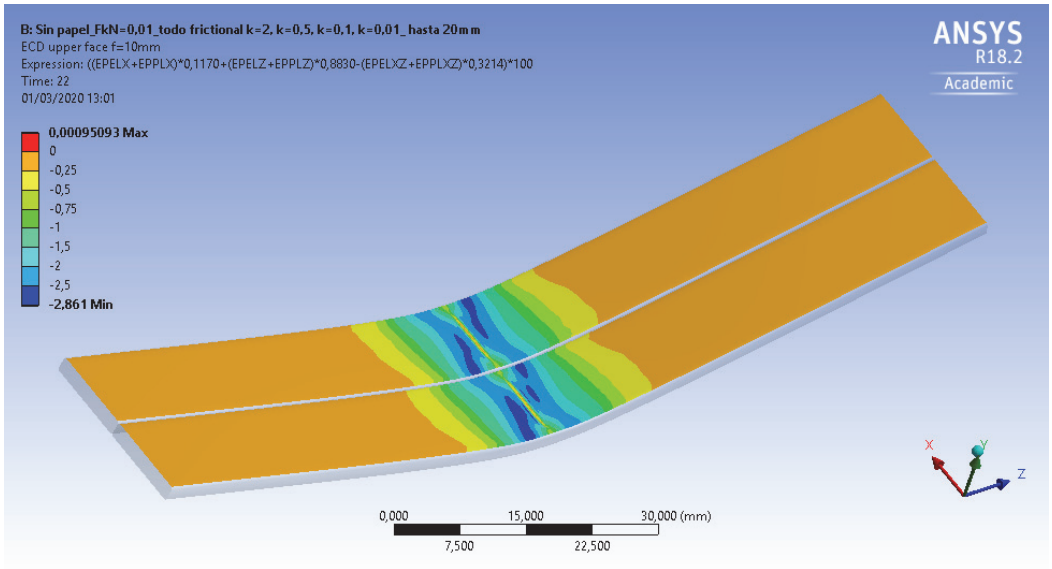

Figure 237. Strain ε_{CD} (%) on the upper face, for a final deflection of 10 mm.

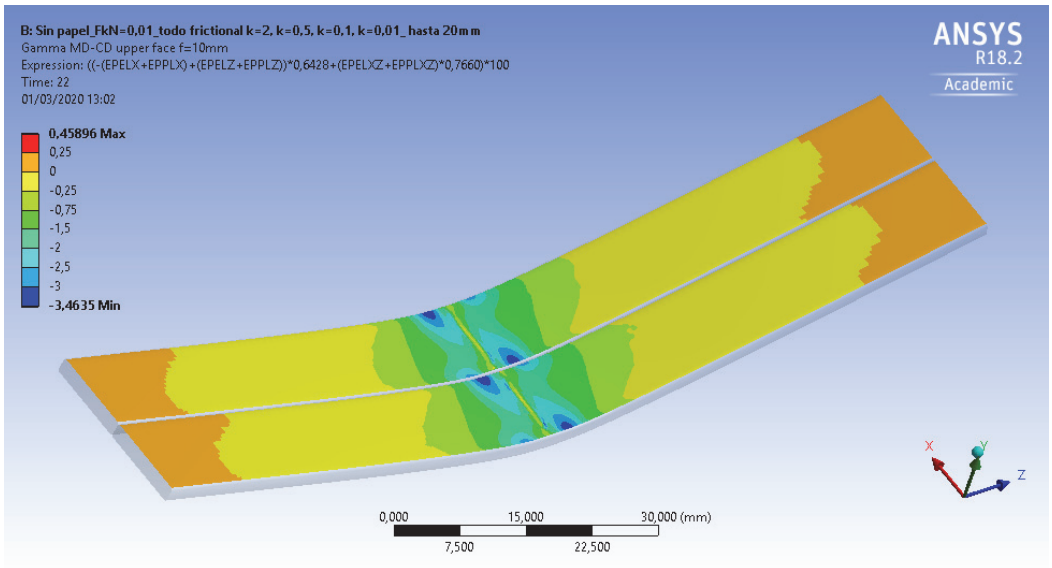

Figure 238. Shear strain γ_{MD-CD} (%) on the upper face, for a final deflection of 10 mm.

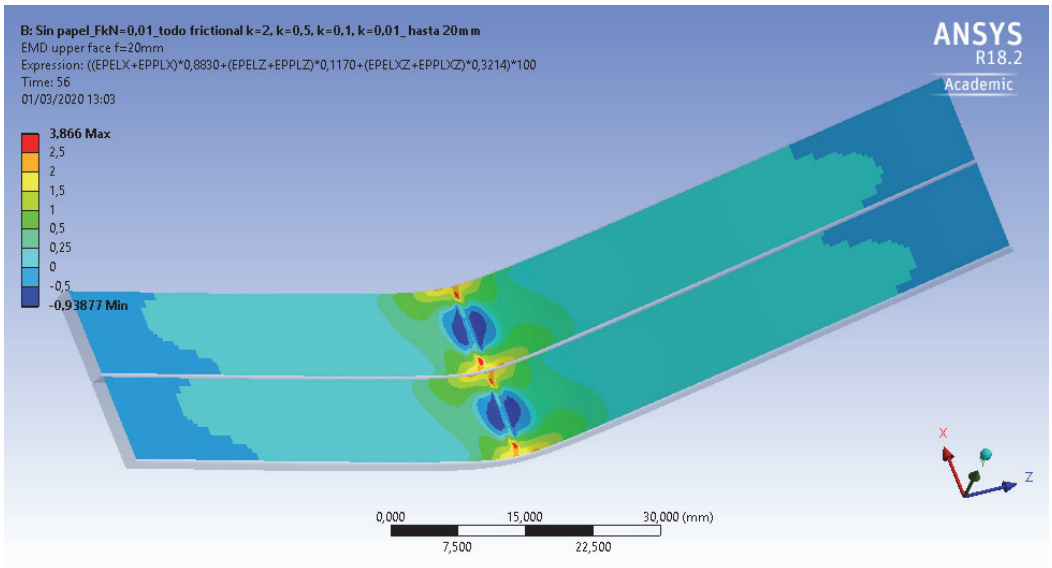

Figure 239. Strain ε_{MD} (%) on the upper face, for a final deflection of 20 mm.

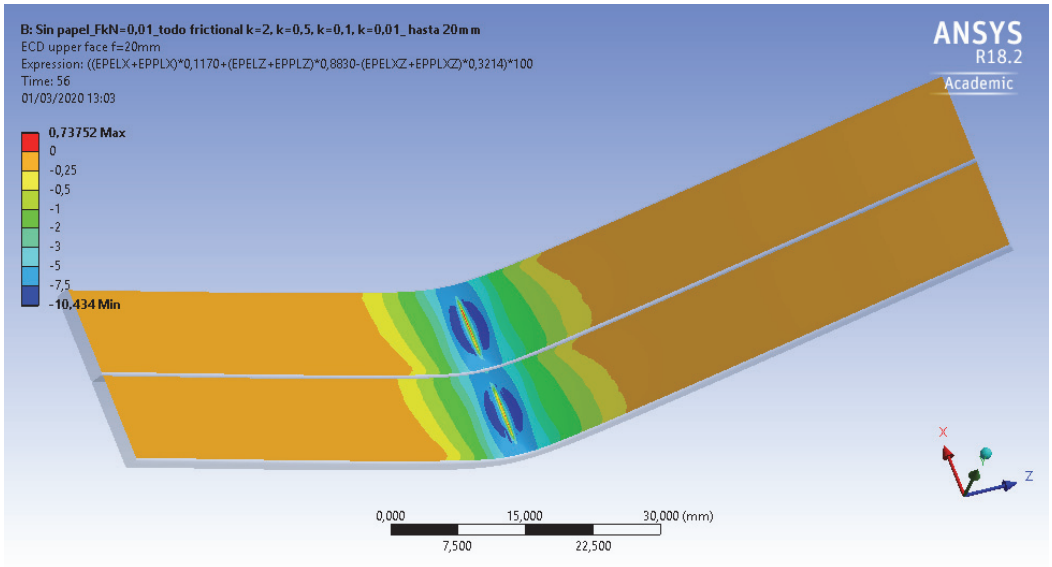

Figure 240. Strain ε_{CD} (%) on the upper face, for a final deflection of 20 mm.

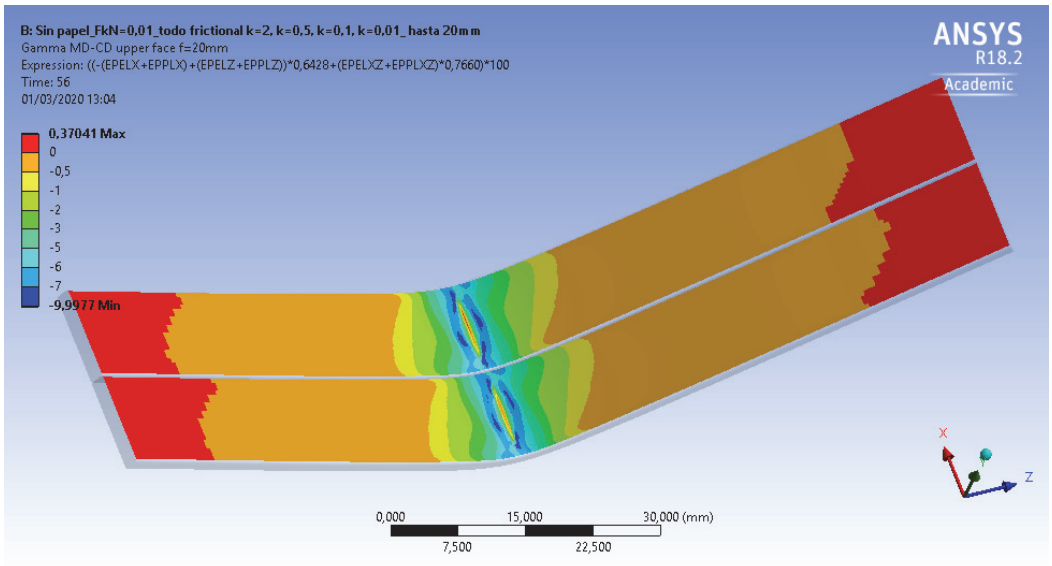

Figure 241. Shear strain γ_{MD-CD} (%) on the upper face, for a final deflection of 20 mm.

The total strains in the main directions of the paper material, on the lower faces of the CTC sample, can be seen in Figure 242-Figure 250. In this area of the CTC sample, the strains in MD are also considerably lower than the strains in CD or the shear strains, for all the deflections. The values of ε_{CD} and $\gamma_{\mathrm{MD}-CD}$ are of a similar order of magnitude. The ends of the lower faces of the CTC sample are subjected to tension and the centre is subjected to compression in MD. The tensile values, which are between ε_{MD}= 0.1% and 0.25%, do not vary much between the maximum deformations of d = 5 mm and d = 20 mm. The compressive values of ε_{MD} increase between -0.2 and -0.427% when d = 5 mm, -0.5 and -0.739% when d = 10 mm, and -1 and -1.451% when d = 20 mm. Regarding the strains in CD, almost the whole lower surface of the CTC sample is subjected to tension and only the ends are subjected to compressions, whose magnitude remain almost constant with a value of -0.5%. The values of ε_{CD} in the centre of the upper faces are between 1-2% when d = 5 mm, 1.5-2% when d = 10 mm, and 2-5 % when d = 20 mm. Furthermore, almost the whole lower surface was subjected to positive strains in shear, and the values of $\gamma_{\mathrm{MD}-CD}$ in the central area of the lower faces in the CTC sample were between 1-1.5% when d = 5 mm, between 1.5-2 % when d = 10 mm, and between 2.5-5 % when d = 20 mm.

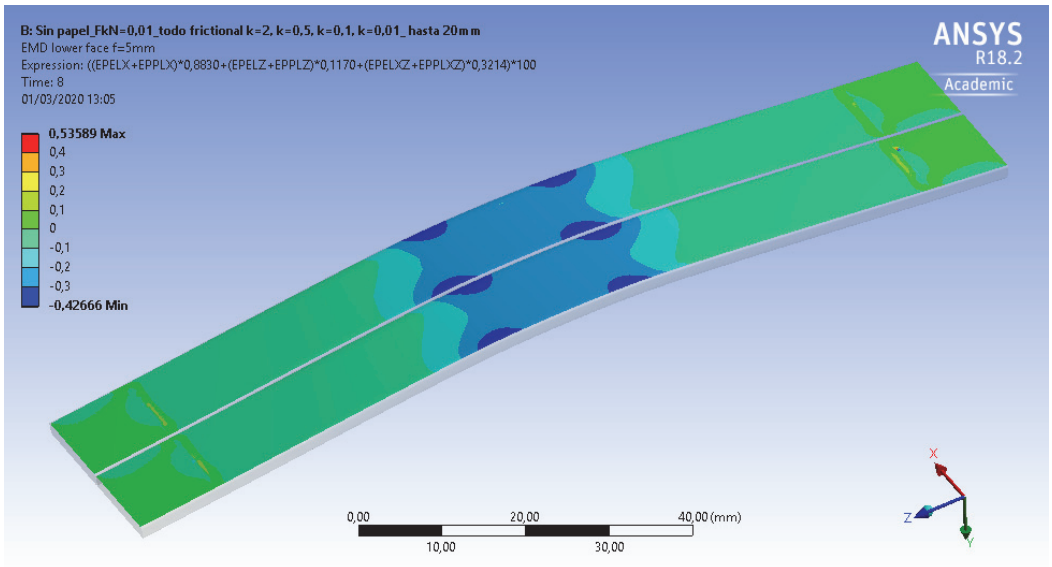

Figure 242. Strain ε_{MD} (%) on the lower face, for a final deflection of 5 mm.

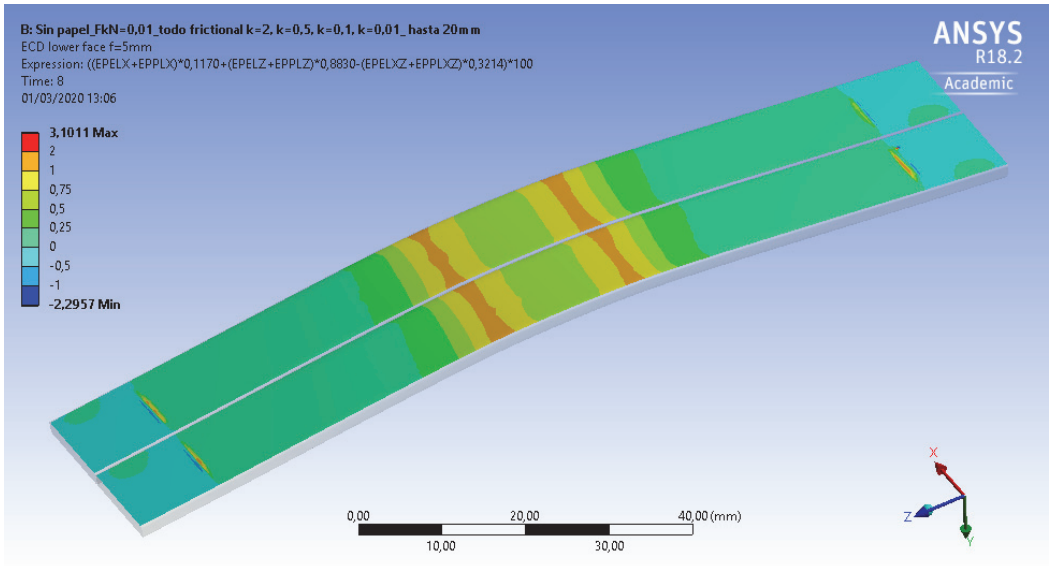

Figure 243. Strain ε_{CD} (%) on the lower face, for a final deflection of 5 mm.

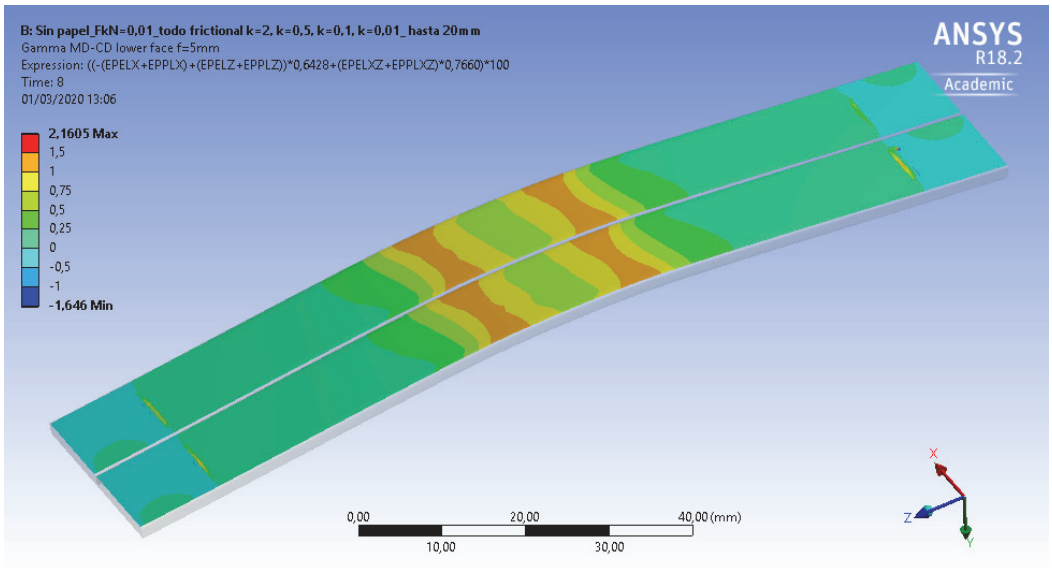

Figure 244. Shear strain γ_{MD-CD} (%) on the lower face, for a final deflection of 5 mm.

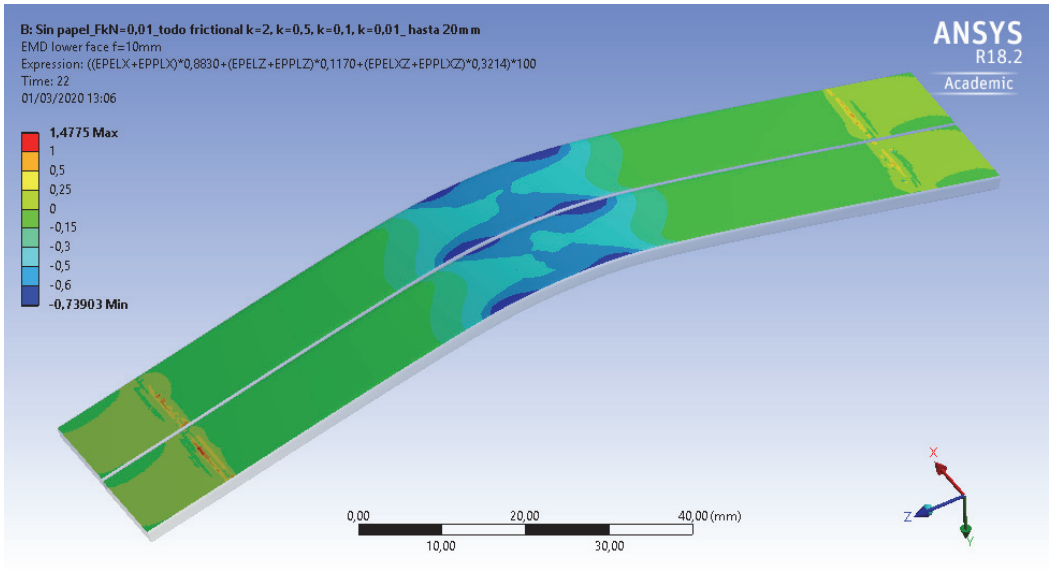

Figure 245. Strain ε_{MD} (%) on the lower face, for a final deflection of 10 mm.

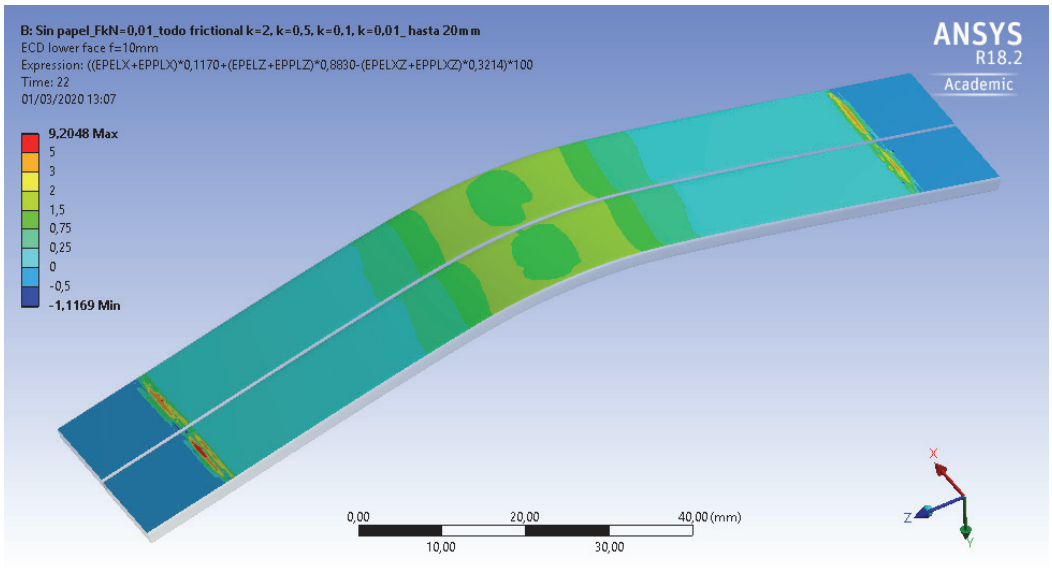

Figure 246. Strain ε_{CD} (%) on the lower face, for a final deflection of 10 mm.

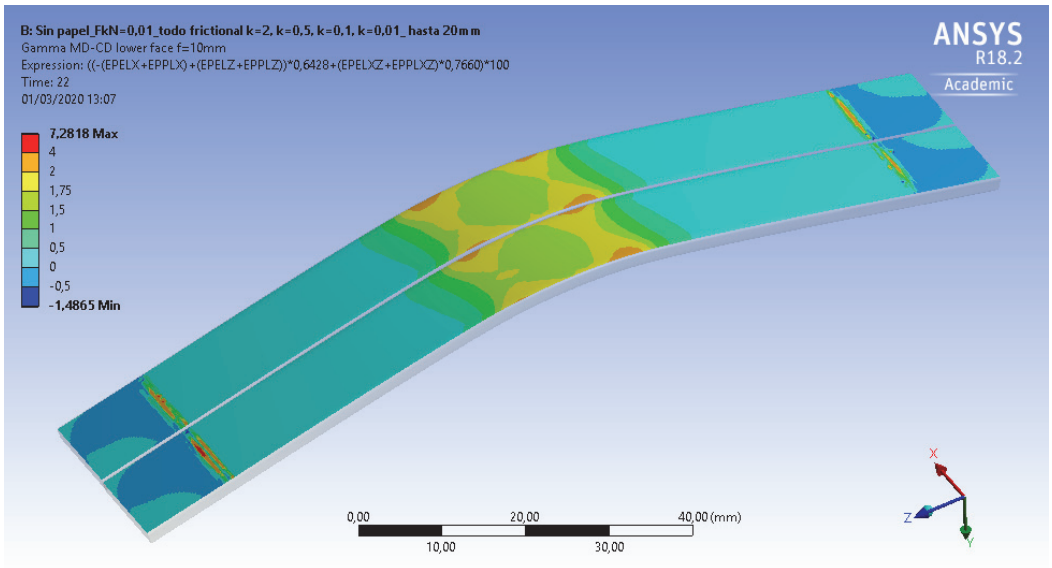

Figure 247. Shear strain γ_{MD-CD} (%) on the lower face, for a final deflection of 10 mm.

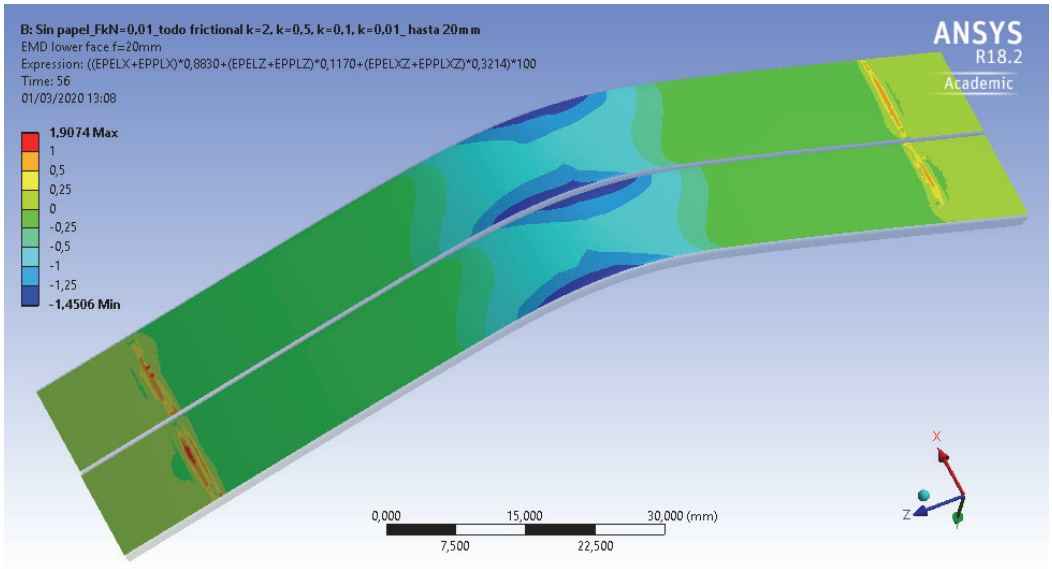

Figure 248. Strain ε_{MD} (%) on the lower face, for a final deflection of 20 mm.

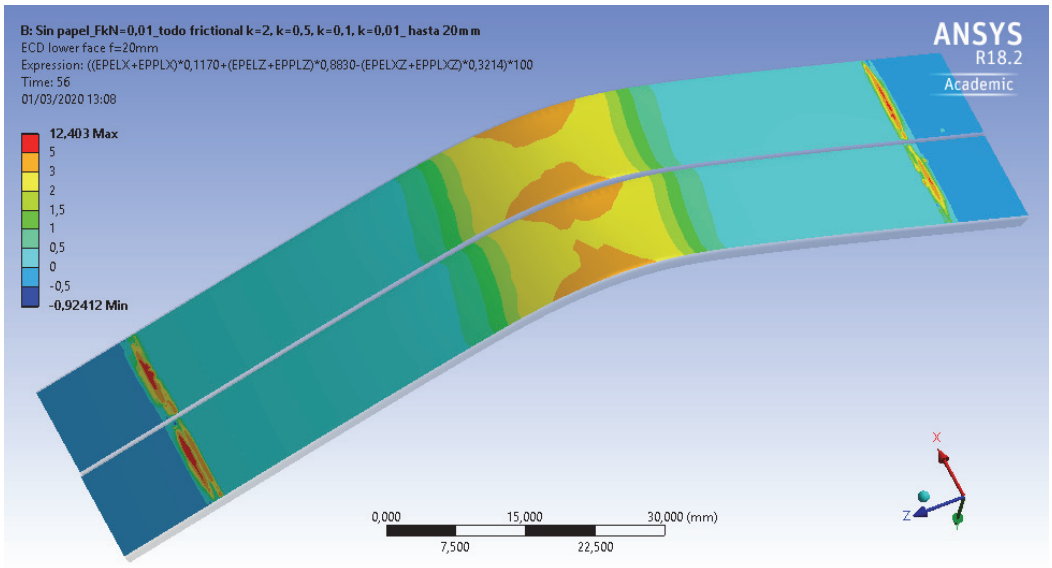

Figure 249. Strain ε_{CD} (%) on the lower face, for a final deflection of 20 mm.

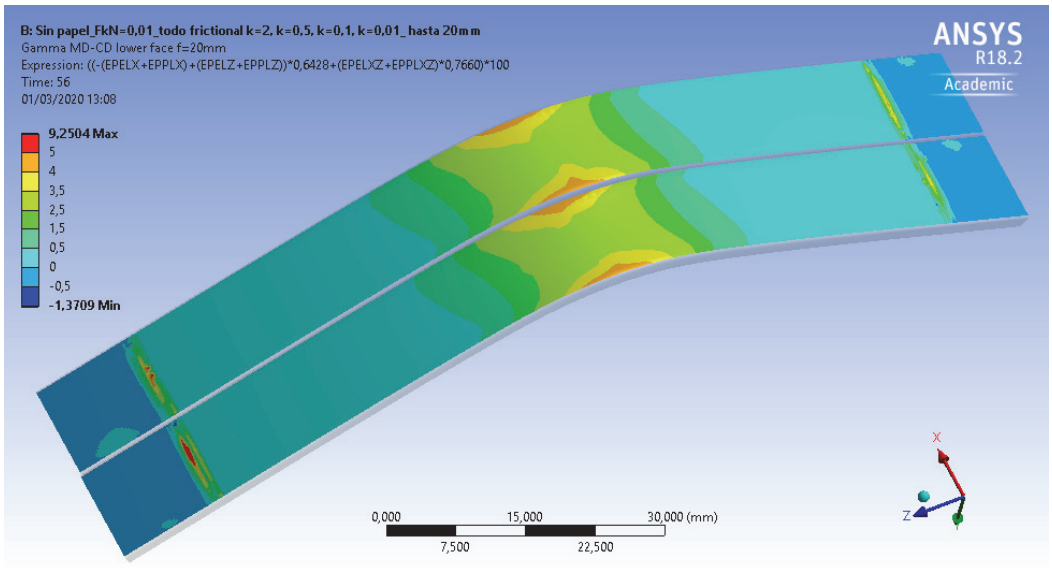

Figure 250. Shear strain γ_{MD-CD} (%) on the lower face, for a final deflection of 20 mm.

The strain results in the main directions of the paper material (MD, CD), for the two lateral sides of the CTC sample can be seen in Figure 251-Figure 256, for a deflection of 5 mm. The strains are very similar in both sides due to the symmetry of the loading and the simplified geometry. In the real CTC, the variable position of the transposed conductor, which is not symmetrical, could produce slightly different strain distributions in both lateral sides. Regarding the field strain in the MD, ε_{MD}, there are parts of the CTC subjected to tension and others subjected to compression. The maximum tensile strains are around $\varepsilon_{MD} \simeq 0.245\%$ and the compressive strains $\varepsilon_{MD} \simeq -0.223\%$. The strains in the CD are also both tensile and compressive strains, and are higher than in the MD: $\varepsilon_{CD} \simeq 0.772\%$ in tension and $\varepsilon_{CD} \simeq -0.649\%$ in compression. The shear strains are the highest ones in the lateral sides, and they vary between 1.464% and −1.205%. As these shear strains are considerably higher than the strains in MD or CD, it is expectable that the failure in the sides of the CTC is dominated by shear deformations.

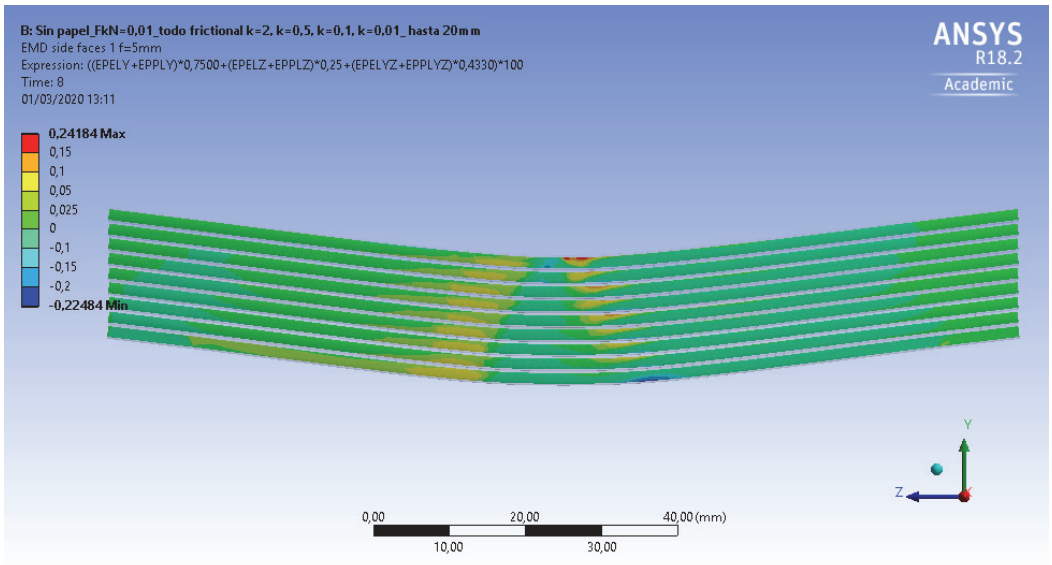

Figure 251. Strain ε_{MD} (%) on the lateral side face 1, for a final deflection of 5 mm.

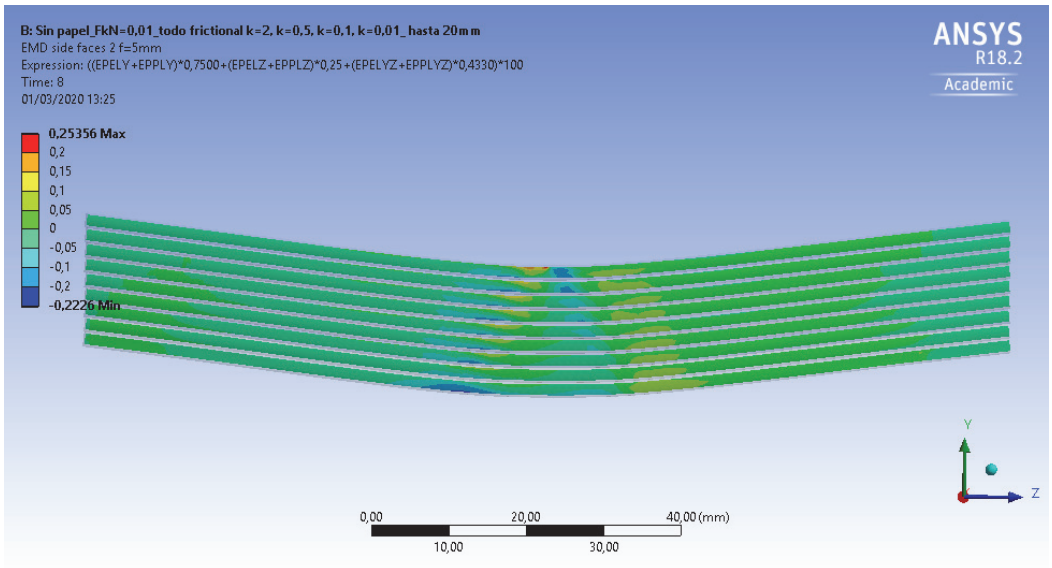

Figure 252. Strain ε_{MD} (%) on the lateral side face 2, for a final deflection of 5 mm.

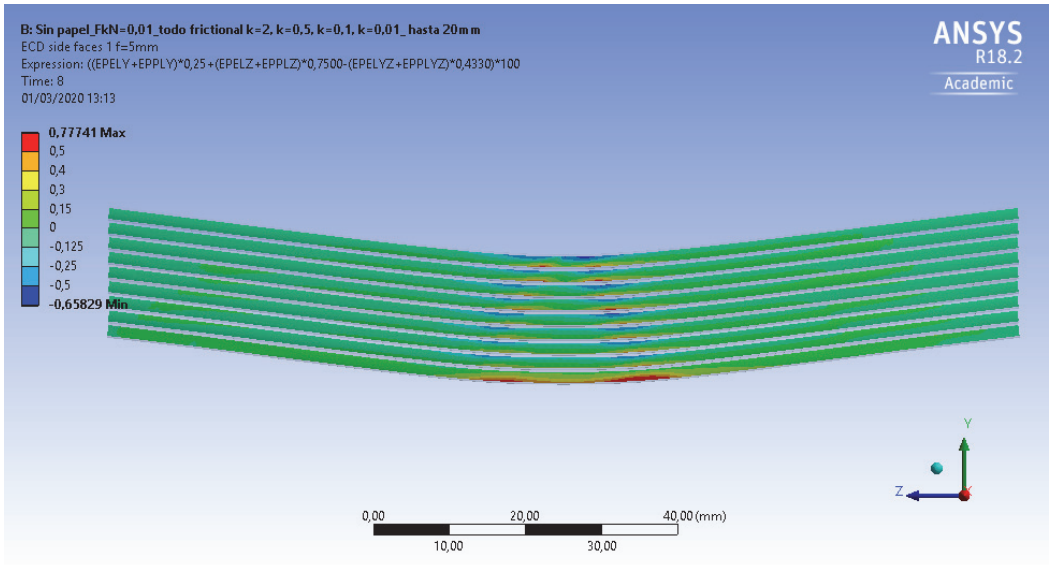

Figure 253. Strain ε_{CD} (%) on the lateral side face 1, for a final deflection of 5 mm.

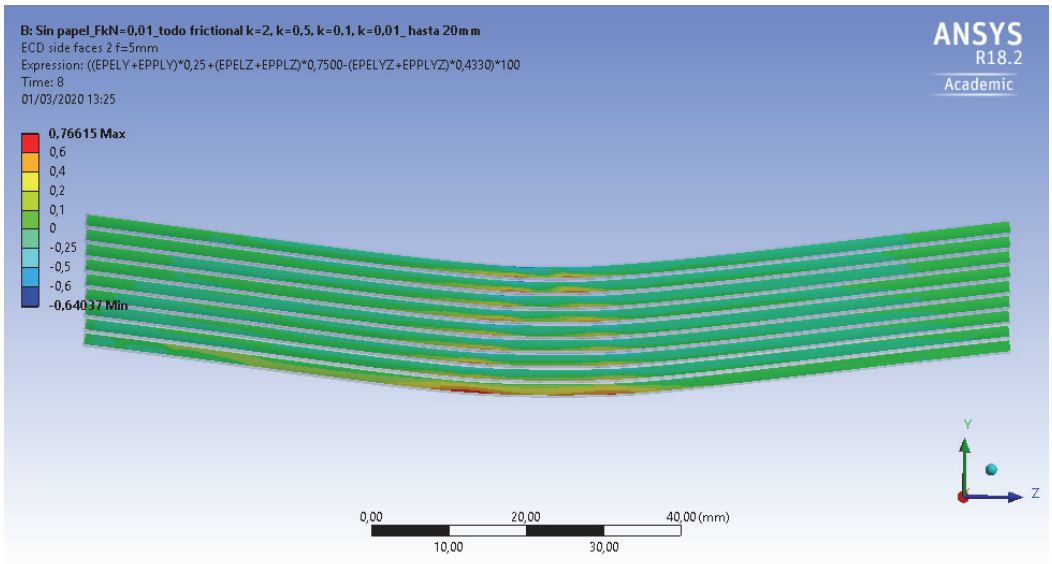

Figure 254. Strain ε_{CD} (%) on the lateral side face 2, for a final deflection of 5 mm.

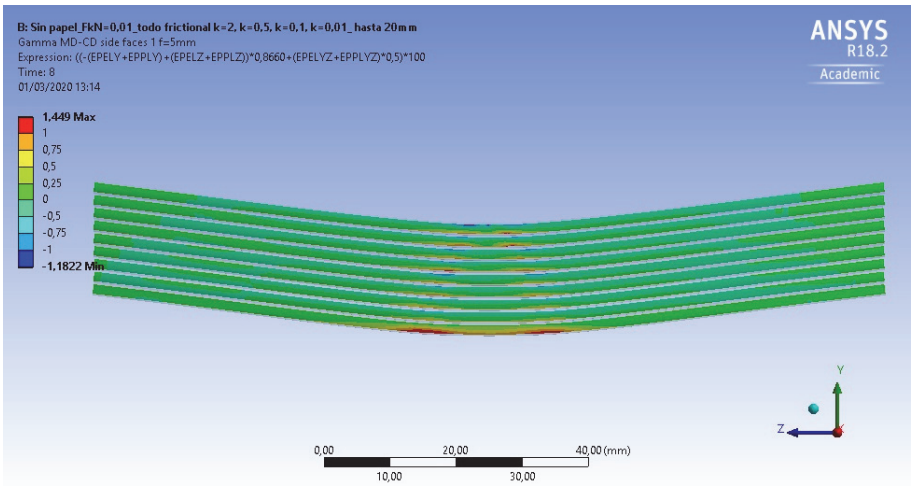

Figure 255. Shear strain γ_{MD-CD} (%) on the lateral side face 1, for a final deflection of 5 mm.

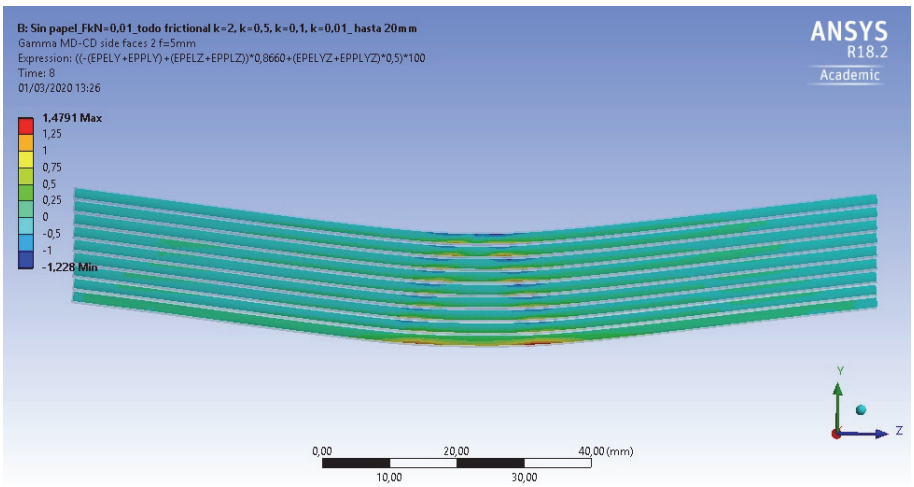

Figure 256. Shear strain γ_{MD-CD} (%) on the lateral side face 2, for a final deflection of 5 mm.

The strains on the lateral sides of the CTC samples when the final deflection is increased up to 10 mm are shown in Figure 257-Figure 262. The strains in MD are more than double the ones obtained for d = 5 mm: the maximum tensile strain is $\varepsilon_{MD} \simeq 0.593\%$, while the maximum compressive strain is $\varepsilon_{MD} \simeq -0.581\%$. The strains in the CD, which are higher than the ones in the MD, are around $\varepsilon_{CD} \simeq 1.694\%$ in tension and $\varepsilon_{CD} \simeq -1.721\%$. When d = 10 mm, the shear strains are also the highest ones, and they had increased up to maximum values of $\gamma_{MD-CD} \simeq 3.308\%$ and $\gamma_{MD-CD} \simeq -3.099\%$.

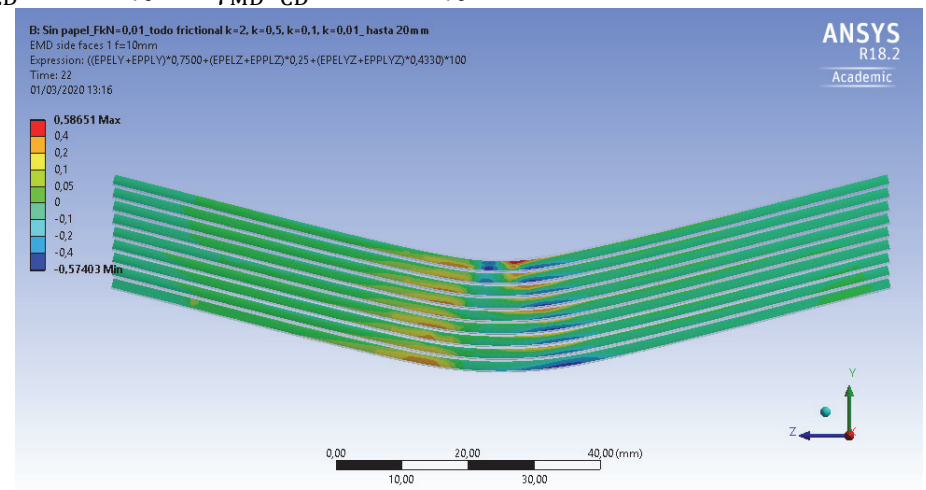

Figure 257. Strain ε_{MD} (%) on the lateral side face 1, for a final deflection of 10 mm.

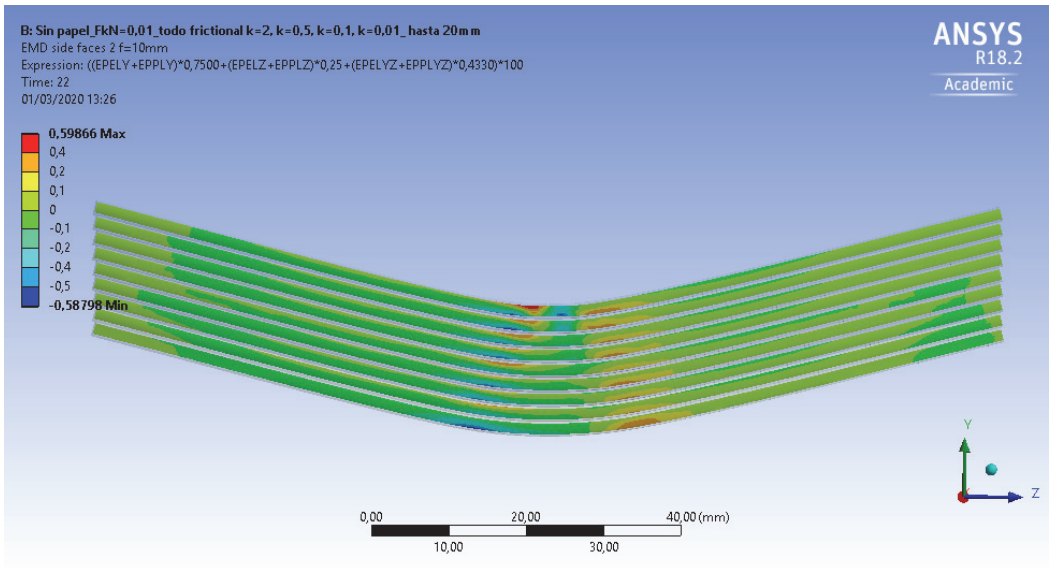

Figure 258. Strain ε_{MD} (%) on the lateral side face 2, for a final deflection of 10 mm.

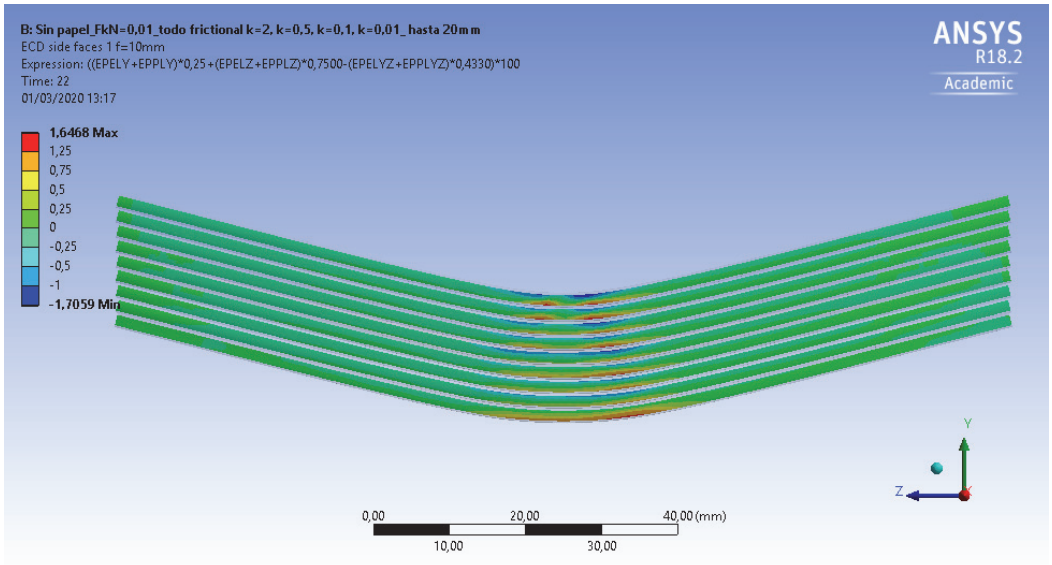

Figure 259. Strain ε_{CD} (%) on the lateral side face 1, for a final deflection of 10 mm.

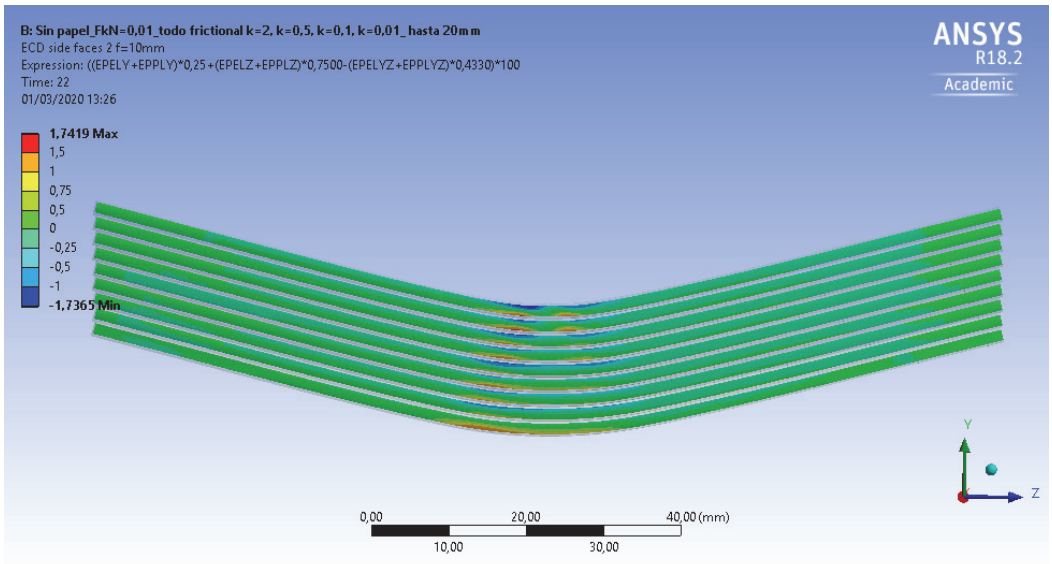

Figure 260. Strain ε_{CD} (%) on the lateral side face 2, for a final deflection of 10 mm.

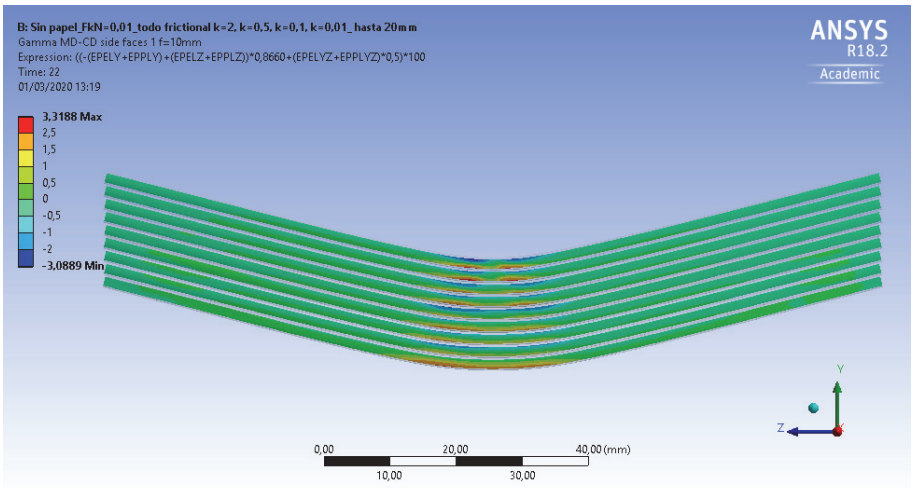

Figure 261. Shear strain γ_{MD-CD} (%) on the lateral side face 1, for a final deflection of 10 mm.

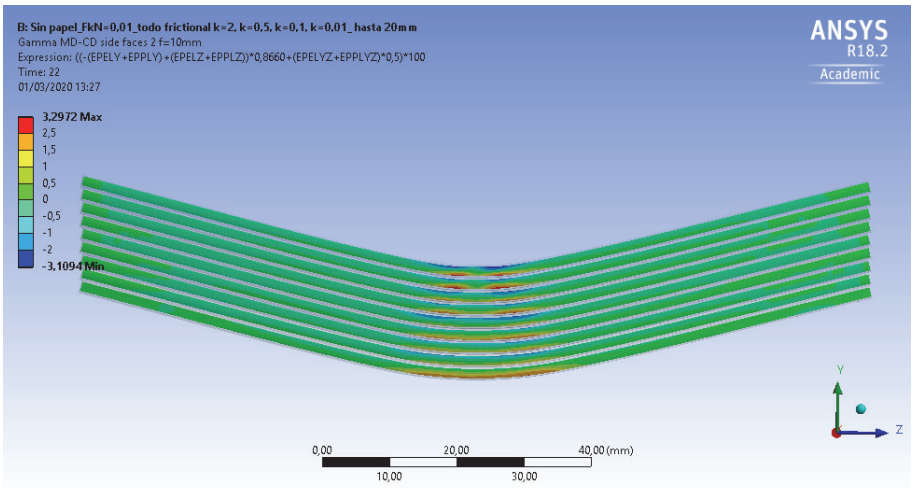

Figure 262. Shear strain γ_{MD-CD} (%) on the lateral side face 2, for a final deflection of 10 mm.

Finally, the strains on the lateral sides of the CTC samples when d = 20 mm are shown in Figure 263 - Figure 268. The maximum tensile strains in MD are around $\varepsilon_{MD} \simeq 1.625\%$, while the maximum compressive strain is $\varepsilon_{MD} \simeq -2.454\%$. The strains in the CD, which are higher than the ones in the MD, are around $\varepsilon_{CD} \simeq 5.854\%$ in tension and $\varepsilon_{CD} \simeq -3.294\%$. When $d = 20\,mm$, the shear strains are between $\gamma_{MD-CD} \simeq 10.754\%$ and $\gamma_{MD-CD} \simeq -5.875\%$.

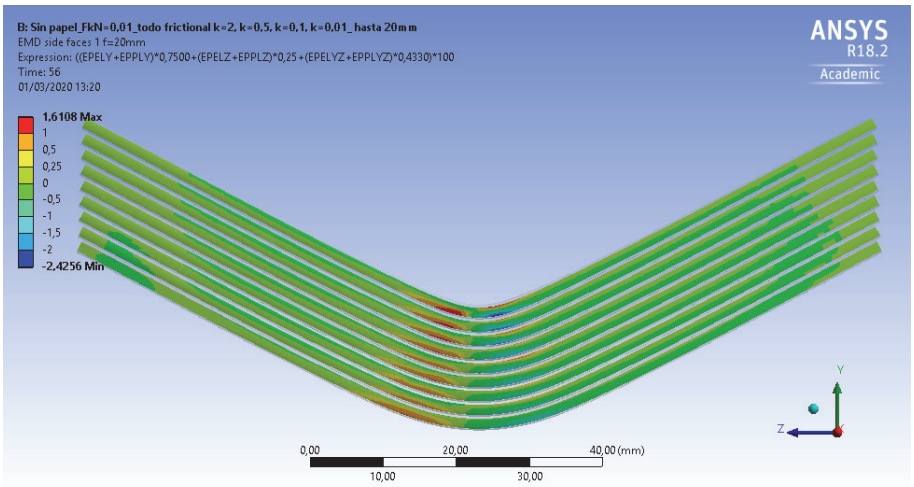

Figure 263. Strain ε_{MD} (%) on the lateral side face 1, for a final deflection of 20 mm.

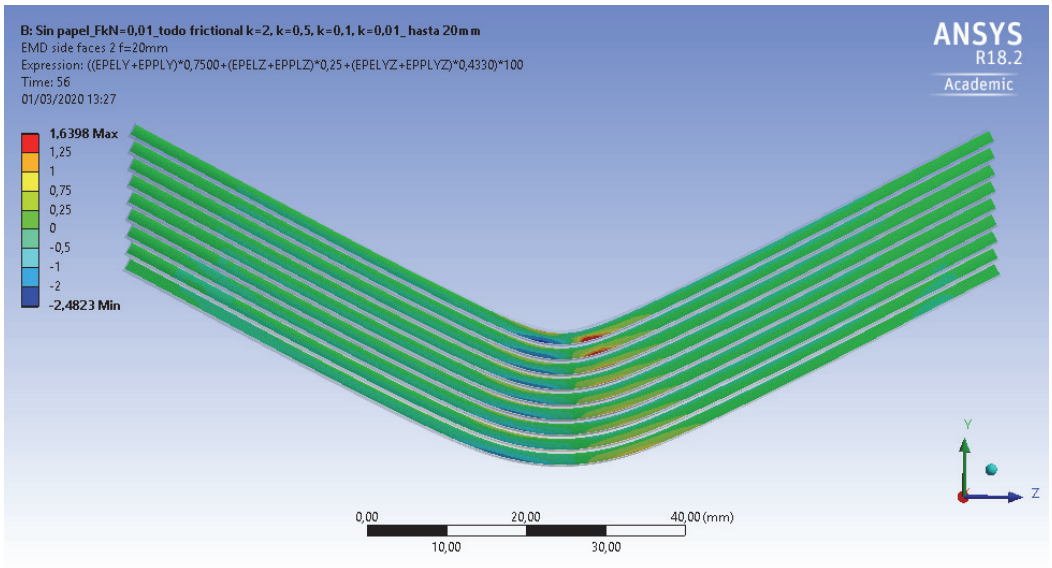

Figure 264. Strain ε_{MD} (%) on the lateral side face 2, for a final deflection of 20 mm.

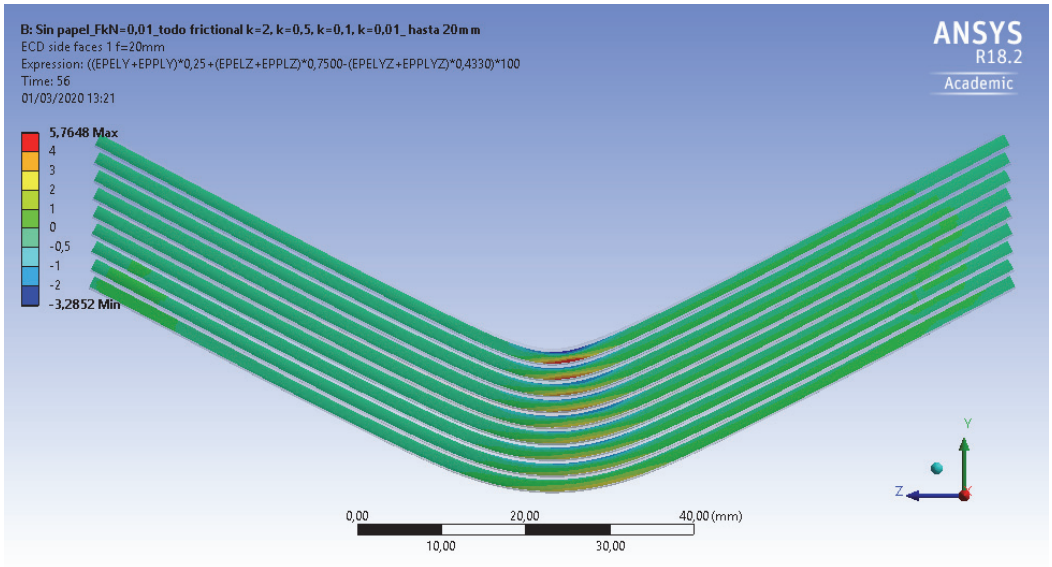

Figure 265. Strain ε_{CD} (%) on the lateral side face 1, for a final deflection of 20 mm.

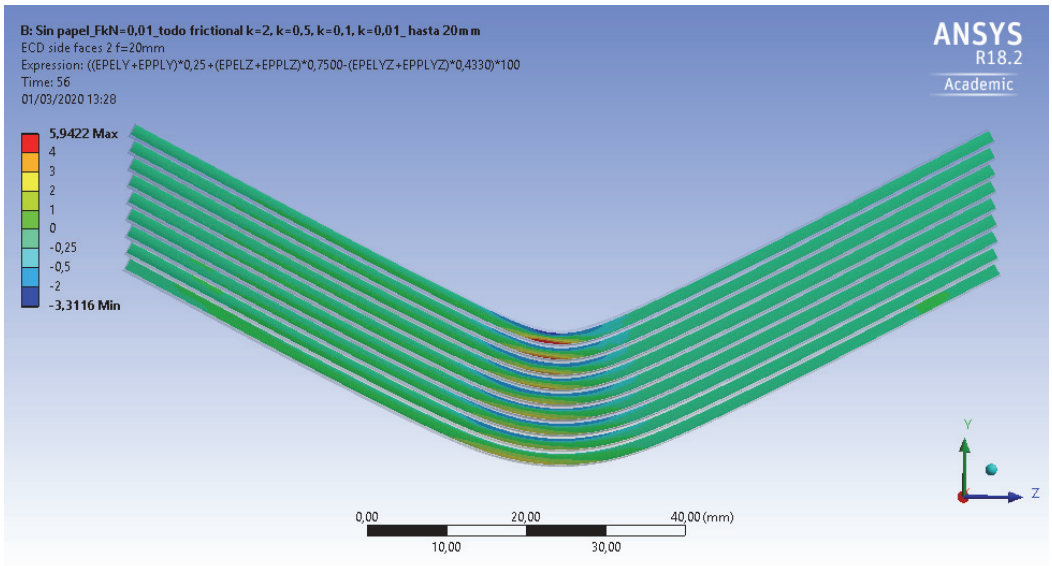

Figure 266. Strain ε_{CD} (%) on the lateral side face 2, for a final deflection of 20 mm.

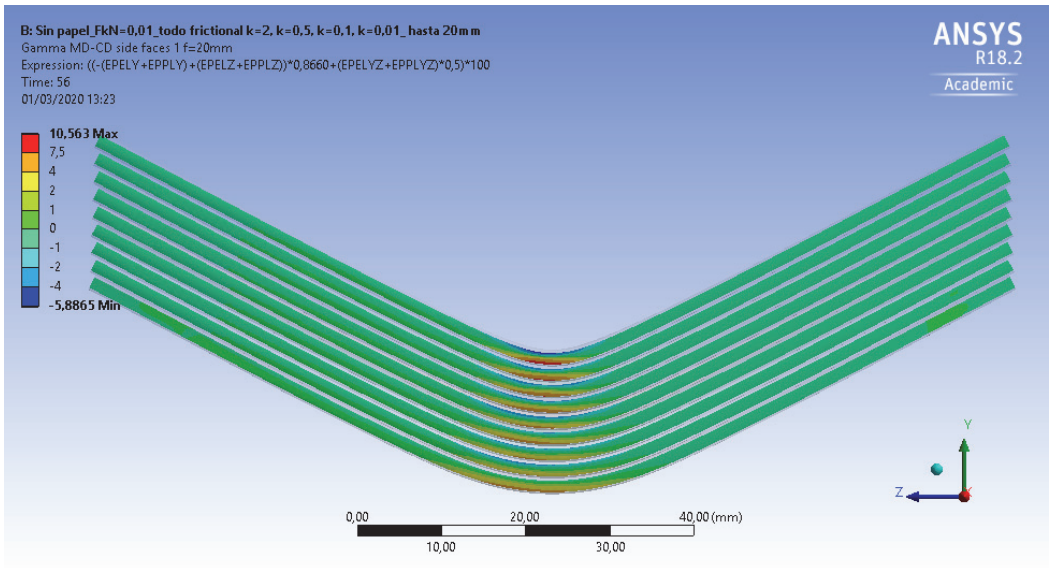

Figure 267. Shear strain γ_{MD-CD} (%) on the lateral side face 1, for a final deflection of 20 mm.

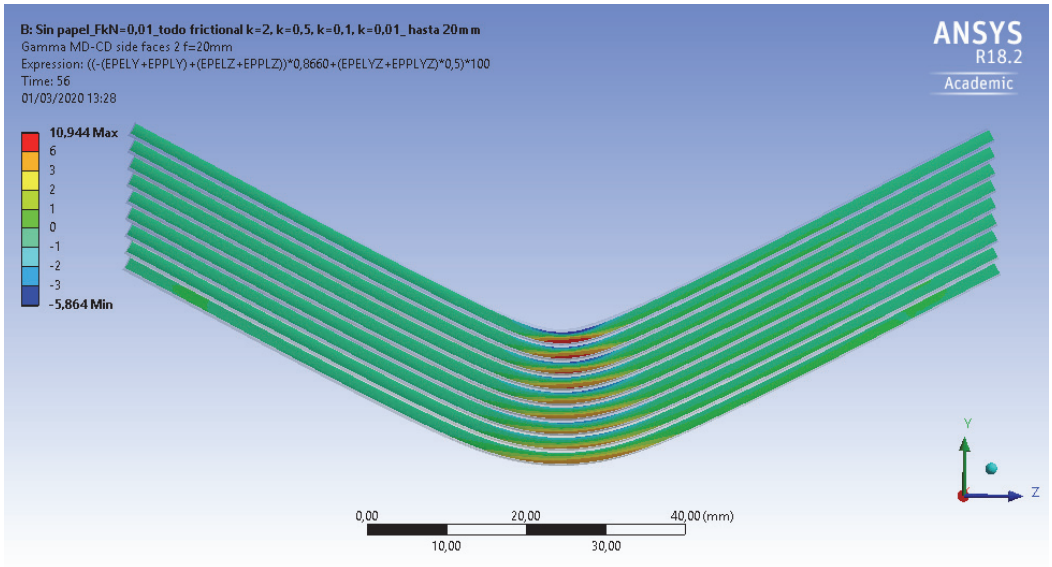

Figure 268. Shear strain γ_{MD-CD} (%) on the lateral side face 2, for a final deflection of 20 mm.

3. Failure criteria for the paper insulation of the CTC

3.1. Introduction

As the paper insulation was not included in the FE numerical model for practical reasons, the stress field over the different layers of paper material wrapping the CTC sample is not known, but it can be assumed that the strain field obtained for the external surface of the copper strands will be approximately similar to the one in the paper insulation. Because of that, all the considered failure criteria have to be expressed in terms of strains. The experimental observations in the insulated CTC samples after the bending tests also showed that there are many different sources for crack initiation in the paper insulation, and it must be considered that, it is not feasible to obtain a failure model which takes all of them into consideration. Some particularities of the geometry of the CTC have not been considered in the numerical model for the sake of simplicity, and the intrinsic heterogeneity of the paper material cannot be easily quantified. Consequently, the aim of this part of the work is to obtain reliable and conservative expressions to predict the occurrence of mechanical failure of the paper insulation.

In a first stage of the experimental work, only the tensile properties of the paper insulation were characterised (see *1.2.2.Tensile mechanical properties of the dielectric paper in the MD and in the CD* in *1.2.Characterisation of the paper insulation samples*). Later on, after the three-point bending tests, relevant fractures were noticed in areas of the CTC samples subjected to compression, such as the upper faces, especially in the most severe ageing states (see *1.3.4.Conclusions after the bending tests*). The numerical simulation also corroborated that the magnitude of compressive and shear strains was not negligible in comparison with the tensile strains (see *2.2.Deformation, stress and strain distributions obtained in the CTC samples through the numerical simulation* in *2.Numerical simulation*). Because of that, the estimation of the compressive and in-plane shear properties was needed for the failure analysis of the insulation of a CTC in a power transformer, and the experimental work was extended (see *1.2.3.Edgewise mechanical compressive properties of the dielectric paper* and *1.2.4.In-plane shear mechanical properties of the dielectric paper* in *1.2.Characterisation of the paper insulation samples*).

Although layers 1 and 2 of the insulation are made of the same material, plain Kraft paper, the first one was more affected by the thermal ageing. The chosen ageing temperature, of 150ºC, melted the enamel of the CTC samples, sticking that layer to the copper conductor. Due to that, the first layer of insulation was artificially more damaged by the ageing process and will not be considered as representative of the mechanical failure of the plain Kraft paper under normal operating conditions. Thus, only the tensile mechanical properties obtained for layer 2 will be considered in the following failure analysis. On the other hand, as it was concluded from the laboratory experiments that there were no noticeable differences between the response to ageing and the mechanical behaviour of layers 3 and 4 of the paper insulation, made of crepe paper, average values obtained from the tensile characterisation will be used here. The characterisation of edgewise compressive properties and the estimation of in-plane shear properties only distinguish between plain Kraft and crepe papers in the different ageing states (the layers of the insulation were not considered in these analyses).

Furthermore, although four ageing states were initially considered (see *1.1.2.Considered ageing states and thermal ageing process*) because it was of interest to determine the ageing duration and temperature that would cause the insulation to lose its mechanical and dielectric properties, the extent of the ageing in State IV is so profound that it will be difficult to reach that situation in an operating power transformer under normal conditions. Therefore, the failure analysis will be focused on Ageing States 0-III, because they represent feasible conditions for the paper insulation during the operating life of a power transformer.

In conclusion, the required parameters for the failure criterion were obtained in *1.2.Characterisation of the paper insulation samples* from *1.Experimental work* and are summarised in Table 41 for four ageing states: Ageing States 0 (new material), I (1 week of ageing at 150ºC), II (2 weeks at 150ºC) and III (9 weeks at 150ºC). $\varepsilon_{MD,t}^{max}$ is the strain at breakage in tension mode in MD, and $\varepsilon_{CD,t}^{max}$ is the strain at breakage in tension mode in CD, which were obtained in section 1.2.2. $\varepsilon_{MD,c}^{max}$ and $\varepsilon_{CD,c}^{max}$ are the compressive strains which correspond to a stress equal to the 50% of the peak compressive stress, as justified in section 1.2.3. γ_{MD-CD}^{max} is the distortion at break in shear mode, or the maximum engineering shear strain, which is twice the tensor shear strain, which was estimated as described in section 1.2.4.

Table 41. Maximum strains for the plain Kraft and crepe papers, in the different orientations and for the different mechanical solicitations.

		In-plane tension		Edgewise compression	In-plane shear
Ageing State	Material	$\varepsilon_{MD,t}^{max}$	$\varepsilon_{CD,t}^{max}$	$\varepsilon_{MD,c}^{max} = \varepsilon_{CD,c}^{max}$	γ_{MD-CD}^{max}
State 0	Plain Kraft	3.42 ± 0.25	8.22 ± 0.81	4.08 ± 0.71	5.60 ± 0.58
	Crepe	23.09 ± 1.46	11.82 ± 0.82	5.21 ± 1.45	28.76 ± 1.92
State I	Plain Kraft	2.54 ± 0.22	7.39 ± 0.67	3.96 ± 1.68	2.94 ± 0.52
	Crepe	22.11 ± 1.02	10.37 ± 0.36	5.06 ± 1.43	11.98 ± 2.18
State II	Plain Kraft	2.03 ± 0.16	6.09 ± 1.09	3.58± 0.92	2.60 ± 0.30
	Crepe	20.43 ± 0.72	7.79 ± 0.24	4.56 ± 1.10	10.20 ± 1.46
State III	Plain Kraft	1.19 ± 0.05	5.50 ± 0.88	2.99 ± 0.95	1.68 ± 0.40
	Crepe	17.68 ± 1.29	3.46 ± 0.34	3.80 ± 0.92	3.23 ± 0.16

3.2. Maximum strain failure criterion

The maximum strain failure criterion is an example of a limit failure criterion expressed in terms of strains and applicable to a lamina (in this case the insulation of a CTC in the windings of a power transformer, made of two different types of paper insulation). This criterion aims at predicting the occurrence of failure and the failure mode by comparing lamina strains (ε_{MD}, ε_{CD}, and γ_{MD-CD}) with the corresponding maximum strains at failure separately, so interaction among the strains is not considered.

- **Failure of the plain Kraft paper insulation:**
- ***Ageing State 0:***

In Ageing State 0, the bending tests in the laboratory did not produce cracks in layer 2 of the insulation for any deflection level. The maximum strain criterion is coherent with that for deflections of 5 and 10 mm. However, when $d = 20\ mm$, this criterion predicts failure in compression in a small area (< 5 mm) of the upper faces, see Figure 269, and failure in shear mode in small areas of the upper and side faces, see Figure 270. One reason for that difference between laboratory observations and predictions of the model could be that the selected compressive and shear strains at failure are conservative ones. Besides, according to expectations, the numerical simulation predicts the strains undergone by the copper CTC, but the strains in layer 2 will be lower because this layer is not glued to the copper conductor and can slide. This contrasts with the behaviour of layer 1 of the insulation, which is stuck to the conductor developing cracks in the bending tests conducted in the laboratory.

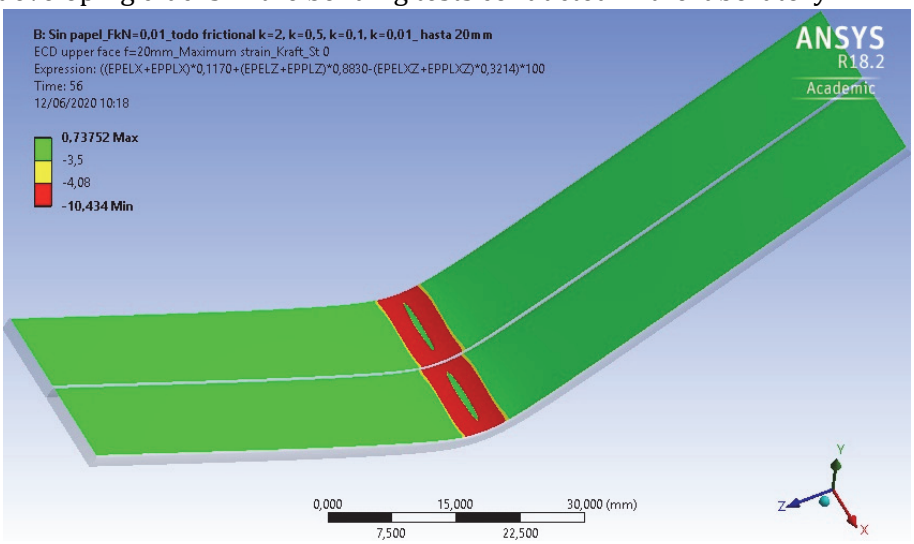

Figure 269. Maximum strain failure criterion in compression mode, $\varepsilon_{CD,c}^{max}$, for the plain Kraft paper in Ageing State 0 on the upper face of the CTC and for d = 20 mm.

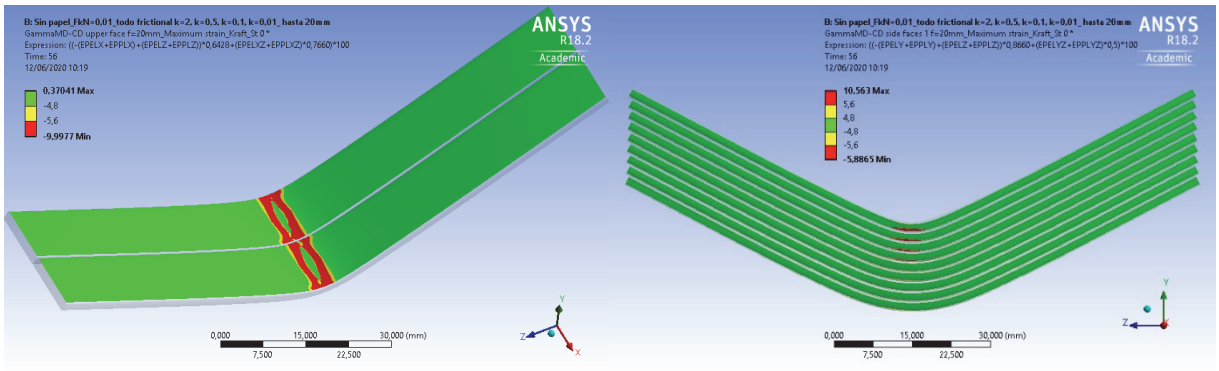

Figure 270. Maximum strain failure criterion in shear mode, γ_{MD-CD}^{max}, for the plain Kraft paper in Ageing State 0 (a) on the upper face and (b) on the lateral side faces of the CTC and for d = 20 mm.

- ***Ageing State I:***

In Ageing State I, for $d = 5\ mm$, no cracks were produced after the tests, and that is coherent with the maximum strain failure criterion. For $d = 10\ mm$, small cracks (< 5mm) were detected in the laboratory for layer 2, and that is coherent with the maximum strain failure criterion, which predicts failure in shear mode in an area of that size in the upper face, see Figure 271.

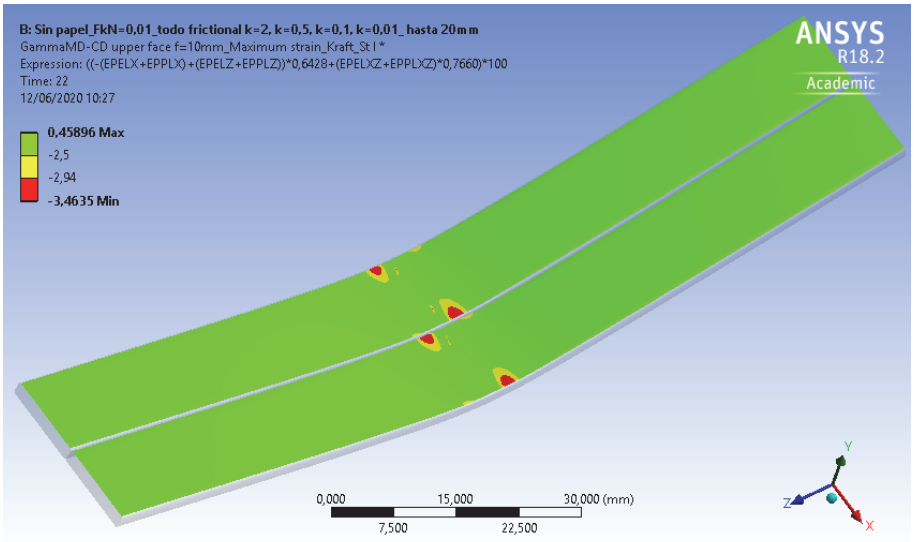

Figure 271. Maximum strain failure criterion in shear mode, γ_{MD-CD}^{max}, for the plain Kraft paper in Ageing State I on the upper face of the CTC and for d = 10 mm.

For $d = 20\ mm$, the cracks produced by the bending tests were of medium size (5-10 mm). The maximum strain criterion predicts failure in tension and compression modes in small areas (< 5 mm) of the upper face, see Figure 272, and in an area of similar size in shear mode, see Figure 273 (a). On the lower and side faces, the area in which failure in shear mode is expected has a length of around 10 mm, see Figure 273 (b) and Figure 274. So, the predictions of the maximum strain failure criterion are in line with experimental observations.

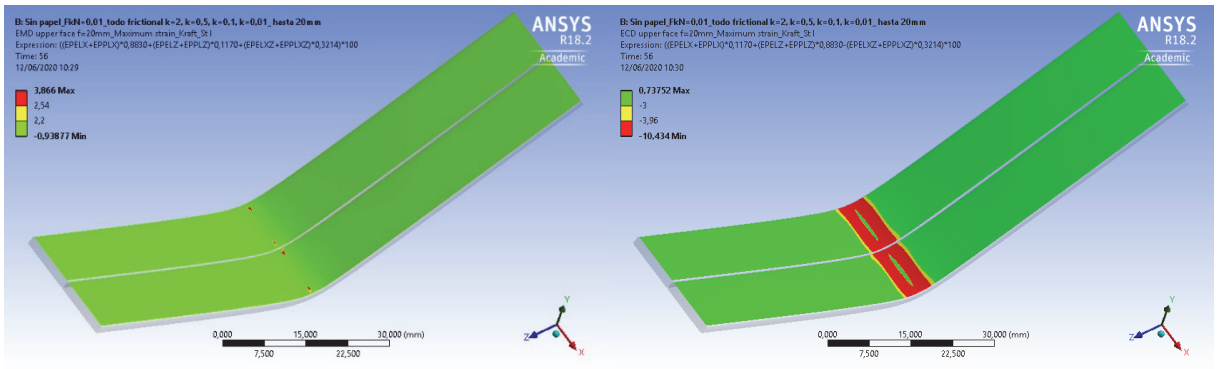

Figure 272. Maximum strain failure criterion (a) in tension mode, $\varepsilon_{MD,t}^{max}$, and (b) in compression mode, $\varepsilon_{CD,c}^{max}$, for the plain Kraft paper in Ageing State I on the upper face of the CTC and for d = 20 mm.

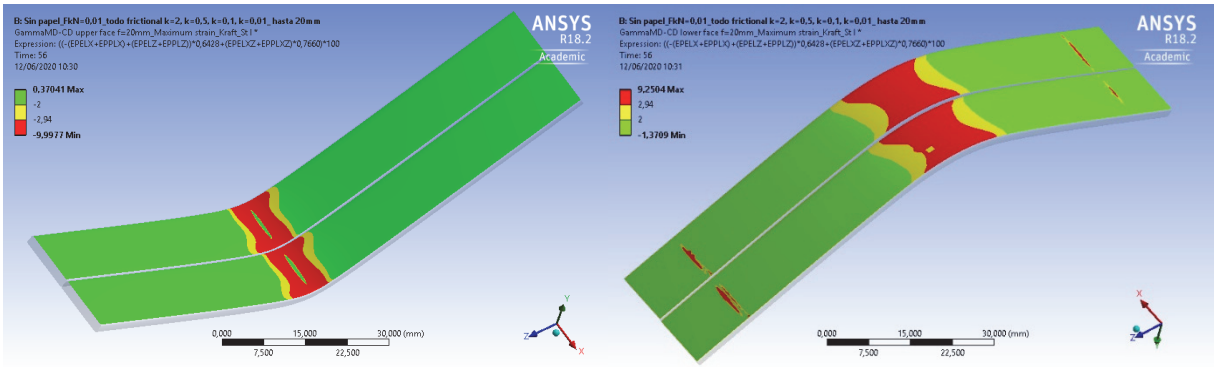

Figure 273. Maximum strain failure criterion in shear mode, γ_{MD-CD}^{max}, for the plain Kraft paper in Ageing State I (a) on the upper face and (b) on the lower face of the CTC and for d = 20 mm.

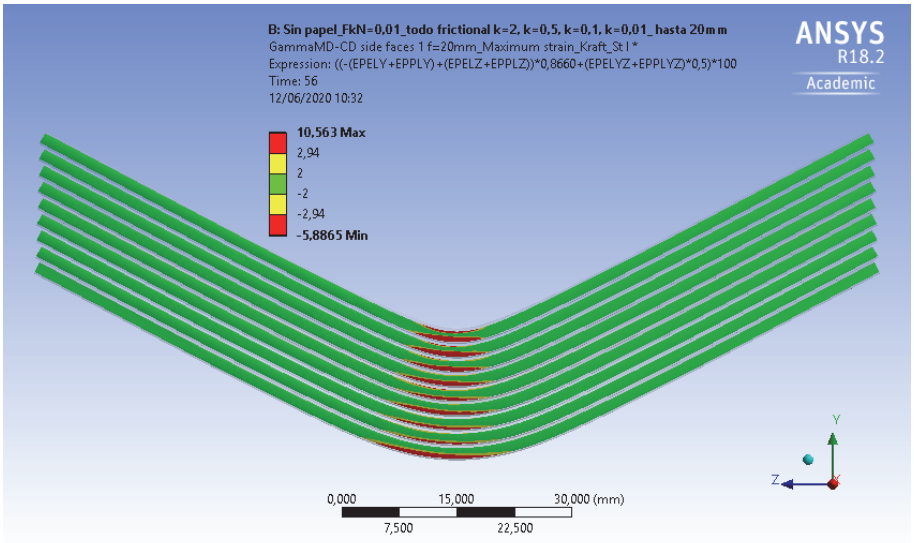

Figure 274. Maximum strain failure criterion in shear mode, γ_{MD-CD}^{max}, for the plain Kraft paper in Ageing State I on the lateral side faces of the CTC and for d = 20 mm.

- ***Ageing State II:***

In Ageing State II, for $d = 5\ mm$, no cracks were produced by the bending tests and that coincides with the predictions of the maximum strain criterion. For $d = 10\ mm$, small cracks (< 5mm) were detected in the plain Kraft insulation after the bending tests. For that deflection level, failure in shear mode is expected in small areas of the upper and lateral side faces, according to the maximum strain failure criterion, see Figure 275. When $d = 20\ mm$, the cracks produced by the bending tests were big (> 10 mm), and that coincides with the forecast of this failure criterion: failure in tension, compression and shear modes on the upper face,

see Figure 276 and Figure 277 (a), and failure in shear mode on the lower and lateral side faces, see Figure 277 (b) and Figure 278.

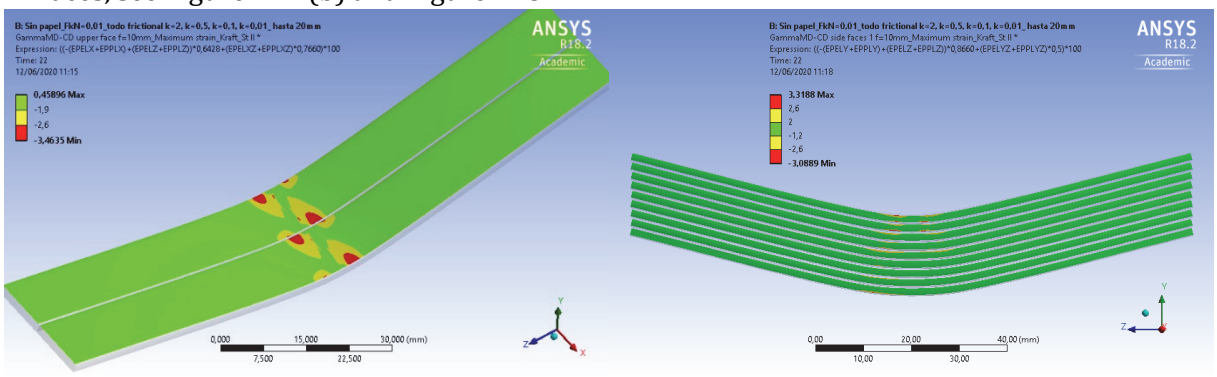

Figure 275. Maximum strain failure criterion in shear mode, γ_{MD-CD}^{max}, for the plain Kraft paper in Ageing State II (a) on the upper face and (b) on the lateral side faces of the CTC and for d = 10 mm.

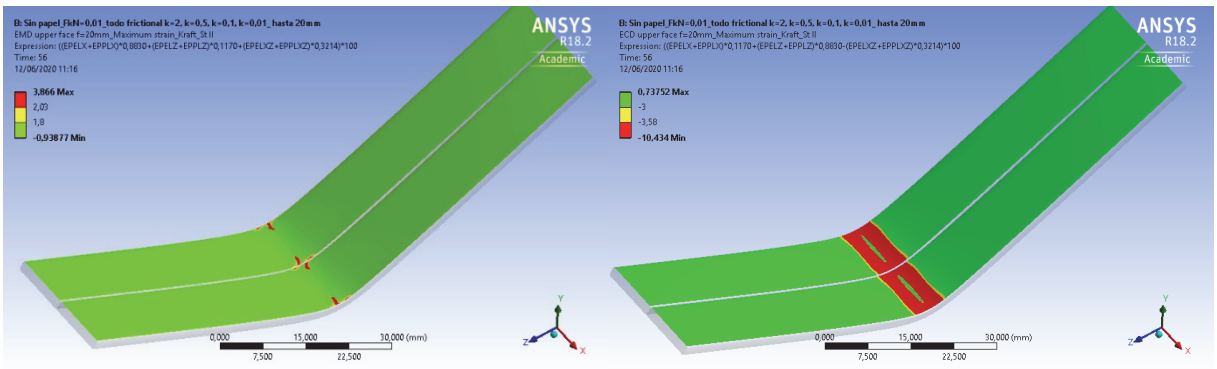

Figure 276. Maximum strain failure criterion (a) in tension mode, $\varepsilon_{MD,t}^{max}$, and (b) in compression mode, $\varepsilon_{CD,c}^{max}$, for the plain Kraft paper in Ageing State II on the upper face of the CTC and for d = 20 mm.

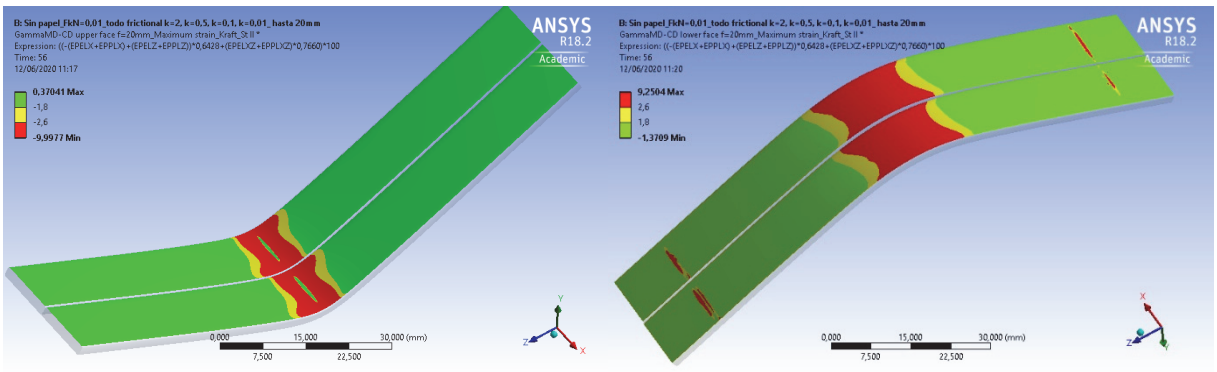

Figure 277. Maximum strain failure criterion in shear mode, γ_{MD-CD}^{max}, for the plain Kraft paper in Ageing State II (a) on the upper face and (b) on the lower face of the CTC and for d = 20 mm.

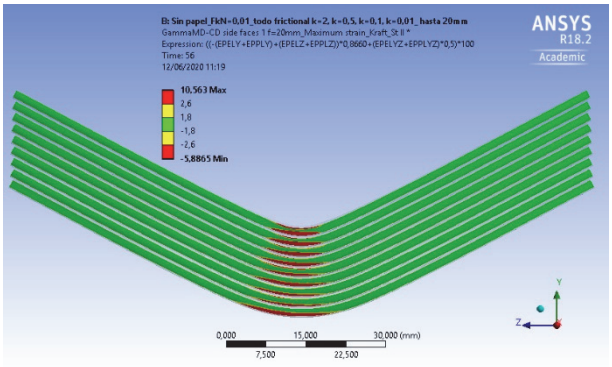

Figure 278. Maximum strain failure criterion in shear mode, γ_{MD-CD}^{max}, for the plain Kraft paper in Ageing State II on the lateral side faces of the CTC and for d = 20 mm.

- ***Ageing State III:***

In Ageing State III, no fractures were observed after the bending tests for layer 2 and for a deflection $d = 5\ mm$, and that is in line with the predictions of the maximum strain failure criterion. For $d = 10\ mm$, big cracks (> 10 mm) arose in the Kraft paper, and that coincides with the predictions of the failure criterion: failure in shear mode in the upper, lower and side faces of the CTC sample, see Figure 279 and Figure 280.

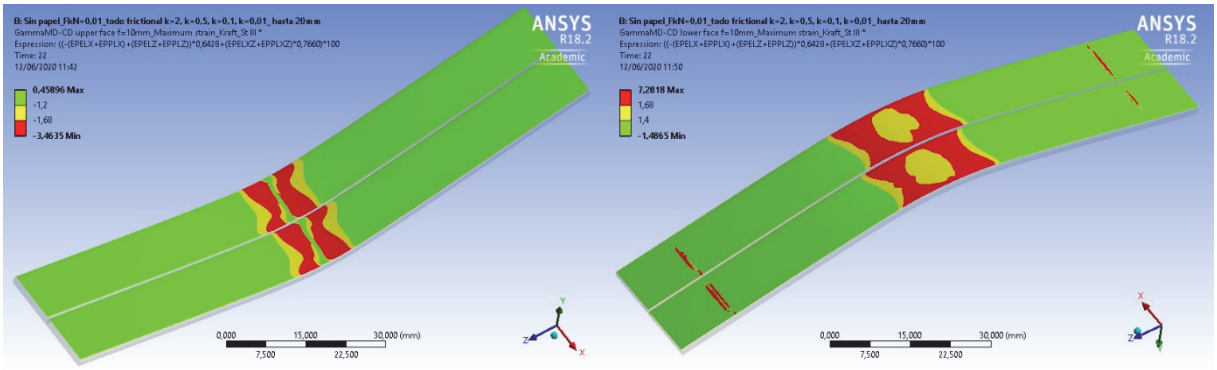

Figure 279. Maximum strain failure criterion in shear mode, γ_{MD-CD}^{max}, for the plain Kraft paper in Ageing State III (a) on the upper face and (b) on the lower face of the CTC and for d = 10 mm.

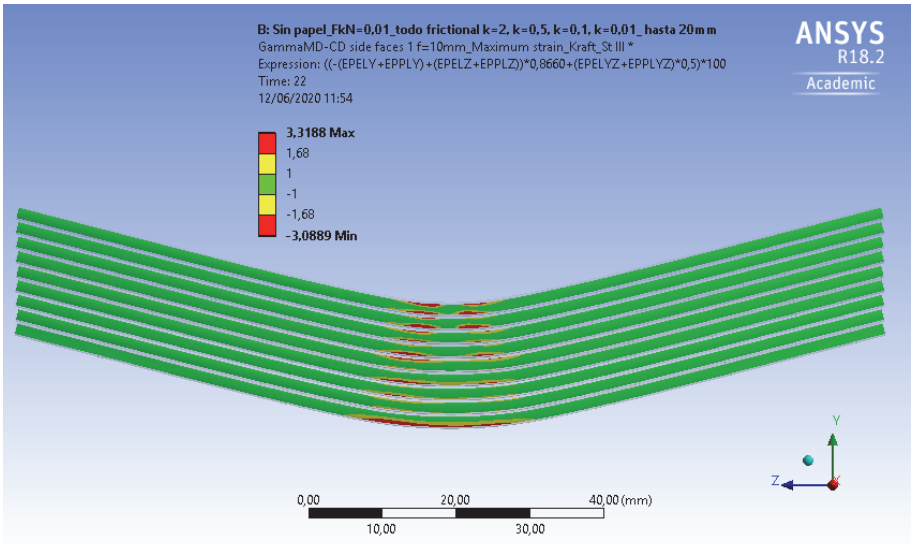

Figure 280. Maximum strain failure criterion in shear mode, γ_{MD-CD}^{max}, for the plain Kraft paper in Ageing State III on the lateral side faces of the CTC and for d = 10 mm.

In this ageing state, the Kraft insulation suffered total fracture after the bending tests with $d = 20\ mm$. The maximum strain failure criterion predicts failure in tensile mode on the upper face and in a small area of the lateral side faces, see Figure 281. Failure in compression mode is also expected on the upper face, see Figure 282 (a). Failure in shear mode is predicted by this criterion on the upper, lower and side faces, see Figure 282 (b) and Figure 283. The interaction among all these failure modes, which cannot be considered with the maximum strain criterion, is probably the cause of the total failure observed in the laboratory.

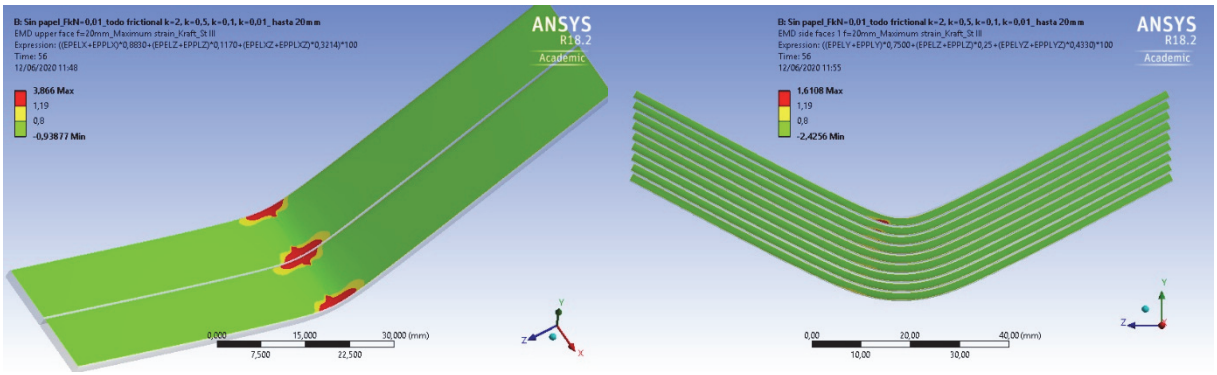

Figure 281. Maximum strain failure criterion in tension mode, $\varepsilon_{MD,t}^{max}$, for the plain Kraft paper in Ageing State III (a) on the upper face and (b) on the lateral side faces of the CTC and for d = 20 mm.

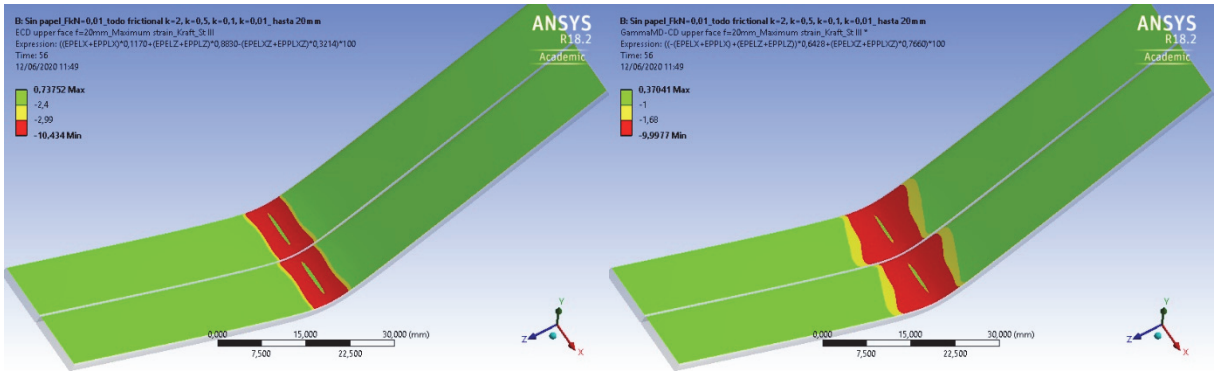

Figure 282. Maximum strain failure criterion (a) in compression mode, $\varepsilon_{CD,c}^{max}$, and (b) in shear mode, γ_{MD-CD}^{max}, for the plain Kraft paper in Ageing State III on the upper face of the CTC and for d = 20 mm.

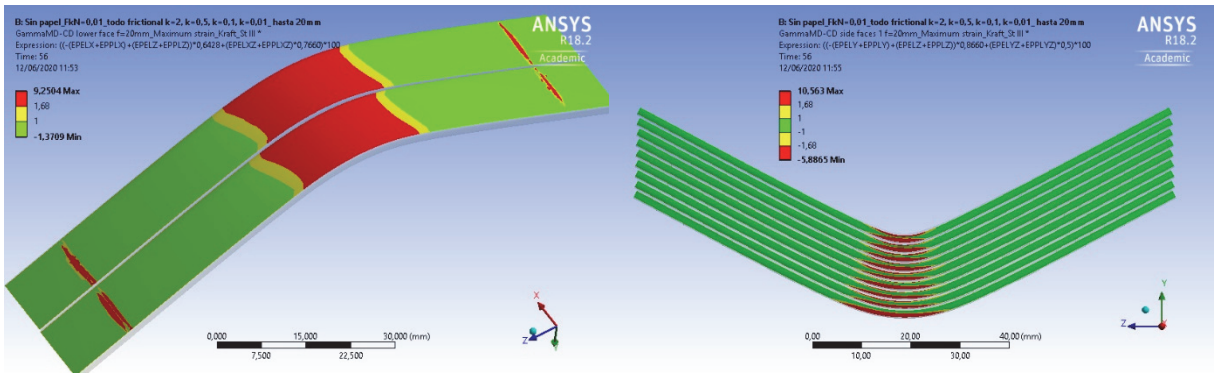

Figure 283. Maximum strain failure criterion in shear mode, γ_{MD-CD}^{max}, for the plain Kraft paper in Ageing State III (a) on the lower face and (b) on the lateral side faces of the CTC and for d = 20 mm.

- **Failure of the crepe paper:**
- ***Ageing State 0:***

In Ageing State 0, no cracks appeared after the bending tests with final deflections of $d = 5\ mm$, $d = 10\ mm$ or $d = 20\ mm$. That coincides with the predictions of the maximum strain failure criterion for deflections of 5 and 10 mm. However, failure in compression mode is predicted in a small area of about 2.5 mm on the upper face for $d = 20\ mm$ by that criterion, see Figure 284. Analogously as in the case of the plain Kraft paper in State 0, there are two reasons for the discrepancy observed between the model predictions and the experimental observations: the compressive strain at failure has been selected in a conservative manner, and, more importantly, the strains that the model predicts on the surface of the CTC sample are higher than the ones that the crepe paper suffers in layers 3 and 4 of the insulation. This is due to the fact that the external layers of the insulation are partially free to slide when the copper CTC deforms.

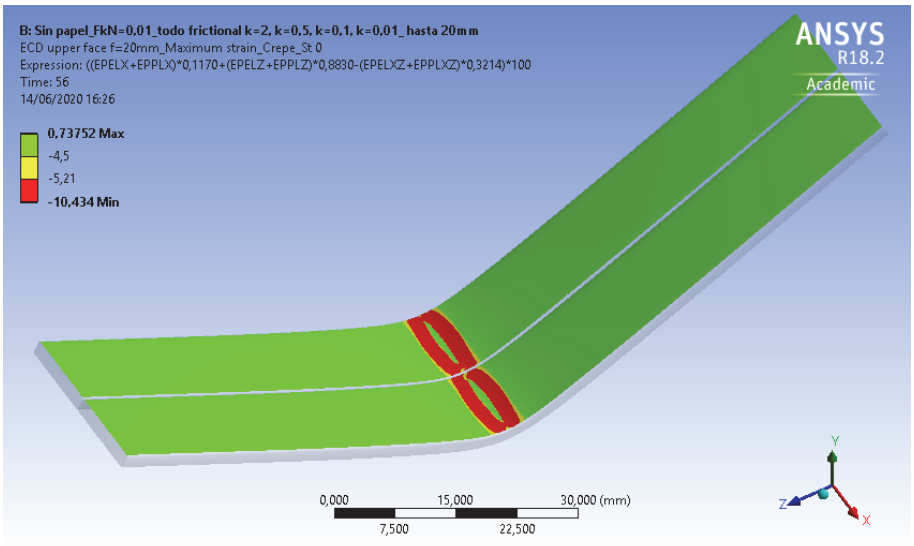

Figure 284. Maximum strain failure criterion in compression mode, $\varepsilon_{CD,c}^{max}$, for the crepe paper in Ageing State 0 on the upper face of the CTC and for d = 20 mm.

- ***Ageing State I:***

In Ageing State I, the bending tests did not produce fracture of the crepe insulation for any deflection level. That coincides with the predictions of the maximum strain failure criterion for final deflections of 5 and 10 mm. Nevertheless, that criterion predicts failure in compression on the upper faces of the CTC for $d = 20\ mm$, also in a small area of about 5 mm, see Figure 285. The reasons for that discrepancy are the same as those mentioned for Ageing State 0.

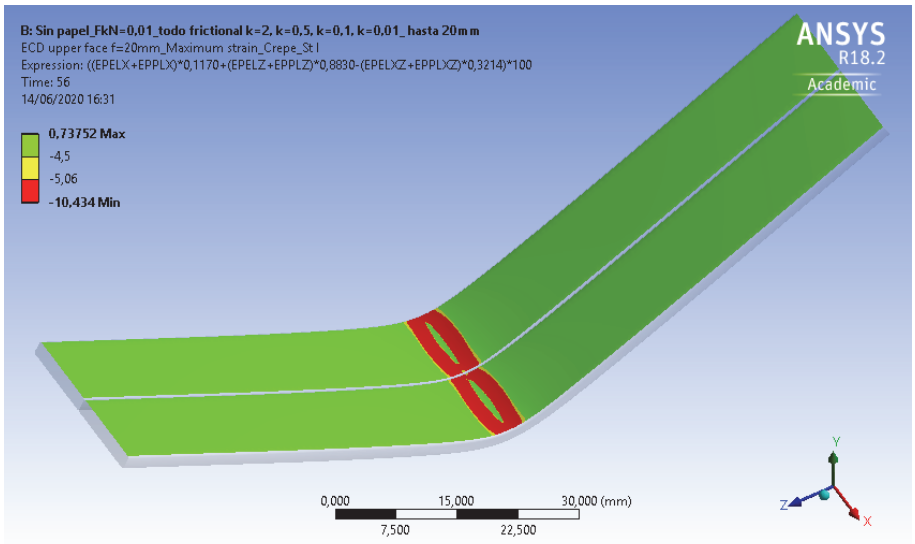

Figure 285. Maximum strain failure criterion in compression mode, $\varepsilon_{CD,c}^{max}$, for the crepe paper in Ageing State I on the upper face of the CTC and for d = 20 mm.

- ***Ageing State II:***

In Ageing State II, no cracks appeared after the bending tests with final deflections $d = 5\ mm$, $d = 10\ mm$ and $d = 20\ mm$. The maximum strain failure criterion is coherent with that for deflections of 5 and 10 mm, but it predicts failure in compression mode in a small area of about 2.5 mm in the upper face, see Figure 286, analogously as in Ageing States 0 and I.

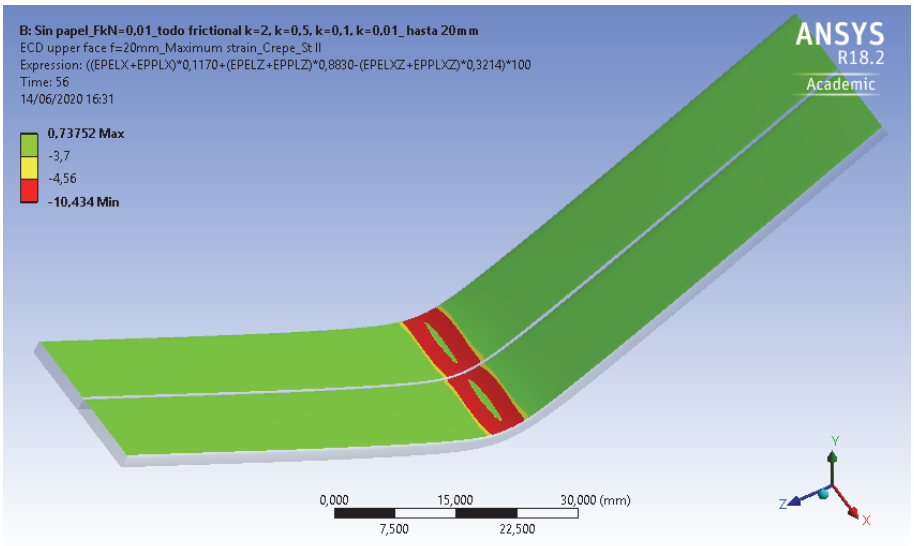

Figure 286. Maximum strain failure criterion in compression mode, $\varepsilon_{CD,c}^{max}$, for the crepe paper in Ageing State II on the upper face of the CTC and for d = 20 mm.

- ***Ageing State III:***

In Ageing State III, no cracks were obtained after the bending tests in the laboratory for $d = 5\ mm$ or $d = 10\ mm$, which agrees with the predictions of the maximum strain failure criterion. After the bending tests, small cracks (< 5 mm) were observed when $d = 20\ mm$. This is in line with the size of the areas in which failure is expected in compression and shear modes in the upper face, see Figure 287, and in the areas in which failure in shear mode is predicted on the lower and lateral side faces, see Figure 288. So, the predictions of the maximum strain failure criterion are in line with experimental observations.

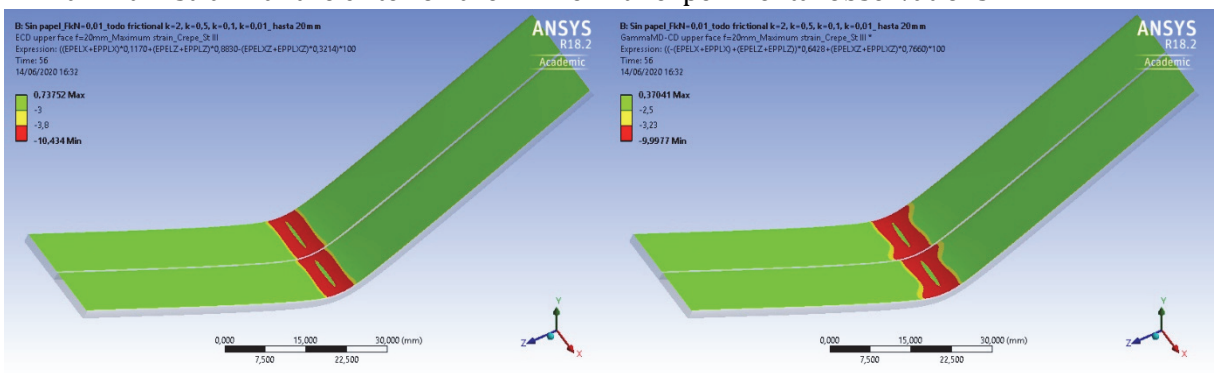

Figure 287. Maximum strain failure criterion (a) in compression mode, $\varepsilon_{CD,c}^{max}$, and (b) in shear mode, γ_{MD-CD}^{max}, for the crepe paper in Ageing State III on the upper face of the CTC and for d = 20 mm.

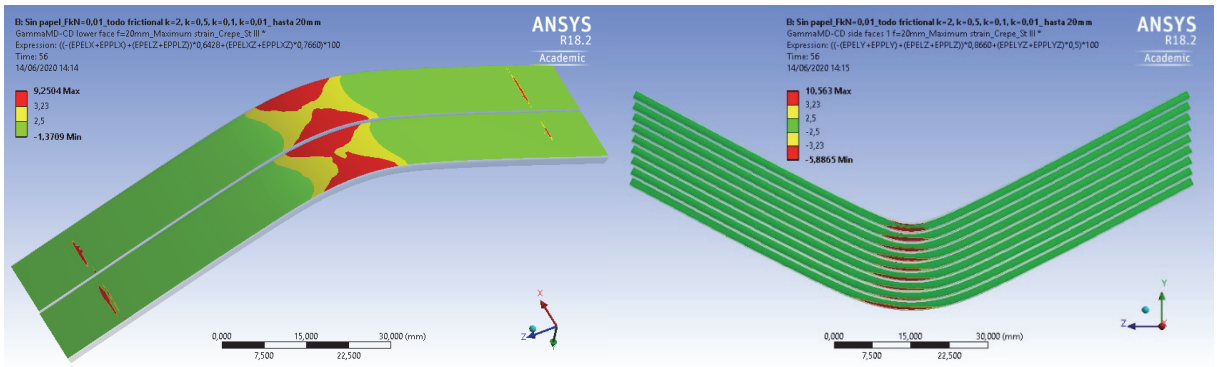

Figure 288. Maximum strain failure criterion in shear mode, γ_{MD-CD}^{max}, for the crepe paper in Ageing State III (a) on the lower face and (b) on the lateral side faces of the CTC and for d = 20 mm.

- **Conclusions about the use of the maximum strain failure criterion:**

Table 42 summarises the validity of the maximum strain criterion for the prediction of failure in the paper insulation, for each insulation material, deflection and ageing state. The meaning of "Yes" in the cells is that the prediction of the criterion was in line with experimental observations.

The meaning of "~" in the cells is that the model predicts failure of the insulation material, but the bending tests did not produce cracks. That happened, for instance, for Ageing State 0. However, it must be noted that the purpose of the present analysis is to obtain a failure criterion for the material in a realistic situation, and in no practical case will the insulation have its factory-new mechanical properties during a failure condition. That discrepancy also happened with the crepe paper in Ageing States I and II is probably caused by higher strains in the numerical model than the ones that really affected the paper insulation during the bending tests. The external layers of the insulation were almost free to slide and it is likely that they were subjected to a lower strain level. In any case, the area in which the failure is predicted by the model is very small and located in the contact region between the load cylinder and the CTC sample, where the strains are the highest; this means that the approach proposed in this study is providing a conservative description of the situation.

In the case of the plain Kraft paper in State III and with d = 20 mm, the extension of the areas of the paper insulation where $\varepsilon > \varepsilon^{max}$ cannot justify the size of the cracks observed in the laboratory. When the size of the areas in which failure is predicted by the model is smaller than the one observed after the bending tests, other mechanisms such as strain interactions, local defects in the material, etc., must have influenced the crack initiation and/or its growth.

Table 42. Validity of the predictions of the maximum tensile strain criterion for the different layers, deflections and ageing states.

Deflection	Plain Kraft paper				Crepe paper			
Ageing	State 0	State I	State II	State III	State 0	State I	State II	State III
d = 5 mm	Yes	Yes	Yes	Yes	Yes	Yes	Yes	Yes
d = 10 mm	Yes	Yes	Yes	Yes	Yes	Yes	Yes	Yes
d = 20 mm	~	Yes	Yes	~	~	~	~	Yes

3.3. A Modification of the Norris failure criterion

It is generally accepted that failure of a lamina is affected by the interaction among different failure modes. The results of the maximum strain failure criterion seemed to be coherent with experimental observations, but they do not consider that interaction, and they simplify the real failure behaviour. The application of an interactive criterion could improve the understanding of the failure mechanism, highlighting other areas of the insulated CTC samples in which failure is expected due to interaction among strains.

Several interactive failure criteria for orthotropic materials subjected to combined stresses have been proposed by different authors following the Hill-type condition. The Tsai-Hill interactive failure criterion, [130], is a simple strength criterion for anisotropic materials, developed from a scalar function of two strength tensors, and originally expressed in terms of stresses. That criterion satisfies the invariant requirements of coordinate transformation, treats interaction terms as independent components, considers the difference in strengths due to positive and negative stresses in the different four quadrants, and can be applied to different materials. The Norris criterion [133] is one of the failure criteria available in the bibliography which is based on the Tsai-Hill interactive failure criterion, and follows equation (89). In the present study, a modification of that failure criterion is proposed for the

insulation paper of a power transformer, based on strains instead of stresses, see equation (88).

$$\left(\frac{\sigma_{MD}}{\sigma_{MD}^{max}}\right)^2+\left(\frac{\sigma_{CD}}{\sigma_{CD}^{max}}\right)^2-\frac{\sigma_{MD}\cdot\sigma_{CD}}{\sigma_{MD}^{max}\cdot\sigma_{CD}^{max}}+\left(\frac{\tau_{MD-CD}}{\tau_{MD-CD}^{max}}\right)^2\geq 1 \quad (125)$$

$$\left(\frac{\varepsilon_{MD}}{\varepsilon_{MD}^{max}}\right)^2+\left(\frac{\varepsilon_{CD}}{\varepsilon_{CD}^{max}}\right)^2-\frac{\varepsilon_{MD}\cdot\varepsilon_{CD}}{\varepsilon_{MD}^{max}\cdot\varepsilon_{CD}^{max}}+\left(\frac{\gamma_{MD-CD}}{\gamma_{MD-CD}^{max}}\right)^2\geq 1 \quad (126)$$

The values of ε_{MD}, ε_{CD} and γ_{MD-CD} can be obtained for each point of the enveloping surface of the CTC sample, by means of the simulation model (see *2.2.Deformation, stress and strain distributions obtained in the CTC samples through the numerical simulation* in *2.Numerical simulation*). The values of ε_{MD}^{max}, ε_{CD}^{max}, γ_{MD-CD}^{max} were listed in Table 41. Consequently, equation (126) will be translated into four equations, in the four quadrants of the strain plane, for each of the insulation materials.

- **Failure of the plain Kraft paper:**
  - ***Ageing State 0:***

Expressions (127)-(130) are to be used, respectively, in the first, second, third and fourth quadrants in the strain plane:

$$\left(\frac{\varepsilon_{MD}}{\varepsilon_{MD,t}^{max}}\right)^2+\left(\frac{\varepsilon_{CD}}{\varepsilon_{CD,t}^{max}}\right)^2-\frac{\varepsilon_{MD}\cdot\varepsilon_{CD}}{\varepsilon_{MD,t}^{max}\cdot\varepsilon_{CD,t}^{max}}+\left(\frac{\gamma_{MD-CD}}{\gamma_{MD-CD}^{max}}\right)^2\geq 1 \quad (127)$$

$$\left(\frac{\varepsilon_{MD}}{3.42}\right)^2+\left(\frac{\varepsilon_{CD}}{8.22}\right)^2-\frac{\varepsilon_{MD}\cdot\varepsilon_{CD}}{3.42\cdot 8.22}+\left(\frac{\gamma_{MD-CD}}{5.60}\right)^2\geq 1$$

$$\left(\frac{\varepsilon_{MD}}{\varepsilon_{MD,c}^{max}}\right)^2+\left(\frac{\varepsilon_{CD}}{\varepsilon_{CD,t}^{max}}\right)^2-\frac{\varepsilon_{MD}\cdot\varepsilon_{CD}}{\varepsilon_{MD,c}^{max}\cdot\varepsilon_{CD,t}^{max}}+\left(\frac{\gamma_{MD-CD}}{\gamma_{MD-CD}^{max}}\right)^2\geq 1 \quad (128)$$

$$\left(\frac{\varepsilon_{MD}}{4.08}\right)^2+\left(\frac{\varepsilon_{CD}}{8.22}\right)^2-\frac{\varepsilon_{MD}\cdot\varepsilon_{CD}}{4.08\cdot 8.22}+\left(\frac{\gamma_{MD-CD}}{5.60}\right)^2\geq 1$$

$$\left(\frac{\varepsilon_{MD}}{\varepsilon_{MD,c}^{max}}\right)^2+\left(\frac{\varepsilon_{CD}}{\varepsilon_{CD,c}^{max}}\right)^2-\frac{\varepsilon_{MD}\cdot\varepsilon_{CD}}{\varepsilon_{MD,c}^{max}\cdot\varepsilon_{CD,c}^{max}}+\left(\frac{\gamma_{MD-CD}}{\gamma_{MD-CD}^{max}}\right)^2\geq 1 \quad (129)$$

$$\left(\frac{\varepsilon_{MD}}{4.08}\right)^2+\left(\frac{\varepsilon_{CD}}{4.08}\right)^2-\frac{\varepsilon_{MD}\cdot\varepsilon_{CD}}{4.08\cdot 4.08}+\left(\frac{\gamma_{MD-CD}}{5.60}\right)^2\geq 1$$

$$\left(\frac{\varepsilon_{MD}}{\varepsilon_{MD,t}^{max}}\right)^2+\left(\frac{\varepsilon_{CD}}{\varepsilon_{CD,c}^{max}}\right)^2-\frac{\varepsilon_{MD}\cdot\varepsilon_{CD}}{\varepsilon_{MD,t}^{max}\cdot\varepsilon_{CD,c}^{max}}+\left(\frac{\gamma_{MD-CD}}{\gamma_{MD-CD}^{max}}\right)^2\geq 1 \quad (130)$$

$$\left(\frac{\varepsilon_{MD}}{3.42}\right)^2+\left(\frac{\varepsilon_{CD}}{4.08}\right)^2-\frac{\varepsilon_{MD}\cdot\varepsilon_{CD}}{3.42\cdot 4.08}+\left(\frac{\gamma_{MD-CD}}{5.60}\right)^2\geq 1$$

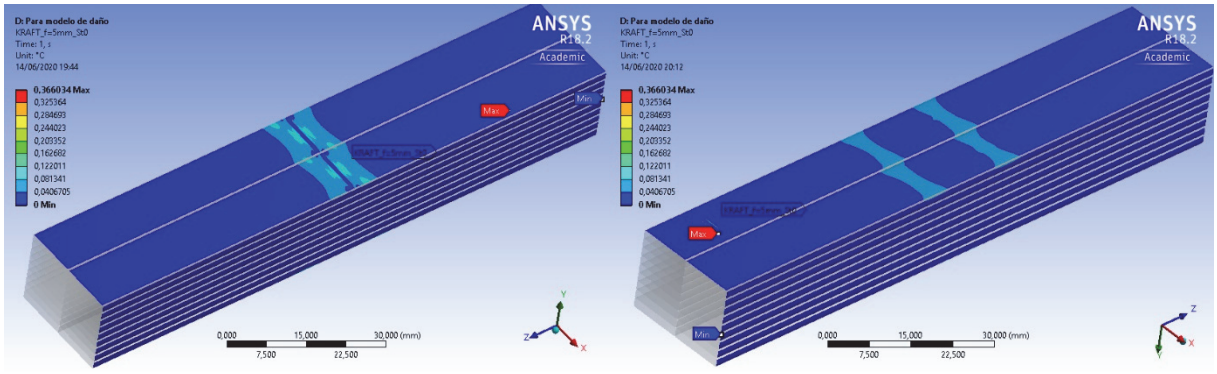

Figure 289. Modification of the Norris criterion for the plain Kraft paper in (a) upper faces and (b) lower faces of the CTC sample for Ageing State 0 and a final deflection of 5 mm.

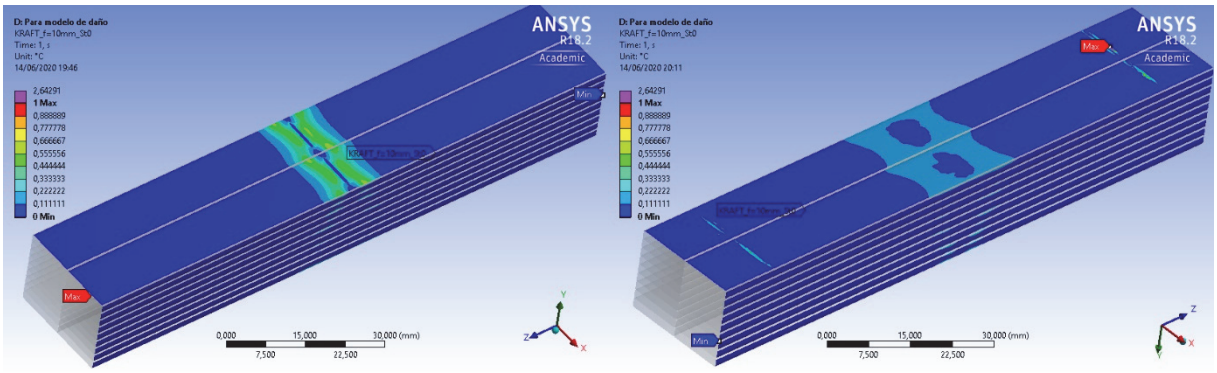

Figure 290. Modification of the Norris criterion for the plain Kraft paper in (a) upper faces and (b) lower faces of the CTC sample for Ageing State 0 and a final deflection of 10 mm.

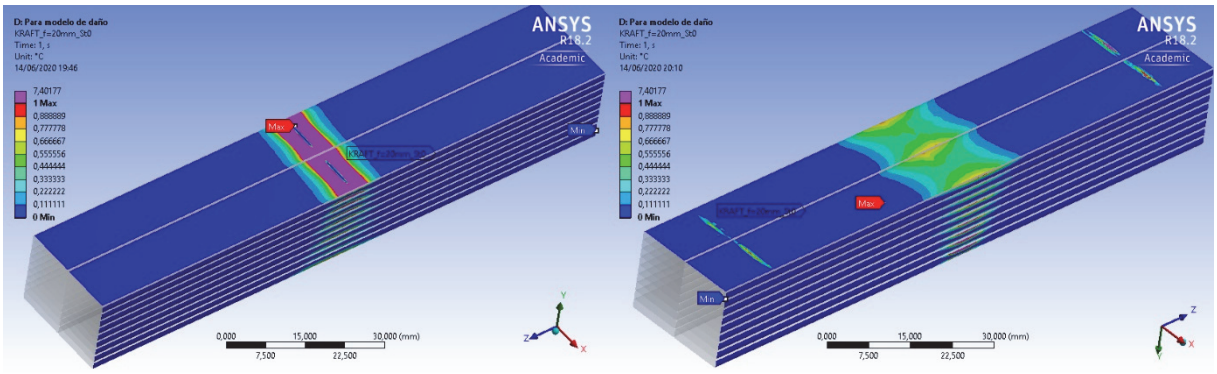

Figure 291. Modification of the Norris criterion for the plain Kraft paper in (a) upper faces and (b) lower faces of the CTC sample for Ageing State 0 and a final deflection of 20 mm.

In Ageing State 0, the bending tests over the CTC samples did not produce any fracture in layer 2 of the insulation for any deflection level. That agrees with the predictions of the Modified Norris Criterion for $d = 5\,mm$, see Figure 289, and for $d = 10\,mm$, see Figure 290, where the area in which the failure criterion is exceeded is insignificant. For $d = 20\,mm$, there is a small area on the upper face where the criterion predicts failure, which agrees with the area of contact of the load cylinder with the CTC copper sample, Figure 291. However, in the bending tests in State 0, the paper insulation was able to slide and did not suffer those high strains predicted by the numerical model.

- ***Ageing State I:***

Expressions (131)-(134) are to be used, respectively, in the first, second, third and fourth quadrants in the strain plane:

$$\left(\frac{\varepsilon_{MD}}{\varepsilon_{MD,t}^{max}}\right)^2 + \left(\frac{\varepsilon_{CD}}{\varepsilon_{CD,t}^{max}}\right)^2 - \frac{\varepsilon_{MD}\cdot\varepsilon_{CD}}{\varepsilon_{MD,t}^{max}\cdot\varepsilon_{CD,t}^{max}} + \left(\frac{\gamma_{MD-CD}}{\gamma_{MD-CD}^{max}}\right)^2 \geq 1 \tag{131}$$

$$\left(\frac{\varepsilon_{MD}}{2.54}\right)^2 + \left(\frac{\varepsilon_{CD}}{7.39}\right)^2 - \frac{\varepsilon_{MD}\cdot\varepsilon_{CD}}{2.54\cdot 7.39} + \left(\frac{\gamma_{MD-CD}}{2.94}\right)^2 \geq 1$$

$$\left(\frac{\varepsilon_{MD}}{\varepsilon_{MD,c}^{max}}\right)^2 + \left(\frac{\varepsilon_{CD}}{\varepsilon_{CD,t}^{max}}\right)^2 - \frac{\varepsilon_{MD}\cdot\varepsilon_{CD}}{\varepsilon_{MD,c}^{max}\cdot\varepsilon_{CD,t}^{max}} + \left(\frac{\gamma_{MD-CD}}{\gamma_{MD-CD}^{max}}\right)^2 \geq 1 \tag{132}$$

$$\left(\frac{\varepsilon_{MD}}{3.96}\right)^2 + \left(\frac{\varepsilon_{CD}}{7.39}\right)^2 - \frac{\varepsilon_{MD}\cdot\varepsilon_{CD}}{3.96\cdot 7.39} + \left(\frac{\gamma_{MD-CD}}{2.94}\right)^2 \geq 1$$

$$\left(\frac{\varepsilon_{MD}}{\varepsilon_{MD,c}^{max}}\right)^2 + \left(\frac{\varepsilon_{CD}}{\varepsilon_{CD,c}^{max}}\right)^2 - \frac{\varepsilon_{MD}\cdot\varepsilon_{CD}}{\varepsilon_{MD,c}^{max}\cdot\varepsilon_{CD,c}^{max}} + \left(\frac{\gamma_{MD-CD}}{\gamma_{MD-CD}^{max}}\right)^2 \geq 1 \tag{133}$$

$$\left(\frac{\varepsilon_{MD}}{3.96}\right)^2+\left(\frac{\varepsilon_{CD}}{3.96}\right)^2-\frac{\varepsilon_{MD}\cdot\varepsilon_{CD}}{3.96\cdot 3.96}+\left(\frac{\gamma_{MD-CD}}{2.94}\right)^2\geq 1$$
$$\left(\frac{\varepsilon_{MD}}{\varepsilon_{MD,t}^{max}}\right)^2+\left(\frac{\varepsilon_{CD}}{\varepsilon_{CD,c}^{max}}\right)^2-\frac{\varepsilon_{MD}\cdot\varepsilon_{CD}}{\varepsilon_{MD,t}^{max}\cdot\varepsilon_{CD,c}^{max}}+\left(\frac{\gamma_{MD-CD}}{\gamma_{MD-CD}^{max}}\right)^2\geq 1 \quad (134)$$
$$\left(\frac{\varepsilon_{MD}}{2.54}\right)^2+\left(\frac{\varepsilon_{CD}}{3.96}\right)^2-\frac{\varepsilon_{MD}\cdot\varepsilon_{CD}}{2.54\cdot 3.96}+\left(\frac{\gamma_{MD-CD}}{2.94}\right)^2\geq 1$$

In Ageing State I, the bending tests with final deflection $d = 5\ mm$ over the CTC samples did not produce any fracture in layer 2 of the insulation, in agreement with the predictions of the Modified Norris criterion, see Figure 292. For this state, small cracks were observed in the laboratory after the bending tests with a final deflection $d = 10\ mm$, which also coincides with the predicted behaviour, see Figure 293. For $d = 20\ mm$, the failure area predicted by the model has a size slightly larger than the one of the cracks observed after the bending tests (5 – 10 mm), see Figure 294, but, again, the predictions are reliable and conservative.

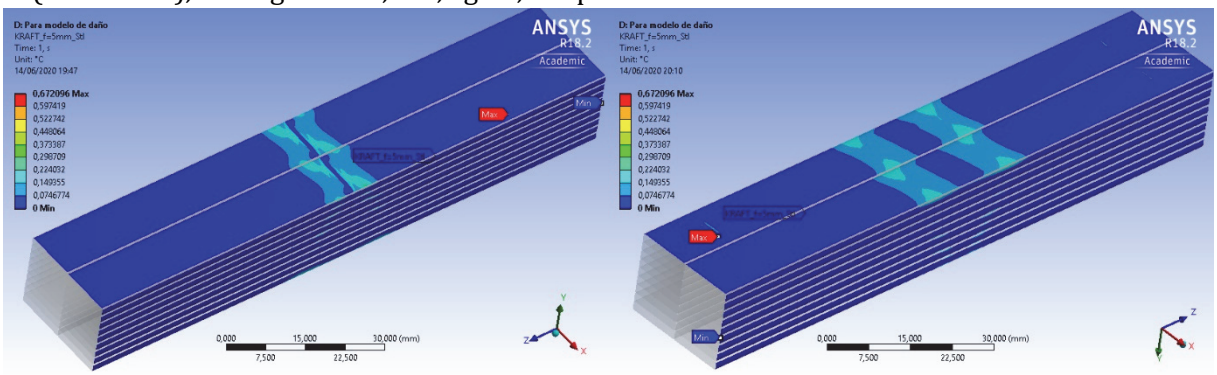

Figure 292. Modification of the Norris criterion for the plain Kraft paper in (a) upper faces and (b) lower faces of the CTC sample for Ageing State I and a final deflection of 5 mm.

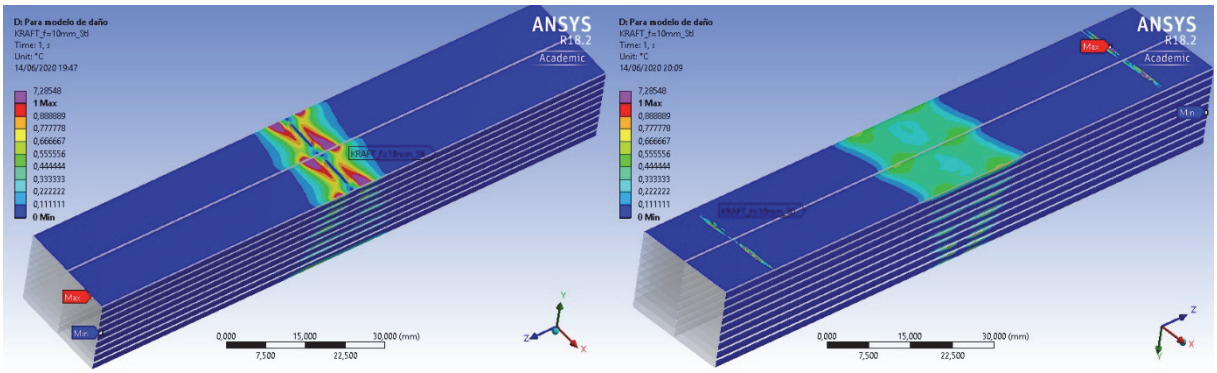

Figure 293. Modification of the Norris criterion for the plain Kraft paper in (a) upper faces and (b) lower faces of the CTC sample for Ageing State I and a final deflection of 10 mm.

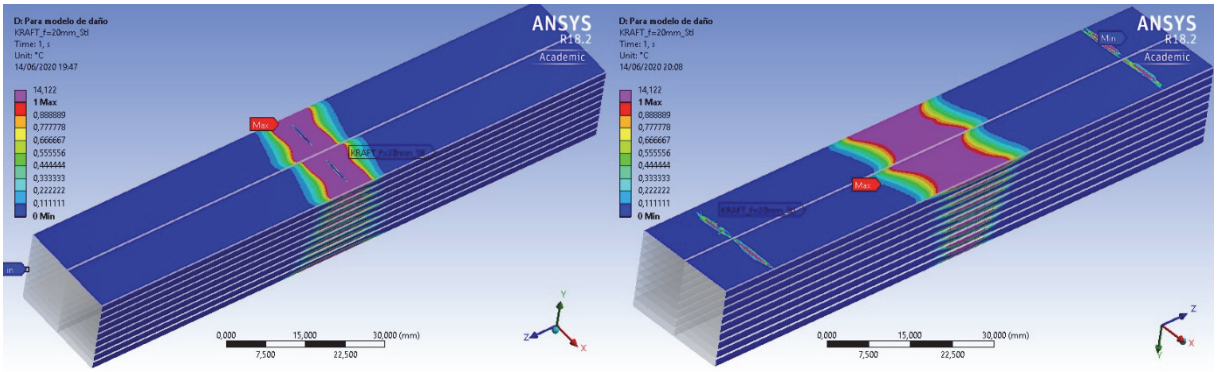

Figure 294. Modification of the Norris criterion for the plain Kraft paper in (a) upper faces and (b) lower faces of the CTC sample for Ageing State I and a final deflection of 20 mm.

- ***Ageing State II:***

Expressions (135)-(138) are to be used, respectively, in the first, second, third and fourth quadrants in the strain plane:

$$\left(\frac{\varepsilon_{MD}}{\varepsilon_{MD,t}^{max}}\right)^2+\left(\frac{\varepsilon_{CD}}{\varepsilon_{CD,t}^{max}}\right)^2-\frac{\varepsilon_{MD}\cdot\varepsilon_{CD}}{\varepsilon_{MD,t}^{max}\cdot\varepsilon_{CD,t}^{max}}+\left(\frac{\gamma_{MD-CD}}{\gamma_{MD-CD}^{max}}\right)^2\geq 1 \quad (135)$$

$$\left(\frac{\varepsilon_{MD}}{2.03}\right)^2+\left(\frac{\varepsilon_{CD}}{6.09}\right)^2-\frac{\varepsilon_{MD}\cdot\varepsilon_{CD}}{2.03\cdot 6.09}+\left(\frac{\gamma_{MD-CD}}{2.60}\right)^2\geq 1$$

$$\left(\frac{\varepsilon_{MD}}{\varepsilon_{MD,c}^{max}}\right)^2+\left(\frac{\varepsilon_{CD}}{\varepsilon_{CD,t}^{max}}\right)^2-\frac{\varepsilon_{MD}\cdot\varepsilon_{CD}}{\varepsilon_{MD,c}^{max}\cdot\varepsilon_{CD,t}^{max}}+\left(\frac{\gamma_{MD-CD}}{\gamma_{MD-CD}^{max}}\right)^2\geq 1 \quad (136)$$

$$\left(\frac{\varepsilon_{MD}}{3.58}\right)^2+\left(\frac{\varepsilon_{CD}}{6.09}\right)^2-\frac{\varepsilon_{MD}\cdot\varepsilon_{CD}}{3.58\cdot 6.09}+\left(\frac{\gamma_{MD-CD}}{2.60}\right)^2\geq 1$$

$$\left(\frac{\varepsilon_{MD}}{\varepsilon_{MD,c}^{max}}\right)^2+\left(\frac{\varepsilon_{CD}}{\varepsilon_{CD,c}^{max}}\right)^2-\frac{\varepsilon_{MD}\cdot\varepsilon_{CD}}{\varepsilon_{MD,c}^{max}\cdot\varepsilon_{CD,c}^{max}}+\left(\frac{\gamma_{MD-CD}}{\gamma_{MD-CD}^{max}}\right)^2\geq 1 \quad (137)$$

$$\left(\frac{\varepsilon_{MD}}{3.58}\right)^2+\left(\frac{\varepsilon_{CD}}{3.58}\right)^2-\frac{\varepsilon_{MD}\cdot\varepsilon_{CD}}{3.58\cdot 3.58}+\left(\frac{\gamma_{MD-CD}}{2.60}\right)^2\geq 1$$

$$\left(\frac{\varepsilon_{MD}}{\varepsilon_{MD,t}^{max}}\right)^2+\left(\frac{\varepsilon_{CD}}{\varepsilon_{CD,c}^{max}}\right)^2-\frac{\varepsilon_{MD}\cdot\varepsilon_{CD}}{\varepsilon_{MD,t}^{max}\cdot\varepsilon_{CD,c}^{max}}+\left(\frac{\gamma_{MD-CD}}{\gamma_{MD-CD}^{max}}\right)^2\geq 1 \quad (138)$$

$$\left(\frac{\varepsilon_{MD}}{2.03}\right)^2+\left(\frac{\varepsilon_{CD}}{3.58}\right)^2-\frac{\varepsilon_{MD}\cdot\varepsilon_{CD}}{2.03\cdot 3.58}+\left(\frac{\gamma_{MD-CD}}{2.60}\right)^2\geq 1$$

In Ageing State II, the predictions of the Modified Norris criterion are in line with the experimental observations for all the deflections levels. No failure is observed when $d = 5\ mm$, see Figure 295; small cracks (< 5 mm) appear when $d = 10\ mm$, see Figure 296; and big cracks (> 10 mm) are produced when $d = 20\ mm$, see Figure 297.

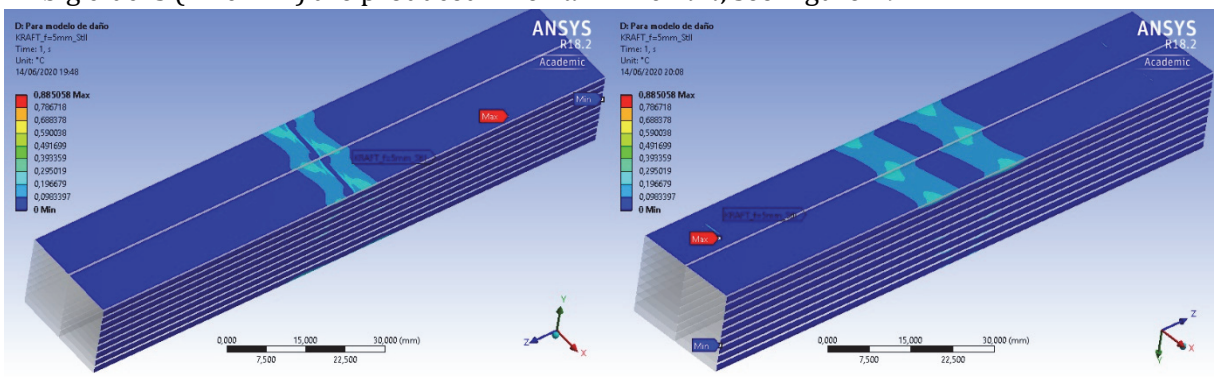

Figure 295. Modification of the Norris criterion for the plain Kraft paper in (a) upper faces and (b) lower faces of the CTC sample for Ageing State II and a final deflection of 5 mm.

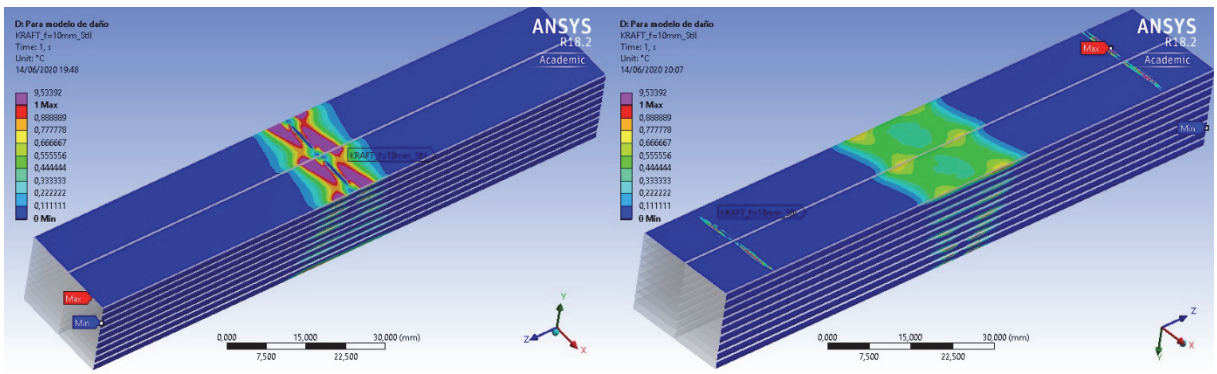

Figure 296. Modification of the Norris criterion for the plain Kraft paper in (a) upper faces and (b) lower faces of the CTC sample for Ageing State II and a final deflection of 10 mm.

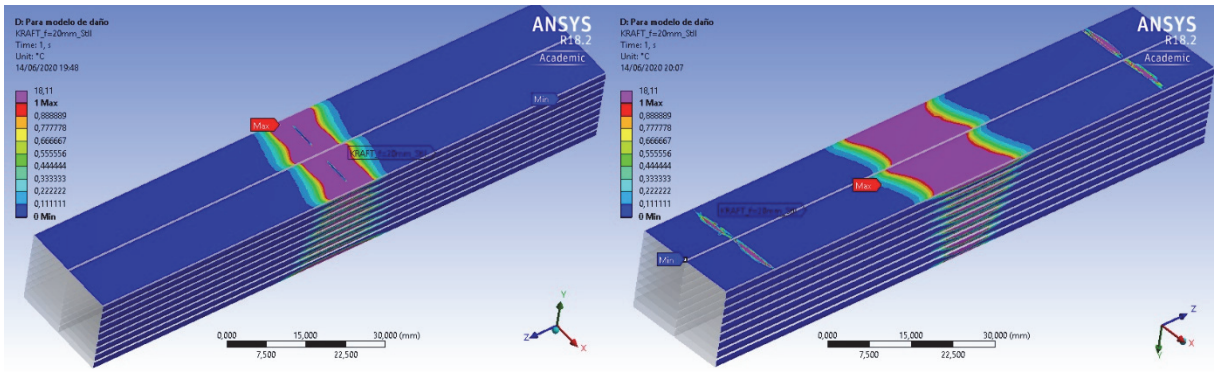

Figure 297. Modification of the Norris criterion for the plain Kraft paper in (a) upper faces and (b) lower faces of the CTC sample for Ageing State II and a final deflection of 20 mm.

- ***Ageing State III:***

Expressions (139) and (142) are to be used, respectively, in the first, second, third and fourth quadrants in the strain plane:

$$\left(\frac{\varepsilon_{MD}}{\varepsilon_{MD,t}^{max}}\right)^2+\left(\frac{\varepsilon_{CD}}{\varepsilon_{CD,t}^{max}}\right)^2-\frac{\varepsilon_{MD}\cdot\varepsilon_{CD}}{\varepsilon_{MD,t}^{max}\cdot\varepsilon_{CD,t}^{max}}+\left(\frac{\gamma_{MD-CD}}{\gamma_{MD-CD}^{max}}\right)^2\geq 1 \tag{139}$$

$$\left(\frac{\varepsilon_{MD}}{1.19}\right)^2+\left(\frac{\varepsilon_{CD}}{5.50}\right)^2-\frac{\varepsilon_{MD}\cdot\varepsilon_{CD}}{1.19\cdot 5.50}+\left(\frac{\gamma_{MD-CD}}{1.68}\right)^2\geq 1$$

$$\left(\frac{\varepsilon_{MD}}{\varepsilon_{MD,c}^{max}}\right)^2+\left(\frac{\varepsilon_{CD}}{\varepsilon_{CD,t}^{max}}\right)^2-\frac{\varepsilon_{MD}\cdot\varepsilon_{CD}}{\varepsilon_{MD,c}^{max}\cdot\varepsilon_{CD,t}^{max}}+\left(\frac{\gamma_{MD-CD}}{\gamma_{MD-CD}^{max}}\right)^2\geq 1 \tag{140}$$

$$\left(\frac{\varepsilon_{MD}}{2.99}\right)^2+\left(\frac{\varepsilon_{CD}}{5.50}\right)^2-\frac{\varepsilon_{MD}\cdot\varepsilon_{CD}}{2.99\cdot 5.50}+\left(\frac{\gamma_{MD-CD}}{1.68}\right)^2\geq 1$$

$$\left(\frac{\varepsilon_{MD}}{\varepsilon_{MD,c}^{max}}\right)^2+\left(\frac{\varepsilon_{CD}}{\varepsilon_{CD,c}^{max}}\right)^2-\frac{\varepsilon_{MD}\cdot\varepsilon_{CD}}{\varepsilon_{MD,c}^{max}\cdot\varepsilon_{CD,c}^{max}}+\left(\frac{\gamma_{MD-CD}}{\gamma_{MD-CD}^{max}}\right)^2\geq 1 \tag{141}$$

$$\left(\frac{\varepsilon_{MD}}{2.99}\right)^2+\left(\frac{\varepsilon_{CD}}{2.99}\right)^2-\frac{\varepsilon_{MD}\cdot\varepsilon_{CD}}{2.99\cdot 2.99}+\left(\frac{\gamma_{MD-CD}}{1.68}\right)^2\geq 1$$

$$\left(\frac{\varepsilon_{MD}}{\varepsilon_{MD,t}^{max}}\right)^2+\left(\frac{\varepsilon_{CD}}{\varepsilon_{CD,c}^{max}}\right)^2-\frac{\varepsilon_{MD}\cdot\varepsilon_{CD}}{\varepsilon_{MD,t}^{max}\cdot\varepsilon_{CD,c}^{max}}+\left(\frac{\gamma_{MD-CD}}{\gamma_{MD-CD}^{max}}\right)^2\geq 1 \tag{142}$$

$$\left(\frac{\varepsilon_{MD}}{1.19}\right)^2+\left(\frac{\varepsilon_{CD}}{2.99}\right)^2-\frac{\varepsilon_{MD}\cdot\varepsilon_{CD}}{1.19\cdot 2.99}+\left(\frac{\gamma_{MD-CD}}{1.68}\right)^2\geq 1$$

In Ageing State III, the predictions of the Modified Norris criterion are in line with experimental observations for all the deflections levels. No failure occurs when $d = 5\,mm$, see Figure 298; big cracks (> 10 mm) are observed when $d = 10\,mm$, see Figure 299; and the total fracture occurs when $d = 20\,mm$, see Figure 300.

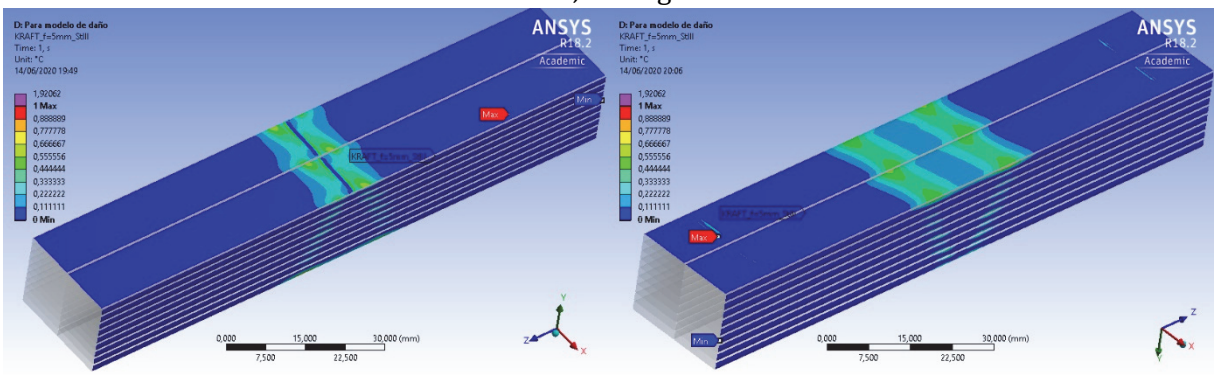

Figure 298. Modification of the Norris criterion for the plain Kraft paper in (a) upper faces and (b) lower faces of the CTC sample for Ageing State III and a final deflection of 5 mm.

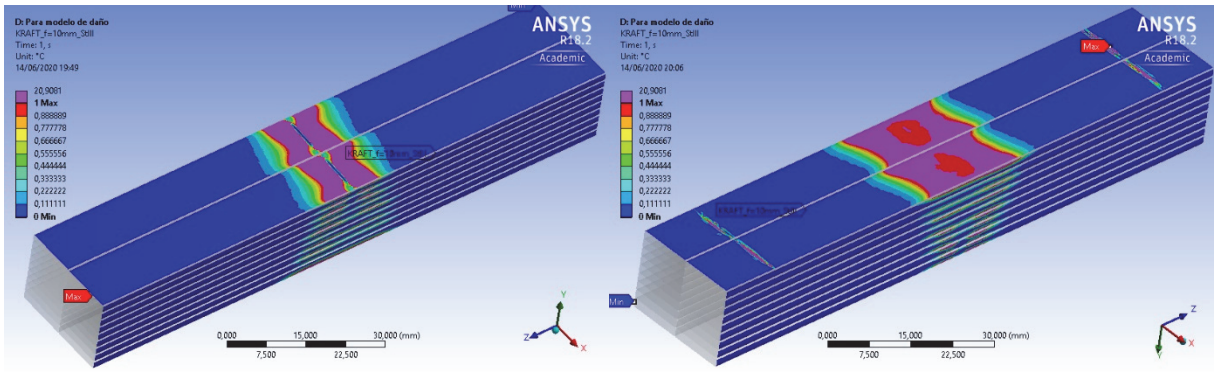

Figure 299. Modification of the Norris criterion for the plain Kraft paper in (a) upper faces and (b) lower faces of the CTC sample for Ageing State III and a final deflection of 10 mm.

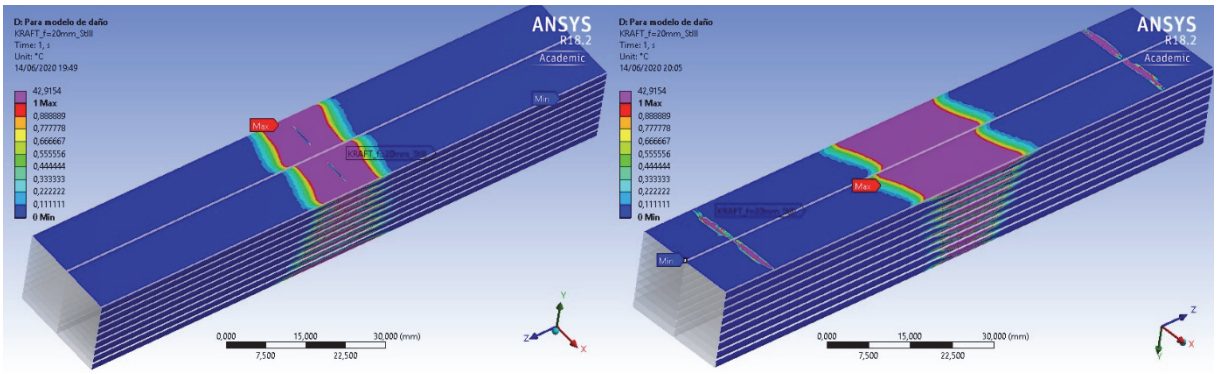

Figure 300. Modification of the Norris criterion for the plain Kraft paper in (a) upper faces and (b) lower faces of the CTC sample for Ageing State III and a final deflection of 20 mm.

- **FAILURE OF THE CREPE PAPER:**

- ***Ageing State 0:***

Expressions (*143*)-(*146*) are to be used, respectively, in the first, second, third and fourth quadrants in the strain plane:

$$\left(\frac{\varepsilon_{MD}}{\varepsilon_{MD,t}^{max}}\right)^2+\left(\frac{\varepsilon_{CD}}{\varepsilon_{CD,t}^{max}}\right)^2-\frac{\varepsilon_{MD}\cdot\varepsilon_{CD}}{\varepsilon_{MD,t}^{max}\cdot\varepsilon_{CD,t}^{max}}+\left(\frac{\gamma_{MD-CD}}{\gamma_{MD-CD}^{max}}\right)^2\geq 1 \tag{143}$$

$$\left(\frac{\varepsilon_{MD}}{23.09}\right)^2+\left(\frac{\varepsilon_{CD}}{11.82}\right)^2-\frac{\varepsilon_{MD}\cdot\varepsilon_{CD}}{23.09\cdot 11.82}+\left(\frac{\gamma_{MD-CD}}{28.76}\right)^2\geq 1$$

$$\left(\frac{\varepsilon_{MD}}{\varepsilon_{MD,c}^{max}}\right)^2+\left(\frac{\varepsilon_{CD}}{\varepsilon_{CD,t}^{max}}\right)^2-\frac{\varepsilon_{MD}\cdot\varepsilon_{CD}}{\varepsilon_{MD,c}^{max}\cdot\varepsilon_{CD,t}^{max}}+\left(\frac{\gamma_{MD-CD}}{\gamma_{MD-CD}^{max}}\right)^2\geq 1 \tag{144}$$

$$\left(\frac{\varepsilon_{MD}}{4.42}\right)^2+\left(\frac{\varepsilon_{CD}}{11.82}\right)^2-\frac{\varepsilon_{MD}\cdot\varepsilon_{CD}}{4.42\cdot 11.82}+\left(\frac{\gamma_{MD-CD}}{28.76}\right)^2\geq 1$$

$$\left(\frac{\varepsilon_{MD}}{\varepsilon_{MD,c}^{max}}\right)^2+\left(\frac{\varepsilon_{CD}}{\varepsilon_{CD,c}^{max}}\right)^2-\frac{\varepsilon_{MD}\cdot\varepsilon_{CD}}{\varepsilon_{MD,c}^{max}\cdot\varepsilon_{CD,c}^{max}}+\left(\frac{\gamma_{MD-CD}}{\gamma_{MD-CD}^{max}}\right)^2\geq 1 \tag{145}$$

$$\left(\frac{\varepsilon_{MD}}{4.42}\right)^2+\left(\frac{\varepsilon_{CD}}{4.42}\right)^2-\frac{\varepsilon_{MD}\cdot\varepsilon_{CD}}{4.42\cdot 4.42}+\left(\frac{\gamma_{MD-CD}}{28.76}\right)^2\geq 1$$

$$\left(\frac{\varepsilon_{MD}}{\varepsilon_{MD,t}^{max}}\right)^2+\left(\frac{\varepsilon_{CD}}{\varepsilon_{CD,c}^{max}}\right)^2-\frac{\varepsilon_{MD}\cdot\varepsilon_{CD}}{\varepsilon_{MD,t}^{max}\cdot\varepsilon_{CD,c}^{max}}+\left(\frac{\gamma_{MD-CD}}{\gamma_{MD-CD}^{max}}\right)^2\geq 1 \tag{146}$$

$$\left(\frac{\varepsilon_{MD}}{23.09}\right)^2+\left(\frac{\varepsilon_{CD}}{4.42}\right)^2-\frac{\varepsilon_{MD}\cdot\varepsilon_{CD}}{23.09\cdot 4.42}+\left(\frac{\gamma_{MD-CD}}{28.76}\right)^2\geq 1$$

In Ageing State 0, the bending tests over the CTC samples did not produce any fracture in layers 3 and 4 of the insulation, made of crepe paper, for any deflection level. That agrees with the predictions of the Modified Norris Criterion for $d = 5\ mm$, see Figure 301, and for

$d = 10\,mm$, see Figure 302. However, analogously as with the plain Kraft paper in this ageing state, for $d = 20\,mm$, there is a small area in the upper face where the criterion predicts failure, coinciding with the area of contact between the load cylinder and the CTC, Figure 302. However, the crepe insulation in State 0 was able to slide and did not suffer those high strains predicted by this conservative model.

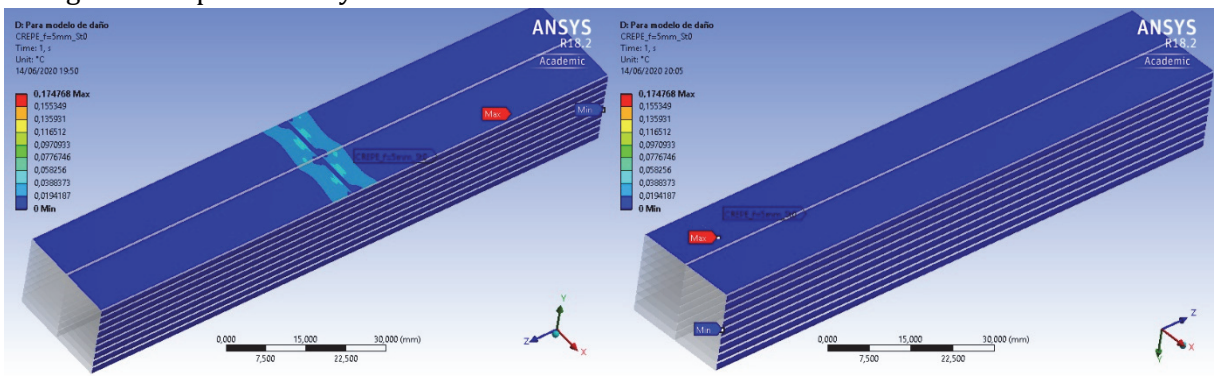

Figure 301. Modification of the Norris criterion for the crepe paper in (a) upper faces and (b) lower faces of the CTC sample for Ageing State 0 and a final deflection of 5 mm.

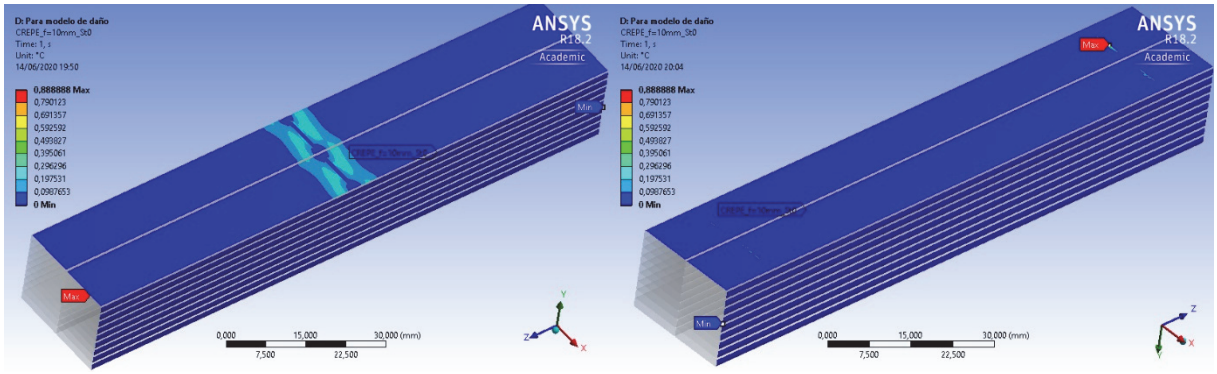

Figure 302. Modification of the Norris criterion for the crepe paper in (a) upper faces and (b) lower faces of the CTC sample for Ageing State 0 and a final deflection of 10 mm.

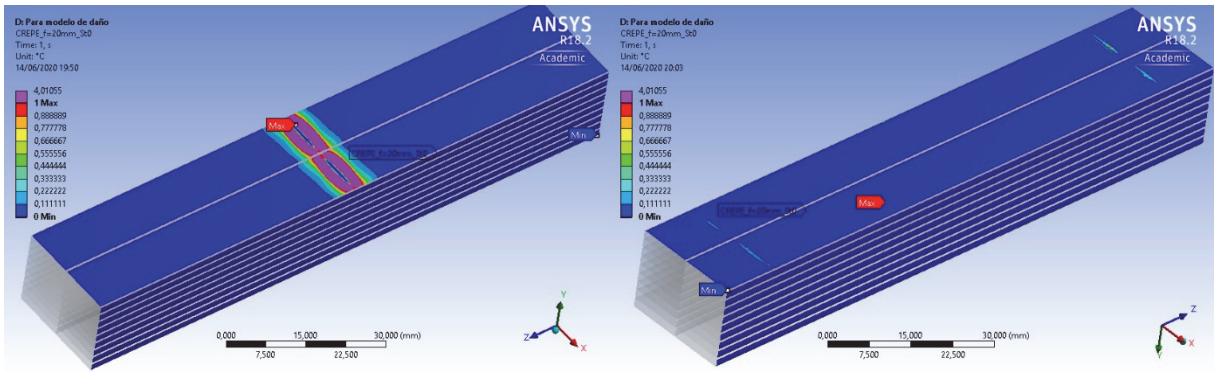

Figure 303. Modification of the Norris criterion for the crepe paper in (a) upper faces and (b) lower faces of the CTC sample for Ageing State 0 and a final deflection of 20 mm.

- ***Ageing State I:***

Expressions (147)-(150) are to be used, respectively, in the first, second, third and fourth quadrants in the strain plane:

$$\left(\frac{\varepsilon_{MD}}{\varepsilon_{MD,t}^{max}}\right)^2 + \left(\frac{\varepsilon_{CD}}{\varepsilon_{CD,t}^{max}}\right)^2 - \frac{\varepsilon_{MD}\cdot\varepsilon_{CD}}{\varepsilon_{MD,t}^{max}\cdot\varepsilon_{CD,t}^{max}} + \left(\frac{\gamma_{MD-CD}}{\gamma_{MD-CD}^{max}}\right)^2 \geq 1 \tag{147}$$

$$\left(\frac{\varepsilon_{MD}}{22.11}\right)^2 + \left(\frac{\varepsilon_{CD}}{10.37}\right)^2 - \frac{\varepsilon_{MD}\cdot\varepsilon_{CD}}{22.11\cdot 10.37} + \left(\frac{\gamma_{MD-CD}}{11.98}\right)^2 \geq 1$$

$$\left(\frac{\varepsilon_{MD}}{\varepsilon_{MD,c}^{max}}\right)^2+\left(\frac{\varepsilon_{CD}}{\varepsilon_{CD,t}^{max}}\right)^2-\frac{\varepsilon_{MD}\cdot\varepsilon_{CD}}{\varepsilon_{MD,c}^{max}\cdot\varepsilon_{CD,t}^{max}}+\left(\frac{\gamma_{MD-CD}}{\gamma_{MD-CD}^{max}}\right)^2\geq 1 \tag{148}$$

$$\left(\frac{\varepsilon_{MD}}{4.35}\right)^2+\left(\frac{\varepsilon_{CD}}{10.37}\right)^2-\frac{\varepsilon_{MD}\cdot\varepsilon_{CD}}{4.35\cdot 10.37}+\left(\frac{\gamma_{MD-CD}}{11.98}\right)^2\geq 1$$

$$\left(\frac{\varepsilon_{MD}}{\varepsilon_{MD,c}^{max}}\right)^2+\left(\frac{\varepsilon_{CD}}{\varepsilon_{CD,c}^{max}}\right)^2-\frac{\varepsilon_{MD}\cdot\varepsilon_{CD}}{\varepsilon_{MD,c}^{max}\cdot\varepsilon_{CD,c}^{max}}+\left(\frac{\gamma_{MD-CD}}{\gamma_{MD-CD}^{max}}\right)^2\geq 1 \tag{149}$$

$$\left(\frac{\varepsilon_{MD}}{4.35}\right)^2+\left(\frac{\varepsilon_{CD}}{4.35}\right)^2-\frac{\varepsilon_{MD}\cdot\varepsilon_{CD}}{4.35\cdot 4.35}+\left(\frac{\gamma_{MD-CD}}{11.98}\right)^2\geq 1$$

$$\left(\frac{\varepsilon_{MD}}{\varepsilon_{MD,t}^{max}}\right)^2+\left(\frac{\varepsilon_{CD}}{\varepsilon_{CD,c}^{max}}\right)^2-\frac{\varepsilon_{MD}\cdot\varepsilon_{CD}}{\varepsilon_{MD,t}^{max}\cdot\varepsilon_{CD,c}^{max}}+\left(\frac{\gamma_{MD-CD}}{\gamma_{MD-CD}^{max}}\right)^2\geq 1 \tag{150}$$

$$\left(\frac{\varepsilon_{MD}}{22.11}\right)^2+\left(\frac{\varepsilon_{CD}}{4.35}\right)^2-\frac{\varepsilon_{MD}\cdot\varepsilon_{CD}}{22.11\cdot 4.35}+\left(\frac{\gamma_{MD-CD}}{11.98}\right)^2\geq 1$$

In Ageing State I, the bending tests with final deflection $d = 5\ mm$ and $d = 10\ mm$ over the CTC samples did not produce any fracture in the crepe insulation, and that coincides with the predictions of the Modified Norris criterion, see Figure 304 and Figure 305, where the area in which the criterion is exceeded is irrelevant. In the same way as in Ageing State 0, there is a small area (the contact between the load cylinder and the CTC sample) in which failure is predicted in the upper faces, see Figure 306, while no cracks were produced by the bending tests.

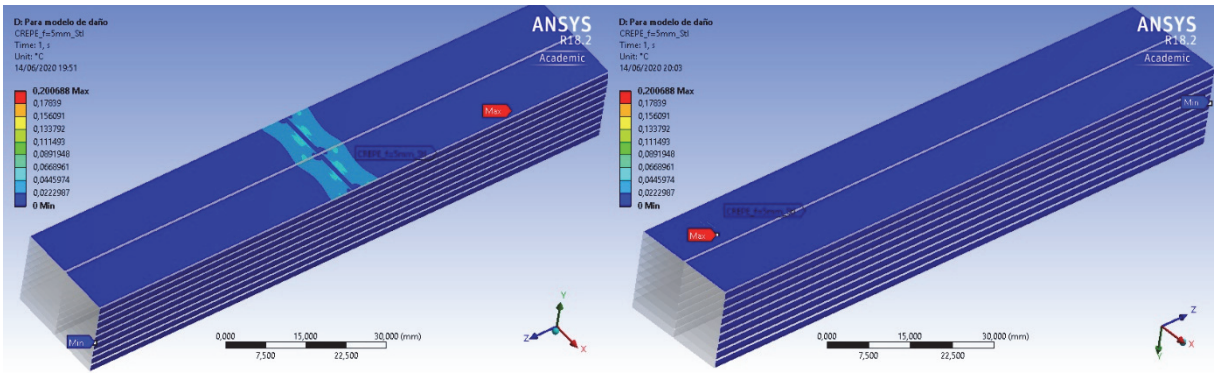

Figure 304. Modification of the Norris criterion for the crepe paper in (a) upper faces and (b) lower faces of the CTC sample for Ageing State I and a final deflection of 5 mm.

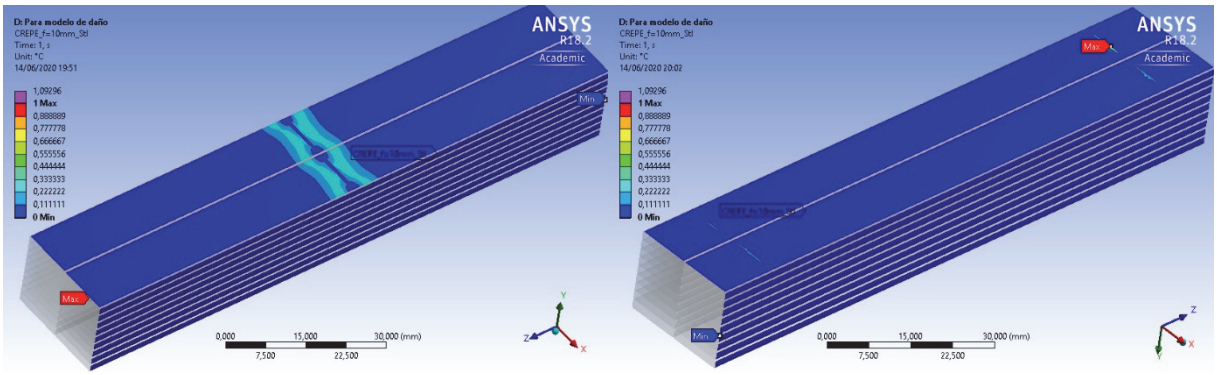

Figure 305. Modification of the Norris criterion for the crepe paper in (a) upper faces and (b) lower faces of the CTC sample for Ageing State I and a final deflection of 10 mm.

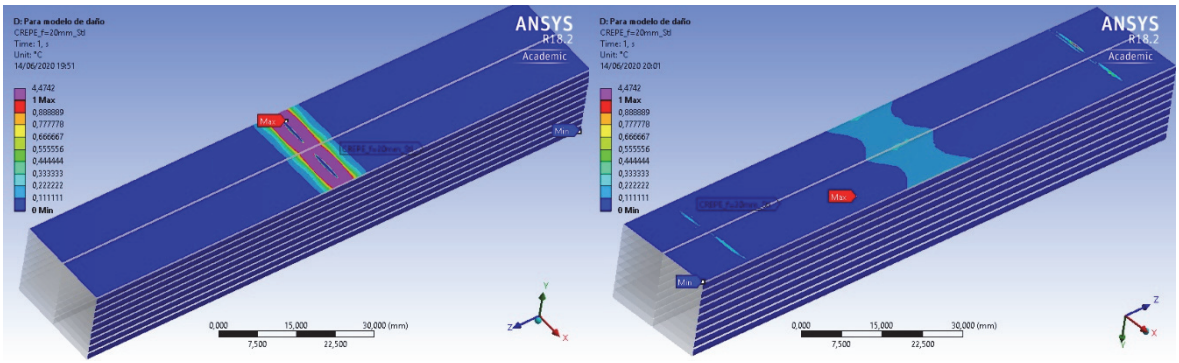

Figure 306. Modification of the Norris criterion for the crepe paper in (a) upper faces and (b) lower faces of the CTC sample for Ageing State I and a final deflection of 20 mm.

- ***Ageing State II:***

Expressions (151)-(154) are to be used, respectively, in the first, second, third and fourth quadrants in the strain plane:

$$\left(\frac{\varepsilon_{MD}}{\varepsilon_{MD,t}^{max}}\right)^2+\left(\frac{\varepsilon_{CD}}{\varepsilon_{CD,t}^{max}}\right)^2-\frac{\varepsilon_{MD}\cdot\varepsilon_{CD}}{\varepsilon_{MD,t}^{max}\cdot\varepsilon_{CD,t}^{max}}+\left(\frac{\gamma_{MD-CD}}{\gamma_{MD-CD}^{max}}\right)^2\geq 1 \quad (151)$$

$$\left(\frac{\varepsilon_{MD}}{20.43}\right)^2+\left(\frac{\varepsilon_{CD}}{7.79}\right)^2-\frac{\varepsilon_{MD}\cdot\varepsilon_{CD}}{20.43\cdot 7.79}+\left(\frac{\gamma_{MD-CD}}{10.20}\right)^2\geq 1$$

$$\left(\frac{\varepsilon_{MD}}{\varepsilon_{MD,c}^{max}}\right)^2+\left(\frac{\varepsilon_{CD}}{\varepsilon_{CD,t}^{max}}\right)^2-\frac{\varepsilon_{MD}\cdot\varepsilon_{CD}}{\varepsilon_{MD,c}^{max}\cdot\varepsilon_{CD,t}^{max}}+\left(\frac{\gamma_{MD-CD}}{\gamma_{MD-CD}^{max}}\right)^2\geq 1 \quad (152)$$

$$\left(\frac{\varepsilon_{MD}}{4.13}\right)^2+\left(\frac{\varepsilon_{CD}}{7.79}\right)^2-\frac{\varepsilon_{MD}\cdot\varepsilon_{CD}}{4.13\cdot 7.79}+\left(\frac{\gamma_{MD-CD}}{10.20}\right)^2\geq 1$$

$$\left(\frac{\varepsilon_{MD}}{\varepsilon_{MD,c}^{max}}\right)^2+\left(\frac{\varepsilon_{CD}}{\varepsilon_{CD,c}^{max}}\right)^2-\frac{\varepsilon_{MD}\cdot\varepsilon_{CD}}{\varepsilon_{MD,c}^{max}\cdot\varepsilon_{CD,c}^{max}}+\left(\frac{\gamma_{MD-CD}}{\gamma_{MD-CD}^{max}}\right)^2\geq 1 \quad (153)$$

$$\left(\frac{\varepsilon_{MD}}{4.13}\right)^2+\left(\frac{\varepsilon_{CD}}{4.13}\right)^2-\frac{\varepsilon_{MD}\cdot\varepsilon_{CD}}{4.13\cdot 4.13}+\left(\frac{\gamma_{MD-CD}}{10.20}\right)^2\geq 1$$

$$\left(\frac{\varepsilon_{MD}}{\varepsilon_{MD,t}^{max}}\right)^2+\left(\frac{\varepsilon_{CD}}{\varepsilon_{CD,c}^{max}}\right)^2-\frac{\varepsilon_{MD}\cdot\varepsilon_{CD}}{\varepsilon_{MD,t}^{max}\cdot\varepsilon_{CD,c}^{max}}+\left(\frac{\gamma_{MD-CD}}{\gamma_{MD-CD}^{max}}\right)^2\geq 1 \quad (154)$$

$$\left(\frac{\varepsilon_{MD}}{20.43}\right)^2+\left(\frac{\varepsilon_{CD}}{4.13}\right)^2-\frac{\varepsilon_{MD}\cdot\varepsilon_{CD}}{20.43\cdot 4.13}+\left(\frac{\gamma_{MD-CD}}{10.20}\right)^2\geq 1$$

In Ageing State II, the tests with deflections of 5 and 10 mm did not produce any fracture of the crepe insulation, and that coincides with the predictions of the Modified Norris criterion, see Figure 307 and Figure 308, where the area in which the criterion is exceeded is negligible. In the same way as in states 0 and I, failure is predicted in the contact between the load cylinder and the CTC sample on the upper faces, see Figure 309, while no cracks were produced by the bending tests for this deflection and ageing state.

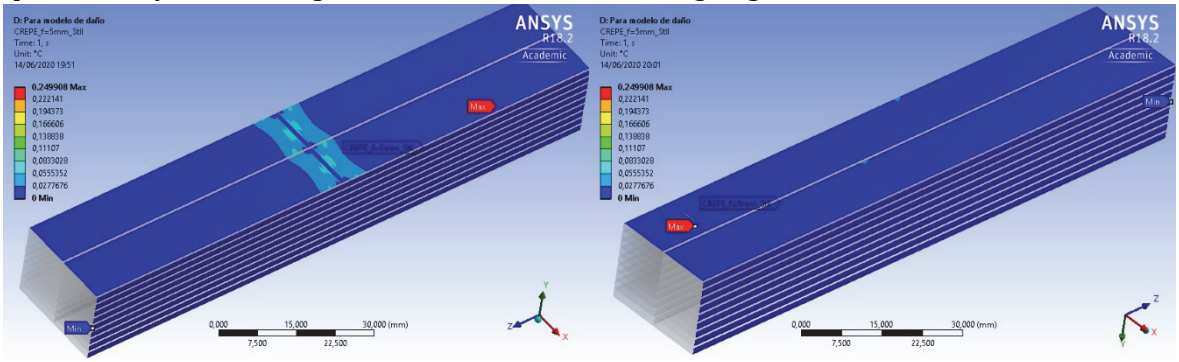

Figure 307. Modification of the Norris criterion for the crepe paper in (a) upper faces and (b) lower faces of the CTC sample for Ageing State II and a final deflection of 5 mm.

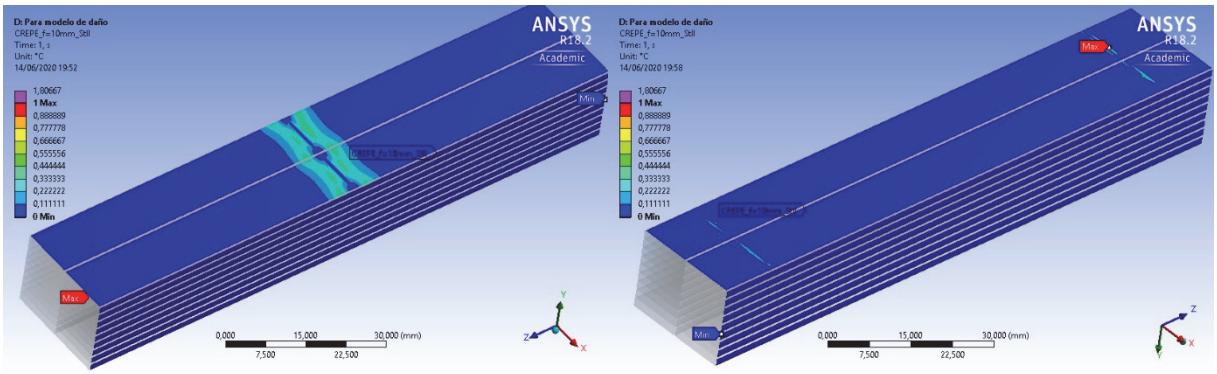

Figure 308. Modification of the Norris criterion for the crepe paper in (a) upper faces and (b) lower faces of the CTC sample for Ageing State II and a final deflection of 10 mm.

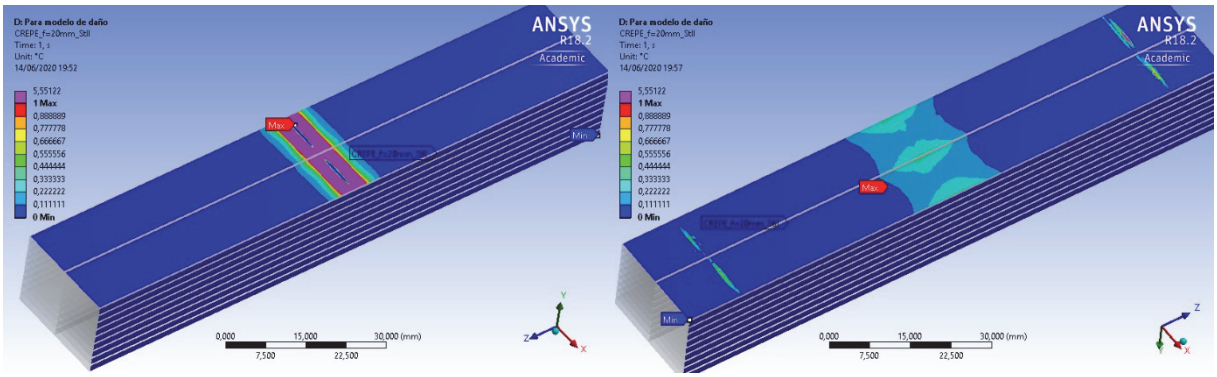

Figure 309. Modification of the Norris criterion for the crepe paper in (a) upper faces and (b) lower faces of the CTC sample for Ageing State II and a final deflection of 20 mm.

- ***Ageing State III:***

Expressions (155)-(158) are to be used, respectively, in the first, second, third and fourth quadrants in the strain plane:

$$\left(\frac{\varepsilon_{MD}}{\varepsilon_{MD,t}^{max}}\right)^2+\left(\frac{\varepsilon_{CD}}{\varepsilon_{CD,t}^{max}}\right)^2-\frac{\varepsilon_{MD}\cdot\varepsilon_{CD}}{\varepsilon_{MD,t}^{max}\cdot\varepsilon_{CD,t}^{max}}+\left(\frac{\gamma_{MD-CD}}{\gamma_{MD-CD}^{max}}\right)^2\geq 1 \quad (155)$$

$$\left(\frac{\varepsilon_{MD}}{17.68}\right)^2+\left(\frac{\varepsilon_{CD}}{3.46}\right)^2-\frac{\varepsilon_{MD}\cdot\varepsilon_{CD}}{17.68\cdot 3.46}+\left(\frac{\gamma_{MD-CD}}{1.15}\right)^2\geq 1$$

$$\left(\frac{\varepsilon_{MD}}{\varepsilon_{MD,c}^{max}}\right)^2+\left(\frac{\varepsilon_{CD}}{\varepsilon_{CD,t}^{max}}\right)^2-\frac{\varepsilon_{MD}\cdot\varepsilon_{CD}}{\varepsilon_{MD,c}^{max}\cdot\varepsilon_{CD,t}^{max}}+\left(\frac{\gamma_{MD-CD}}{\gamma_{MD-CD}^{max}}\right)^2\geq 1 \quad (156)$$

$$\left(\frac{\varepsilon_{MD}}{1.67}\right)^2+\left(\frac{\varepsilon_{CD}}{3.46}\right)^2-\frac{\varepsilon_{MD}\cdot\varepsilon_{CD}}{1.67\cdot 3.46}+\left(\frac{\gamma_{MD-CD}}{1.15}\right)^2\geq 1$$

$$\left(\frac{\varepsilon_{MD}}{\varepsilon_{MD,c}^{max}}\right)^2+\left(\frac{\varepsilon_{CD}}{\varepsilon_{CD,c}^{max}}\right)^2-\frac{\varepsilon_{MD}\cdot\varepsilon_{CD}}{\varepsilon_{MD,c}^{max}\cdot\varepsilon_{CD,c}^{max}}+\left(\frac{\gamma_{MD-CD}}{\gamma_{MD-CD}^{max}}\right)^2\geq 1 \quad (157)$$

$$\left(\frac{\varepsilon_{MD}}{1.67}\right)^2+\left(\frac{\varepsilon_{CD}}{1.67}\right)^2-\frac{\varepsilon_{MD}\cdot\varepsilon_{CD}}{1.67\cdot 1.67}+\left(\frac{\gamma_{MD-CD}}{1.15}\right)^2\geq 1$$

$$\left(\frac{\varepsilon_{MD}}{\varepsilon_{MD,t}^{max}}\right)^2+\left(\frac{\varepsilon_{CD}}{\varepsilon_{CD,c}^{max}}\right)^2-\frac{\varepsilon_{MD}\cdot\varepsilon_{CD}}{\varepsilon_{MD,t}^{max}\cdot\varepsilon_{CD,c}^{max}}+\left(\frac{\gamma_{MD-CD}}{\gamma_{MD-CD}^{max}}\right)^2\geq 1 \quad (158)$$

$$\left(\frac{\varepsilon_{MD}}{17.68}\right)^2+\left(\frac{\varepsilon_{CD}}{1.67}\right)^2-\frac{\varepsilon_{MD}\cdot\varepsilon_{CD}}{17.68\cdot 1.67}+\left(\frac{\gamma_{MD-CD}}{1.15}\right)^2\geq 1$$

In Ageing State III, the tests with deflection of 5 did not produce fracture of the crepe insulation, and that is in line with the predictions of the Modified Norris criterion, see Figure 310. When $d = 10\ mm$, the bending tests did not produce cracks of the crepe paper, but the Modified Norris criterion predicts a very small failure area on the upper face, see Figure 311.

For this ageing level, the first cracks of small size (< 5 mm) appeared in the crepe paper. However, the area in which this failure model predicts failure is larger than that, see Figure 312. In all cases, the reason for that discrepancy is that the strains and deformations which affect the external layers of the CTC insulation are smaller to the ones predicted by the numerical simulation, in which it is assumed that the paper is adhered to the copper surface. The implication is that the presented failure model is conservative in all cases.

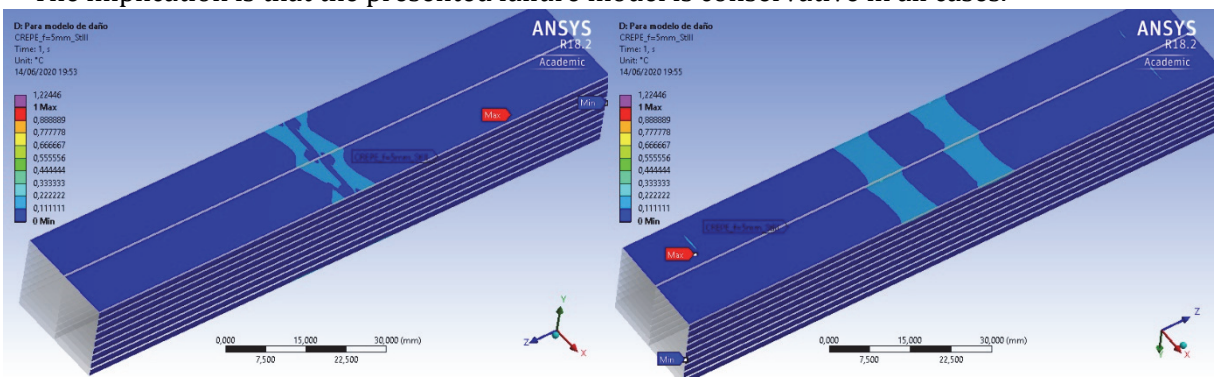

Figure 310. Modification of the Norris criterion for the crepe paper in (a) upper faces and (b) lower faces of the CTC sample for Ageing State III and a final deflection of 5 mm.

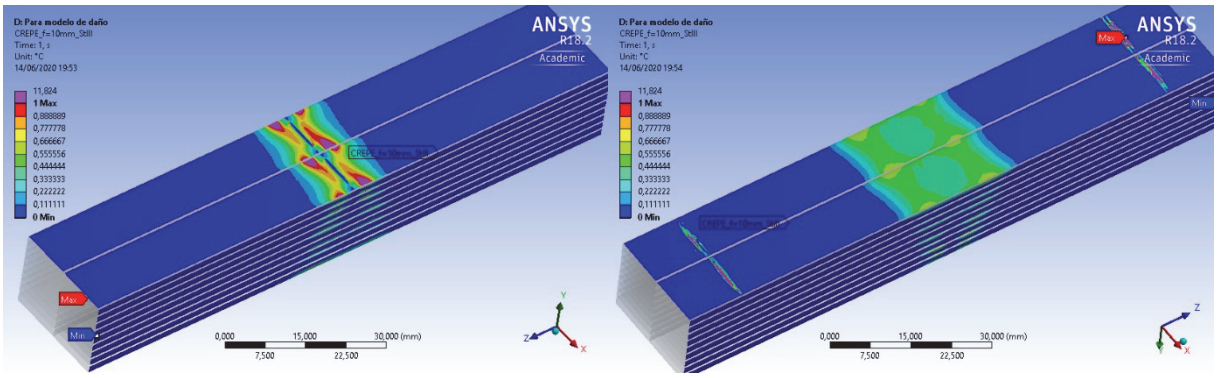

Figure 311. Modification of the Norris criterion for the crepe paper in (a) upper faces and (b) lower faces of the CTC sample for Ageing State III and a final deflection of 10 mm.

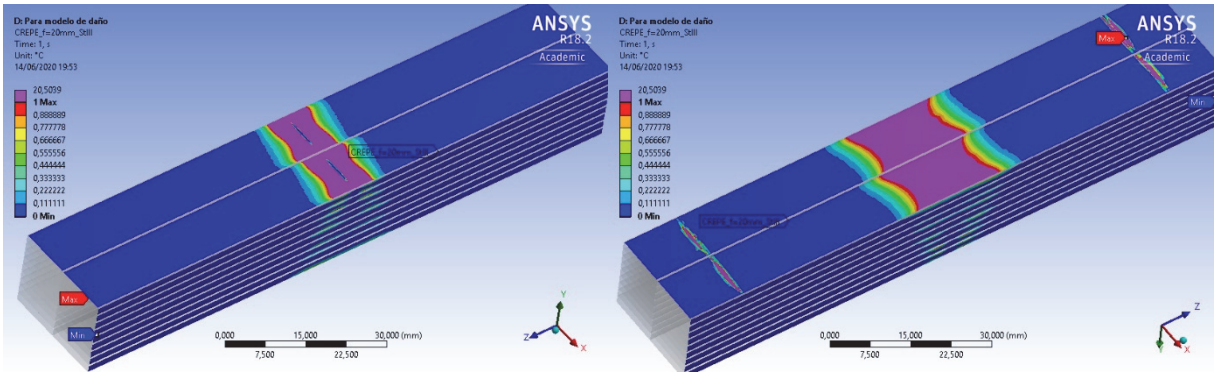

Figure 312. Modification of the Norris criterion for the crepe paper in (a) upper faces and (b) lower faces of the CTC sample for Ageing State III and a final deflection of 20 mm.

- **Conclusions about the use of the modification of the Norris failure criterion:**

Table 43 summarises the validity of the modified Norris criterion for the prediction of failure of the cellulosic insulation (plain Kraft and crepe papers) for all the ageing states. The cells with "Yes" mean that the criterion was in line with experimental observations. The cells with "~" mean that the model predicts a larger area for failure occurrence than the one

produced by the bending tests. In some cases, there is a small area in which the failure criterion is exceeded but no failure occurred in the laboratory (such as in State 0 with d = 20 mm for the plain Kraft paper; and in State III with d = 10 mm, and in States 0, I and II with d = 20 mm for the crepe paper). In other cases, the area in which failure is expected according to the model is slightly larger than the real one (such as in State I with d = 20 mm for the plain Kraft paper). In all cases, the use of the modification of the Norris failure criterion gave conservative predictions.

The combination of the finite element model developed in this research with the mechanical models that were calibrated from the results obtained in the laboratory provides a reliable and conservative description of the response undergone by the Kraft and crepe papers when a CTC is subjected to bending. This is well proven for deformations up to 10 mm (which can be produced by a short circuit or other kinds of electrical or mechanical faults in the windings of power transformers). When the deflection of the CTC sample is 20 mm, the compressive strains in the contact between the load cylinder and the conductor are very high. It is not to be expected that the strains which affect the paper insulation be that extreme, as the paper is much more flexible than the copper and is able to slide; this is the cause of the discrepancy between the failure model and the observations. Besides, the failure criterion consists of several fractions with critical strains obtained experimentally in their denominators. The maximum compressive strain at failure is the most conservative parameter introduced in that failure criterion, and the component of the criterion which depends on the compressive strain is the term which causes that the criterion is exceeded when the compressive strains are high. In general, it can be considered that the presented model is reliable, conservative and can describe failure of these kinds of paper insulation in situations of interest.

Table 43. Validity of the predictions of the modified Norris criterion for the different layers, deflections and ageing states.

Deflection	Plain Kraft paper				Crepe paper			
Ageing	State 0	State I	State II	State III	State 0	State I	State II	State III
d = 5 mm	Yes	Yes	Yes	Yes	Yes	Yes	Yes	Yes
d = 10 mm	Yes	Yes	Yes	Yes	Yes	Yes	Yes	~
d = 20 mm	~	~	Yes	Yes	~	~	~	Yes

IV. CONCLUSIONS

1. Problem statement

Although it is generally agreed that the condition of the solid insulation in the windings of power transformers is one of the factors that has a more relevant impact on their life expectancy, there is a lack of understanding about how the ageing derived from normal operation and electrical faults affects the performance of that insulation. The ageing of the paper insulation produced by high temperatures and chemical reactions in the insulating oil deteriorates both its electrical and mechanical properties. The deformations caused by electromagnetic forces acting over power transformers can result in breakage of the paper insulation, which is a mechanical phenomenon, and that can cause a subsequent electrical failure, if the insulation stops complying its dielectric purpose.

If we assume that the mechanical performance of the insulation has an impact on the reliability of power transformers, a mechanical failure model for that insulation could be a useful tool for the estimation of the condition of power transformers, to be used in combination with other existing methods (see *1.2.1.Methods for the estimation of the condition of power transformers* in part *II.STATE OF THE ART*). However, before the present work, there was no study which took into consideration all the factors that have a role in that mechanical failure model (properties of the material under different kinds of mechanical solicitations, different ageing states and influence of a particular insulating liquid, impact of large deformations which could be produced by short-circuit forces, real geometry of the insulated conductors, etc.).

2. Research strategy

In the present work, the performance of a commercial insulated CTC, wrapped in four layers of dielectric paper (two internal layers made of plain Kraft paper and two external layers made of crepe paper) was studied from a triple approach: experimental, numerical and analytical.

In the experimental analysis, samples of that insulated CTC were obtained from the coil of a core-type power transformer, introduced into vessels filled with naphthenic oil, and aged isothermally in temperature-controlled ovens at 150°C for four different ageing periods (see *1.1.Accelerated thermal ageing of the paper insulation* in *III.MATERIALS, METHODS AND RESULTS*). The ageing level of the insulation (plain Kraft and crepe papers) was quantified through the Degree of Polymerisation (DP) (see *1.2.1.Degree of Polymerisation (DP) of the dielectric paper*). Later on, the mechanical properties of the paper material were obtained under tensile and compressive testing (see *1.2.2.Tensile mechanical properties of the dielectric paper in the MD and in the CD* and *1.2.3.Edgewise mechanical compressive properties of the dielectric paper*), and the shear mechanical properties were estimated from the tensile properties, as suggested by [140] (see *1.2.4.In-plane shear mechanical properties of the dielectric paper*). Then, insulated CTC samples were subjected to three-point bending tests producing deformations which could be caused by a short circuit in the windings of a power transformer (see *1.3.Three-point bending tests of the insulated CTCs*), and the fractures produced in the paper material were macroscopically and microscopically analysed.

In the numerical analysis, the bending test over an insulated CTC sample was simulated by means of ANSYS AIM Static Structural. That simulation made it possible to estimate the strains that the paper insulation suffers, which will be needed as input in a failure model for the paper insulation. In the analytical approach, the existing failure models applicable to a

lamina were reviewed and classified (see *5.4.3.Different criteria for the failure of paper materials* in part *II.STATE OF THE ART*) and two of them were adapted to the studied insulation materials (see *3.Failure criteria for the paper insulation of the CTC* in part *III.MATERIALS, METHODS AND RESULTS*). The experimental analysis provided the material properties introduced in the failure model, while the numerical analysis gave the strains at each node of the simulated geometry, and was also used to represent the result of the analytical failure criterion in each of the nodes of the CTC sample.

3. Contributions derived from the experimental research

3.1. Thermal ageing of the paper insulation

The DP of the plain Kraft and crepe papers, which is a widely used measure of the deterioration of its dielectric properties, was determined for each ageing state. The mechanical failure of the insulation paper has been studied for DPs comprised between 650 – 1000, catalogued as "good" in [55], and up to DPs lower than 350, catalogued as "aged". That means that the present study covers the mechanical response of the paper insulation during its whole lifespan. The experimental results showed that the position of the paper material in the different layers of the insulation did not have any impact on the ageing, except in the case of layer 1. This layer is in direct contact with the copper CTC and its deterioration was artificially increased due to the high temperature that was selected for the ageing process to achieve an ageing level equivalent to a whole lifetime of operation of a real power transformer.

The DP makes it possible to link the experimental work carried out with many other studies which report values of the DP measured in the insulation of real power transformers after some years of operation. It can be considered that, when the DP of Kraft paper (or crepe paper) of a particular class is around one particular value, its mechanical performance will be similar to the one described in the present study. Although the DP is a "destructive" method, as it requires a piece of the insulation paper from the transformer under analysis, and that can cause local failure and is not a feasible method for an operating transformer, there are many non-destructive methods in the literature which measure other parameters which are directly linked to the DP and can be used in operating transformers (for instance, [33], [59], [60], [62], [63]).

3.2. Tensile, edgewise and in-plane shear mechanical testing of the paper insulation

Samples of plain Kraft and crepe insulation papers were subjected to tensile testing in MD and CD, following standard [137]. Average values and standard deviations for the strain at breakage in tension, $\varepsilon_{MD,t}^{max}$ and $\varepsilon_{CD,t}^{max}$, were obtained and plugged into the failure criterion. The difference in the responses to tension in MD of the plain Kraft and crepe papers was noticeable. The maximum strain at breakage in MD, $\varepsilon_{MD,t}^{max}$ was considerably higher for the crepe paper (6.8 times higher when the material was not aged, and almost 2.8 times higher in Ageing State IV). Due to the geometry of the insulation of the CTC, where the MD coincides with the principal edge in the paper insulation strips, and the CD coincides with the transversal direction, in which the width of the material is only about 20 mm, failure in tension in MD and CD is governed by different mechanisms. While failure in tension in MD is brittle, failure in tension in CD is a progressive process which resembles the ductile tearing mechanism in metallic materials. The aspect of the stress-strain curves of the plain Kraft and crepe papers was not noticeably different. The values of the maximum strain at breakage in CD, $\varepsilon_{CD,t}^{max}$, are 1.4 times higher for the crepe insulation when the material was not aged , and 1.1 times higher in Ageing State IV. In the crepe paper, the CD is the preferential direction for

crack propagation under tension, as both the strain at breakage and the tensile strength are lower in CD.

An experimental method inspired by [139] was presented for the estimation of the compressive properties of the insulation paper which uses cylindrical paper samples with two concentric layers of insulation. The observed failure mechanism was local buckling and wrinkle formation in the cylinders, which was the cause for the reduction in the mechanical strength that can be seen in the stress-strain compressive curves. The compression tests showed that the deformation capacity of the paper remained beyond the peak stress, and the material still displayed a relevant compressive strength. As failure in compression mode is not a sudden phenomenon, a conservative value was selected here as the ultimate strain of the material, ε_c^{max}, which was defined as the strain corresponding to 50% of the peak compressive stress, $0.5 \cdot \sigma_c^{max}$, after reaching that peak stress. The tests showed a great variability of about 27.8% among the values of $\varepsilon(0.5 \cdot \sigma_c^{max})$ from the curves obtained for the same material in one particular orientation and ageing state. The average ε_c^{max} values were slightly higher for the crepe paper than for the plain Kraft during the whole ageing duration, and the influence of ageing was less relevant here than with the tensile properties. The difference between the estimated ε_c^{max} in MD and CD was not clear, in contrast to what was observed for the tensile properties; therefore, it was not justified to introduce different values for those material directions into the failure model. ε_c^{max} was modelled by means of a linear relationship over time during the whole ageing duration; the values provided by this line were introduced into the failure criterion.

The shear properties were experimentally estimated from tensile testing at 35º from the MD, as suggested in [140], for different kinds of thin paper, considering that $\varepsilon_{35^o}^{\max} \simeq \varepsilon_{\mathrm{MD-CD}}^{\max}$. Both the plain Kraft and the crepe papers displayed sudden breakages, but the strain at breakage, $\varepsilon_{35^o}^{\max}$, was more than 5 times higher for the crepe insulation when the material was not aged, and that ratio reduced to around 1.4 times in Ageing State III. Although the initial mechanical performance of the crepe insulation was superior, that material was also more affected by the ageing process.

3.3. Three-point bending tests over the insulated CTCs and fracture analysis

The effect of the radial component of a short-circuit force over insulated CTC samples previously aged was experimentally modelled by three-point bending tests, producing final deflections of 5, 10 and 20 mm in the conductor. The force-deflection curves showed that the aged conductor displayed a more rigid response than the non-aged one; this is explained as a consequence of the bonding between copper strands induced by the ageing at high temperature. However, if the deformation continues, that bonding breaks, producing a sudden drop in the force-deflection curve. Failure of the insulation paper always started in layer 1, as it was glued to the copper conductor and suffered the highest strains, while the external layers were able to slide up to some extent.

Common sources for crack initiation after the three-point bending tests were the presence of the transposed conductor, which suffered higher deformations than more rigid parts of the CTC, and the wrapping of the paper around the copper CTC. In areas of the CTC samples subjected to tension, the kind of failure was the sudden onset of cracks, such as in the paper samples under tensile testing. However, when the paper is heavily aged, areas subjected to compression were more critical for crack initiation and growth. When the deformation of the CTC was not very high, the first defects in compressed areas were wrinkles and local buckling of the insulation, very similar to the ones observed in the experimental characterisation in compression. When the CTC deformation increased, the insulation could

not continue buckling, because it was constrained due to its wrapping around the CTC, and the failure mode changed, producing cracks in areas subjected to compression. Other conclusions were that a very high temperature and duration of the ageing is needed for the cracks to grow, to produce the end-of-life of the insulation. Crepe insulation has a much better response to ageing and big deformations of the CTCs than the plain Kraft paper. However, if the thermal ageing is very extreme, the final condition of the crepe paper is similar to the one of the plain Kraft.

The cracks produced for each deformation level and ageing state were macroscopically analysed and classified into small cracks (< 5 mm), medium-size cracks (5-10 mm), big cracks (> 10 mm), and total fracture. The insulation did not suffer any cracks in the non-aged CTC samples, illustrating the good mechanical performance of the manufactured paper. However, the influence of the thermal ageing was very marked, especially in the plain Kraft, which suffered total fracture for a deflection of 20 mm in Ageing State III. The response of the crepe insulation was considerably better, as a really profound ageing state (about 7 months at 150ºC) and a deformation of 20 mm were needed to produce big cracks. The failure mechanism was also microscopically analysed by means of a Scanning Electron Microscope, see *1.4.Analysis of the microstructure and fracture patterns in the paper insulation with Scanning Electron Microscope*, which showed that crack formation and growth in the insulation is mainly a local phenomenon, where the cellulose fibres break in areas subjected to tension, or as a consequence of wrinkles and buckling in areas subjected to compression. In contrast, the matrix and fibres in the insulation nearby the local defect, but outside the affected area, remain in a very good condition, even when the material is heavily aged.

4. Contributions derived from the FE numerical study

The studied copper CTC subjected to a bending test was modelled by means of ANSYS AIM Static Structural, see *2.Numerical simulation* in *III.MATERIALS, METHODS AND RESULTS*. One of the most challenging aspects of the numerical simulation was to properly model the contacts among the copper strands during the bending test, and to define an adequate mesh which makes it possible to obtain results with sufficient quality while improving convergence. It was essential to model the sliding between the adjacent copper layers, as the deformation of the CTC increases, in order to capture the average force-deflection curve obtained in the bending tests in the laboratory. That was introduced by means of a variable frictional coefficient during the different steps of the loading, and the agreement between the simulated response and the experimental one is considered to be quite good, despite the approximations considered in the numerical model for the sake of simplicity. The numerical model permitted the calculation of the strains ε_{MD}, ε_{CD} and γ_{MD-CD} on the external surfaces of the CTC, where the paper insulation is wrapped.

For all the numerical simulations with final deflections between 5 and 20 mm, ε_{CD} and γ_{MD-CD} were considerably higher than ε_{MD}. Besides, the compressive strains seem to be more critical for failure initiation than the tensile strains, something that coincides with experimental observations after the bending tests. The strains in the upper faces of the CTC sample are higher in CD than in MD, and almost the whole surface is subjected to compression in CD. The shear strains, γ_{MD-CD} , are of a very similar order of magnitude to ε_{CD}, with maximum values of around -10% when the CTC deflection is 20 mm. On the lower face of the CTC, the strains in CD are also higher than the ones in MD, and almost the whole lower surface is subjected to tension, with maximum values of about $\varepsilon_{CD} \simeq$ 2-5% in tension. The magnitude of γ_{MD-CD} in the central area of the lower faces is similar. On the lateral sides, it is to be expected that the failure is governed by γ_{MD-CD}, as they are considerably higher than the

strains in MD or CD. Only when d = 20 mm, could the tensile strains also be critical for crack initiation.

These results highlighted the need for obtaining the mechanical properties of the insulation material in compression and shear modes, which is something really novel, as no reference was found in the literature dealing with that characterisation in the case of thin paper. The classic references which take into consideration the mechanical properties of the paper insulation of power transformers only consider the tensile strength and the maximum strain at failure, but it has been proved in the present work that other stresses or strains could be more critical for the mechanical failure.

5. Contributions derived from the analytical study

There are many models in the literature for the failure of a lamina in a state of combined stress, although they are not specific to paper materials and they are applicable to different types of polymers, it is to be expected that the failure mechanism are similar for both. However, these failure criteria are traditionally expressed in terms of stresses. It is not easy to introduce the thin layers of insulation paper, with a thickness of about 80-82 μm, into the geometry in the numerical simulation, because a copper strand is around 24 times thicker than one layer of paper insulation, and the size of the elements required in the mesh would be very small, leading to an unmanageable number of elements and an enormous time required for the resolution process. Even if that had been feasible, we would have needed to solve different simulations, varying the paper material properties in accordance with the ageing state. Thus, in the present study, the insulation paper was not included in the numerical model, and the strain field on the external faces of the CTC sample was obtained, which will be higher or equal to the strains suffered by the wrapped paper insulation, as it has a certain capacity to slide around the copper conductor. That means that the failure criterion, which needs to be expressed in terms of strains, will be conservative in any case.

Two failure criteria were applied to the two insulation papers studied in this work: one limit criterion, the maximum strain failure criterion; and one interactive criterion, a modification of the Norris failure criterion, see *3.Failure criteria for the paper insulation of the CTC* in *III.MATERIALS, METHODS AND RESULTS*. In the first case, the strains obtained on each of the surfaces of the CTC sample (ε_{MD}, ε_{CD} and γ_{MD-CD}) were compared with the maximum strains at break derived from the mechanical characterisation, and areas in which the values were exceeded were pictured by means of ANSYS AIM Static Structural. The predictions of this criterion are in line with experimental observations, except in the case of d = 20 mm, where the areas in which failure is predicted by the model are smaller than the ones observed after the bending tests. The modification of the Norris failure criterion was more complex, as different analytical expressions considering the interactions among strains were needed in the different quadrants of the strain plane. These equations were introduced into the different nodes of the geometry of the simulated CTC sample, where the values of the strains ε_{MD}, ε_{CD} and γ_{MD-CD} are known, by means of conditional functions, and the obtained results were represented in the geometry in ANSYS. The predictions of the modified Norris failure criterion were in line with experimental observations up to a deformation of 10 mm, and conservative in all cases. In some cases, the area in which failure is expected according to the model is slightly larger than the real one, especially when d = 20 mm.

6. Implications of this work for the estimation of the condition of power transformers in operation

We consider that this PhD thesis provides a consolidated methodology and highly valuable experimental information for the assessment of power transformers under

operating conditions. Thus, the failure criterion proposed for plain Kraft and crepe insulating papers under different ageing states and with different deformations levels of the copper conductor is a very innovative contribution and could serve to improve the understanding of the processes that lead to the failure of the insulation of a power transformer. The main characteristics of the CTC modelled in the numerical simulation (such as the contact definition among copper strands) are common for other conductors used in power transformers with different geometries. The magnitude and kind of load applied to the conductor can be modified, and different strain distributions could be obtained for a wide range of situations. Therefore, the Finite Element approach that we have followed in this study could be extended to different boundary conditions. Moreover, the failure criterion could be calibrated with other material properties for the prediction of mechanical failure of any kind of paper insulation.

Regarding this subject, one of the conclusions derived from this study is that the tensile behaviour of the insulation paper is not the only relevant factor. Quite the contrary, the response to compression and shear stresses is also relevant, and that has implications for manufacturers of paper insulation. Some more precise methods for the quantification of the shear strength of the paper material are required. We have experimentally verified that the shear strains suffered by the insulation are relevant for the mechanical failure, and that they are affected by the angle selected for the wrapping of the paper insulation around the copper conductor. This issue opens the door for future lines of research.

All the tools developed and validated in this PhD thesis can be used by manufacturers in order to improve constructive characteristics in CTCs for the windings of a core-type power transformer. Specifically, it is now feasible to develop predictive models to predict the estimated lifespan of power transformers depending on the materials employed and on the in-service conditions. This will be useful for the advancement of the techniques currently used in the management of power transformers in the electrical system.

BIBLIOGRAPHY

[1] K. Karsai, D. Kerényi, and L. Kiss, *Large Power Transformers*. Budapest: Elsevier, 1987.

[2] C. Oria, A. Ortiz, D. Ferreño, I. Carrascal, and I. Fernández, "State-of-the-art review on the performance of cellulosic dielectric materials in power transformers: Mechanical response and ageing," *IEEE Trans. Dielectr. Electr. Insul.*, vol. 26, no. 3, pp. 939–954, 2019.

[3] E. Borgqvist *et al.*, "Dielectric properties of polymers," *Tappi*, vol. 19, no. 1, p. 634, 2014.

[4] O. Girlanda, K. Wei, T. Brattberg, and L. E. Schmidt, "Influence of Density on the Out-of-Plane Mechanical Properties of Pressboard," in *Conference on Electrical Insulation and Dielectric Phenomena (CEIDP) Proceeding*, 2012, pp. 247–250.

[5] O. Girlanda *et al.*, "Analysis of the Micromechanical Deformation in Pressboard performed by X-ray Microtomography," *Electr. Insul. Conf.*, pp. 89–92, 2015.

[6] T. Joffre, O. Girlanda, F. Forsberg, F. Sahlén, M. Sjödahl, and E. K. Gamstedt, "A 3D in-situ investigation of the deformation in compressive loading in the thickness direction of cellulose fiber mats," *Cellulose*, vol. 22, no. 5, pp. 2993–3001, 2015.

[7] O. Girlanda, K. Wei, M. Evenbom, L. E. Schmidt, and J. Forslin, "Static and quasi-static behavior of dry and oil-impregnated pressboard," in *2016 Electrical Insulation Conference (EIC)*, 2016, pp. 105–108.

[8] C. Oria *et al.*, "Experimental and numerical analysis of the failure of the cellulosic insulation of continuously transposed conductors under the effects of short circuits and thermal ageing in power transformers," *IEEE Trans. Dielectr. Electr. Insul.*, vol. 27, no. 1, pp. 325–333, 2020.

[9] "International Standard: Power transformers – Part 1: General. IEC 60076-1." 2011.

[10] L. F. Blume, A. Boyajian, G. Camilli, T. C. Lennox, S. Minneci, and V. M. Montsinger, *Transformer engineering*. New York: John Wiley and Sons, 1951.

[11] P. S. Georgilakis, *Spotlight on Modern Transformer Design*. London: Springer Dordrecht Heidelberg London New York, 2009.

[12] "IEEE standard terminology for power and distribution transformers.," *IEEE Standard C57.12.80*. IEEE, New York.

[13] "IEC 60076-2:2011. Power transformers - Part 2: Temperature rise for liquid-immersed transformers." IEC, 2011.

[14] G. Bertagnolli, *Power Transformers and Short Circuits. Evaluation of the short-circuit performance of power transformers*, ABB. 2014.

[15] A. E. B. Abu-Elanien and M. M. A. Salama, "Asset management techniques for transformers," *Electr. Power Syst. Res.*, vol. 80, p. 456, 2010.

[16] L. Lundgaard, W. Hansen, D. Linhjell, and T. Painter, "Aging of Oil-Impregnated Paper in Power Transformers," *IEEE Trans. Power Deliv.*, vol. 19, no. 1, p. 230, 2004.

[17] M. Muhr and C. Sumereder, "Transformer Condition Determination Methods," *Proc. 2008 Int. Symp. Electr. Insul. Mater.*, p. 479, 2008.

[18] M. Arshad and S. M. Islam, "Significance of Cellulose Power Transformer Condition Assessment," *IEEE Trans. Dielectr. Electr. Insul.*, vol. 18, no. 5, p. 1591, 2011.

[19] I. Fofana, A. Bouaïcha, and M. Farzaneh, "Characterization of aging transformer oil–

pressboard insulation using some modern diagnostic techniques," *Eur. Trans. Electr. Power*, vol. 21, p. 1110, 2011.

[20] R. E. Mark, C. C. Habeger, J. Borch, and M. B. Lyne, *Handbook of Physical Testing of Paper (Volume 1)*, Marcel Dek. United States of America, 2002.

[21] Y. Kamata *et al.*, "Development of low-permittivity pressboard and its evaluation for insulation of oil- immersed EHV power transformers," *IEEE Trans. Electr. Insul.*, vol. 26, no. 4, p. 819, 1991.

[22] Y. Yoshida and M. Nishimatsu, "Power capacitors," *IEEE Trans. Electr. Insul.*, vol. 21, no. 6, p. 963, 1986.

[23] *EN 13601 : Copper and copper alloys - Copper rod, bar and wire for general electrical purposes*. 2013.

[24] J. Borch, M. B. Lyne, R. E. Mark, and C. C. Habeger, *Handbook of Physical Testing of Paper (Volume 2)*. New York: Marcel Dekker, 2002.

[25] G. L. Link, "Dielectric properties of polymers," *J. Appl. Polym. Sci.*, p. 1281, 1972.

[26] C. C. Habeger and G. A. Baum, "The microwave dielectric constant of water-paper mixtures: The role of sheet structure and composition," *J. Appl. Polym. Sci.*, vol. 28, p. 969, 1983.

[27] D. A. Seanor, "Electrical properties of polymers," *J. Appl. Polym. Sci.*, p. 1187, 1972.

[28] Y. Take, Y. Suzuki, and F. Itohara, "The effects of lignin contents on the dielectric properties of insulating paper," *J. Inst. Electr. Eng.*, vol. 84, no. 4, p. 601, 1964.

[29] Y. Take, Y. Suzuki, and F. Itohara, "Effects of hemicellulose on the dielectric properties of insulating paper," *J. Inst. Electr. Eng.*, vol. 84, no. 4, p. 609, 1964.

[30] Y. Take, "Investigations of dielectric losses in insulating paper," 1960.

[31] S. V. Kulkarni and S. A. Khaparde, *Transformer Engineering*, Marcel Dek. New York, 2004.

[32] A. M. Emsley, X. Xiao, R. J. Heywood, and M. Ali, "Degradation of cellulosic insulation in power transformers. Part 3: Effects of oxygen and water on ageing in oil," *IEE Proc. - Sci. Meas. Technol.*, vol. 147, no. 3, p. 115, 2000.

[33] P. J. Baird, H. Herman, and G. C. Stevens, "Non-Destructive Measurement of the Degradation of Transformer Insulating Paper," *IEEE Trans. Dielectr. Electr. Insul.*, vol. 13, no. 1, p. 309, 2006.

[34] M. Eklund, N. Naphthenics, P. Jarman, and M. Edwall, *Transfomer oil handbook*. 2004.

[35] "IEC 60296. Fluids for electrotechnical applications - Unused mineral insulating oils for transformers and switchgear." IEC, 2012.

[36] H. P. Gasser, C. Krause, M. Lashbrook, and R. Martin, "Aging of Pressboard in Different Insulating Liquids," in *IEEE International Conference on Dielectric Liquids*, 2011, p. 978.

[37] A. A. Abdelmalik, "Analysis of Thermally Aged Insulation Paper in a Natural Ester-based Dielectric Fluid," *IEEE Trans. Dielectr. Electr. Insul.*, vol. 22, no. 5, pp. 2408–2414, 2015.

[38] S. Tenbohlen and M. Koch, "Aging performance and moisture solubility of vegetable oils for power transformers," *IEEE Trans. Power Deliv.*, vol. 25, pp. 825–830, 2010.

[39] "IEC 60076-7. Power transformers – Part 7: Loading guide for mineral-oil-immersed power transformers." IEC, 2018.

[40] R. E. Benson, "Effects of relative humidity and temperature on tensile stress-strain properties of kraft linerboard," *Tappi*, vol. 54, no. 4, p. 699, 1971.

[41] K. Miners, "Particles and moisture effect on dielectric strength of transformer oil using VDE electrodes," *IEEE Trans. Power Appar. Syst.*, vol. 101, no. 3, p. 751, 1982.

[42] H. Yoshida, Y. Ishioka, and T. Suzuki, "Degradation of Insulating Materials of Transformers," *IEEE Trans. Electr. Insul.*, vol. EI-22, no. No.6, p. 795, 1987.

[43] J. K. Nelson, "An assessment of the physical basis for the application of design criteria for dielectric structures," *IEEE Trans. Electr. Insul.*, vol. 24, no. 5, p. 835, 1989.

[44] C. Krause, "Dielectric strength of transformer oil: Impact of oil flow, moisture and cellulose particles," in *conf*, Rapperswil, Switzerland, 1996.

[45] M. Mandlik and T. S. Ramu, "Moisture Aided Degradation of Oil Impregnated Paper Insulation in Power Transformers," *IEEE Trans. Dielectr. Electr. Insul.*, vol. 21, no. 1, p. 186, 2014.

[46] M.-H. Glomm, K. Liland, and L. Lundgaard, "Oxidation of Paper Insulation in Transformers," *IEEE Trans. Dielectr. Electr. Insul.*, vol. 17, no. 3, p. 939, 2010.

[47] H. P. Dixson and J. C. Nelson, "An accelerated aging study of several writing papers," *Tappi*, vol. 45, no. 10, p. 753, 1962.

[48] Y. Li *et al.*, "Insulation Performance of Aging Transformer Winding under Transient Impulse," in *19th IEEE International Conference on Dielectric Liquids (ICDL)*, 2017, pp. 1–4.

[49] H. Ye *et al.*, "Insulation Characteristics of Deformed Transformer Winding under Transient Impulse," in *2017 IEEE Conference on Electrical Insulation and Dielectric Phenomenon (CEIDP)*, 2017, pp. 552–555.

[50] V. M. Montsinger, "Effects of time and frequency on insulation test of transformers," *AIEE Trans.*, vol. 43, pp. 337–347, 1924.

[51] G. Maier, "The electric strength of insulating oil with power-frequency voltage, switching surges and standard impulses," *Brown Boveri Rev.*, vol. 103, p. 33, 1967.

[52] Y. Kamata and Y. Kako, "Flashover characteristics of extremely long gaps in transformer oil under non-uniform field conditions," *IEEE Trans. Electr. Insul.*, vol. EI-15, no. 1, pp. 18–26, 1980.

[53] R. J. Heywood, A. M. Emsley, and M. Ali, "Degradation of cellulosic insulation in power transformers. Part 1 : Factors affecting the measurement of the average viscometric degree of polymerisation of new and aged electrical papers," *IEE Proc. - Sci. Meas. Technol.*, vol. 147, no. 2, p. 86, 2000.

[54] "ASTM D1795-13, Standard Test Method for Intrinsic Viscosity of Cellulose," West Conshohocken, 2013.

[55] "IEC 60450:2007. Measurement of the average viscometric degree of polymerization of new and aged cellulosic electrically insulating materials." IEC, 2007.

[56] ASTM International, "ASTM D3394-16, Standard Test Methods for Sampling and Testing Electrical Insulating Board." West Conshohocken, 2016.

[57] A. M. Emsley, X. Xiao, R. J. Heywood, and M. Ali, "Degradation of cellulosic insulation in power transformers. Part 2: Formation of furan products in insulating oil," *IEE Proc. - Sci. Meas. Technol.*, vol. 147, no. 3, p. 110, 2000.

[58] A. M. Emsley and G. C. Stevens, "Review of chemical indicators of degradation of cellulosic electrical paper insulation in oil-filled transformers," *Proc. IEEE Inst. Electr. Eng.*, vol. 141, no. 5, p. 324, 1994.

[59] M. Mirzaie, A. Gholami, and H. Tayyebi, "Thermal Degradation of Cellulose Paper Insulation in Power Transformers," *2007 Int. Conf. Solid Dielectr.*, p. 673, 2007.

[60] S. Y. Matharage, Q. Liu, and Z. D. Wang, "Aging Assessment of Kraft Paper Insulation through Methanol in Oil Measurement," *IEEE Trans. Dielectr. Electr. Insul.*, vol. 23, no. 3, pp. 1589–1596, 2016.

[61] "IEC 60567:2011. Oil-filled electrical equipment - Sampling of gases and analysis of free and dissolved gases - Guidance." IEC, 2011.

[62] J. Jalbert, R. Gilbert, P. Tétreault, B. Morin, and D. Lessard-Déziel, "Identification of a chemical indicator of the rupture of 1,4-?-glycosidic bonds of cellulose in an oil-impregnated insulating paper system," *Cellulose*, vol. 14, no. 4, pp. 295–309, 2007.

[63] J. Scheirs, G. Camino, M. Avidano, and W. Tumiatti, "Origin of furanic compounds in thermal degradation of cellulosic insulating paper," *J. Appl. Polym. Sci.*, vol. 69, pp. 2541–2547, 1998.

[64] "IEC 61198:1993. Mineral insulating oils - Methods for the determination of 2-furfural and related compounds." IEC, 1993.

[65] M. Bruzzoniti, R. Maina, R. De Carlo, C. Sarzanini, and V. Tumiatti, "GC Methods for the Determination of Methanol and Ethanol in Insulating Mineral Oils as Markers of Cellulose Degradation in Power Transformers," *Chromatographia*, vol. 77, no. 15–16, pp. 1081–1089, 2014.

[66] S. Y. Matharage, Q. Liu, Z. D. Wang, P. Mavrommatis, G. Wilson, and P. Jarman, "Ageing Assessment of Transformer Paper Insulation through Detection of Methanol in Oil," in *IEEE 11th International Conference on the Properties and Applications of Dielectric Materials*, 2015.

[67] D. Laurichesse, Y. Bertrand, C. Tran-Duy, and V. Murin, "Ageing diagnosis of MV/LV distribution transformers via chemical indicators in oil," in *2013 IEEE Electrical Insulation Conference (EIC)*, 2013, pp. 464–468.

[68] J. Jalbert, R. Gilbert, Y. Denos, and P. Gervais, "Methanol: A Novel Approach to Power Transformer Asset Management," *IEEE Trans. Power Deliv.*, vol. 27, pp. 514–520, 2012.

[69] M. Kohtoh, G. Ueta, and S. Okabe, "Transformer Insulating Oil Characteristic Changes Observed Using Accelerated Degradation in Consideration of Field Transformer Conditions," *IEEE Trans. Dielectr. Electr. Insul.*, vol. 17, no. 3, p. 808, 2010.

[70] G. Ueta, T. Tsuboi, and S. Okabe, "Study on Degradation Causing Components of Various Characteristics of Transformer Insulating Oil," *IEEE Trans. Dielectr. Electr. Insul.*, vol. 19, no. 6, p. 2216, 2012.

[71] M.-L. Coulibaly, C. Perrier, M. Marugan, and A. Beroual, "Aging Behavior of Cellulosic Materials in Presence of Mineral Oil and Ester Liquids under Various Conditions," *IEEE Trans. Dielectr. Electr. Insul.*, vol. 20, no. 6, pp. 1971–1976, 2013.

[72] I. Fofana, J. S. N'cho, J. C. Olivares-Galván, R. Escarela-Pérez, and P. S. Georgilakis, "Comparative Studies of the Stabilities to Oxidation and Electrical Discharge between Ester Fluids and Transformer Oils," in *2011 North American Power Symposium*, 2011.

[73] M. M. Ariffin, M. T. Ishak, M. H. A. Hamid, N. I. A. Katim, and A. M. Ishak, "Ageing Effect of Vegetable Oils Impregnated Paper in Transformer Application," *Int. Conf. High*

Volt. Eng. Power Syst., pp. 183–187, 2017.

[74] O. H. Arroyo *et al.*, "Aging Characterization of Electrical Insulation Papers Impregnated with Synthetic Ester and Mineral Oil: Correlations Between Mechanical Properties, Depolymerization and Some Chemical Markers," *IEEE Trans. Dielectr. Electr. Insul.*, vol. 25, no. 1, pp. 217–227, 2018.

[75] M. Maharana, S. K. Nayak, and N. Sahoo, "Karanji Oil as a Potential Dielectrics Liquid for Transformer," *IEEE Trans. Dielectr. Electr. Insul.*, vol. 25, no. 5, pp. 1871–1879, 2018.

[76] M. Maharana, N. Baruah, S. K. Nayak, and N. Sahoo, "Comparative Study of Mechanical and Electrical Strength of Kraft Paper in Nanofluid Based Transformer Oil and Mineral Oil," *Int. Symp. Electr. Insul. Mater.*, pp. 646–649, 2017.

[77] ASTM, "ASTM D149 - 09. Standard Test Method for Dielectric Breakdown Voltage and Dielectric Strength of Solid Electrical Insulating Materials at Commercial Power Frequencies." 2013.

[78] D. J. Allan, W. A. Sharpley, F. C. Pratt, and M. E. Woollard, "Short-Circuit Performance of Transformers - a Contribution To the Alternative To Direct Testing.," *Int. Conf. Large High Volt. Electr. Syst.*, vol. 1, no. 02, 1980.

[79] D. O. Swihart and D. V. Wright, "Dynamic stiffness and damping of transformer pressboard during axial short circuit vibration," *IEEE Trans. Power Appar. Syst.*, vol. 95, no. 2, p. 721, 1976.

[80] Y. Tournier, M. Richard, A. Ciniero, S. Yakov, A. B. Madin, and J. D. Whitaker, "A study of the dynamic behavior of transformer windings under short-circuit conditions," *CIGRE*, vol. 134, 1964.

[81] "International Standard: Power transformers – Part 5: Ability to withstand short circuit. IEC 60076-5." IEC, 2006.

[82] N. Stenberg, "On the Out-of-Plane Mechanical Behaviour of Paper Materials," Department of Solid Mechanics, Royal Institute of Technology, Stockholm, 2002.

[83] K. Persson, "Material Model for Paper: Experimental and Theoretical Aspects. Diploma report.," *Diploma report. Lund Institute of Technology*. Lund Institute of Technology, Lund, Sweden, 1991.

[84] D. D. Tjahjanto, O. Girlanda, and S. Östlund, "Anisotropic viscoelastic-viscoplastic continuum model for high-density cellulose-based materials," *J. Mech. Phys. Solids*, vol. 84, 2015.

[85] P. Mäkela and S. Östlund, "Orthotropic elastic–plastic material model for paper materials," *Int. J. Solids Struct.*, vol. 40, p. 5599, 2003.

[86] P. Verma, D. S. Chauhan, and P. Singh, "Effects on Tensile Strength of Transformer Insulation Paper under Accelerated Thermal and Electrical Stress," *Annu. Rep. Conf. Electr. Insul. Dielectr. Phenom.*, p. 619, 2007.

[87] H. T. Banks, S. Hu, and Z. R. Kenz, "A Brief Review of Elasticity and Viscoelasticity for Solids," *Adv. Appl. Math. Mech.*, vol. 3, no. 1, 2011.

[88] B. Miled, I. Doghri, and L. Delannay, "Coupled viscoelastic–viscoplastic modeling of homogeneous and isotropic polymers: Numerical algorithm and analytical solutions," *Comput. Methods Appl. Mech. Eng.*, vol. 200, p. 3381, 2011.

[89] J. Tryding, "In-plane fracture of paper," Lund University, 1996.

[90] R. C. Neagu, E. K. Gamstedt, and M. Lindström, "Characterization methods for elastic

properties of wood fibers from mats for composite materials," *Wood Fiber Sci.*, vol. 38, no. 1, p. 95, 2006.

[91] J. Alfthan, "Experimental study of non-linear stress relaxation and creep of paper materials and the relation between the two types of experiments," *Nord. Pulp Pap. Res. J.*, vol. 25, no. 3, p. 351, 2010.

[92] D. Geissler and T. Leibfried, "Mechanical breakdown of aged insulating paper around continuously transposed conductors for power transformers under the influence of short-circuit forces - Analysis by numerical simulations," *Electr. Insul. Conf.*, pp. 401–406, 2015.

[93] N. Stenberg and C. Fellers, "The out-of-plane Poissons ratios of paper and paperboard," *Nord. Pulp Pap. Res. J.*, vol. 17, no. 4, p. 387, 2003.

[94] N. Stenberg, C. Fellers, and S. Östlund, "Plasticity in the thickness direction of paperboard under combined shear and normal loading," *J. Eng. Mater. Technol.*, vol. 123, no. 2, p. 184, 2001.

[95] N. Stenberg, C. Fellers, and S. Östlund, "Measuring the stress–strain properties of paperboard in the thickness direction," *J. Pulp Pap. Sci.*, vol. 27, no. 6, p. 213, 2001.

[96] M. Nygårds, "Modelling the out-of-plane behaviour of paperboard," *Nord. Pulp Pap. Res. J.*, vol. 24, no. 1, p. 72, 2009.

[97] O. Girlanda, D. D. Tjahjanto, S. Östlund, K. Wei, and L. E. Schmidt, "Characterization and Modelling of the Mechanical Properties of Pressboard," *Annu. Rep. Conf. Electr. Insul. Dielectr. Phenom.*, p. 563, 2013.

[98] O. Girlanda, D. D. Tjahjanto, S. Östlund, A. Ask, J. Forslin, and L. E. Schmidt, "Modeling and experimental validation of the mechanical behavior of pressboard," in *2014 IEEE Electrical Insulation Conference (EIC)*, 2014.

[99] O. Girlanda, D. D. Tjahjanto, S. Östlund, and L. E. Schmidt, "On the transient out-of-plane behaviour of high-density cellulose-based fibre mats," *J. Mater. Sci.*, p. 8131, 2016.

[100] Q. S. Xia, M. C. Boyce, and D. M. Parks, "A constitutive model for the anisotropic elastic–plastic deformation of paper and paperboard," *Int. J. Solids Struct.*, vol. 39, p. 4053, 2002.

[101] A. Harrysson and M. Ristinmaa, "Large strain elasto-plastic model of paper and corrugated board," *Int. J. Solids Struct.*, vol. 45, p. 3334, 2008.

[102] E. Borgqvist, M. Lindström, J. Tryding, M. Wallin, and M. Ristinmaa, "Distortional hardening plasticity model for paperboard," *Int. J. Solids Struct.*, vol. 51, p. 2411, 2014.

[103] N. Stenberg, "A model for the through-thickness elastic-plastic behaviour of paper," *Int. J. Solids Struct.*, vol. 40, p. 7483, 2003.

[104] T. P. Nevell and S. H. Zeronian, *Cellulose chemistry and its applications*. UK: Ellis Horwood, 1985.

[105] J. J. Aklonis and W. J. MacKnight, *Introduction to Polymer Viscoelasticity*. New York: Wiley, 1983.

[106] M. Htun and C. Fellers, *The in-plane anisotropy of paper in relation to fiber orientation and drying restraints*. New York: Marcel Dekker, 1986.

[107] H. W. Haslach, "Time-dependent mechanisms in fracture of paper," *Mech. Time-Dependent Mater.*, vol. 13, pp. 11–35, 2009.

[108] F. J. Schmied, C. Teichert, L. Kappel, U. Hirn, W. Bauer, and R. Schennach, "What holds paper together: Nanometre scale exploration of bonding between paper fibres," *Sci. Rep.*,

vol. 3, no. 2432, 2013.

[109] M. Rigdahl and N. L. Salmén, "Dynamic mechanical properties of paper: Effect of density and drying restraints," *J. Mater. Sci.*, vol. 19, p. 2955, 1984.

[110] A. P. Karafillis and M. C. Boyce, "A general anisotropic yield criterion using bounds and a transformation weighting tensor," *J. Mech. Phys. Solids*, vol. 41, no. 12, p. 1859, 1993.

[111] P. Mäkela, "The effect of moisture ratio and drying restraint on the stress relaxation of paper," in *61st Appita Annual Conference and Exhibition*, 2007, pp. 169–177.

[112] K. Kurita, T. Kuriyama, K. Hiraishi, S. Kusumoto, S. Shida, and Y. Hori, "Mechanical strength of transformer windings under short-circuit conditions," *IEEE Trans. Power Appar. Syst.*, vol. 88, no. 3, pp. 222–230, 1969.

[113] H. Kojima, H. Miyata, S. Shida, and K. Okuyama, "Buckling strength analysis of large power transformer windings subjected to electromagnetic force under short circuit," *IEEE Trans. Power Appar. Syst.*, vol. 99, no. 3, pp. 1288–1297, 1980.

[114] H. Zhang *et al.*, "Dynamic Deformation Analysis of Power Transformer Windings in Short-Circuit Fault by FEM," *IEEE Trans. Appl. Supercond.*, vol. 24, no. 3, 2014.

[115] D. Geissler and T. Leibfried, "Short-Circuit Strenght of Power Transformer Windings-Verification of Tests by a Finite Element Analysis-Based Model," *IEEE Trans. Power Deliv.*, vol. 32, no. 4, pp. 1705–1712, 2017.

[116] D. Geissler and T. Leibfried, "Short circuit tests to derive the buckling strength of Continuously Transposed Cable for power transformers under the influence of the paper insulation thickness," in *Power Engineering Conference (UPEC)*, 2014, vol. 32, no. 4.

[117] L. J. Gibson and M. F. Ashby, *Cellular Solids: Structure and Properties*. Cambridge Universtity Press, 1999.

[118] N. Stenberg and Q. S. Xia, "Communications between Stenberg and Xia." 2001.

[119] A. De Ruvo, L. Carlsson, and C. Fellers, "The bi-axial strength of paper," *Tappi*, vol. 63, no. 5, p. 133, 1980.

[120] S. W. Tsai and E. M. Wu, "A General Theory of Strength for Anisotropic Materials," *J. Compos. Mater.*, vol. 5, p. 58, 1971.

[121] O. Girlanda, "Experimental Study and Numerical Simulation of Delamination in Multiply Paperboard during Offset Printing," Karlstad University, 2006.

[122] W. J. McNutt, W. M. Johnson, R. A. Nelson, and R. E. Ayers, "Power transformer short-circuit strenght - requirements, design and demonstration," *IEEE Trans. Power Appar. Syst.*, vol. PAS-89, no. 8, pp. 1955–1969, 1970.

[123] M. R. Patel, "Dynamic reponse of power transformers under axial short-circuit forces," *IEEE Trans. Power Appar. Syst.*, vol. PAS-92, no. 5, pp. 1558–1576, 1973.

[124] B. Steenberg, "Behaviour of paper under stress and strain," *Pulp Pap. Mag. Canada*, vol. 50, p. 220, 1949.

[125] J. Goldschmidt and D. Wahren, "On the rupture mechanism of paper," *Sven. Papperstidning*, vol. 71, p. 477, 1968.

[126] D. H. Page, "A theory for the tensile strength of paper," *Tappi J.*, vol. 52, no. 4, pp. 674–681, 1969.

[127] O. J. Kallmes, *Theory and Design of Wood and Fiber Composite Materials*. Syracuse Wood Science Series, 1972.

[128] I. B. Sachs and T. A. Kuster, "Edgewise compression failure mechanism of linerboard observed in a dynamic mode," *Tappi J.*, vol. 63, no. 10, pp. 69–73, 1980.

[129] C. T. Sun, B. J. Quinn, J. Tao, D. W. Oplinger, and W. J. Hughes, "Comparative Evaluation of Failure Analysis Methods for Composite Laminates," Washington, D.C., 1996.

[130] V. D. Azzi and S. W. Tsai, "Anisotropic strength of composites," *Exp. Mech.*, vol. 5, no. 9, pp. 283–288, 1965.

[131] N. T. Mascia and R. A. Simoni, "Analysis of failure criteria applied to wood," *Eng. Fail. Anal.*, vol. 35, pp. 703–712, 2013.

[132] R. C. Neagu, E. K. Gamstedt, S. L. Bardage, and M. Lindström, "Ultrastructural features affecting mechanical properties of wood fibres," *Wood Mater. Sci. Eng.*, vol. 1, pp. 146–170, 2006.

[133] C. B. Norris, "Strength of orthotropic materials subjected to combined stresses," 1962.

[134] O. Hoffman, "The brittle strength of ortotropic materials," *J. Compos. Mater.*, vol. 1, pp. 200–206, 1967.

[135] J. Tryding, "A modification of the Tsai-Wu failure criterion for the biaxial strength of paper," *Tappi J.*, vol. 77, no. 8, pp. 132–134, 1994.

[136] "IEC 60814:1997. Insulating liquids - Oil-impregnated paper and pressboard - Determination of water by automatic coulometric Karl Fischer titration." IEC, 1997.

[137] "Paper and board. Determination of tensile properties. Part 2: Constant rate of elongation method (20 mm/min)." ISO 1924-2:2008, 2008.

[138] "Paper and board — Determination of compressive strength — Ring crush method." ISO 12192:2011, 2011.

[139] "An investigation of test methods for determining the edgewise compression strength of the components of combined board. Part II. Development of a modified ring compression test and its relationship to combined board strength. Compression Report 78.," 1963.

[140] H. Yoshihara and M. Yoshinobu, "Off-axis tensile strength and evaluation of the in-plane shear strength of paper," *Holzforsch. - Gruyter*, vol. 68, no. 5, pp. 583–590, 2014.

[141] V. C. Setterholm, R. Benson, and E. Q. Kuenzi, "Method for measuring edgewise shear properties of paper," *Tappi*, vol. 51, no. 5, pp. 196–202, 1968.

[142] N. Pan and X. Zhang, "Shear Strength of Fibrous Sheets: An Experimental Investigation," *Text. Res. J.*, vol. 67, no. 8, pp. 593–600, 1997.

[143] T. Yokoyama and K. Nakai, "Evaluation of in-plane orthotropic elastic constants of paper and paperboard," 2007.

[144] H. Yoshihara and M. Yoshinobu, "In-plane shear strength of paper measured by asymmetric four-point bending test," *Holzforsch. - Gruyter*, vol. 69, no. 1, pp. 41–46, 2015.

[145] H. Yoshihara and M. Yoshinobu, "Evaluation of the in-plane shear strength of paper measured by tensile-loaded shear test," *Nord. Pulp Pap. Res. J.*, vol. 32, no. 1, pp. 126–131, 2017.

[146] C. Oria, A. Ortiz, I. Fernández, I. Carrascal, and D. Ferreño, "Mechanical Behaviour of the Cellulosic Dielectric Materials of Windings in Power Transformers in Operation," in *2018 XIII International Conference on Electrical Machines (ICEM)*, 2018, pp. 2400–2406.

[147] D. H. Johnson, "Principles of Simulating Contact Between Parts using ANSYS." Erie, Pennsylvania, 2012.

[148] "ANSYS Meshing User's Guide." ANSYS, Inc., Canonsburg, Pennsylvania, 2017.

[149] "ANSYS Mechanical APDL Contact Technology Guide." ANSYS, Inc., Canonsburg, Pennsylvania, 2017.

[150] R. Afshar, N. P. Van Dijk, I. Bjurhager, and E. K. Gamstedt, "Comparison of experimental testing and finite element modelling of a replica of a section of the Vasa warship to identify the behaviour of structural joints," *Eng. Struct.*, vol. 147, pp. 62–76, 2017.

[151] D. Roylance, "Transformation of Stresses and Strains," Cambridge, 2001.

APPENDIX: SCIENTIFIC CONTRIBUTIONS

1. Publications related to this PhD thesis

- "State-of-the-art review on the performance of cellulosic dielectric materials in power transformers: Mechanical response and ageing". C. Oria, A. Ortiz, D. Ferreño, I. Carrascal, and I. Fernández. IEEE Transactions on Dielectrics and Electrical Insulation, vol. 26, no. 3, pp. 939–954, 2019.

- "Experimental and numerical analysis of the failure of the cellulosic insulation of continuously transposed conductors under the effects of short circuits and thermal ageing in power transformers". C. Oria; I. Carrascal; A. Ortiz; I. Fernández; D. Ferreño; R. Afshar; K. Gamstedt. IEEE Transactions on Dielectrics and Electrical Insulation, vol. 27, no. 1, pp. 325–333, 2020.

2. Contributions to international conferences related to this PhD thesis

- "Mechanical behaviour of the cellulosic dielectric materials of windings in power transformers in operation". C. Oria, A. Ortiz, I. Fernández, I. Carrascal, and D. Ferreño. 2018 XIII International Conference on Electrical Machines (ICEM), 2018, pp. 2400–2406. Alexandroupoli, Greece.

3. Research stays related to this PhD thesis

- Uppsala University. Department of Materials Science and Engineering, Applied Mechanics, in Ångströmlaboratoriet, under the supervision of Professor Kristofer Gamstedt. From August 15 to September 30, 2018.

- Uppsala University. Department of Materials Science and Engineering, Applied Mechanics, in Ångströmlaboratoriet, under the supervision of Professor Kristofer Gamstedt. From August 4 to September 16, 2019.

4. Research projects

- Análisis de procesos de impregnación de materiales celulósicos y de generación de gases en fluidos dieléctricos de origen vegetal y mineral. Grupo de Investigación en Transformadores Eléctricos de Potencia (GITEP). Departamento de Ingeniería Eléctrica y Energética. Responsable: Alfredo Ortiz Fernández. Año 2017.

- Análisis comparativo del rendimiento de aceites biodegradables frente a aceites de origen mineral. Grupo de Investigación en Transformadores Eléctricos de Potencia (GITEP). Departamento de Ingeniería Eléctrica y Energética. Responsable: Alfredo Ortiz Fernández. Años 2018-2019.

APÉNDICE: RESUMEN, RESULTADOS Y DISCUSIÓN

1. Planteamiento del problema

A pesar de que se acepta de forma generalizada que el estado de los materiales dieléctricos sólidos (papel y cartón) utilizados en transformadores de potencia es uno de los factores que tiene un mayor impacto en su esperanza de vida, no se sabe con precisión cómo influyen en su desempeño los procesos de envejecimiento o las tensiones mecánicas derivados de la operación en condiciones normales, o debidos a la ocurrencia de fallos eléctricos. Las altas temperaturas y las reacciones químicas que tienen lugar en el aceite dieléctrico degradan las propiedades mecánicas y dieléctricas del aislamiento celulósico. Las fuerzas electromagnéticas que actúan sobre un transformador de potencia pueden producir la fractura del aislamiento celulósico cuando está envejecido, siendo éste un fenómeno mecánico, que a su vez puede ser el causante de un fallo eléctrico si este material deja de cumplir su propósito dieléctrico.

Si se asume que la integridad mecánica del aislamiento celulósico es uno de los factores que afecta a la confiabilidad de los transformadores de potencia, pues guarda relación con las propiedades dieléctricas, un modelo de fallo mecánico para el aislamiento de papel podría ser una herramienta útil que contribuyese en el diagnóstico indirecto del estado de un transformador, que puede emplearse en combinación con otros métodos existentes (véase *1.2.1.Methods for the estimation of the condition of power transformers* en el apartado *II.STATE OF THE ART*). Sin embargo, antes de la realización el presente trabajo de investigación, no se tenía constancia de que existiese ningún estudio publicado que tuviese en cuenta todos los factores más importantes que influirían en ese modelo de fallo mecánico (las propiedades del material dieléctrico bajo diferentes solicitaciones mecánicas, diferentes estados de envejecimiento del papel y la influencia de un líquido dieléctrico en particular, el impacto de grandes deformaciones que podrían generarse debido a la ocurrencia de un cortocircuito, la geometría real de los conductores con su aislamiento, etc.).

2. Estrategia de investigación

En esta tesis doctoral, se analiza la respuesta mecánica de un conductor continuamente transpuesto fabricado y cedido por la empresa Imefy, cuyo aislamiento consta de cuatro capas de papel dieléctrico (las dos capas interiores están hechas de papel dieléctrico tipo Kraft normal, y las capas dos exteriores de papel dieléctrico tipo crepe), desde una triple perspectiva: experimental, numérica y analítica.

En la parte experimental del estudio, se extrajeron probetas de una bobina de un transformador de potencia, fabricada con el conductor continuamente transpuesto previamente mencionado, con su aislamiento de papel. Estas probetas se introdujeron en vasijas llenas de aceite dieléctrico nafténico y fueron envejecidas isotérmicamente en hornos a 150°C durante cuatro periodos de envejecimiento diferentes (véase *1.1.Accelerated thermal ageing of the paper insulation* en el apartado *III.MATERIALS, METHODS AND RESULTS*). El grado de envejecimiento del aislamiento (papeles Kraft normal y crepe) se cuantificó mediante el grado de polimerización (véase *1.2.1.Degree of Polymerisation (DP) of the dielectric paper*). Posteriormente, las propiedades mecánicas del papel se obtuvieron mediante ensayos de tracción y compresión (descritos en los apartados *1.2.2.Tensile mechanical properties of the dielectric paper in the MD and in the CD* y *1.2.3.Edgewise mechanical compressive properties of the dielectric paper*), y las propiedades mecánicas bajo una solicitación de esfuerzo cortante fueron estimadas de forma indirecta a partir de las propiedades de tracción, como se sugiere en [140] (véase *1.2.4.In-plane shear mechanical*

properties of the dielectric paper). Por otro lado, probetas del conductor con su aislamiento celulósico, una vez envejecidas, fueron sometidas a ensayos de flexión a tres puntos cuyo objetivo era reproducir las deformaciones que podrían haber sido ocasionadas por un cortocircuito que actuase sobre los devanados de un transformador de potencia (véase *1.3.Three-point bending tests of the insulated CTCs*). Las fracturas que se produjeron en el papel como resultado de estos ensayos se analizaron macroscópicamente y microscópicamente.

En el análisis numérico, se simuló el ensayo de flexión sobre la probeta de conductor utilizando *ANSYS AIM Static Structural*. Esta simulación permitió estimar las deformaciones que sufre el aislamiento de papel dieléctrico, que a su vez serán necesarias como input en un modelo de fallo mecánico que pueda aplicarse a ese aislamiento. En lo que respecta al estudio analítico, los modelos de fallo mecánico existentes que pueden aplicarse a una lámina han sido revisados y clasificados (véase *5.4.3.Different criteria for the failure of paper materials* en el apartado *II.STATE OF THE ART*) y dos de ellos han sido adaptados a los materiales dieléctricos celulósicos estudiados en esta tesis (véase *3.Failure criteria for the paper insulation of the CTC* en el apartado *III.MATERIALS, METHODS AND RESULTS*). El análisis experimental ha proporcionado los parámetros del material necesarios para calibrar los modelos de fallo; mientras que el análisis numérico ha proporcionado las deformaciones en cada uno de los nodos de la geometría en la simulación, que también eran necesarios para poder evaluar cada criterio analítico de fallo en cada uno de esos nodos.

3. Contribuciones derivadas de la investigación experimental

3.1. Envejecimiento térmico del papel dieléctrico

Se ha medido el grado de polimerización (DP) para los aislamientos celulósicos tipo Kraft y crepe, que es un indicador ampliamente utilizado, para cuantificar el nivel de deterioro de las propiedades dieléctricas del papel en cada uno de los niveles de envejecimiento considerados. El fallo mecánico del aislamiento ha sido estudiado para diferentes valores del DP, desde aquellos considerados como "buenos" en [55] (DP entre 650 y 1000), hasta los catalogados como "envejecidos" (DP inferior a 350). Esto quiere decir que el presente estudio pretende cubrir el análisis de la respuesta mecánica del aislamiento celulósico durante toda su vida útil. Los resultados experimentales han demostrado que la posición del papel en cada una de las capas del aislamiento no tuvo ningún impacto en su envejecimiento, excepto en el caso de la capa 1. Esta capa estaba en contacto directo con el conductor transpuesto de cobre y su nivel de deterioro fue artificialmente incrementado por la elevada temperatura elegida para el proceso de envejecimiento, de 150ºC, que derritió el esmalte aislante del conductor, pegando la primera capa del aislamiento al cobre. El motivo de elegir una temperatura tan elevada era que se quería lograr un estado de envejecimiento en las otras capas del aislamiento equivalente a toda una vida útil de operación de un transformador de potencia real, en un periodo de envejecimiento acelerado razonable (véase *1.1.Accelerated thermal ageing of the paper insulation* en el apartado *III.MATERIALS, METHODS AND RESULTS*).

La medida del DP permite comparar los resultados experimentales obtenidos en la presente tesis con otros muchos estudios disponibles en la bibliografía que presentan valores del grado de polimerización del papel medidos en el aislamiento de transformadores de potencia reales tras varios años de operación. Puede considerarse que, cuando el DP de un papel dieléctrico tipo Kraft (o crepe) utilizado en un transformador de potencia está alrededor de un determinado valor, su desempeño mecánico será parecido al que tiene el material analizado en el presente estudio que presente un DP similar. Aunque la medida del DP es un método destructivo, pues requiere muestras del papel dieléctrico del aislamiento

analizado, que no siempre pueden extraerse, ya que pueden ser la causa de un fallo local en un transformador en operación, existen muchos métodos no destructivos en la literatura que miden otros parámetros que pueden relacionase directamente con el DP y ser medidos en transformadores en operación (por ejemplo, [33], [59], [60], [62], [63]).

3.2. Ensayos mecánicos a tracción, compresión y cortante sobre el aislamiento celulósico

Se han realizado ensayos de tracción uniaxial en MD y CD sobre muestras del aislamiento celulósico tipo Kraft y tipo crepe en los distintos estados de envejecimiento considerados, siguiendo el proceso descrito en [137], véase *1.2.2.Tensile mechanical properties of the dielectric paper in the MD and in the CD*. Se obtuvieron los valores promedio y las desviaciones estándar de la deformación en rotura a tracción, $\varepsilon_{MD,t}^{max}$ y $\varepsilon_{CD,t}^{max}$, que fueron posteriormente introducidos en el criterio de fallo. Las diferencias en las respuestas a tracción en MD para los papeles Kraft y crepe son muy notables. La deformación máxima en rotura en MD, $\varepsilon_{MD,t}^{max}$, es muy superior para el aislamiento tipo crepe (unas 6,8 veces superior cuando los materiales no habían sido envejecidos, y casi 2,8 veces superior en el estado de envejecimiento IV). Debido a la geometría del aislamiento del conductor continuamente transpuesto, en la que la dirección MD coincide con el eje longitudinal de las tiras de papel dieléctrico, y la dirección CD es la transversal, en la cual la anchura del papel es de solo unos 20 mm, el fallo del material a tracción en MD y CD está gobernado por mecanismos diferentes. El fallo a tracción en MD es frágil, mientras que el fenómeno de rotura a tracción en CD es progresivo, y se asemeja al mecanismo de desgarro dúctil en materiales metálicos. El aspecto de las curvas de tensión-deformación en CD para el papel Kraft ordinario y para el papel crepe no difiere notablemente. Los valores de la deformación máxima en rotura en CD, $\varepsilon_{CD,t}^{max}$, son aproximadamente 1,4 veces superiores para el aislamiento tipo crepe cuando el material no está envejecido, y 1,1 veces superiores en el estado de envejecimiento IV. Para el aislamiento tipo crepe, queda claro que la dirección CD va a ser la dirección preferente para la propagación de las grietas cuando el material está sometido a tracción, ya que, tanto la deformación máxima como la tensión máxima en rotura son inferiores en CD.

En el presente estudio, se ha presentado un método experimental inspirado en [139] para la estimación de las propiedades mecánicas del aislamiento celulósico a compresión, que emplea muestras cilíndricas formada por dos capas concéntricas de aislamiento (veáse *1.2.3.Edgewise mechanical compressive properties of the dielectric paper*). Los mecanismos de fallo observados fueron abolladura local y formación de arrugas en los cilindros, que fueron la causa de la reducción en la resistencia mecánica que puede apreciarse en las curvas de tensión-deformación a compresión. Los ensayos de compresión muestran que la capacidad del aislamiento celulósico de deformarse a compresión se mantenía tras haber alcanzado la tensión máxima de compresión, y el material seguía mostrando una resistencia a esfuerzos de compresión considerable. Como el mecanismo de fallo a compresión de este material no es un fenómeno instantáneo, se decidió seleccionar un valor conservativo como deformación última del material a compresión, ε_c^{max}, que se definió como la deformación correspondiente al 50% de la tensión pico de compresión, $0{,}5 \cdot \sigma_c^{max}$, tras haber superado esa tensión pico. Los ensayos muestran una gran variabilidad, de aproximadamente el 27,8%, en los valores de $\varepsilon(0{,}5 \cdot \sigma_c^{max})$ obtenidos de las curvas de tensión-deformación para un mismo papel en una orientación (MD o CD) y estado de envejecimiento determinados. Los valores promedio de la deformación última a compresión estimada, ε_c^{max}, fueron ligeramente superiores para el papel crepe que para el papel Kraft en todos los diferentes estados de envejecimiento, y la influencia de éste fue menos relevante en este caso que con las propiedades a tracción. En contraposición con lo que ocurrió en el caso de la deformación en rotura a tracción, la

diferencia entre la ε_c^{max} estimada en MD y CD no queda clara tras los ensayos a compresión, por lo que se considera que no está justificado introducir valores diferentes para las propiedades a compresión en las dos direcciones principales del material en el modelo de fallo. Se considera que la deformación última a compresión sigue una variación aproximadamente lineal durante toda la duración del envejecimiento, y los valores que se introducen en el modelo de fallo han sido obtenidos mediante esta interpolación lineal a partir de todos los resultados de los ensayos a compresión.

Las propiedades del material a cortante se han estimado experimentalmente a partir de ensayos a tracción en muestras de papel dieléctrico cuya dirección longitudinal coincide con un ángulo de 35º con respecto a la dirección MD, como sugiere [140], para los distintos tipos de papel dieléctrico, considerando que la deformación en rotura a 35º coincide con la deformación tangencial en rotura, $\varepsilon_{35^o}^{\max} \simeq \varepsilon_{\mathrm{MD-CD}}^{\max}$, veáse *1.2.4.In-plane shear mechanical properties of the dielectric paper*. Para ambos tipos de papel, se produjo rotura frágil en los ensayos de tracción a 35º de MD, pero la deformación máxima en rotura fue más de 5 veces superior para el aislamiento tipo crepe cuando el material no había sido envejecido, y este factor se redujo hasta aproximadamente 1,4 veces en el estado de envejecimiento III. En este caso, también ocurre que, aunque las propiedades mecánicas iniciales del papel tipo crepe son mejores, éste se ve más afectado por el proceso de envejecimiento que el papel tipo Kraft común.

3.3. Ensayos de flexión a tres puntos sobre las muestras de conductor continuamente transpuesto con aislamiento de papel y análisis de las fracturas generadas

Los ensayos de flexión a tres puntos tratan de representar las deformaciones que produciría la componente radial de una fuerza de cortocircuito sobre las probetas de conductor con el aislamiento de papel, cuando las flechas finales son de 5, 10 y 20 mm, véase *1.3.Three-point bending tests of the insulated CTCs*. Las curvas fuerza - flecha muestran que el conductor presenta una mayor rigidez cuando ha sido envejecido, lo cual se debe a la unión entre las láminas de cobre contiguas que se produce debido al envejecimiento a alta temperatura, que funde el esmalte aislante que recubre las láminas de cobre. Sin embargo, según va aumentando la deformación, esa unión se va rompiendo entre algunas de las láminas adyacentes, produciendo reducciones súbitas en la fuerza de flexión que son apreciables en las curvas de los ensayos de flexión a tres puntos.

En todos los casos, el fallo del papel dieléctrico comienza en la capa 1, porque ésta ha quedado pegada al núcleo de cobre debido al envejecimiento acelerado y, por eso, sufre las mayores deformaciones, mientras que, en las capas de aislamiento exteriores el deslizamiento es posible hasta cierto grado. Algunas de las causas más comunes para la formación de las primeras grietas tras los ensayos a flexión son: la presencia del conductor transpuesto, que sufre unas deformaciones superiores que el resto del conductor, en el que la unión entre las láminas de cobre que conforman su sección hace que trabaje solidariamente hasta que esta unión se rompe; y, también, el arrollamiento del papel dieléctrico alrededor del conductor continuamente transpuesto. En zonas de las probetas del conductor que se ven sometidas a deformaciones de tracción debido a los ensayos de flexión, el mecanismo de fallo observado es la generación de grietas, de forma similar al tipo de fallo observado en los ensayos a tracción. Sin embargo, cuando el papel está profundamente envejecido, las zonas del conductor en las que aparecen deformaciones de compresión son más críticas para la aparición y propagación de grietas. Cuando la deformación de las probetas del conductor no es muy elevada, los primeros defectos que aparecen en zonas sometidas a compresión son arrugas y abolladuras locales en el aislamiento dieléctrico, muy similares a las que se han

observado tras la caracterización experimental del papel a compresión. Cuando la deformación del conductor aumenta, el papel dieléctrico no puede continuar abollándose, pues está fuertemente enrollado alrededor del cobre, y el modo de fallo cambia, siendo este el origen de las grietas que se observan en zonas del conductor sometidas a compresión. Otra de las conclusiones obtenidas tras los ensayos de flexión a tres puntos, es que la temperatura y duración del envejecimiento térmico necesarios para que las grietas del papel dieléctrico crezcan hasta llegar al punto de producir el final de la vida útil del aislamiento son muy elevadas. El aislamiento tipo crepe tiene una respuesta al envejecimiento y a las grandes deformaciones mucho mejor que la del aislamiento tipo Kraft. Sin embargo, si el envejecimiento se prolonga hasta llegar a ser extremo, las propiedades del aislamiento tipo crepe al final del proceso son similares que las del papel Kraft.

Las grietas que se producen para cada nivel de deformación y profundidad del envejecimiento térmico han sido analizadas macroscópicamente y clasificadas en: grietas pequeñas (< 5 mm), de tamaño mediano (5-10 mm), grietas grandes (> 10 mm) y fractura total. En las probetas de cobre no envejecidas, el aislamiento dieléctrico no sufrió rotura para ninguno de los niveles de deformación considerados, lo cual ilustra las buenas propiedades mecánicas del papel tras la manufactura del conductor transpuesto. Sin embargo, la influencia del envejecimiento térmico fue muy notable, especialmente en el caso del papel Kraft, que sufrió fractura total para una flecha de 20 mm en el estado de envejecimiento II. La respuesta del aislamiento tipo crepe fue considerablemente mejor, ya que fueron necesarios un profundo estado de envejecimiento (cerca de 7 meses a 150°C) y una flecha sobre la probeta del conductor de 20 mm para producir grietas grandes en este material dieléctrico. Los mecanismos de fallo fueron analizados también microscópicamente, utilizando un microscopio electrónico de barrido, véase *1.4.Analysis of the microstructure and fracture patterns in the paper insulation with Scanning Electron Microscope*, llegándose a la conclusión de que de que la formación y el crecimiento de las grietas en el aislamiento dieléctrico son mayoritariamente fenómenos locales. Las grietas se producen en los puntos en los que se rompen las fibras de celulosa en las áreas sometidas a esfuerzos de tracción, o como consecuencia de la formación de arrugas y abolladuras en las áreas sometidas a esfuerzos de compresión. Por el contrario, en las zonas que están cerca de un defecto local, pero fuera del área afectada, tanto la matriz como las fibras que conforman la estructura microscópica del papel se mantienen en buenas condiciones, incluso cuando el material ha sido sometido a un intenso envejecimiento térmico.

4. Contribuciones derivadas del análisis numérico mediante elementos finitos

El conductor continuamente transpuesto de cobre estudiado, sometido a un ensayo de flexión, ha sido modelado mediante *ANSYS AIM Static Structural*, véase *2.Numerical simulation* in *III.MATERIALS, METHODS AND RESULTS*. Uno de los aspectos más complejos en lo que respecta a la simulación numérica fue conseguir un modelado apropiado de los contactos entre las láminas de cobre adyacentes, cuyo comportamiento fuese similar al observado experimentalmente durante el ensayo de flexión, y la definición de un mallado adecuado que hiciese posible la obtención de resultados con suficiente calidad y mejorase la convergencia del modelo. Fue esencial representar adecuadamente en la simulación el deslizamiento entre las láminas de cobre adyacentes que se producía al ir aumentando la deformación sobre el conductor, para aproximarse a la curva fuerza-flecha promedio obtenida a partir de los ensayos de flexión experimentales. Ese deslizamiento se introdujo en el modelo mediante un coeficiente de fricción variable en los diferentes *steps* del proceso de carga. Se considera que, a pesar de las aproximaciones y simplificaciones consideradas en el modelo numérico, la respuesta obtenida de la simulación consigue aproximarse de forma

aceptablemente buena a la respuesta obtenida de los ensayos de laboratorio. El modelo numérico permitió calcular las deformaciones (ε_{MD}, ε_{CD} y γ_{MD-CD}) en las superficies exteriores del conductor de cobre continuamente transpuesto, en las zonas en las que está enrollado el papel dieléctrico.

En todas las simulaciones numéricas con flechas finales comprendidas entre 5 y 20 mm, las deformaciones en dirección CD y tangencial (ε_{CD} y γ_{MD-CD}) fueron considerablemente superiores que la deformación en MD (ε_{MD}). Además, las deformaciones de compresión parecen ser más críticas para el inicio del fallo mecánico que las deformaciones de tracción, lo que coincide con las observaciones experimentales tras los ensayos de flexión. Las deformaciones en las caras superiores de la probeta del conductor son superiores en CD que en MD, y casi toda la superficie está sometida a compresión en CD. Las distorsiones tangenciales, γ_{MD-CD}, son de un orden de magnitud similar a las deformaciones en CD, ε_{CD}, con valores máximos alrededor de -10 % cuando la flecha en la probeta es de 20 mm. En las caras inferiores del conductor, las deformaciones en CD son también superiores que las deformaciones en MD, y prácticamente toda el área de las caras inferiores está sometida a deformaciones de tracción, con valores máximos de $\varepsilon_{CD} \simeq$ 2-5%. El valor de γ_{MD-CD} en el área central de las caras inferiores es similar. En las caras laterales, se espera que el mecanismo de fallo mecánico esté gobernado por las deformaciones tangenciales, ya que éstas son considerablemente superiores que las deformaciones en MD o CD. Las deformaciones de tracción solo son críticas para la aparición de grietas cuando la flecha de la probeta de cobre obtenida en los ensayos a flexión alcanza los 20 mm.

Los resultados anteriores destacan la necesidad de caracterizar las propiedades mecánicas del papel dieléctrico sometido a esfuerzos de compresión y de corte, lo que es algo bastante novedoso, ya que no se ha encontrado ninguna referencia en la literatura que se ocupe de esta caracterización en el caso de papel dieléctrico, o cualquier otro tipo de papel de pequeño espesor. Las referencias clásicas que estudian las propiedades mecánicas del papel dieléctrico en transformadores de potencia solo tienen en cuenta la tensión de rotura y la máxima deformación en rotura a tracción, pero este análisis demuestra que otras tensiones y deformaciones pueden tener una contribución más crítica en el fallo mecánico del material.

5. Contribuciones derivadas del estudio analítico

Hay muchos modelos en la literatura que tratan de predecir el fallo mecánico de una lámina en un estado tensional complejo, aunque no son específicos para el papel, sino que pueden aplicarse a diferentes tipos de polímeros o materiales compuestos, es esperable que los mecanismos de fallo sean similares en ambos casos. Estos criterios para el fallo mecánico vienen tradicionalmente expresados en términos de tensiones. Sin embargo, no es una tarea trivial introducir las delgadas capas de papel, con espesores de 80-82 µm, en la geometría de la simulación numérica, ya que, cada una de las láminas que constituyen el conductor de cobre es aproximadamente 24 veces más gruesa que una capa de papel dieléctrico. El tamaño de los elementos requeridos en un mallado, si se hubiese introducido el papel dieléctrico en el modelo, habría sido muy pequeño, requiriendo un número inmanejable de elementos y un enorme tiempo necesario para el proceso de cálculo. Incluso aunque lo anterior hubiese sido factible, habría sido necesario realizar varias simulaciones con diferentes propiedades de los materiales, una para cada material dieléctrico y estado de envejecimiento considerados en el análisis. Consecuentemente, en el presente estudio, el papel dieléctrico no se incluyó en el modelo numérico y se obtuvo el campo de deformaciones en las caras externas del conductor de cobre. Estas deformaciones van a ser mayores o iguales que las que sufre el aislamiento enrollado, ya que éste tiene una cierta capacidad de deslizarse alrededor del conductor de

cobre. Esto significa que el modelo de fallo obtenido, que debe estar expresado en términos de deformaciones, será conservativo en cualquier caso.

Se han aplicado dos criterios de fallo al papel dieléctrico analizado en el presente estudio: un criterio límite, el criterio de máxima deformación; y un criterio interactivo, que es una modificación del criterio de Norris, véase *3.Failure criteria for the paper insulation of the CTC* en el apartado *III.MATERIALS, METHODS AND RESULTS*. En el primer caso, las deformaciones obtenidas en cada una de las caras exteriores de la probeta de conductor de cobre (ε_{MD}, ε_{CD} y γ_{MD-CD}) fueron comparadas con las deformaciones últimas en rotura obtenidas de la caracterización mecánica, y las áreas del conductor en las que estos valores son superados fueron representadas gráficamente mediante *ANSYS AIM Static Structural*. Las predicciones obtenidas mediante este criterio están en línea con las observaciones experimentales, excepto para el caso de los ensayos de flexión con flecha máxima de 20 mm, en los que las áreas en las que se predice la ocurrencia de fallo son más pequeñas que las áreas en las que, efectivamente, se produce el fallo tras los ensayos experimentales.

La modificación del criterio de fallo de Norris ha sido más compleja, pues fueron necesarias diferentes expresiones analíticas que considerasen las interacciones entre deformaciones en los diferentes cuadrantes del plano de deformaciones. En cada uno de los nodos de la geometría del modelo numérico, se han introducido las ecuaciones del criterio de Norris, una vez que los valores de deformaciones (ε_{MD}, ε_{CD} y γ_{MD-CD}) eran conocidos, mediante funciones condicionales, implementadas en Excel. Los resultados del criterio de fallo en cada uno de los nodos de la geometría se han representado gráficamente en ANSYS. Las predicciones del criterio de fallo de Norris modificado coinciden con las observaciones experimentales, hasta una flecha de 10 mm producida por los ensayos de flexión en la probeta de cobre, y son conservativas en todos los casos. En algunos casos, el área en el que se espera que se produzca el fallo del material es ligeramente más grande que el área en el que realmente se produjo el fallo experimental, especialmente cuando la flecha final es de 20 mm.

6. Contribuciones de este trabajo para el diagnóstico de transformadores de potencia en operación

Consideramos que esta tesis doctoral aporta una metodología sólida e información experimental muy valiosa para el análisis del estado de los transformadores de potencia en operación. El criterio de fallo propuesto para papel dieléctrico tipo Kraft y crepe, en diferentes estados de envejecimiento y sometidos a diferentes niveles de deformación del conductor en el que trabajan como aislantes, es una contribución innovadora que podría servir para mejorar la comprensión de los procesos que desembocan en el fallo mecánico del aislamiento de un transformador de potencia. Las características principales del conductor continuamente transpuesto modelado en la simulación numérica en el presente estudio (como, por ejemplo, la definición de los contactos entre las diferentes láminas de cobre que lo conforman) son comunes para otros tipos de conductores que se utilizan en transformadores de potencia y que pueden tener otras geometrías. La magnitud y el tipo de carga mecánica aplicada al conductor pueden variarse, y obtener así distintas distribuciones de deformaciones para un amplio número de situaciones que podrían producirse en un transformador de potencia en operación. En consecuencia, el enfoque mediante el modelo de elementos finitos que se ha seguido en este estudio podría extenderse y aplicarse con diferentes condiciones de contorno. Además, el criterio de fallo podría calibrarse con las propiedades de otros materiales, para predecir el fallo mecánico de cualquier tipo de papel dieléctrico.

Con respecto a la respuesta mecánica del papel dieléctrico, una de las conclusiones que se derivan de este estudio es que el comportamiento del aislamiento celulósico a tracción no es el único factor relevante. Las respuestas mecánicas del material a compresión y corte son también importantes, lo cual tiene implicaciones para los fabricantes de papel dieléctrico para transformadores de potencia. Son necesarios métodos más precisos para la cuantificación de la resistencia al corte del papel que la estimación empleada en este estudio. Hemos comprobado experimentalmente que las deformaciones tangenciales sufridas por el aislamiento celulósico son relevantes para el fallo mecánico, y el valor de éstas depende del ángulo elegido para el arrollamiento del papel dieléctrico alrededor del conductor de cobre en el proceso de manufactura. Este problema es una puerta abierta para líneas de investigación futuras.

Todas las herramientas desarrolladas y validadas en esta tesis doctoral pueden ser adaptadas y empleadas por los fabricantes, con el objetivo de mejorar las características constructivas en los conductores continuamente transpuestos que se utilizan en los devanados de los transformadores de potencia. En concreto, es posible desarrollar modelos predictivos que permitan estimar la vida útil de los transformadores de potencia de acuerdo con el material dieléctrico utilizado y las condiciones de operación. Esto puede ser útil para mejorar las técnicas que se emplean en la actualidad para la gestión de los transformadores de potencia en el sistema eléctrico.